Boletim da Sociedade Astronômica Brasileira

Vol. 30
2018

ISSN 0101-3440

Boletim da Sociedade Astronômica Brasileira

Objetivos

A Sociedade Astronômica Brasileira (SAB) é uma entidade científica sem fins lucrativos, fundada em 1974, cujas finalidades são:

- Congregar os astrônomos do Brasil;
- Zelar pela liberdade de ensino e pesquisa;
- Zelar pelos interesses e direitos dos astrônomos;
- Zelar pelo prestígio da ciência do País;
- Estimular as pesquisas e o ensino de Astronomia no País;
- Manter contato com institutos e sociedades correlatas no País e no exterior;
- Promover reuniões científicas, congressos especializados, cursos e conferências;
- Editar um boletim informativo sobre as atividades da SAB e assuntos gerais relacionados com a Astronomia.

Política Editorial

O Boletim da Sociedade Astronômica Brasileira (ISSN 0101-3440) é o periódico oficial da SAB e visa registrar a memória de atuação profissional da Sociedade Astronômica Brasileira e da pesquisa em Astronomia no país, publicando o seguinte conteúdo:

- Artigos científicos em Astronomia, seja em português ou inglês.
- Artigos de revisão, em português
- Revisão de conferências, colóquios e eventos científicos
- Resenhas de livros sobre Astronomia
- Artigos de opinião sobre política científica em Astronomia
- Artigos sobre História da Astronomia no Brasil
- Artigos técnicos, em português, sobre instrumentos de uso da comunidade
- Relatórios institucionais
- Resumos de teses e dissertações
- Notas de pesquisa ou comentários sobre outros artigos em Astronomia.
- Resumos da Reunião Anual da SAB

Os artigos de revisão poderão ser submetidos por membros ou solicitados a membros pela Comissão Editorial.

Relatórios institucionais podem ser opcionalmente enviados à Comissão Editorial, para publicação no Boletim pelo chefe de departamento ou responsável pela instituição.

Todos os artigos deverão ser aprovados por relatores ad hoc indicados pela Comissão Editorial.

Editorial

O Boletim da SAB (BSAB) é um periódico quase tão antigo quanto a própria Sociedade Astronômica Brasileira. Previsto como uma das atribuições da Diretoria da SAB em seu próprio regimento, o primeiro número foi publicado em 1977, tendo como editor o Dr. Roberto Vieira Martins. Durante seus primeiros vinte anos, teve importante papel como registro do amadurecimento da Astronomia Brasileira, contendo notícias, artigos de divulgação, relatos de importância histórica, propostas de normatização da terminologia astronômica, além de artigos de pesquisa. O tamanho da sociedade era pouco menos de 1/3 de seu tamanho atual, e boa parte de seus membros eram da geração de sócios fundadores ou alunos diretos destes. Houve muita colaboração para manter o BSAB ativo, o que permitiu a publicação de 4 ou 5 edições por ano, que eram enviadas por correio aos sócios quites. Uma dessas edições costumava ser inteiramente destinada aos resumos submetidos à Reunião Anual. A partir de fins dos anos 90, a frequência do BSAB começou a diminuir, chegando a apenas 1 ou 2 edições ao ano, na década seguinte. Eventualmente, vários fatores podem ter contribuído para isso, como a ascensão de uma nova geração de astrônomos mais distantes do evento de fundação da SAB, a maior internacionalização da sociedade, que passou a privilegiar a produção de textos exclusivamente em Inglês para as revistas de impacto, e a maior facilidade de acesso aos artigos científicos através da internet. Em 2008, a então Diretoria da SAB propôs a modernização do BSAB, tornando-o mais parecido com uma revista científica aos moldes do antigo *The Quarterly Journal of the Royal Astronomical Society*, um veículo para a publicação de artigos científicos, resenhas e de registro da memória da SAB, com um macro latex próprio. Todavia, os mesmos problemas que afetavam a frequência do BSAB nos anos anteriores continuaram, e o novo formato só teve uma única edição, de número 29, em 2008. Esperamos agora retomar esse percurso donde ele parou. O número 30 corresponde a uma edição especial, contendo trabalhos apresentados na XLI Reunião Anual da SAB, agora não apenas como resumo, mas sim como miniartigos. Esperamos que esse volume inaugure uma nova fase para o BSAB e para nossa sociedade.

A Diretoria

Maio de 2018

Instruções a autores

Manuscritos devem ser submetidos em formato eletrônico a qualquer um dos membros do corpo editorial:

Daniela B. Pavani
(dpavani@if.ufrgs.br)

Eliade Lima
(eliadeliu@gmail.com)

Leandro Kerber
(lokerber@uesc.br)

Helio J. Rocha-Pinto
(helio@astro.ufrj.br)

Manuscritos

Todos os manuscritos devem usar o macro latex sab.cls, disponível para download na página da SAB:
https://www.sab-astro.org.br/sab/publicacoes/instrucoes-aos-autores/

Recomenda-se que os autores baixem o macro e o arquivo de exemplo, usando-o como modelo para a redação de seu manuscrito.

A primeira página do manuscrito deve conter:

1. Título
2. Nome do(s) autor(es)
3. Afiliação institucional do(s) autor(es)
4. endereço eletrônico do(s) autor(es)
5. Quaisquer notas de rodapé com créditos a observatórios ou outras informações relevantes

Os manuscritos devem conter um resumo tanto em português, quanto em inglês.

Ilustrações

As ilustrações devem ser produzidas em formato eps, para permitir a inserção no documento latex. Toda ilustração deve ser acompanhada de legenda e ser referenciada no texto.

Tabelas

As tabelas devem conter título e legenda. Preferencialmente, as tabelas devem conter apenas delimitadores horizontais e separador horizontal entre os títulos das colunas. Não é recomendado usar separadores entre linhas da tabela ou entre colunas.

Material online

Material online deve ser mantido em links permanentes. Tabelas e outros dados devem ser sediados no CDS (http://cdsweb.u-strasbg.fr/), quando relevantes. Animações cujo conteúdo seja resultado do artigo submetido ao boletim devem ser submetidas conjuntamente com o manuscrito, devendo ser sediadas em link permanente no servidor da SAB.

Boletim da Sociedade Astronômica Brasileira, **30**, no. 1, 3-7

UEFS Professional Master Program in Astronomy

CAPES First Four-Year Achievements

V. A. Fernandes-Martin, M. G. Pereira, & P. C. Rocha-Poppe

[1] Universidade Estadual de Feira de Santana, Departamento de Física, Observatório Astronômico Antares
e-mail: vmartin@uefs.br, e-mail: mariIdogp@gmail.com, e-mail: paulopoppe@uefs.br

Abstract. Since 2000, the various actions developed by the Astronomy group of the Department of Physics of the State University of Feira de Santana (UEFS), aimed at the dissemination and popularization of science in schools, culminated in 2007 with the creation of the Specialization in Astronomy, and in 2013, with the creation of the Professional Master in Astronomy (MPAstro). From the first moment, the target audience is directed to teachers of basic education, as well as higher education with graduate education, preferably in the 6 areas of knowledge: Physics, Chemistry, Biology, Mathematics, History and Geography. After 4 years of operation and the graduation of 2 classes (18 students), we present here an extract of MPAstro from the point of view of the projects and educational products developed. The MPAstro explores both the interdisciplinary characteristics that Astronomy has, and the flexibility that it presents in questions related to university teaching, research and extension actions.

Resumo. Desde 2000, as várias ações desenvolvidas pelo grupo de Astronomia do Departamento de Física da Universidade Estadual de Feira de Santana (UEFS), voltadas à divulgação e popularização de ciências nas escolas, culminaram em 2007 com a criação da Especialização em Astronomia, e posteriormente, em 2013, com a criação do Mestrado Profissional em Astronomia (MPAstro). Desde o primeiro momento, o público alvo é voltado aos professores da educação básica, assim como do ensino superior com a formação graduada, de preferência, em 6 áreas do conhecimento: Física, Química, Biologia, Matemática, História e Geografia. Após 4 anos de operação e o egresso de 2 turmas (18 discentes), o presente trabalho se destina a apresentar um extrato do MPAstro além dos projetos e produtos educacionais desenvolvidos. O MPAstro explora tanto as características interdisciplinares que a Astronomia possui, como a flexibilidade que a mesma apresenta em questões relativas ás ações de ensino, pesquisa e extensão universitárias.

Keywords. Astronomy education – Teacher formation – Outreach

1. Introduction

The students' lack of interest in basic education through studies related to science has global dimensions (Yano, 2011) which presents itself as a worrying scenario observed in schools, going against the current moment in which society is immersed in an environment deeply immersed in technology. In addition to this the school performance evaluation indicators such as PISA[1], ROSE[2] and ENEM[3], which without restrictions show major deficiencies in basic education students'.

Since 1971, the Antares Astronomical Observatory (OAA) has been developing a role of disseminating the sciences to the visiting public; mostly elementary and middle school students. One of the good points was that in 1992 the OAA was incorporated at the Feira de Santana State University (UEFS), Bahia, Brazil, as an Organizational Development Unit, linked directly to the superior administration of the University. In 1997 the research and extension activities were coordinated by the professors of the UEFS physics department aided by the monitors (students from the Physics Course).

Using the structure of the OAA, the PECS project "Education, Science and Society: Teaching and Outreach of Astronomy" was structured and financed in 2003 by the Vitae Foundation, which would allow a greater projection and amplitude of the actions aimed at arousing interest in Science & Tecnology.

The various actions developed by the Astronomy group of the Department of Physics at UEFS, aimed at the outreach and popularization of science in schools, culminated in 2007 with the creation of the specialization in Astronomy (lato sensu) to teachers of basic education formed in one of these areas: Physics, Chemistry, Biology, Mathematics, History and Geography.

This specialization project aimed to contribute to the academic training of physics, chemistry, biology, mathematics, history and geography teachers of the public and private teaching networks of the State of Bahia. The course covered theoretical and observational, classical and modern themes of Astronomy, which allowed the teacher-student to understand the main scientific contributions of this interdisciplinary science to humanity. Concomitant to this, in a partnership with the Anísio Teixeira Institute of the Bahia State Department of Education, two continuing astronomy courses were held for teachers of basic education in the state. In the two editions of these courses about 400 teachers of the public basic education system were involved in all regions of Bahia.

In 2009 the MACT (Antares Museum of Science and Technology) was inaugurated. Nowadays, at the MACT, there are 07 permanent exhibitions: "Espaço Natureza"; "Bedengó"; "Dinossauros e Pterossauros do Brasil"; "Era dos mamíferos: a Aurora da Humanidade"; "Stonehenge" , "Relóógio Solar" and "A Conquista Espacial". We have also a planetarium and a auditorium for school attendance.

Finally, in 2013 a further step is taken to strengthen the area of Astronomy with the creation of the Professional Master in Astronomy (MPAstro). It was approved at CAPES with the concept 3.0 in 2013 March and at 2013 August we stared the first class with 10 studentes selected from 50.

[1] http://inep.gov.br/pisa
[2] http://roseproject.no
[3] http://enem.inep.gov.br

Table 1. Subjects Distribution per semester

Semester	hour/semester	Subjects	hours/week
First	09h	Professional Practice	03h
		Astronomy: a general vision	03h
		Astronomy Instrumentation	03h
Second	08h	Computer Applications in Astronomy Teachings	03h
		Development and Production of Teaching Materials	03h
		01 elective (depending on the goal of the Dissertation (TFC))	02h
Third	07h	A History of Astronomy	03h
		02 electives (depending on the goal of the TFC)	2x02h
Fourth	03h	Special Topics	03h

2. The professional Master's degree in Astronomy (stricto sensu)

There was a latent feeling that academic masters in teaching do not meet the needs of teachers who are in the classroom. In this context, the particular case of those who need the specific contents of Astronomy, as well as the relations of this with other areas of knowledge.

The experiences in teaching, extension and research resulting from the teachers' activities in the OAA, as well as the Interdisciplinarity Lato Sensu Course in Astronomy, together with the demand for specific contents, mainly coming from teachers of the basic education, culminated in the Stricto Sensu in Astronomy (Professional Master's Degree) – MPAstro[4].

With the Astronomy interdisciplinarity natural character we can select our target audience teachers from the following areas: Physics, Chemistry, Biology, Mathematics, Geography or History and also Professionals from Science Centers and Museums that work with Astronomy in their daily lives.

It aims is to contribute to the training of teachers and improvement of science teaching, having Astronomy as the main subject. We have also the goal to explore the interdisciplinarity characteristic of Astronomy and to extend the professional qualification of the teachers in the different levels of education - Fundamental, Middle and/or Higher. At the end of the course, the academic title received is "Master in Astronomy Teaching".

The MPAstro is a part-time program in which the majority of the teacher & student must maintain their professional activities, not departing from the schools where they teach. For this, all the activities of the Master course are concentrated in two days of the week (Friday and Saturday).

The MPAstro concentration area is "Teaching and Diffusion of Astronomy Description" having the research line: Interdisciplinarity Teaching of Astronomy and the Scientific-Technological Diffusion. We have 11 themes linked to the research line. They are:

1. Conceptual Astronomy Mistakes in the Classroom
2. History of Astronomy
3. The Big Bang: The Origin of the Universe
4. New Technologies applied to Teaching Astronomy
5. Elements of Applied Physics and Mathematics in Astronomy
6. Textbooks on Teaching Science and Geography
7. Brazilian Space Program
8. Chemical Evolution of the Universe: Formation of Chemical Elements and First Molecules
9. Production and Use of Didactic Materials in Astronomy
10. Outreach in Astronomy
11. Solar Energy: Uses and Applications

After 4 years of operation and the graduation of 2 classes (18 students), we have our first CAPES evaluation at this year. We present here an extract of the MPAstro besides the projects and educational products developed in this professional stricto sensu program that must to be related with 1 or more of the 11 themes mentioned above.

3. The master course characteristics

The total duration of the MPAstro is 30 months, i.e., 24 months with, if necessary, extension of 6 months. The course composition are: 7 compulsory subjects, each one corresponding to 45 hours (3 hours per week for 15 weeks) and 3 electives (2 hours per week).

Beyond the subjects and the electives, the students need to participate in the "update seminars" (75% presence) and in the "qualification seminars" (each 6 months; mandatory presence).

The Subjects Distribution per semester is presented in the following table (Table 1). At the fourth semester the student must finish the TFC. If it is not possible he/she need to request for an extension for up to 6 months not exceeding the total of 30 months.

4. Some results

Throughout the training process, it is sought to provide the students with the maximum tools from an instrumental, observational and experimental point of view, enabling them to take knowledge that has been solidly established in the classroom.

Over the four-year period of MPAstro's action, the demand for the program has been steady, around 50 candidates per selection (Table 02). The selections, in order to contemplate the diversity of the target audience, are concerned with accessing basic knowledge and exploring the ability to interpret and apply elementary concepts needed in basic science education. Until 2015, 10 annual vacancies were offered. After that, 12 annual vacancies are being offered and the average defense time is around 27 months, that is very good according to CAPES. One of the main results is that, during the course, the students are constantly encouraged to develop materials for direct application in the classroom as well as the socialization of the projects and their results in scientific events.

Concerned to events, at 2016 August we organized the "2o Seminário Nacional dos Mestrados Profissionais da área de ensino da CAPES" (2nd National Seminar of Professional Masters

[4] http://pg-astro.uefs.br

Table 2. MPAstro demand

Year	Applications	Approved	Registered/Vacation
2013	50	36	10/10
2014	42	22	10/10
2015	49	28	10/10
2016	47	31	12/12
2017	59	37	12/12

of CAPES' teaching area). The event[5] was organized by the MPAstro/UEFS and it took place from August 7 to 9, 2016 in the dependencies of the Anisio Teixeira Institute/SEC/BA, in Salvador. There were both oral and banners presentations. The participation of MPAstro's students was very representative and we count on the participation of coordinators of the various regions of the country as well as the students of the courses stricto sensu professionals from the CAPES teaching area.

5. The projects and educational products developed

As a requirement of the CAPES teaching area, associated with any dissertation must have an educational product. Since 2013 August until 2017 February were developed at MPAstro 18 projects and educational products related to these projects[6].

Following we can see the titles and a breaf abstract of each project:

Handling of astronomic images with the use of Aladin for Astronomy Education. *Abstract:* The software Aladin was used to visualize and manipulate astronomical images developed by CDS of Strasbourg and to elaborate teaching activities involving astronomical concepts, such as distance, brightness, image manipulation, colors as well as to explain the nature of different objects showing their images in different filters, among others. In the total, it were elaborated four activities that were applied to students of the 6th year of elementary school, high school and undergraduate ones for the Engineering and Pedagogy courses. All activities and the results of their evaluation with students are detailed, discussed and analyzed; a teacher guide is also provided. The results show that in the four activities, the students have a significant learning supporting the use of such methodology. Also, it was elaborated two memory games, based on Java platform, with the images of some astronomical objects. This research also made the translation of Aladin to Portuguese.

Educational process in the teaching of sciences and biology in the perspective of Astrobiology. *Abstract:* From astronomy topics listed in Elementary Education curriculum and finding that there is deficiency in teacher's training on basic knowledge of this science, it is proposed to draw up a paradidactic grounded in scientific conceptions, to be used in Basic Education. The paradidactic material was thought to be developed in comic format in view of the official documents governing the Brazilian education when it is proposed the use of different languages in teaching. We have consulted the bibliography and have used the methods of qualitative and quantitative research. For the preparation of the paradidactic, there was a concern to support it at assumptions of the Theory of Meaningful Learning. We justified the preparation of the paradidactic and themes chosen from discovering that there is little use of this science, which is interdisciplinary in basic education, since their subjects are part of the Basic Education curriculum, so they are attractive and offer possibilities to change the way education is conceived, pointing to the development of transdisciplinary proposals.

Proposal for paradidactical material on the origins of the Universe and life. *Abstract:* This work is a proposal of educational process, developed through applied research in order to seek the improvement about teaching Science and Biology in Basic School implementing current themes and concepts, interrelated to cross-cutting issues, going back to the origin of life, living beings, their interaction with the physical environment and the prospects for life elsewhere other than Earth. The project had as target students from elementary and high school from two public schools in the district of Feira de Santana-BA.

Kepler's laws of the planetary movement in the teaching books of physics of the 2014 national book program: a study based on conceptual, didactic-methodological and historical aspects. *Abstract:* The Physics textbooks constitute the main teacher's working tool, although surveys indicate the need to prepare own teaching materials prepared by the teacher and the use of the textbook as support. We conducted a study of Kepler's Laws of Planetary Motion in Physics textbooks recommended by the National Textbook Program (PNLD in Portuguese) in 2014. The main objective is to verify how that content is addressed in these works. We use as conceptual, didactic-methodological and historical aspects analysis criteria. They are linked to that recommended by the PNLD Guide, the National Curriculum Guidelines for Secondary Education, and academic papers that focus urges that a History of Science in teaching Physics.The methodology was qualitative in nature.

Astronomy in middle school. Science and the Ludic: challenging and educating. *Abstract:* This work presents the results of the use of a didactic material called Experimental Activity Kit (KAE), which was intended to draw up an Experimental Activities Manual (MAE) for teaching astronomy, physics and mathematics. This material was influenced by the teachings of David Ausubel about meaningful learning and Lev Vygotsky, with the theory of acquiring knowledge through practical activity in a social environment. In order to measure the knowledge acquired by the participants in the training process, we perform pre and post-tests with questions that allowed extract important results and conclusions. The results of the exams and evaluation of the methodology, submitted to a content analysis, indicated that students who saw reasoning as emerging through the assembly of the kits developed higher cognitive functions and showed greater interest and excitement in class, confirming that experimentation is one of the factors that most pleased the students during the lessons.

Teaching of Astronomy mediated by information and communication technologies (ICT): proposal of approach and analysis. *Abstract:* We are experiencing a period of transformation of teaching and learning techniques in school as an institution. Beyond its "walls", new technologies are developed and gradually incorporated into the daily lives of people. These same educational institutions try to keep up with changes upgrading themselves technologically acquiring equipment such as computers, tablets, televisions and internet connections so that teachers can use these media in the classroom. Despite this, the reflection on the best approaches to use these technologies

[5] `https://sites.google.com/site/ensinocapes/`

[6] They can be find at `https://sites.google.com/a/uefs.br/mp-astro/dissertacoes` and `https://sites.google.com/a/uefs.br/mp-astro/produtos-educacionais`

for education is set aside.

Insertion of cosmic background radiation in middle school through the use of skyviewer and planck applications mission in virtual reality. *Abstract:* The Cosmic Background Radiation (CBR) is considered one of the great discoveries of modern astronomy. Their study is to better understand the Universe and the refinement of observational techniques. Satellites Cosmic Background Explorer (COBE) and the Wilkinson Microwave Anisotropy Probe (WMAP) mapped more accurately the distribution of the cosmic background radiation.The present work is to develop a process of teaching and learning by introducing modern astronomy by analyzing the CBR Sky maps obtained by COBE and WMAP satellites using Skyviewer and Planck Mission in Virtual Reality.

Construction of a digital game connected with the scientific disclosure of Astronomy. *Abstract:* The purpose of this work in Astronomy at the Universidade Estadual de Feira de Santana, Bahia, is to offer a pleasant alternative to the introduction of contents related to astronomy in the classroom. With this in mind, we designed an digital educational quiz of questions and answers, applied in computers, with the theme of astronomy, inserted into three groups with three different methods, having as target the students of 1st year of Rotary Public School in Feira de Santana, Bahia, during some physics classes. We realized that different classes can be estimulated in different ways still getting almost identical results. It was noticeable in this work that the motivation in part of the students and teachers makes a difference for a change in education, thus making significant proposition for everyone involved.

Bromélia: multifunctional bench for Astronomy Laboratories. *Abstract:* This project aims at the development of educational kits for science laboratories, with a focus on astronomy. We intend to provide critical experiential opportunities that will facilitate learning. This will clarify concepts sometimes misunderstood solely by lecture and make connections between diverse disciplines, such as Geography, Physics, Mathematics, Biology and Chemistry. In specific, the proposed kits to the areas cited are: Seasons, Lambert-Beer and Pasnpermia. In this paper we will emphasize the Chemistry and Geography kit, as well as display the details of a kit to assemble electrotechnology to evaluate the proposed methodology.

Geometry and Astronomy: a proposal of didactic sequence for interdisciplinary education. *Abstract:* This work presents a proposal of work for students of primary and secondary education with the main work tool a Didactic Sequence, seeking to solve a major difficulty learning reversed in the low-income mathematics discipline in the first unit. This work seeks to improve viewing issues and application of geometry in a real trouble showing how the geometry was used for the solution of issues in Astronomy. This work was applied to the class of third year of the Technical Course in Agriculture of the Territorial Center for Professional Education at Chapada Diamantina involving 32 students after the low-income index identifying the first unit, which brings in its curriculum proposal notions of Geometry / Initial trigonometry, in order to help the teacher making pleasant and interesting the lesson for students.

The teachers of sciences and their practices: a didactic proposal for the teaching of the contents of the year's seasons. *Abstract:* In this work, we analyze the understanding of Science, Geography and Education teachers of São Miguel das Matas, Bahia, about teaching and learning process of Seasons content that has been reflected on the construction and using of a didactic material (model System Earth-Sun), developed from a workshop with teachers who teach science classes in elementary school. The methodology has been based in questionnaires, videos and experimental demonstrations. The results showed that many science teachers have difficulties regarding to the understanding of the Seasons content. As a result, we can say that a didactic workshop in Seasons concept could make better the understanding of this content.

Study of eletromagnetic radiation in the light of Astronomy, in the context of physics lessons, in the 3rd series of middle school. *Abstract:* This study was to investigate how the introduction of modern physics in high school, mediated by the study of astronomy, may favor the practice of teaching and learning of physics, from the perspective of the Theory of Meaningful Learning (TML), through the use of Sequence Didactic . It was developed in a senior high school class, in a public school from Santo Antonio de Jesus town, State of Bahia, and entitled "Knowing the Universe Through the Colors". The same had as its central theme Electromagnetic Radiations and constituted both an instrument and product of this research. This research has been prepared under qualitative and quantitative approach, from which have developed a descriptive understanding work of the investigated object. Finally, this study shows a very positive result of the methodology chosen and can say that the Didactic Sequence elaborate contributed to a meaningful learning of concepts covered in Modern Physics, mediated by Astronomy, enabling students to build knowledge that can serve as anchors for future concepts.

Workshop of rocket: interdisciplinary aspects among astronomy, astronautics and physics. *Abstract:* This work discusses aspects of Astronautics and Astronomy in the Science and Physics classes of Elementary and Middle School in public and private schools in Feira de Santana. Astronomy is an interdisciplinary and necessary science in the curriculum of Brazilian schools. As such, we have a workshop where students build and launch rockets made of low-cost materials such as PET pickups and PVC pipes. The meaningful learning (Ausubel, 1976) was the theoretical reference of this study. Therefore,, we started the work by collecting information from the students through questionnaires to create a profile about their knowledge about astronomy and, after that, we propose activities where students are able to develop skills for understanding the physical phenomena that can be observed during the launch of a rocket, such as Oblique Motion and Newton's Laws. The workshop was very positive, arousing students' interest in participating in the Brazilian Astronomy and Astronautics Olympiads and obtaining better grades in the disciplines of Science and Physics. The students also realized the importance of astronomy in the development of humanity.

Didactic book and ludic activities: a relevant combination for the teaching-learning of the contents of Astronomy. *Abstract:* This work analyzed the combination of textbook Geography with ludic activities in the teaching-learning of Astronomy contents in the 6th year of elementary school. Geography is an example of discipline that presents astronomy content in primary and secondary education. Thus, it presented the pedagogical importance of textbooks for teachers and students, as well as the playful in contemporary educational practice may be potentiating the resource development and student learning in the school environment. The theoretical

basis for the study of recreational activities such as mediation and learning tool for this research work was based on the theory of sociointeractionist of Lev Vygotsky Semonovich. Our research approach is qualitative and quantitative, as we believe that there is an interdependence between quantifiable indicators and qualitative aspects and so they complement each other. For the development and completion of research we seek tools that made it possible: observe and analyze facts or relevant tools, collect and analyze statistical data that contributed to the target audience of the teaching and learning process.

The use of educational video and play as an instrument of teaching and dissemination of Astronomy. *Abstract:* Currently, due to the various technological options, the vast access to information and the demotivation of some students, much is discussed in the literature about the way of teaching so that it becomes diversified and attractive. The teacher / classroom model with traditional teaching has leaved to be the main medium in the teaching-learning process. Faced with this new educational paradigm, the need arises to seek strategies that increase the interest, the motivation and consequently the level of learning of the students. In this sense, we have the ludic forms of teaching, such as the application of didactic games, which are increasingly present in the school environment. From this context, a didactic game, entitled "Space Track" and an educational video called "Unraveling the Universe", was created.

Basic Astronomy as a starting point for the introduction of concepts of physics in middle school. *Abstract:* This work is the result of a research that aims to analyze strategies of teaching Physics using Astronomy as a motivational agent for its learning, establishing a relationship of transversality between Physics and Astronomy. The teaching methodologies included teaching strategies for scientific research, observation and practical experimental activities, executed in a high school in the city of Salvador-Bahia in the years 2015 and 2016. All research work was based on the theoretical principles of John Dewey, which advocated participatory learning where ideas should be shared - and this is only possible when there is no barrier to free expression of thought -, and David Ausubel's Theory of Meaningful Learning, according to which to have meaning it is necessary that the new knowledge has connection with what the student already knows. As a product of the construction work, we have as final production the elaboration of a practical manual containing the experiments in which shared the methods and procedures employed.

The teaching of physics in the light of Astronomy: a pedagogical practice research and experimental. *Abstract:* Scientific Literacy is one of the big challenges in contemporary world. This project promote a diffusion of this manner of learning though practice in Physical class and Basic Education Science, as well practice of experiments involving basic astronomical tools, observation of astronomical phenomena, planetarium sections, presentations, participations in Astronomy and Astronautic Brazilian Olympiad, science fairs and confection of didactic material for Teaching Astronomy are some activities include on this project.

The educational products related to each project already produced are: Didactics sequences; Facebook Pages; Products for the blinds; Educational workshops; Electronic games; Multifuncional bench for laboratories; Activity manuals; Board games; Educational Portals; Educational videos; Comics; Book for children and Models.

6. Conclusion

The MPAstro explores both the interdisciplinarity characteristics that Astronomy has, and the flexibility that it presents in questions related to university teaching, research and extension actions. Throughout the training process, the teacher will be able to provide the maximum tools from an instrumental, observational and experimental point of view, enabling the teacher-student to take knowledge that has been solidly established in the classroom. All the educational products are validated by the defense judges.

Acknowledgements. We are so gratefull to Vitae Fundation that provided financial support in the beginning of the research activities at the Antares Observatory at 2003 that culminated in the MPAstro at 2013.

References

Yano, C., 2011, Revista Ciência Hoje, 282, 2011

Boletim da Sociedade Astronômica Brasileira, **30**, no. 1, 8-9

Use of tactile materials for Astronomy teaching for visually- and hearing-impaired public schools in Minas Gerais

A. Paganotti[1,2], C. Reis[1], & M. Voelzke[2,3]

[1] Instituto Federal de Minas Gerais, Brazil. e-mail: crislaynemodesto@hotmail.com
[2] Universidade Cruzeiro do Sul, Brazil. e-mail: arilson.paganotti@ifmg.edu.br
[3] Institut fuer Geophysik und extraterrestrische Physik, Technische Universitaet Braunschweig, Germany. e-mail: m.voelzke@tu-braunschweig.de

Abstract. This work deals with the use of tactile materials as a pedagogical tool for the teaching of Astronomy, and this material was used in a didactic activity with 44 students of the public elementary school in Minas Gerais. A visually impaired student and another hearing impaired participated, being these the focus of the research. With the tactile visual material elaborated, the objective was to develop themes such as phases of the Moon, eclipses and Solar System. Two questionnaires were applied and revealed an improvement in the concepts related to Astronomy and in the socialization of disabled students with the group after the didactic activity.

Resumo. Este trabalho aborda o uso de materiais táteis como ferramenta pedagógica para o ensino de Astronomia, sendo este material utilizado em uma atividade didática com 44 alunos do Ensino Fundamental de uma escola pública de Minas Gerais. Um aluno deficiente visual e outro deficiente auditivo participaram, sendo esses o foco da pesquisa. Com o material tátil visual elaborado objetivou-se desenvolver temas como fases da Lua, eclipses e Sistema Solar. Dois questionários foram aplicados e revelaram uma melhora nos conceitos relacionados à Astronomia e na socialização dos alunos deficientes com a turma após a atividade didática realizada.

Keywords. Teaching of Astronomy

1. Introduction

Being a teacher goes far beyond teaching a class. It becomes necessary for the teacher to adapt to a new problem every day and to find a way to solve it. Often teachers come across a class with a great diversity of students, with different skills, experiences, cultures and limitations (Dickman& Ferreira 2008). Public Inclusion Policies (Brazil 2008) ensure the entry and permanence of persons with disabilities in regular schools, having the right to have their educational needs met. Thus, a change in the teaching method is necessary, both to achieve a better development of students with disabilities, and to the regular students. This work deals with the use of tactile materials as a pedagogical tool for the teaching of Astronomy. It was carried out with students of the public elementary school in Minas Gerais, with 20 students from a group of eighth and 24 from the ninth grade of Elementary School. In these classes there are two disabled students being one blind and one deaf.

2. Objectives

The objective of this study was to analyze the Astronomy knowledge of a group of students in which students with visual impairment and deafness are enrolled, as well as to verify the contribution of the tactile materials produced to the learning of concepts related to Astronomy.

3. Metodology

In this work two questionnaires were used, the first one being applied to verify the students' knowledge on Astronomy subjects. From the analysis of this questionnaire, tactile materials were prepared for use by the students during the proposed pedagogical activity. The use of tactile materials for the teaching of Astronomy was a proposal to try to alleviate the difficulties presented by the deficient students, visual and auditory, verified in the first questionnaire applied. The second questionnaire applied was aimed at verifying students' learning during the development of the proposed didactic activity. Figures 1 and 2 show part of the materials used.

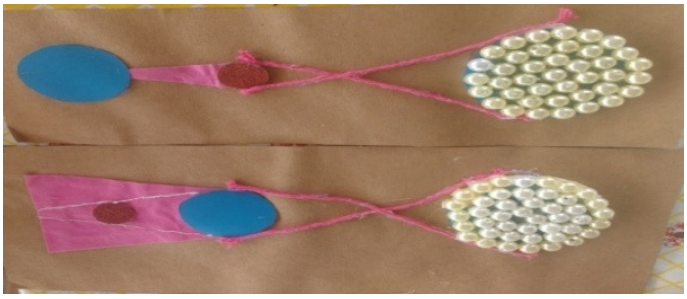

Figure 1. Representative assembly of the Solar System using low cost materials.

4. Results and Discussions

With question 6 was aimed to verify the students' knowledge regarding the phases of the Moon. An image of the four phases of the Moon was provided where students were to write the name corresponding to each phase. The data of this question are expressed in the graph in figure 3.

In general, most students scored between two and three phases of the Moon, and it was possible to see that the greatest confusion in the answers occurred in the waning and growing phases, in which only twelve students of the total hit Crescent

Figure 2. Representative assembly of Lunar and Solar eclipse using low cost materials.

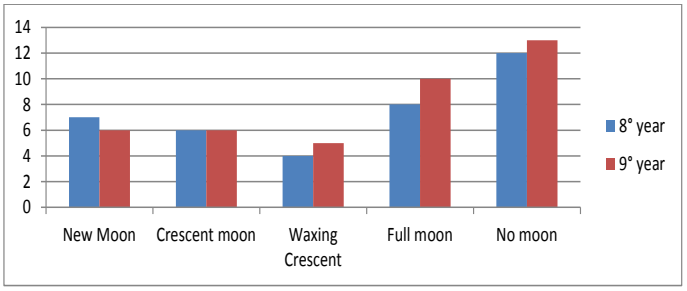

Figure 3. Representative chart of the answers given to question 6 of the first questionnaire.

Moon and nine students of the total matched the Waning Crescent. The blind student could not identify any of the phases, while the deaf student was able to identify only the Full Moon.

5. Final Considerations

There was a significant improvement in the students' responses to the second questionnaire applied and in the socialization of the disabled with the class. It was observed that the material assembled to aid the disabled students also helped the other students of the class with regard to learning the concepts related to Astronomy.

References

BRAZIL. Code. *Decree No. 6,571*, dated September 17, 2008. Available at: <http://www.planalto.gov.br/ccivil_03/leis/L7853.html>. Accessed on: 04 February 2016.

Dickman, A. G., & Ferreira, A. 2008, Revista Brasileira de Pesquisa em Educação em Ciências, 8 (2), 1

Boletim da Sociedade Astronômica Brasileira, **30**, no. 1, 10-11

The astronomy press release system of UFRJ/SAB

Douglas F. Martins[1], Eduardo M. Pereira[1], Catarina V. Lencioni[2], & Thiago S. Gonçalves[1]

[1] Observatório do Valongo, Univerisidade Federal do Rio de Janeiro, e-mail: douglasm13@astro.ufrj.br
[2] Escola de Comunicação, e-mail: catarinalencioni@gmail.com

Abstract. The outreach of the Brazilian astronomers researches is a fundamental key for bringing visibility to astronomy wide nationally. Not only it raises public awareness regarding the work performed in Brazil, the astronomy dissemination promotes and stimulates the science produced here. However, the currently main astronomy diffusion sources in Brazil have been enthusiasts and amateurs, what devalues the role of the professional astronomer. As part of the issue is due to the absence of an intermediate for astronomers and the press, this project precisely aims to play the role of a communicator agent, acting between science research and outreach. Our team focuses particularly on press releases production through a simple and direct template: we contact the authors of a potentially public-interesting research; if agreed, we step into the process of producing an accessible comprehension text about the research, in order to deliver it to journalists. Moreover, we also make use of modern tools, such as and especially social media, aiming to increase the trustworthy information reach. Since the beginning of this project, last February, two press releases have been finished, and two others are currently under production process. Furthermore, the use of social media has brought satisfying results, as we shall present using the available statistics tools.

Resumo. A divulgação da pesquisa feita por astrônomos brasileiros é peça fundamental para a visibilidade da astronomia em âmbito nacional. Além de promover e estimular a ciência feita no Brasil, a difusão traz conscientização por parte da população sobre os estudos realizados pelos pesquisadores do nosso país. Entretanto, as principais fontes de divulgação astronômica no Brasil vêm sendo entusiastas e amadores, desvalorizando o papel do astrônomo profissional. Como parte do problema se deve à ausência de um mediador entre astrônomos e jornalistas, nosso projeto visa justamente desempenhar o papel de agente comunicador intermediário entre a pesquisa e a divulgação. O foco principal deste trabalho é levar a pesquisa em astronomia desenvolvida no país à grande imprensa, mais especificamente investindo na produção de press releases. Seguindo o modelo linear para o processo de comunicação científica, consideramos a seguinte metodologia: estabelecemos contato com um autor de uma pesquisa em astronomia com potencial midiático; uma vez concordado, redigimos um texto de compreensão acessível sobre o estudo para que possa ser distribuído aos jornalistas. Através deste procedimento, produzimos em média um release a cada duas semanas. Além disso, também buscamos aproveitar as mídias sociais através de publicações de notícias sobre astronomia em um contexto geral, objetivando ampliar o alcance da informação fidedigna. Até agora este ferramental retornou considerável sucesso, como apontaremos através das estatísticas disponíveis, apresentando os resultados e conclusões obtidos nos primeiros seis meses de trabalho.

Keywords. Miscellaneous

1. Who are the science communicators?

One can easily notice that all major astronomy outreach channels in Brazil are led by enthusiasts and amateurs. In great part, this is due to a lack of interest from the academic community in bridging the gap between scientists and the press. The end result is that the public is more aware of research developed in North America and Europe than that originated in Brazil. In that context, this project aims to play the role of a communicator agent, or a public information officer (PIO), acting as said connection between scientific research and the public.

2. The linear model for science communication

The linear model is one of the simplest and most used models to describe the communication process. It depicts a unidirectional flow of information in which the message follows a straight line, starting at the sender and ending at the receiver, without any feedback from the latter (Christensen, 2007). The layout displayed in Figure 1 represents the information flow from the scientist (sender) down to the public (receiver). The gradient from blue to orange denotes a simplification of the information. Once the journalists obtain the final word from the PIOs, the information may be published. Thus, our biggest concern as PIOs is to ensure that the information produced by the scientists becomes accessible and attractive to the journalists, which leads us to the main stage of this project.

3. Production of press releases

Our main focus is to take astronomy research developed in Brazil to the mainstream media, more specifically investing in production of press releases. The process occurs through the following steps:

1. Contact with the author(s) of a study with high potential to attract public interest;
2. following an interview with the author(s), composition of an accessible text (in layman's terms) about the research;
3. editing, and (with the author's consent) distribution of the text to the press.

4. Finished releases

For six months, starting in February, we have tested our methodology and functionality, resulting in press releases on the following scientific papers:

– "Segregation effects in DEEP2 galaxy groups", Nascimento et al., 2016

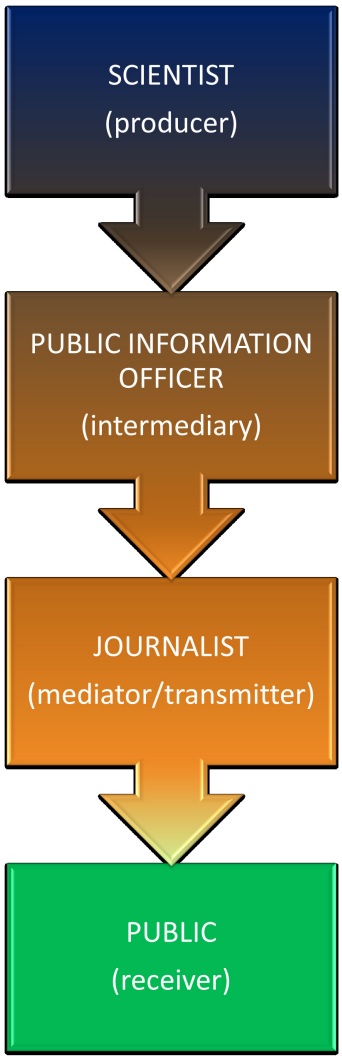

Figure 1. Representation of the linear model of communication applied for science outreach: the information path from the scientist to the public.

- "The fate of the gaseous disks of galaxies that fall into clusters" (published on SAB's webpage), Ruggiero&Lima-Neto, 2017
- "Gemini NIFS survey of feedind and feedback processes in nearby Active Galaxies: I - Stellar kinematics", Riffel et al., 2017
- "The abundance of compact quiescent galaxies since z ~ 0.6", Charbonnier et al., 2017

5. Social media support

We also emphasize the relevance of social media (such as Facebook) regarding the popularization and visibility of activities developed in scientific institutions. Since February we have also produced content for the Valongo Observatory Facebook fanpage; Figure 2 (above) shows individuals reached during and before this period. The blue points indicate cumulative reach for all publications after our project started, while the red points show these values for a similar duration preceding this work.

6. Perspectives for the future

Following this initial phase of training, we expect to increase our output and achieve an average rate of one release every two weeks, in order to establish a continuous dialog with the press. We also plan to establish partnerships with the major main science outreach actors in Brazil, in an attempt to take advantage of their reach and extended audience while providing content that reflects national research projects.

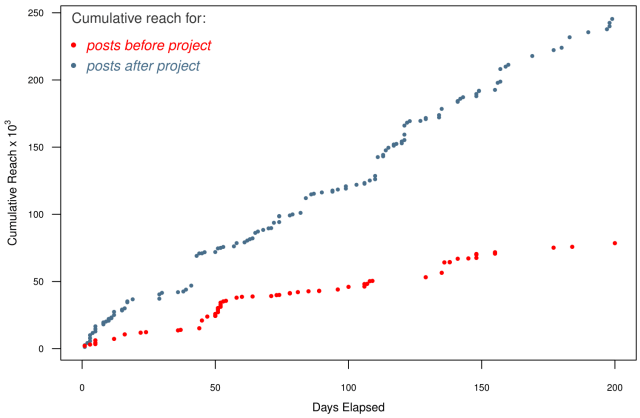

Figure 2. Plot comparing the cumulative reaches before and after our work for the Valongo Observatory facebook fan page.

Acknowledgements. We would like to thank PROFAEx, from Federal University of Rio de Janeiro, for financial support.

References

Christensen, L. L. 2007, in The hands-on guide for science communicators: A step-by-step approach to public outreach, Springer Science & Business Media
Nascimento, Ribeiro & Lopes 2016, Monthly Notices of the Royal Astronomical Society, 464, 183
Ruggiero & Lima Neto 2017, Monthly Notices of the Royal Astronomical Society, 468, 4107
Riffel et al. 2017, Monthly Notices of the Royal Astronomical Society, 470, 992
Charbonnier et al. 2017, Monthly Notices of the Royal Astronomical Society, 469, 4523

Boletim da Sociedade Astronômica Brasileira, **30**, no. 1, 12-13

The possible social representations of astronomy by students from integrated high school

José Isnaldo de Lima Barbosa[1,2] & Marcos Rincon Voelzke[1,3]

[1] Universidade Cruzeiro do Sul, Brazil, e-mail: joseisnaldo@gmail.com
[2] Instituto Federal de Alagoas, Brazil
[3] Institut für Geophysik und extraterrestrische Physik, Technische Universität Braunschweig, Germany, e-mail: mrvoelzke@hotmail.com

Abstract. In this paper, we present the possible Social Representations, which students of the Integrated High School of the Federal Institute of Alagoas (IFAL) have on the term inductor Astronomy, as well as identifying how they were probably elaborated. Therefore, in agreement with Moscovici (2010) is used the Theory of Social Representations.

Resumo. Neste trabalho, apresentamos as possíveis Representações Sociais, que alunos do Ensino Médio Integrado do Instituto Federal de Alagoas (IFAL) têm sobre o termo indutor Astronomia, assim como, busca identificar como elas foram provavelmente elaboradas. Portanto, de acordo com Moscovici (2010) é utilizada a Teoria das Representações Sociais.

Keywords. Teaching of Astronomy

1. Introduction

A Social Representation (SR) is an organized and structured set of information, beliefs, opinions and attitudes; It is a particular sociocognitive system, composed of two subsystems: a central system (or central nucleus) and a peripheral system (Abric, 2003).

2. Methodology

In order to identify the Social Representations of Astronomy by students of Integrated High School, the Central Nucleus Theory was adopted, so according to this theory, the data were collected through a questionnaire of free association or free avocational and hierarchical. This instrument was applied to 653 students from IFAL, 267 from the 1 st year, 219 from the 2nd year and 167 from the 3rd year. The predominant age groups are: 1st year (14 to 17 years); 2nd year (15 to 18 years); 3rd year (16 to 19 years). The questionnaire was structured with the following questions:

1. When thinking about the term *Astronomy*, write all the words you have remembered and try to register as many of them in the following table (32 spaces) in order to complete it. Beware, **do not** fix your attention on the last word you wrote, but on the term *Astronomy*.
2. Among those words recorded in question 1, select and rewrite in the first column of the following table the eight words that you consider most important, that is, more related to the term *Astronomy*. Next to the second column, classify each one by its degree of importance from 1 to 8, with grade 1 being the most important, grade 2 being the 2nd most important, and so on until grade 8, which will be the least important.

3. Results and discussions

After tabulation of the data, we have 419 different words, out of a total of 5224 evocations, in the sequence the data were introduced in the software IRAMUTEQ, and with this was carried out a prototypical analysis with the objective of detecting the possible social representations of the researched students in relation to the object Astronomy. For each word cited, its frequency (F) was calculated, that is, the number of times that word was mentioned, as well as the average order of recall (AOR), which considers the position in which the term evoked was hierarchized by the respondent, in this way, the AOR represents the degree of importance given to each word.

For this work were considered evocations with frequency greater than or equal to twenty. Thus, an average frequency of 89.4 and an AOR of 4.4 was calculated (Table 1). Therefore, these were the parameters used for the construction of the four houses, where the elements belonging to the possible central core and the peripheral region, highlighted in the table below.

4. Final considerations

In this sense, we conclude that the researchers have social representations of the object Astronomy, and these were based on elements that made or are part of the experience lived by the students within the formal space of education, as well as their interaction with the media of mass communication. It is also verified that the students possess information and a valuation position in relation to astronomical science.

References

Abric, J. C. 2003, in Social Representations and Educational Practices, Campos, P.H.F. & Loureiro, M. C. S., eds., (Goiânia: Ed. da UCG), pg. 38

Moscovici, S. 2010, in Social Representations: Investigations in social psychology, (Petrópolis: Vozes)

Table 1. Four-house chart showing the social representations of Astronomy elaborated by the students surveyed.

Central Core			1st Periphery		
Frequency ≥ 89.4 e AOR < 4.4			Frequency ≥ 89.4 e AOR ≥ 4.4		
Words	Frequency	AOR	Words	Frequency	AOR
Planets	446	4.1	Stars	312	4.4
Astros	217	3.1	Moon	173	5.1
Galaxies	200	4.1	Sun	173	4.4
Universe	184	2.9	Satellites	156	5.4
Space	166	4.2	Gravity	140	4.5
Study	157	3.2	Constellations	130	4.8
Physical	101	3.3	Meteors	117	5.6
Earth	95	4.2	Astronauts	110	4.6
			Telescopes	95	5.5
			Movement of the astros	94	5.1
Contrast Zone			2nd Periphery		
Frequency < 89.4 e AOR < 4.4			Frequency < 89.4 e AOR ≥ 4.4		
Words	Frequency	AOR	Words	Frequency	AOR
Solar System	81	3.5	Comets	88	5.7
Astronomers	69	3.7	Rockets	65	5.1
Life	57	4.1	Milky Way	59	4.8
Research	52	3.5	Time	57	5.0
Technology	50	3.7	Black Hole	56	5.7
Science	50	3.4	Sky	54	5.1
Big Bang	37	4.0	Observations	53	4.7
Scientists	21	3.9	Calculus	48	4.5
Celestial Bodies	20	3.5	NASA	45	4.7
			Discoveries	41	5.0
			Climate	40	5.6
			Phenomena	39	4.9
			Light	38	4.8
			Eclipses	38	6.0
			Atmosphere	36	4.9
			Material	32	4.9
			Asteroids	31	5.6
			Speed	28	5.0
			Gases	27	5.5
			Spacecraft	26	6.1
			Light years	26	5.5
			Vacuum	21	5.3
			Cosmos	20	4.9

Boletim da Sociedade Astronômica Brasileira, **30**, no. 1, 14-15

The study of topics of Astronomy in Physics teaching that addresses the significant learning

M. L. Santos Neta[1] & Marcos Rincon Voelzke[1,2]

[1] Universidade Cruzeiro do Sul, Brazil, e-mail: mlsneta@yahoo.com.br
[2] Institut für Geophysik und extraterrestrische Physik, Technische Universität Braunschweig, Germany, e-mail: mrvoelzke@hotmail.com

Abstract. In this work are discussed the results of the case study on the oceanic tides for which it was used didactic sequences, based on the Cycle of Experience of George Kelly (Kelly 1963), applied in four groups of the first year of the integral medium teaching. The data obtained in two same tests - Pre and Post-Test - before and after the application of the didactic sequences, as well as the verification of the significant learning analysed as for the conditions of the previous knowledge considering authors Boczko (1984), Horvath (2008) and Kepler & Saraiva (2013). Also the values were analysed obtained the Post-Test II applied to the long period. The results reveal that the worked groups presented previous knowledge in conditions adapted for the understanding of the event, as well as, for they be used in the situation-problem resolution that demands the understanding. Verify also that the idea of the didactic sequence can be used as tool in the relationship teaching-learning addressed to the significant learning.

Resumo. Neste trabalho são discutidos os resultados do estudo de caso para o qual foi utilizado sequências didáticas, baseados no Ciclo de Experiência de George Kelly (Kelly 1963), para o estudo das marés oceânicas, aplicada em quatro turmas do primeiro ano do Ensino Médio integral. Os dados obtidos em dois testes iguais — Pré e Pós-Teste I — antes e depois da aplicação das sequências didáticas, como também a verificação da aprendizagem significativa foram analisados quanto às condições dos conhecimentos prévios considerando os autores Boczko (1984), Horvath (2008) e Kepler & Saraiva (2013). Também foram analisados os valores obtidos no Pós-Teste II aplicado em longo prazo. Os resultados revelam que as turmas trabalhadas apresentaram conhecimentos prévios em condições adequadas para a compreensão do evento, como também, para serem utilizados na resolução de situações-problema que exigem sua compreensão. Constata também que a idéia da sequência didática pode ser utilizada como ferramenta na relação ensino-aprendizagem direcionada a aprendizagem significativa.

Keywords. Teaching of Astronomy

1. Introduction

This work had as purpose to study topics of Astronomy (Mourão 2008) in Physics discipline with students of the 1st year of the Medium Teaching of a located school in the city of Sirinhaém – PE in the period between August 2015 and May 2017.

2. Objectives

To analyse and to understand as the study of topics of Astronomy in Physics Teaching can be significant.

3. Methodological Procedures and Results

The Pre-Test was applied to 112 students, soon afterwards the application of the didactic sequences happened: antecipation of the knowledge, investment in the result, encounter with event, confirmation or not of the hypothesis and formation of new constructions (Kelly 1963) and at the end of the intervention the Post-Test I was applied; after five months the situations problems were introduced and, one year and one month later, the Post-Test II was applied to 86 students. The results can be observed in the Figures.

4. Results and discussions

In the Post-Test I it happened a variation of percentile between 36.0% and 100.0% for the adequate answers; as to the construction of the significant learning oscillated from 3.1% to 88.9% for the developed category; and in relation to the Post-Test II it varied among 40.7% to 54.7% for the correct answer. So the application of the methodology is pertinent, but need to be adjusted to obtain a deepening of the topics.

References

Boczko, R. 1984, Concepts of Astronomy, (São Paulo: Edgard Blucher)
Horvath, J. E. 2008, The abcd of the astronomy and astrophysics, (São Paulo: Livraria da Física)
Kelly, G. A. 1963, A theory of personality: the psychology of personal constructs, (New York: W. W. Norton)
Kepler, S. O, Saraiva, M. F. O. 2013, Astronomia e Astrofísica, (São Paulo: Livraria da Física)
Mourão, R. R. F. 2008, Dicionário Enciclopédico de Astronomia e Astronáutica, (Rio de Janeiro: Saraiva)

Table 1: Question one: what is tide?

	A		B		C		F	
	Pre-Test	Post-Test I	Pre-Test	Post-Test I	Pre-Test	Post-Test I	Pre-Test	Post-Test I
Appropriate	8.0%	48.0%	2.8%	75.0%	0.0%	71.9%	5.3%	63.1%
More or less Appropriate	48.0%	28.0%	27.8%	19.4%	28.1%	25.0%	15.8%	21.1%
Inadequate	44.0%	24.0%	69.4%	5.6%	71.9%	3.1%	78.9%	15.8%

Table 2: Significant learning: question one.

	A	B	C	F
Developed	48.0%	44.4%	68.8%	52.7%
Developing	36.0%	50.0%	28.1%	38.6%
Non developed	16.0%	5.6%	3.1%	10.5%

Table 3: Significant learning: question two.

	A	B	C	F
Developed	44.0%	88.9%	71.9%	78.9%
Developing	36.0%	8.0%	3.1%	5.3%
Non developed	20.0%	2.8%	25.0%	15.8%

Table 4: Post-Test II – Question I

	A	B	C	F
Correct	38.9%	46.7%	33.3%	42.9%
Incorrect	61.1%	53.3%	66.7%	57.1%

Boletim da Sociedade Astronômica Brasileira, **30**, no. 1, 16-17

Sundials as a teaching tool to understand time, calendar, seasons and Earth orbit

M. P. Ferreira & G. R. Hickel

[1] Federal University of Itajubá e-mail: mauriciopereiraferreira@hotmail.com, gabrielhickel@unifei.edu.br

Abstract. The sundial was constructed in the classroom and used in a flat location with a good solar incidence during the whole daytime period, where the students use the following knowledge: mathematics; art; ecology, geography, history and physics (astronomical), that is, in this project interdisciplinarity was necessary for a good development. For this work, it was decided to make the horizontal sundial. The work obtained a satisfactory result, with a better understanding of the seasons of the year and of the movements of rotation and translation of the Earth. Interdisciplinarity contributed to the development of this work and the classes taught. Another important factor was the realization of a class outside the classroom, providing a break in the traditional classroom routine.

Resumo. O relógio de Sol foi construído em sala de aula e utilizado em um local plano com uma boa incidência solar durante todo o período diurno, onde os educandos utilizam os seguintes saberes: matemática; artes; ecologia, geografia, história e física (astronômicos), ou seja, nesse projeto a interdisciplinaridade foi necessária para um bom desenvolvimento. Para esse trabalho, escolheu-se confeccionar o relógio de Sol horizontal. O trabalho obteve um resultado satisfatório, com uma melhor compreens´ ao das estações do ano e dos movimentos de rotaç ao e translaç ao da Terra. A interdisciplinaridade contribuiu para o desenvolvimento desse trabalho e das aulas ministradas. Outro fator importante foi a realizaç ao de uma aula fora da sala de aula, proporcionando uma quebra na rotina da aula tradicional.

Keywords. History and philosophy of astronomy – Time – *(Sun:)* solar-terrestrial relations

1. Introduction

One of the first marking mechanisms of the passage of time to be constructed was the sundial. By determining the bright part of the day, the Sun was already used as a qualitative marker of time, even by the nomadic tribes. But it is with the first set civilizations (and the advent of numerical symbology) that the first sundial were built. From the systematic observation of these clocks, the early civilizations also perceived that the shade of these artifacts varied significantly with the seasons of the year, allowing also a marker of the tropic year (time interval between two consecutive springs). Even with the hassle of not working on cloudy days, the sundial was a key element in the organization of early societies.

The sundial is a useful tool to determine not only the time during the day, but also the seasons and even the geographic position. Today, the sundial has a historical value (in pieces built centuries and even millennia) and is still made as a decorative piece (in reduced sizes) and also as an architectural element, in great monuments.

Its use as a teaching tool has been rescued over the past 50 years, especially in Europe and the USA. In Brazil, with the greatest diffusion of astronomical knowledge, especially in the last 20 years (with good participation of the schools in the Brazilian Astronomy Olympics - OBA) where the students came to have greater contact with the subject, there was a certain rescue of the importance in the construction and use of sundial for the understanding of issues relating to the movements of the Earth (Oba.org.br 2016).

2. Procedures

The sundial should be constructed in the classroom and later used in a flat location with a good solar incidence during the whole daytime period, where students should use the following knowledge: mathematics; art; ecology, geography, history and physics (astronomical). With the use of the sundial, it will be possible the interdisciplinarity, where it consists in the interaction of the contents of several disciplines, thus providing a new knowledge (Azevedo 2012). Already as a teaching tool, it can be used to explain the following topics: day movement, apparent movement of the Sun, time, gnomon, latitude and longitude, cardinal points, solstices and equinoxes, seasons of the year.

2.1. Materials

For this work, it was decided to make the horizontal sundial, which can be easily transported and used anywhere within the 21’ latitude, which is the latitude of the city of Alfenas - MG, Brazil. For the preparation of the horizontal sundial, the following materials were used:

- pencil;
- protractor;
- ballpoint pen;
- stylet;
- drawing of the horizontal sun clock printed on A4 paper using *Shadows 4.0* software;
- compass;
- hand level;
- plywood of 15 mm and 10 mm thickness.

The *Motion of the Sun Simulator* software was also used to simulate the apparent motion of the Sun, and it is possible to visualize the projection of a person’s shadow throughout the year in any latitude that is. The figure below shows the main screens of such software, the drawing of the horizontal sundial printed on four A4 paper and the sundial finished.

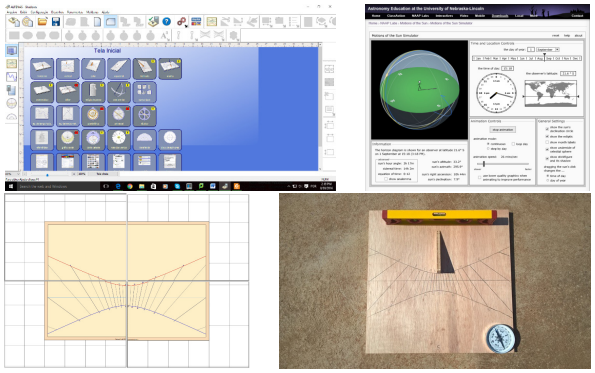

Figure 1. *Shadows 4.0* software (top left); *Motion of Sun Simulator* software (top right); drawing of the horizontal sun clock printed on A4 (botton left); sundial finished (botton right)

3. Results and discussion

The classes were developed at the State School Padre José Grimminck, in the city Alfenas – MG, in class 1 of the 1st year of High School. The students initially showed a lack of interest in the sundial, but in the course of the classes developed, especially in the first class, where with the use of the earth globe, we tried to explain the seasons and the projection of the shadows on the surface of the planet, thus recovering , which they had previously learned about solstices and equinoxes, they began to be curious about the subject, asking questions about what they were witnessing in that lesson. Already, when the *Motions of the Sun Simulator* software was introduced, students easily understood the projection of the surplus generated by it, but not with the same enthusiasm as using the globe. At the end of the study, the following questionnaire was distributed to analyze the fixation of what had been learned during the classes:

1. What is solstice? What do you mean by summer and winter solstice?
2. What is an equinox? What do you mean by spring and autumn equinox?
3. What are the seasons?
4. Why do we have 4 seasons of the year?
5. How and why did you start counting time?
6. What is the sundial for?

The results of the questionnaires are presented in the following graphs, considering the correct answers, incorrect answers and no answer:

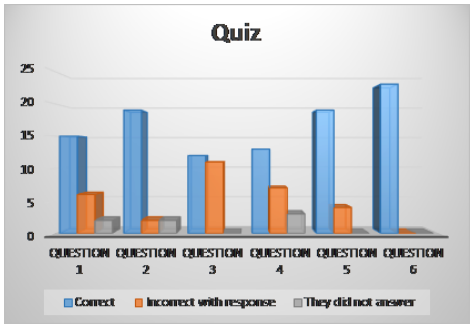

Figure 2. Graph of the quiz applied at the end of classes.

It is possible to note on the graph that everyone understood what the sundial is for, followed, but not 100% of the students, by equinoxes and how and why they started counting time. Question 3, *what are the seasons*, was the one that had almost 50% of error and correctness. Even with the classes developed with the use of the terrestrial globe and the use of the sundial and simulators softweres, 50% of the students still can not understand, what are the seasons of the year.

4. Conclusion

The work obtained a satisfactory result, because with the use of the sundial it made possible a more palpable lesson, and a better understanding of the seasons of the year and of the movements of rotation and translation of the Earth. Interdisciplinarity contributed to the development of this work and the classes taught. Another important factor was the holding of a class outside the classroom, providing a break in the traditional classroom routine.

References

Azevedo, S. S. M. 2012. Relógio de Sol Analêmico: Método Pedagógico Interdisciplinar. (Campos dos Goytacazes: Universidade Estadual do norte Fluminense Darcy Ribeiro), 1: 50 p.

Astro.unl.edu. Motions of the Sun Simulator. Program of simulation of apparent movement of the Sun. Available in:`http://astro.unl.edu/naap/motion3/animations/sunmotions.html`. Acess in August 03, 2016.

Oba.org.br. Atividades Práticas da X Olimpíada Brasileira de Astronomia e Astronáutica. Avaliable in: `http://www.oba.org.br/downloads/atividade_pratica_xoba.pdf`. Acess in May 20, 2016.

Shadows 4.0. Program for the design of Sundial and Astrolabe. Available in: `http://www.shadowspro.com/en/index.html`. Acess in August 30, 2016.

Boletim da Sociedade Astronômica Brasileira, **30**, no. 1, 18-19

Look to the sky, see the universe: A university extension project in a non-formal teaching space

M. P. Ferreira, A. J. Roberto Jr., & J. C. Silva

[1] Universidade Federal de Alfenas, Minas Gerais.
e-mail: mauriciopereiraferreira@hotmail.com, arturjustiniano@gmail.com,jcarlos1905@gmail.com

Abstract. In this work the main actions developed in the scope of a project of university extension aimed at the scientific dissemination and the teaching of astronomy in non formal spaces of teaching, as well as some results are discussed. The "Look at the sky, see the universe" project is developed at the Astronomical Observatory (OA) of the Federal University of Alfenas (UNIFAL—MG) – OA-UNIFAL-MG. It is a non-formal teaching space aimed at teaching and disseminating astronomy. two cassegrain telescopes, a CCD camera, a camera for observing objects from the solar system, three newtonian telescopes and three filters for the observation of the Sun.

Resumo. Neste trabalho são apresentadas as principais ações desenvolvidas no âmbito de um projeto de extensão universitária voltado à divulgação científica e ao ensino de astronomia em espaços não formais de ensino, bem como são discutidos alguns resultados. O projeto "Olhe para o céu, veja o universo" é desenvolvido no Observatório Astronômico (OA) da Universidade Federal de Alfenas (UNIFAL—MG) – OA-UNIFAL-MG. Trata-se de um espaço não formal de ensino voltado para o ensino e a divulgação da astronomia e que conta atualmente com dois telescópios cassegrain, uma câmera CCD, uma câmera para observaç ao de objetos do sistema solar, três telescópios newtonianos e três filtros para observação do Sol.

Keywords. Cosmology: observations – Telescopes – Teaching of Astronomy

1. Introduction

The Astronomical Observatory (OA) of the Federal University of Alfenas (UNIFAL-MG) – OA-UNIFAL-MG – was built with resources from the institution and two development agencies, Foundation for Research Support of Minas Gerais (FAPEMIG) and National Council for Scientific and Technological Development (CNPq). It is a space for teaching, research and extension activities in astronomy because this science has enormous potential to spark young people's interest in scientific subjects. In this sense, the importance of the dissemination and teaching of astronomy in non-formal spaces of education, such as the OA-UNIFAL-MG, becomes evident since one of the main roles of these places is to motivate students for science by offering an attractive environment. For this reason, the project Look to the sky, see the universe has as mission to make the dissemination of the science allied to the public utility. In Figure 1 present the OA-UNIFAL-MG.

Figure 1. Left image: OA-UNIFAL-MG; Right image: Students who visited the OA-UNIFAL-MG.

The dissemination of the achievements and the process of production of scientific knowledge can promote the human being's awareness of citizenship, rights and duties towards society, the environment and contribute to the problem-solving of each community. It is about providing opportunities for learning through the confrontation of conceptions and prejudices arising from personal experience with the perspective presented by science. Astronomy may be the science that has the greatest potential to contribute to these opportunities. It is one of the areas that most attracts attention and awakens the curiosity of students, from the first years of school to their graduation courses. The following figure shows a visit made by students from a high school to OA-UNIFAL-MG.

Figure 2. Left image: Students using the 11-inch cassegrain telescope at the OA-UNIFAL-MG; Right image: Untreated images taken from the Moon using telescopes.

Therefore, this project has as its mission to reach large sections of the population and introduce them in the subjects of science and shows them that all this knowledge that has been acquired over the centuries has influenced the way we see ourselves as thinking beings before the universe.

2. Theoretical reference

According to Schivani and Zanetic (2011) non-formal educational spaces such as the observatory have the role of making

naive curiosity advance to an epistemological curiosity that is of utmost importance in the learning process, whether formal or non- formal.

In this sense, the activities proposed in this project will have as theoretical reference the Three Pedagogical Moments (Delizoicov 1991) and (Delizoicov et al. 2002) since this referential allows the progressive monitoring of the critical distance of the visitors in relation to alternative conceptions, or intuitive concepts, for the correct assimilation of knowledge. In the first pedagogical moment, the initial problematization, the visitor will be encouraged to confront his alternative conceptions with scientific interpretations so that he feels the need to acquire knowledge that he does not yet possess to understand the astronomical phenomenon that he is observing. According to Delizoicov et al. (2002):

The problematization can occur in at least two ways. On the one hand, it may be that the student already has notions about the questions posed, the result of his previous learning, in school or outside. Their notions may or may not be in accordance with the theories and explanations of science, characterizing what have been called "alternative conceptions" or "intuitive concepts" of students. The problematizing discussion can allow these conceptions to appear. On the other hand, problematization may allow the student to feel the need to acquire other knowledge that he does not yet possess; that is to say, it poses a problem for him to solve. This is why issues and situations must be problematized.

In the second pedagogical moment, the knowledge organization, this alternative knowledge is studied through various activities - telescope observation, Astro3D and conversation with the teacher - with the objective of developing the physical conceptualization to understand the problematized situations, being necessary the study of the scientific knowledge involved in the first moment. Thus:

The approach to scientific concepts is the point of arrival, both in the structuring of the programmatic content and in the students' learning, leaving the point of departure with the themes and the significant situations that originate, on the one hand, the selection and organization of the content roll, when they are articulated with the structure of scientific knowledge, and, on the other hand, the beginning of the dialogic and problematizing process (Delizoicov et al. 2002).

The third pedagogical moment, the application of knowledge, aims to verify the ability of visitors to use the knowledge acquired in real situations. In the case of the observation activities of the sky with telescope the potential that the visitors acquire to understand the astronomical phenomena when they come across news of the media and also in the formal education.

3. Resources used

This is a non-formal teaching space aimed at the teaching and dissemination of astronomy and currently has two cassegrain telescopes, one of 11 and another 14 inches, 3, a CCD camera, a camera for observing system objects solar, three Newtonian telescopes of 180 millimeters and three filters for observation of the Sun. The project organizes periodic observation sessions and lectures, in the OA-UNIFAL-MG as much in schools and in other places. During the activities the contact with the public makes possible debates on astronomical subjects divulged by the media, demystifying preconceptions and pseudosciences. For nocturnal observations the Stellarium software is used - projecting it on a screen - for the presentation of the constellations and the position of the stars.

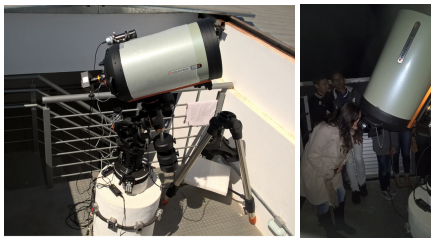

Figure 3. 14-inch cassegrain telescope in equatorial mount found at OA-UNIFAL-MG.

4. Results and discussion

In terms of results, we highlight the systematic progress in the number of schools and students attended, which has contributed to arouse interest in science and scientific careers.

References

Delizoicov, D. Conhecimento, tensões e transições. 1991. 219f. PhD thesis (Education). Faculty of Education, University of São Paulo, São Paulo, 1992.

Delizoicov, D.; Angotti, J. A. P.; Pernambuco, M. M. Ensino de ciências: Fundamentos e métodos. São Paulo: Cortez, 2002.

Schivani, M. e Zanetic, J. 2011. In I Simpósio nacional de educação em astronomia.

Boletim da Sociedade Astronômica Brasileira, **30**, no. 1, 20-21

Sky observation using the moon as a guide

A practical activity proposal for the teaching of astronomy in basic education

Sérgio Mascarello Bisch[1], Marconi Frank Barros[2], & Thiago Pereira da Silva[3]

[1] Departamento de Física da UFES
e-mail: sergiobisch@gmail.com
[2] Escola Estadual de Ensino Fundamental e Médio João Crisóstomo Beleza, SEDU/ES
e-mail: marconibarros05@gmail.com
[3] Centro Estadual de Ensino Médio em Tempo Integral São Pedro, SEDU/ES
e-mail: thiagopereiradasilva@yahoo.com.br

Abstract. The development of practical activities of observation and recognition of the sky has been recommended in Brazilian curricular references, such as PCNs and BNCC. However, its effective implementation by teachers of Basic Education faces several difficulties, one of the main being the lack of training of these teachers in the area of Astronomy and their little or no experience with activities of observation and recognition of the sky. As a strategy to allow teachers, even without familiarity with the recognition of the sky, to promote and carry out such activities, the Astronomy Teaching Laboratory, linked to the UFES Department of Physics, developed a didactic strategy that uses the Moon as a guide for observations. This strategy has been applied, with good results, by teachers of the state education network of Espírito Santo since 2013.

Resumo. A realização de atividades práticas de observação e reconhecimento do céu tem sido recomendada nos referenciais curriculares brasileiros, como os PCNs e a BNCC. Contudo, sua efetiva realização por parte de docentes da Educação Básica enfrenta diversas dificuldades, uma das principais sendo a falta de formação destes docentes na área da Astronomia e sua pouca ou nula experiência com atividades de observação e reconhecimento do céu. Como estratégia para permitir que professores, mesmo sem familiaridade com o reconhecimento do céu, possam promover e por em prática tais atividades, o Laboratório de Ensino de Astronomia (LEA), ligado ao Departamento de Física da UFES, desenvolveu uma estratégia didática que utiliza a Lua como guia para as observações. Essa estratégia vem sendo aplicada, com bons resultados, por professores da Rede Estatual de Ensino do Espírito Santo desde 2013.

Palavras-chave. Teaching of Astronomy, Moon

1. Introduction

The use of the sky as a natural laboratory for performing practical astronomy teaching activities is strongly recommended in Brazilian curricular references, such as the National Curricular Parameters (PCNs) and the current National Curricular Common Base (BNCC), however, the effective implementation of this type of activity faces a great difficulty: the small, or null, training of teachers of Basic Education regarding contents and methodologies of Astronomy teaching and, especially, in relation to the accomplishment of practical activities of sky observation. The teacher, in general, does not know how to carry them out and what can be worked and taught through them. In this sense, the Laboratory of Astronomy Teaching (LEA), linked to the UFES Department of Physics, developed a strategy that aims to allow the accomplishment, with good didactic use, of these activities by teachers with little or no experience with sky observation, but that are interested in carrying them out.

2. Methodology

The strategy takes advantage of the fact that anyone, even having no experience with the location and recognition of stars and constellations, can easily locate the Moon in the sky. In the first step of the proposed methodology, the teacher responsible for the activity, preferably with the advice of an institution dedicated to the public outreach of Astronomy, as a planetarium or didactic observatory, should plan the most favorable nights to carry out the activity, choosing dates in which the Moon is in its crescent phase - which allows it to be observed early in the night - and when it is passing through some of the most conspicuous and easily recognizable constellations, and preferably on a date when one of the planets visible to the naked eye in this same region. A script should then be written and passed on in the classroom to the students with directions on how to observe the sky with the naked eye and drawing record of the Moon and the brightest "stars" of the nearby region to it.

In the next step, the students perform the observations and make records of what they saw in drawings (Figure 1), making notes of the brightest stars and their colors. These observations are carried out outside the school, outdoors, next to the residences in which the students live.

Then, a debate and questioning about what was recorded in the drawings are carried out in the classroom, especially questioning whether all the bright stars recorded would be stars. With the aid of software such as Stellarium, the main stars represented in the drawings are then identified. One of the highlights of the work is the realization by students that one or more of the registered stars are planets, something that most were completely unaware of. This awareness promoted a reconciliation between what is experienced and what is learned in books, between heaven and the Universe.

Ideally, as a final step, the following month, after a lunation, when the Moon has returned, roughly, to the same region of the sky, a new observation, with the naked eye and telescope, should be made at school to apply the knowledge learned in the class-

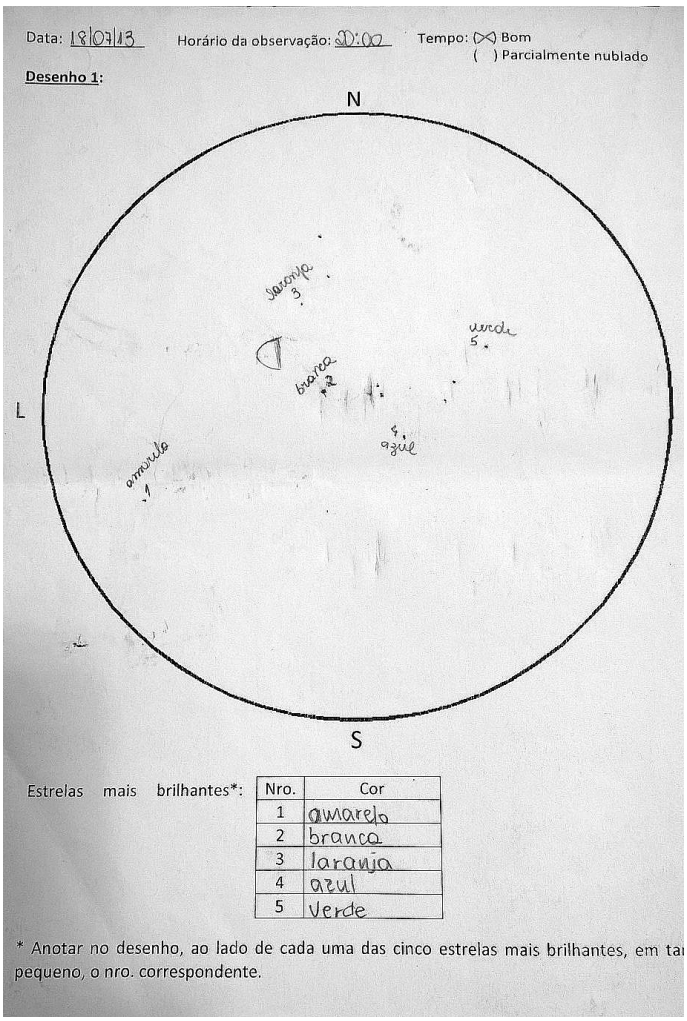

Figura 1. Student drawing, representing the Moon and the brightest stars in the sky.

room and to make the recognition of this sky region and the main constellations and celestial objects in it.

3. Results and Conclusions

The strategy has been successfully applied to High School classes of the Espírito Santo State Education Network since 2013, succeeding in challenging and motivating students to study astronomy and yielding numerous debates in the classroom. One of the most striking results is the students' learning of the existence of planets among the "stars" recorded in their drawings, that several planets are visible to the naked eye and that, in synthesis, the sky is our window to the Universe, through which we can learn about its nature and composition.

Agradecimentos. The authors would like to thank the students and collegues of the schools EEEFM João Crisóstomo Beleza and Centro Estadual de Ensino Médio em Tempo Integral São Pedro who gently supported and enthusiastically participated in the activities of sky observation.

References

Barros, M. F. Os movimentos dos planetas e os modelos de Universo: uma proposta de sequência didática para o ensino médio. 167 f. Masters dissertation (Mestrado Profissional em Ensino de Física) — UFES, Vitória, 2014.

Silva, T. P. da. Nossa posição no universo: uma proposta de sequência didática para o ensino de astronomia no ensino médio. 160 f. Masters dissertation (Mestrado Profissional em Ensino de Física) — UFES, Vitória, 2015.

Boletim da Sociedade Astronômica Brasileira, **30**, no. 1, 22-23

Astronomy in the park

Public outreach activity during the partial solar eclipse of february 26, 2017

Ana Elisa Ferreira[1], Aline Costalonga Gama[2], Fábio Bianchi de Moura[3], & Sérgio Mascarello Bisch[1]

[1] Departamento de Física da UFES. e-mail: elizabrum@yahoo.com.br, sergiobisch@gmail.com
[2] Instituto Federal do Espírito Santo. e-mail: alinecga@yahoo.com.br
[3] EEEFM Aristóbulo Barbosa Leão, SEDU/ES. e-mail: orionchess@gmail.com

Abstract. During the solar eclipse of February 26, 2017, an outreach activity of eclipse observation directed at the public that frequents the park at the weekends was held at Parque da Cidade, Serra, ES. The activity, coordinated by representatives of UFES, SEDU/ES and IFES, was carried out using several resources: reflecting e refracting telescopes for projection of the Sun; solar telescope and special glasses for direct observation of the Sun; masks with soldering filter 14 and sundials. Other activities of dissemination of astronomy, using banners and an interactive model of the solar system, were also promoted. Altogether, about 150 people of all ages were attended in the park between 10 a.m. and 1 p.m. on Sunday.

Resumo. Durante o eclipse solar do dia 26 de fevereiro de 2017, foi realizada no Parque da Cidade, Serra, ES, uma atividade de observação do eclipse voltada ao público que frequenta o parque nos fins de semana. A atividade, coordenada por representantes da UFES, SEDU/ES e IFES, foi realizada usando diversos recursos: telescópio refletor e luneta para projeção do Sol; telescópio solar e óculos especiais para observação direta do Sol; máscaras com filtro de soldador 14 e relógios de Sol. Outras atividades de divulgação da Astronomia, utilizando banners e um modelo interativo do sistema solar, também foram promovidas. Ao todo, cerca de 150 pessoas de todas as idades foram atendidas no parque entre as 10 e 13 horas do domingo.

Keywords. Teaching of Astronomy — Eclipses

1. Introduction

Special astronomical events such as eclipses, due the interest they arouse in the public, are excellent opportunities for the implementation of Astronomy public outreach activities. During the solar eclipse that occurred on February 26, 2017, Carnival Sunday, visible as a partial eclipse in southeastern Brazil, an Astronomy public outreach action was carried out in a public park — the "Parque da Cidade" — in the municipality of Serra, ES, involving the observation of the eclipse and other astronomy teaching activities aimed at the public that attends the park on weekends.

2. Developed Activities

The action was promoted by a network of collaborators made up of students connected to the Astronomy club of IFES-Vitória and the State Teaching Network of the Municipality of Serra, ES, coordinated by representatives of UFES, IFES-Vitória and SEDU/ES.

The observation of the eclipse was performed by various means: by projection of the Sun, with reflector and refractor telescopes; by direct observation, with a Coronado solar telescope, special glasses with filters for observation of the Sun and masks made with cardboard folded in size A4 and made with welder filter number 14. Inside these masks were printed safety guidelines on its use and information on the eclipse.

In addition to the observation of the eclipse itself, other activities of teaching and outreach of Astronomy were also carried out, such as: demonstrations of use and construction of sundials, of the horizontal type and equatorial type, made with a pet bottle; exhibition of banners about the Sun, from the exhibition "Cosmic Landscapes: from Earth to the Big Bang", elaborated in celebration of the International Year of Astronomy 2009; using an interactive model of the solar system, with information about its components and showing the real scale of sizes and distances, elaborated by the Laboratory of Astronomy Teaching (LEA) of UFES (Bisch & Santos Jr. 1993), with the objective of working with children, in a playful and concrete way, concepts associated with the solar system.

3. Results

The public showed good receptivity and participated actively in the observations of the eclipse and other promoted activities. Individual and family attendments were made, explaining the eclipse and working with the interactive model of the solar system, which has a carpet (the Sun itself, with a diameter of 1.60 m) on which are exposed the real-scale size of planets, being that, to each of them, there was also a connected string representing their distances to the Sun, to demonstrate the real scale of distances of the planets to the Sun. This model was used by monitors of the IFES-Vitória, attending mainly to children and working in ludic and concrete way to teach concepts associated with the solar system, such as the new classification of the bodies of this system, which includes the dwarf planets, and the actual proportions of size and distance of its main components relative to the Sun.

The use of A4 size masks made with welder filters was monitored individually, emphasizing the observation duration (10 seconds) and the necessary rest period to the eyes to avoid injuries.

The activities attracted the attention and aroused the interest of the public that was in the park, having been attended, approximately, 150 people of all ages, between 10 a.m. and 13 p.m. on Sunday, February 26, 2017.

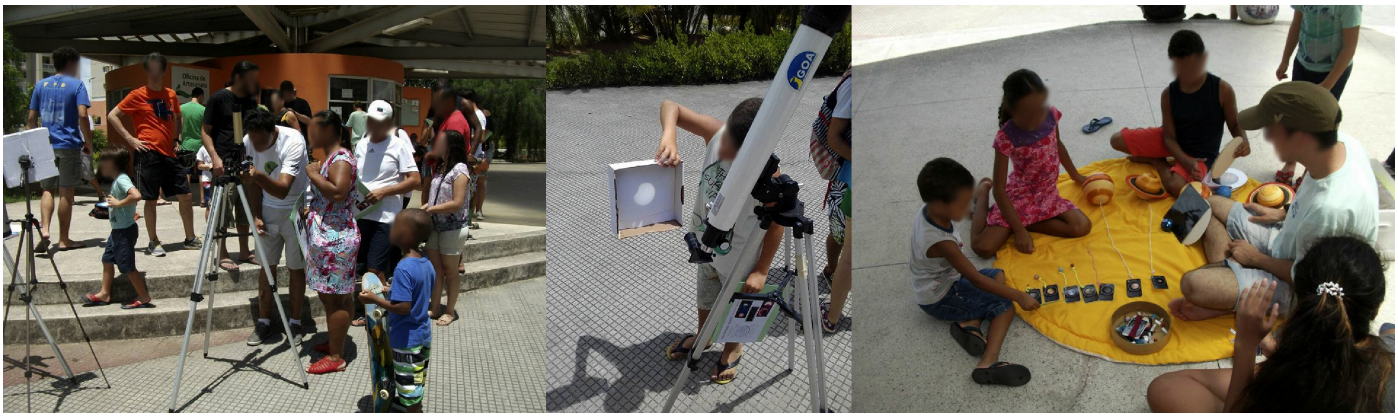

Figure 1. Public outreach of Astronomy at the Parque da Cidade, Serra, ES, during the solar eclipse of February 26, 2017. From left to right: direct observation of the Sun with solar telescope, observation of the sun by projection and ludic activity with the interactive model of the solar system, where the yellow "carpet" represents the Sun.

4. Conclusion

The work accomplished fully achieved its objectives, attending a significant number of people, publicizing knowledges, arousing public curiosity and interest in Astronomy and contributing to the training of students who acted as monitors during the event.

Acknowledgements. The authors would like to thank to the Federal University of Espírito Santo, the Federal Institute of Espírito Santo – Vitória and the Espírito Santo's State Secretariat of Education for their support to the actions of education and public outreach of Astronomy.

References

Bisch, S. M., & Santos Jr., A. A., 1993, in: Atas do X SNEF, SBF (São Paulo: Sociedade Brasileira de Física), p. 575.

Boletim da Sociedade Astronômica Brasileira, **30**, no. 1, 24-25

Application of the restricted problem of the three bodies in teaching physics and astronomy

G. S. Macedo & A. J. Roberto Jr.

[1] Federal University of Alfenas, e-mail: gabrielmacedo154@yahoo.com.br, arturjustiniano@gmail.com

Abstract. In this work, we will present a construction of a small code, which aims to numerically solve the restricted problem of the three bodies. Theme with numerous publications that lodge methods to solve. Here we go beyond solving them apply them in two systems, Sol-Jupiter-Trojan Jupiter and Sol-Neptune-Pluto.

Resumo. Neste trabalho vamos apresentar a construção de um pequeno código, que visa resolver numericamente o problema restrito dos três corpos. Tema com inúmeras publicações que apresentam metodos de como resolver. Aqui vamos alem de resolver aplica-los em dois sistema, Sol-Jupiter-Troiano Jupiteriano e Sol-Netuno-Plutão.

Keywords. Celestial mechanics – Teaching of Astronomy – Chaos

1. Introduction

Isaac Newton (1643-1727) when he published his book: "Philosophiae naturalis principia mathematica", also referred to as principia, wrote the laws of the motion and the law of universal gravitation and also showed the main problem of celestial mechanics, the problem of n bodies (Prazeres 2010). The problem of n bodies can be described as, given to a system with n point masses, that is, points of mass that have their movements governed by gravitation and also given their initial conditions, their position and its speed, what is desired is to know its position and velocity moment future. Mathematically translating is to solve the Ordinary Differential Equations (ODE's) which govern the movement of the body in question. On a system with n bodies there are multiple near collisions make the problem extremely complex, which even present moment, there is no analytical solution (Prado 2001). For n> 2 there is no analytical solution to the problem, but a particular case of the three-body problem (n = 3) has, is the denominated the Three-Body Restricted Problem (PRTC).

The PRTC is a theme with numerous publications in magazines specialized and some in the area of physical education and astronomy. However, in relation to the latter we do not find in the publications application examples of this problem, only the development of methods for solve the related ODE's and it. What for us is a misunderstanding, since the PRTC is an as- directly related to the contents of the subjects of classical mechanics, astronomy and numerical methods and which has great potential to contextualize the study content. Thinking about that, in this work we go present a teaching strategy that can be used to include the PRTC in teaching physics and astronomy. It is, development of a small numerical code for to solve the ODE's of the PRTC by the Cauchy method and graphically simulate the solution found. To exemplify and contextualize we apply in two cases. The system Jupiter, one of its Trojan asteroids and the Sun and the other composed by the Sun, Neptune and Pluto.

2. Restricted problem of the three bodies

Euler in 1772, in his book "Theoria motuum lunae, new methodo pertractata ", proposed a reformulation for the problem of three bodies. This particular case is a version simplified from the three-body problem and became the studied in celestial mechanics due to its applications and was later named by Henri Poincaré (1854 - 1912) of Restricted Problem of the Three Bodies (Prazeres 2010).

Such a problem can be described as follows, given three mass bodies m_1, m_2 (called primary) and m_3 that move under mutual gravitational action and knowing their initial conditions, position and velocity, desires to determine their subsequent motions (Prado 2001).

The three-body problem has no analytical solution due to unsurpassed mathematical complications, but a particular case it has solution and multiple applications this and the Restricted Problem of Three Bodies. There are several cases of PRTC, but we will be concerned about the problem restricted circular plane of the three bodies. Hellings (1994) describes the simplifications made in the problem of three bodies which are:

1. The mass of the third body is practically zero, that the third body has no in the orbits of the primary.

2. The orbits of the circular primaries.

3. The third body moves in the orbital plane of the primaries. This restriction implies an important simplification mathematics, since now the complete description of the prob- lems becomes two-dimensional.

3. Methodological Procedures

The equation that governs the movement of bodies is the Law of Universal Gravitation, this is the most important equation because all others derive from it. Based on the declarations 1,2 3 we can discard equations of motion of the primary staying only with the equation of the third body and equating Newton's second Law with the Law of Universal gravitation and using the coordinate system dimensionless to simplify the equations of motion as described by Hellings (1994), we arrive at the equations that govern the movement of the third body.

$$x'' = -(1-\mu)\frac{x-\mu}{R_1^3} - \mu\frac{x+1-\mu}{R_2^3} + x + 2y' \quad (1)$$

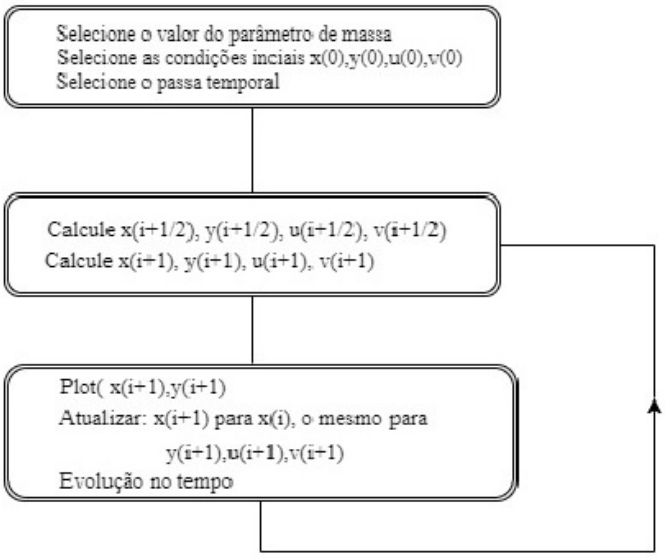

Figure 1. Cauchy numerical method

$$y'' = -(1-\mu)\frac{y}{R_1^3} - \mu\frac{y}{R_2^3} + y - 2x' \tag{2}$$

onde

$$R_1 = \sqrt{(x-\mu)^2 + y^2} \tag{3}$$

$$R_2 = \sqrt{(x+1-\mu)^2 + y^2} \tag{4}$$

In order to solve equations 1 and 2 it was de- developed a small algorithm that uses the Cauchy method, being necessary as initial parameters the ratio mass, initial position, x_0 and y_0, and the speeds initials x_0' and y_0'. The method used is described in the figure follow.

4. Results

We apply the algorithm developed in system the Sol–Jupiter–Asteroid and we managed to trace the periodic orbit of a Jupiterian asteroid, see Fig. 2.

And also in the Sun–Netuno–Pluto system we to calculate the Pluto's libration due to Neptune, as shows 3.

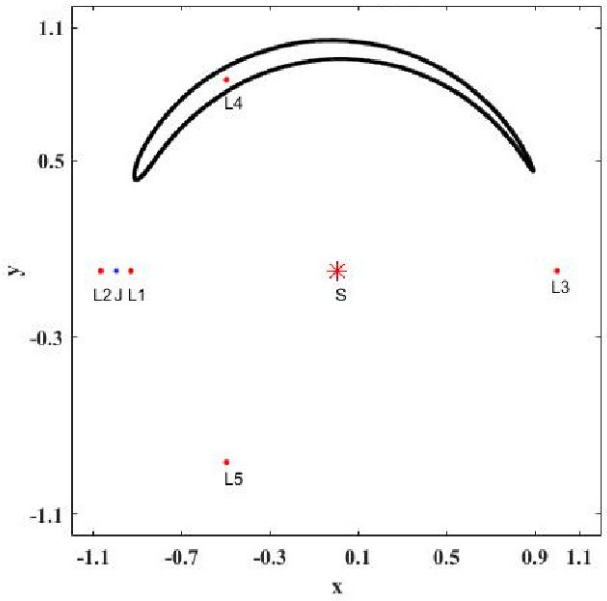

Figure 2. Orbit of a Jupiterian Trojan asteroid

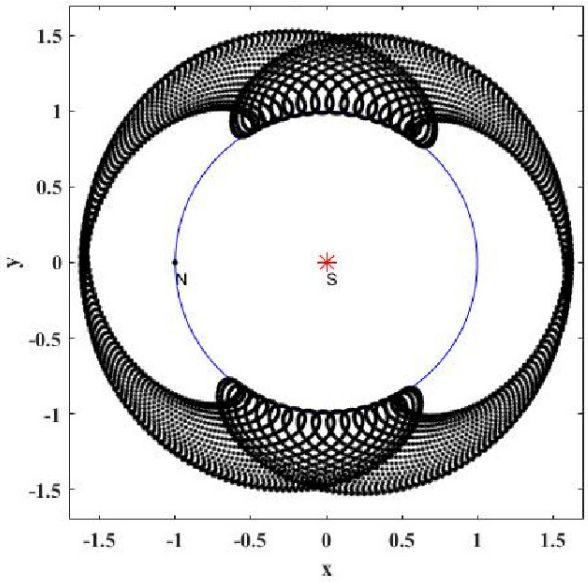

Figure 3. Pluto Orbit disturbed by Neptune

5. Conclusion

With the results we noticed that the present work has a potential in the teaching of physics and astronomy, aiming mainly at the dynamics of celestial bodies. Therefore, our project is to transfer this code to a more attractive graphical platform to be used as a teaching tool and the construction of a teaching sequence that can be applied in the disciplines of physics and astronomy.

References

Prado, A. F. B. A. 2001, Trajetórias Espaciais e Manobras Assistidas por Gravidade. Instituto Nacional de Pesquisas Espaciais — INPE, 2001.

Hellings, P. 1994, Astrophysics with a PC: An Introduction to Computational Astrophysics, 1994.

Prazeres, R. F. 2010, Métodos Clássicos e Qualitativos no Estudo do Problema dos Três Corpos, 2010.

Boletim da Sociedade Astronômica Brasileira, **30**, no. 1, 26-27

Binary Stars 3D

An app for teaching astronomy

G. S. Macedo, H. L. C. Pinto, A. J. Roberto Jr., & P. A. Bressan

[1] Federal University of Alfenas, MG. e-mail: gabrielmacedo154@yahoo.com.br, e-mail: hugo.lcpinto@gmail.com, e-mail: arturjustiniano@gmail.com, e-mail: Paulo.Bressan@gmail.com

Abstract. In this work we will present an app that can be used for both teaching and research. This app simulates a compact binary stellar system and also the light curve of such a system. The app is operated in three different modes. With the app we hope to contribute with the insertion in the market of pedagogical tool that uses a smartphones and tablets technology increasingly present in the hands of researchers, students and teachers.

Resumo. Neste trabalho vamos apresentar um aplicativo que para ser utilizado como ferramenta didática, um aplicativo que simula de forma tridimensional um sitema estelar binário compacto e também a curva de luz deste sistema. O aplicativo é operado em três diferentes modos e foi desenvolvido para aparelhos que possuem o sistema operacional android. Com o aplicativo esperamos contribuir com a inserção no mercado de uma ferramenta didática que utiliza os smartphones e tablets, tecnologia cada dia mais presente nas mãos de pesquisadores, alunos e professores.

Keywords. Stars: mass-loss – binaries: general – Teaching of Astronomy

1. Introduction

A binary stellar system it is composed of two stars that are connected under attraction of mutual gravity and which orbit a center of mass common . Currently, we know that more than half of the stars in the sky, about 60% of the stars of the Milky Way are in systems like these or with more stars as described by osorio.

Such systems are great laboratories in which to study diverse physical contents as Law of Universal Gravity and at Laws of Kepler. However, systems like these are studied by direct observation, which depends on some variables such as climate, power of the telescope used, whether the system is eclipsed or not, among others. Images and animations for computers such as "StarLightPro", which are used for systems studies, but without much interaction with the user and the use of a resource anywhere in the classroom and easily in the hands of the students.

Taking into account the various variables that involve the study of systems like these and the fact that the number of users of mobile devices has been increasing exponentially and that the use of mobile technologies makes it possible for learning to occur at any time, by anyone as pointed out by Neves et al. (2014) and supported by the National Curriculum Parameters (PCN's) and its complementary guidelines (PCN +), specifically in the theme "Universe, Earth and Life", which presents the teaching of astronomy, we will present in this work an application that simulates three-dimensional and interactive form a compact binary stellar system designed for mobile devices, smartphones and tablets, which use Android technology.

2. App Description

Binary Stars 3D is an app developed in the programming language C sharp (C#) on the Unity 3D platform that simulates a compact binary stellar system composed of a white ana star and a low main sequence star, also called primary and secondary respectively. The app is operated in three different modes.

In mode 1 (Fig. 1) the two stars of the main sequence they fill the lobe of Roche (LR).

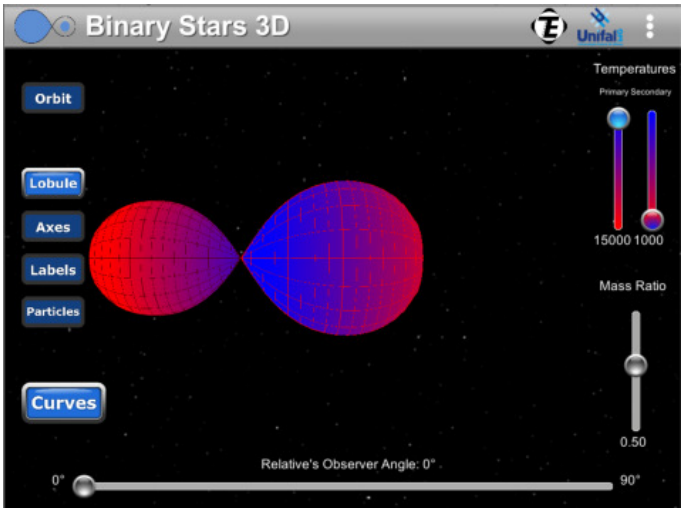

Figure 1. Semi-Contact Binary System.

In mode 2 (Fig. 2) the secondary star fills LR and the primary star is a white dwarf.

At last (Fig. 3), the secondary star expands beyond its LR, and we see the shape of the disk of acretion around the white dwarf. This acretion disk is formed due to the mass loss of the secondary star by the lagrangian point L_1.

In all three modes it is possible to place the system to orbit around the center of mass, visualize the spatial dimensions x, y, z, vary the angle of observation, the three collinear lagrangian points, L_1,L_2 e L_3, vary the ratio of masses of the system, $q = \frac{m_1}{m_2}$, the temperature of the stars and simulate the light curve (Fig. 4) and send the data by e-mail.

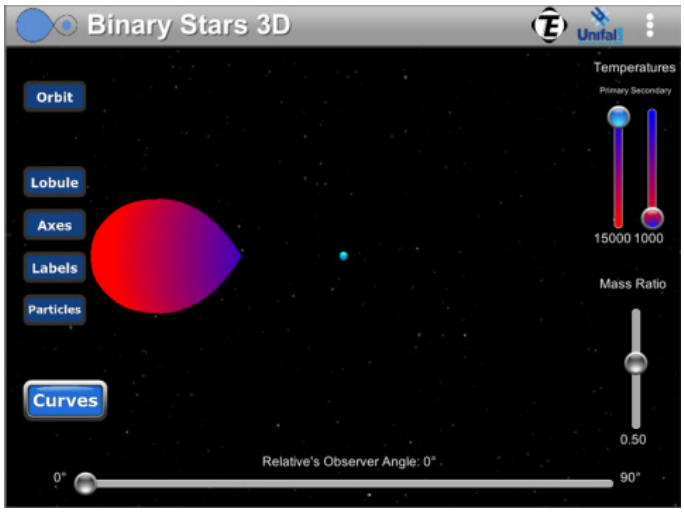

Figure 2. Roche lobes of the Binary System.

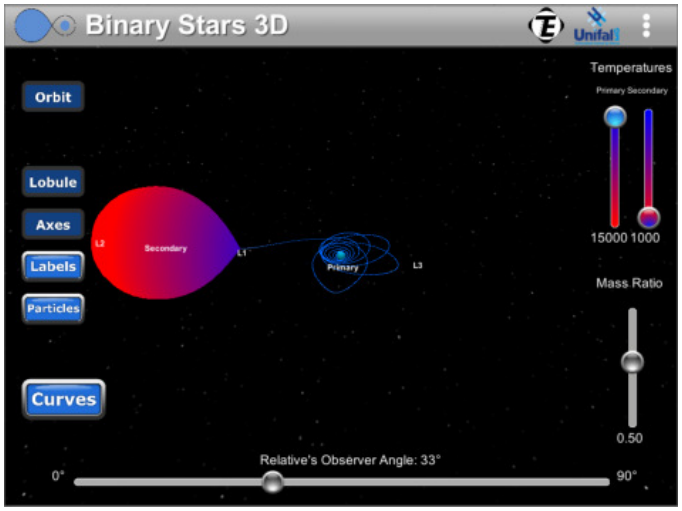

Figure 3. Formation of the Accretion Disc.

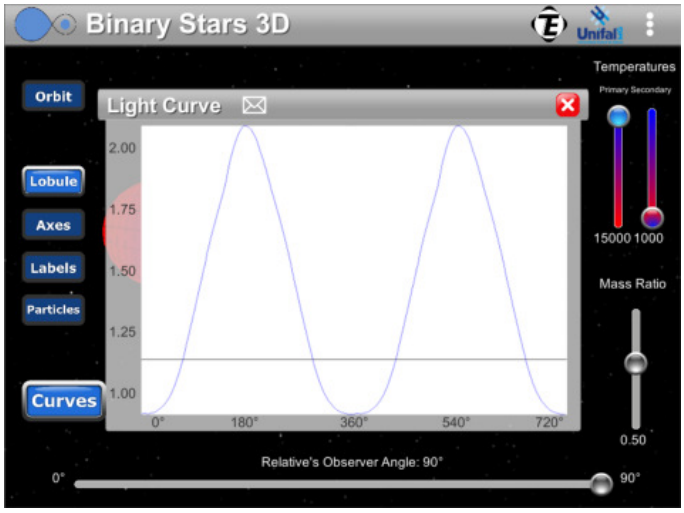

Figure 4. Binary System Light Curve.

3. Conclusion

The app showed great feedback regarding interactivity, performance, graphics and we expect contribute to the teaching of astronomy. With the introduction of contents related to stellar astrophysics in higher education and in the medium, using as teaching tool a technology that is widely used by students, smartphones and tablets.

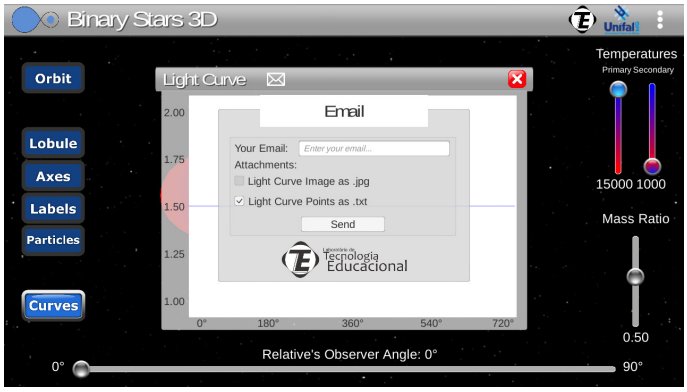

Figure 5. Data upload screen.

Acknowledgements. The Foundation for Support of Research of the State of Minas Gerais - FAPEMIG for the financial assistance. To the Laboratory of Educational Technology - LTE and the Federal University of Alfenas for the structure and support.

References

Osorio, Y. F. M. 2009, Determinação do Período Orbital de Sistema Binários Eclipsantes.

Gálvez, J. C. T. 2012, Análise de binárias eclipsantes no bojo da galáxia com dados OGLE-II usando o código Eilson-Devinney.

Neves, B. G. B., Melo, R. S., & Machado, A. F. 2014, Universo Móvel: um aplicativo educacional livre para dispositivos móveis. **Texto Livre**: Linguagem e Tecnologia, 7, 34

Kepler, S. O., Saraiva, M. F. O. 2000, Astronomia e Astroísica, Porto Alegre: Editora da Universidade/UFRGS, 2000.

BRASIL, Orientação Educacionais Complementares aos Parâmetros Curriculares Nacionais para Ensino Médio (PCN+). Ciências da Natureza e Matemática e suas tecnologias. Braília: MEC. 2002.

Boletim da Sociedade Astronômica Brasileira, **30**, no. 1, 28-28

Verification of Titius-Bode Law in exoplanetarian system and determination of functions that describes star-planets distances

Vinícius Lima dos Santos & Marcos Rogerio Calil

[1] Colégio Dante Alighieri, e-mail: vini.lima.santos@uol.com.br, e-mail: astronomocalil@gmail.com

Abstract. The Titius-Bode Law can determinate the star-planets distances of the Solar System planets with precision. However, this law does not work in exoplanetiarian systems. This project discovered that using equations of degrees 2 to 6 is possible to determinate the star-planets distances with precision in relation with the data disclosed by NASA Exoplanet Archive

Resumo. A Lei de Titius-Bode consegue determinas as distâncias planetas-estrela dos planetas do Sistema Solar com precisão. Entretando, tal lei não funciona em sistemas exoplanetários. Este projeto descobriu que, utilizando equações de graus 2 até 6, é possível determinar as distâncias planetas-estrela com precisão em relação aos dados divulgados pela NASA Exoplanet Archive

Keywords. Planets and satellites: detection – History and philosophy of astronomy – History of Astronomy

1. Introduction

In 1766, Johan Daniel Tietz began calculations to determine the distances between planets and Sun (From Mercury to Uranus). In 1766, Johann Bode improved the calculations that become known as Titius-Bode Law. Compared to the current data, the formula, described by $d_n=4+3\cdot2^n$, can determine the star-planets distances, without exceeding 5.5% of the actual values. However, from the planet Neptune, the calculated values diverge more than 29.08%.

2. Methodology

The initial objective of this project was to verify if the Titius-Bode Law applies to exoplanetary systems with more than three planets. Fifteen exoplanetary systems were selected. As the formula, even when altered to adapt itself to the exoplanetarian system, did not obtain accurate results in the selected sample, we started to describe the star-planets distances based on linear and non-linear regression, plotted in scatter plots. After the tests, a low margin of error was obtained in linear systems, however, a high margin of error was obtained in non-linear systems. Then, other formulas were created based on polynomial calculations of degrees 2 to 6 to adquire more precise results to non-linear systems.

3. Conclusion

It was found that equations of second and third degree have the most accurate results compared to degrees 3 to 6. In addition, compared with the NASA Exoplanet Archive, the calculations presented a smaller margin of error or equal to the data disclosed by that institution. The exception occurred with thirds and fourths planets, where the error reaches more than 8% of the reveled by NASA. However, due to the diameter of the planets, even the thirds and fourths planets are found using the equations of each system. About the firsts and seconds planets, it is not possible create equations for them due to insufficient number of elements to assemble a chart. As a result, with the project effectiveness it is possible to determine star-planet distances regardless of the exoplanetarian system.

References

Bonnet, C. 1764, in Contemplation de la nature, (Amsterdam : Chez M.-M. Rey), 4
Bovair, T. Linewaver, C. H. 2013, in Monthly Notices of the Astronomical Society
Chang, H. 2010, in Journal of Astronomy and Space Sciences, 27, 1
Fernandes, J. 2000, in Jornal electrónico publicado pelo Observatório Astronómico da Universidade de Coimbra, 3
Kepler, S. O. Saraiva, M. F. O. 2000, in Astronomia e Astrofisica
Gaenier-Malet, J. P. 2006, in Double Cause
Godoi, V. M. S. in viXra.org
Huang, C. X. Bakos, G. 2010, in Cornell University Library
Lam, A. 2014, in Astrobites
Naficy, K., Ayubinia, A. Saeedi, M. 2012, in Iranian Journal of Physics Research, 12, 3
Varella, I. G. 2005, in Uranometria Nova
Voisey, J. 2011, in Universe Today

Boletim da Sociedade Astronômica Brasileira, **30**, no. 1, 29-30

The state of art of research on conceptual errors of Astronomy in Brazilian didactic books (1986-2016)

P. H. A. Sobreira[1]

[1] Planetarium of the Federal University of Goiás e-mail: sobreiracosmografia@yahoo.com.br

Abstract. Conceptual errors in Astronomy had been appearing in didactic books after the 1930s, and the worst level of quality occurred in the 1980s and 1990s. Methodology of this research was the state of the art between 1986 and 2016. At this period, there were 10 almost triennial evaluations of the PNLD (Sciences and Geography) and PNLEM (Physics and Geography), which was interleaved by an increasing number of academic works that show the continuity of conceptual errors in didactic books.

Resumo. Erros conceituais na Astronomia apareceram em livros didáticos após a década de 1930, e o pior nível de qualidade ocorreu nos anos 80 e 90. A metodologia desta pesquisa foi o estado da arte entre 1986 e 2016. Neste período, foram realizadas 10 avaliações quase trienais do PNLD (Ciências e Geografia) e PNLEM (Física e Geografia), que foram intercaladas por um número crescente de trabalhos acadêmicos que mostram a continuidade dos erros conceituais nos livros didáticos.

Keywords. Publications – Bibliography – Teaching of Astronomy

1. Introduction

The didactic books have short and imprecise texts; they propagate authors' mental models and conceptual errors. The figures are two-dimensional and out-of-scale; this prevents understanding of some phenomena and concepts that needs to be shown three-dimensionally. Conceptual errors in Astronomy had been appearing in didactic books after the 1930s, and the worst level of quality occurred in the 1980s and 1990s, when the academic community produced 9 critical papers before the official assessments of the PNLD (National Textbook Plan) and PNLEM (High School).

2. Metodology

The methodology of this research was the state of the art between 1986 and 2016, from 7 publications about High School books and 41 from Elementary School II. Sources were journals, Meeting Minutes of SNEA's, SNEF's and ENPEC's, abstracts of SAB's annual meetings and the Database of dissertations and theses about Astronomy Education of the UFSCar (Academics).

3. Results

At this period, there were 10 almost triennial evaluations of the PNLD (Sciences and Geography) and PNLEM (Physics and Geography), which was interleaved by an increasing number of works that show the continuity of conceptual errors in didactic books, notably after the 2010s with the SNEA's meetings (11 works). In the last few years, the quality of information has improved, common conceptual errors have disappeared from the didactic books, but some still persist, and astronomers need to increase their participation in the MEC assessment teams. The spatial distribution of the researches membership is: SP (28), PR (4), RJ (4), DF (2), MG (2), BA (1), GO (1) and RS (1).

4. Bibliography used

The following is a list of sources that deals with this problem.

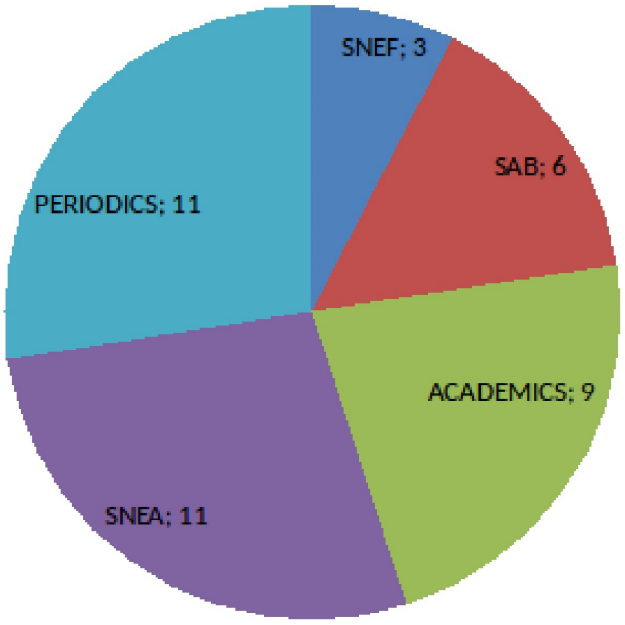

Figure 1. Sources of publications

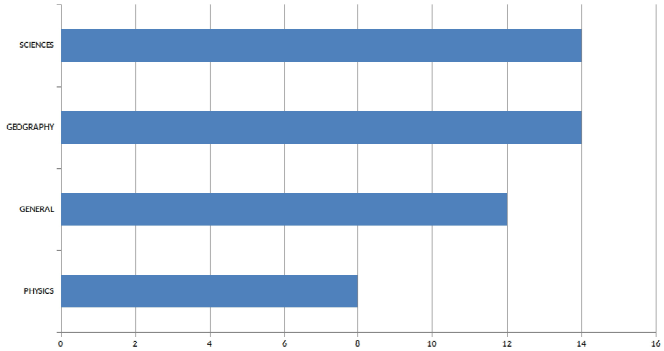

Figure 2. Number of evaluating publications acording to the didactic books areas

– Amaral, P.; Oliveira, C. E. Q. V. de. Astronomia nos livros didáticos de Ciências – Uma análise do PNLD 2008. RELEA, 2011, n. 12
– Bezerra, R. M.; Sobreira, P. H. A. Astronomia no livro didático de Ciências. In: XXX Reunião anual da SAB. Boletim da SAB, 2004, v. 24. p. 81
– Boczko, R. Erros comumente encontrados nos livros didáticos do ensino fundamental. In: EXPOASTRO98 Astronomia: educação e cultura, Anais...SAAD, 1998, p.29
– Canalle, J. B. G. Técnicas de análise de livros didáticos do 1º grau e dos seus conteúdos de Astronomia. Boletim da SAB, 1998, vol. 17, n. 3, p. 37
– Canalle, J. B. G.; Trevisan, R. H.; Lattari, C. J. B. Análise do conteúdo de astronomia de livros de Geografia de 1º grau. Caderno Brasileiro de Ensino de Física, 1997, v. 14, n. 3, p. 254
– Daminelli Neto, A.; Toma, E. Y. O conteúdo de Astronomia nos livros de Geografia do 1o grau. In: XII Reunião anual da SAB, 1986, Resumos. p.60
– Lago, L.; Mattos, C. M. Apresentação das fases da Lua nos livros didáticos de Ciências e Física: Uma amostra dos últimos trinta anos. I Simpósio Nacional de Educação em Astronomia, 2011, p.28
– Langhi, R. Nardi, R. Ensino de Astronomia: erros conceituais mais comuns presentes em livros didáticos de Ciências. Caderno Brasileiro de Ensino de Física, 2007, v. 24, p. 87
– Leite, C.; Hosoume, Y. Astronomia nos livros didáticos de Ciências – Um panorama atual. In: XVI Simpósio Nacional de Ensino de Física, Anais - internet. SBF, 2005
– Morais, P. V. de; Moreira, M. D.; Sales, N. L. L. Análise de erros conceituais e desatualizações de livros de Ciências e Geografia após a análise do PNLD. II Simpósio Nacional de Educação em Astronomia, 2012, p.24
– Oliveira, A. P. de. Abordagem da Astronomia nos livros aprovados pelo PNLD. III Simpósio Nacional de Educação em Astronomia, 2014, p.21
– Oliveira, E. A. G., Leite, C. Ensino de Astronomia nos anos iniciais do Ensino Fundamental – Análise de livros e documentos oficiais. III Simpósio Nacional de Educação em Astronomia, 2015, p.21
– Oliveira, P. H. P. Leis de Kepler do movimento planetário nos livros didáticos de Física do PNLD de 2014: Um estudo à luz de aspectos conceituais, didático-metodológicos e históricos. Dissertação (Mestrado Profissional) – Programa de Pós-Graduação em Astronomia, UEFS, 2015
– Prestes, P. M. de A.; Braga, A. O.; Barros, V. P.; Moreau, A. Conteúdos de Astronomia nos livros didáticos: Uma análise a partir dos PCN+. II Simpósio Nacional de Educação em Astronomia, 2012, p.24
– Rodrigues, M. A. Os planetas do sistema solar em livros didáticos de ciências da quinta série do ensino fundamental. Experiências em Ensino de Ciências, 2007, v.2, n.2, p.1
– Rodrigues, M. de S.; Leite, C. Astronomia cultural em livros didáticos de Física aprovados no PNLEM 2012. II Simpósio Nacional de Educação em Astronomia, 2012, p.24
– Selles, S. E., Ferreira, M. S. Influências histórico-culturais nas representações sobre as estações do ano em livros didáticos de Ciências. Ciência e Educação, 2004, v.10, n.1, p.101
– Silva, R. O.; Sobreira, P. H. A.; Barrio, J. B. M. Orientação geográfica: análise crítica dos livros didáticos de Geografia do PNLD 2011. In: XXXVII Reunião anual da SAB, Boletim da SAB, 2012, p. 79
– Simões, C. C. Elementos de Astronomia nos livros didáticos de Física. Dissertação (Mestrado). Programa de Pós-Graduação em Ensino de Ciências e Matemática, PUC-Minas, 2009
– Sobreira, P. H. A. Astronomy in Brazilian didactic books of Geography. In: International Astronomical Union XXVII General Assembly, Abstract Book, 2009, p. 432
– Trevisan, R. H. Assessoria na avaliação do conteúdo de Astronomia nos livros didáticos de Ciências do primeiro grau. Boletim da SAB, 1995, vol. 15, n. 1
– Trevisan, R. H.; Lattari, C. J. B., Canalle, J. B. G. Assessoria na avaliação do conteúdo de Astronomia dos livros de Ciências do primeiro grau. Caderno Brasileiro de Ensino de Física, 1997, v. 14, n. 1

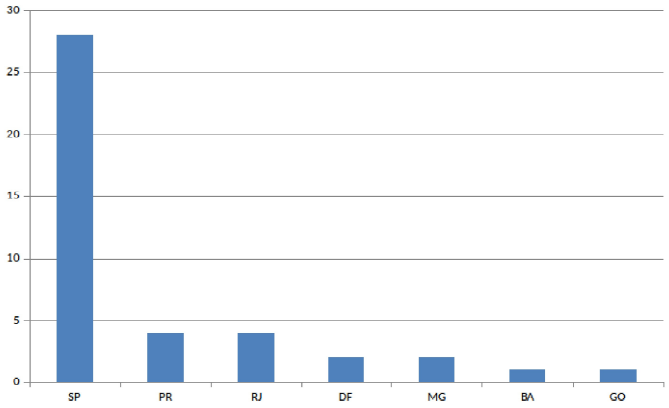

Figure 3. Spatial distribution of the research institutions in Brazil

Boletim da Sociedade Astronômica Brasileira, **30**, no. 1, 31-32

Description of variable stars visible in small observatories for teaching purposes

M. M. de Brito & A. J. Roberto Junior

[1] Federal University of Alfenas (UNIFAL-MG). e-mail: monique15brito@gmail.com, arturjustiniano@gmail.com

Abstract. In this work we present a methodology to identify which variable stars of the General Catalog of Variable Stars (GCVS) can be observed in a given observatory, with a certain instrumental configuration and what is the best time of the year for observation. In order to exemplify the developed method, we present the results obtained for the Astronomical Observatory (OA) of the Federal University of Alfenas, Brazil.

Resumo. Neste trabalho apresentamos uma metodologia para identificar quais estrelas variáveis do General Catalogue of Variable Stars (GCVS) podem ser observadas em um determinado observatório, com uma determinada configuração instrumental e qual a melhor época do ano para a observação. A fim de exemplificar o método desenvolvido, apresentamos os resultados obtidos para o Observatório Astronômico (OA) da Universidade Federal de Alfenas, Brazil.

Keywords. Astrometry - Stars: variables

1. Introduction

Although they are a minority among all stars in the universe, variable stars constitute a very important area of stellar astrophysics (Kepler & Saraiva 2014). By analyzing the nature of the variability of these stars it is possible to obtain information about stellar properties such as mass, radius, luminosity, temperature, internal and external structure, composition and evolution (Lopes 2013).

An important source of information about variable stars is the catalog developed by a variable star research group at the Moscow State University in Russia, the General Catalog of Variable Stars (GCVS) (Samus et al. 2017). This catalog relies on a vast set of data regarding the variable stars mapped in the Milky Way and also neighboring galaxies.

In this work we present a strategy to identify the GCVS variable stars that can be monitored in na astronomical observatory, according to its location and instrumental configuration. The work is divided into 3 parts. In the first one will be presented the main concepts on variable stars. In the second the concepts about position astronomy, important for the understanding of the methodology developed. n the third part we will determine the variable stars that can be monitored in the UNIFAL-MG astronomical observatory. In the final considerations will be presented suggestions of teaching and research activities, at postgraduate level in teaching physics and astronomy about variable stars.

2. Variable Stars

Most stars have luminosity virtually unchanged in time. Occurs the slow variation of brightness due to the own process of stellar evolution, which entails in the change of stars deposition in the HR diagram. But there is a class of stars, the variable stars, whose luminosity varies in a short period of time.

The variable star concept applies only to the observable phase of the star throughout human existence. By measuring and recording the variability of the magnitude of the variable stars as a function of time, it allows the stellar light curve to be established. The behavior of this type of star can be studied by analyzing its light curve, making possible the determination of the period of variability of the star. The period is the amount of time it takes the star to pass through a complete cycle — from maximum magnitude to minimum magnitude — to return the maximum magnitude.

Variable stars are divided into two groups: intrinsic variables and extrinsic variables. The intrinsic variables are those in which the variability of its brightness stems from the star's own physical structure (contractions, expansions, eruptions and explosions in its outer layers). The extrinsic variables are those in which the variability of their brightness results from factors external to the stellar physical constitution (partial or total eclipses in binary or multiple systems, spots in the star's chromosphere).

3. Position Astronomy

The Sun in its movement through the ecliptic, apparent trajectory that the star travels throughout the year, presents different configurations in the sky. In the passage of the Sun by the vernal point (or Aries point), which occurs when the ecliptic intercepts the celestial equator, the star has a right ascension (α) equal to 0h (zero hours). The day of the year in which this event occurs is called the march equinox. The right ascension of a star is the angle measured on the celestial equator between the meridian of the vernal point and the meridian in which the star is found, varies between $0\text{h} \leq \alpha \leq 24\text{h}$. When a star has $\alpha = \pm\ 12\text{h}$ than the right ascension that the Sun is, that is, it is diametrically opposite to the Sun in the celestial sphere at that date, the star is in the best position for its observation.

Why use the Sun as a reference? Knows if approximately the day of the year in which the Sun has $\alpha = 0h$, so it is possible to determine the Julian date corresponding to that day. By means of the julianed equinox date of march it will be possible to find the julian day corresponding to the best date for the observation of each star. After being found the julian day it will be easy to define the julian date of each of the stars. Then, by means of some simple calculations, we will convert that date julian to gregorian date.

3.1. Determination of the best Julian day for observation

The following is the step-by-step guide for determining the best date of the year for stargazing. More detailed information on julian date conversion, position astronomy concepts can be found in Boczko (1984).

1. Determine the Julian date (JD) dated 03/20/2017:

$$\mathrm{JD} = \mathrm{int}(365,25 * \mathrm{Year} - T) + \mathrm{int}(30,6001 * (\mathrm{Month} + 1)) + \mathrm{Day} + 1720994,5 + \frac{\mathrm{Hour}}{24} \quad (1)$$

2. Days (D) passed from day 0 to 20/03 in the Julian calendar:

$$\mathrm{D} = \mathrm{JD} - \mathrm{JDO} \quad (2)$$

   The JD0 finds a value based on the date 0/1/Year at 12h (Bierrenbach 2017). The JD0 is obtained by the same equation used to calculate the JD, considering that it will only have changes regarding the value of the date and time.
3. Star diametrically opposed to the sun:

$$\alpha < 12\mathrm{h}, \mathrm{soon}\ \ \alpha_{\mathrm{Sun}} = \alpha - 12 \quad (3)$$

$$\alpha > 12\mathrm{h}, \mathrm{soon}\ \ \alpha_{\mathrm{Sun}} = \alpha + 12 \quad (4)$$

4. For the Sun to vary by 1h to α Sun:

$$\alpha * \mathrm{number\ of\ days} = 365,25/24\mathrm{h} \approx 15,219\mathrm{days/hour} \quad (5)$$

5. Julian day corresponding to the value of α Sun:

$$\alpha_{\mathrm{Sun}} * \mathrm{number\ of\ days} = \mathrm{X} \quad (6)$$

   We should point out that the above calculation is made from the date of the equinox in March, that is, by that date a certain amount of days will have passed. Thus, the result of equation 5 should be summed with the result found in equation 2.
6. Julian day:

$$\mathrm{Julian\ Day} = X + D \quad (7)$$

   A consequence of the result obtained by equation 6 is that this value can exceed the quantity of 365 days. If so, admit the following condition:
   If Julian day < 365 days: Julian day = Julian day;
   If Julian day > 365 days: Julian day = Julian day – 365.
7. Julian Date (JD) corresponding to the best day for stargazing:

$$\mathrm{JD} = \mathrm{JD0} + \mathrm{Julian\ Day} \quad (8)$$

8. The last step is the conversion of julian date to Gregorian date (day, month, year) for each of the variable stars. Detailed and detailed step-by-step explanations of how to do this conversion is found in reference (Bierrenbach 2017).

4. Variable Stars of the GCVS observable in the OA of UNIFAL-MG

Monitoring any celestial body requires that at least two conditions be allowed: location on planet Earth and instrumentation used. For the location of the Astronomical Observatory (OA) of the Federal University of Alfenas (latitude 21°25′45″ south of the equator and longitude 45°56′50″ West of the Greenwich meridian) the best candidates have declination in the range $-40° \leq \delta \leq 10°$.

The other criterion for the selection of stars concerns the potentiality of the instrument of observation. A relevant feature when it comes to a telescope is the size of your mirror or lens. The larger the aperture of the telescope, the greater the amount of light it can capture. The OA has as its main observation instrument a reflecting telescope with a 14"(fourteen-inch) mirror, a small telescope. Weak light stars, that is to say with an apparent magnitude higher than 10, are unfeasible and unlikely to be observed in the OA telescope. In this way, variable stars with a minimum apparent magnitude of less than 10 were selected.

5. Conclusions

A total of 1807 GCVS variable stars were possible to be observed in the OA of the Federal University of Alfenas. In this mapping appeared stars of different types of variability, with 70.6% of intrinsic nature, 26.1% have extrinsic variability and 3.3% without identification by GCVS. Of the total intrinsic variable stars, 49.09% correspond to long-period Mira and semi-regular variables. Among the stars of extrinsic variability the eclipsing binary systems of the Algol type appeared more frequently, corresponding to 8.23% of this group. The method to characterize the variable stars as described in this work seems to be a good proposal for the teaching of astronomical concepts, making possible that teaching and research activities at the undergraduate and graduate levels regarding the variable stars are performed.

References

Kepler, S. O., Saraiva, M.F.O. 2014, Astronomia e Astrofísica, (São Paulo: Editora Livraria da Física), pg. 282

Lopes, C. E. F. 2013, in Estudo sistemático de estrelas variáveis na era dos grandes surveys. UFRN: Tese de doutorado, pg. 1-2

Samus, N. N., Kazarovets E. V., Durlevich O. V., Kireeva N. N., & Pastukhova E. N. 2017, Astronomy Reports, 61, 80

Bierrenbach, G.L.N. 2017, Astronomia de Posição — notas de aula, versão 01/02/2017, IAG/USP. Disponível em `http://www.astro.iag.usp.br/~gastao/AstroPosicao/Curso2016.pdf`, acesso em 28/6/2017. pg. 12-13.

Boczko, R. 1984, Conceitos de astronomia, (São Paulo: Editora Edgard Blücher), pg. 44-45.

Boletim da Sociedade Astronômica Brasileira, **30**, no. 1, 33-34

Digital resources and low cost of teaching materials for astronomical education

Ludemar Paladino[1] & Marcos Rincon Voelzke[1,2]

[1] Universidade Cruzeiro do Sul, São Paulo. e-mail: ludemarp@yahoo.com.br
[2] Geophysik und Institut fur extraterrestrische Physik — Technische Universitat Braunschweig, Germany. e-mail: mrvoelzke@hotmail.com

Abstract. This work presents the results of the application of two questionnaires about Astronomical concepts in three classes in the first year High School of a public school in the periphery of São Paulo. In the first questionnaire was verified the prior knowledge of students. Then the intervention strategies were carried out: use of digital resources of the school, construction of mock-ups using low cost materials and the use of educational books, such as Couper & Henbest (1997), Horvath (2008). After four months, the second questionnaire was applied to verify the occurence of meaningful learning.

Resumo. Este trabalho apresenta os resultados da aplicação de dois questionários sobre conceitos de Astronomia em três turmas do primeiro ano do Ensino Médio de uma escola pública na periferia de São Paulo. No primeiro questionário foram verificados os conhecimentos prévios dos alunos. Então as estratégias de intervenção foram realizadas: uso de recursos digitais da escola, construção de maquetes usando materiais de baixo custo e a utilização de livros educativos, tais como Couper & Henbest (1997), Horvath (2008). Depois de quatro meses, o segundo questionário foi aplicado para verificar a ocorrência de aprendizagem significativa.

Keywords. Teaching of Astronomy

1. Introducion

The theory of a meaningful learning is a theory developed to be used in practice inside the classroom, using the students' previous knowlwdge. In order check the occurrence of that learning in Astronomy classes using the facilities which school provides. The teacher might guide the digital resources at his or her fingertips to improve the Astronomy teachings, and he or she might understand the reality that students belongs of. According with Moran et al. (2002), the biggest challenge to an educator is to help the meaningful information reaches the students. The application of low cost materials in the construction of Solar System mock-ups makes the learning process easy. According to Dickman et al. (2009), the application of low cost materials can encourage teachers to adopt that practice as a learning tool. That research takes up of the use of that facilities like pedagogic methods in the Astronomy learning.

2. Objectives

The present work aims to analyse if the use of digital resources combined with the application of low cost materials in the accomplishment of projects and the use of pedagogic books colaborate to the occurance of a meaningful learning in the Astronomy learning.

3. Methodology

It was drafted two questionnaires with 21 questions, therefore 20 closed questions; success rates, Figure 4. And discursive ones; success rates, Figura 5. The first is to check the Astronomy previous knowledge. To stem from the questionnarie analysed it was apllied the pedagogic strategies, so the second one was used. Three classes were studied in a amount of 78 students among 14 and 15 years old. The result os success rates of the classes is on the Figures 1, 2 and 3.

4. Results and Discussion

After the application of the second questionnaire, the results presented an evolution in right answers to the question, except to class C (question 14 and 20) and class D (question 1 and 10), in closed questions, the rates incresed from 16.7% to 49.7%. In the second test, in the open question the result was from 0.0% to 28.2%. And in the second phase just class C did not have evolution in the considered satisfactory results (above from 50.0% of successes in the questionnaire), success rates, Figure 6. Indicated that the strategies have achieved positive results, but they need adjustments to improve the meaningful learning.

5. Final Remarks

The teaching of Astronomy serve as boost to achieve a meaningful learning, in a wider context in the Science learning. After the second questionnarie application there was an improvement in the results. And during the application of the strategies the students started to relate each other in a better way, showing socialization and great interest among students in astronomical science.

References

Dickman, A. G, Menezes, A. R., Guimarães, A. M. S. T, Belchior, E. A, & Silva, M. B. R. 2009, SNEF, XVIII, Simpósio Nacional de Ensino de Física, pg.1

Couper, H. & Henbest, M. T. 1997, Buraco Ngro: Uma viagem ao centro de um buraco negro, (São Paulo: Ed. Moderna)

Horvath, J. E. 2008, OABCD ABCD da Astronomia e Astrofísica, (São Paulo: Livraria da Física)

Moran, J. M., Masetto, M. T. & Behrens, M. A. 2002, Novas tecnologias e mediação pedagógica, (Campinas: Papirus), pg.23

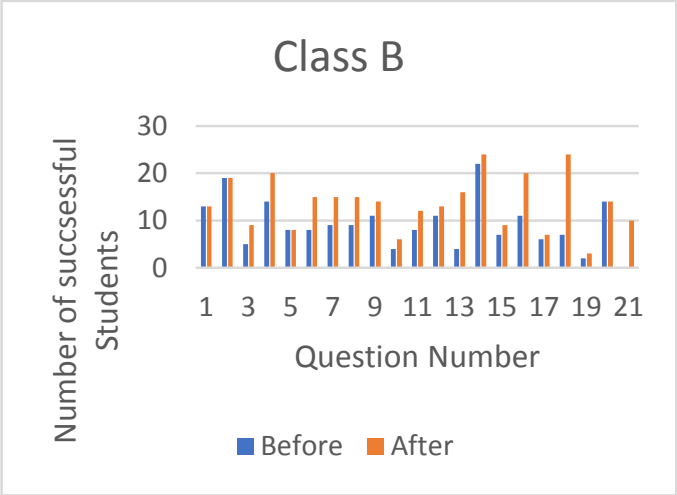

Figure 1. Correct answer before and after the quuestionnarie application.

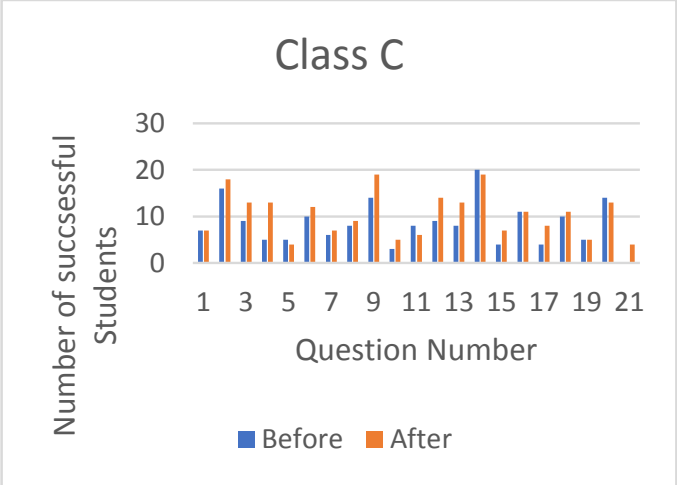

Figure 2. Correct answer before and after the questionnarie application.

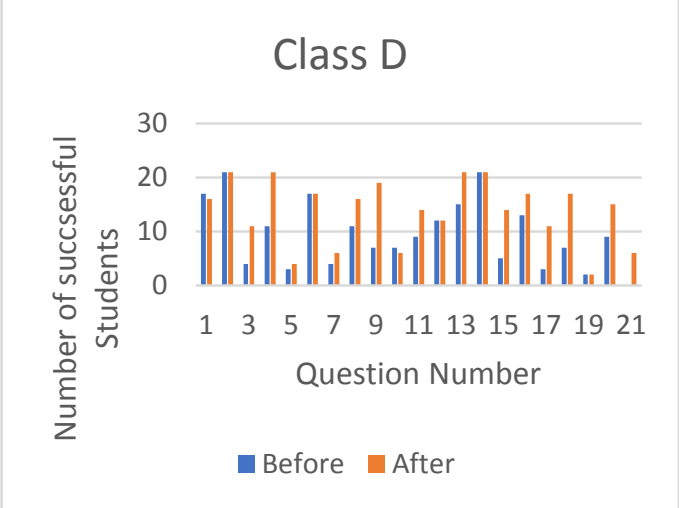

Figure 3. Correct answer before and after the questionnarie application.

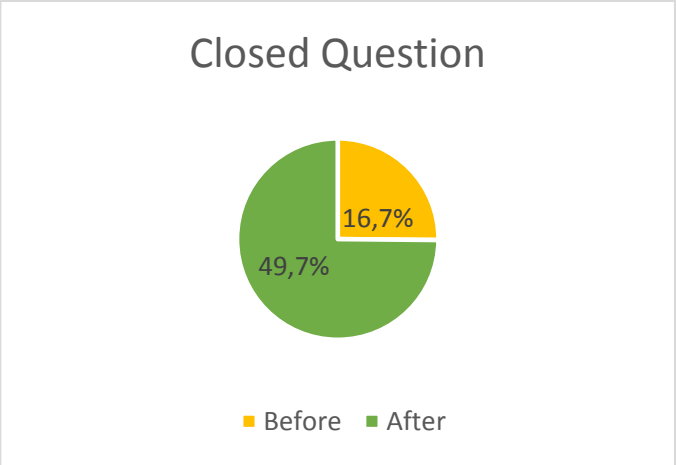

Figure 4. Porcentage of students answered closed questions, before and after.

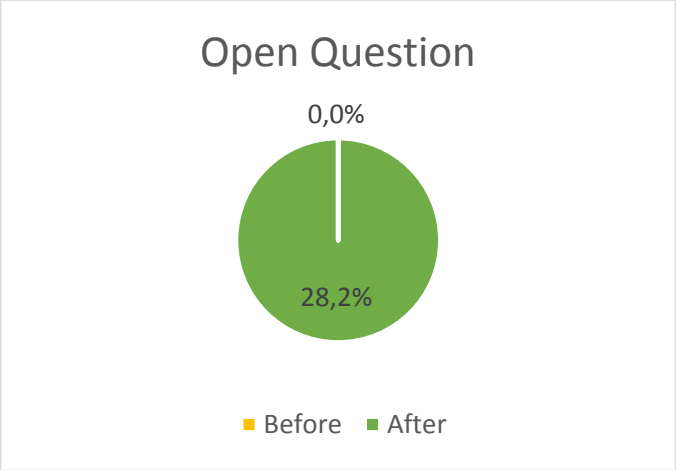

Figure 5. Porcentage of students answered open questions, before and after.

Figure 6. Students whose achieve satisfactory rates in the second phase.

Boletim da Sociedade Astronômica Brasileira, **30**, no. 1, 35-36

A proposal for an Astronomy basic course for secondary school students

Rafael Domingues & Artur Justiniano Jr.

[1] University of Alfenas, MG — Brazil. e-mail: rafaelpassosdomingues@gmail.com

Abstract. We present results from a long-term Astronomy foundation course taught to high school students at a private college in Alfenas-MG. This project began in 2014 through a partnership between the teaching group of Astronomy of UNIFAL-MG and the teacher of physics of the college. Each year about 40 students take part in the course, where we work on fundamental topics of Astronomy in a constructivist approach.

Resumo. Apresentamos resultados de um curso de longa duração de fundamentos de Astronomia ministrado para alunos do ensino médio de um colégio particular em Alfenas-MG. Este projeto teve início em 2014 através de uma parceria entre o grupo de ensino de Astronomia da UNIFAL-MG e a professora de Física do colégio. Por ano, cerca de 40 alunos participam do curso, onde trabalhamos tópicos fundamentais da Astronomia numa abordagem construtivista.

Keywords. Teaching Astronomy — Secondary school

1. Introduction

From childhood, we have conceptions about the universe around us. We seek to shape the things around us, to recognize patterns, and to use them for our own safety, searching tirelessly for answers. The goal is to use Astronomy to insert the teaching of the evolution of the ideas of Physics, providing a contextualized learning of the law of universal gravitation and the laws of Kepler.

2. Results

Fig. 2 show some students that participated in the annual course, all medalists of the Brazilian Astronomical and Astronautical Olympiad of the year 2016.

In 2016, three of the participants of the course (Andrade, Carolline, Marinho, Lucas & Brassi, Pedro; Fig. 1), were selected to participate in the Space Journey in Barra do Piraí - RJ, where they received an award for their rocket to reach the horizontal reach of 101.8 meters.

There has been growing participation over the years (Fig. 4). The interdisciplinary character of Astronomy instigates and favors meaningful learning by student parts, deconstructing any stigmas that might create a misconception of what science is.

There is significant progress over the years (Fig. 3), one can observe the annual achievement of medals from the Brazilian Astronomy and Astronautics Olympiad.

3. Conclusion

We observed that the students began to behave more skeptically, seeing science as a human construct, a more critical view of pseudo-sciences, understanding their inherences, above all, about the importance of using the scientific method for the development of science. In addition to contributing to the scientific training of students, the course has contributed to improve the performance of students in the discipline of Physics in high school. Add to this the increasing participation of these students in the Brazilian Astronomy and Astronautics Olympiad and also in the Brazilian Show Rockets.

Acknowledgements. Teacher Porto, Mersia, for support and complicity in the project.

Figure 1. Space journey — Barra do Piraí / RJ (2016).

References

Justiniano, A., & Botelho, R. 2016, Revista Brasileira de Ensino de Física, 38 (4), 8

Justiniano, A. et al. 2017, Revista Brasileira de Ensino de Física, 39 (4), 11

Nussenzveig, H. M. 2002, Curso de Física Básica 1 — Mecânica, (São Paulo: Edgard Blücher), 336

Oliveira, S. K, & Saraiva O. M, 2010, Astronomia e Astrofísica, (Porto Alegre: Livraria da Física), 768

Figure 2. Some participating students.

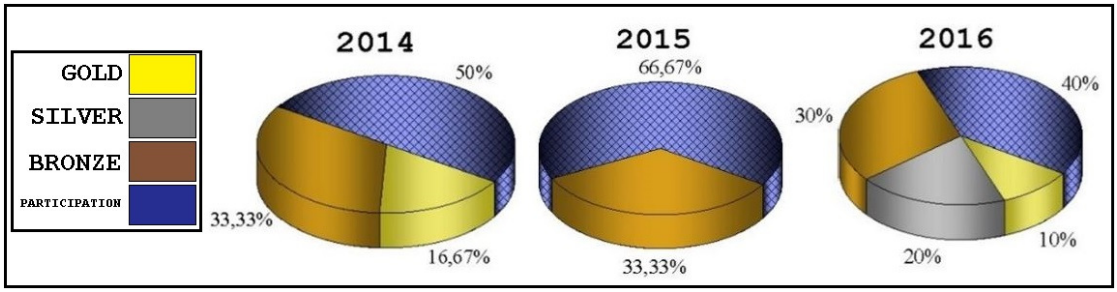

Figure 3. Annual medal win — Brazilian Astronomy and Astronautics Olympiad.

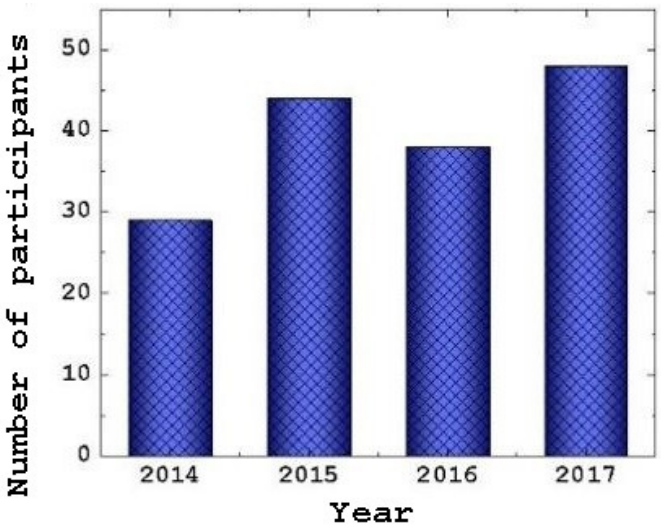

Figure 4. Annual shareholdings.

Boletim da Sociedade Astronômica Brasileira, **30**, no. 1, 37-38

Observation of planetary transit in miniobservatories: a proposal for inserting the study of the exoplanets in physics teaching

José C. da Silva & Artur Justiniano

[1] Universidade Federal de Alfenas, e-mail: jcarlos1905@gmail.com

Abstract. In this work we are proposal a strategy to insert the study of exoplanets in the training courses of physics teachers and in the master's degree in physics teaching. For this we estimate a magnitude limit (10 mag) from an analysis of the observatory site light pollution and evaluation of the optical set technical features, detector CCD and telescope. We set a range of declination, $-60° < \delta < +15°$, due the urban area near observatory's site and using the Exoplanet Archive database we select 13 stars that can be observed by Unifal Astronomical Observatory. With this informations, we can obtain and analyze the light curve originated by the planetary transit and estimate the radius and orbital parameters of the exoplanet.

Resumo. Neste trabalho estamos propondo uma estratégia para inserir o estudo dos exoplanetas nos cursos de formação de professores de física e no mestrado em ensino de física. Para isso estimamos uma magnitude limite (10 mag) a partir de uma análise da poluição luminosa do sítio do observatório e da avaliação das características do conjunto óptico, detector CCD e telescópio. Definimos um intervalo de declinação, $-60° < \delta < +15°$, devido à zona urbana próxima ao sitio do observatório e utilizando o banco de dados Exoplanet Archive selecionamos 13 estrelas que podem ser observadas pelo Observatório Astronômico da Unifal. Com estas informações, podemos obter e analisar a curva de luz originada pelo trânsito planetário e estimar o raio e os parâmetros orbitais do exoplaneta.

Keywords. miniobservatories – exoplanets – planetary transit

1. Introduction

Since the first discovery in the 90's, Wolszczan et al. (1992), there are already more than 3500 exoplanets detected. Among them, there is a great diversity of characteristics already measured, such as, orbital parameters, the mass and the planet radius. This and other parameters are essential links to test formation models, structure and evolution of exoplanet (Maxted et al. 2010).

Some planet in the Solar System have a strong brightness, due to solar radiation reflected in their atmospheres or surfaces, besides being close to us favoring the obtaining of good images. But, detecting exoplanet is not an easy task, because the distance, the small size and bright contrast of the host star are just a few of the obstacles that must overcome. Facing this challenger, the technological development and the improvement of detection techniques are fundamental to overcome them. And currently the search and characterization of exoplanet have become one of the most attractive areas of modern astronomy.

Among the techniques used to detect them, we highlight the transit planetary (PTT), used in the Kepler Mission and that allowed the detection hundreds of exoplanets and with data still under analysis (Fischer et al. 2015). In 2018, the promising TESS (*Transiting Exoplanet Survey Satellite*) Mission propose to catalog more than 2000 exoplanets and of these, it is expected to detect about 300 with up to twice the Earth size. In this work, we will present a proposal to identify the exoplanets that can be observed in miniobservatories using the planetary transit technique as a strategy to insert the study of exoplanets in the training courses of physics teachers and in the master's degree in physics teaching.

In the section 2 we will highlight PTT. In section 3, we will describe our methodology. In section 4, we will present the preliminary results obtained for the Unifal Astronomical Observatory (UAO) and finally, in section 5 we will present the next step for this work.

2. Planetary Transit Technique

PTT is based on a simple phenomenon, just as it is observed in solar eclipses and occultations of Venus and Mercury. Thus, The PTT consists of the detection of exoplanet by means of the analysis of the light curve of the host star (see 1). Therefore, PTT is preferably employed to detect large mass exoplanets that are close to the host star (Fischer et al. 2015). And even PTT being limited to the exoplanets that are in the line of sight between the observer and star, in last year it has overcoming other techniques regarding number of techniques (Fischer et al. 2015).

From light curve analysis we can extract planetary parameters such as, exoplanet radius (Vanderburg et al. 2011), the orbital semi-major axis (Maxted et al. 2010) and orbital period (Martioli, 2006).

From the stellar structure theories to determine the star radius (R_*) and measure of maximum depth d, we obtain the planet radius (R_p).

$$R_p = R_* \left(\frac{\triangle F}{F}\right)^{1/2} \tag{1}$$

Measuring the time of consecutive transits, we determine the period, P.

$$P = \frac{\pi G M_* t^3}{4R_*^3} \tag{2}$$

And, finally, by applying Kepler's third law, we can obtain the orbital semi-major axis, a.

$$a = \left(\frac{GM_* P^2}{4\pi^2}\right)^{1/3} \tag{3}$$

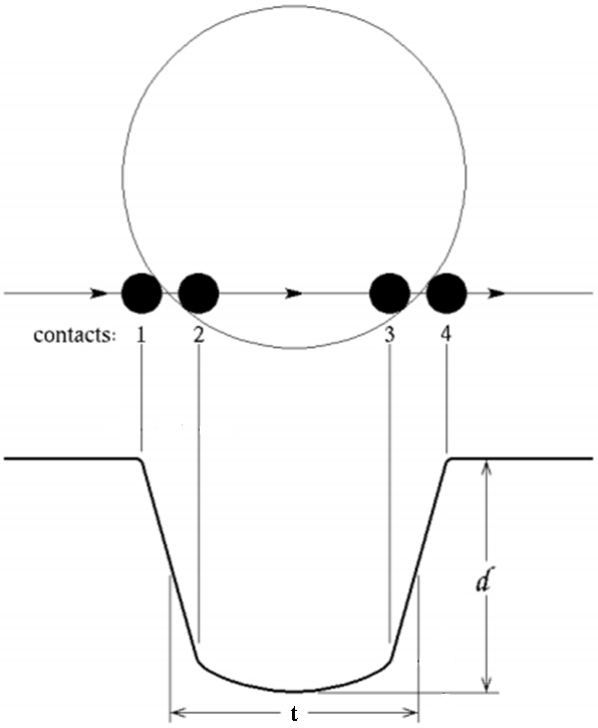

Figure 1. Light curve with observational parameters. (Brown et al. 2001)

3. Metodology

The UAO site is located in the urban area, it was necessary to measure the local light pollution using the technique of recording the limit magnitude with the naked eye. With this technique we have to identify the magnitude of the bright star to identify. From this analysis and evaluation of the optical set technical features, detector CCD and telescope, we estimate that the local limit magnitude as 10 mag.

Due the local light pollution, we have defined that the best objects to be observed should be located to the north. Thus, we defined the declination interval between $-60° < \delta < +15°$.

4. Results

With these parameters, we use the Exoplanets Archive database and select 13 stars that can be observed in the UAO.

Table 1. Stars with observation parameters

	Estrela	α (h m s)	δ (m s)	Mag
1	WASP-18	01 37 23.03	-45 40 40.4	9.30
2	WASP-7	20 44 10.23	-39 13 31.0	9.51
3	WASP-8	23 59 36.07	-35 01 53.0	9.79
4	KELT-11	10 46 49.74	-09 23 56.5	8.03
5	WASP-136	00 01 18.18	-08 55 34.8	9.98
6	WASP-69	21 00 06.19	-05 05 39.9	9.87
7	WASP-74	20 18 09.32	-01 04 32.4	9.70
8	HD106315	12 13 53.39	-00 23 36.5	8.95
9	WASP-76	01 46 31.86	+02 42 01.9	9.50
10	HD3167	00 34 57.52	+04 22 53.3	8.94
11	WASP-38	16 15 50.36	+10 01 57.2	9.44
12	HIP41378	08 26 27.85	+10 04 49.4	8.93
13	KELT-11	08 22 28.21	+13 44 07.1	9.28

5. Conclusion

Our next step to this work, it will be determine the best date to observe each star, and then, using PTT, estimate the radius and orbital parameters of the exoplanet.

References

Fischer D. A. et al. Exoplanet Detection Techiques. (2015). arXiv:1505.06869v2.

Brown. T.M. et al. Hubble Space Telescope time-series photometry of the transiting planet of HD209458. *Astrophysical Journal*, 552:699-709, 2001.

Martioli. E. Exoplanetas: O que são e como detectá-los. *Instituto Nacional de Pesquisas Espaciais*. Brazil. 2006.

Maxted. P. F. L. et al. WASP-32b: A Transiting "hot Jupiter" planet orbiting a lithium-poor, solar-type star. (2010). arXiv: 1010.1742v1.

Nasa. TESS Mission. https://www.nasa.gov/content/about-tess. Accessed: 28/10/2017.

Vanderburg. A. et al. Two small planets transiting HD 3167. arXiv:1607.05248v2.

Wolszczan. A. Frail. D.A. A planetary system around the millisecond pulsar PSR1257+12. Nature, 145-147, 1992.

Boletim da Sociedade Astronômica Brasileira, **30**, no. 1, 39-41

The Biological Impact of Kepler-96 Superflares in a planet in the habitable zone

R. Estrela & A. Valio

[1] Mackenzie Presbyterian University. e-mail: rlf.estrela@gmail.com, adrivalio@gmail.com

Abstract. We present the analysis of superflares seen on the lightcurve of the active star Kepler-96. Its age of 2.4 Gyr is the same as the Sun when there was a sudden increase in the oxygen level on Earth atmosphere. Our analysis is based on the four years of continuous short cadence observation of the star by the Kepler telescope. The model used here simulates a planetary transit and allows the insertion of a flare in the stellar disk with different size, amplitude, and position. By fitting the observational data with this model, it is possible to infer the physical properties of the superflares, such as its duration (few minutes) and energy released. In addition, we analyze the biological impact of these superflares in an hypothetical Earth in the habitable zone of the star assuming it has protection via various atmospheres scenarios (an Archean and Present-day atmospheres) and an ocean. We estimated the UV flux increase produced by the strongest superflare and concluded that life would only survive on the surface if there was already an ozone layer present on the planet atmosphere or at ocean depths higher than 10m.

Resumo. Nós apresentamos o estudo de superexplosões magnéticas observadas na curva de luz da estrela Kepler-96. Esta estrela tem uma idade de 2,4 Ga, a mesma idade que o Sol tinha quando a Terra teve um aumento repentino no nível de oxigênio em sua atmosfera. Nossa análise é baseada em quatro anos de observação contínua desta estrela pelo telescópio Kepler. O modelo utilizado neste trabalho simula trânsitos planetários e permite a inserção de explosões com diferentes tamanhos, amplitudes e posições no disco da estrela. Ao realizar o ajuste entre o dado observacional e o modelo, é possível inferir propriedades físicas das superexplosões, como a duração (alguns minutos) e a energia liberada. Além disso, nós também analisamos o impacto biológico destas superexplosões em uma planeta hipotético tipo Terra localizado na zona habitável da estrela, supondo que a vida no planeta tem proteção através de uma atmosfera (Archeana ou atual com ozônio) ou de um oceano. Nós estimamos o aumento do fluxo de UV devido à superexplosão mais forte e concluímos que a vida só seria possível na superfície se tivesse ozônio presente na atmosfera do planeta ou em profundidades maiores que 10m no oceano.

Keywords. Astrobiology, Planets and satellites: atmospheres, Stars: solar-type, Sun: flares, Sun: UV radiation

1. Introduction

Kepler-96 is a solar analogue star harbouring a Super-Earth planet in close orbit. Its age of 2.3 Gyr is the same as the Sun when there was a considerable increase of oxygen in Earth's atmosphere in the end of the Archean era due to micro-organisms living under the sea. This star is still very active and has several superflares on its lightcurve. Some authors (Airapetian et al. (2016), Lingam & Loeb (2017)) discussed about the possibility of such superflares occurring in the young Sun and their impact on the primitive Earth. Thus, Kepler-96 is an interesting target to study because (i) the Archean Earth conditions if the Sun had such superflares at that time and (ii) a planet in the habitable zone with Archean conditions, considering that this planet had already enough time for life to evolve.

Here, we analyze the superflares of Kepler-96 using the transit model developed by Silva (2003). Properties of the superflares, such as duration, size, amplitude, and position will be intrinsically studied with this model. From these parameters it is possible to estimate the power released by the superflare. The increase in the UV flux due to superflares is also inferred. Then, we study how different atmospheres from the primitive and present-day Earth and an ocean could attenuate the increased UV flux arriving at a planet in the habitable zone (HZ, at 1AU) of Kepler-96. Finally, we estimate the biological impact of the superflares on two very resistant microorganisms, *Deinococcus radiodurans* and *Escherichia coli*, living in the surface or in the ocean of this planet.

2. Methods

2.1. Modelling superflares

Kepler-96 has a Super-Earth planet orbiting very close to this star, with P_{orb} = 16.23 days. By analyzing the 86 transits detected of Kepler-96b, three of them (30th, 48th, and 67th) show flares signatures, and in particular transit 48th has a high intensity flare that causes an increase of 4% in the total luminosity flux of the star. We have modelled the flares using the transit model described in Silva (2003), in which a stellar flare is added to the disk of the star outside the planet transit band. This model was already applied to model starspots in Kepler and CoRoT stars (Silva-Valio & Lanza 2011; Estrela & Valio 2016; Valio et al. 2017). A Gaussian profile was chosen to model the flare in time, t, as described below:

$$I_{\rm flare} = A \exp\left[\frac{(t-t_0)^2}{2\sigma_t^2}\right] \quad (1)$$

where A is the amplitude of the flare, t_0 represents the peak time as measured from midtransit time and σ_t is the temporal duration of the flare.

The three parameters that characterize the flare (A, t_0, and σ_t) were obtained by minimizing the χ^2 between the modelled transit lightcurve and the observed data.The results are summarized in Table 1.

In addition, we computed the total energy released by the flare using the following formula:

$$E_{\rm flare} = AL_{\rm star} \int_{-\infty}^{+\infty} \exp(t - t0^2/2\sigma_t^2)\mathrm{dt} \quad (2)$$

Table 1. Characteristics of the Kepler-96 superflares

Flare	Transit	Midtransit [BJD - 2.454.833 days]	Time position [hours]	Time duration [hours]	Time duration [min]	Amplitude [I_c]	Energy [ergs]
A	30th	674.41007	-0.0714 ± 0.006	0.118 ± 0.006	7.1 ± 0.4	39627 ± 0.00002	2.0×10^{33}
B	48th	966.70310	0.2402 ± 0.006	0.161 ± 0.003	9.7 ± 0.2	2986143 ± 0.002	1.8×10^{35}
C	67th	1275.2347	-0.108 ± 0.016	0.088 ± 0.017	5.3 ± 1.0	32885 ± 0.00006	1.2×10^{33}

Table 2. Biological effective irradiance from Kepler-96, E_{eff} [J/m^2]

	No atmosphere	Archean atmosphere	Present atmosphere with O_3
	Contribution of 5400% to the UV flux (Flare A)		
E. coli	$8 \times 10^4 \pm 0.020$	$1.3 \times 10^4 \pm 0.019$	$22 \pm 6.96 \times 10^{-8}$
D. radiodurans	$8.2 \times 10^4 \pm 0.15$	$1.3 \times 10^3 \pm 0.019$	$7.5 \pm 8.4 \times 10^{-8}$
	Contribution of 60% to the UV flux (Flare B)		
E. coli	$3 \times 10^3 \pm 10^{-4}$	$338 \pm 4 \times 10^{-4}$	$5 \pm 1.2 \pm 10^{-8}$
D. radiodurans	$2 \times 10^3 \pm 4 \times 10^{-4}$	$282 \pm 5 \times 10^{-4}$	$1.5 \pm 9.18 \times 10^{-8}$

2.2. Superflares contribution to the UV flux

To estimate the UV flux contribution of the Kepler-96 flares, we used the UV flux measured on the most intense solar flares observed. Woods et al (2004) reported one of the largest flares found in the Sun, a X17 GOES class flare with total energy of $E = 4 \times 10^{32}$ ergs, that increased by 12% the solar MUV flux. As the total thermal blackbody flux of Kepler-96 and the Sun are very similar, we considered that the superflares found in Kepler-96 would increase the UV flux proportionally. Therefore, a superflare found in Kepler-96 with $E = 1.8 \times 10^{35}$ ergs would increase by about 5400% the solar MUV flux.

3. Biological Impact

Stellar flares can give a significant contribution to the total UV flux of the star. For this reason, we analyzed here the possible impact that the superflares produced by Kepler-96 could have in life present in a planet on its habitable zone (1 AU).

Fortunately, this incident stellar UV flux (F_{inc}) can be attenuated by a planetary atmosphere depending on its composition. Here we used different atmospheric scenarios found in Earth adopted from Cnossen et al. (2007): an Archean atmosphere composed of 80% N_2 and 20% CO_2, with concentrations of 2.09×10^{19}cm^{-3} and 5.24×10^{18}cm^{-3} respectively, and a Present day atmosphere with ozone with concentrations of 2.09×10^{19}cm^{-3} for N_2, 5.62×10^{18}cm^{-3} for O_2, and 1.35×10^{12}cm^{-3} for O_3. These atmospheres contain molecules, such as N_2, CO_2 and O_2, that can absorb short wavelengths.

The UV radiation can also be attenuated by the water. Therefore, the UV flux in the ocean varies considerably with depth, and can be determined by the equation:

$$I(\lambda, z) = I_0(\lambda) e^{-K(\lambda), z} \quad (3)$$

where I(λ, z) is the UV spectral irradiance at a depth z, $I_0(\lambda)$ is the UV spectral irradiance with the superflare contribution passing through an Archean atmosphere and K(λ) is the diffuse attenuation coefficient for water adopted by Smyth (2011).

We used the attenuated UV flux with the superflares contribution to estimate the biological impacts in a hypothetical Earth in the HZ either for life on the planet surface or under the ocean surface. In both cases, we weighted the increased UV flux with the action spectrum of the microorganisms to get information about the total flux in the UV band that falls onto unit area of these biological bodies, known as biological effectiveness irradiance (E_{eff}):

$$E_{\rm eff} = \int F_{inc}(\lambda) S(\lambda) d(\lambda) \quad (4)$$

Table 3. UV Irradiation at Ocean depths

	Ocean Depth [m] (increase of 5400%)	Ocean Depth [m] (increase of 60%)
E. coli	28	10
D. radiodurans	12	surface

where F_{inc} is the total incident MUV flux with the superflare contribution arriving at the planet surface/ocean depth, S is the action spectra of a biological body and λ is the MUV wavelengths. Here we used the action spectra of two microorganisms that define the surviving zone for life: *Deinococcus radiodurans* (Setlow & Boling (1965); Calkins & Barcelo (1982); O'Malley-James & Kaltenegger (2017)) and *Escherichia coli* (Giller (2000)).

Then, we verified if the estimated E_{eff} can be tolerated by *D. radiodurans* and *E. coli*.

4. Results

We estimated the biological effective irradiance (E_{eff}) for two resistant microorganisms (*D. radiodurans* and *E. coli*) present in an Earth-like planet in the HZ of Kepler-96. The threshold for the E_{eff} is defined using the maximum UV flux for 10% survival of these microorganisms, which is $F_{10}^{UV} = 5.53 \times 10^2$ J/m^2 for *D. radiodurans* (Ghosal et al. 2005) and $F_{10}^{UV} = 22.6$ J/m^2 for *E. coli* (Gascón et al. 1995). These results are shown in Table 2, note that to obtain the values in Joules, we multiplied the values in Watts by the total duration of the superflare.

For the contribution of the strongest superflare (increase of 5430% in the MUV flux), the E_{eff} shows that *D. radiodurans* would only survive in the surface of a hypothetical Earth at 1AU if there is an ozone layer present on the planet atmosphere (see Table 2). Considering the effects of a smaller superflare (increase of 60% in the MUV flux), *D. radiodurans* could survive in the surface even if the planet has an Archean atmosphere.

Moreover, we also analyzed the ocean depths that could harbour extremophile life in this planet without being damaged by the strongest superflare of Kepler-96 (see Table 3). Thus, considering the effects of this superflare (flare B) in a planet in the HZ, an ocean depth of 28m would be necessary to absorb the UV irradiation such that *E. coli* could survive and 12m for *D. radiodurans*.

5. Conclusion

We detected and modelled flares present in the transits of Kepler-96b. All of them showed an energy range that corresponds to superflares.

The study of the biological impact suggests that the stellar UV Flux (increased by the contribution of the strongest superflare) received by a biological body would allow the presence of life in the surface only for a planet with ozone. An ocean in this planet can also attenuate the UV radiation and protect the microorganisms from the increased UV radiation due to the superflares. Thus, although a hypothetical Earth-like planet orbiting Kepler-96 receives an increased UV radiation due to the superflares, life could still survive in depths inside the photic zone (up to 200m) of an Archean ocean present in these planets.

In a future work we will consider the cumulative effects of all superflares from the star.

Acknowledgements. This work has been supported by grant from the Brazilian agency FAPESP (#2013/10559-5) and from MackPesquisa. Raissa Estrela acknowledges a FAPESP fellowship (#2016/25901-9).

References

Airapetian, V. S., Glocer, A., Gronoff, G., Hébrard, E., & Danchi, W. 2016, Nature Geoscience, 9, 452
Calkins J., & Barcelo J. A., 1982, The Role of Solar Ultraviolet Radiation in Marine Ecosystems. Springer US, p.14
Cnossen, I., Sanz-Forcada, J., Favata, F., et al. 2007, Journal of Geophysical Research (Planets), 112, E02008
Estrela, R., & Valio, A. 2016, ApJ, 831, 57
Gascón, J., Oubiña, A., Pérez-Lezaun, A., & Urmeneta, J. 1995, Current microbiology, 30(3), 177-182.
Ghosal, D., et al. 2005, FEMS microbiology reviews, 29(2), 361-375.
Giller, H. 2000, Proceedings of the Water Environment Federation 2000.2, 41-47.
Lingam, M., & Loeb, A. 2017, ApJ, 848, 41
O'Malley-James, J. T., & Kaltenegger, L. 2017, MNRAS, 469, L26
Setlow J. K., & Boling M. E. 1965, Biochimica et Biophysica Acta, 108, 259
Silva, A. V. R. 2003, ApJ, 585, L147
Silva-Valio, A., & Lanza, A. F. 2011, A&A, 529, A36
Smyth, T. J. 2011, Journal of Geophysical Research (Oceans), 116, C11020
Valio, A., Estrela, R., Netto, Y., Bravo, J. P., & de Medeiros, J. R. 2017, ApJ, 835, 294
Woods, T. N., Eparvier, F. G., Fontenla, J., et al. 2004, Geophys. Res. Lett., 31, L10802

Boletim da Sociedade Astronômica Brasileira, **30**, no. 1, 42-43

Identification of organic molecules in the protostellar region NGC 1333-IRAS 4A

Heidy M. Quitián-Lara[1], Bertrand Lefloch[2], & Heloisa M. Boechat-Roberty[1]

[1] Obsertavatório do Valongo, Universidade Federal do Rio de Janeiro, Brazil e-mail: heidyql@astro.ufrj.br
[2] l'Institut de Planétologie et d'Astrophysique de Grenoble, France

Abstract. Here we present the first results of the survey in the protostellar region NGC 1333-IRAS 4A. This object shows the presence of a variety of complexe organic molecules (COMs), such as: CH_3CCH, c-C_3H_2, CH_3HOH, H_2CCO, CH_3OH and HC_3N. We confirm the detection of COMs and molecules of pre-biotic interest, such as: PN, methyl formate ($HCOOCH_3$), dimethyl ether (CH_3OCH_3), formic acid (HCOOH) and acetonitrile (CH_3CN). Given the wide range of detected transitions, it is possible to construct the rotational diagrams by estimating the excitation temperatures and column densities of each of these species. The identification of a wide variety of molecules containing C and O, as well as S, N, and P atoms indicates a chemical complexity increase in these so-called "hot cores" objects, for having relatively heated environments (T > 100 K) and high densities.

Resumo. Apresentamos os primeiros resultados do survey feito na região protoestelar NGC 1333-IRAS 4A. Este objeto mostra a presença de uma grande variedade de moléculas orgânicas, como: CH_3CCH, c-C_3H_2, CH_3HOH, H_2CCO, CH_3OH eHC_3N. Confirmamos a detecção de COMs e moléculas com interesse prebiótico, como: PN, formiato de metila ($HCOOCH_3$), dimetil éter (CH_3OCH_3), ácido fórmico (HCOOH) e acetonitrila (CH_3CN). Dada a ampla gama de transições detectadas, é possível construir os diagramas de rotação estimando as temperaturas de excitação e as densidades colunares de cada uma dessas espécies. A identificação de uma grande variedade de moléculas contendo C e O, além de S, N e P, é indicadora do aumento na complexidade química nesses objetos nomeados de "núcleos quentes", por se tratarem de ambientes relativamente aquecidos (T> 100 K) e apresentarem altas densidades.

Keywords. physical data and processes: astrochemistry — ISM: singular object IRAS 4A — Molecules: abundances — Stars: formation

1. Introduction

The low-mass class 0 protostellar object NGC 1333 IRAS 4A is a binary source located in the Perseus molecular complex, at the distance of 235 pc. The two components, IRAS 4A1 and IRAS 4A2, have a separation of only about 1.8" (~ 420 AU) and a total luminosity of a few solar luminosities. The IRAS 4A system is associated with a spectacular large-scale (a few arcminutes) bipolar molecular outflow. High-angular resolution observations by Santangelo et al. 2014 have disentangled two distinct molecular jets powered by each of the two components. IRAS 4A is the second hot core protostar identified after IRAS 16293-2422 (Bottinelli et al. 2007). The identification of complex organic molecules (COMs) is of great importance in the study of the first stages of the formation of low mass stellar objects (Taquet et al. 2015). In this work, the molecular content of IRAS 4A was investigated as part of the Large Program ASAI[1] (PIs: B. Lefloch and R. Bachiller), carrying out a highly sensitive, unbiased survey of the spectral windows 72-115GHz, 130-172 GHz, 205-272 GHz using the IRAM 30m telescope (Sierra Nevada, Spain).

2. Methodology and Results

Spectral line surveys of the source were carried out with the IRAM 30m telescope over six semesters from September 2012 to March 2015, using the broad-band EMIR receivers E090, E150 and E230, connected to the Fast Fourier Transform Spectrometers (FTS) either in the high (50 kHz) or low (200 kHz) spectral resolution mode. The 3mm (72–116 GHz) and 2mm (126–170 GHz) bands were observed simultaneously. The 1mm (200-276 GHz) band was covered observing both LSB and USB simultaneously using the FTS in its 200 kHz resolution mode. We used the CASSIS software (Vastel et al. 2015) for the line identification, using the CDMS and JPL databases, considering all the lines detected with an intensity higher than 3σ. The diversity of spectral signatures reflects the diversity of excitation and chemical conditions among the source. We examine here the molecular content based on the molecular line identification in the 1, 2 and 3mm bands.

The spectra exhibit many different molecular lines with presences of isotopologues, reflecting the evolutionary stage and the physical conditions of the source. This is illustrated in Figure 1, which displays the emission in the spectral bands 86–89.5 GHz (top), 144–147 GHz (center), 250.25–252.75 GHz (bottom). In this context, the number of detected isotopologues and molecular lines are indicators of the excitation conditions, whereas the number of main isotopologues traces the molecular complexity of the source (see Table 1).

2.1. Carbon chains

We identified carbon chains of the polyyne type, with a maximum of 4 carbon atoms. Both linear and cyclic conformations of these species were observed. In addition, it was also observed that the number of identified lines is higher for hydrogen-rich carbon chains (see Table 2). Furthemore, the identification of isopologues species is an indicative of the presence of the deuterated fossil stage (Codella et al. 2012) in the outflowing gas (see Table 1).

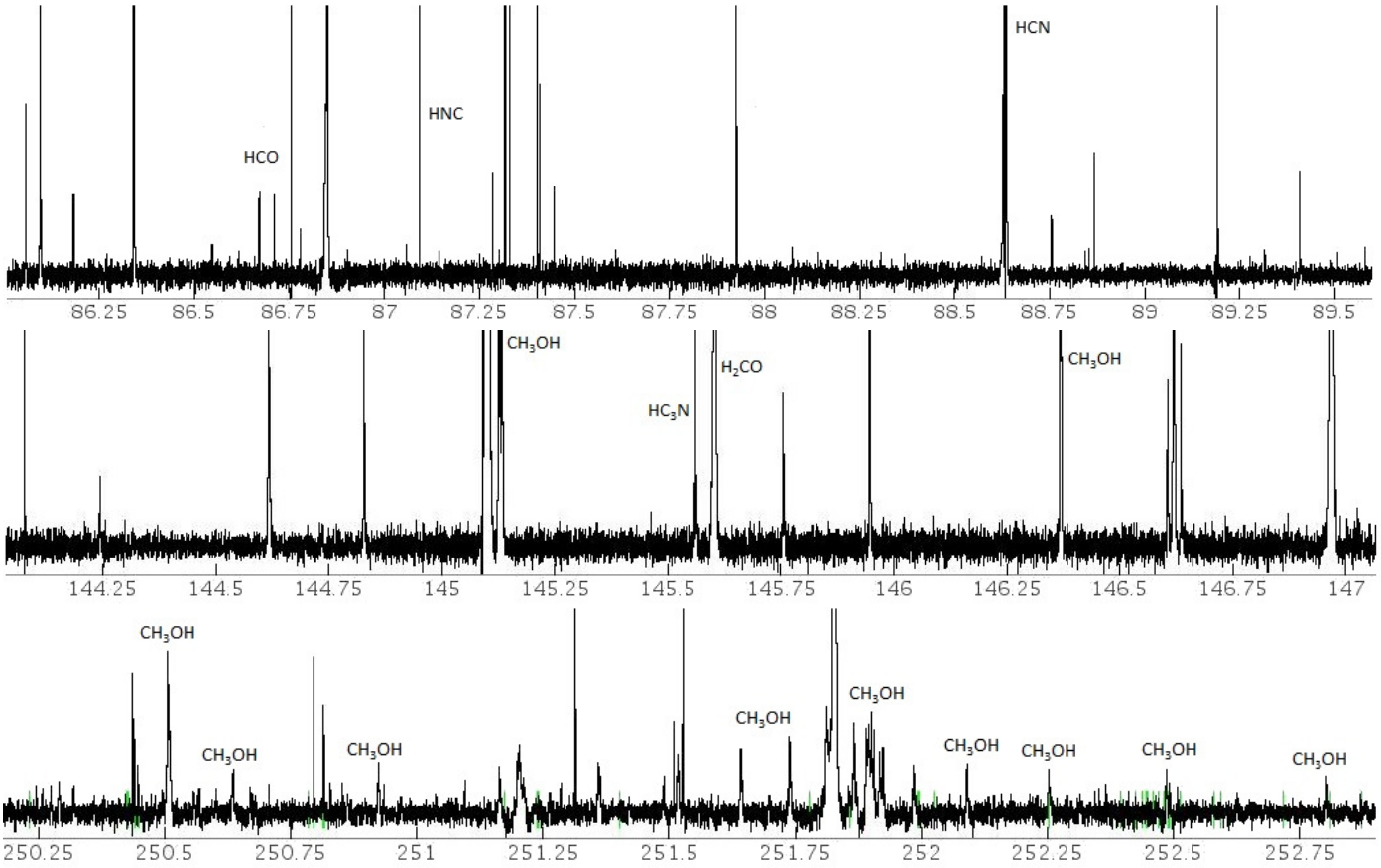

Figure 1. Example of molecular line emission detected with ASAI in IRAS 4A in the spectral bands 86–89.5 GHz (top), 144–147 GHz (center), 250.25–252.75 GHz (bottom)

Table 1. Number of lines identified for each species (selected isotopologues included) per spectral band. The identified species were distributed in four groups according to the main atom. Being observed that oxygenated species are dominant in the three spectral bands studied in IRAS 4A. The ξ letter denotes S, Si and P.

Species	3mm	2mm	1mm	Total
O-bearing	55	85	104	244
N-bearing	13	1	25	39
C-bearing	30	27	48	105
ξ-bearing	5	9	11	25
Isotopologues				
D_2CO	1	1	5	7
DCO^+	-	1	1	2
$^{13}CH_3OH$	9	8	14	31
^{34}SO	3	3	5	11
c-C_3HD	4	5	-	9

3. Conclusions

The number of identified lines in the source shows that IRAS 4A is a region dominated by O-bearing species, which is characteristic of a hot core. Polyyne species with up to 4 carbons were identified, showing an upper limit to their abundances, x, of 10^{-11} to 10^{-13}. Our preliminary results show that the source IRAS 4A is rich in complex organic molecules, species that play an important role in the formation of pre-biotic molecules in young objects.

Table 2. Carbon chains identified per spectral band and the results obtained from the Rotational Diagram.The x letter denotes the relative abundances with respect H_2 assuming an H_2 column density in the hot core of N(H_2)= $1.6x10^{24}$ cm^2 (Bottinelli et al 2004)

Species	Total lines	T_{ex} (K)	N (cm^2)	x
C_2H	11	5.3	$1.4x10^{14}$	$8.8x10^{-11}$
c-C_3H	15	6.5	$1.9x10^{12}$	$1.2x10^{-12}$
l-C_3H	9	5.9	$5.9x10^{11}$	$3.7x10^{-13}$
C_4H	8	5.5	$6.2x10^{13}$	$3.9x10^{-11}$
c-C_3H_2	28	15.4	$3.7x10^{12}$	$2.3x10^{-12}$
CH_3C_2H	34	31.7	$5.3x10^{13}$	$3.2x10^{-11}$

References

[1] ASAI website: http://www.oan.es/asai
Bottinelli, S. et al. 2004, The Astrophysical Journal, 615, 354.
Bottinelli, S. et al. 2007, Astronomy & Astrophysics, 463, 601.
Codella, C. et al. 2012, The Astrophysical Journal, 757, L9.
Santangelo, G. et all. 2014, Astronomy & Astrophysics, 568, A125.
Taquet, V. et al. 2015, The Astrophysical Journal, 804, 81.
Vastel, C. et al. 2007, Proceedings of the Annual meeting of the French Society of Astron. and Astrophysics. Eds.: F. Martins, S. Boissier, V. Buat, L. Cambrésy, P. Petit, pp.313-316.

Boletim da Sociedade Astronômica Brasileira, **30**, no. 1, 44-45

Protonation and hydrogenation of benzene molecule on a surface grain

Heidy M. Quitián-Lara[1], Fabio Ribeiro[2], Diana Andrade[1], Maria L. Rocco[3], Wania Wolff[4], & Heloisa M. Boechat-Roberty[1]

[1] Observatório do Valongo, Universidade Federal do Rio de Janeiro, Brazil e-mail: heidyql@astro.ufrj.br
[2] Instituto de Química, Universidade Federal do Rio de Janeiro, Brazil
[3] Instituto Federal de Educação, Ciência e Tecnología do Rio de Janeiro, Brazil
[4] Instituto de Física, Universidade Federal do Rio de Janeiro, Brazil

Abstract. In this work, we studied the formation of the hydrogenated and protonated benzene molecule (C_6H_6), the basic unit of polycyclic aromatic hydrocarbons (PAHs), through the interaction of electrons with frozen benzene on the surface of interstellar and circunstellar dust grains. It was used the electron-stimulated ion desorption technique (ESID) where benzene molecules are condensed on a substrate at low temperatures and are bombarded with electrons with energies at 2.1-2.9 keV. We analyzed the desorbed ions from the ice using the mass spectrometry by time of flight (TOF-MS). By the mass spectra we observed the ions resulting from the loss of hydrogen ($C_6H_5{}^+$, $C_6H_4{}^+$ and etc.); the protonated benzene ($C_6H_6H^+$) and the sequence of ions resulting from the hydrogenation until complete saturation of its structure, thus leading to loss of aromaticity and formation of the ionized cyclohexane ($C_6H_{12}{}^+$) and protonated cyclohexane ($C_6H_{12}H^+$).

Resumo. Neste trabalho estudamos a hidrogenação e protonação da molécula do benzeno (C_6H_6), unidade básica dos hidrocarbonetos policíclicos aromáticos (PAHs), através da interação de elétrons com moléculas congeladas de benzeno na superfície de grãos de poeira interestelar e circunstelar. Para isto, foi utilizada a técnica de dessorção de íons estimulada por elétrons (ESID), onde moléculas de benzeno são condensadas sobre um substrato metálico a baixas temperaturas e bombardeadas com elétrons com energias de 2,1-2,9 keV. Os íons dessorvidos do gelo foram analisados usando a tecnica de espectrometria de massas por tempo de vôo (TOF-MS). Pelos espectros de massas foram observados os íons decorrentes da perda de hidrogênio ($C_6H_5^+$, $C_6H_4^+$,etc.); o benzeno protonado, ($C_6H_6H^+$), e a sequência de íons decorrentes da hidrogenação até a completa saturação da sua estrutura, levando assim à perda da aromaticidade e formação do ciclohexano ionizado, $C_6H_{12}^+$, e do ciclohexano protonado ($C_6H_{12}H^+$).

Keywords. physical data and processes: astrochemistry – ISM - CSM - benzene and hydrogenated benzene - experimental techniques: ESID-TOF-MS

1. Introduction

To date, more than 200 different molecules have been identified in the interstellar (ISM) and circunstellar (CSM) media[1]. Some of these molecules freeze out at the cold temperatures (10–20 K) of both ISM and CSM to form molecular ices on the surface of dust grains (Herbst et al. 2009). In such ices, complex organic molecules (COMs) are efficiently formed by chemical transformation processes catalyzed by external agents (Fedoseev et al 2012). In this context, cosmic rays, photons and charged particles induce ionization, dissociation, desorption and protonation of molecules on the surface of grains producing neutral, ionized and radical fragments (Burke and Brown 2010). Some of these fragments, mainly of smaller sizes, become mobile at temperatures >30 K and undergo combination reactions on the grain surface to form more complex species (Garrod et al. 2008).

On the other hand, in the infrared spectra of several astrophysical objects the features at 3.3; 3.4; 6.2; 7.7; 8.6; 11.3 and 12.7 μm are present. These bands can be attributed to the vibrational transitions of the C-H and C-C bonds in fused benzene (C_6H_6) aromatic rings of a mixture of neutral (PAHs) and ionized (PAH^+) polycyclic aromatic hydrocarbons, as well as to their hydrogenated (H_n-PAHs) and protonated (H^+-PAHs) analogues. In this work, we used experimental methods to examine the interaction of high energetic electron beam with a C_6H_6 solid sample, simulating the electron-driven chemical transformations that occur on the surface of interstellar and circumstellar benzene-rich ices.

2. Methodology and Results

The electron-stimulated ion desorption (ESID) technique was used to determine the positively charged fragments desorbed from a pure benzene ice at 125 and 127K into a ultrahigh vacuum (UHV) chamber at 10^{-9} mbar base pressure, bombarded by a focused electron beam at 2.1, 2.3 and 2.9 keV of impact energies. Electrons colliding on a surface transfer part of their energy and momentum to the sample, thus inducing excitation and ionization processes that may cause bond breakage and desorption of neutral and ionic species. The positively charged ions desorbed from the ice were analyzed using the mass spectrometry by time of flight (TOF-MS) technique. A top view schematic diagram of the experimental setup is showed in Figure 1. More details about the available experimental setup can be found elsewhere (Ribeiro et al. 2014).

The results are summarized in Figure 2. It is possible to see that the protonated benzene ion, $C_6H_7^+$ (or $C_6H_6H^+$) is predominantly formed. Moreover, a competition between the primary processes of dehydrogenation and protonation of the benzene molecule are also evidenced. The most produced products from dehydrogenation are the benzyl cation, $C_6H_5^+$, and the C_6H^+ species. The formation of $C_6H_4^+$, $C_6H_3^+$, $C_6H_2^+$ and the cyclohexatriyne cation, C_6^+, is also observed. On the other hand, hydrogenation was observed until the complete loss of aromaticity, with the formation of the aliphatic cyclohexane ($C_6H_{12}^+$) and protonated cyclohexane ($C_6H_{12}H^+$) species. We suggest that interstellar cyclohexane could be formed as a desorption product of benzene-rich ices.

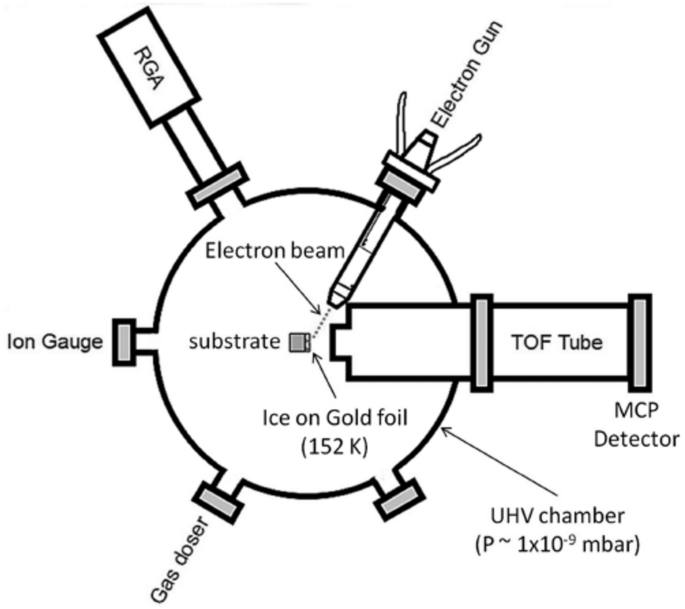

Figure 1. Experimental setup. Adapted from Ribeiro et al. 2014.

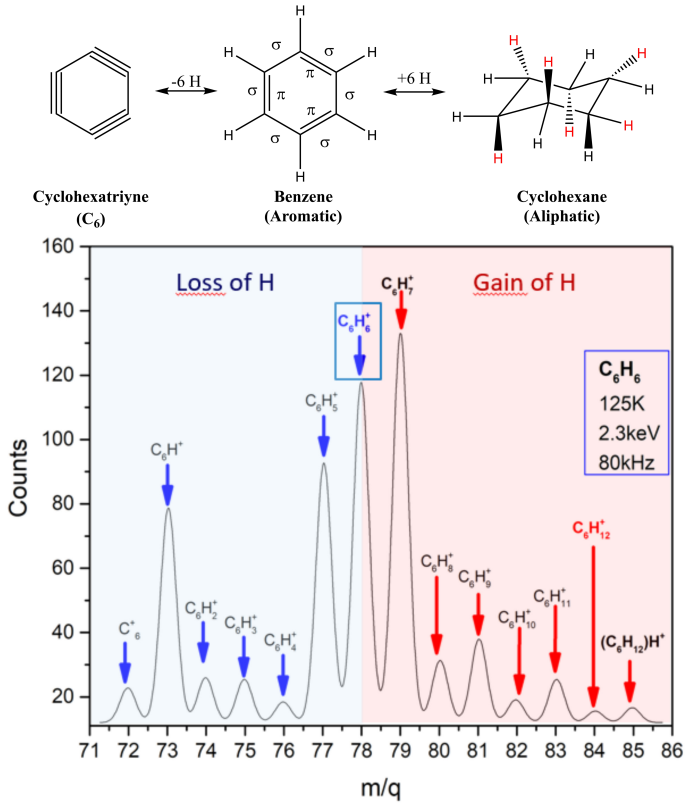

Figure 2. Dehydrogenation, protonation and hydrogenation of condensed benzene at 2.3 keV.

3. Conclusions

In the condensed phase, the protonation, hydrogenation and dehydrogenation processes of benzene ice submitted to electron impact are highly efficient. The formation of the protonated benzene ($C_6H_7^+$) and its subsequent desorption are favored. These ions are formed on the surface of the frozen grain and are desorbed and released in the gas phase. Ion desorption is presented in terms of desorption yield, Yi, the number of ions emitted by incident electron, shown in Figure 3. Therefore, we suggest that

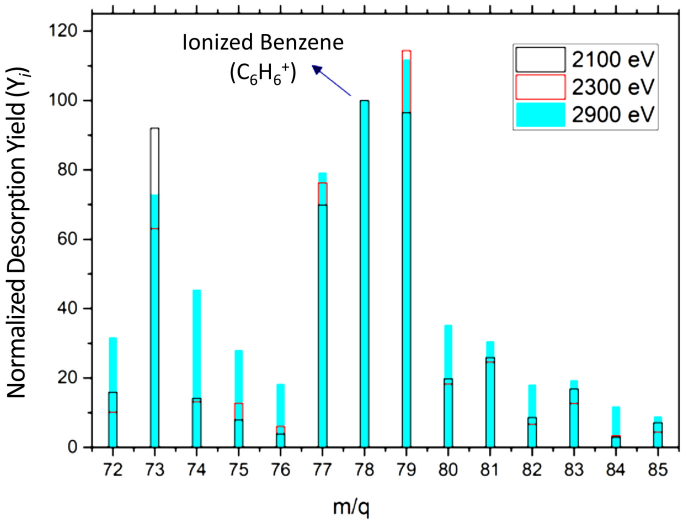

Figure 3. Normalized ion desorption yield, Yi (ions/impact), from benzene ice at 125 K stimulated by electrons at impact energies of 2.1, 2.3 and 2.9 KeV

it is possible to detect such fragments in the radio frequency range. The formation of fragments with odd number of hydrogen atoms is clearly dominant in both dehydrogenated and hydrogenated ionic groups. These closed-shell fragments present a higher structural stability with respect to the even open-shell fragments. Finally, the formation of H-rich species, such as the cyclohexane ion ($C_6H_{12}^+$) and the protonated cyclohexane ion ($C_6H_{12}H^+$), suggests a possible route of formation of the PAH structures with the presence of aliphatic moieties.

Acknowledgements. The authors would like to acknowledge the staff of the Laboratório de Química de superfícies (LaQuiS) of Universidade Federal do Rio de Janeiro (UFRJ), CNPq and CAPES by the financial support.

References

[1] https://www.astro.uni-koeln.de/cdms/molecules
Burke, D. et al. 2010, Physical Chemistry Chemical Physics,12, 5947.
Fedoseev, G. et al. 20012, The Journal of Chemical Physics, 137, 054714.
Garrod, R. et al. 2008, The Astrophysical Journal, 682, 283.
Herbst, E. et al. 2009, Annual Review of Astronomy and Astrophysics, 47, 427.
Ribeiro, F. et all. 2014, The Journal of Physical Chemistry C, 118, 25978.

Boletim da Sociedade Astronômica Brasileira, **30**, no. 1, 46-47

Ages as an attribute of planetary habitability

L. L. Amorim[1] and J. -D. Jr. do Nascimento[2]

[1] Dep. de Física, Universidade Federal do Rio Grande do Norte, UFRN e-mail: larissal.pesquisa@gmail.com
e-mail: jdonascimento@fisica.ufrn.br

Abstract. In the study of the climatic evolution of the planets and search for life, a key concept is the habitable zone (HZ). The standard definition of HZ is considered, a range of distances from a star to a planet for which liquid water could exist. Physically this corresponds to take into account temperature conditions of about 273 - 373 K for a specific static evolutionary point. Here, based on an evolutionary model, we investigate the evolution of the climate region of a hypothetical Earth around a solar analog star whose masses and metallicities are close to the solar values. We follow the luminosity and temperature model evolution as a function of time (age) for one solar mass star. Our first results used recently GAIA distance and luminosities measurements for a sample of analogs and twins and showing an HZ growing of approximately 20% in size from the Zero Age Main Sequence (ZAMS) to the current age of the Sun. In this study, we are presenting our HZ estimative for a sample of solar analogs and twins. The stability of life and habitability of planets like Earth around solar analogs seems to be a function of age.

Resumo. No estudo da evolução climática de planetas e busca por vida, um conceito fundamental é o de Zona Habitável (ZH). A definição de ZH considerada padrão é de uma faixa de distâncias da estrela em que um planeta pode sustentar água no estado líquido. Fisicamente isso corresponde a levar em consideração condições de temperatura entre 273-373 K para um específico estágio de evolução estelar. Aqui, baseado em um modelo de evolução estelar, nós investigamos a evolução da região climática de uma Terra hipotética ao redor de análogas solares nas quais a massa e a metalicidade são próximas dos valores do Sol. Nós seguimos modelos evolutivos de luminosidade e temperatura como função do tempo (idade) para estrelas de uma massa solar. Nossos resultados usam dados recentes do GAIA para distância e consequentemente luminosidade para uma amostra de gêmeas e análogas e mostram um crescimento da ZH de aproximadamente 20% em tamanho desde a ZAMS até a idade atual do Sol. Nesse poster nós apresentamos nossa estimativa de ZH para gêmeas e análogas. A estabilidade da vida e a habitabilidade de planetas como a Terra ao redor de estrelas como o Sol aparenta ser uma função da idade.

Keywords. (Stars): planetary systems – Stars: evolution

1. Introduction

In order to study planetary habitability we commonly use habitable zone (HZ) as the main parameter. Habitability is quantitatively defined as a measure of the ability of a specific planet orbiting a star develop and sustain life (Schulze-Makuch et al., 2011). However, this concept is under construction. The standard concept of habitable zone (HZ) is conservatively defined as a region where a planet can support liquid water on the surface (Huang 1959). G-type stars evolve along the first 100 Myr reaching the ZAMS, and it is well-known that first billion years of their life the activity is enhanced. The life conditions at this stage are hostile. At this phase, continuous flares, EUV radiation and much denser and faster stellar winds are present (do Nascimento *et al.* 2013). An example of this evolutionary effect driven by the Sun can be found in the Mars evolution. Mars has undergone three main climatic stages throughout its geological history. First, beginning with a water-rich epoch, followed by the Archean cold and semi-arid era. Third, transitioning into present-day arid and very cold desert conditions. These global climatic periods represent three different stages of planetary habitability. The evolution of the habitable zone as a function of stellar age is important and a fundamental step to study habitability. Age of a planet is a major attribute of the habitability status, along which, factors like liquid water or an equivalent solvent, rocky mantle and temperature and other can be considered. The sample selection is critical step to understand our own life evolution as a function of age. Local conditions for the developing of life are thought to include liquid water, magnetic and particles protection, rock, minerals and other aspects connected with the onset of biological requirements. Star-planetary age is a necessary condition and stars with the same properties as for the Sun, and in a range of ages it is one of the good choices to study the habitability evolution as a function of age. In this context, we used the sample composed by 81 solar analogs and twins as proposed by dos Santos et al. (2016). These stars have temperatures between 5662 and 5918K and ages ranging between 0.60 and 10.10 Gyrs.

2. Habitable zone and stellar age

In our approach, to study how HZ changes with the stellar evolution, we used a simple model, in which we consider the flux from a star of radius as $R = \sqrt{\frac{L}{4\pi\sigma T^4}}$, where T is the temperature due to the radiation of a point in the spherical surface of radius R centered in the star that has luminosity L. We use temperatures of 273 and 373 K to compute the internal and external limits of the HZ. These limits represent the temperatures at which water is liquid under a pressure of 1 atm.This is a rough first order approximation. We compare our numbers for the Sun with the ones obtained by Kopparapu et al. (2013), and we realized that they are in good agreement and could be used as a qualitative first study. Concerning distances and evolutionary status of our primary targets, we used information of distance obtained by the GAIA (ESA) mission. We computed luminosities by using the standard expression

$$\log\left(\frac{L}{L_\odot}\right) = \frac{M_\odot(BC + M_V)}{2.5} \quad (1)$$

where BC is the bolometric correction and has been obtained as a function of the T_{eff} and mass, based on the expressions

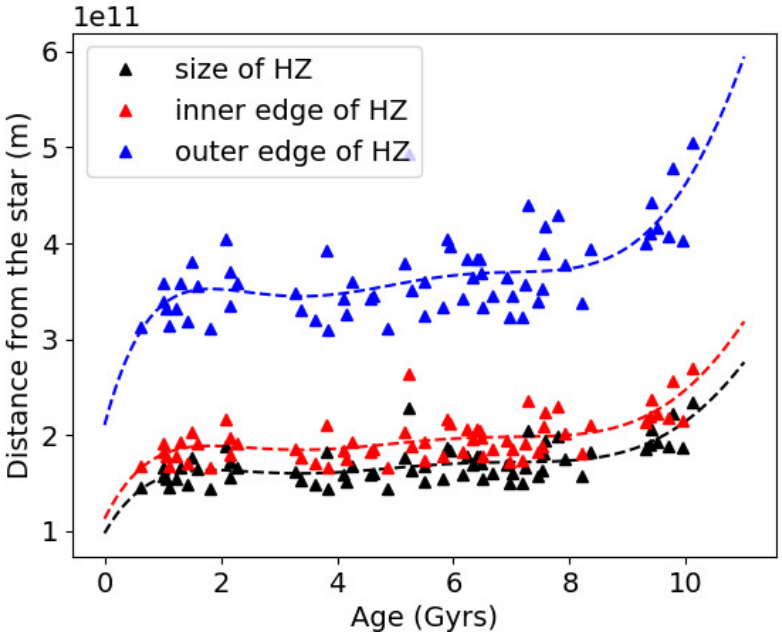

Figure 1. Distance as a function of age. Triangles represent solar analogs and twins which its age and habitable zone has been computed. The dotted lines are trend lines.

described by Flower (1996). The M_V is the visual magnitude and described by

$$M_V = V + 55 \log\left(\frac{1000}{\pi}\right) AV. \quad (2)$$

For close targets with low (π) parallaxes, we can consider absolute extinctions as zero. To understand how these properties vary in an evolving star, we used evolutionary models computed by the Toulouse-Geneva evolutionary code (TGEC), as described in Hui-Bon-Hoa (2008) and do Nascimento *et al.* (2013). These models used an initial composition as Grevesse & Noels (1993). Transport of chemicals and angular momentum due to rotation-induced mixing are computed as described in (Vauclair 2003). The angular momentum evolution follows the Kawaler (1988) prescription. We calibrated a solar model as in Richard *et al.* (1996). With this models, we computed the relation between HZ and some fundamental parameters. The resulting evolutionary model of the HZ as a function of age is shown in Fig. 1.

3. Results and Conclusions

The Figs. 1 show how the HZ evolve as a function of age. From our simple model, we determined a habitable zone size increase of 20% from the ZAMS to the current age of our sun. In this study, we used only stars with new GAIA parallaxes. This first results, allow us to conclude that our theoretical prevision is actually in agreement with the expected for G-type stars. The studies will be continuing to found a promising way to trace the habitability evolution on exoplanets.

Acknowledgements. The authors wish to thank the CNPq and CAPES.

References

Hui-Bon-Hoa, A. 2008, Ap&SS, 316, 55
Flower, P. J. 1996, ApJ, 469, 355
dos Santos, L. A., Meléndez, J., do Nascimento, J.-D., et al. 2016, A&A, 592, A156
Kopparapu, R. K., Ramirez, R., Kasting, J. F., et al. 2013, ApJ, 765, 131
Richard, O., Vauclair, S., et al. 1996, A&A, 312, 1000
Huang, S.-S. 1959, PASP, 71, 421
Schulze-Makuch, D., Mndez, A., Fairn, A. D, et al. 2011 Astrobiology, 11, 1041
do Nascimento, J. -D., Jr., Takeda, Y., et al. 2013, ApJ, 771, 31
Grevesse, N., & Noels, A. 1993, Origin and Evolution of the Elements,eds. N. Prantzos, E. Vangioni–Flam, and M. Cassé, Cambridge Univ. Press, p. 15
Vauclair, S., Théado, S. 2003, A&A, 587, 777
Kawaler, S.D. 1988, ApJ, 333, 236

Boletim da Sociedade Astronômica Brasileira, **30**, no. 1, 48-49

Earth-size planet formation in the 'habitable zone' of binary stars systems

G. O. Barbosa[1a], O. C. Winter[2b], A. Amarante[2c], A. Izidoro[2d], R. C. Domingos[3e], & E. E. N. Macau[1f]

[1] National Institute for Space Research (INPE), São José dos Campos, SP, Brazil.
e-mail: [a]gerson.barbosa@inpe.br, [f]elbert.macau@inpe.br
[2] State University of São Paulo (UNESP), Guaratinguetá, SP, Brazil.
e-mail: [b]ocwinter@gmail.com, [c]amarante@feg.unesp.br, [d]izidoro.costa@gmail.com
[3] State University of São Paulo (UNESP), São João da Boa Vista, SP, Brazil.
e-mail: [e]rdomingos95@gmail.com

Abstract. It is well known that most of the stellar systems have two or more stars. From the binary cases only about 20 have planets in P-type orbits, i.e. in circumbinary trajectories. In the present work we are concerned with the possibility of having Earth-like planets in the habitable zone of circumbinary star systems. These systems have planets with masses in the range from mini-Neptunes to a few times the Jupiter's mass. Then, the work was divided into two parts. The first was to study the stability of the habitable zone of each system. The second one was to explore the possibility of formation of an Earth-like planet in the habitable zone. The stability was studied considering the permanence or not of massless particles in the habitable zone. Therefore, considering the last stage of planetary formation, we explored the evolution of a disk of planetesimals and planetary embrios that under collision with each other accrete and grow. The results are presented in terms of simulations of different disk profiles in order to identify conditions that could possibly form planets with mass similar to the Earth in the habitable zone.

Resumo. É bem sabido que a maioria dos sistemas estelares tem duas ou mais estrelas. Dos casos binários, apenas cerca de 20 têm planetas em órbitas de tipo P, ou seja, em trajetórias circumbinárias. No presente trabalho, estamos preocupados com a possibilidade de ter planetas parecidos com a Terra na zona habitável de sistemas estelares circumbinários. Estes sistemas têm planetas com massas na gama de mini-Neptunes para algumas vezes a massa de Júpiter. Então, o rabalho foi dividido em duas partes. O primeiro foi estudar a estabilidade da zona habitável de cada sistema. O segundo foi explorar a possibilidade de formação de um planeta terrestre na zona habitável. A estabilidade foi estudada considerando a permanência ou não de partículas sem massa na zona habitável. Portanto, considerando a última etapa da formação planetária, exploramos a evolução de um disco de planetesimais e embriões planetários que, sob colisão, se acumulam e crescem. Os resultados são apresentados em termos de simulações de diferentes perfis de disco para identificar condições que poderiam formar planetas com massa semelhante à Terra na zona habitável.

Keywords. Celestial mechanics – Stars binaries: general – Planets and satellites: formation – Methods: numerical

1. Introduction

Recent research has shown that most planetary systems are composed of multiple stellar systems of which 50% are binary. Thus, questions concerning the formation of planets in these systems and the possible existence of life bring us many issues and challenges. In Haghighipour & Kaltenegger (2013), a generalization model of the Habitable Zone (HZ) calculation was proposed in circumbinary systems (P-Type), in which planets rotate around the center of mass of the binaries. This calculation shows the internal and external limits in which a planet of the Earth type (the same mass of the Earth) is capable of harboring life as we know it. However, our work seeks to study the possibility of formation of terrestrial planets in these regions.

2. Methods

We aim to study the last stage of formation of binary stellar systems through computational simulations. For this, we initially studied all binary stellar systems and calculated their HZ's for Earth-like planets (Earth's same mass), and selected the systems that had the possibility of forming and harboring planets within their HZ's, Table 1.

3. Initial Conditions

With the selected systems, the total mass of the protoplanetary disk was distributed within its habitable zones of each system.

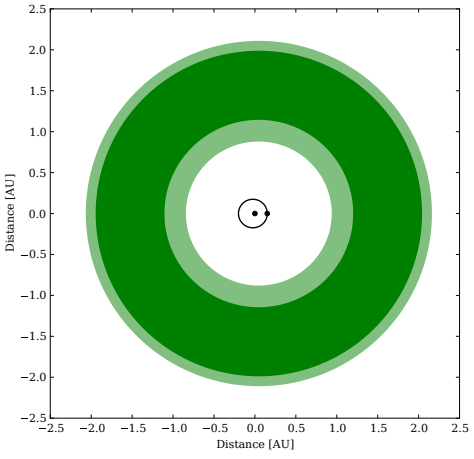

Figure 1. HZ of the binary system Kepler-35 using http://astro.twam.info/hz/.

We used a bi-modal distribution of mass, composed of planetesimals and embryos, 50% of the mass of the disk is formed by planetesimals and 50% by embryos. The radius of the bodies is given from an assumed density of 3.344 gcm^{-3}, and all other elements besides the mass and semi-major axis were randomly distributed, with eccentricity varying between 0-0.01 and inclination between 0^o-0.5^o relative to the plane of the binaries. We used discs with surface profilesgiven by $\Sigma_1 r^{-x}$, where x = 1.5.

System	M_A ($M_\odot$)	M_B ($M_\odot$)	a_{bin} (AU)	e_{bin}	a_p (AU)	e_p	M_p (M_j)	HZ range (AU)
K-34	1.048	1.021	0.229	0.521	1.089	0.182	0.220	1.25-2.80
K-35	0.890	0.810	0.176	0.142	0.603	0.042	0.127	0.90-2.10
K-38	0.949	0.249	0.147	0.103	0.464	0.030	0.380	1.25-2.95
K-38*	0.949	0.249	0.147	0.103	0.464	0.030	0.016	1.25-2.95
K-413	0.820	0.542	0.102	0.037	0.355	0.118	0.210	0.30-0.90
K-453	0.944	0.195	0.185	0.052	0.790	0.036	0.030	0.51-1.30
K-1647	1.221	0.968	0.128	0.160	2.720	0.058	1.520	1.40-4.00

Table 1. Selected binary systems with the potential to form Earth-like planets in their HZ and their respective parameters. The diference between K38 and K38* is the mass, where the mass of K38 is a superior limit and K38* is the reasonable mass.

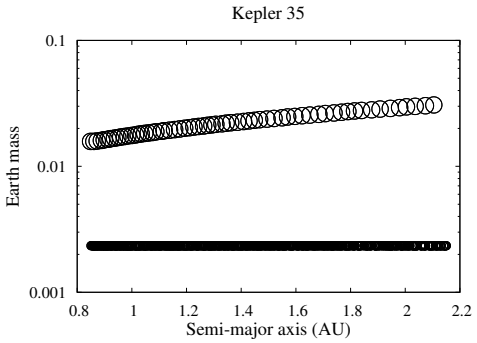

Figure 2. Initial conditions for a disk of the system Kepler-35 containing 65 embryos and 597 planetesimals. Embryos and more massives than planetesimals with their sizes proportional to their mass.

The Σ_1 is the solid surface density at 1 AU and was used to ajusted to fix the total mass in the disc of each HZ region at $2.8 M_\oplus$, comparable to the sum of the masses of the terrestrial planets. Planetary embryos are assumed to have formed by oligarchic growth and are thus randomly spaced by 3.5–6.5 mutual Hill radii. Individual planetesimals were given masses of $7.04\text{x}10^{-9}$ $M_\odot$ ($\approx 2.34\text{x}10^{-3}$ $M_\oplus$). Planetesimals are assumed to interact gravitationally only with the protoplanetary embryos, giant planets and the stars, but not with each other. The masses of the planetary embryos scale as $M \approx r^{3(2-x)/2}\Delta^{1.5}$ (Kokubo & Ida 2002; Raymond et al. 2009; Izidoro et al. 2009) where Δ is the number of mutual Hill radii separating adjacent orbits. This amounts to roughly 60 planetary embryos and 600 planetesimals. Figure 2 shows the initial mass distribution of our simulations.

4. Numerical Simulation

In our simulations are used the planets belonging to each of the systems with their respective real parameters. For each system we performed 5 simulations with slightly different randomly generated initial conditions for planetary embryos and planetesimals. The simulations were integrated for 200 Myr using an adaptation (made by us) in the MERCURY package (Chambers 1999; Chambers et al. 2002).

5. Results

Figure 3 shows in 60 Myr a Earth-like planet with semi-major axis = 1.8 AU, eccentricity = 0.05 and 1.2 $M_\oplus$ in the HZ.

6. Concluding Remarks

One of the most important things for the impossibility of the formation of planets within the HZ is the gravitational effect

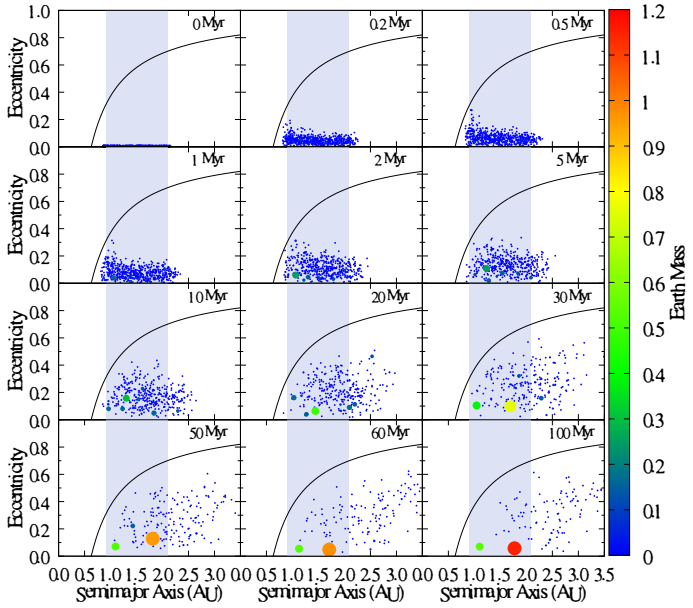

Figure 3. Snapshot in the time of the Kepler-35 system. The size of the each body is proportional to its mass. The region shaded in blue represents the HZ range and the black line represents the semi-major axis as a function of the eccentricity given by $a = [a_p(1 + e_p)]/(1 - e)$.

caused by the planet present in each system. Thus in the case of Kepler-34 and Kepler-1647 systems, we will need to increase the mass in the disk in the next steps to compensate for the ejections caused by the planet's presence of the system. Figure 3 shows that is possible to form a Earth-like planet in the HZ of a real binary star system (Kepler-35 in the case). In the systems Kepler-38, 413 and 453 we can see the same results (planets with mass varying between 0.8-1.3 $M_\oplus$).

Acknowledgements. The authors acknowledge the financial support by CAPES, CNPq and FAPESP.

References

Chambers, J. E. 1999, MNRAS, 304, 793
Chambers, J.E, Quintana, E.V., Duncan, M.J. and Lissauer, J.J. 2002, AJ, 123, 2884
Izidoro A., Raymond S. N., Morbidelli A., Winter, O. C. 2009, MNRAS, 453, 3619
Kokubo E., & Ida S. 2002, ApJ, 581, 666
Haghighipour, N. & L. Kaltenegger, L. 2013, ApJ, 777, 166
Raymond S. N., O'Brien D. P., Morbidelli A., & Kaib N. A. 2009, Icarus, 203, 644

Boletim da Sociedade Astronômica Brasileira, **30**, no. 1, 50-51

Planetary transit model and light curve analysis

N. Vinicius Santos, Israel Florentino, Adriana Valio

[1] Universidade Presbiteriana Mackenzie, São Paulo, SP. e-mail: 41486501@mackenzista.com.br

Abstract. The analysis of light curve based on planetary transit is directly associated to the variation of the light emitted by a star when an exoplanet eclipses its orbit. Each system involves exoplanets (they may have moons, rings, etc.) and stars with numerous features. These variables together generate the light curve, and from it, its possible to calculate the planet radius, orbit slope angle, and the larger semi-axis.

Resumo. A análise de curva de luz baseada no trânsito planetário está diretamente associada á variação da luz emitida por uma estrela quando um exoplaneta movimenta-se por sua órbita. Cada sistema envolve exoplanetas (podem ter luas, aneis, e etc) e estrelas com inúmeras caracteristicas. Estas variáveis em conjunto geram a curva de luz, e a partir dela, pode-se calcular o raio do planeta, ângulo inclinação da órbita e semieixo maior.

Keywords. light curve – planetary systems – model

1. Introduction

More than 3600 planets have been discovered orbiting around other stars. Of these, 75% were detected by the planetary transits method, when the planet eclipses its host star. Given this favorable percentage, this project aims to organize in a single tool the calculations, variables, functions, constants and so on. in a documented way, in order to consolidate the concepts used to calculate the transit of planets based on light curve analysis. Such a model will be implemented and made available in the python language, and will allow the user to perform partial calculations or simulations with analytical results, graphical animations and navigable 3D displays as well as graphs related to the light curve. The Python language was agreed because of the high utilization rate by the academic community. It will also be using a Python branch named Visual Python (VPython). The tool used for the development and eventual compilation of codes that use graphic resources is the Jupyter Notebook. Jupyter is a client-server application that allows the execution of VPython documents through the browser. The development of the tool will be under the paradigm of object oriented programming respecting the design patterns.

2. Light Curve Model

The first step in light curve analysis is when the planet eclipses its host star. During a transit the brightness of the star is diminished by a few hours of less than 1% periodically depending on the orbital period of the planet. This decrease in the amount of light allows the extraction of the data needed to construct the relative light flux as a function of time, as exemplified in Figure 1 (1). The light curve generated by traffic is not always uniform. The light flux may undergo minor changes due to the chemical-physical characteristics of the stars involved in the analysis. Planets may have moons and rings, stars usually have spots, and these characteristics are directly linked to the results generated. When these factors are involved, we can visualize the perturbations in the graph according to Figure 2 (1). Once these variables are parameterized, we are able to infer relevant results, such as the planet radius, the larger semi-axis and the inclination angle of the planet orbit.

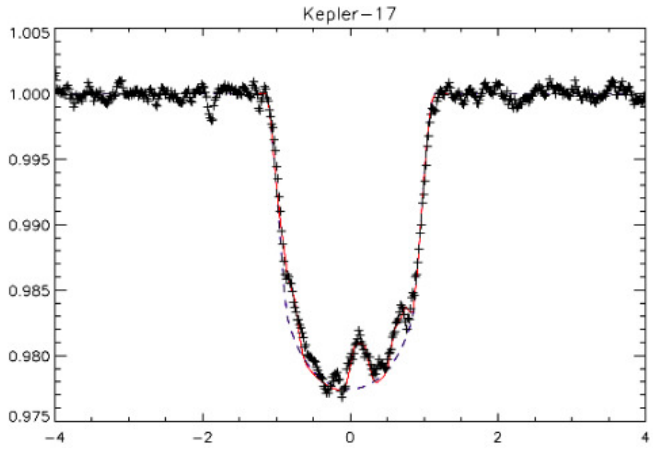

Figure 1. Light curve model without disturbance

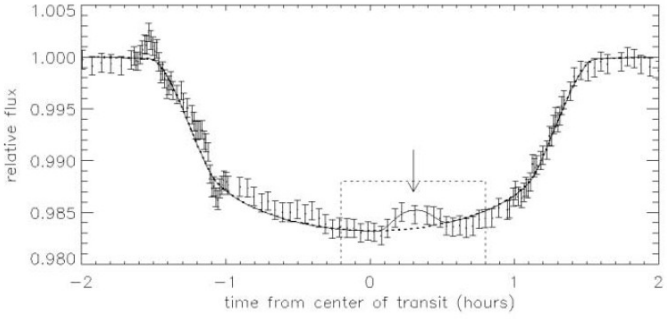

Figure 2. Light curve model with disturbance of a spot light

3. Model, Documentation and Methodology

The application documentation provides all the necessary objects for the best representation of the problems involving the model. Objects such as Magnetic Field, Types of Spots, Flake and Rotation are properly associated so that there is total control and manipulation of the classes. For use of functions, all calls will be properly documented (Figure 3), informing who uses them, what are the arguments that should be passed as a

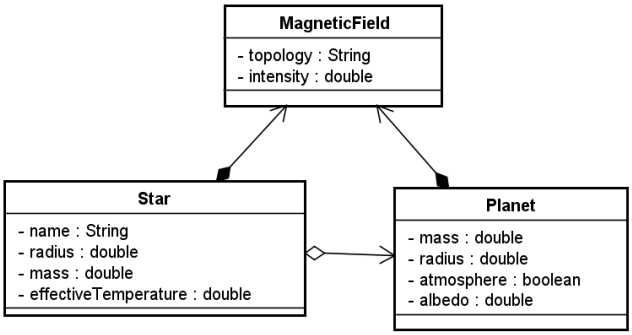

Figure 3. Part of Class Diagram

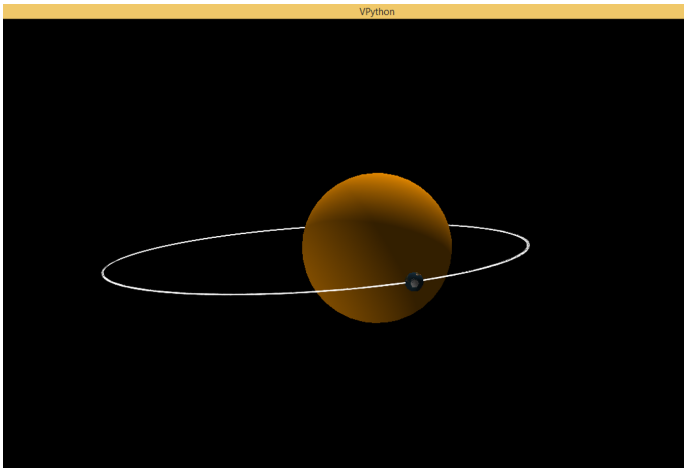

Figure 4. Transit Representation

parameter, as well as what the return of the function and a brief summary of what was done. The animation generated involving 3D (Figure 4) objects will be given dynamically, where the colors, shapes and characteristics of the objects will be defined from the inputs made by those who call the function. The animations will not fit into perfect scales, since such a property would make it difficult to see the planet in front of the star, given its dimensions. The methodology to be used to consolidate all the needs of the application on a single scope will be the analysis and transcription of codes already existing in programming languages, mostly oriented to the work involving astronomy and astrophysics The library will be available to the entire community downloading by Github

4. Expected results

All the asymmetric and mathematical models used were designed through the work by researchers very concepts. Given this, it is intended to consolidate these adaptation models of a use and propagation of the light curve model, using a technology as allied in the process. The largest object and scope is related to the expansion of the planetary transit model under the light curve to be created by users of simple and functional formats, from undergraduate to postdoctoral students. The major difficulties and those faced are associated with the workflow of processes and documentation, since it is a physical and mathematical involved are not trivial. Nevertheless, assuming that future projects involving planetary transit will save precious developing time when the library proposed here is completed, it is sufficient motivation to move forward.

Acknowledgements. Thanks to all friends and teachers for help, time, affection, and especially patience.

References

Silva, A.V.R (2003). Method For Spot Detection On Solar-Like Stars, The Astrophysical Journal.
Tusnski, L. R. M. (2011). Modelo para simulação de trânsitos de planetas com luas e anéis. page 56.
Gamma, E. Helm, R. Johnson, R. Vlissudes, J. Design patterns: elements of reusable object-oriented software
Boss, A. P. (2002). Stellar metallicity and the formation of extrasolar gas giant. pages 50–55.
Ghezzi, C., Jazayeri, M., and Mandrioli, D. (2002). Fundamentals of software engineering.
Marcus, A. and Gould, E. W. (2000). Crosscurrents: cultural dimensions and global web user-interface design. interactions, 7(4):32–46.

Boletim da Sociedade Astronômica Brasileira, **30**, no. 1, 52-53

Unraveling the Astrophotography: Physical Principles and Techniques for Processing Astronomical Images from CCD and DSLR

L. de Almeida[1] & J. R. S. Leão[1]

[1] Federal University of Rio Grande do Norte, Natal, RN, Brazil e-mail: dealmeida.l@fisica.ufrn.br

Abstract.
This work aims to present the methodology used by us as ministrants of telescope and astrophotography workshops. Our mini-course empowers participants to perform a basic operation of motorized telescopes, maintenance, and optics collimation and also provides an average knowledge of the main processing techniques used today in astrophotography. Here, we present the main topics of those courses, that goes from the basics of the optics of all kinds of telescopes to the final processing procedure of the astrophotography.

Resumo. Este trabalho tem como objetivo apresentar um relato de curso e metodologia utilizada por nós enquanto ministrantes de mini cursos de Telescópio e Astrofotografia. Nosso minicurso capacita seus participantes a operação básica de telescópios motorizados, manutenção e colimação das óticas envolvidas e também proporciona um conhecimento médio das principais técnicas de processamento de astrofotografias utilizadas nos dias de hoje. Aqui, apresentamos os principais tópicos de nosso mini-curso, desde ótica básica de todos os tipos de telescópio, até o processamento final de astrofotografias.

Keywords. Teaching of Astronomy – Techniques: image processing – Miscellaneous

1. Introduction

Today, it is not very easy for us to take a break from our modern life and look the night sky, much so because of the visual pollution from the city's lights as also for the lack of interest caused by the false common knowledge that there is nothing interesting to see. Most people also believe that you need crazy expensive equipment to click some quality pictures of the sky. Some schools and universities in Brazil have observation projects but don't have qualified personnel to operate the telescopes. As we don't have a specific course to operate telescopes, most teachers find themselves with great equipment but no experience on the subject. Since 2012 (Leão et al. 2016), our Astronomy and Astrophysics group (SOFIA Observatory) hosts courses about telescopes and astrophotography with the idea of enabling those teachers and students to operate such equipment the best way possible. Since the first time this workshop was given (de Almeida & Leão. 2012), we have always received good feedback from participants regarding the methodology and material used. Our methodology gave light to some related works as Amaral et al. (2016) and Santos et al. (2012).

By the end of each workshop, all participants will have learned: basic and intermediate definitions of OTAs (Optical Tube Assembly), telescope handling and maintenance, concepts and use of DSLRs (Digital Single Lens Reflex), getting astronomical images using reflecting telescopes and main techniques of image processing. Finally, we hope that the participants can leave the course with enough knowledge to be able to make their own astrophotography using the techniques of recording and processing given. Thus, knowing how to mount the telescope, register astronomical objects and process these files revealing the recorded images.

2. Physical principles of telescopes and DSLRs

In this first step, we approach the optics of our image acquisition equipment that is divided into two main parts: the lens; and the sensor. The lens can be interpreted as the optical instrument that converges the light of the object to be photographed at a focus point where the sensor is mounted. The sensor can be interpreted as the analog or electronic device that collect the light coming from the optical instrument. We discuss some types of OTAs used for observation and astronomical recording. First, we must understand what the optics of a telescope consists of. This is the system of lenses and/or mirrors that converge light from the object to a focal point. There are several types of OTAs that differ by the construction and path that the light makes to the focal point. This section of the workshop focus on: OTAs (Optical Tube Assembly), mounts, refractor telescopes (chromatic objective, chromatic aberration, apochromatic APO-ED), reflector telescopes (Newtonian, Cassegrain, Gregorian, Catadioptric, Schmidt, Maksutov), barlows, prisms and filters. The physical principles related to telescopes covered during the workshop are: focal Ratio, magnitude, optical magnitude limit, brightness, resolution, the principle of diffraction, airy disk, Dawes limit, magnification, field of view.

Once we have seen everything we can about OTAs and mounts, we cover the equipment responsible for the acquisition of light from the telescopes and the transformation of this raw signal into digital signals that will be further processed. There are several types of camera with different types of sensors and lenses. Before getting onto the cameras, we need to understand how the digital sensors that store these images work. Regardless of whether it is CCD or CMOS the working principle of these sensors is the photoelectric effect. All the physical principles of CCD and CMOS are covered during the workshop with practical and theoretical problems. This section of the workshop covers: cameras (PowerShot, SLR and DSLR), sensors (CCD and CMOS) and lenses. The physical principles are: lenses, aperture, ISO, the photoelectric effect,A/D (Analog to Digital) and exposure time.

3. Techniques for Processing Astronomical Images

Astrophotography exists for several reasons, and each astrophotographer develops his own motives and ideas about this activity. But we all have in common the desire to do the best possible job with the equipment that we can afford. Good astrophotography can take days, weeks and even months to go the way we want. There are several registration techniques that help us get better RAW images so that, in the processing, we have less work. This part of the workshop aims to give a better understanding of the acquisition techniques and the processing procedures at the final stage of the work. This is the most extensive part of the workshop and here we list just the main topics: registration techniques, afocal, PowerShot and cellphones,direct focus, CCD (equipment adjustment, collimation, auto guider, periodic error correction, focus, darks, bias, luminance, nebulae and galaxies, exposure time, number of frames, preview on DS9, planets and Moon, the maximum number of frames, RGB), DSLR (nebulae and galaxies, T-ring, universal support, camera settings, mosaic, high dynamic range (HDR)), image processing techniques (direct processing, RGB image processing, stacking in 3 colors, level Adjustment in Liberator FITs, processing in Photoshop, mosaic methods in Photoshop, HDR with Photomatix and Photoshop, stacking images in DeepSkyStacker, adjust levels in Lightroom, final Settings in Photoshop, acquisition and processing Techniques with DSLR only, acquisition of the Milky Way), visual pollution. Once we cover all these topics we are able to produce a good quality astrophotography.

4. Results

We show next one example of how the knowledge provided with our workshop and of course, some time, can helps us to create a fine astrophotography. The Fig. 1 shows our earliest attempt to photograph the Trifd Nebula M20 in 2011 with a 12 inch telescope.

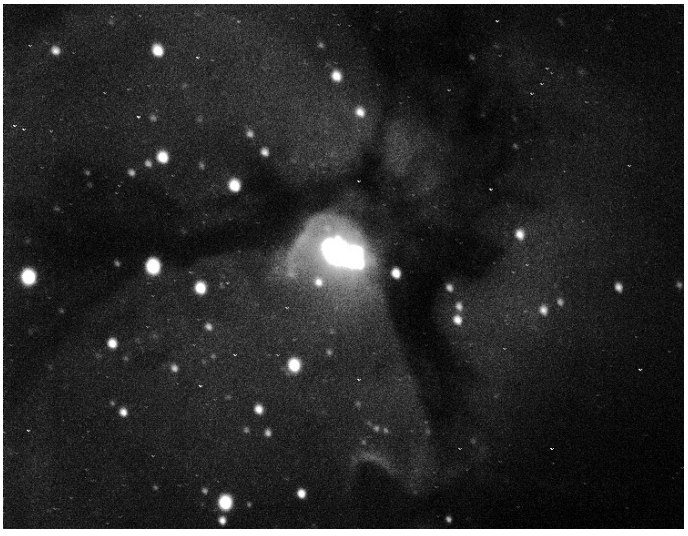

Figure 1. M20 - Single frame of Trifd Nebula by Leandro de Almeida using a 12 inches Telescope with a DSI II camera.

Now, by using all the knowledge available in our workshop, the result is quite fascinating. We can see the final result in Fig. 2, and that same astrophotography received the Nacional Astrophotography prize in 2013.

Figure 2. M20 - Mosaic of the Trifid Nebula in RGB by Leandro de Almeida using a 12 inches Telescope with 2 and 3x barlow and a DSI II camera.

5. Conclusion

The conclusion of this work is that it doesn't matter the price of your equipment if you don't have the knowledge to extract the results. All pictures shown during our workshops were produce using only a meade LX90 12, and a Greika telescope 6 with a DSI B&W with RGB filters.

Acknowledgements. We acknowledge Fabricio Ferrari, Laura Amaral and Jessica dos Santos for helping to maintain the SOFIA Observatory alive all these years. We thank the Federal University of Rio Grande (FURG) and CNPq for providing the means to create this observatory and CAPES and the University of Rio Grande do Norte (UFRN) for the financial support from 2015 to 2017.

References

de Almeida, L., Leão, J.R.S. Métodos Observacionais, Astrofotografia e Utilização de Telescópios de Porte Médio. SNEA 2012. USP.

Amaral, L., Leão, J. R. S., Ferrari, F. (2016) O uso da astrofotografia para a divulgação de astronomia: técnica e metodologia. In: IV Simpósio Nacional de Educação em Astronomia, 2016, Goiânia-GO. anais do IV SNEA

Leão, J. R. S., de Almeida, L., Amaral, L., Ferrari, F., Brito, L. H. 2016, Os primeiros 7 anos do observatório sofia: gênese, observações, divulgação, astrofotografia e impacto. In: IV Simpósio Nacional de Educação em Astronomia, 2016, Goiânia-GO. Anais do IV SNEA.

Santos, J., de Almeida, L., Leão, J. R. S. (2012) Observação do Céu do Extremo Sul do Brasil. In: 21 congresso de Iniciação Científica da Universidade Federal de Pelotas, 2012, Pelotas - RS - BRASIL. Caderno de Resumos do 21 Congresso de Iniciação Científica, CIC.

Boletim da Sociedade Astronômica Brasileira, **30**, no. 1, 54-55

Searching for exoplanet candidates around the evolved binary

QS Vir: a pilot study

E. S. Pereira[1] & L. A. Almeida[1,2]

[1] Instituto de Astronomia, Geofísica e Ciências Atmosféricas, Universidade de São Paulo. e-mail: elielson.pereira@usp.br
[2] Departamento de Física Teórica e Experimental, UFRN. e-mail: leonardodealmeida.andrade@gmail.com

Abstract. The present work was developed with the purpose of identifying and characterizing exoplanets around evolved compact binary systems using the eclipse time variation (ETV) method and, in addition, to develop an algorithm to study the secular dynamic of such systems. As a pilot project, we chose the QS Vir system. This binary consists of a white dwarf as primary with mass of ~0.78 $M_\odot$ and a main-sequence red-dwarf star with mass of ~0.43 $M_\odot$. The binary has a short orbital period $P_{orb;bin}$ = 3.168 hours. Photometric observations were performed between 2010 and 2017 by our group using the facilities of the Pico dos Dias Observatory (OPD/LNA). Light curves of the system were obtained using standard tools in Astronomy. The essential measure for our study, the mid eclipse time, was derived using a binary light curve generation code (Wilson & Devinney, 1971) and an MCMC algorithm (Monte Carlo with Markov Chain). We use a linear ephemeris to fit the mid eclipse times and obtain the (O-C) diagram, which showed a complex variation of ~ 200 seconds of amplitude. The best solution for this variation yields two circumbinary bodies: a brown dwarf (~0.05 $M_\odot$), with an orbital period of ~19 years, and a super-Jupiter (~6 M_{Jup}) with orbital period of ~4.8 years. The solution is close to the 4/1 mean-mean resonance which can be an evidence of secular stability. Additional observations are being done to confirm this findings.

Resumo. O presente trabalho foi desenvolvido com o intuito de identificar e caracterizar exoplanetas ao redor de sistemas binários compactos e evoluídos a partir do método variação dos instantes dos eclipses (VIE), bem como desenvolver um algoritmo para estudar a dinâmica secular associada à tais sistemas. Como um projeto piloto, nós escolhemos o sistema QS Vir. Este sistema é constituído por uma anã branca, como primária, com massa de $0.78 \pm 0.04\ M_\odot$ e por uma anã vermelha da sequência principal, de tipo espectral M e massa de $0.43 \pm 0.04\ M_\odot$. A binária possui uma órbita cerrada de $P_{orb;bin}$ = 3.168 horas (O'Donoghue et al. 2003). Observações fotométricas do alvo foram realizadas entre 2010 a 2017 pelo nosso grupo usando as facilidades do Observatório do Pico dos Dias (OPD/LNA). Curvas de luz do sistema foram obtidas usando ferramentas padrões em Astronomia. A medida essencial para o nosso estudo, o centro do instante do eclipse da primária, foi determinada usando um código de geração de curva de luz de binária (Wilson & Devinney, 1971) e um algoritmo de minimização MCMC (Monte Carlo with Markov Chain). Usando-se uma efeméride linear para ajustar aos instantes de eclipses obtivemos o diagrama (O-C), pelo qual notou-se uma complexa variação de amplitudes de 200 s. A melhor solução para esta variação, resulta em dois corpos circumbinários: uma anã marrom (~0.05 $M_\odot$) com período orbital de ~19 anos e um super Júpiter (~6 M_{Jup}) com período orbital de ~4.8 anos. A solução está próxima da ressonância de movimentos médios de 4/1, que pode ser uma evidência de estabilidade secular. Observações adicionais estão sendo feitas para confirmar essas descobertas.

Keywords. exoplanets — planetary systems — binaries — QS Vir — resonance

1. Introduction

The formation and evolution of planets around binary systems is one of the open questions in the field of exoplanet research. Because of the Kepler mission, it is now known that some non-evolved binaries (both main sequence stars) do host exoplanets.

For example, the Kepler 47 binary has two planets that orbit the system with semi-major axes larger than 1 AU (Orosz et al. 2012) and the binary system Kepler 16 houses a Saturn-type planet with a semi-major axes of 3.9 AU (Doyle et al. 2011). However, the questions that arise are: do exoplanets survive the most energetic phases in the evolution of the host binary? If so, what would be the dynamic evolution of these bodies?

Thus, the present work was developed aiming to identify and characterize exoplanets around evolved compact binary systems from the eclipses times variations (ETV). As a pilot project, we chose the QS Vir binary system. This system consists of a white dwarf as primary with mass of $0.78 \pm 0.04\ M_\odot$ and a main-sequence red dwarf with mass of $0.43 \pm 0.04\ M_\odot$. The binary has a short orbital period of 3.168 hours (O'Donoghue et al. 2003).

An artistic conception of the QS Vir system is illustrated in Fig. 1.

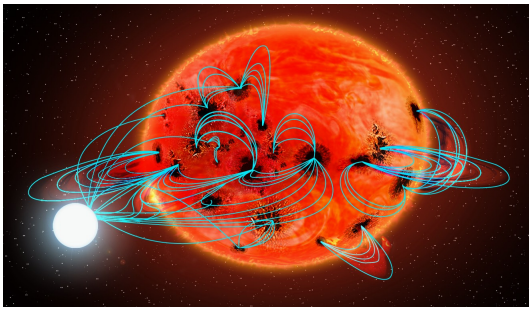

Figure 1. Artistic conception for QS Vir system. Adapted from https://www.noao.edu/outreach/press/pr07/pr0701.html.

2. Analysis, Results and Discussion

2.1. Observations and database

Photometric observations of QS Vir were performed between 2010 and 2017 using the facilities of the Pico dos Dias Observatory (OPD/LNA). Light curves (e.g., Fig. 2) of the system were obtained using standard tools for data reduction from Image Reduction and Analysis Facility (IRAF).

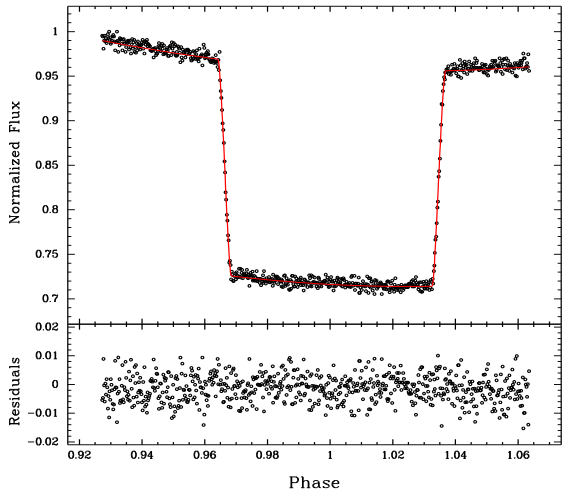

Figure 2. Top panel: White dwarf eclipse of QS Vir superimposed with the best solution obtained with the Wilson-Devinney code. Bottom panel: Residuals from the fitting.

The essential measurement for our study, the primary mid-eclipse time, was determined using a binary light curve generation code (Wilson & Devinney, 1971) and a Monte Carlo with Markov chain (MCMC) algorithm. One example of this procedure is shown in Fig. 2.

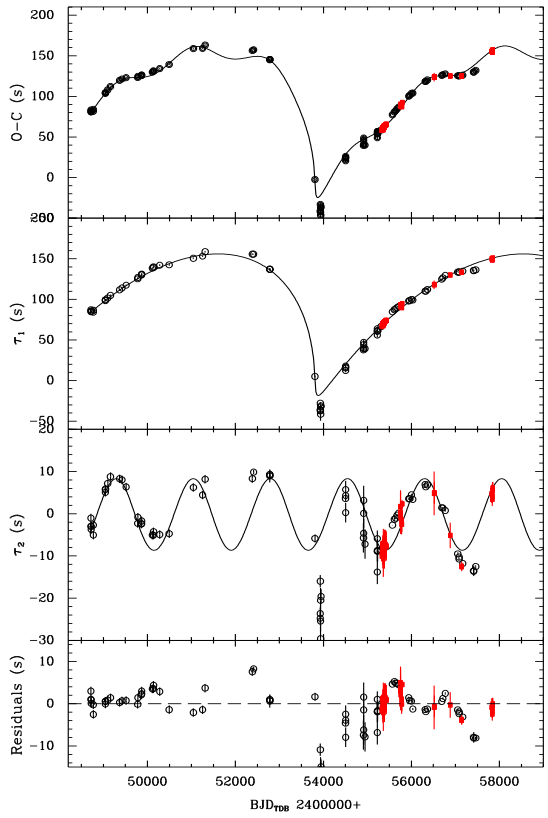

Figure 3. Top panel: QS Vir primary eclipse superimposed with the best solution obtained with the Wilson-Devinney code. Bottom panel: Residuals from the fitting.

2.2. Orbital period variation

Fitting a linear ephemeris to the eclipse times, we obtained the residuals, also called the (O-C) diagram. This diagram show a complex orbital period variation of ~200 seconds of amplitude. After modeling under the assumption of circumbinary bodies, we obtained as a good preliminary solution: a brown dwarf and a super Jupiter. Figure 3 and Tab. 1 show the best solution and the main parameters derived from the fit.

Table 1. Adjusted parameters from the linear ephemeris and the two time-light effect terms to the QS Vir eclipse times.

Linear ephemeris		
Parameter	Value	Unit
P	$0.150757486 \pm 1 \times 10^{-9}$	days
T_0	$2448689.63996 \pm 2 \times 10^{-5}$	MJD(BTDB)
term τ_1		
Parameter	Value	Unit
P	18.96 ± 0.38	years
T	2453831 ± 30	MJD(BTDB)
$a_{\rm bin} \sin i$	0.36 ± 0.01	AU
e	0.95 ± 0.02	
ω	206 ± 1	$^\circ$
$f(m)$	$(1.3 \pm 0.4) \times 10^{-4}$	$M_\odot$
$m \sin i$	52.7 ± 2.0	$M_{\rm Jup}$
$a \sin i$	7.1 ± 0.6	AU
term τ_2		
Parameter	Value	Unit
P	4.78 ± 0.09	years
T	2453956 ± 70	MJD(BTDB)
$a_{\rm bin} \sin i$	0.017 ± 0.002	AU
e	0.10 ± 0.03	
ω	337 ± 1	$^\circ$
$f(m)$	$(2.15 \pm 0.3) \times 10^{-7}$	$M_\odot$
$m \sin i$	6.3 ± 0.6	$M_{\rm Jup}$
$a \sin i$	2.8 ± 0.8	AU

The next step will be to refine the solution and test the dynamic stability in order to confirm the discovery.

Acknowledgements. Ao CNPq pela bolsa de IC concedida durante a execução deste projeto (Processos: 151184/2015-1, 144440/2016-4.).

References

Bours et al, 2016, MNRAS, 460, 3873-3887.
Doyle et al, 2011, Science, 333, 6049, 1602-1606.
O'Donoghue et al, 2003, MNRAS, 345, 506-528.
Orosz et al, 2012, ApJ, 758, 2.
Wilson & Devinney, 1971, ApJ, 166, 605.

Boletim da Sociedade Astronômica Brasileira, **30**, no. 1, 56-57

Atmospheric spectroscopy at Gale Crater on Mars

V. A. Oliveira[1] & P. H. Mombelli

[1] Universidade Federal do Pampa, Caçapava do Sul, Brazil; e-mail: viniciusoliveira@unipampa.edu.br

Abstract. Currently, Mars is the celestial object with the biggest quantity of devices made by mankind. This fact explain the astronomical quantity of data available about this planet, which allows several studies in several lines of research. Here we present the result of a monograph in Space Geophysics, in a graduation in Geophysics, the data used were collected by the device PFS (Planetary Fourier Spectrometer) in the mission MEX (Mars Express) launched in 2006. The main aim was the verification of the existence of methane (CH_4) in a specific region in the atmosphere of the Red Planet. The target region, Gale Crater, is where the Rover Curiosity is right now. Therefore, the choice was because the strong evidence of liquid water in the past on this site, and because Curiosity has identified an unusual amount of methane in the local atmosphere.

Resumo. Atualmente, Marte é o objeto celeste com a maior quantidade de objetos feitos por humanos. Este fato explica a quantidade astronômica de dados disponíveis sobre este planeta, o que permite vários estudos em várias linhas de pesquisa. No estudo atual, apresenta-se o resultado do Trabalho de Conclusão de Curso em Geociência Espacial, do curso de Geofísica, os dados usados foram coletados por um dispositivo PFS (Espectrômetro Planetário de Fourier) na missão MEX (Mars Express) lançada em 2006. O objetivo principal deste trabalho foi a verificação da existência de metano (CH_4) em uma região específica na atmosfera do Planeta Vermelho. A região-alvo, Cratera Gale, é onde o Rover Curiosity está. Sendo assim, a escolha foi devido a forte evidência de água líquida no passado deste local, e porque a Curiosity identificou uma quantidade incomum de metano na atmosfera do local.

Keywords. Planets and Satellites: atmosphere – Planets and Satellites: Mars – Planets and Satellites: Gale Crater

1. Introduction

The term 'GEO' has ceased to be exclusive to Earth studies, inclusive there is a new term: 'Space Geoscience' to explain studies of celestial objects with detectable geological proprieties. In fact, there is increasingly non-stellar objects like moons, asteroids and exoplanets have been studied using Geology, besides to the first targets in the Solar System.

This way, in 2015 was created the Laboratório de Geociências Espaciais e Astrofísica, with the purpose of encouraging and facilitating the studies in Spacial Geoscience. In an effort to start this initiative, we begin a spectroscopic study, in infrared, of the atmosphere of Mars. This study presents the direct objective to analyze and identify methane (CH_4) in the Martian atmosphere, first in a specific region and after over all the planet. In later stages the study intends to determine the abundance of this substance, since it is an organic tracer with fragile survival in atmospheres as that of Mars. This characteristic could be an indicative of a methane source active nowadays.

2. Mars

Mars is the fourth planet of the Solar System, from the Sun, its name is in honor of the god of war of Ancient Rome. Its reddish color is because the large quantity of powder of iron oxide III (Fe_2O_3), which cover almost all the planet (Christensen et al., 2003) Although in many aspects Mars is similar to Earth, the spatial dimension is smaller, especially the diameter (53.2% of the Earth), the mass (10.7% of the Earth) and the mean surface gravity, only 3.71 m/s^2 (Williams, 2004).

Mars presents a rarefied atmosphere, being estimate to be 100 times less dense than Earth's (NASA, 2005). The chemical composition is practically equal to terrestrial, but the abundances differ considerably. The main discrepancies, estimated by Owen (1992), are the CO_2 abundance of 95% in the Mars' atmosphere, against 0.04% in Earth; the N_2 about 2.7% in Mars and 78% in Earth; and the O_2 0.13% and 21%, respectively.

The time coordinates of Mars were adapted to the specific situation of the planet, then it was defined an unity named Solar Longitude (L_S). This unity is proportional to the angle between an imaginary line linked Mars and the Sun with the equinox line in Mars. Then, the Martian months correspond to the variation of L_S of 30º, however each month has different quantities of Martian days (suns). These, in their turn, are equal to 24 hours and 34 minutes. At last, the Martian year is defined in 669 suns.

By contrast, the spacial coordinates system follows the same pattern as Earth, longitude and latitude, always referencing the planetary equator (zero latitude) and a central meridian (zero longitude). Whether the equator is easy to be identified, the central meridian must be choice arbitrary – like did in Earth – and, in 1972, the one chosen in that pass over a crater named Airy-0.

The main selection criterion to Gale Crater was the detection of unusual amounts of methane plumes by the Rover Curiosity in 2012. Considering that (Krasnopolsky et al., 2004) estimated the lifetime of methane in the Martian atmosphere in approximately 340 terrestrial years. Therefore, the planet's atmosphere would not be able to maintain this element for a long period, this implies in a continuous production of CH_4. In fact, (Webster et al., 2015) suggest that Mars is continually producing and releasing methane into the atmosphere.

3. Observations

We used the data collected with the Planetary Fourier Spectrometer (PFS), a device aboard the mission Mars Express (MEX) sent by European Space Agency (ESA) in partnership with *Agenzia Spaziale Italiana*. These data are available in the digital repository Planetary Science Archives (PSA).

According to (Formisiano et al., 2004), from all the observable CH_4 bands using PFS, only the 3 000 cm^{-1} band has a suitable SNR, in addition to having a prominent absorption peak of

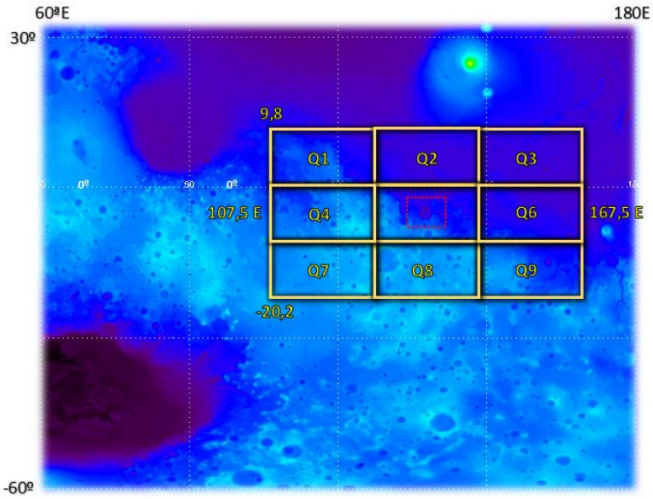

Figure 1. The division of the study area, Q5 indicates the Gale Crater, the figure image shows all the adjacent regions used in this work.

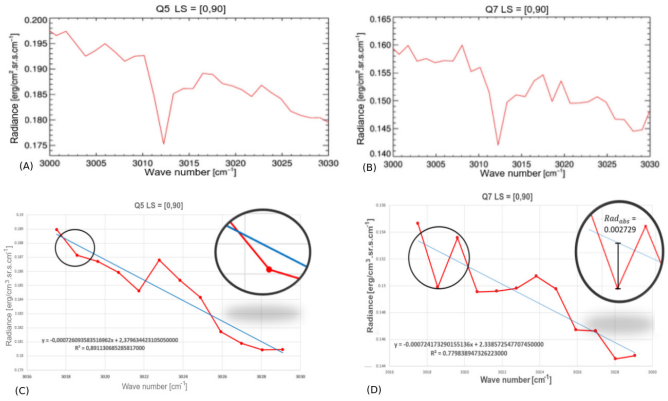

Figure 2. Integrate spectrum obtained (A) for the Q5 region and (B) for Q7 region. Qualitative result (C) in Q5 region and (D) in Q7 region, all of them during the Martian spring.

methane at 3 018 cm^{-1}. For statistical and comparison purposes, it was chosen to work only with integrated spectrum over each region. The adjacent sections were chosen to verify the edge effects, since the Martian atmosphere is not static. Figure 1 brings the visual information of all the chosen regions.

4. Results

Considering that the present study aims at a qualitative analysis, it was decided to estimate a regression curve in the section around the methane line in the spectrum for its correct identification. In this way it was possible to separate noise from true line, i.e., whenever the measured value exceeded a bias value the line was classified as true, otherwise it would just be noise. The cut-off is equivalent SNR measured (SNR_{med}) greater than twice the SNR intrinsic (SNR_{int}) of the equipment, in this case SNR_{int} is equal to 80 erg/s.cm^3.sr.cm^{-1}.

Two of the results calculated by us are showed in Figure 2, both are to Spring Season in Martian North Hemisphere; one over Gale Crater (Q5) and other to Q7 (our better measure). The other graphics are available, please demand the authors if you would to see.

Table 1 indicates the regions studied in which the presence of methane was identified, it is possible to note a seasonal variation of CH_4.

Table 1. Qualitative results found in this work

Seasonal Period	Region with indication of CH_4	SNR_{med}
Spring	Q1, Q3, Q7	2, 4, 3
Summer	–	–
Fall	Q3, Q7	4, 2
Winter	Q1	2

Germinale et al. (2011) indicated sections over Mars where it was detected methane, our results are in a good agreement with them, always during the spring. In fact, this season showed the best situation to determinate methane plumes on Mars.

5. Conclusion

In any season studied in this work, there was no detectable amount of methane at Gale Crater (Q5), sometimes in sections around Q5, specially Q7 (the most promising of all them). A possible reason of this is that this study only used data from the Extended Mission 2 (EXT2) of MEX, from October 2007 to December 2009. It is worth pointing out that Curiosity does the cited detection of CH_4 only in 2014, five years after the data we have used was collected. Therefore, a more detailed analysis, over all the planet, could bring more information about the existence of methane in Mars. Likewise to use data from several mission, including many years, would be useful too.

Acknowledgements. To MEX-M-PFS-2-EDR-NOMINAL-V1.0, a database available in the Planetary Data System (PDS); Dr. Giuseppe Sindoni and Dr. Marco Giuranna for the kindness of responding to the questioning emails, as well as giving some IDL scripts to start the analysis; and to the Department of Geophysics of the Universidade Federal do Pampa – UNIPAMPA.

References

Christensen, P.R. et al. 2003, Science Magazine, 300, 2056
Formisiano, V. et al. 2004, Science Magazine, 306, 1758
Germinale, A. et al. 2011, Elsevier, 59, 137
Krasnopolsky, V. et al. 2004, Iacrus, 172, 537
NASA 2005, "Exploration of the Planet Mars: Mars Facts"
Owen, T. 1992, Mars, 1, 818
Webster, C. et al. 2015, Science Magazine, 347, 415
Williams, D. R 2004, NASA Goddard Space Flight Center, 1

Boletim da Sociedade Astronômica Brasileira, **30**, no. 1, 58-61

How typical is the Solar magnetic cycle?

J. -D. Jr., do Nascimento[1,2], F. Anthony[1], S. Meibom[2], S. Saar[2], & X. Dumusque[3]

[1] Dep. de Física. Universidade Federal do Rio Grande do Norte, UFRN, CP 1641, 59072-970, Natal, RN, Brazil
[2] Harvard-Smithsonian Center for Astrophysics, 60 Garden St., Cambridge, MA 02138, USA
[3] Observatoire Astronomique de l'Université de Genève, 51 Chemin des Maillettes, 1290 Versoix, Switzerland

Abstract. The 11-year activity cycle is a major continuous feature of the Sun. It is the result of a complex temporal evolution of the solar magnetic field intensity, which is controlled by dynamo, that is the physical process generating and maintaining solar magnetic field. The magnetic cycle has consequences in the variations of the Ca II H & K emission line cores and lower chromosphere heating. Long-term Ca II emission variability is also observed in other stars. Combining a star sample from HARPS planet-search program with high-precision Ca II chromospheric activity measurements we selected a large number of reliable Pcyc, and we revisit the relation between rotation periods $P_{\rm rot}$ and $P_{\rm cyc}$, and we discuss about the question of How typical is the Solar magnetic cycle.

Resumo. O ciclo de 11 anos de atividades magnética é uma das mais importantes características continua do Sol. É o resultado de uma complexa evolução temporal da intensidade do campo magnético solar, que é controlado pelo dínamo, que é o processo físico que gera e mantém o campo magnético solar. O ciclo magnético tem consequências nas variações dos núcleos das linha de emissão Ca II H & K e aquecimento da cromosfera inferior. A variabilidade de emissão de longo prazo também é observada em outras estrelas. Nese trabalho, combinando uma amostra de estrelas do programa HARPS de busca por planeta, para as quais fizemos as medidas da emissão de Ca IIreferente à atividade cromosférica associadas à um um grande número de estrelas selecionadas com Pcyc confiáveis, e revisados. Estudamos a relação entre períodos de rotação $P_{\rm rot}$ e $P_{\rm cyc}$, assim como discutimos neste artigo questões referentes a quão típico é o ciclo magnético solar.

Keywords. Stars: activity – Stars: rotation – Stars: solar-type

1. Introduction.

A milestone towards the spectroscopy study of chromospheric activity was given when Eberhard & Schwarzschild (1913) confirmed the presence of Ca II H&K absorption lines in the spectrum of several stars. The Ca II H&K flux became a very important parameter for the understanding stellar activity. Over three decades from the 1960 at the Mt. Wilson Observatory, and using the 100-inch Hooker telescope, Olin Wilson and his collaborators began a long-term program to monitoring Ca II line emission of 91 cool dwarf stars, included the Sun (Wilson 1978). This project became known as the "HK Project" and after 1978 was transferred to the Mount Wilson 60-inch telescope, which was dedicated entirely to study stellar chromospheric activity and variability, and has become identified with a particular methodology known as the *solar-stellar connection*. Along the decades, part of the raw data was lost, and thanks to the cooperative effort at the National Solar Observatory, a large amount was recovered in 2015. Now, a data set complete, calibrated, and self-consistent cover almost 2300 HK Project stars, from 1966 to mid-1995.

Another important step was taken by Skumanich et al. (1975) in established a correlation between the Ca II emission and solar magnetic fields. Today Ca II emission is a well-known proxy indicator for stellar magnetic activity. Long-term variations in the chromospheric Ca II emission can provide information on the nature and strength of magnetic activity. The Mt. Wilson monitoring programme (cf., Baliunas et al. 1995) was the longest-running program to monitor stellar activity cycles. This programme has been monitoring stars continuously since 1966 and demonstrated that the Sun is not the only star with a periodic activity cycle, but rather such periodic behavior is quite common, among the solar type stars. At the same time, for many other solar-like stars, was described an absence of activity or stars do not show any periodic activity cycles like. Wilson (1978); Baliunas & Vaughan (1985); Baliunas et al. (1995), and others have devoted major parts of their research efforts to study the variations of the Ca II emission and determine of $P_{\rm cyc}$ and $P_{\rm rot}$. Brandenburg et al. (1998) critically discussed the available data. Saar & Brandenburg (1999) judged the reliability of the available data and graded them accordingly. Saar & Baliunas (1992) have also studied the data from the extended Wilson survey and find that, while 10-15% of stars in the survey show no periodic variation.

The "HK Project" has shown many interesting features. The quasi-regular cyclic activity demonstrated that many active solar-type stars do not behave cyclically and some exhibit solar-type cyclic behaviour, and other stars vary irregularly. The "HK Project" has shown that quasi-regular cyclic activity is by no means unique to the Sun, but it has also demonstrated that many active solar-type stars do not behave cyclically. A natural path at this point was to assume that by studying the different parameters of these stars (e.g. age, mass, luminosity, rotation periods, convective structure), it should be possible to identify which parameters control cyclic activity, and from that, understand the mechanism responsible for the stellar cycle. In this context, along the recent years, stellar activity surveys have been produced a huge quantity of Ca II H&K observations from the Doppler exoplanet programs and new studies have been conducted to investigate magnetic activity of solar-type stars (Santos et al. 2000; Wright et al. 2004; Hall et al. 2007). The merge of all these data brings a fundamental question: which of these stars are really similar to the Sun in terms of structure and evolution? The Mt. Wilson sample mainly consists of solar-type, main-sequence (MS) stars and the crucial point in this context is clearly found stars that can be considered comparable to the Sun from their mass, effective temperature, metallicity and rotation rate. From this early studies, it is almost clear the dependence of magnetic activity patterns on both rotation and convection, and

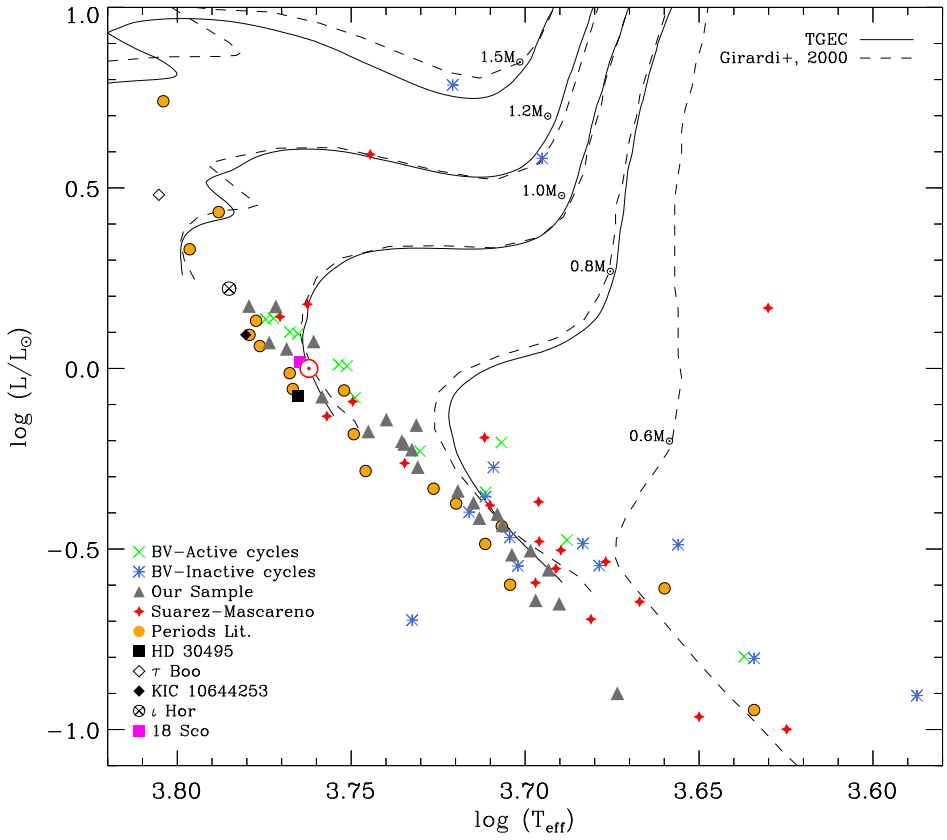

Figure 1. The distribution of the analog sample stars in the Hertzsprung-Russell diagram. Luminosities have been derived from the Hipparcos parallaxes. Evolutionary tracks at [Fe/H] = 0 are shown for stellar masses between $0.6M_{\odot}$ and $1.5M_{\odot}$. Crosses and asterixes indicate stars in Böhm-Vitense (2007) on the active and inactive sequences, respectively.

this suggests the presence of some kind of dynamo action, but it is still a challenger explain a few number of hypothesis, as for exemple those tars that are completely inactive, or those stars with extremely irregular activity. Using new cycle lengths of stellar activity from Mt. Wilson and HARPS FGK high-precision sample (Udry et al. 2000; Lovis et al. 2011) which include some stars nearly indistinguishable from the Sun (Cayrel de Strobel 1996), call solar twins, we can study how typical is the Sun's magnetic cycle length.

2. Evolutionary status and mass

In this sections, we discuss about the sample evolutionary status and some specific observational characteristics of stars used in this study. Part of our data and analysis is based on the high-quality data as selected by Saar & Brandenburg (1999); Lorente & Montesinos (2005); Lovis et al. (2011) and collected by do Nascimento et al. (2015). The Fig.1 shows the HR diagram with the evolutionary tracks computed for different metallicity values ([Fe/H] = 0.15, 0.0, -0.20, and -0.40), and presented here only for [Fe/H] = 0.0, which encompasses most of the stars contained in the present working sample. For comparison raisons, we presenting TGEC models (do Nascimento et al. 2009) and those from (Girardi et al. 2000). The work sample is composed for stars with masses between $0.6M_{\odot}$ and $1.5M_{\odot}$. Crosses indicate stars on the active sequence, and asterisks indicate stars on the Inactive sequence as in Böhm-Vitense (2007). The bright star 18 Sco (HD 146233, HIP 79672, HR 6060) is represented by a square and was the first star identified as a solar twin by Porto de Mello & da Silva (1997). 18 Sco has been observed for chromospheric activity (e.g. Hall et al. 2007), magnetic fields (Petit et al. 2008). 18 Sco which has physical characteristics similar to solar, a lithium abundance about three times solar (Meléndez & Ramírez 2007), a younger age (Baumann et al. 2010), $P_{\rm rot}$ of 22.7 days (Petit et al. 2008) and a Sun-like activity cycle of 7 years (Hall et al. 2007), is found here that along border line of the inactive sequence.

3. Rotation Periods and Cycle Lengths of Stellar Activity relation

In Fig. 2 we present the lengths of the activity cycles, $P_{\rm cyc}$ in years as a function of the rotation periods in days as originally published by Böhm-Vitense (2007). In Fig. 3 we present an updated version of this Fig. 2. Here we use the same observational data as used by Saar & Brandenburg (1999) and Lorente & Montesinos (2005), but with new $P_{\rm cyc}$ and $P_{\rm rot}$ from Lovis et al. (2011). We from found a distinct segregation of active and inactive stars into two approximately parallel bands A(active) and I (inactive) sequences and a remarkable scattering of points. Crosses indicate stars on the A sequence, and asterisks indicate stars on the I sequence from Böhm-Vitense (2007). Squares

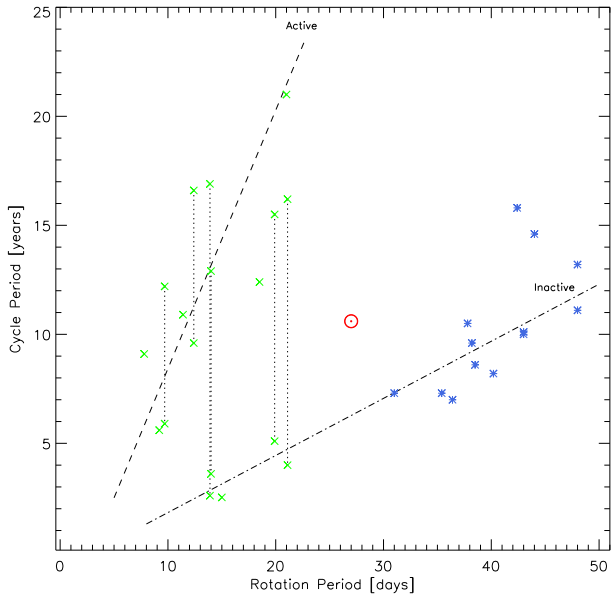

Figure 2. Relation between rotation periods $P_{\rm rot}$ (in days) and cycle Lengths $P_{\rm cyc}$ (in years) of stellar Activity as suggested by Böhm-Vitense (2007). Two sequences are defined by Böhm-Vitense (2007) as relatively young, active A sequence (dashed line) and the older, less active I sequences (dash-dotted line). The solar point is represented by the usual symbol ⊙.

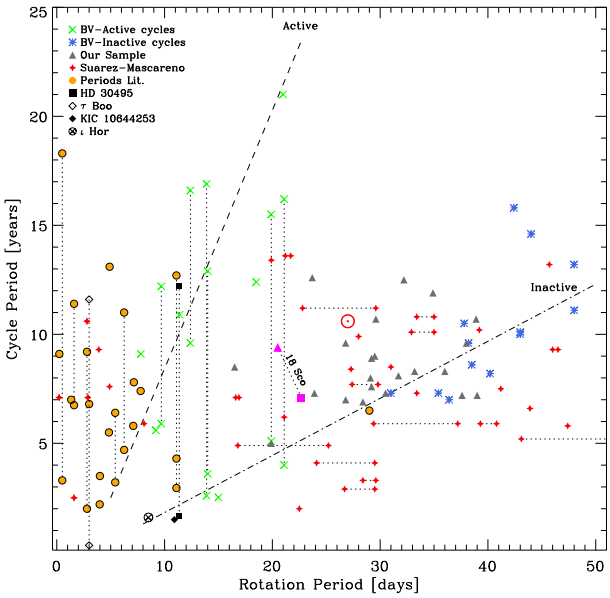

Figure 3. Updated version of the Figure 2, presented originally presented by Böhm-Vitense (2007). Squares around the crosses show stars with $(B-V) < 0.62$. Gold points are cycles from Saar (2011) and more recent data for other single dwarfs seen in HK and photometry, gathered since Saar & Brandenburg (1999) & Brandenburg (1999) represented by green and blue symbols. We also included data from Hall et al. (2007); Metcalfe et al. (2010, 2013); Egeland et al. (2015); Suárez Mascareño et al. (2016); Salabert et al. (2016). Triangles indicate secondary periods for some stars on the A sequence. The vertical lines connect multiple cycles observed for the same star, while the horizontal lines connect multiple $P_{\rm rot}$ observed for the same star. The shaded area indicates the variation of the solar period of rotation caused by differential rotation. The solar twin 18 Sco is represented by the a magenta symbol. For 18 Sco the triangles indicate activity cycles and rotation periods values range.

around the crosses show stars with $(B-V) < 0.62$. Triangles indicate secondary periods for some stars on the A sequence. The Sun position on this diagram is represented by the usual symbol. Inactive I sequence, as defined by Böhm-Vitense (2007) are composed by cooler and more slowly rotating stars. We need to highlight a particular star in this plot, the star 18 Sco. This object it is a solar twin, that is defined as stars nearly spectroscopic indistinguishable from the Sun (Cayrel de Strobel 1996). This target was first identified as a solar twin by Porto de Mello & da Silva (1997). 18 Sco chromospheric activity has been measured for decades (e.g. Hall et al. 2007; Petit et al. 2008). For 18 Sco, authors obtain an age of 2.89 ± 1.09 Gyr, using Li abundances and stellar parameters from high S/N spectroscopy. The mass derived is 1.04 ± 0.02 $M_{\odot}$. 18 Sco has physical characteristics really close to solar. A lithium abundance about three times the solar (Meléndez & Ramírez 2007), a younger age (Baumann et al. 2010), $P_{\rm rot}$ of 22.7 days (Petit et al. 2008) and a Sun-like activity cycle of 7 years determined by Hall et al. (2007). This solar twin is found here at the border line of the inactive sequence. From the Fig. 4 we can see a clear 7 years cycle for 18 Sco, but possibilities of a longer cycle exist, and further observation of 18 Sco is needed.

4. Summary and discussions

As seen in Fig. 3 the observed relation between rotation periods and lengths of activity cycles for main-sequence G and K stars based on recent $P_{\rm cyc}$ and $P_{\rm rot}$ also shows an intermediate scattering (new branch?), besides the two mainly sequences, which Saar & Brandenburg called the active, A, and the inactive, I, sequences. We suggested a "new branch", that it may be a splitting of the Inactive branch. As a main result, we conclude that the Sun is not anomalous, when compared to the magnetic cycles that have been seen in other stars, but potentially a member of a new intermediate branch. An important next step will be evaluated this new $P_{\rm cyc}$ and determined how reliable they are. 18 Sco shows a cycle close to to the lower sequence, however further observation of 18 Sco is needed to confirm (or not) an existence of a longer cycle for this solar twin. A critical analysis on the cycle "quality" is urgently needed.

Acknowledgements. JDN was partially supported by CNPq grants.

References

Baliunas, S. L., Donahue, R. A., Soon, W. H., et al. 1995, ApJ, 438, 269
Baliunas, S. L. & Vaughan, A. H. 1985, ARA&A, 23, 379
Baumann, P., Ramírez, I., Meléndez, J., Asplund, M., & Lind, K. 2010, A&A, 519, A87
Böhm-Vitense, E. 2007, ApJ, 657, 486
Brandenburg, A., Saar, S. H., & Turpin, C. R. 1998, ApJ, 498, L51
Cayrel de Strobel, G. 1996, A&A Rev., 7, 243
do Nascimento, J. D., Castro, M., Meléndez, J., et al. 2009, A&A, 501, 687
do Nascimento, J. D., Saar, S. H., & Anthony, F. 2015, in Cambridge Workshop on Cool Stars, Stellar Systems, and the Sun, Vol. 18, 18th Cambridge Workshop on Cool Stars, Stellar Systems, and the Sun, ed. G. T. van Belle & H. C. Harris, 59–64
Eberhard, G. & Schwarzschild, K. 1913, ApJ, 38
Egeland, R., Metcalfe, T. S., Hall, J. C., & Henry, G. W. 2015, ApJ, 812, 12
Girardi, L., Bressan, A., Bertelli, G., & Chiosi, C. 2000, A&AS, 141, 371
Hall, J. C., Henry, G. W., & Lockwood, G. W. 2007, AJ, 133, 2206
Lorente, R. & Montesinos, B. 2005, ApJ, 632, 1104
Lovis, C., Dumusque, X., Santos, N. C., et al. 2011, ArXiv e-prints
Meléndez, J. & Ramírez, I. 2007, ApJ, 669, L89
Metcalfe, T. S., Basu, S., Henry, T. J., et al. 2010, ApJ, 723, L213
Metcalfe, T. S., Buccino, A. P., Brown, B. P., et al. 2013, ApJ, 763, L26
Petit, P., Dintrans, B., Solanki, S. K., et al. 2008, MNRAS, 388, 80

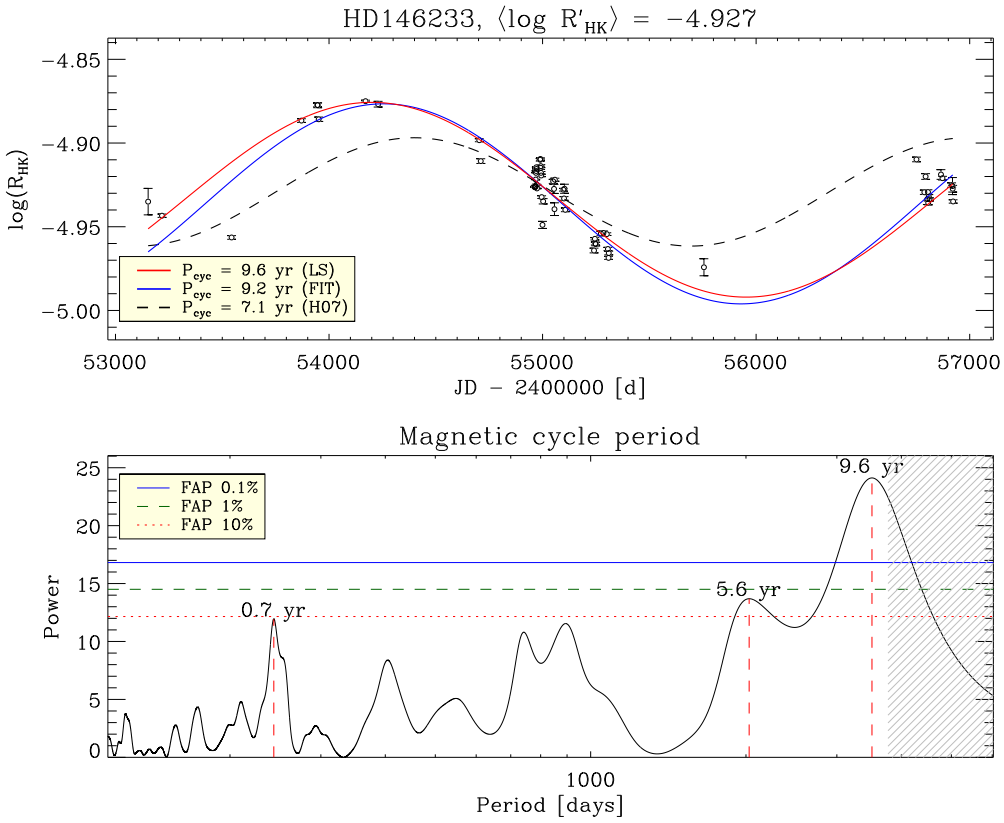

Figure 4. HARPS $log(R_{HK})$ measurements and periodogram for 18 Sco (HD146233).

Porto de Mello, G. F. & da Silva, L. 1997, ApJ, 482, L89
Saar, S. H. 2011, in IAU Symposium, Vol. 273, Physics of Sun and Star Spots, ed. D. Prasad Choudhary & K. G. Strassmeier, 61–67
Saar, S. H. & Baliunas, S. L. 1992, in Astronomical Society of the Pacific Conference Series, Vol. 27, The Solar Cycle, ed. K. L. Harvey, 150–167
Saar, S. H. & Brandenburg, A. 1999, ApJ, 524, 295
Salabert, D., Régulo, C., García, R. A., et al. 2016, A&A, 589, A118
Santos, N. C., Mayor, M., Naef, D., et al. 2000, A&A, 361, 265
Skumanich, A., Smythe, C., & Frazier, E. N. 1975, ApJ, 200, 747
Suárez Mascareño, A., Rebolo, R., & González Hernández, J. I. 2016, A&A, 595, A12
Udry, S., Mayor, M., Naef, D., et al. 2000, A&A, 356, 590
Wilson, O. C. 1978, ApJ, 226, 379
Wright, J. T., Marcy, G. W., Butler, R. P., & Vogt, S. S. 2004, ApJS, 152, 261

Boletim da Sociedade Astronômica Brasileira, **30**, no. 1, 62-66

The rotational evolution of single and binary solar twins using HARPS spectra

Leonardo A. dos Santos[1,2] & Jorge Meléndez[2]

[1] Observatoire de l'Université de Genève, e-mail: Leonardo.dosSantos@unige.ch
[2] Universidade de São Paulo, e-mail: jorge.melendez@iag.usp.br

Abstract. Recent discoveries of extra-solar planets around cool stars show that they have unusual properties which are unseen in the Solar System. In light of this fact, many questions have been posed regarding if the Sun is a typical star for its type and age. In particular, assessing if the Sun is a common rotator has important implications for gyrochronology and our understanding of the rotational evolution of Sun-like stars. In The Solar Twin Planet Search program we observed more than 80 Sun-like stars using the HARPS spectrograph with the objective of procuring extra-solar planets. The high-quality spectra obtained in this program allowed us to perform an unprecedent study on the rotational evolution of stars strictly similar to the Sun, and thus assess if it is a regular rotator. Our results show that the Sun indeed rotates tipically for its age, but the solar twins in general seem to plateau in their rotational velocity evolution after the solar age; the rotational periods, on the other hand, should continue to evolve through the main sequence. In addition, we found that the solar binaries do not follow a distinct evolutionary path in their rotation, and we discuss the outliers in our sample.

Resumo. Descobertas recentes de planetas extrassolares em estrelas do tipo solar mostram que eles têm propriedades incomuns quando comparadas com o Sistema Solar. Em vista desse fato, muitas questões foram feitas se o Sol é uma estrela típica para o seu tipo e idade. Em particular, avaliar se o Sol tem uma rotação comum tem implicações importantes para girocronologia e nosso entendimento sobre a evolução rotacional de estrelas similares. No programa *Solar Twin Planet Search* nós observamos mais de 80 gêmeas solares com o espectrógrafo HARPS com o objetivo de procurar planetas extrassolares. Os espectros de alta qualidade obtidos nesse programa permitiram um estudo sem precedentes sobre a evolução rotacional de estrelas estritamente similares ao Sol, e portanto verificar se ele é um rotador regular. Nossos resultados mostram que o Sol realmente rota tipicamente para sua idade, mas as gêmeas solares em geral parecem estagnar em sua evolução rotacional depois da idade solar; os períodos de rotação, por outro lado, devem continuar evoluindo ao longo da sequência principal. Além disso, também verificamos que as gêmeas solares binárias não seguem um caminho evolutivo distinto em sua rotação, e discutimos os principais casos de desvios da norma.

Keywords. Stars: solar-type – Stars: fundamental parameters – Stars: evolution – Stars: rotation – *(Stars:)* binaries: spectroscopic – Sun: evolution

1. Introduction

The wealth of high-quality photometric and spectroscopic data produced by the search for extra-solar planets fueled a growing interest in questions regarding the magnetic and rotational evolution of Sun-like stars (e.g., Gallet & Bouvier 2013; do Nascimento et al. 2014; Amard et al. 2016). The Sun is the only star for which we have wide access to accurate and precise direct measurements of its physical properties, thus we rely heavily on the knowledge of our star to infer about other stars and their planetary systems. Such indirect inferences are made, however, based on the premise that the Sun is a typical star; it is thus crucial that we assess this assumption by comparing the Sun with other stars, preferably those that display similar physical properties.

Past studies in the rotation of the Sun rendered conflicting results, often suggesting that it either rotates too slowly (Smith 1979; Leão et al. 2015) or regularly for its age (e.g., Soderblom 1983; Barnes 2003). However, such comparisons were made against stars with relaxed degrees of similarity to the Sun, thus precluding us of drawing reliable conclusions on the conformity of the solar rotation.

Simple models of stellar wind and rotational evolution for Sun-like stars predict that, during the main sequence, their rotational velocities and chromospheric activity correlate with stellar ages according to a power-law ($v_{\rm rot} \propto t^{-\beta}$, Kawaler 1988). This power-law index β is related to the magnetic field configuration of the star, which in turn controls how much angular momentum is lost through stellar wind (Charbonneau 1992; Barnes 2003; Gallet & Bouvier 2013). The first strong observational evidence for this evolution was obtained in the seminal work of Skumanich (1972), in which they found that $\beta = 1/2$. This strong connection between rotational rate and stellar age gave life to gyrochronology, which is calibrated to match the solar values (Barnes 2007; Mamajek & Hillenbrand 2008). This relation allows us to reliably derive stellar ages if we know the rotational rate of a star and if we assume that the Sun is a typical rotator. Moreover, we expect that Sun-like stars orbited by close-in stellar or sub-stellar companions have enhanced rotational velocity and chromospheric activity due to interaction with their companions (e.g., Ferraz-Mello et al. 2015).

In the Solar Twin Planet Search program we used the HARPS spectrograph (High-Accuracy Radial velocity Planet Searcher, Mayor et al. 2003) to observe more than 80 solar twins aiming to procure extra-solar planets orbiting bright ($V < 10$) Sun-like stars (Ramírez et al. 2014; Bedell et al. 2015; Tucci Maia et al. 2016; dos Santos et al. 2016, 2017; Meléndez et al. 2017). When corrected for barycentric radial-velocities, the spectra of each star can be combined to produce extreme high signal-to-noise ratio (median SNR $\sim$ 1000 at 600 nm), which in turn allowed us to precisely measure the physical parameters of the solar twins using differential analysis (Bedell et al. 2014). This sample contains 18 spectroscopic binaries, of which three display high rotational velocities for their ages.

We used this large sample of solar twins with high-precision physical parameters to reliably infer if the Sun is a typical rotator for its age, as well as to study the rotational evolution of Sun-like stars. In addition, we employed the radial velocities (RVs) data from HARPS to obtain the orbital parameters of the solar twin binaries and measure the orbital parameters of these systems. In the following sections we discuss our main results and their implications for stellar evolution of Sun-like stars and binary systems.

2. Data analysis of MIKE and HARPS spectra

Initially, we observed 88 solar twins with the MIKE spectrograph (Magellan Inamori Kyocera Echelle, Bernstein et al. 2003) and from these spectra derived the stellar parameters – effective temperature $T_{\rm eff}$, surface gravity $\log g$, metallicity [Fe/H] and stellar ages t – following the procedure described in Ramírez et al. (2014). Later we noticed that the spectral resolution of MIKE is not stable enough to measure rotational velocities $v \sin i$, leading us to use the HARPS spectra to perform this measurement. The other stellar parameters derived from the HARPS spectra are going to be published in a forthcoming paper (Spina et al. 2017).

Since rotational velocities of solar twins are usually lower than 4 km s^{-1}, it is necessary to use spectra with high resolving power ($R > 10^5$) and high signal to noise (SNR > 500) to reliably measure rotational velocities (see figures 1 and 2 in dos Santos et al. 2016). The HARPS spectra are initially processed with the Data Reduction Software (DRS) available for the instrument's users; this software also computes barycentric radial velocities by cross-correlating the spectra with a binary mask of a solar-type star. Further description of the data processing and details on how rotational velocities are measured can be found in dos Santos et al. (2016). Essentially, we combined the HARPS spectra after the radial velocity Doppler correction and the rotational velocities were measured by comparing five observed spectral lines with synthetic lines computed with MOOG (Sneden 1973) and atmosphere models by Castelli & Kurucz (2004). These measurements took into account the contribution of macroturbulence velocity for each star, which is computed following an empirical relation (see equation 1 in dos Santos et al. 2016).

The stellar ages were computed from the MIKE spectra by fitting the stellar parameters with Yonsei-Yale isochronal tracks (Yi et al. 2001), following the procedures of Ramírez et al. (2013, 2014). There are many concerns with the use of isochrones to estimate stellar ages. As shown by Brown (2014), these Bayesian age estimates may be biased towards larger values, although this problem can be minimized by using specific techniques (see Ramírez et al. 2013, and references therein). It is also important to consider that stellar evolution models used to generate the isochrone tracks have limitations, which are mainly related to uncertainties in the input physics and the lack of non-standard physics; for a detailed analysis of the main differences between different stellar evolution models and their limitations, we refer to Stancliffe et al. (2016). Nevertheless, most of these concerns should not be important for stars extremely similar to the Sun, especially for stellar ages near solar age (4.56 Gyr, Bahcall et al. 1995), as the isochrones we use were calibrated to reproduce the solar age and mass (Meléndez et al. 2012).

The orbital parameters of the spectroscopic binaries were estimated following the formalism of Murray & Correia (2010). The best fit parameters are obtained using an implementation of the Nelder-Mead algorithm to minimize the residuals of the fit to a Keplerian reflex motion; the uncertainties of the fit were estimated with `emcee`, an implementation of the Affine Invariant Markov Chain Monte Carlo Ensemble sample (Foreman-Mackey et al. 2013). In addition, we also included radial velocities obtained in other instruments in order to extend the time coverage of the data. More details in the implementation of this method can be found in dos Santos et al. (2017).

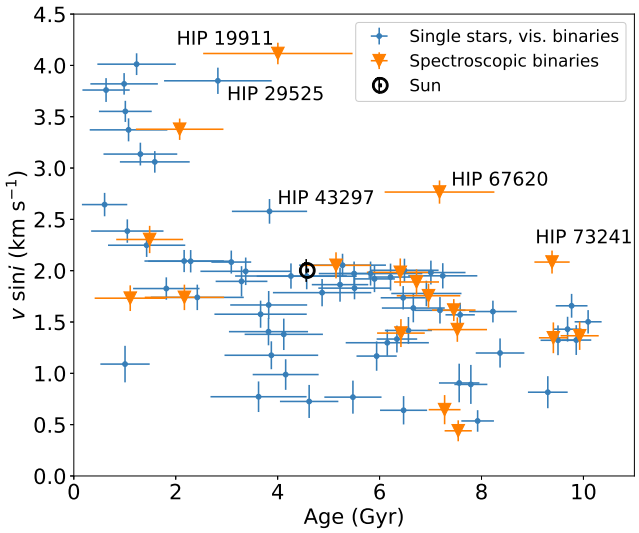

Figure 1. The rotational velocities and stellar ages of all solar twins that were observed with HARPS.

3. The relation between rotational velocities and stellar ages

Rotational velocities measured with stellar spectra are multiplied by $\sin i$, where i is the inclination angle of the rotational axis of the star and the reference plane; this angle is unknown for most stars in our sample, and this limitation introduces a significant spread in the $v \sin i$ versus age relation (see Fig. 1). An isotropic distribution of inclination angles i results in a distribution of $\sin i$ that is biased towards 1; in fact, it is expected that all stars above the 70th percentile of $v \sin i$ in a given interval of ages have $\sin i$ above 0.9. This allows us to select the stars that have the highest chances of having $\sin i \approx 1$ inside age bins with widths of 2 Gyr (see Section 5 in dos Santos et al. 2016). In addition, we remove spectroscopic binaries from the sample, since we start from the premise that these may display distinct evolutionary paths due to interactions with their close-in companions.

We then proceeded to fit an empirical relation between rotational velocities and ages similar to the one inferred by Skumanich (1972). We decided to utilize the functional form of a power-law added of a constant[1]: $v = v_{\rm f} + m\, t^{-b}$, where v is the rotational velocity (km s^{-1}), t is the age (Gyr), and $v_{\rm f}$ (asymptotic velocity, km s^{-1}), m and b are free parameters. The best-fit values for the free parameters were obtained by fitting the data using the the method of orthogonal distance regression (ODR, Boggs & Rogers 1990), which takes into account the uncertainties in both $v \sin i$ and ages.

We found that the best-fit parameters are $v_{\rm f} = 1.224 \pm 0.447$, $m = 1.932 \pm 0.431$, and $b = 0.622 \pm 0.354$ (see Fig. 2). This result is in contrast with the previous empirical studies on the rotational

[1] This same funcional form is also used by Pace & Pasquini (2004) and Guinan & Engle (2009) in their chromospheric activity and $v \sin i$ vs. age relations.

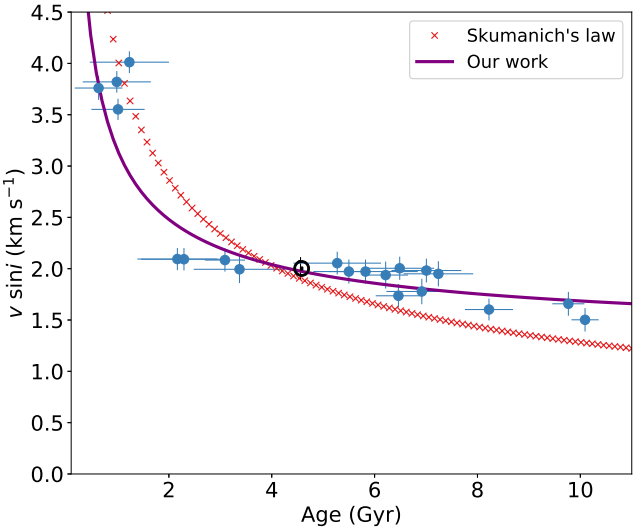

Figure 2. The rotational braking law that we obtained for the *selected sample* of solar twins. The light gray region is composed of 300 curves that are created with parameters drawn from a multivariate Gaussian distribution defined by the mean values of the fit parameters and their covariance matrix.

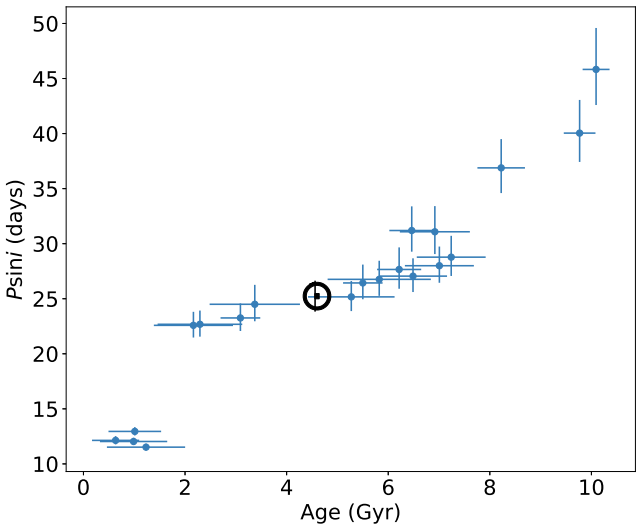

Figure 3. Expected evolution of rotational periods for the *selected sample* of solar twins, taking into account the theoretical evolution of radii from do Nascimento et al. (2014).

evolution of solar-type stars (Barnes 2001, 2003; Lanzafame & Spada 2015), which either found or assumed that the Skumanich law describes well the rotational braking of Sun-like stars. This conflict can be explained by the fact that using solar-type stars, which are not as similar to the Sun as solar twins, may introduce larger uncertainties in the $v \sin i$ and age relation; other line-broadening terms, such as macroturbulence velocities, may also contribute as a confounding factor.

Our results reinforce the idea that the Sun is indeed a normal star regarding its rotational velocity when compared to solar twins; this, in turn, validates the use of the Sun to calibrate gyrochronology relations. The solar twins, on the other hand, do not seem to follow the Skumanich law: their rotational velocities decay more steeply during the early ages, and plateau after the solar age. This result imposes a challenge for gyrochronology, since stars effectively older than the Sun have rotational velocities similar to solar, thus increasing the uncertainties of gyro ages. The rotational braking law we obtained agrees strongly with the theoretical model proposed by do Nascimento et al. (2014), and qualitatively with the empirical power-law index derived by Pace & Pasquini (2004, see Fig. 2).

A similar behavior of rotational stagnation after the solar age was also observed by van Saders et al. (2016) using rotational periods of *Kepler* stars and open clusters. However, due to the evolution of stellar radii during the end of the main sequence (do Nascimento et al. 2014), we expect that the rotational periods of Sun-like stars should become larger after 8 Gyr (see Fig. 3). Thus, although the rotational velocities saturate after the solar age, the rotational periods seem to increase, likely validating gyrochronology.

Among the non-spectroscopic binaries in our sample (blue symbols in Fig. 1), we noticed that HIP 29525 and HIP 43297 displayed rotational velocities significantly higher than the expected for their ages. A careful analysis of their stellar parameters using the HARPS spectra revealed that their ages were overestimated (Spina et al. 2017), which means that these are young stars (0.8 and 1.8 Gyr, respectively, for HIP 29525 and HIP 43297) with consistent rotational rates for their ages. The other fast-rotating stars in our sample are spectroscopic binaries and are discussed in Section 4.

4. Spectroscopic binaries

For the purposes of this study, spectroscopic binaries are those that show a significant modulation in their HARPS radial velocities that can be traced to the presence of a close-in companion or those with companions detected directly in separations smaller than 1 arcsec, which is the angular aperture of the HARPS spectrograph. We observed 18 spectroscopic binaries in our sample, and at least three of them display rotational velocities and chromospheric activity significantly higher than the expected for their ages: HIP 19911, HIP 67620, and HIP 103983 if we consider its updated age estimate (Spina et al. 2017; dos Santos et al. 2016; Freitas et al. 2017; Ramírez et al. 2014). In addition, the radial velocities fit for these three binaries display residuals larger than the expected for the high-quality data they have.

The orbital parameters we measured for the spectroscopic binaries with complete or near-complete phase coverage are shown in Table 1, including the fast-rotating binaries. With the exception of HIP 30037, we found that these systems display moderate orbital periods of more than one year and the minimum masses of their companions indicate that these are, in general, red or white dwarfs.

For HIP 19911 and HIP 67620, the direct detection of bright companions around them (Riddle et al. 2015; Tokovinin 2014; Hartkopf et al. 2012) suggest that their companions are red dwarfs, thus weakening the hypothesis of blue straggler phenomena to explain their anomalies. Further analysis of HIRES spectra of HIP 19911 reveals that this is a double-lined binary (see Fig. 4), which was not visible in the HARPS spectra because of unfavorable observation windows. A similar case is observed for HIP 67620, in which Fuhrmann et al. (2017) found that this is also a double-lined binary, displaying a weak Doppler separation of -7 km s^{-1}. For HIP 103983, a careful analysis of the HARPS spectra revealed that this is also a double-lined binary (see Fig. 5), but with a small Doppler separation that is only discernible when the system is near the periapse.

Table 1. Orbital parameters of the binaries with complete or near-complete orbital phases in their RV data. Results for HIP 83276 come from Duquennoy & Mayor (1991).

HIP	HD	T (days)	e	$m \sin i$ ($M_\odot$)	a (AU)
6407	8291	$1852.3^{+3.3}_{-3.1}$	$0.682^{+0.009}_{-0.010}$	0.119 ±0.002	3.070 ±0.005
14501	19467	–	–	> 0.043	–
18844	25874	–	–	> 0.075	–
19911	26990	2074.15 ±0.09	0.8188 ±0.0003	0.313 ±0.002	6.16 ±0.02
30037	45021	31.61112 ±0.00006	0.30205 ±0.00008	0.0610 ±0.0002	0.1971 ±0.0003
54102	96116	> 5110	–	0.012	–
54582	97037	> 37000	–	0.03	–
62039	110537	–	–	> 0.018	–
64150	114174	–	–	0.258	–
65708	117126	207.273 ±0.004	0.311 ±0.002	0.170 ±0.001	0.851 ±0.001
67620	120690	3803.3 ±0.4	0.3428 ±0.0002	0.578 ±0.002	5.50 ±0.01
72043	129814	> 38000	–	> 0.40	–
73241	131923	> 7670	–	> 0.49	> 0.72
79578	145825	6681.8 ±1.5	0.3322 ±0.0003	0.1014 ±0.0002	7.216 ±0.007
81746	150248	3246.5 ±0.7	0.6644 ±0.0005	0.1079 ±0.0002	4.387 ±0.003
83276	153631	386.72	0.185	0.24	–
87769	163441	> 30000	–	> 0.30	–
103983	200565	10278^{+274}_{-247}	0.50 ±0.01	0.210 ±0.005	9.8 ±0.2

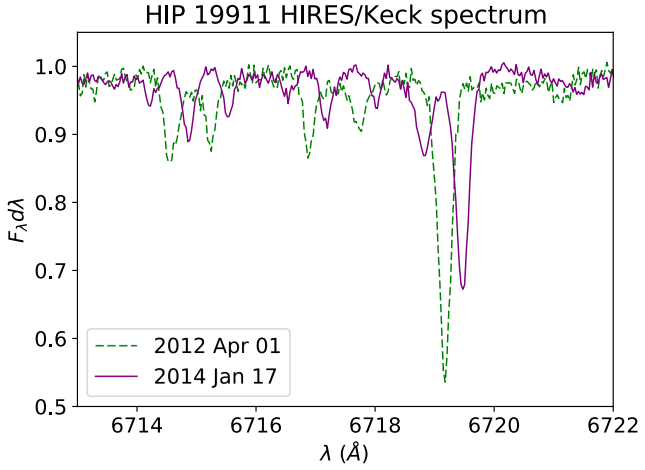

Figure 4. HIRES spectra for the double-lined solar twin binary HIP 19911 taken at two different orbital phases: lowest Doppler separation corresponds to the green spectrum, and the largest separation is represented by the purple spectrum.

These results indicate that solar twin binaries with low-mass companions at moderate or large orbital periods (> 30 days), either eccentric or not, do not seem to follow a distinct rotational evolutionary path than single solar twins. This is an expected outcome, since tidal acceleration caused by interaction with a stellar companion is only important for orbital periods of only a few days, depending on how massive the companion is (see, e.g., Ferraz-Mello et al. 2015).

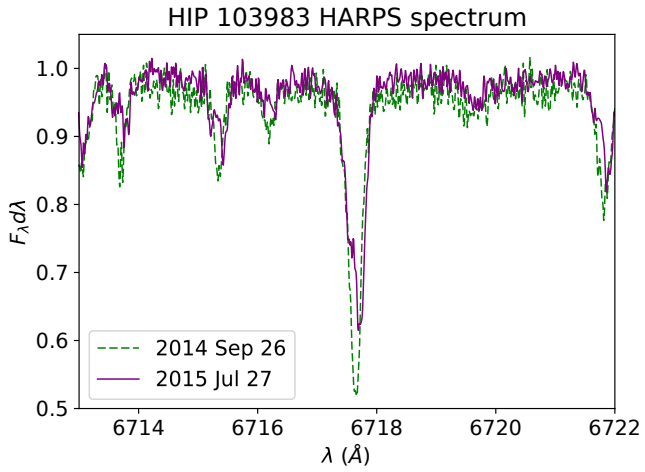

Figure 5. Same as Fig. 4, but for HARPS spectra of the double-lined solar twin binary HIP 103983.

Among the 18 spectroscopic binaries we studied, four of them have new companions that were not previously reported in the literature. These are: HIP 6407, HIP 30037, HIP 54582 and HIP 62039. For the first one, its companion is likely an eccentric red dwarf with minimum mass 0.12 $M_\odot$. The last three binaries likely have very low-mass companions that are either brown dwarfs or giant planets. The last two have very large orbital periods (> 100 yr) that are not easily constrained with the radial velocities data available. Such long period binaries are viable targets for further characterization using direct imaging methods.

5. Conclusions

By employing high-quality HARPS spectra and radial velocities of bright stars strictly similar to the Sun, we have performed the largest study on the rotational evolution of solar twins using spectroscopic data. We concluded that the Sun is indeed a regular rotator for its age when compared to solar twins, and that it is thus viable to use it to calibrate empirical relations such as gyrochronology.

We also found that the solar twins seem to follow an evolutionary path that differs from the widely used Skumanich law: their rotational velocities decay faster during the first 1 Gyr, but even more striking is the observation that these velocities stagnate into a plateau after the solar age. This has strong implications for gyrochronology, since the ages inferred from $v \sin i$ may have large uncertainties for Sun-like stars. On the other hand, based on theoretical models of stellar evolution, we expect that the rotational periods of Sun-like stars continue evolving after the solar age, especially by the end of the main sequence; thus our results do not rule out gyrochronology based on rotational periods.

Among the 18 spectroscopic binaries in our sample, we found that three of them, HIP 19911, HIP 67620 and HIP 103983, display a significantly high rotational velocity for their respective ages. After a careful analysis of the radial velocities and spectra, we concluded that these and other anomalies, such as high chromospheric activity and large RV residuals, are likely due to contamination by their bright nearby companion – i.e., these are double-lined spectroscopic binaries. This means that the other binaries in the sample, which have low-mass companions ($m \sin i$ < 0.6 $M_\odot$) at moderate to large orbital (> 30 days)

periods are likely to follow the same evolutionary path of rotation that single stars do.

Acknowledgements. This research was possible owing to financial support from the São Paulo Research Foundation (FAPESP), grants no. 2012/24392-2, 2014/26908-1 and 2016/01684–9. We would also like to thank our collaborators M. Bedell, J. L. Bean, L. Spina, A. Alves-Brito, S. Dreizler, I. Ramírez, M. Asplund, J.-D. do Nascimento and L. Casagrande.

References

Amard, L., Palacios, A., Charbonnel, C., Gallet, F., & Bouvier, J. 2016, A&A, 587, A105
Bahcall, J. N., Pinsonneault, M. H., & Wasserburg, G. J. 1995, Reviews of Modern Physics, 67, 781
Barnes, S. A. 2001, ApJ, 561, 1095
Barnes, S. A. 2003, ApJ, 586, 464
Barnes, S. A. 2007, ApJ, 669, 1167
Bedell, M., Meléndez, J., Bean, J. L., et al. 2015, A&A, 581, A34
Bedell, M., Meléndez, J., Bean, J. L., et al. 2014, ApJ, 795, 23
Bernstein, R., Shectman, S. A., Gunnels, S. M., Mochnacki, S., & Athey, A. E. 2003, in Society of Photo-Optical Instrumentation Engineers (SPIE) Conference Series, Vol. 4841, Instrument Design and Performance for Optical/Infrared Ground-based Telescopes, ed. M. Iye & A. F. M. Moorwood, 1694–1704
Boggs, P. T. & Rogers, J. E. 1990, Contemporary Mathematics, 112, 183
Brown, D. J. A. 2014, MNRAS, 442, 1844
Castelli, F. & Kurucz, R. L. 2004, ArXiv Astrophysics e-prints
Charbonneau, P. 1992, in Astronomical Society of the Pacific Conference Series, Vol. 26, Cool Stars, Stellar Systems, and the Sun, ed. M. S. Giampapa & J. A. Bookbinder, 416
do Nascimento, Jr., J.-D., García, R. A., Mathur, S., et al. 2014, ApJ, 790, L23
dos Santos, L. A., Meléndez, J., Bedell, M., et al. 2017, MNRAS, 472, 3425
dos Santos, L. A., Meléndez, J., do Nascimento, J.-D., et al. 2016, A&A, 592, A156
Duquennoy, A. & Mayor, M. 1991, A&A, 248, 485
Ferraz-Mello, S., Tadeu dos Santos, M., Folonier, H., et al. 2015, ApJ, 807, 78
Foreman-Mackey, D., Hogg, D. W., Lang, D., & Goodman, J. 2013, PASP, 125, 306
Freitas, F. C., Meléndez, J., Bedell, M., et al. 2017, submitted
Fuhrmann, K., Chini, R., Kaderhandt, L., & Chen, Z. 2017, ApJ, 836, 139
Gallet, F. & Bouvier, J. 2013, A&A, 556, A36
Guinan, E. F. & Engle, S. G. 2009, in IAU Symposium, Vol. 258, The Ages of Stars, ed. E. E. Mamajek, D. R. Soderblom, & R. F. G. Wyse, 395–408
Hartkopf, W. I., Tokovinin, A., & Mason, B. D. 2012, AJ, 143, 42
Kawaler, S. D. 1988, ApJ, 333, 236
Lanzafame, A. C. & Spada, F. 2015, A&A, 584, A30
Leão, I. C., Pasquini, L., Ferreira Lopes, C. E., et al. 2015, A&A, 582, A85
Mamajek, E. E. & Hillenbrand, L. A. 2008, ApJ, 687, 1264
Mayor, M., Pepe, F., Queloz, D., et al. 2003, The Messenger, 114, 20
Meléndez, J., Bedell, M., Bean, J. L., et al. 2017, A&A, 597, A34
Meléndez, J., Bergemann, M., Cohen, J. G., et al. 2012, A&A, 543, A29
Murray, C. D. & Correia, A. C. M. 2010, Keplerian Orbits and Dynamics of Exoplanets, ed. S. Seager (The University of Arizona Press), 15–23
Pace, G. & Pasquini, L. 2004, A&A, 426, 1021
Ramírez, I., Allende Prieto, C., & Lambert, D. L. 2013, ApJ, 764, 78
Ramírez, I., Meléndez, J., Bean, J., et al. 2014, A&A, 572, A48
Riddle, R. L., Tokovinin, A., Mason, B. D., et al. 2015, ApJ, 799, 4
Skumanich, A. 1972, ApJ, 171, 565
Smith, M. A. 1979, PASP, 91, 737
Sneden, C. A. 1973, PhD thesis, The University of Texas at Austin
Soderblom, D. R. 1983, ApJS, 53, 1
Spina, L., Meléndez, J., Karakas, A., et al. 2017, submitted
Stancliffe, R. J., Fossati, L., Passy, J.-C., & Schneider, F. R. N. 2016, A&A, 586, A119
Tokovinin, A. 2014, AJ, 147, 86
Tucci Maia, M., Ramírez, I., Meléndez, J., et al. 2016, A&A, 590, A32
van Saders, J. L., Ceillier, T., Metcalfe, T. S., et al. 2016, Nature, 529, 181
Yi, S., Demarque, P., Kim, Y.-C., et al. 2001, ApJS, 136, 417

Boletim da Sociedade Astronômica Brasileira, **30**, no. 1, 67-68

Solar radius at sub-THz frequencies and its relation to solar activity

F. Menezes & A. Valio

[1] Center for Radio Astronomy and Astrophysics Mackenzie (CRAAM), Mackenzie Presbyterian University
e-mail: fabian.menezes@mackenzista.com.br, avalio@craam.mackenzie.br

Abstract. In the optical wavelengths, the solar radius is 695 700 km and this is what defines the photosphere. However, as the altitude increases, the electromagnetic radiation is produced at other frequencies, causing the solar radius to change as function of wavelength. The radius measurements and its dependence on the solar cycle enable a better understanding of the solar atmosphere. We measure the solar radius at the subterahertz frequencies of 0.212 and 0.405 THz – *i.e.*, the altitude where these emissions are primarily generated – and also analyse the radius variation over the 11-year solar activity cycle. For this, we used radio maps of the solar disk for the period between 1999 and 2017, reconstructed from daily scans made by the *Solar Submillimeter-wave Telescope* (SST), located at the Argentinean Andes. Our measurements yield radii of 966.5″ ± 2.8″ for 0.2 THz and 966.5″ ± 2.7″ for 0.4 THz. This implies a height of (5.0 ± 2.0) $\times 10^6$ m above the photosphere. Furthermore, we also observed strong anti-correlation between the radius variation and the solar activity at both frequencies.

Resumo. Em comprimentos de onda visíveis, o raio solar com um valor de 695 700 km define a fotosfera, a superfície visível do Sol. No entanto, à medida que a altitude aumenta, a radiação eletromagnética é produzida em outras frequências, fazendo com que o raio solar varie em função do comprimento de onda. As medidas do raio e sua dependência com ciclo solar permitem uma melhor compreensão da atmosfera solar. Medimos o raio solar nas frequências de subterahertz de 0,212 e 0,405 THz, isto é, a altitude onde essas emissões são geradas dominantemente - e analisamos a variação do raio ao longo do ciclo de atividade solar de 11 anos. Para isso, utilizamos mapas de rádio do disco solar para o período entre 1999 e 2017, reconstruídos a partir de exames diários realizados pelo *Telescópio Solar Submilimétrico* (SST), localizado nos Andes argentinos. Nossas medições revelaram raios de 966.5″ ± 2.8″ para 0,2 THz e 966.5″ ± 2.7″ para 0,4 THz. Isso implica uma altura de (5, 0 ± 2, 0) $\times 10^6$ m acima da fotosfera. Além disso, observamos uma forte correlação entre a variação do raio e a atividade solar em ambas as frequências.

Keywords. Sun: atmosphere – Sun: chromosphere – Sun: fundamental parameters – Sun: radio radiation

1. Introduction

The solar radius is a very important parameter for the calibration of solar atmospheric models.

In this work, we measure the solar radius at subterahertz frequencies of 0.212 and 0.405 THz throughout 18 years, from 1999 to 2017, and its variations due to solar activity. More information on this work is available in Menezes & Valio (2017).

2. Observations and Data

The data used for this study are from the Solar Submillimeter-wave Telescope (SST) [Kaufmann et al. (2002)], installed at El Leoncito Astronomical Complex, Argentina. SST is a multi-beam radio telescope operating at 0.212 and 0.405 THz, with a HPBW [1] of 2′ and 4′, respectively.

To determine the solar radius, we used 67 000 maps of the whole Sun, which were created from azimuthal scans (Figure 1, *top-left*). First, we set the background and quiet-Sun values (respectively first and second highest peaks in Figure 1, *top-right*) so that the solar limb level is set as the mean value of them (*middle horizontal line* in Figure 1, *bottom-left*). Then, the coordinates corresponding to the solar limb level are fit by a circle yielding the circumference center (Figure 1, *bottom-right*) and the radius, that is the mean distance between limb coordinates and the center. After this procedure (for all the maps), the resulting radii values were corrected for the Earth's orbit eccentricity.

We used the Pearson correlation coefficient (PCC) to check for any correlation between solar activity and solar radius variations. The solar activity proxy used for this was the sunspot number (SSN; SILSO data, Royal Observatory of Belgium, Brussels).

[1] Half-Power Beam Width

Table 1: Values of mean sub-THz radii, optical radius [Mamajek et al. (2015)] and altitude above the photosphere.

Frequency	**R** (arcsec)	**R** ($R_\odot$)	**R** (10^8 m)	**Altitude** (Mm)
212 GHz	966.5 ± 2.8	1.007 ± 0.003	7.01 ± 0.02	5.0 ± 2.0
405 GHz	966.5 ± 2.7	1.007 ± 0.003	7.01 ± 0.02	5.0 ± 2.0
Optical	959.63	1	6.957	0

3. Results and discussion

The mean radius obtained for both 0.212 and 0.405 THz was 966.5″ with rms of 2.8″ and 2.7″, respectively (Figure 2). These results are also summarised in Table 1.

To check for consistency, we ploted our results with those from other authors in Figure 3. As can be seen from the figure, the emission altitude decreases exponentially with frequency. Our results, shown as stars in the plot, are in good agreement with previous ones.

We also compared our results to a simple model of the Sun – *i.e.* a solar disk with constant intensity over the disk and a radius of 966″. Then this model was convolved with SST's reconstructed beams. Lastly, we also calculated the solar radius from ALMA's 0.239 THz solar map that resulted in a radius of 964.9″ ± 2.8″, *i.e.* a difference of 1.6″.

In addition to the solar average radius, we investigated the dependence of the solar radius on solar activity (or sunspot number). The temporal series are shown in Figure 4, where the PCC yield correlation coefficients of $\rho_{0.212\mathrm{THz}} = -0.755$

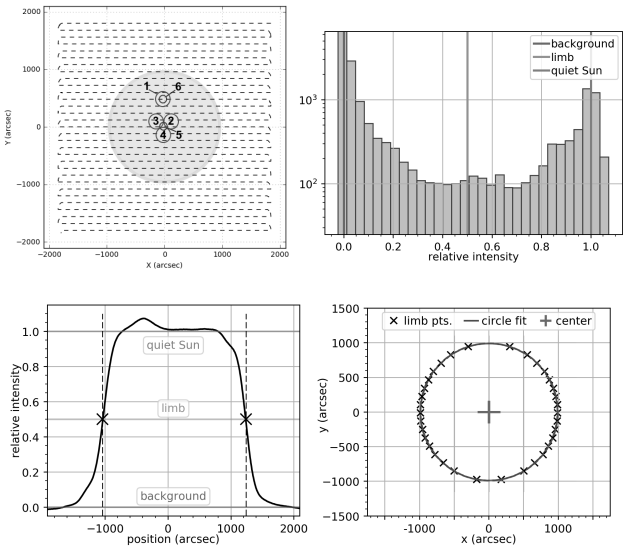

FIGURE 1: *Top-left*: Scans over the solar disk made by SST. *Top-right*: Histogram of the temperature values from the scans. *Bottom-left*: Definition of the solar limb points of a single scan. *Bottom-right*: Limb coordinates with circle fit.

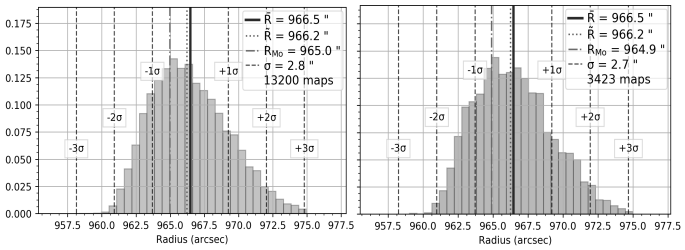

FIGURE 2: Histogram of the solar radius values at 0.212 THz (*left*) and at 0.405 THz (*right*).

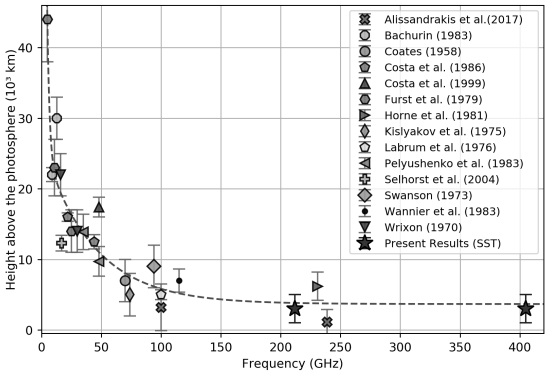

FIGURE 3: Previous altitude values as a function of the frequency from other authors and including our present results. The dashed line represents a double exponential curve fit to the points.

and $\rho_{0.405\mathrm{THz}} = -0.853$. These values indicate a strong anti-correlation between the 11-year solar activity cycle and the temporal variation of sub-THz radii.

4. Conclusions

The mean sub-THz radii estimated in this work implies that most of the emission originates in the chromospheric layer of the solar atmosphere considering the measurements uncertainty. On the other hand, the anti-correlation between the radius and solar activity may be related to the existence of polar brightenings that are anticorrelated to the solar magnetic cycle.

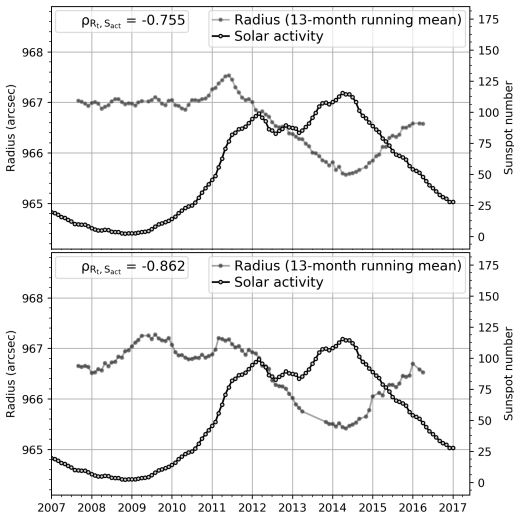

FIGURE 4: Radius temporal variations (*gray lines*) and sunspot number (*black lines*) from 2007 to 2017. *Top*: 212 GHz. *Bottom*: 405 GHz.

Acknowledgements. Thanks to **MackPesquisa** for the financial support to participate in this event and to **CAPES** for the scholarship during the master's degree.

References

Alissandrakis, C. E., Patsourakos, S., Nindos, A., & Bastian, T. S. 2017, A&A, 605, A78
Bachurin, A. F. 1983, Bulletin Crimean Astrophysical Observatory, 68, 61
Coates, R. J. 1958, ApJ, 128, 83
Costa, J. E. R., Homor, J. L., & Kaufmann, P. 1986, Solar Flares and Coronal Physics Using P/OF as a Research Tool,
Costa, J. E. R., Silva, A. V. R., Makhmutov, V. S., et al. 1999, ApJ, 520, L63
Fuerst, E., Hirth, W., & Lantos, P. 1979, Sol. Phys., 63, 257
Horne, K., Hurford, G. J., Zirin, H., & de Graauw, T. 1981, ApJ, 244, 340
Kaufmann, P., Costa, J., Giménez de Castro, G., et al. 2002, Revista Mexicana de Astronomia y Astrofisica Conference Series, 14, 149
Kaufmann, P., Levato, H., Cassiano, M. M., et al. 2008, Proc. SPIE, 7012, 70120L
Kisliakov, A. G., Kulikov, I. I., Fedoseev, L. I., & Chernyshev, V. I. 1975, Soviet Astronomy Letters, 1, 79
Labrum, N. R. 1976, Solar Activity Observations and Predictions, by P.S. McIntosh and M. Dryer. Translated from the English edition. Moskva: Mir., pp.93-116, 93
Mamajek, E. E., Prsa, A., Torres, G., et al. 2015, arXiv:1510.07674
Menezes, F., & Valio, A. 2017, Sol. Phys., 292, #195
Pelyushenko, S. A., & Chernyshev, V. I. 1983, Soviet Ast., 27, 340
Selhorst, C. L., Silva, A. V. R., & Costa, J. E. R. 2004, A&A, 420, 1117
Swanson, P. N. 1973, Sol. Phys., 32, 77
Wannier, P. G., Hurford, G. J., & Seielstad, G. A. 1983, ApJ, 264, 660
Wrixon, G. T. 1970, Nature, 227, 1231

Boletim da Sociedade Astronômica Brasileira, **30**, no. 1, 69-70

Flare parameters inferred with 3D loop models database

V. A. Cuambe[1,3], J. E. R. Costa[1], & P. J. A. Simões[2]

[1] INPE, Astrophysics Division, National Institute for Space Research, Av. dos Astronautas 1758, 12227-010, São José dos Campos, Brazil . e-mail: joaquim.costa@inpe.br
[2] SUPA School of Physics and Astronomy, University of Glasgow, G12 8QQ, Glasgow, UK. e-mail: paulo.simoes@glasgow.ac.uk
[3] UEM, Physics Division, Eduardo Mondlane University, Av. Julius Nyerere 1569, Maputo, Mozambique. e-mail: valente.cuambe@uem.mz

Abstract. We characterize a solar flare based on key parameters of their microwave emission in a structured 3D geometry of a magnetic loop. Due to the high number of the parameters involved we propose a large database of pre-calculated elements (~ 250.000) to better explore the range of those parameters that explain the observables. This database was constructed based on NoRP and NoRH observations (but not restricted to) including known general properties of a solar flare.

Resumo. Caracterizamos uma explosão solar baseado em parâmetros-chave de sua emissão em microondas usando uma geometria estruturada em 3D de um arco magnético. Devido ao elevado número de parâmetros envolvidos, propomos um banco de dados (~ 250.000 elementos pré-calculados) para melhor explorar o intervalo desses parâmetros que explicam os observáveis. Este banco foi construído com base nas observações do NoRP e NoRH (não restritos a estas), incluindo propriedades gerais das explosões solares.

Keywords. Sun: radio radiation – Sun: flares, sun: magnetic fields – sun: atmosphere, catalogs.

1. Introduction

A solar flare is an energetic phenomenon in the solar atmosphere, manifested as a sudden and rapid enhancement of intensity in almost all electromagnetic wavelengths (Fletcher et al. 2011). The excess of energy in tens of seconds is on the order of 10^{32} ergs (e.g. see reviews by Bastian et al. 1998; Fletcher et al. 2011). The process occurs in a magnetic loop or arcades over active regions. Therefore, the lack of knowledge on the detailed coronal magnetic field usually leads to simple homogeneous source model to analyse the emission. This yields to incorrect inferred parameters as analysed in Costa et al. (2013).

To describe a spatially varying flare source, it is necessary to define the strength and geometry of the magnetic field, spatial distribution of the non-thermal electrons, and to a lesser importance for microwave emission, the thermal plasma density and temperature, which can be relevant to the free-free absorption and Razin effect.

Following the work of Costa et al. (2013), we constructed a database based on a simplified 3D loop geometry and distribution of the parameters. We calculated more than two hundred and fifty thousands elements to become a catalogue for flare analyses. In this current database, we upgraded their geometry by inserting two new parameters to describe the magnetic dipole model. Although we know the properties of the gyrosynchrotron emission (the theory); we know that we need information about the geometry and strength of B field in the corona B(x,y,z), and the distribution of the non-thermal electrons, in space and energy it is very complicated and time-consuming to implement in practice as reported in the literature (e.g. Alissandrakis & Preka-Papadema 1984; kucera et al. 1993; Lee et al. 1994). Therefore, past and current observations cannot constrain the models well, even the simplest, uniform source model. That makes the space of parameters for forward-fitting modelling huge. Thus, the proposed large pre-calculated database of 3D simplified models result into a faster search of the parameters in a flare analysis.

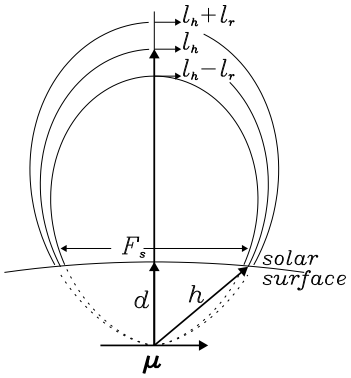

Figure 1. Magnetic dipole model

2. Model description

The loop is modelled as a dipole magnetic field. The magnetic induction of any voxel in space at position ($\mathbf{r}$), from the dipole magnetic momentum (μ), is calculated by

$$B = \frac{3(\mu\mathbf{r})\mathbf{r} - \mu\mathbf{r}^2}{\mathbf{r}^5} \quad (1)$$

The absolute value of the magnetic moment is adjusted to give the desired magnetic field to the loop foot-point. The dipole is placed below the solar surface at some depth d as shown on Figure 1. The flaring volume is constructed around the central field line with a circular cross-section with radius at the apex (l_r). Thus, the geometrical free parameters are the loop height ($H_{arc} = l_h - d$, where l_h is the distance from the dipole momentum to the central field line at the loop apex), feet separation (F_s) and apex radius.

The electron distribution is defined by its energy distribution in the form of a power-law (with power index δ as a free param-

Table 1. Best database representation.

Parameter	ie	δ	N_{nth} (log)	q (%)	Az (Deg)
Mean	1.91	3.12	6.72024	5.65	44.00
Solution	1.94	2.49	6.00277	1.00	-80.60
	R_{Arc} ($\times 10^9$cm)	F_{sep} ($\times 10^9$cm)	H_{Arc} ($\times 10^9$cm)	t (Deg)	B (G)
Mean	0.58	2.20	2.97	4.33	2231
Solution	0.27	2.51	1.74	0.00	2297

eter) from 10 keV to 100 MeV, in a homogeneous pitch angle distribution. The spatial distribution of non-thermal electrons is symmetric in relation to the loop apex. The ambient density is defined as an exponential decay from 10^{13} to 10^8 cm^{-3}. Thus, for a given set of reference values of the parameters, the gyrosynchrotron is calculated following Ramaty (1969), using a code by Simões & Costa (2006); Costa et al. (2013) to obtain the emission and self-absorption coefficients and the 3D radiative transfer. Details are given in those papers.

3. Application to 20020531_000725 UT Flare

We analysed an M2.4 GOES class flare observed on the East limb of the Sun on May 31, 2002 with our 3D database. This M2.4 event clearly shows a loop-like geometry. The maximum peak in 9.4 GHz at NoRH were observed at 00:07:25 UT. We collected the four fluxes at 3.75, 9.4, 17 and 34 GHz at NoRP website without any additional calibration, and both images at 17 and 34 GHz at NoRH. From the magnetogram, we found that the maximum positive and negative B is $\sim$ 2200 G, that suggests low asymmetry. The inferred parameters of the observation (computed weighted mean) from our database search can be seen in Table 1. This Table 1 also shows the refined parameters (solution) obtained after calculating new elements that are not in the database using a genetic algorithm known as Pikaia (Charbonneau 1995) to improve the image and spectrum matches.

We found a microwave looptop emission that is quite clear from the image of this May 31, 2002, flare near the limb. This effect might be explained by an enhancement of energetic electrons at the top of the loop occurring as a result of a transverse pitch angle anisotropy caused by the accelerating mechanism as suggested in the work of Melnikov et al. (2002).

Figure 2 shows plots of the spectra. The asterisks show the observed spectrum obtained by NoRP website, the continuous line shows our refined solution.

Figure 3 shows the observed NoRH maps at 34 and 17 GHz on red scale, respectively. The maps are overlaid with white contour at 50% of NoRH image maximum and black contours plots of the model for comparison. It is clearly seen that the contours not perfectly match but it reproduces the shape of the observed loop. This may imply that many of the geometric parameters (see Table 1) of the model are roughly in the same range of the observable.

4. Conclusions

We conclude that, this database speeds up the search for the best geometrical representation of the observed brightness temperature of NoRH maps and the best spectral fit of NoRP, by using a reasonably large volume of pre-constructed models with different scenarios.

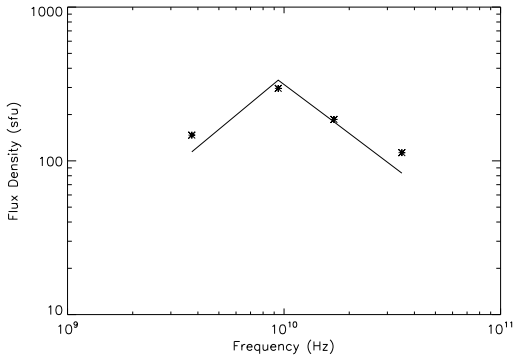

Figure 2. Plots of the calculated and observed spectra. The asterisks are the observed NoRP spectrum, thick line is the fitting.

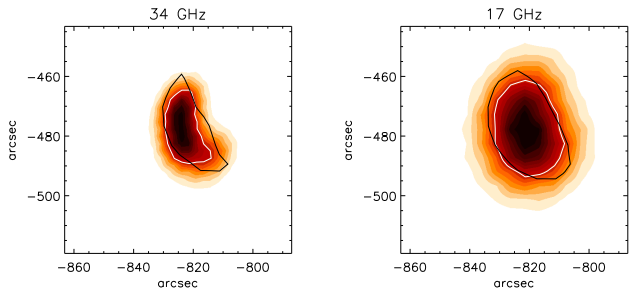

Figure 3. Images of NoRH 34 and 17 GHz (red scale) brightness temperature with contours overlaid (white) at 50% of image maximum and model (black) at 50%.

Acknowledgements. We would like to thank the SKA SA for all the support they have offered and the Brazilian agency CAPES for financial support of the fellowship of one of us (V.A.C).

References

Alissandrakis, C. & Preka-Papadema, P. 1984, A&A, 139, 507
Bastian, T. S., Benz, a. O., & Gary, D. E. 1998, A&A, 36, 131
Costa, J., Simões, P., Pinto, T., & Melnikov, V. 2013, PASJ, 65, 5
Charbonneau, P. 1995, ApJS,101,309
Fletcher, L.; Dennis, B. R.; Hudson, H. S.; Krucker, S.; Phillips, K.; Veronig, A.; Battaglia, M.; Bone, L.; Caspi, A.; Chen, Q.; Gallagher, P.; Grigis, P. T.; Ji, H.; Liu, W.; Milligan, R. O.; Temmer, V. 2011, Space Sci. Rev., 159
Kucera, T. A. and Dulk, G. A. and Kiplinger, A. L.,et al. 1993, ApJ, 412,853
Kuznetsov, A. A. and Kontar, E. P. 2015, Sol. Phys., 290, 79
Lee, J. W., Gary, D. E., & Zirin, H. 1994, Sol. Phys., 152, 409
Melnikov, V. F., Reznikova, V. E., Yokoyama, T., & Shibasaki, K. 2002, in ESA Special Publication, 506, 339–342
Ramaty, R. 1969, ApJ, 158, 753
Simões, P. & Costa, J. 2006, A&A, 453, 729

Boletim da Sociedade Astronômica Brasileira, **30**, no. 1, 71-72

Studying spot-induced modulations of active solar analog stars

E. N. Velloso[1] & J.-D. do Nascimento Jr.[1,2]

[1] Universidade Federal do Rio Grande do Norte e-mail: diofanto@ufrn.edu.br
[2] Harvard-Smithsonian Center for Astrophysics e-mail: jdonascimento@cfa.harvard.edu

Abstract. Modulations of stellar light in cool stars are the result of spots crossing the visible stellar disc. Due to differential rotation, spots at different latitudes have different rotation periods. Using synthetic light curves generated with a starspot modeling code we confirm that for cool stars spot latitude and stellar inclination are challenging to be determined uniquely from the photometry alone. We emphasize that spectroscopic rotation measurements are essential. As a first result, we performed a comparative analysis of parameters obtained for κ^1 Cet, a young solar analog observed by MOST, and we show that at least for stars at the same range of magnetic activity, starspot modeling gives coherent solutions. These first results open a door to revisit an entire population of similar stars observed by CoRoT and Kepler (and soon by TESS) and a possibility to constrain parameters of limb darkening and differential rotation at this mass and evolutionary stage. These parameters are fundamental for stellar evolution and exoplanet science.

Resumo. Modulações da luz de estrelas frias são resultantes de manchas cruzando o disco estelar visível. Devido à rotação diferencial, manchas em diferentes latitudes possuem períodos de rotação diferentes. Usando curvas de luz sintéticas geradas por um código de modelagem de manchas, confirmamos que para estrelas frias a latitude e a inclinação são difíceis de determinar apenas pela fotometria. Enfatizamos que medidas espectroscópicas de rotação são essenciais. Como um primeiro resultado, realizamos uma análise comparativa dos parâmetros obtidos para κ^1 Cet, uma jovem análoga solar observada pelo MOST, e mostramos que ao menos para estrelas na mesma faixa de atividade magnética, a modelagem das manchas produz soluções coerentes. Esses primeiros resultados abrem uma porta para revisitar toda uma população de estrelas semelhantes observadas pelo CoRoT e pelo Kepler (e em breve pelo TESS) e a possibilidade de restringir parâmetros de escurecimento de limbo e rotação diferencial nessa massa e estágio evolutivo. Tais parâmetros são fundamentais para evolução estelar e ciência de exoplanetas.

Keywords. Methods: miscellaneous – Stars: solar-type – starspots

1. Introduction

Since the dawn of the starspot hypothesis to explain distortions in some lightcurves, including solar data, astronomers have been deeply interested in the subject in order to obtain some insight about the stellar magnetic field behaviour. Several attempts to approach the problem through the study of lightcurves were made ever since, each one with different assumptions. Some prefer to use numerical integration over the spot areas, which usually are in rectangular shape in a uniform grid, as in the case of Matrix Lightcurve Inversion techniques (Harmon & Crews 2000), while others assume circular spots with a given set of parameters (position and size) and work out analytical models based on the geometry of the problem (Eker 1994).

In the case of analytical models, software has been created in order to find and visualize optimal solutions, as for instance `SpotModeL` (Ribárik, Oláh & Strassmeier 2003) and `StarSpotz` (Croll et al. 2006). In this context, the `Cheetah` code was developed focusing on speed over model visualization, seeking to be suitable for a large scale study of the Kepler dataset, implemented in the widely used programming language Python. Its performance was tested for synthetic lightcurves (Walkowicz, Basri & Valenti 2013) and now we extend the project using real lightcurves for solar-type young stars applying also a Markov Chain Monte Carlo (MCMC) method for assessing the parameter uncertainties.

In section 2 we will discuss the analytic model chosen to parameterize the spotted stars as well as the underlying algorithm used to calculate the best fit plus uncertainties. In section 3 we will take a look at first results from the solar analog κ^1 Cet. At last, in section 4 we will further discuss our conclusions and some future directions.

2. Model and Algorithm

We used the analytic formulation for a single circular spot as in Eker (1994). We assume there are $n_{\rm spots}$ contributing to modulations in a given lightcurve, so our set of parameters is going to be

$$\theta = \left[i \;\; T_{\rm eq} \;\; k \;\; \beta_1 \;\; \lambda_1 \;\; R_1 \;\; \cdots \;\; \beta_{n_{\rm spots}} \;\; \lambda_{n_{\rm spots}} \;\; R_{n_{\rm spots}} \right],$$

where i, $T_{\rm eq}$ and k are stellar parameters (inclination, rotational period at equator and differential rotation coefficient, respectively) and for each spot there are position (latitude β and longitude λ) and size (angular radius R). Each parameter has its boundaries according to the physics of the problem, and the differential rotation profile is given by:

$$T(\beta) = \frac{T_{\rm eq}}{1 - k \sin^2 \beta},$$

which implies that we need at least two spots to fix a single rotation pattern.

Using normalized units for flux (maximum at 1.00) we are able to derive the expected noiseless flux $f(\theta, u_1, u_2, \kappa_\omega)$ for a given set of parameters, where u_1 and u_2 are limb-darkening coefficients and κ_ω is the spot-to-photosphere flux ratio. These were fixed and assumed to be near solar values ($u_1 = 0.70$, $u_2 = 0.00$, $\kappa_\omega = 0.29$).

Each spot is fitted sequentially to the lightcurve via Levenberg-Marquardt non-linear least squares optimization, and every time an additional spot is fitted the whole vector of parameters used so far is optimized simultaneously. In addition to the original boundaries on the nature of the parameters, constraints can be made to the valid parameter space (e.g. a known $v \sin i$

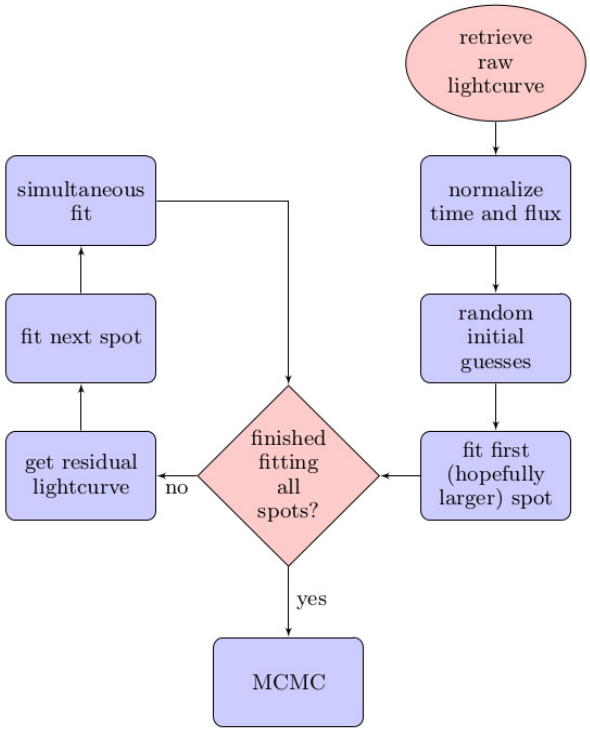

Figure 1. The greedy algorithm used to fit efficiently a given number of spots.

range) to reduce degeneracies. In the end, we apply a MCMC method using the `emcee` python library (Foreman-Mackey et al. 2013) to assess the model goodness of fit. The whole process behind the developed algorithm is indicated schematically in fig. 1.

More details on the multi-fit process can be found on the original documentation for `Cheetah` online[1].

3. First Results

In the direction of evaluating the validity of the proposed algorithm, we elected the solar analog κ^1 Cet as our first case study, mainly because it is a very young and active solar analog, which means it can be reasonably modeled with few (2 or 3) starspots and the assumptions about rotation profile and limb-darkening are justified, but also because there are many such studies in the literature whose results we intend to compare with ours to estimate accuracy. In tab. 1 we compare our findings using a very simple MCMC (500 walkers, 3000 iterations) to the minimum χ^2 solutions reported in Walker et al. (2007). Our solution is shown in fig. 2.

4. Conclusions

We have shown that the greedy algorithm indeed produces coherent solutions according to known results and that the constraints on parameter space reduce errors due to degeneracies. If we apply the same method with a fixed set of parameters we might be able to find the optimal limb-darkening coefficients and κ_ω. We intend to keep perfecting the method and study young open clusters in order to draw conclusions about starspot physics in active stars at the same evolutionary stage.

[1] `https://github.com/lmwalkowicz/Cheetah`

Table 1. Comparative results of fitted parameters.

Parameter	Prior range	MCMC	(Walker et al. 2007)
i (deg) . . .	30 – 80	51.33 – 62.56	60.6
T_{eq} (days)	8.0 – 10.5	8.61 – 8.91	8.784
k	0.00 – 0.30	0.13 – 0.23	0.087
β_1 (deg) .	−10 – 60	14.47 – 27.69	32.4
λ_1 (deg) .	0 – 360	293.74 – 300.45	298[a]
R_1 (deg) .	5 – 30	11.83 – 12.68	11.75
β_2 (deg) .	−10 – 60	44.88 – 58.80	37.2
λ_2 (deg) .	0 – 360	54.21 – 94.15	105[a]
R_2 (deg) .	5 – 30	5.88 – 6.67	5.95

[a] Derived from relative epoch and period.

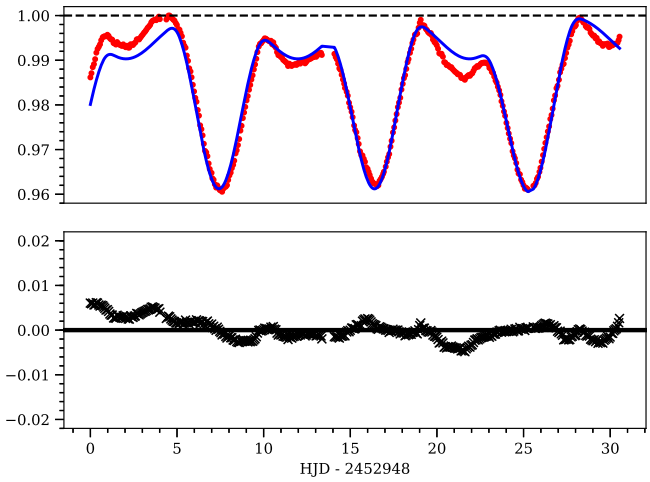

Figure 2. Model fit of two-spot solution for the κ^1 Cet lightcurve of 2003. In the lower panel, residuals on the same scale.

References

Croll, B. et al. 2006, Bulletin of the American Astronomical Society 38, p. 1217.
Eker, Z. 1994, The Astrophysical Journal 420, p. 373.
Foreman-Mackey, D., Hogg, D.W., Lang, D. & Goodman, J., 2013, Publications of the Astronomical Society of the Pacific 125(925), p. 306.
Harmon, R.O. & Crews, L.J., 2000, The Astronomical Journal 120(6), p. 3274.
Ribárik, G., Oláh, K. & Strassmeier, K.G., 2003, Astronomische Nachrichten 324(3), p. 202.
Walker, G.A.H. et al. 2007, The Astrophysical Journal 659, p. 1611.
Walkowicz, L.M., Basri, G. & Valenti, J.A. 2013, The Astrophysical Journal Supplement Series 205(2), p. 17

Boletim da Sociedade Astronômica Brasileira, **30**, no. 1, 73-74

Magnetic activity in main sequence and evolved stars

B. F. O. Gonçalves[1], J. S. da Costa[1] & J.-D. Jr. do Nascimento[1]

[1] Universidade Federal do Rio Grande do Norte e-mail: odlavson@ufrn.edu.br

Abstract. The complexity of cool star's magnetic field demands an investigation of magnetic activity along the stellar evolution. In this work, we use Least-Squares Deconvolution (LSD) to look for magnetic signal in a base composed of 63 (main sequence, giant, and supergiant) stars. We also computed the chromospheric activity index (S-index) — based on Ca II H and K lines — for the stars in our base. It was found magnetic field signature for eight main sequence stars and nine evolved stars. Our preliminary results show an evident decay of magnetic field and chromospheric activity with age for main sequence stars. For evolved stars, we find what seems to be a trend between S-index and Teff.

Resumo. A complexidade do campo magnético das estrelas frias demanda uma investigação da atividade magnética ao longo da evolução estelar. Neste trabalho utilizamos o método do LSD (do inglês *Least-Squares Deconvolution*) com o intuito de procurar por sinal magnético em uma base composta por 63 estrelas que se encontram em três estágios evolutivos distintos: sequência principal, gigantes e supergigantes. Nós também calculamos o índice de atividade cromosférica (S-index) — baseado nas linhas H e K do Ca II — para as estrelas da nossa base. Foi encontrado sinal de campo magnético para 8 estrelas da sequência principal e para 9 estrelas evoluídas. Nossos resultados preliminares mostram um decaimento claro do campo magnético e da atividade cromosférica com a idade para as estrelas da sequência principal. Para as estrelas evoluídas, encontramos o que parece ser uma tendência entre S-index e Teff.

Keywords. Stars: activity – Stars: magnetic field – Stars: late-type

1. Introduction

It is a known fact to the astronomical community that the magnetic field plays a crucial role in the formation and evolution of stars. However, it has been only in the last two decades that we became capable of investigating the real influence of magnetism in the lives of stars. The construction of high-resolution spectropolarimeters such as ESPaDOnS (CFHT) and NARVAL (TBL) has been providing the scientific community with an amount of data never seen before. As a result, the quality of the work done grew significantly along with the development of new methods of data analysis. In this way, stellar magnetism is today a well-established field of research, where observational results feed theorists with new constraints to their models.

However, despite significant advances, there remain many unsolved questions. We do not have yet the complete awareness of the differences between the solar dynamo and other kinds of dynamos operating in cool stars. Moreover, some renowned researchers are also not sure about the reliability of the tomographic imaging methods currently used to reconstruct magnetic maps of stars, Zeeman-Doppler Imaging (ZDI) as an example.

This work was set up to investigate other unsolved questions not mentioned above, but also important. At what stage during the evolutionary track a star switch from being magnetic active to becoming magnetic inactive? Are our methods limited to detect magnetic fields only in low-mass stars? This article does not intend to solve those questions but rather show what the possible answers based on the results obtained are.

2. Sample

We selected 63 cool stars (except for two stars that present T_{eff} greater than 7000 K) from different luminosity classes: main sequence, giants and supergiant stars (Figure 1). Some of the giant stars studied here were select from Aurière et al. (2015). Meanwhile, all main sequence stars were extracted from

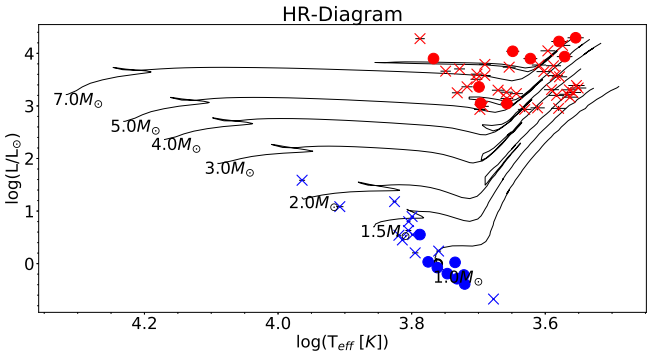

Figure 1. Hertzsprung-Russel diagram with evolutionary tracks showing our data base of 63 stars.

Boyajian et al. (2012). We downloaded the spectra utilized in this work from PolarBase (Petit et al. 2014).

3. Methods

We used two methods to instigate signs of magnetic activity in our database. First we calculated the S-index as described in Tsvetkova et al. (2017) in order to identify chromospheric activity in the stars of our base (Equation 1 and Table 1).

Then, we applied the Least-Squares Deconvolution (LSD) method (Donati et al. 1997) to compute longitudinal magnetic field for the stars that showed at least marginal field detection (Equation 2).

$$S_{index} = \frac{aF_H + bF_K}{cF_{R_{HK}} + cF_{V_{HK}}} + e \quad (1)$$

$$B_l = 2.14 \times 10^{11} \frac{\int vV(v)dv}{\lambda gc \int [1 - I(v)]\, dv} \quad (2)$$

Table 1. Constant values used in the calculation of the S-index (Refer to Equation 1).

coefficients	values
a	-6.394
b	164.816
c	94.996
d	20.665
e	0.03253

4. Results

Some of our results can be seen in Figures 2 and 3, both related to the main sequence stars, and Figure 4, related to evolved stars.

There is a natural relation between magnetic field intensity and chromospheric activity. We expect that stars with field detection present higher S-index than stars that did not present field detection. However, it is possible that spectra with high noise give us a false high value for the chromospheric activity even though a magnetic field does not exist on the atmosphere of the star or is too low to be detected. It would be necessary to look spectrum by spectrum to identify for this kind of problem.

Figure 2 presents the expected result: as the stars evolve, its angular momentum loss makes it spin slower. As a consequence, the dynamo effect gets weaker, and we end up measuring a decrease in the magnetic field.

The result shown in Figure 3 is in complete accordance with Figure 2. In other words, a decrease in the magnetic field is directly related to a decrease in chromospheric activity what results in lower values for the S-index.

In Figure 4 we seem to have a low decrease of the S-index with T_{eff}. However, this result needs further analysis to be confirmed.

The results obtained from this work lead us to believe that more massive stars situated on the main sequence either do not present a global magnetic field or our methods cannot resolve it. For the evolved stars, we need further investigation to see if there is any trend between physical structure features of giant stars and the presence of a magnetic field.

5. Perspectives

We intend to continue to investigate the presence (or not) of magnetic fields in more massive stars. Nonetheless, we know that a radiative envelope might be the reason why we cannot detect such fields. Furthermore, we will also study the physical differences that exist in the top layers of the atmosphere of giant and supergiant stars — what ends up creating a dividing line (Linsky & Haisch 1979) in the cool region of the HR-diagram — and the role magnetic fields play in this feature.

Acknowledgements. I acknowledge the graduate student Leandro de Almeida (PPGF - UFRN), aka Ted, for the constant support regarding the Python language and other issues. I also thank CNPq for the financial support during my master's degree.

References

Aurière, M., Konstantinova-Antova, R., Charbonnel, C., et al. 2015, A&A, 574, A90
Boyajian, T. S., McAlister, H. A., van Belle, G., et al. 2012, ApJ, 746, 101
Donati, J.-F., Semel, M., Carter, B. D., Rees, D. E., & Collier Cameron, A. 1997, MNRAS, 291, 658
Linsky, J. L., & Haisch, B. M. 1979, ApJ, 229, L27
Petit, P., Louge, T., Théado, S., et al. 2014, PASP, 126, 469
Tsvetkova, S., Petit, P., Konstantinova-Antova, R., et al. 2017, A&A, 599, A72

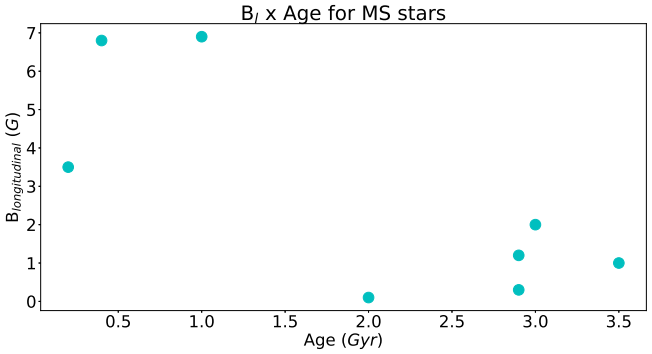

Figure 2. $B_{longitudinal}$ vs Age for main sequence stars.

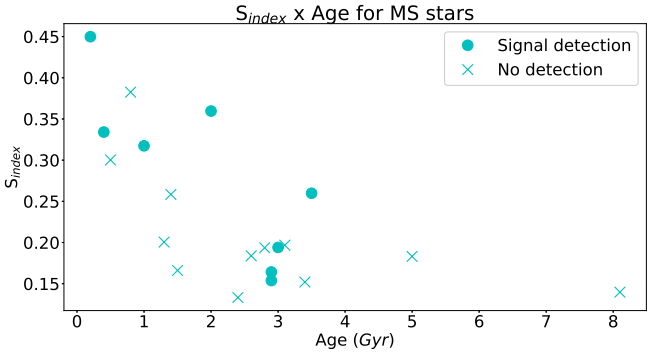

Figure 3. S_{index} vs Age for main sequence stars.

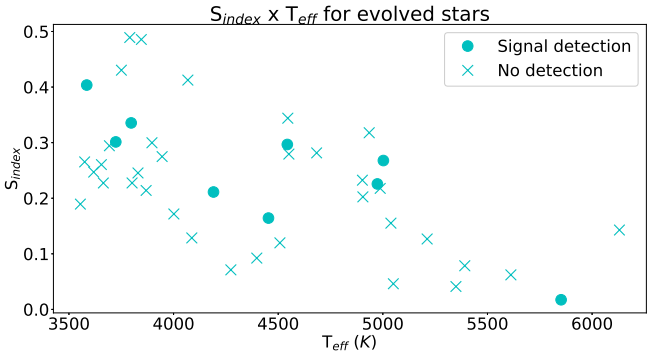

Figure 4. S_{index} vs T_{eff} for evolved stars.

Boletim da Sociedade Astronômica Brasileira, **30**, no. 1, 75-76

Heating mechanisms of protostellar accretion disks

N. F. S. Andrade & V. Jatenco-Pereira

[1] Instituto de Astronomia, Geofísica e Ciências Atmosféricas e-mail: natalia.fernanda.andrade@usp.br e-mail: vera.jatenco@iag.usp.br

Abstract. Accretion disks are commonly found around young stars, such as T Tauri stars. In order to occur the transport of matter to the star, the particles of the disk need to loose some of their rotational energy and fall towards the central object. The most promising mechanism of angular momentum transport is the magneto-rotational instability (IMR). However, this instability requires that the particles be coupled to the magnetic field lines. For this to happen, at least a fraction of the particles needs to be charged. As the temperatures through the disk are low, the ionization rates are also very small. Thus for the IMR to occur through the whole disk, the temperatures must be higher. There are in the literature models that include the damping of Alfvén waves as an additional heating source, besides the viscous heating mechanism, in particular, the non linear, turbulent and dust-cyclotron damping. In this work, a numerical code was developed to simulate the disk using the four mechanisms cited. It was then made an analysis of their efficiency as a function of the radial distance and the initial conditions.

Resumo. Discos de acreção são comumente encontrados ao redor de estrelas jovens, como as estrelas T Tauri. Para com que ocorra o transporte de matéria, as partículas necessitam de perder um pouco de sua energia de rotação e "cair" em direção ao objeto central. O mecanismo mais promissor de transporte de momento angular é a instabilidade magneto-rotacional (IMR). Entretanto, para com que esta instabilidade ocorra, as partículas necessitam de estar acopladas às linhas do campo magnético. Para com que isso ocorra, pelo menos uma fração das partículas necessitam de estar carregadas. Poranto, para que a IMR ocorra em toda a extensão do disco, as temperaturas necessitam de ser mais altas. Na literatura, existem diversos modelos que incluem o amortecimento de ondas Alfvén como uma fonte adicional de calor, além da dissipação viscosa, em particular, os amortecimentos não linear, turbulento e cíclotron da poeira. No presente trabalho, um código numérico foi desenvolvido que simula os quatro mecanismos supracitados. Foi, então, realizada uma análise de suas eficiências em função da distância radial e das condições iniciais.

Keywords. accretion disks – Alfvén waves – heating mechanisms

1. Introduction

The formation process of low-mass stars envolves the collapse of molecular clouds as well as the formation of a accretion diks, which will be responsible for the transport of matter towards the central object. In order for the transport to happen, it is necessary that the particles of the disk loose some of their rotation energy and fall towards the star. The most promising mechanism of angular momentum transport is the magneto-rotational instability (IMR), proposed by Balbus & Hawley (1991). However, in order for the instability to take place it is necessary that the temperature in the disk increases to ensure that there is a minimal fraction of ionization (Gammie, 1996). There are several works in the literature that use the damping of Alfvén waves as an extra heating mechanism for the disk.

In this work, we use the standard model proposed by Shakura & Sunyaev (1973) and the layered model proposed by Gammie (1996) along with three extra heating mechanisms of damping of Alfvén waves, non-linear, turbulent and dust-cyclotron damping, studied by Vasconcelos et al. (2000) and Jatenco-Pereira (2013), in order to make an analysis of the efficiency of these mechanisms as a function of the radial distance.

2. Material and methods

Assuming a geometrically thin and optically thick disk (Shakura & Sunyaev, 1973) divided in layers (Gammie, 1996) and adopting the opacity law given by Bell & Lin (1994), a numerical code was constructed to simulate the disk. The numerical code computed the parameters of the disk, such as the intensity of the magnetic field, the central temperature, the volumetric and superficial density and the scale height, the temperatures given by the viscous dissipation alone and the temperatures generated by the damping of Alfvén waves. In order to calculate the temperatures we supposed that the disk irradiates as a black body, so that the temperature is obtained as follows:

$$T^4 = \frac{D}{\sigma} \quad (K), \tag{1}$$

where D is the energy flux dissipated by the viscosity and by the damping of Alfvén waves and σ is the Stefan-Boltzmann constant.

The energy flux dissipated by the damping of the waves is Φ/L, where L is the damping lenght and Φ is the wave flux, which is given by:

$$\Phi = \rho < \delta\, v^2 > v_A, \tag{2}$$

where ρ is the disk volumetric density, v_A is the Alfvén velocity and δv is the magnitude of the velocity perturbation.

Knowing that the density energy of the Alfvén waves is:

$$\epsilon_A = \frac{1}{2}\rho < \delta v^2 > + \frac{1}{2} < \delta B^2 > /(4\pi), \tag{3}$$

and using the equipartition of energy

$$\frac{1}{2}\rho < \delta v^2 > = \frac{1}{2} < \delta B^2 > /(4\pi), \tag{4}$$

we have that:

$$\Phi = \frac{< \delta B^2 >}{(4\pi)} v_A. \tag{5}$$

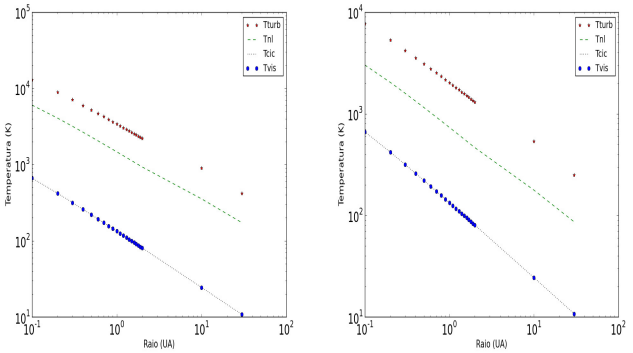

(a) Temperature profile with $f = 0,01$.

(b) Temperature profile with $f = 0,005$.

Figure 1. Temperature profile for wave fluxes of 0.01 and 0.005. In red, are the temperatures generated by the turbulent damping, in green the temperatures generated by the non-linear damping and in black the temperatures generated by the dust-cyclotron damping. The blue dots represents the temperatures of the viscous dissipation, which is invariant with the wave flux.

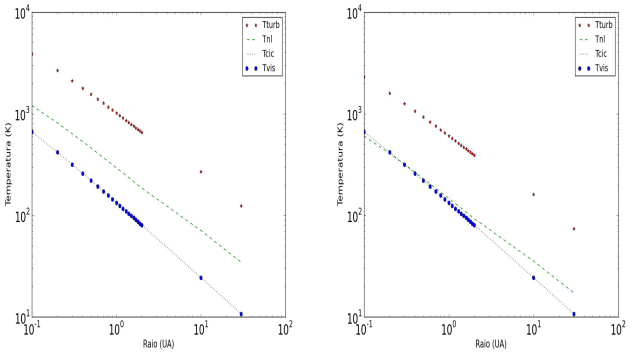

(a) Temperature profile with $f = 0,002$.

(b) Temperature profile with $f = 0,001$.

Figure 2. Temperature profile for wave fluxes of 0.002 and 0.001. In red, are the temperatures generated by the turbulent damping, in green the temperatures generated by the non-linear damping and in black the temperatures generated by the dust-cyclotron damping. The blue dots represents the temperatures of the viscous dissipation, which is invariant with the wave flux.

But, as the perturbation of the magnetic field has to be a fraction of the initial magnetic field, we can write:

$$< \delta B^2 > /(4\pi) \; = \; f^2 B^2/(4\pi), \tag{6}$$

where f is a free parameter. Hence, we have that the wave flux if given by:

$$\Phi = \frac{f^2 B^2}{(4\pi)} v_A = f^2 \rho v_A^3 \quad (erg\ cm^{-2}\ s^{-1}). \tag{7}$$

3. Results

For a non-dusty disk and considering only viscous dissipation and the turbulent and non-linear mechanisms, as proposed by Vasconcelos et al. (2000), it was obtained that the most efficient mechanism is the turbulent, which shows temperatures of $\sim$ 1000 K at the innermost regions and $\sim$ 50 K at 100 AU.

For a dusty disk (Jatenco-Pereira, 2013) and considering viscous dissipation and the non-linear, turbulent and dust-cyclotron mechanisms, it was obtained the temperature profile shown in Figure 1.

4. Conclusions and perspectives

For a dusty disk we can see that the dust-cyclotron damping is the less efficient among the mechanisms of damping of Alfvén waves, since that even for small values of the Alfvén waves flux, the turbulent and non-linear mechanisms still produce temperatures superiors to the cyclotron. Besides, we obtained that the dust-cyclotron damping shows similar temperatures of viscous dissipation.

In the continuity, we intend to investigate a way of coupling the three mechanisms of damping of Alfvén waves, in order to maximize the heating of the disk.

Acknowledgements. N.F.S. Andrade would like to thanks the brazilian agency FAPESP (under grant 2016/22092-2) for the support.

References

Balbus, S. A. & Hawley, J. F. 1991, ApJ, 376, 214
Bell K. R., Lin D. N. C., 1994, ApJ, 427, 987
Gammie, C. F. 1996, ApJ, 457, 355
Jatenco-Pereira, V. 2013, MNRAS, 431, 3150
Shakura, N.I. & Sunyaev, R. A. 1973, A&A, 24, 33
Vasconcelos, M., Jatenco-Pereira, V. & Opher, R. 2000, ApJ, 534, 967

Boletim da Sociedade Astronômica Brasileira, **30**, no. 1, 77-78

DogsHeaven Observatory international cooperation – Wind structure : The cases of ζ Puppis and γ^2 Velorum

Paulo Cacella[1]

[1] DogsHeaven Observatory, e-mail: dogsheaven@tachyonweb.net

Abstract. We show in this paper some results of DogsHeaven Observatory, a private observatory in Brasília, Brazil. From supernova discoveries to stellar occultations of solar system bodies, from millisecond pulsar optical detection to support with spectroscopic data on stellar research, the observatory operates in several distinct fields. In this paper we highlight two works that will have an impact on stellar astrophysics field. In the first work, headed by Noel D. Richardson, we report on the first multi-color precision light curve of the bright Wolf-Rayet binary γ^2 Velorum, obtained over six months with the nanosatellites in the BRITE-Constellation fleet. In parallel, we obtained 488 high-resolution optical spectra of the system. The second work, headed by Tahina Ramiaramanantsoa, was a study of the early-O-type supergiant ζ Puppis and it was based on 5.5 months of dual-band optical photometric monitoring at the 1 mmag level and ground-based multi-site spectroscopic monitoring in eight observatories.

Resumo. Nós mostramos nesse trabalho alguns resultados do Observatório DogsHeaven, instituição privada, situado em Brasília, Brasil. De descoberta de supernovas até ocultações estelares de corpos do Sistema Solar, de detecção óptica de pulsares de milisegundos ao suporte com dados espectroscópicos em pesquisa estelar, o observatório opera em campos diversos. Nesse trabalho nós destacamos dois trabalhos, os quais terão impacto no campo de astrofísica estelar. No primeiro trabalho, liderado por Noel D. Richardson, apresentamos a primeira curva multiespectral de precisão da binária Wolf-Rayet γ^2 Velorum, obtida com dados de seis meses da constelação de nanosatélites BRITE. Em paralelo foram obtidos 488 espectros de alta resolução do sistema. O segundo trabalho, liderado por Tahina Ramiaramanantsoa, foi um estudo da estrela supergigante ζ Puppis, e foi baseado em monitoramento fotométrico em duas bandas por 5.5 meses com resolução de 1 mmag e com monitoramento espectroscópico feito em oito observatórios.

Keywords. Stars:winds, outflows – Stars:Wolf-Rayet – Stars:supergiants

1. Introduction

DogsHeaven Observatory is a private observatory located in Brasília, Brazil. The observatory has activities in several astronomical and astrophysical fields. From TNO's occultations, as in Braga-Ribas et al.(2013) and Ortiz et al.(2012), to supernovae and novae search, from stellar low and medium resolution spectra to software development, the observatory has been participating in several current researches with worldwide active specialists.

The observatory has a set of telescopes up to a diameter of 50cm and several science appliances, from spectroscopes to ugriz and johnson photometric filters. The site has clear nights usually from April to September with the rainy season between October and March and, as a consequence few available nights. However, during the season is frequent daily availability, what is a very important asset when we are doing research that needs worldwide or timely coverage.

The first discovery of a supernova in Brazil happened at DogsHeaven Observatory in 2002 by Cacella et al. (2002). It was a nearby Ia supernova in Leo called 2002bo. It was located in NGC3190, some 80 millions light years away. This supernova was discovered 13 days prior to maximum and had a very extensive coverage. Due to a very detailed study in visual and infrared wavelenghts this supernova is one of reference stars used today in supernova reasearch.

More recently, the observatory discovered a more distant, 800 millions light years away, supernova type Ic in Antlia. This supernova is called 2017dgk, Cacella (2017) and spectroscopic confirmation was done by ePESSTO ESO-NTT. This supernova is currently object of a study as is located in a dwarf galaxy.

The observatory also was an important player in the discovery of the optical counterpart of the millissecond pulsar XTE J0929-314, reported by Cacella (2002), after RXTE ASM Team reported the discovery of a faint x-ray transient in Antlia. Data from Very Large Array showed that the astrometry of the observatory were favorably compared with a much larger professional facility.

DogsHeaven Observatory is currently particpating in several programs and international cooperations. The main research currently at the observatory is the search of transient objects, solar system objects, photometric imaging and spectroscopy.

The observatory is currently cooperating with ASAS-SN in confirming transients, as reported in Holoien (2017), mainly supernovae.

With SASER, the the Southern Astro Spectroscopy Email Ring, we participate in a worldwide coverage of spectroscopic research of some specific targets, mainly visible in southern hemisphere, as in Molnár et al. (2016). This cooperation with professional astronomers allowed the observatory to participate actively in the two papers shown in this paper.

With Akira Karai, from Koyama Astronomical Observatory at Kyoto Sangyo University, we are conducting a research looking for detection of C2 and CN lines in Novae, as reported in Akira & Cacella (2016).

With RIO group we are collaborating with observations of stellar occultations of TNOs and Centaurs.

Currently we are following early B supergiant μ Sgr at lines C II $\lambda\lambda$6578/6583 , Si II $\lambda\lambda$6347/6371, Hα and He I λ6678.

Beyond that, the Observatory developed a software that is helping to automatically detect new transients, moving objects or variable stars. 2017dgk supernova was discovered with this tool.

2. The variability of the BRITE-est Wolf-Rayet binary, γ^2 Velorum I. Photometric and spectroscopic evidence for colliding winds

In the first work, headed by Richardson (2017), the observatory generated 56 spectra for the research. We report on the first multi-color precision light curve of the bright Wolf-Rayet binary γ^2 Velorum, obtained over six months with the nanosatellites in the BRITE Constellation fleet. In parallel, we obtained 488 high-resolution optical spectra of the system. In this first report on the datasets, we revise the spectroscopic orbit and report on the bulk properties of the colliding winds. We find a dependence of both the light curve and excess emission properties that scales with the inverse of the binary separation. When analyzing the spectroscopic properties in combination with the photometry, we find that the phase dependence is caused only by excess emission in the lines, and not from a changing continuum. We also detect a narrow, high-velocity absorption component from the He I λ5876 transition, which appears twice in the orbit. We calculate smoothed-particle hydrodynamical simulations of the colliding winds and can accurately associate the absorption from He I to the leading and trailing arms of the wind shock cone passing tangentially through our line of sight. The simulations also explain the general strength and kinematics of the emission excess observed in wind lines such as C III λ5696 of the system. These results represent the first in a series of investigations into the winds and properties of γ^2 Velorum through multi-technique and multi-wavelength observational campaigns.

3. BRITE-Constellation high-precision time-dependent photometry of the early-O-type supergiant ζ Puppis unveils the photospheric drivers of its small- and large-scale wind structures.

The second work, headed by Ramiaramanantsoa (2017), and which the Observatory contributed with 164 spectra, was based on 5.5 months of dual-band optical photometric monitoring at the 1 mmag level, BRITE-Constellation has revealed two simultaneous types of variability in the O4I(n)fp star ζ Puppis: one single periodic non-sinusoidal component superimposed on a stochastic component. The monoperiodic component is the 1.78 d signal previously detected by Coriolis/SMEI, but this time along with a prominent first harmonic. The shape of this signal changes over time, a behaviour that is incompatible with stellar oscillations but consistent with rotational modulation arising from evolving bright surface inhomogeneities. By means of a constrained non-linear light curve inversion algorithm we mapped the locations of the bright surface spots and traced their evolution. Our simultaneous ground-based multi-site spectroscopic monitoring of the star unveiled cyclical modulation of its He II λ4686 wind emission line with the 1.78-day rotation period, showing signatures of Corotating Interaction Regions (CIRs) that turn out to be driven by the bright photospheric spots observed by BRITE. Traces of wind clumps are also observed in the He II λ4686 line and are correlated with the amplitudes of the stochastic component of the light variations probed by BRITE at the photosphere, suggesting that the BRITE observations additionally unveiled the photospheric drivers of wind clumps in ζ Pup and that the clumping phenomenon starts at the very base of the wind. The origins of both the bright surface inhomogeneities and the stochastic light variations remain unknown, but a subsurface convective zone might play an important role in the generation of these two types of photospheric variability.

4. Final Remarks

In this work we show how a private observatory can contribute with research data and discoveries to the astronomical community. DogsHeaven Observatory is open to cooperation on diverse astronomical fields with capabilities ranging from imaging to spectroscopy.

References

Arai Akira, Cacella P. 2016, ATEL, 9359
Braga-Ribas, F. et al. 2013, ApJ, 773, 26
Cacella, P. et al. 2002, IAUC, 7847
Cacella, P. 2002, IAUC, 7893
Cacella, P. 2017, TNS, 2017dgk, 2017-464
Holoien, T. W.-S. et al. 2016, MNRAS, 471, 4966
Molnár, L. et al. 2016, MNRAS, 466, 4009
Ortiz J. L. et al. 2012, Nature, 491, 566
Ramiaramanantsoa T. et al. 2017, MNRAS, Accepted
Richardson, N. et al. 2017, MNRAS, 471, 2715

Boletim da Sociedade Astronômica Brasileira, **30**, no. 1, 79-80

Rotation periods and variability properties of active KEPLER stars

P. P. Cabral, E. N. Velloso, D. T. da Costa, L. L. Amorim, F. A. J. de Lima, J. M. Varela, J. V. Ferreira, L. de Almeida, A. C. Matiucci, F. Anthony, J. S. da Costa, M. Castro, & J.-D. Jr. do Nascimento

[1] Dep. de Física. Universidade Federal do Rio Grande do Norte, UFRN, CP 1641, 59072-970, Natal, RN, Brazil

Abstract. *Solar analogs are major targets to understand the solar dynamo*. The KEPLER NASA satellite observed continuously thousands of stars and providing a unique dataset for which stellar variability can be studied. In this paper, we present the first results from the under-graduation project at the GE^3 UFRN team, to perform a semi-automated variability analysis of the full KEPLER dataset. We analyzed thousands of light curves (all quarters) to derive rotation periods and a proxy of activity. Our data set is composed by main-sequence with masses around 1 solar mass. Our method to detected rotation periods was based on autocorrelation function and Lomb-Scargle analysis. Our goal it is to derive consistently rotation period and a proxy of variability for a large sample of active solar analog stars for further spectroscopic studies.

Resumo. *Análogas solares são objetos importantes na compreensão do dínamo solar.* O satélite KEPLER da NASA observou continuamente milhares de estrelas e forneceu um conjunto de dados exclusivos para o qual a variabilidade estelar pode ser estudada. Apresentamos aqui os primeiros resultados do projeto de graduação de alunos do GE^3 da UFRN, onde uma análise da variabilidade estelar foi feita de forma semi-automatizada e com os dados do KEPLER. Analisamos milhares de curvas de luz (todos os trimestres) para derivar períodos de rotacão e um indicador da atividade. Nosso conjunto de dados é composto por estrelas de 1 massa solar na sequencia principal. Os períodos de rotacão foram determinados com funcão de autocorrelacão e análise Lomb-Scargle. Nosso objetivo é derivar consistentemente a rotacão e um variabilidade para uma grande amostra de análogas solares ativas para estudos espectroscópicos.

Keywords. Stars: activity – Stars: rotation – Stars: solar-type

1. Introduction.

The stellar rotation period reflects the history of the angular momentum evolution of the star. Along the early phases of stellar evolution, and on the main-sequence lifetime, stars lose angular momentum and spin down. For stars like the Sun, also known as low-mass stars, this angular momentum loss is driven by a magnetized wind that is connected to the stellar outer convection zone evolution (e.g., Kawaler 1988; Bouvier et al. 1997). In recent years, the stellar rotation study has significantly developed thanks to new observational efforts and new techniques. Specifically, 4 years of uninterrupted photometry with a high level of precision and time sampling, for a large stellar sample by KEPLER space mission (Borucki et al. 2010) has improved a lot the study of stellar rotation. KEPLER space telescope obtained the light curves of the stars in the selected region of the sky and each star was photometrically observed along the wavelength band from 423 to 897 nm (Borucki et al. 2010). Brightness variations detected by KEPLER are commonly attributed to the presence of magnetic structures (sunspots, active regions, etc) in the surface of main-sequence cool dwarfs. As for the Sun, G-type star observed by KEPLER presents a similar behavior. The dark sunspots correspond to the concentrated strong magnetic field that emerges on the photosphere. The bright faculae correspond to the enhanced network magnetic field (Solanki et al. 2006). Sunspots and solar active regions have lifetimes of days to weeks and are used as tracers of solar surface rotation. In this context, this new data of stellar variability allows rotation periods to be detected for several types of stars. Period measurements for older stars remain very rare and hard to be measured, because old stars rotate slowly and are less active than their younger counterparts. Active regions and spots on the stellar surface drive the variability and effects can all lead to a complex periodogram structure, with spurious peaks from jumps and long-term systematics, and multiple or split peaks from spot evolution or differential rotation. Typical stellar light curves are complex, and we can say that there are neither sinusoidal nor strictly periodic ones and the time-evolving nature of these active regions distribution needs to be deeply studied. Young stars are more active, and rotation period determination can be straight. Extremely active stars can also be complex and challenging to determine which peak in the periodogram corresponds to the to the stellar rotation period. Active moderate stars in the KEPLER dataset gives reliable rotation measurements for from F-, G-, and K-type to M-type stars. In this study, we took data from KEPLER mission to analyze light curves from solar-type stars in order to determine (and verify) its rotation periods P_{rot} and relations with their variability ΔV, obtained by a stellar signal model methods. Those are solar analogs, stars with around 1 solar mass, an effective temperature between 5700 and 5900 Kelvin and a surface gravity between 4.3 and 4.5.

2. Extracting the surface rotation rates and the variability index.

Starspots and active regions are present over rotations of cool stars. Continuous observation of a star with a high cadence photometric satellite produces a light curve, which could be analyzed as a time series by specific techniques and then revealing systematic variations. Rotation, planets and systematic phenomena will produce a peak the periodogram of the time series. Assuming starspots trace surface rotation, this provides a way to measure the rotation rate of the star. In this study, the average surface P_{rot} is obtained from light curve modulation analysis. To extract the P_{rot}, we analyze PDC-MAP and simple aperture photometry light curves that are corrected for outliers, drifts, and

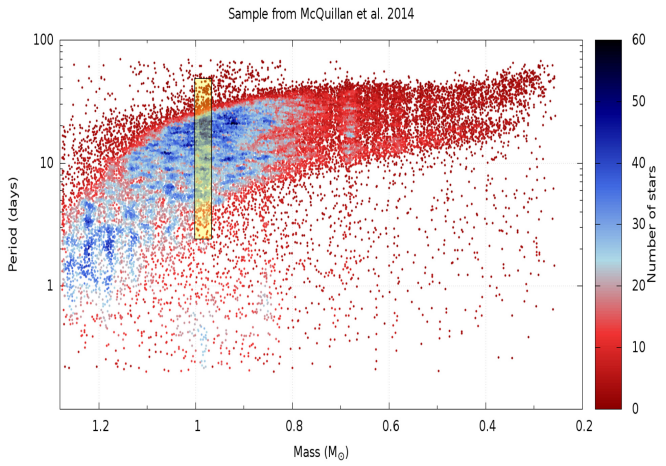

Figure 1. Rotation period versus mass for 34 000 field stars from McQuillan et al. (2013) and McQuillan et al. (2014). Rotation periods derived using AutoACF. The mass was derived from models of Baraffe et al. (1998). We included the yellow shaded regions representing our selected data set.

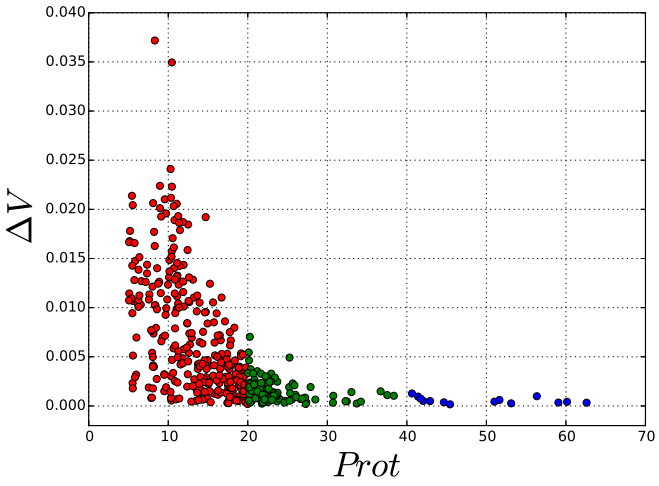

Figure 2. Variability ΔV versus rotation period P_{rot} in the rotation range 1–20 days (red); 20–40 days (green); and 40–70 days (blue) blown up from Fig. 1 for around 1 solar mass. Red symbols are the most active stars.

discontinuities and stitched together following the procedures described by do Nascimento et al. (2014). The light curves are then high-pass filtered using a triangular smooth function with a cutoff that can change from 40 to 100 days. Finally, we computed the autocorrelation of the signal (McQuillan et al. 2013) in order to cross-check the results. We fit a Gaussian function to the global wavelet, i.e., the projection into the frequency domain of the time-frequency analysis, and the uncertainty was obtained from the full width at half-maximum of the Gaussian profile. This uncertainty includes the P_{rot} variation due to differential rotation.

The gradual fluctuations due to magnetic features (starspots and faculae) dynamics on stellar surfaces could be also used as a proxy of activity (He et al. 2015). Fluctuation amplitude of a stellar light curve is generally not uniform, we define a quantity, ΔV, to represent the effective range of the light-curve modulation, based on the splined model of the light curve. These quantities were used to construct the Fig. 2, for a range of stars with masses around 1 solar mass, as indicated by the yellow region on the Fig. 1. This proxy describes the degree of periodicity and effective fluctuation range of the light curve. The combination of rotation and amplitude modulation are complementary on the analysis of solar-type stars.

3. First look conclusions.

We produce a first catalog of active start with rotation and activity measurements. We have presented an analysis of rotation-activity connection, so far extensively studied and well established for field stars observed from the ground. Here we are presenting an unprecedented sample of solar-type stars with rotation period determined from space-borne mission and mass around 1 solar mass. Study of stellar activity-rotation relation is important because it can provide new constraints for dynamo models when combined with surface rotation rates and the depth of the convection zone.

As a main result, we show that the KEPLER light curve amplitude variation for solar analogs can be adopted as an indicator of photospheric magnetic activity. The scattering observed in the Figs. 1 and 2 seem to show manifestations of spot dynamics and stellar cycle. The complexities related to the light-curve modulations by magnetic features on the Sun, exist on other solar-type stars, and need to be better understood. Spectroscopy observations seem to be essential to better define the mass, metallicity, convection profile for those stars.

Acknowledgements. The authors thank CAPES/CNPq and the Federal University of Rio Grande do Norte for financial support.

References

Baraffe, I., Chabrier, G., Allard, F., et al. 1998, A&A, 337, 403
Borucki, W. J., Koch, D., Basri, G., et al. 2010, Science, 327, 977
Bouvier, J., Forestini, M., & Allain, S. 1997, A&A, 326, 1023
do Nascimento, J.-D., Jr., García, R. A., et al. 2014, ApJ, 790, L23
He, H., Wang, H., & Yun, D. 2015, ApJS, 221, 18
Kawaler, S. D. 1988, ApJ, 333, 236
McQuillan, A., Mazeh, T., & Aigrain, S. 2013, ApJ, 775, L11
McQuillan, A., Mazeh, T., & Aigrain, S. 2014, ApJS, 211, 24
Solanki, S. K., Inhester, B., & Schüssler, M. 2006, Reports on Progress in Physics, 69, 563

Boletim da Sociedade Astronômica Brasileira, **30**, no. 1, 81-82

Does environment matter? The rotational scenario of low mass stars in the young Cygnus OB2 association

J. Roquette[1], S. H. P Alencar[1], J. Bouvier[2], L. P. V. Vaz.[1], & M. G. Guarcello[3]

[1] Departamento de Física, ICEx, UFMG, Brazil; e-mail: juliaroquette@gmail.com
[2] Univ. Grenoble Alpes, CNRS, IPAG, France
[3] INAF, Osservatorio Astronomico di Palermo, Italy

Abstract. As part of the results of a near-infrared variability survey (WFCAM/UKIRT JHK bands) in the Cygnus OB2 association, we investigated the rotational properties of low mass candidate members in the association. The general scenario for the rotational evolution of young stars seen in other regions is confirmed by Cygnus OB2 rotational period distributions, with disk-bearing stars rotating on average slower than diskless stars. A mass-rotation dependence was also verified, but as in NGC 6530, very low mass stars rotate on average slower than higher mass stars. The disk and mass-rotation connection were also analyzed while considering the incident UV radiation arising from O-type stars in the association. Results compatible with the disk-locking scenario were verified only for stars with low UV incidence, suggesting that massive stars may have an important role on regulating the rotation of nearby low mass stars.

Resumo. Como parte dos resultados de um levantamento de variabilidade no infravermelho (WFCAM/UKIRT nas bandas JHK) na associação Cygnus OB2, investigamos as propriedades rotacionais das estrelas de baixa massa candidatas a membro da associação. O cenário geral para a evolução da rotação de estrelas jovens observado em outras regiões foi confirmado pelas distribuições de períodos rotacionais em Cygnus OB2, com estrelas com disco girando em média mais devagar do que estrelas sem disco. Uma dependência da rotação com a massa também foi verificada, mas conforme em NGC 6530, as estrelas de massa muito pequena giram em média mais lentamente do que as estrelas com maior massa. A dependência da rotação com a presença do disco também foi analisada considerando-se a radiação UV incidente vinda das estrelas tipo O na associação. Resultados compatíveis com o cenário do trancamento por disco foram verificados apenas para estrelas com baixa incidência de radiação UV, o que sugere que as estrelas de massa muito grande podem ter um importante papel na regulação da rotação de estrelas de massa pequena em sua vizinhança.

Keywords. Stars:Low-mass – Stars:Rotation – Stars: Pre-Main sequence

1. Context

Along with the mass and initial composition, the angular momentum is a fundamental stellar parameter and it influences directly the stellar structure and its evolution. The study of the angular momentum evolution of magnetically active low mass stars is heavily based on the study of their rotational properties, which is a direct product from observations, and the current angular momentum evolution models are constrained by observations of the rotational properties of groups of coeval stars assembled as an evolutionary sequence. The use of such observational constraint assumes that the environmental conditions do not influence the angular momentum evolution of low mass stars, in the last decade this assumption has been put in check by observational evidences that the rotational properties of low mass stars in the early pre main sequence, such as the mass dependence of rotation and disk-locking scenario, can be sensitive to environmental conditions such as the presence of ionizing sources in their neighborhood.

2. Cygnus OB2, a 'massive' environment

Cygnus OB2 is 1.33 kpc away from the Sun (Kiminki et al. 2015). Wright et al. (2014, 2016) suggested that the association formed as it is today: a highly sub-structured, globally unbound association. Cygnus OB2 is a notoriously massive OB association with more than 160 confirmed OB stars among its members(Wright et al. 2015). Beyond the interest on its rich massive population, Cygnus OB2 is also a valuable target for studying the environmental influence during low mass star formation and early evolution. Guarcello et al. (2016) recently investigated the dissipation timescale of protoplanetary disks around low mass stars in the vicinity of massive stars and found evidences that disks are more rapidly dissipated in regions with higher stellar density and more intense UV radiation within the Cygnus OB2 association. They also found that disk dissipation due to close encounters is negligible, and that disk dissipation is dominated by photoevaporation. While some massive stars have ages under 2 Myr (Hanson 2003), the low mass population ages are in the range 2.5-6.7 Myr (Wright et al. 2010).

OB stars are ionizing sources and can influence their environment due to their strong UV field. Far ultraviolet (FUV) photons (6 eV $< h\nu <$ 13.6 eV) can dissociate H_2 molecules, and extreme ultraviolet (EUV) photons ($h\nu >$ 13.6 eV) are capable of ionizing hydrogen atoms. A higher concentration of OB stars would therefore imply a higher UV radiation local incidence, that in turn could influence the evolution of neighbor low mass stars. The environmental influence of OB stars is exemplified in Figure 1. For example, regions with intense local UV field can be hostile to the evolution of circumstellar disks, and to the processes of star formation (e.g. Guarcello et al. 2016).

3. The rotational scenario of Cygnus OB2

The observational dataset used was obtained through the 3.8 m United Kingdom Infrared Telescope equipped with the Wide Field Camera (programs U/07A/H16 and U/07B/H60), and covers a field of 0.87 squared degrees centered on Cygnus OB2. We measured reliable periods for 894 stars among the candidate

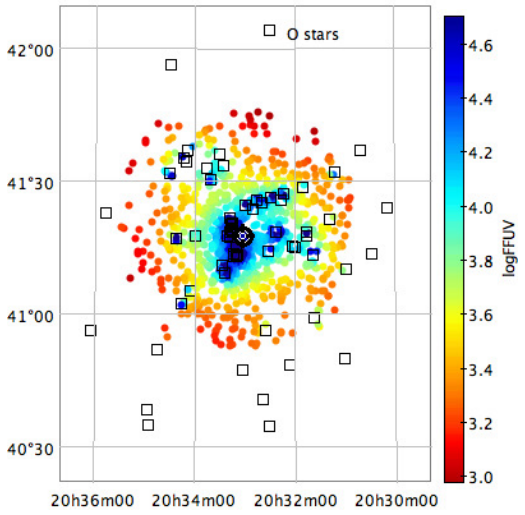

Figure 1. OB stars FUV incident flux in the Cygnus OB2 association. As in Guarcello et al. (2016): the FUV flux of each O and WR stars (shown as black empty squares) was propagated to the position of each low mass candidate member by using 2D-projections for the distance between each pair of sources. The position of each low mass star is shown as a dot, and the color of each dot indicates the FUV incident flux on that position according to the color bars to the right of the plot. Using the FUV local fluxes as criteria, we defined as stars submitted to high UV incidence those with $\log(F_{FUV}) > 3.7\ G_0$, and low UV incidence those with $\log(F_{FUV}) \leq 3.7\ G_0$.

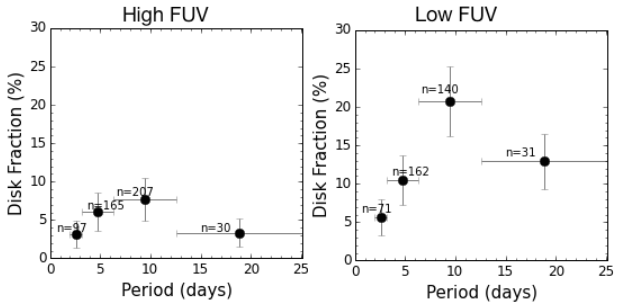

Figure 2. While the difference between the rotational properties of disk-bearing and diskless stars is stronger in regions with low UV incidence, in regions with high UV incidence it was not possible to statistically distinguish between the two samples. The increase of the disk fraction with period is stronger for the former than for the later. A maximum disk fraction of ~21%, and ~7.3% for slow rotators was found for low and high local UV incidence respectively.

members in the association, with periods in the range 2.0 – 32.5 d, and in the mass range 0.1 – $1.4 M_{\odot}$. Due to some completeness and contamination issues, most of our analysis was limited to the intermediate ($3.1 \leq P \leq 6.3$ d) and slow ($P > 6.3$ d) rotators, with detected fast rotators only in the range 2 – 3.1 d. Disk-bearing and diskless stars in our sample are statistically distinct in their rotational properties, with the former rotating slower than the later and with a Kolmogorov-Smirnov test resulting in a probability of only 0.4% that the two samples came from same parent distribution. The disk fraction increases as a function of period, except for the very-slow rotator bin, which has smaller statistics number and seems to suffer from contamination from field stars. In the full sample, the disk fraction varies from ~4% for fast rotators to ~13% for slow rotators. In Figure 2 the disk-locking scenario is re-examined by considering samples of stars submitted to low and high incident FUV flux as defined in Figure 1.

A mass-rotation connection was supported by a KS-test, but lower mass stars ($M \leq 0.4 M_{\odot}$) in Cygnus OB2 rotate on average slower than higher mass stars ($M > 0.4 M_{\odot}$). Also, the statistic distinction between the two mass ranges is stronger for samples of stars submitted to higher UV incidence. This mass-rotation connection is different from most other similarly aged regions (e.g. Herbst et al. 2001), but it is not novel as it was observed before in the younger NGC 6530 (~2 Myr; Henderson & Stassun 2012).

4. Does Environment matter?

Yes, it seems it does! As in Littlefair et al. (2010), we raised the hypothesis that the environmental conditions could act on regulating the rotational evolution of young stars. Indeed environment is a common component between Cygnus OB2 and NGC 6530 as both regions have a higher concentration of ionizing sources than other young regions of similar age: As mentioned, Cygnus OB2 is a notoriously massive OB association with hundreds of OB stars among its members and NGC 6530 is a core cluster of the Sgr OB1 association (Sung et al. 2000) and it is 3-4 times richer in OB stars than ONC (Damiani et al. 2004). Future studies correlating the UV incidence levels with the rotational properties of such clusters will help testing this hypothesis.

5. Conclusions

Our results suggest a link between environmental conditions and the rotational evolution of young stars. However, it is urgent to complement the sample presented in this study for fast rotators and lower masses, in order to achieve a better understanding of the rotational scenario in the association, and to confirm such suggestions.

Acknowledgements. More details on the development of this study can be found in the source paper: Roquette et al. (2017), and on JR PhD thesis which was granted by CNPq and CAPES. S.H.P.A acknowledges financial support from CNPq, CAPES, and FAPEMIG. JB acknowledges the support of ANR grant 2011 Blanc SIMI5-6020 01 Toupies: Towards understanding the spin evolution of stars. We thank Bo Reipurth for providing us with the WFCAM/UKIRT dataset used.

References

Damiani, F., Flaccomio, E., Micela, G., et al. 2004, ApJ, 608, 781
Guarcello, M. G., Drake, J. J., et al. 2013, ApJ, 773, 135
Guarcello, M. G., Drake, J. J., et al. 2016, arXiv:1605.01773
Hanson, M. M. 2003, ApJ, 597, 957
Henderson, C. B., & Stassun, K. G. 2012, ApJ, 747, 51
Herbst, W., Bailer-Jones, C. A. L., & Mundt, R. 2001, ApJ, 554, L197
Littlefair, S. P., Naylor, T., et al. 2010, MNRAS, 403, 545
Kiminki, D. C., Kobulnicky, H. A., et al. 2015, ApJ, 811, 85
Roquette, J., Bouvier, J., Alencar, S.H.P., et al. 2017, A&A, 603, A106
Sung, H., Chun, M.-Y., & Bessell, M. S. 2000, AJ, 120, 333
Wright, N.J., Drake, J. J., et al. 2010, ApJ, 713, 871
Wright, N.J., Drew, J. E., & Mohr-Smith, M. 2015, MNRAS, 449, 741
Wright, N.J., Parker, R. J., et al. 2014, MNRAS, 438, 639
Wright, N.J., Bouy, H., Drew, J. E., et al. 2016, MNRAS, 460, 2593

Boletim da Sociedade Astronômica Brasileira, **30**, no. 1, 83-84

Rotation and tide equilibrium

A statistical analysis of the observations

Ana Carolina Mattiuci Figueiredo[1], José Ronaldo Pereira da Silva[2] and José Dias do Nascimento Jr[3]

[1] Universidade Federal do Rio Grande do Norte e-mail: carol.mattiuci@gmail.com
[2] Universidade Estadual do Rio Grande do Norte e-mail: jzeronaldo@gmail.com
[3] Harvard-Smithsonian Center for Astrophysics e-mail: jdonascimento@cfa.harvard.edu

Abstract. WWe used an unprecedented new sample of 1538 binaries of spectral types O-K, and luminosity class V, IV and III. The goal here is to find the period which binaries reach the synchronization between rotational and orbital periods, and orbital circularization. Our results are confronted with tidal theory by Zahn.

Resumo. Nós usamos uma nova amostra sem precedentes de 1538 binárias dos tipos espectrais de O a K, e classe de luminosidade V, IV e III. O objetivo aqui é achar o período que as binárias alcançam a sincronização entre os períodos rotacional e orbital, e circularização orbital. Nossos resultados são confrontados com a teoria de maré de Zahn.

Keywords. Spectroscopic binaries – Rotation – Star evolution

1. Introduction

Binary systems can provide sufficient observable for tests of stellar evolution models. It is estimated that more than half of the stars are components of multiple systems. In a binary system the two components are gravitationally bound to each other move in elliptical orbits around their common center of mass. These stars can provide more observable than simple stars.

All binary system, as well as all physics system, search the equilibrium. For binary systems are necessary three conditions: synchronization, circularization and all spins, orbital and rotational, aligned. All these parameters pass by process of evolution, these process are: the tidal effect, angular momentum loss by magnetically coupled, stellar wind and by gravitational wave radiation, strong wind accretion and Roche-lobe overflow characterizing mass transfer (Duquennoy, Mayor, & Mermilliod, 1992).

Zahn relates the efficiency of the tidal effect to the turbulent friction in the convection zone of the star, states the theoretical period for most likely system be synchronized and circularized, and calculates the time of synchronization and circularization.

$$\frac{1}{t_{sinc}} \approx 6\frac{k_2}{t_f}q^2\left(\frac{MR^2}{I}\right)\left(\frac{R}{a}\right)^6, \quad (1)$$

$$\frac{1}{t_{circ}} = -\frac{d\ln(e)}{dt} = \frac{21}{2}\frac{k_2}{t_f}q(1+q)\left(\frac{R}{a}\right)^8, \quad (2)$$

We evaluated the relationship between orbital period, rotational velocity and eccentricity. For different subsamples based on spectral type, we found a critical period of synchronization and we discuss about circularization and statical properties regarding this spectral type and luminosity class.

2. Sample

The spectral types and luminosity class was collected of the data base from SIMBAD.

The orbital period and eccentricity was collected from the online version of the Ninth Catalog of the Orbital Elements of Spectroscopic Binaries. (Pourbaix et al., 2004). The mean rotations were collected from Catalog of Projected Rotational Velocities (Glebocki & Gnacinski, 2003).

Table 1. Quantity of stars by spectral type, evolved and not evolved.

S. T.	V	(IV and III)
O0 to O9	26	17
B0 to B4	85	89
B5 to B9	95	59
A0 to A4	174	49
A5 to A9	47	29
F0 to F4	68	28
F5 to F9	194	45
G0 to G4	128	66
G5 to G9	84	133
K0 to K9	109	201

3. Results and conclusions

The main sequence stars synchronize with periods about 17 days, in other hand the subgiants and giants synchronize about 580 days.

For the values of circularization we find about 14 days for main sequence and 400 days for subgiants and giants range.

The correlations among period and rotation, and among excentricity and rotation are more significant starting in spectral type F5, for not evolved stars and starting in spectral type G for evolved stars.

Acknowledgements. We acknowledge CAPES and CNPQ for the scholarship

References

Duquennoy, A., Mayor, M., & Mermilliod, J.C. 1992, in Binaries as Tracers of Stellar Formation, ed. A. Duquennoy, & M. Mayor (Cambridge: Cambridge Univ. Press), 52

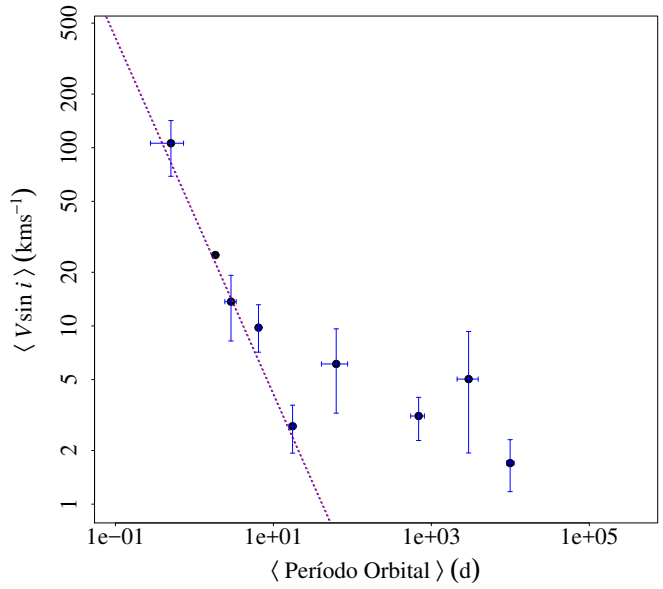

Figure 1. Syncronization of main sequence G stars. The red lines indicate the greatest radii and the blue lines indicate the smallest radii

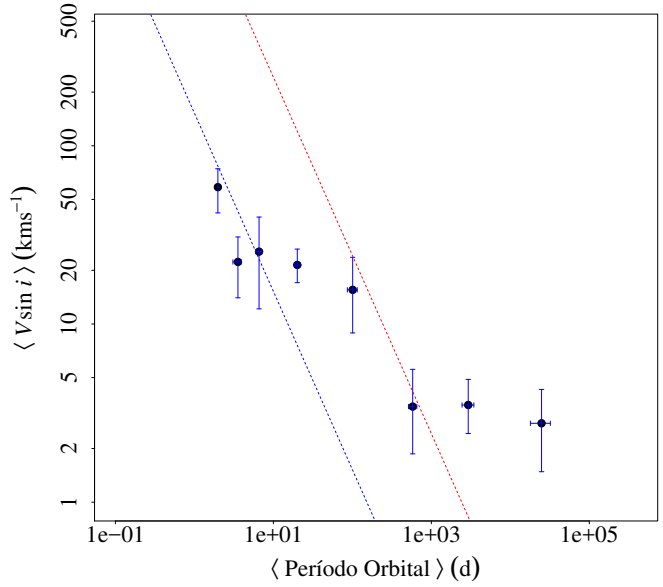

Figure 2. Syncronization of K giants and subgiants. The red lines indicate the greatest radii and the blue lines indicate the smallest radii

Glebocki R., & Gnacinski, P. 2003, The Catalogue of Rotational Velocities of Stars in Clusters, eds. A. Brown, G.M. Harper, and T.R. Ayres, Cambridge Workshop, p. 823

Pourbaix, D., Tokovinin, A. A., Batten, A. H., Fekel, F. C, Hartkopf, W. I., Levato, H., Morrell, N. I., Torres, G. & Udry, S., 2004, A&A, 424, 727

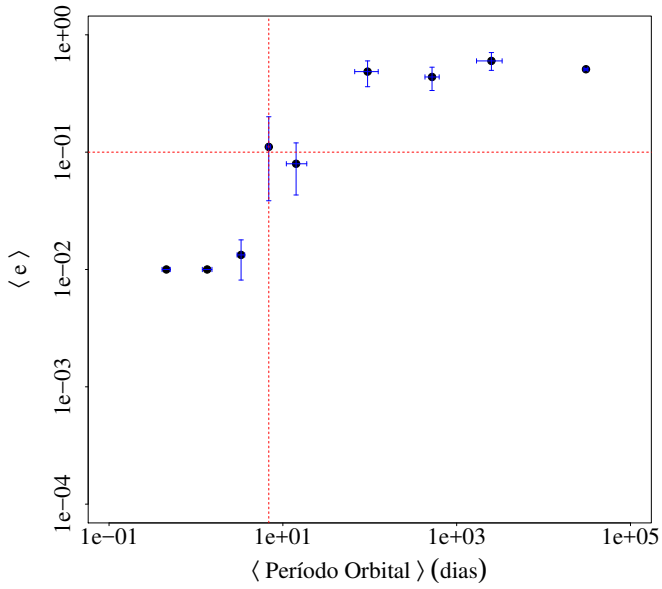

Figure 3. Circularization of main sequence K stars. The horizontal line indicates the circularization and the vertical line indicates the critical period.

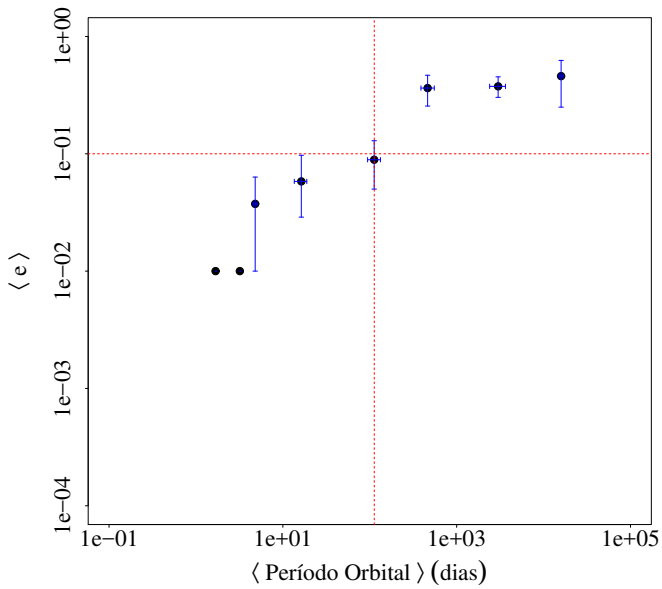

Figure 4. Circularization of G giants and subgiants. The horizontal line indicates the circularization and the vertical line indicates the critical period.

Boletim da Sociedade Astronômica Brasileira, **30**, no. 1, 85-86

The activity of possibles Maunder minimum candidates

R. Ferreira[1], M. Castro[1] & J.-D do Nascimento Jr.[1,2]

[1] Departamento de Física Teórica e Experimental – Universidade Federal do Rio Grande do Norte
CP 1641, 59072-970, Natal, Rio Grande do Norte, Brazil. e-mail: rafaelferreira@fisica.ufrn.br

Abstract. Among several aspects related to the Sun activity history, there was a period of the Sun evolution with a low chromospheric activity level and a low number of observed sunspots. This period was between 1645 and 1715, (well known as Maunder Minimum period, MM), and remains as a puzzle for the stellar evolution theory. In this work, we investigate the evolutionary status of 30 sun-like type stars that are possible MM candidates due to their low chromospheric activity as compared with stars at same evolutionary status. These stars present activity index measurements along 50 yrs from the Mount Wilson program and others. They have very low chromospheric activity as $\log R'_{HK} \leq 5.0$, $< S > \simeq 0.15$ and $(B-V)$ between 0.61 and 0.71 (for the Sun the $< S >_{\odot} = 0.167$ and a color index $(B-V)_{\odot} = 0.65$). At this phase, we also revisited CoRoT and Kepler databases to enhance the number of Maunder minimum candidate stars presenting flat light curves and low activity profile.

Resumo. Dentre os vários aspectos relacionados com o histórico de atividade do Sol, houve um período da evolução do Sol com baixa nível de atividade cromosférica e um baixo numero de manchas solares observadas. Esse período foi entre 1645 e 1715, (conhecido como mínimo de Maunder, MM), e permanece como um enigma para a teoria da evolução estelar. Neste trabalho, nós investigamos o status evolucionário de 30 estrelas do tipo solar que são consideradas possíveis candidatas MM devido aos seus baixos níveis de atividade cromosférica ao longo dos últimos 50 anos. Estas estrelas apresentam índices de atividade extremamente baixos, tais como: $\log R'_{HK} \leq 5.0$, $< S > \simeq 0.15$ e $(B-V)$ entre 0.61 e 0.71 (para o Sol $< S >_{\odot} = 0.167$ e o índice de cor $(B-V)_{\odot} = 0.65$). Neste estágio, nós também revisaremos as bases de dados dos satélites CoRoT e Kepler para aperfeiçoarmos o número de estrelas candidatas MM, que apresentem curvas de luz "flat" e perfil de baixa atividade.

Keywords. Stars: activity – Stars: evolution – Stars: chromospheres

1. Introduction

The problem of extremely low activity in main sequence stars is a puzzle for the stellar astrophysics. It is known that young stars have a strong activity. When these stars present an extremely low activity, along many years, it could be the first evidence of Maunder Minimum (MM hereafter), which defines a phase of the solar activity during 70 yrs between XVI and XVII centuries when almost no sunspots have been observed (see Fig.1).

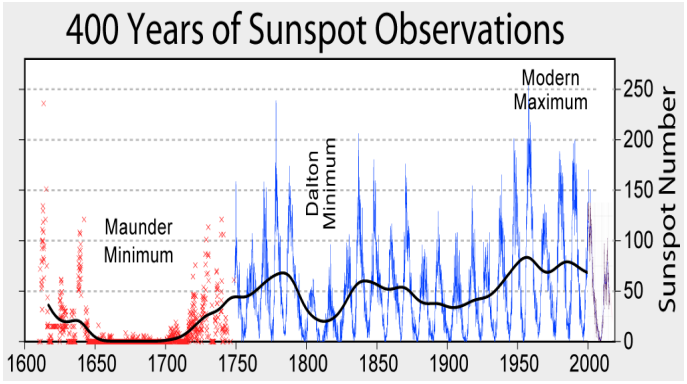

Figure 1. *All measurements for sunspots along 400 yrs. The red dots show the MM period. We also have the others minimums in this figure.*

Many surveys in Sun-like stars have been a good opportunity to study the Sun's activity history (Wright (2004)). They are very important to detect extremely low activity analogous to MM period in young stars. In fact, the MM state has been investigated since 1970's (Eddy (1976)). Through the Mt. Wilson (MW) program (see Fig. 2) and the California and Carnegie Planet Search program, it has been possible to analyze the activity evolution along the last 50 yrs. The S-index of MW is the standard index of activity and has been very useful to investigate the activity evolution of these stars.

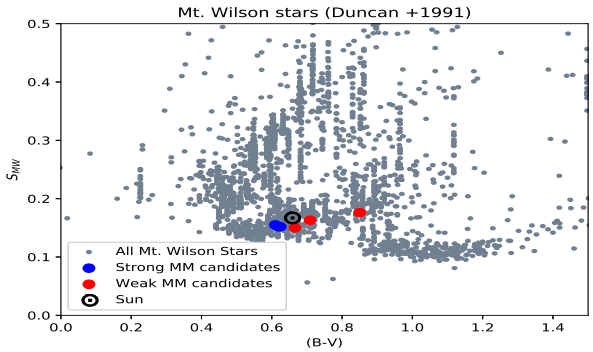

Figure 2. In this figure, we can see the MW sample stars. The inferior envelope contains the MM candidates, divided into strong MM candidates and weak MM candidates according to the literature (Ferreira et al. 2018, in prep.)

This work is organized as follows: in section 2 we present our sample of stars, in section 3 we show many results and discussion about some selected stars of our sample, finally the last session is the conclusion and perspectives.

2. The sample

Our sample presented in Fig. 2 is composed by Sun-like stars (see Duncan et al. (1991); Hall et al. (2009); Isaacson & Fischer

(2010); Lubin et al. (2010); Pace (2013)). We use the long-term programs for monitoring the activity along many years. The most important was the MW project. Currently, there are some short-term activity programs, that observe stars for some days only.

The better MM candidates in the sample					
Star	Type	log n (Li)	B-V	$< S >$	Age [Gyr]
HD 10307	G2	1.92	0.618	0.152	7.00
HD 43587	G0	1.83	0.610	0.155	6.12
HD 95128	G0	1.81	0.624	0.152	7.11
HD 3651	K0	0.59	0.850	0.176	6.91
HD 115617	G5	1.20	0.709	0.163	6.53
HD 217014	G5	1.32	0.666	0.150	7.24

3. Results and discussion

We investigate about 30 Sun-like stars that have a flat activity profile and may be considered MM candidates to according to Lubin et al. (2010) and others. From the spectroscopic S-index measurements variability, we calculate the Long-Scargle Periodograms (Horne & Baliunas (1986)) and we found several possible periods of activity. We first investigate the star HD 43587, that was a primary CoRoT target. After this, we found five more stars that can be considered MM candidates.

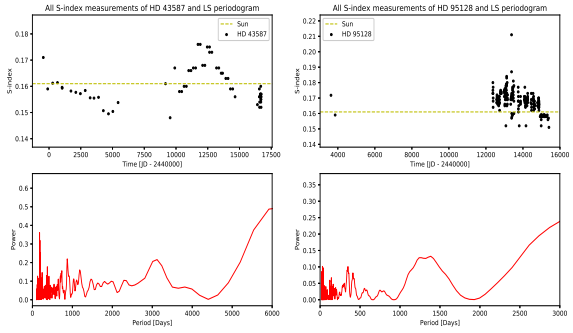

Figure 3. All S-index spectroscopic measurements for HD 43587 and HD 95128 (above) with its respectively Lomb-Scargle (LS) periodograms (below).

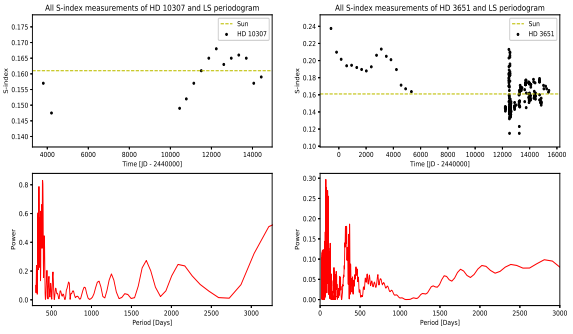

Figure 4. All S-index spectroscopic measurements for HD 10307 and HD 3651 (above) with its respectively Lomb-Scargle (LS) periodograms (below)

Lubin et al. (2010) analyse the MM candidates under the perspective of lithium abundances and classified three of these stars as strong MM candidates and Weak MM candidates according to the standard deviation of log n(Li). Here, we show the Lomb-Scargle periodogram for the "strong" MM candidates, from the activity measurements of long-term programs (see Figs. 3,4,5).

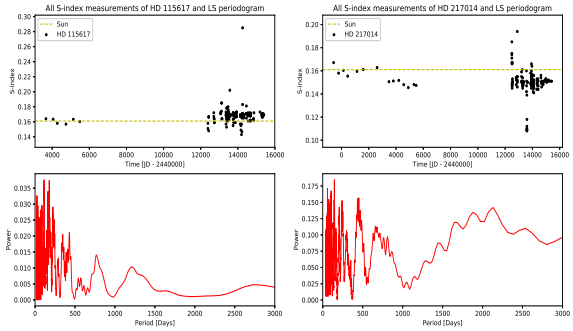

Figure 5. All S-index spectroscopic measurements for HD 115617 and HD 217014 (above) with its respectively Lomb-Scargle (LS) periodograms (below)

4. Conclusion and perspectives

These stars are considered strong MM candidates by many authors and they have lithium abundance that is within the normal range for their color (Lubin et al. (2010)). The analyze of the lithium abundances suggests that stars with normal lithium abundance and low activity profile are good MM candidates. In addition, it is not possible to determine the activity cycle period, which is an indication that the star is in a long period of flat activity. We pretend to continue with the time-series spectroscopic measurements and proposals for long-term observational campaign.

Acknowledgements. The authors thanks GE^3 Team (DFTE/UFRN) and CAPES/CNPq agencies for the financial support since the beginning of this research.

References

Wright, J. T. 2004, AJ, 128, 1273
Eddy, J. A. 1976, Science, 192, 1189
Lubin, D., Tytler, D., & Kirkman, D. 2010, ApJ, 716, 766
Duncan, D. K., Vaughan, A. H., Wilson, O. C., et al. 1991, ApJS, 76, 383
Hall, J. C., Henry, G. W., Lockwood, G. W., Skiff, B. A., & Saar, S. H. 2009, AJ, 138, 312
Isaacson, H., & Fischer, D. 2010, ApJ, 725, 875
Pace, G. 2013, A&A, 551, L8
Horne, J. H., & Baliunas, S. L. 1986, ApJ, 302, 757

Boletim da Sociedade Astronômica Brasileira, **30**, no. 1, 87-88

Solar analogs and twins: a spectroscopic analysis in the violet and ultraviolet

M. L. Ubaldo-Melo[1], G. F. Porto de Mello[1], D. Lorenzo-Oliveira[2], & R. E. Giribaldi[1,3]

[1] Observatório do Valongo, Universidade Federal do Rio de Janeiro, Ladeira do Pedro Antônio 43, CEP 20080-090 Rio de Janeiro, RJ, Brazil, e-mail: mariamelo13@astro.ufrj.br, gustavo@astro.ufrj.br
[2] Departamento de Astronomia do IAG, Universidade de São Paulo, Rua do Matão 1226, Cidade Universitária, CEP 05508-900 São Paulo, SP, Brazil, e-mail: diego.lorenzo@iag.usp.br
[3] ESO – European Southern Observatory, Karl-Schwarzhild-Strasse 2, 85748 Garching bei München, Germany, e-mail: rescateg@eso.org

Abstract. Solar type stars are fundamental objects in astrophysics. We perform a spectroscopic analysis in the regime bellow 4500 Å of 85 solar type stars aiming to determine which solar analog and twin candidates of our sample, characterized by means of a spectroscopic analysis in the visible, are similar to the Sun in the mentioned region. The violet/ultraviolet region is very sensitive to small variations of the atmospheric parameters of the stars and is still poorly explored in the literature in the context of solar type stars. We use the spectral indexes method with a principal component analysis calibration to derive the atmospheric parameters of a select sample of objetcs and determine that the stars HD 98649, HD 118598, HD 138573 and HD 140690 are the most similar to the Sun between 3995 and 4500 Å. Besides that, we use the molecular features of CN (3850 Å) and CH (4310 Å) to study similarities between a set of stars and the Sun.

Resumo. Estrelas do tipo solar são objetos fundamentais na astrofísica. Reportamos uma análise espectroscópica da região abaixo de 4500 Å de 85 estrelas do tipo solar com o objetivo de determinar quais candidatas a análogas e gêmeas solares da amostra, assim classificadas por análises espectroscópicas no visível, mantêm semelhanças com o Sol no regime mencionado. A região violeta/ultravioleta é muito sensível à pequenas variações dos parâmetros atmosféricos estelares e ainda é pouquíssimo explorada na literatura no contexto de estrelas do tipo solar. Utilizamos o método dos índices espectrais aplicando uma calibração a partir de uma análise de componentes principais para derivar os parâmetros atmosféricos de uma amostra seleta de objetos e determinar que as estrelas HD 98649, HD 118598, HD 138573 e HD 140690 mais se assemelham ao Sol entre 3995 e 4500 Å. Além disso, usamos as bandas moleculares do CN (3850 Å) e do CH (4310 Å) para estudar similaridades entre um conjunto de estrelas e o Sol.

Keywords. Stars: solar-type – Stars: fundamental parameters – Stars: atmospheres

1. Introduction

Stars similar to the Sun are fundamental objects in astrophysics as they play an important role in characterizing the properties of the Sun among the stars; in studies of Galaxy evolution (Edvardsson et al. 1993a,b); and they are astrobiologically interesting objects (Porto de Mello, del Peloso & Ghezzi 2006).

We pay special attention to the so-called solar analogs and twins (Cayrel de Strobel & Bentolila 1989; Cayrel de Strobel 1996). Solar analogs are stars with atmospheric parameters, such as effective temperature, metalicity, surface gravity and photometric colors, similar to the solar ones. Solar twins are objects that have all fundamental parameters — mass, age, effective temperature, chemical composition, surface gravity, luminosity, and others — identical to the Sun within the observational uncertainties.

Although the study of stars similar to the Sun started in the ultraviolet region with Hardorp (1978), the majority of stars classified as solar analogs and twins were characterized by means of a spectroscopic analysis in the visible spectrum. However, the regime below 4500 Å is interesting in solar type stars for their great sensitivity to the atmospheric parameters (Dragon & Mutschlecner 1980). This regime is, therefore, a useful tool in the identification of this kind of stars, being still poorly explored in the literature in this context (Altamore et al. 1990).

2. Methodology

Our sample contains 85 solar type stars, including interesting solar analog and twin candidates (Porto de Mello et al. 2014), and a total of 120 FEROS spectra with atmospheric parameters determined in the literature and compiled in the work of Lorenzo-Oliveira et al. (2016). We first degraded the original resolving power of FEROS of 48000 to 15000 — due to the high density of transitions below 4500 Å and in order to simplify our analysis and increase the S/N — and normalized the spectra.

Thereafter, we identified the spectral indexes visually. A spectral index is a spectral characteristic composed by a group of atomic or molecular transitions showing sensitivity to the variation of one or more atmospheric parameters (Ghezzi et al. 2014). We built a calibration using the principal component analysis method applied to the EW of the 103 best indexes (of a total of 336) and the atmospheric parameters of the calibration sample (it didn't include the solar analog and twin candidates), this result is shown in Fig. 1.

To estimate the EW error we used stars with multiple observations. Then, we applied a Monte Carlo simulation to the measurements of the spectral indexes of the solar analog and twin candidates to generate synthetic measurements of the indexes and build distributions of EWs. With these values we determined their atmospheric parameters and its errors using the calibration.

Moreover, we isolated the region of greater influence of the molecular features of CH and CN — they are the main molecular bands observed in solar type stars and whose sensitivities

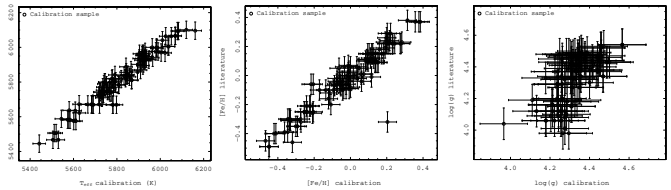

Figure 1. Comparison between the effective temperature, metalicity and surface gravity values, respectively, derived from the calibration and their values from the literature for the calibration sample.

to the atmospheric parameters are high (Hardorp 1978) — in order to quantitatively determine, though in a preliminary manner, similarities between the solar analog and twin candidates and the Sun. We measured the EW of these regions and analyzed its correlation with effective temperature, metalicity and surface gravity.

3. Results

Table 1. Atmospheric parameters of solar analog and twin candidates derived using the 3995 to 4500 Å regime. The letters a, b, c, d, and e hold for distinct observations of the same object, and Ganimedes and Vesta are used as Sun templates.

Identification	$T_{eff} \pm 30$ (K)	[Fe/H] ± 0.051	$\log g \pm 0.120$
HD 71334 a	5762	−0.025	4.384
HD 71334 b	5744	−0.047	4.389
HD 98649 a	5753	−0.038	4.396
HD 98649 b	5754	−0.046	4.387
HD 115382	5772	−0.125	4.415
HD 118598	5818	+0.004	4.366
HD 138573	5762	−0.017	4.390
HD 140690	5784	+0.039	4.353
HD 146233 a	5766	+0.025	4.357
HD 146233 b	5820	+0.038	4.352
HD 146233 c	5800	+0.025	4.342
HD 146233 d	5825	+0.069	4.314
HD 146233 e	5812	+0.032	4.343
HD 150248 a	5739	−0.074	4.399
HD 150248 b	5814	+0.019	4.362
HD 164595	5774	−0.068	4.397
BD+15 3364	5748	+0.070	4.334
Ganimedes a	5746	+0.004	4.387
Ganimedes b	5751	−0.019	4.382
Vesta	5744	−0.018	4.385

We compared the results of Tab. 1 with Porto de Mello et al. (2014) (obtained using the visible region) analyzing the statistical significance of each atmospheric parameter with respect to the literature parameters: in general our results agree with those from Porto de Mello et al. (2014).

Likewise, we performed the comparison mentioned with respect to the Sun (T_{eff} = 5777 K, [Fe/H] = 0.00 and $\log g$ = 4.44), and we also compared the literature values with the solar ones. The result was that all the stars are similar to the Sun in the visible spectrum, suggesting that this regime exhibits a lower capacity to discriminate spectral features. However, using the violet region, we could discriminate more finely between the stars and we found that only the stars HD 98649, HD 118598, HD 138573, and HD 140690 are similar to the Sun in all parameters in 1σ confidence level. This indicates that this domain is potentialy very sensitive to discriminate subtle differences of the spectral features in solar type stars.

Figure 2. Relation between CH EW and effective temperature for a set of solar analog and twin candidates. The error bars were evaluated using spectra of the star HD 146233.

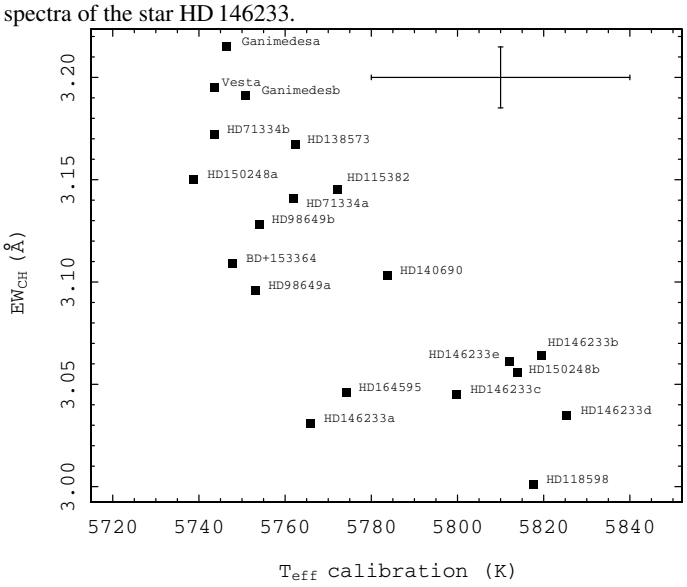

About the study using CH and CN features, we observed a low correlation between its strenghts and the atmospheric parameters, with the CH showing a small trend with effective temperature as shown in Fig. 2.

4. Conclusions

1. We stablished a tool to analyze the short spectral range of solar type stars.
2. The atmospheric parameters derived using spectral indexes in the violet region are in agreement with those in the visible.
3. The visible domain is poorer than the violet to discriminate between spectral feature differences.
4. The violet regime showed a significant sensitivity, revealing that the stars HD 98649, HD 118598, HD 138573, and HD 140690 are the best solar analog and solar twin candidates of our sample, and we strengthen the classification of these stars as solar analogs.
5. The analysis using the CH and CN features were inconclusive, but they should be explored in more detail.

Acknowledgements. MLUM thanks FAPERJ for undergraduate fellowship, DLO acknowledges the support from FAPESP, and REG from CAPES.

References

Altamore A., Rossi C., Rossi L., Villada de Arnedo M., 1990, A&A, 234, 332
Cayrel de Strobel G., 1996, A&A, 7, 243
Cayrel de Strobel G., Bentolila C., 1989, A&A, 211, 324
Dragon J. N., Mutschlecner J. P., 1980, ApJ, 239, 1045
Edvardsson B., Andersen J., Gustafsson B., Lambert D. L., Nissen P. E., Tomkin J., 1993a, A&AS, 102, 603
Edvardsson B., Andersen J., Gustafsson B., Lambert D. L., Nissen P. E., Tomkin J., 1993b, A&A, 275, 101
Ghezzi L., et al., 2014, AJ, 148, 105
Hardorp J., 1978, A&A, 63, 383
Lorenzo-Oliveira D., Porto de Mello G. F., Dutra-Ferreira L., Ribas I., 2016, A&A, 595, A11
Porto de Mello G., del Peloso E. F., Ghezzi L., 2006, Astrobiology, 6, 308
Porto de Mello G. F., da Silva R., da Silva L., de Nader R. V., 2014, A&A, 563, A52

Boletim da Sociedade Astronômica Brasileira, **30**, no. 1, 89-90

A study of likeness: The solar twin 18 Sco and the Sun

G. T. Ponte & G. F. Porto de Mello

[1] Observatório do Valongo, Universidade Federal do Rio de Janeiro
e-mail: geisaponte.astro@gmail.com, gustavo@astro.ufrj.br

Abstract. The objective of this work is to make a direct empirical comparison between the solar twin 18 Sco and the Sun, using spectra of high signal-to-noise ratio (S/N), high resolution (R) and wide spectral coverage.

Resumo. O objetivo deste trabalho é fazer uma comparação empírica direta entre a gêmea solar 18 Sco e o Sol, usando espectros de alta sinal ruído (S/N), alta resolução (R) e ampla cobertura espectral.

Keywords. Stars: fundamental parameters – Stars: abundances – Stars: solar-type – Techniques: spectroscopic

1. Introduction

The detailed study of solar twins has direct applications both in the understanding of the chemical evolution of the Galaxy and the evolution of the properties of the Sun over time (such as Monroe et al., 2013), besides being a powerful tool in the study of exoplanetary systems. Due to their characteristics similar to solar, the detailed spectroscopic analysis of these stars becomes less dependent on the uncertainties present in the modeling of theoretical parameters, maximizing small spectral differences and making it possible to detail features of distinction or similarity. The objective of this work is to make a direct empirical comparison between the solar twin 18 Sco and the Sun.

2. Working sample

Using spectra of high signal-to-noise ratio (S/N), high resolution (R) and wide spectral coverage, we evaluate how the impact of different sources of error in the analysis can influence the classification of a particular star as a solar twin.

Instrument: FEROS/ESO, R = 48.000

Spectral coverage: 4500 to 6850 Å with S/N > 350

Objects: Ganymede, Vesta, 18 Sco, HD 150248,
HD 164595, HD 138573, HD 98649, HD 118598

2.1. More than one solar proxy

We are using Ganymede and Vesta as solar proxy to test if their intrinsic caracteristics (e.g. chemical composition, albedo) influence the obtained solar spectra.

2.2. Wide spectral coverage

To minimize the uncertainties, we are analysing a sufficient number of isolated lines of same species (Fe I, Fe II, Cr I, etc.) (Porto de Mello, 1996)

2.3. Systematics in continum normalization

This allows us to estimate biases induced by systematic particular choices of continuum on manual normalization. Each person may have a distinct perspective of the spectra when inspecting and fitting a low-degree polynomial to estimate its continuum.

2.4. Careful manual measurements

It has been shown in the literature that manual fitting profiles (such as Gaussian and Voigt), line by line, seems to be more precise than automatic methods. (e.g. Tucci Maia et al., 2017)

3. Analysis

First of all, we made a careful analysis of our data searching for gaps in spectra (such as very strong lines or instrumental problems), and then we split the spectra into 16 blocks ($\Delta\lambda$ = 70-200 Å). In this process, we used Solar Atlas (Kurucz et al., 1984, Wallace et al., 2011) looking for suitable solar continuum regions with the view to anchor a global consistency. Later, the spectra were normalized using IRAF/Pyraf interactive curve fitting package "continuum". Then, we started to fit manually, line-by-line, Gaussian profiles in alpha elements, iron peak and s-process lines: Ca I, Co I, Cr I, Cr II, Fe I, Fe II, Mn I, Ni I, Sc I, Sc II, Ti I, Ti II, YI, and Y II in order to measure full width half maximum (FWHM), line depth (d_r) and equivalent widths (EW). Below (Fig. 1 and Fig. 2) we can see how different spectra can result in similar distributions and spreads. However, its similarity allows us to understand its differences.

4. Results and perspectives

One basic criteria to determine how close is a star to the Sun is to look at the similarities between their spectral lines. A perfect solar twin should have median $<d_r> = 0$ (Meléndez et al., 2006) and although we can see (Fig. 3 and 4) 18 Sco compared to Sun (with Ganymede as our best proxy) show some differences.

Another aspect of this work is to analyze the correlation between line-depth differences and their respective excitation potentials. We will apply this method to the new twins HD 150248, HD 164595, HD 138573, HD 98649 and HD 118598 proposed by Porto de Mello et al., 2014. This approach will allow us to map some of the sources of uncertainties and degrees of subjectivity involved in determinations of spectroscopic similarity between the twins stars.

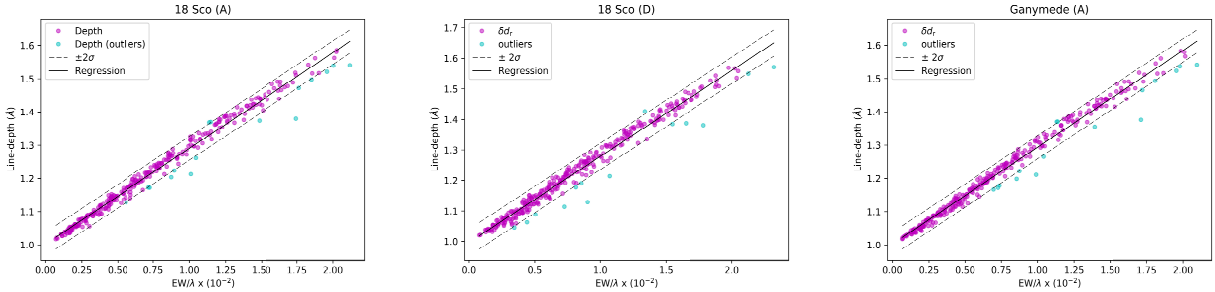

Figure 1. Testing line-depth vs EW/λ to 18 Sco (two different spectra) and Sun (Ganymede) at 2σ confidence level.

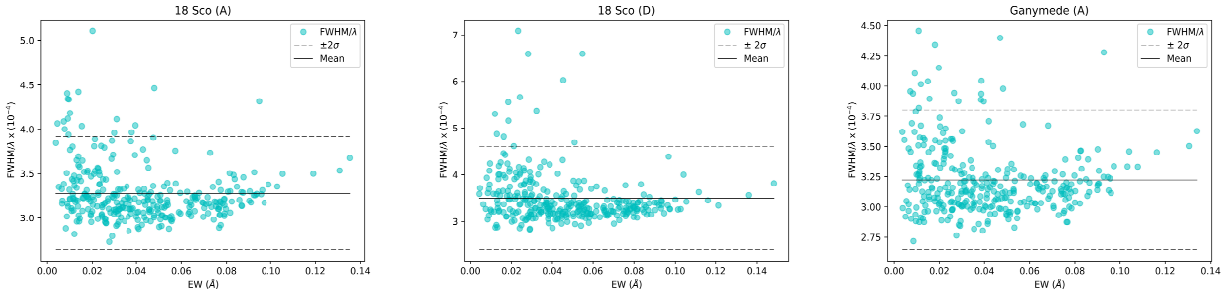

Figure 2. Test FWHM/λ vs EW showing us lines to be eliminated (out of 2σ) at the same spectra seen above in Fig. 1.

References

Kurucz, R. L., Furenlid, I.,& Brault, J, 1984, Solar Flux Atlas from 296 to 1300 nm, NSO Atlas No. 1.
Meléndez, J., Dodds-Eden, K. & Robles., J. A., 2006, ApJ, 641, L133-L136
Monroe, T., Meléndez, J., Ramírez, I. et al. 2013, ApJL, 774, L32
Porto de Mello, G. F., 1996, PhD Thesis, Observatório Nacional, Rio de Janeiro
Porto de Mello, G. F., Da Silva, R., & Nader, R., 2014, A&A, 563, A52
Tucci Maia, M., Meléndez, J., Spina, L. & Lorenzo-Oliveira, D., 2017, MNRAS, submited
Wallace, L., Hinkle, K., Livingston, W., & Davis, S. P., 2011, A Solar Flux Atlas for the Visible and Near Infrared, NSO Tech.

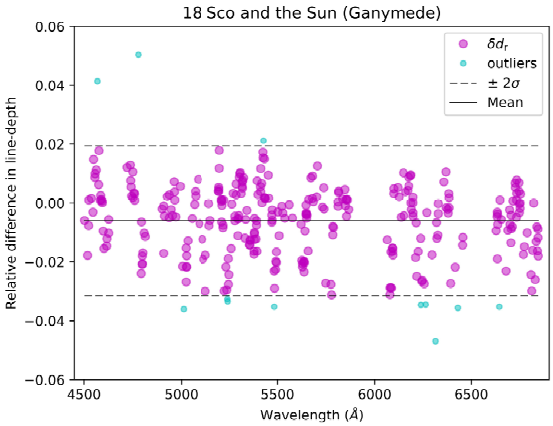

Figure 3. Line-depth differences of a solar spectrum (Ganymede) and 18 Sco.

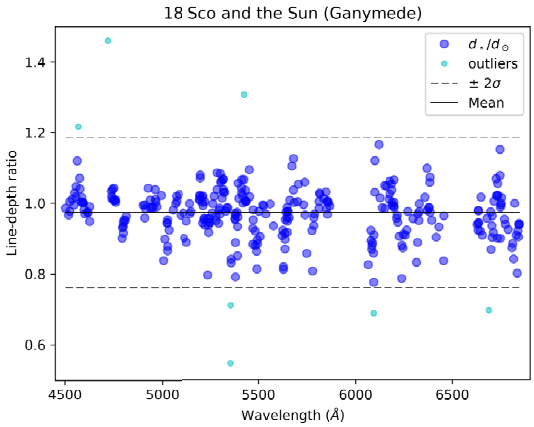

Figure 4. Line-depth ratios of a solar spectrum (Ganymede) and 18 Sco.

Boletim da Sociedade Astronômica Brasileira, **30**, no. 1, 91-92

Seismic and spectroscopic analysis of 9 bright red giant stars observed by Kepler and Gaia.

H. R. Coelho[1], A. Miglio[2], & J. D. do Nascimento Jr.[1]

[1] Departamento de Física Teórica e Experimental - UFRN - Brazil e-mail: hugo.pesquisa@gmail.com
[2] School of Physics and Astronomy - University of Birmingham - UK

Abstract. Space-based observatories such as CoRoT and Kepler can provide nearly uninterrupted time series for thousands red giants, allowing the extraction of seismic constraints related to global stellar properties. This can be carried over a large number of targets by combining seismic and spectroscopic constraints by using the so-called scaling relations. The combinations of asteroseismology and spectroscopy can also be used to understand extra-mixing process that occur inside red-giant stars. Therefore, it is important to characterize individual red giants using high S/N data. In this work, we conduct a detailed seismic analysis of nine bright red giant stars observed by Kepler. We extracted the period spacing of mixed modes for 7 stars. Distances estimated by seismology are compared with Hipparcos and Gaia distances.

Resumo. Observatórios espaciais como CoRoT e Kepler podem fornecer séries temporais quase ininterruptas para milhares de gigantes vermelhas, permitindo a extração de vínculos sísmicos relacionados a propriedades estelares globais. Isso pode ser repetido para a um grande número de estrelas, combinando restrições sísmicas e espectroscópicas usando as chamadas relações de escala. A combinação de asterosismologia e espectroscopia também pode ser usada para entender os processos de mistura extra que ocorrem dentro de estrelas gigantes vermelhas. Portanto, é importante caracterizar gigantes vermelhas individividualmente usando dados de alta qualidade. Neste trabalho, realizamos uma análise sísmica detalhada de nove estrelas gigantes vermelhas brilhantes observadas pelo satélite Kepler. Nós extraímos o espaçamento de períodos de modos mistos para 7 estrelas. As distâncias estimadas pela sismologia são comparadas com as distâncias medidas pelos satélites Hipparcos e Gaia.

Keywords. Asteroseismology – Stars: late-type – Stars: distances

1. Introduction

Asteroseismology of red-giant stars has proven to be a very successful tool to place tight constraints on fundamental stellar properties, including radius, mass, evolutionary state, internal rotation and age. While ideally one would conduct an analysis of individual frequencies on a star-by-star basis, the very large number of stars observed by CoRoT and Kepler makes this impractical with current analysis procedures. Most studies have so far relied on using the so-called average seismic parameters. Such parameters are related to global stellar properties and can be combined with estimations of surface temperature in the so-called scaling relations to infer masses and radii for a large sample of field stars. Scaling relations can be combined with apparent magnitudes and effective temperature to derive seismic estimation for distances. This is particularly useful for targets which cannot rely on high-precision parallaxes. It has thus become increasingly important to test the scaling relations and the seismic inferred distances by using bright giants with accurate parallaxes and robust spectroscopic estimations of surface temperature.

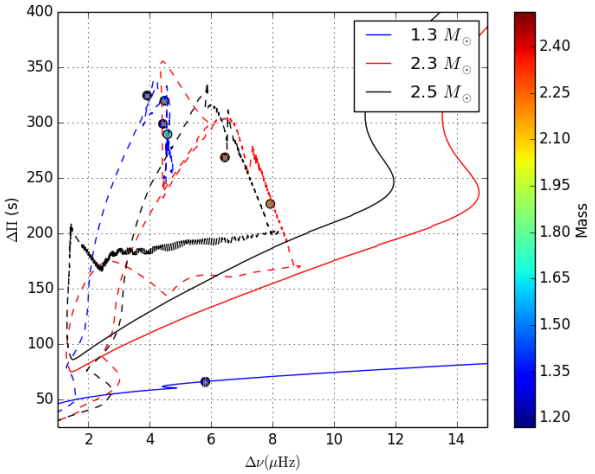

Figure 1. Period spacing (ΔΠ) versus large separation (Δν). The coloured solid lines indicate evolutionary tracks computed by the Modules for Experiments in Stellar Astrophysics (MESA) code. The models have solar composition and three different masses (1.30, 2.30 and 2.50 $M_\odot$).

2. Sample

Our sample consists of 9 bright red giant stars observed by the Kepler space telescope. The data obtained for the target stars have high signal to noise ratio (S/N > 200), allowing a detailed study with high quality seismic data.

All stars in our target sample have accurate values of parallaxes measured by Hipparcos, and 8 stars have parallaxes from Gaia.

We also measured the period spacing (ΔΠ) of mixed modes for 7 giants. Measuring period spacings allows us to clearly discriminate between red giants with similar luminosities but different evolutionary states .

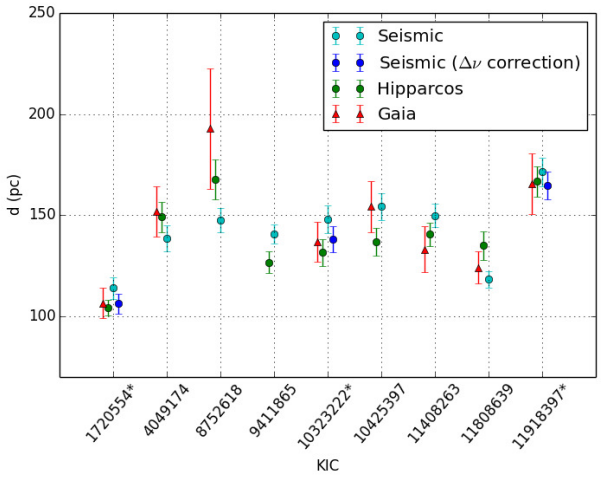

Figure 2. Comparison between distances obtained using three estimates: two from parallaxes, one from asteroseismology. Light blue dots are the distances determined by combining asteroseismic constraints and spectroscopic temperatures. The dark blue dots are the three RGB stars with applied corrections on $\Delta\nu$, also indicated by asterisks in the KIC numbers.

3. Results and Conclusions

Figure 1 shows the measured period spacing for 7 stars in our sample. Six stars are confirmed as clump stars ($\Delta\Pi > 200$) and one star is ascending the red giant branch ($\Delta\Pi > 50$). The other two stars are assumed to be ascending RGB stars, since they don't show a clear mixed mode patern in their power spectrum.

Figure 2 shows estimations of distance obtained by various methods. We computed estimations of distances using average seismic parameters.

From Figure 2, we see that the seismic estimations of distances have a reasonably good agreement with distances measured by Hipparcos and Gaia. We also computed corrections applied to the large separation in three RGB stars, which slightly improves the estimations of seismic distances.

Acknowledgements. This work has made use of data from the European Space Agency (ESA) mission Gaia, processed by the Gaia Data Processing and Analysis Consortium (DPAC). Funding for the DPAC has been provided by national institutions, in particular the institutions participating in the Gaia Multilateral Agreement.

References

Bedding, T. et al. 2011, Nature, 471, 608
Miglio, A. et al. 2013, MNRAS, 429, 423
White, T. R. et al. 2013, MNRAS, 433, 1262
Coelho, H. R., Chaplin, W. J., Basu, S., Serenelli, A., Miglio, A., Reese, D. R. 2015, MNRAS, 451, 3011
Paxton, B., et al. 2011, ApJS, 192, 3
Bossini, D., et al. 2015, MNRAS, 453, 2290

Boletim da Sociedade Astronômica Brasileira, **30**, no. 1, 93-94

The impact of GAIA astrometry on the evolutionary status of the seismic analog HD 42618

M. Castro[1], F. Baudin[2], J. Marques[2] & J. D. do Nascimento Jr.[1]

[1] Universidade Federal do Rio Grande do Norte (Natal, Brazil) e-mail: mcastro@fisica.ufrn.br
[2] Institut d'Astrophysique Spatiale (Orsay, France) e-mail: frederic.baudin@ias-psud.fr

Abstract. Last year, the satellite Gaia from ESA released its first data in astrometry (Gaia DR1), including new parallax measurements of millions of stars. Among these results, we were interested in the new parallax measurement of the CoRoT target HD 42618. This parallax, which is 1.5 mas lower than the one measured by Hipparcos, therefore corresponds to a greater distance and consequently to a larger luminosity. This implies a change in its evolutionary status, that we have studied from spectroscopic data, seismic analysis from photometric CoRoT data, and stellar evolution models. We show that the Gaia astrometric measurements can have an impact on the estimated evolutionary status of a solar-type star and, in the case of HD 42618, it implies some disagreements with the seismic data.

Resumo. No ano passado, o satélite Gaia da ESA disponibilizou seus primeiros dados em astrometria (Gaia DR1), incluindo novas medidas de paralaxe de milhões de estrelas. Entre estes resultados, nós interessamos na nova medida de paralaxe do alvo CoRoT HD 42618. Esta paralaxe, que é 1,5 mas menor que a medida por Hipparcos, corresponde, portanto, a uma maior distância e consequentemente a uma maior luminosidade. Isso implica uma mudanạ em seu estatuto evolutivo, que estudamos a partir de dados espectroscópicos, análise sísmica de dados fotométricos CoRoT e modelos de evolução estelar. Mostramos que as medidas astrométricas de Gaia podem ter um impacto sobre o estado evolutivo estimado de uma estrela de tipo solar e, no caso da HD 42618, isso implica alguns desentendimentos com os dados sísmicos.

Keywords. astrometry – solar analog – evolutionary status – asteroseismology

1. Introduction

New parallaxes from Gaia DR1 allow to analyze the impact of this parameter on the evolutionary status of stars. For the CoRoT target HD 42618, the new parallax is 1,5 mas lower than the one measured by Hipparcos. It implies a larger luminosity, which has an impact on the stellar age. We calculated evolutionary models with the Toulouse-Geneva Evolution Code (TGEC, see Hui-Bon-Hoa 2008) to study the evolutionary status of HD 42618 in a HR diagram using spectroscopic parameters from Morel et al. (2013). We calculated the theoretical frequencies of our models to compare to the observed frequencies of the analog star (Barban et al. 2013).

2. Data

To construct the HR diagram, we used the fundamental parameters inferred by Morel et al. (2013) from spectroscopic data obtained with HARPS ($T_{\rm eff}$ = 5765 ± 17 K, $[Fe/H]$ = −0.10 ± 0.02) and the luminosity calculated from the apparent magnitude V = 6.839 (SIMBAD database), the parallaxes from Hipparcos (p = 42.55 mas, case 1 hereafter) and Gaia DR1 (p = 41.05 mas, case 2), and the bolometric corrections calculated according to VandenBerg & Clem (2003). The observed frequencies have been inferred from the CoRoT light curve by Barban et al. (2013).

3. Results and conclusions

Our models calculated with the TGEC include atomic diffusion, meridional circulation (Théado & Vauclair 2003) and tachocline (Brun et al. 1998), which calibration allows to match the solar lithium abundance in a solar model. The models matching the observed point in a HR diagram (Fig. 1) have similar masses in both cases, in agreement with the seismic-inferred mass M = 0.9 ± 0.1 $M_\odot$ by Barban et al. (2013), but diverge in age by around 2 Gyr. In both cases, the surface lithium is completely destroyed. Large separations of the frequencies of the models do not agree with observed ones in both cases, showing models with larger density in case 1 and with lower density in case 2, compared to the observed large separations (Fig. 2). Differences in the large separations of both set of models are consistent with the differences on age. Small separations of the frequencies of the models, which are sensitive to the age of the model, account for the observations only in case 1. In case 2, the calculated small separations are significantly lower than the observed ones, indicated a model too old.

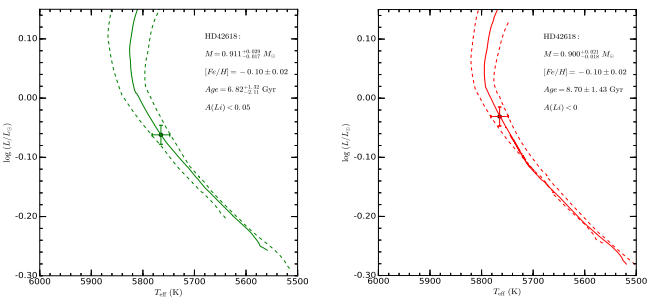

Figure 1. HR diagram for HD 42618, on the left using the Hipparcos parallaxe (case 1), on the right using the Gaia parallaxe (case 2). Mass, metallicity, age and lithium abundances of the models are indicated in the figure.

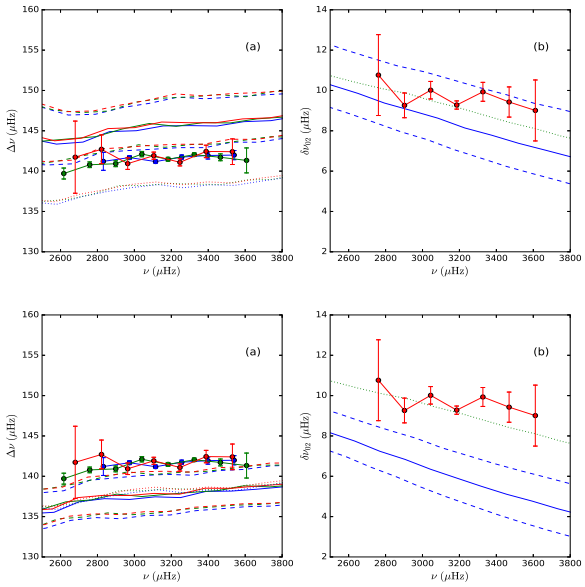

Figure 2. (a) large separations $\Delta\nu$ (blue for $l = 0$, green for $l = 1$, and red for $l = 2$), and (b) small separations $\delta\nu_{02}$ of the oscillation frequencies of the HD 42618 model in case 1 (up) and in case 2 (bottom). Continuous and dashed lines are for calculated models in the range of masses determined by Fig. 1. Dotted line is a solar model and linked circles are the separations of the observed frequencies.

As an additional constraint, we calibrated the tachocline thickness of the models to account for the observed lithium abundance (A(Li) = 1.28 ± 0.06, Morel et al. 2013). Tachocline thicknesses, which model the shear layer of differential rotation below the convective zone, have been reduced by a factor of 1.4±0.2 in case 1 and 1.6±0.2 in case 2, which seems reasonable. Calibrated models are presented in Figs. 3 and 4. The masses are still very similar and the difference in ages is smaller (around 1.5 Gyr). In both cases, large separations are slightly larger for models with calibrated tachocline (about 1 μHz larger), improving the comparison with observation in the case 2 accounting for the model with the larger mass in our range of masses ($M = 0.930$ $M_\odot$). Small separations of case 2 are still lower than the observed ones.

These results show that we have a better agreement of the large separations with the models of the case 2 (Gaia parallax), and in particular with the models with the calibration of the tachocline thickness to account for the observed lithium abundance. It suggests that the tachocline thickness, which depends on the differential rotation, is an important parameter to calibrate for the characterization of solar analog stars. However, the small separations of our models account for the observed ones only with the models of the case 1 (Hipparcos parallax).

In conclusion, even if the models with calibration of the tachocline are better matching the observations in the case of Gaia parallax, the large difference of the small separations with the observations are indicating that our modeling of the evolutionary status is not completely satisfactory. The same study but considering a 2σ error bar on the spectroscopic parameters could allow to have a larger set of models, to find the better one that account for both spectroscopic and seismic observations.

Acknowledgements. MC and JDN acknowledge the supports by continuous grants from CNPq (Bolsas de produtividade) and Capes (Capes/Cofecub project n°820-14) Brazilian Agencies.

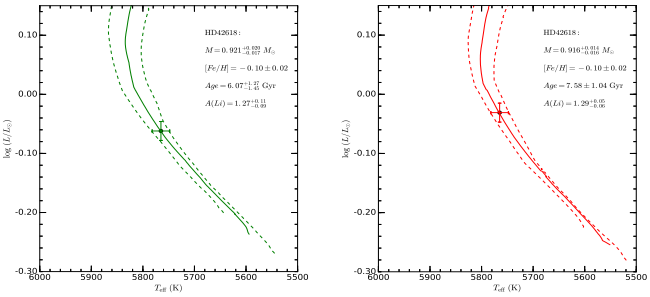

Figure 3. Same as Fig. 1 but using models with calibrated tachocline thickness to match the observed lithium abundance.

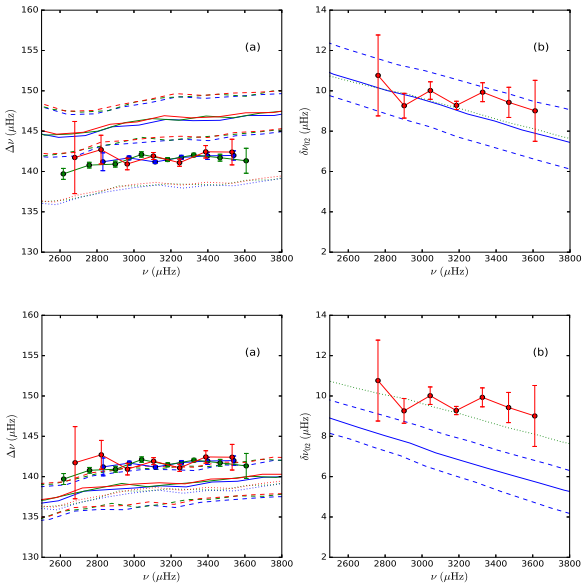

Figure 4. Same as Fig. 2 but using models with calibrated tachocline thickness to match the observed lithium abundance.

References

Barban, C., Deheuvels, S., Goupil, M.-J., et al. 2013, JPhCS, 440, 2030
Brun, A. S., Turck-Chièze, S., Zahn, J.-P. 1998, in *Structure and Dynamics of the Interior of the Sun and Sun-like Stars* ESA Publications Division, SP-418, 439
Hui-Bon-Hoa, A. 2008, Ap&SS, 316, 55
Morel, T., Rainer, M., Poretti, E., Barban, C., Boumier, P. 2013, A&A, 552, A42
Théado, S., Vauclair, S. 2003, ApJ, 587, 784
VandenBerg, D. A., Clem, J. L. 2003, AJ, 126, 778

Boletim da Sociedade Astronômica Brasileira, **30**, no. 1, 95-96

Simultaneous modelling of X-ray emission and optical polarization of intermediate polars: the case of V405 Aur

Isabel J. Lima[1], Cláudia V. Rodrigues[1], Karleyne M. G. Silva[2], G. Juan M. Luna[3], Flávio D'Amico[1], Joaquim E. R. Costa[1], & Jaziel G. Coelho[1]

[1] Instituto Nacional de Pesquisas Espaciais, Brazil e-mail: isabel.lima@inpe.br
[2] Gemini Observatory, Chile
[3] Instituto de Astronomia y Física del Espacio, Argentina

Abstract. We present a simultaneous modelling of X-ray and optical (UBVRI) emission of V405 Aurigae, the intermediate polar with the highest magnetic field, using the CYCLOPS code. Our preliminary fit to V405 Aur suggests that is possible to model its data using only one post-shock region, differently from literature results.

Resumo. Apresentamos a simultânea modelagem da emissão em raios-X e no óptico (UBVRI) de V405 Aurigae, a polar intermediária de maior campo magnético, usando o código CYCLOPS. Nosso resultado preliminar sugere que é possível modelar os dados usando apenas uma região pós-choque, diferentemente dos resultados na literatura.

Keywords. magnetic fields — polarization — radiative transfer — methods: numerical — novae, cataclysmic variables.

1. Introduction

Intermediate polars (IPs) are a subset of magnetic cataclysmic variables in which the white-dwarf (WD) spin period is much shorter than the orbital period. The material flows along the magnetic field lines forming columns or curtains. The compressed material — the post-shock region — near the WD is responsible by most of the system emission in high energies: Bremsstrahlung and lines emission dominate in X-rays. In optical and IR spectral region, other components are the main emitters, as the disk, when present. Some IPs present optical polarization that comes from cyclotron emission from the post-shock region.

In this study, we present our modelling of the optical polarization and X-ray emission of V405 Aurigae, the intermediate polar that has the highest magnetic field. The observational characteristics of V405 Aur (Evans & Hellier 2004; Piirola et al. 2008) are: flux presents a double-peaked modulation in optical and X-rays; optical circular polarization is variable and alternates between positive and negative values; XMM-Newton spectra show two components with a strong soft X-rays excess. The optical polarization indicates a magnetic field of ~30 MG and two post-shock regions. X-rays data were also modelled using two regions, however the geometry is not the same in terms of inclination and colatitude: $i = 65°$ and $\beta = 60°$ from X-rays data and $i = 30 - 50°$ and $\beta = 90°$ from optical data.

The cyclotron emission of polars (CYCLOPS) code calculates the radiative transport in the magnetic accretion columns considering free-free and cyclotron as emission processes and photoelectric absorption and electron scattering as extinction processes. CYCLOPS permits the fitting of multiband data (Costa & Rodrigues 2009; Silva et al. 2013). This code adopts a 3D-representation treatment and non-homogeneous post-shock region in terms of density, temperature and magnetic field. Hence auto-eclipse, projection effects, and absorptions internal to the binary system are consistently considered. The code also considers the interstellar extinction in X-ray and optical wavelengths. Up to the present time the cyclops is a unique tool.

Table 1. Parameters of v405 Aur model.

CYCLOPS input parameters	Fitted values
i	52.0°
β	52.0°
Δ_{long}	2.0°
h	0.11 R_{WD}
$B_{\rm Pole}$	45 MG
$B_{\rm lat}$	78.0°
$B_{\rm long}$	288.0°
$T_{\rm max}$	128 keV
$\log(N_{\rm max})$	12.5 cm^{-3}
$\delta_{\rm phase}$	0.194
Model results	**Values**
$B_{\rm reg}$	24 –34 MG
$\langle T \rangle$	52.4 keV
$T_{\rm pond}$	26.2 keV
$T_{\rm range}$	10 – 128 keV
$Att(MI)$	0.158
χ^2_{norm}	0.068

2. V405 Aur modelling

Our goal is to find a model that explains both optical and X-rays V405 Aur data. We show the Table 1 a set of parameter a preliminary fit of V405 Aur data. The fitting was performed using the PIKAIA genetic algorithm and AMOEBA (Charbonneau 1995; Press et al. 1992).

Figures 1 and 2 show a good model obtained by a simultaneous fitting of U, B, V, R, and I light and polarization curves and X-ray spectra.

3. Conclusions and Prospects

A preliminary fit to V405 Aur suggests that is possible to model its data using only one post-shock region, unlike previous studies.

The present models consider each band represented by only one wavelength. Multiwavelength correction may be the key to

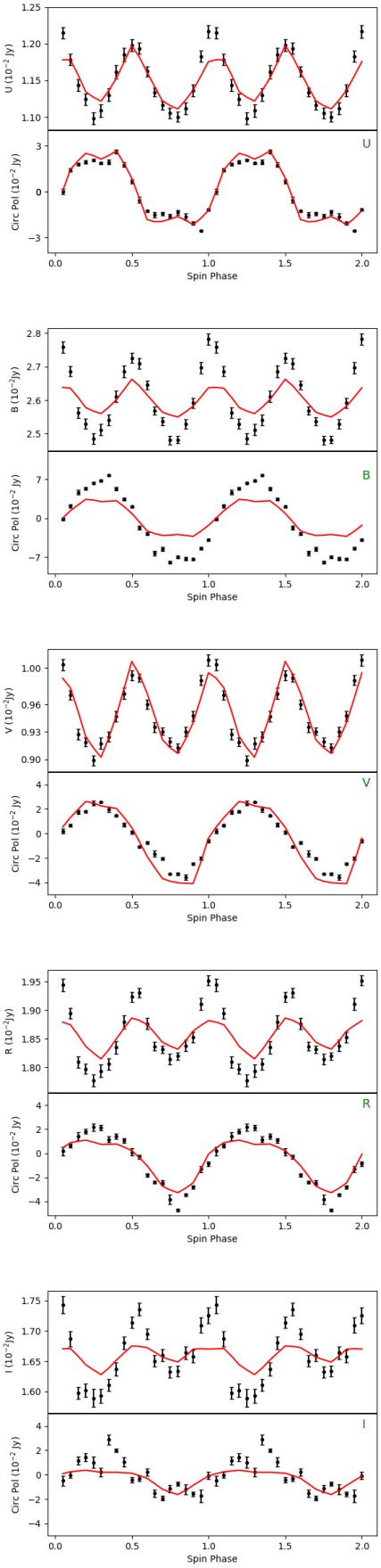

Figure 1. A good model obtained by a simultaneous fitting of UBVRI light and polarization curves of V405 Aur.

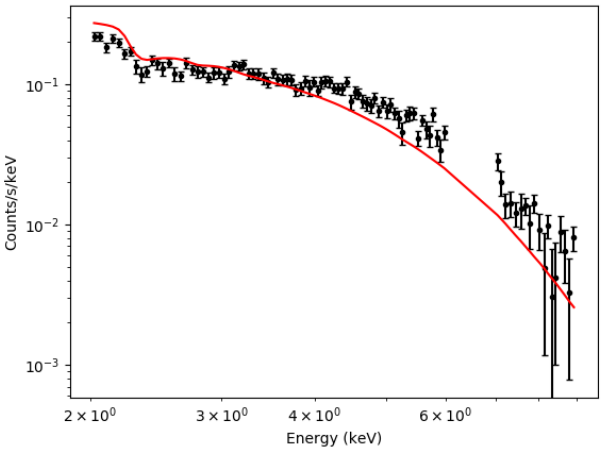

Figure 2. Our best model fit for the X-rays spectra of V405 Aur.

better fit some bands such as B and I. We also intend to fit simultaneously the light curves in X-rays.

Acknowledgements. We are indebted to Vilppu E. Piirola for providing the V405 Aur optical data. IJL: FAPESP (Procs. 2015/24393-7, 2013/26258-4), CVR: CNPq (Procs. 306701/2015-4), FAPESP (Procs. 2017/05610-2) and JGC: FAPESP (Procs.13/15088-0).

References

Charbonneau, P., 1995, ApJS, 101, 309
Costa, J. E. R., Rodrigues, C. V. 2009, MNRAS, 398, 240
Evans, P. A. & Hellier, C. 2004, MNRAS, 353, 447
Piirola, V., Vornanen, T., Berdyugin, A., & Coyne, G. V. 2008, ApJ, 684, 558
Press, W. H., Teukolsky, S. A., Vetterling, W. T., Flannery, B. P., 1992, Numerical recipes in FORTRAN. The art of scientific computing, 29, 32
Silva, K. M. G. et al., 2013, MNRAS, 432, 1587

Boletim da Sociedade Astronômica Brasileira, **30**, no. 1, 97-98

Project and development of the architectural model for CRAAM Solar Virtual Observatory

Luis Felippe Backer[1], Israel Santos[1,2], & Leandro Pupo Natale[1]

[1] Faculdade de Computação e Informática Mackenzie
[2] Centro de Rádio Astronomia e Astrofísica Mackenzie - CRAAM

Abstract. Disruption of communication technologies have brought a new perspective to the way information is treated. With the adoption of new technologies it became essential the democratic access to knowledge for better results and the continuous and faster growth of the research community. In the astronomy field, the need of access to data and information impulsed labs to engineer software platforms to simplify access to collected data. In this article we will discuss about the challenges of the software development, maintenance and the adoption of new technologies to remodel and optimize the current architecture.

Resumo. A disrupção de tecnologias de comunicação trouxeram uma nova perspectiva no modo como abordamos o acesso a informação. Com a adoção de novas tecnologias passou a ser essencial a democratização do acesso ao conhecimento para trazer à sociedade de pesquisadores melhores resultados e garantir o crescimento contínuo da comunidade. No campo da astronomia, a necessidade de acesso a dados e informação impulsionou o desenvolvimento de plataformas de software para simplificar o acesso aos dados coletados. Neste artigo vamos discutir sobre os desafios do desenvolvimento e manutenção de software e adoção de novas tecnologias para remodelar e otimizar a arquitetura atual.

Keywords. Containers – Docker – Micro services – Software Architecture – SVO

1. Introduction

The era of communication technologies and information dissemination resulted in a new culture of sharing and democratization of knowledge, allowing users to access information from diversified sources. With this scenario it becomes essential, in the astronomy field, the development and adoption of solar virtual observatories (SVO) aiming the data sharing.

The Solar Virtual Observatory of Mackenzie University's Center of Radio, Astronomy and Astrophysics (CRAAM-SVO), initially created to structure and share collected data from the SST (Solar Submillimeter Telescope) (Kaufmann et al. 2001) and POEMAS (Polarization Emission of Millimeter) (Valio et al. 2013)telescopes, has been working with software computational resources to integrate with the International Virtual Observatory Alliance (IOVA), however the need for high availability of services and capacity to handle numerous request demand require an architectural review.

2. Solar Virtual Observatory Architecture

As explained by (Santos 2017) the current CRAAM-SVO architecture is composed of one application server that addresses requests from labs, partners and researchers. The development is based on Java Enterprise Edition architecture with frameworks such as JPA and Jena for a Virtuoso database integration, through SQL and RDF/XML, alongside with API's to generate FITS (Flexible Image Transport System) files for data sharing.

The software Architecture process and standards goes through constant upgrades aiming to better attend new services and to guarantee a flexible software architecture to be enhanced with the use of new disruptive technologies. The most popular approach in software development has been the use of containers united with the application development in micro services, allowing to execute in modules and gain high availability and scalability.

2.1. Microservices vs Service Oriented Architecture

The best choice for the SVO architecture development relies between Service Oriented Architectures (SOA), Microservices Architecture (MSA) and the analysis of which better fits with the software roadmap proposal.

(Erl et al. 2014) defines the SOA architecture model as a design paradigm model that comprises the design principles of the service orientation to enhance efficiency, productivity and agility guaranteeing a separation of concerns with low coupling services. With SOA services are agnostic, reusable and compose a service inventory where each service is responsible for a specific logic. The combination of SOA and Web Services leverage's the potential of re-usability by allowing access to the service logic through a communication framework.

The Microservices Architecture, according to (Bonerér 2016), is a system based on small, independent and connected services, this allow to divide the system into groups, removing the development complexity.

Both Microservices and SOA are verry simillar, (Bonerér 2016) says both share same goals such as decoupling, isolation, composition, integration and autonomous services, however microservices are an application of Reactive principles, this means that microservices are responsive, resilient, elastic (can adapt to larger workloads) and massage driven.

2.2. Containers vs Virtual Machines

According to (Dua et al. 2014), Virtual Machines (VM) are the virtualization of the operating system (OS) layer in which hypervisors allow for multiple guest OS to run in a single machine (Figure 1), which may result in performance issues due to the fact that VM's suffer from overhead in instructions translated to the host and it requires large amount of storage to maintain the OS, kernel and programs. Virtual machines are popular in the market but it's being over throned by the rise of containers.

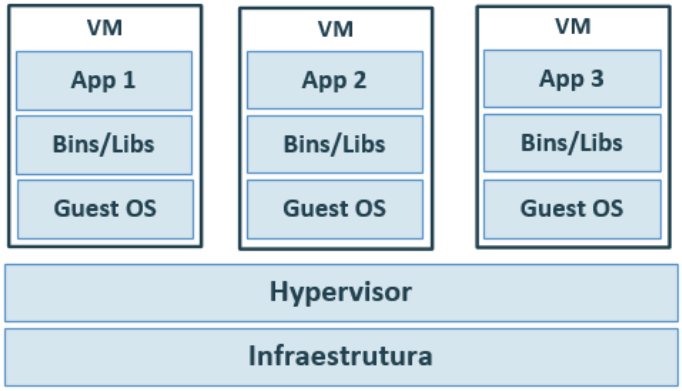

Figure 1. Virtual Machine architecture based on Docker.com diagram.

Figure 2. Start up time result of PostgreSQL database.

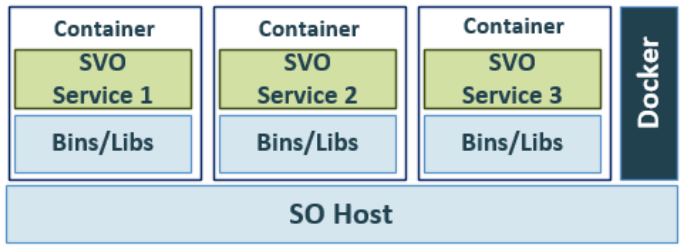

Figure 3. Docker architecture based on Docker.com diagram.

Containers aren't a new industry technology, but it was only with the invention of Docker platform, that the market began adhere. Containers are stateless components that works creating packages with applications, its dependencies and executable files (Dua et al. 2014). The fact that containers work as processes sharing the same OS and kernel (Figure 3) makes it a preferable option to VM's because it presents better performance in terms of hardware requirements and start up time. To take as an example, when running simple PostgreSQL data base , Docker takes only 3 seconds to start a PostgreSQL (Figure 2).

3. Technical approach

Each software architecture model presents it's benefits and issues, whether it's for implementation, performance or maintenance purposes. In the goal of reaching a manageable and flexible architecture, it's much needed a remodelling of the current SVO architecture so we introduce both container and micro services to build a new, flexible and optimized model CRAAM's SVO (Santos 2017).

To incorporate the new technologies into the architectural design, the study of the current application is imperative for a better understanding of the solution's functionalities and their integrations so we can build a modular version of application based on micro services.

With a good understanding of the solution, the development process will require a re-engineering of the current code in order to allow the use of micro services, guaranteeing that each service is independent and yet they interact efficiently as a single system at the user's perspective. Having a micro service architecture permits the optimized use of the container technology, by separating each service as a container, communicating between each other and enabling a faster scaling of the most requested service.

The container technology adopted will be Docker. The open source platform simplifies the build and management of containers and allows a communication between containers so the application services may interact during system execution.

4. Conclusion

This proposed model facilitates the DevOps practice, allowing to devide the SVO system development in groups, and simplifies upgrades and new functionality builds by initializing new containers and ending the old versions. The project reduces risks of downtimes, allowing rollback to previous stable containerized versions, and provides the choice of deployment in any environment: physical and virtual machines or public and private clouds.

Acknowledgements. I would like to thank MackPesquisa for the finantial support.

References

Strimbei, C., Dospinescu, O., Strainu, R. M., Nistor, A. 2015, Informatica Economica, 19 (4), 13
Morris, D., Voutsinas, S., Hambly, N. C., Mann, R. G. 2017, Astronomy and Computing, 20, 105
Dua, R., Raja, A. R., Kakadia, D. 2014, In Cloud Engineering (IC2E), 610
De Carvalho, Reinaldo R. et al. 2010, Journal of Computational Interdisciplinary Sciences, 1, 187
Kaufmann, P. et al. 2001, IMOC 2001: Proceedings of the 2001 SBMO/IEEE MTT-S International. IEEE, p. 439.
Santos, I. F. 2017, Construção Iterativa de uma Ontologia com Integração Semântica para o Observatório Solar Virtual do Centro de Rádio Astronomia e Astrofísica Mackenzie. Tese de Doutorado, Universidade Presbiteriana Mackenzie
Valio, A. et al. 2013, Solar Physics, 283, 651
Almeida, M. B., Bax, Marcello P. 2003, Ciência da Informação, Brasília, 32 (3), 7
Berner-Lee, T., Hendler, J. 2003, Nature, 410, 1023
Borst, W. N. 1997, Construction of engineering ontologies for knowledge sharing and reuse. Universiteit Twente
Erl, T., Gee, C., Normann, H., Kress, J., & Maier, B. 2014, Next generation SOA: A concise introduction to service technology & service-orientation, Pearson Education
Bonerér, J. 2016, *Reactive microservices architecture: design principles for distributed systems*

Boletim da Sociedade Astronômica Brasileira, **30**, no. 1, 99-100

Spatially- and velocity-resolved emission line disk spectra of V2051 Oph along outburst

E. L. Andrade & R. Baptista

[1] Universidade Federal de Santa Catarina
e-mail: eduardo.andrade@astro.ufsc.br, raybap@gmail.com

Abstract. We report the analysis of time series of optical spectroscopy of the eclipsing dwarf nova V2051 Oph along three consecutive nights covering the maximum, and the decline of its 2002 July outburst. We present spatially- and velocity-resolved disk spectra of the $H\gamma$ emission line along the outburst using eclipse mapping techniques. Emission line profiles are asymmetric and vary with distance from disk center. Presence of P Cygni profile in the spectra suggests mass loss in a highly collimated disk wind (opening angle $\theta \sim 15 \pm 5°$) originating from the inner disk regions ($\sim 0.15\ R_{L_1}$).

Resumo. Relatamos a análise de séries temporais de espectroscopia óptica da novã anã eclipsante V2051 Oph ao longo de três noites consecutivas cobrindo o máximo e o declínio de sua erupção de julho de 2002. Apresentamos espectros do disco na linha de emissão de $H\gamma$ resolvido por velocidade e espacialmentealmente ao longo de uma erupção usando técnica de mapeamento por eclipse. Os perfis de linha de emissão são assimétricos e variam com a distância do centro do disco. A presença de perfil P Cygni nos espectros sugere perda de massa altamente colimado (ângulo de abertura $\theta \sim 15 \pm 5°$) proveniente das regiões interna do disco ($\sim 0.15\ R_{L_1}$).

Keywords. Stars: dwarf novae – binaries: eclipsing – novae, cataclysmic variables

1. Introduction

Dwarf novae (DNs) are close binary stars in which a white dwarf that accretes matter from a solar-type companion. They show repeated outbursts lasting from days to weeks and recurring on timescales from weeks to years, in which their accretion disk brighten by factors 20-100. Outbursts are unpredictable, and observations covering such events are rare and precious.

V2051 Oph is an eclipsing DN with $P_{orb} \simeq 90$ min undergoing sparse outbursts a few days long, possibly in response to sudden changes in mass-transfer from the mass donor star (Baptista et al. 2007). It was observed for four consecutive nights in July 2002 with the optical spectrograph Boller & Chivens coupled to the 1.5 m ESO telescope with spectral range of 3600 - 5950 Å. By fortunate coincidence, these observations coincided with the binary outburst covering the rise to maximum and the subsequent decline back to quiescent state. Due to the good spectral resolution and good temporal resolution, the data allows for the use of the indirect image technique to map the brightness distribution of the accretion disk along the outburst. Here we report the analysis of spectral mapping of the $H\gamma$ emission line of the three last nights of that outburst.

2. Analysis

Light curves of $H\gamma$ were sampled from -2000 km s^{-1} to +2000 km s^{-1} using velocity bin of 500 km s^{-1} centered at the rest wavelength, $v = 0$ km s^{-1}. Maximum-entropy eclipse-mapping techniques (Horne 1985; Baptista 2001) were used to solve for a map of the disk brightness distribution at each velocity bin. We adopted the binary parameters of Baptista et al. (1998), $q = 0.19$ and $i = 83.3°$, and a square eclipse map with 51×51 pixels centred at the white dwarf position.

Each of the eclipse maps yields the information about the emitting region on a specific velocity bin. By combining 8 velocity maps we are able to isolate the shape of $H\gamma$ line emission line at any desired position on the dis. In order to separate the disk spectra at different distances from the disk center, we sliced the eclipse map in a set of five concentric annular sections of width $\Delta R = 0.1\ R_{L_1}$ and computed the average intensity inside each annulus. The statistical uncertainties affecting the average intensities are estimated with Monte Carlo simulations.

Figure 1 shows the resulting $H\gamma$ line profiles for outburst maximum (top panel), early decline (middle panel) and late decline (bottom panel). $H\gamma$ appears in emission at all disk radii, with a typical broad, double-peaked disk profile in the outer disk regions. The line profile is asymmetric and varies with distance from disk center; the red peak is stronger at smaller radii and the blue peak becomes progressively stronger with increasing radius. The innermost disk regions show a P Cygni profile indicating origin in an outflowing gas, probably a disc wind (Cordova & Mason 1985). From the binary parameters we estimate the disk wind opening angle θ using $\theta = i - \arccos(V_{escape}/V_{observed})$, where $V_{escape} = \sqrt{G\,M_1\,R^{-1}}$ and $V_{observed}$ is the observed velocity of the absorption component. We find a highly collimated disk wind (opening angle of $\theta \sim 15 \pm 5°$) originating from the inner disk regions ($\sim 0.15\ R_{L_1}$).

3. Conclusion

Our preliminary data analysis show that the $H\gamma$ emission line profiles are asymmetric and vary with distance from disk center. Presence of P Cygni profile in the spectra suggests mass loss in a highly collimated disk wind. Spectral mapping is a powerful probe of the physical and dynamical conditions in an outbursting accretion disk. By extending the analysis to the full wavelength and time coverage of our data we will be able to test the connection between the suggested disk wind outflow and the onset of the outburst, and we will search for signals of spiral arms in the outbursting accretion disk (as suggested by the asymmetric double-peaked line profile).

Acknowledgements. We thank CNPq and CAPES for financial support through scholarships.

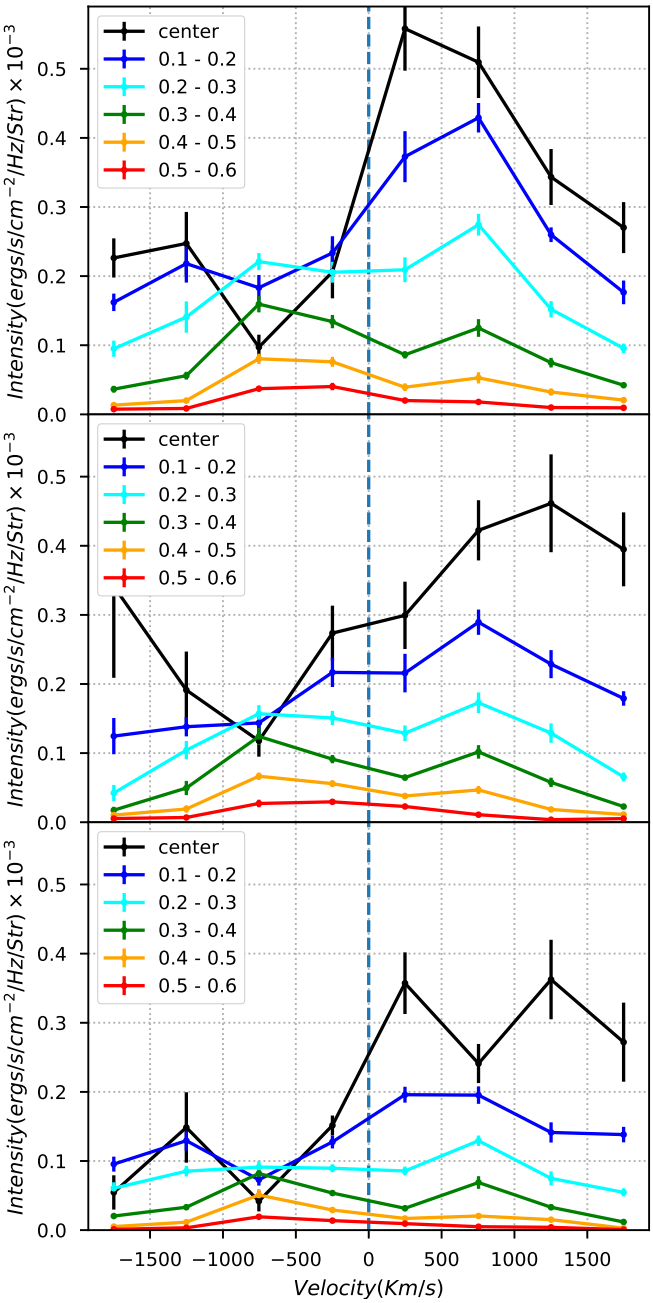

Figure 1. Disc spectrum as function of radius plotted in velocity centered in $H\gamma$, marked by vertical dashed line. Top panel corresponds to outburst maximum, second and third are decline to quiescence. Colors of each curve are indicated in the graph where each value correspond to an annulus disc radius as function of L_1. From the center of the disc increasing in steps of $0.1L_1$ up to $0.6L_1$, outer parts of the accretion disc.

References

Baptista, R., Santos, R. F., Faúndez-Abans, M., & Bortoletto, A. 2007, AJ, 134, 867
Baptista, R., Catalan, M. S., Horne, K., & Zilli, D. 1998, MNRAS, 300, 233
Horne, K. 1985, MNRAS, 213, 129
Baptista, R. 2001, Astrotomography, Indirect Imaging Methods in Observational Astronomy, 573, 307
Cordova, F. A., & Mason, K. O. 1985, ApJ, 290, 671

Boletim da Sociedade Astronômica Brasileira, **30**, no. 1, 101-102

Identification and spectral classification of brown dwarfs in the Dark Energy Survey data

M. Dal Ponte[1,2], B. X. Santiago[1,2], A. Carnero Rosell[2], B. Burningham[3], & L. N. da Costa[2]

[1] Departamento de Astronomia (UFRGS) e-mail: marina.ponte@ufrgs.br, e-mail: basilio.santiago@ufrgs.br
[2] Laboratôrio Interinstitucional de e-Astronomia (LIneA) e-mail: carnero@linea.gov.br, e-mail: ldacosta@linea.gov.br
[3] University of Hertfordshire e-mail: burninghamster@gmail.com

Abstract. Brown dwarfs are low-mass, cool and intrinsically very faint sources compared to H-burning main-sequence stars. Here present our the first attempts to draw a sample of LT dwarf candidates using Dark Energy Sruvey (DES) data in conjunction with near and mid infrared surveys. We devise cuts in colour space and test them using known MLT dwarfs and QSOs. We also develop a simulation tool that generates synthetic samples of MLT dwarfs, against which to test our selection criteria. Finally, we briefly describe a simple likelihood analysis tool to further refine the sample of LT dwarfs.

Resumo. As anãs marrons são objetos de baixa massa, frios e instrinsicamente muito fracos quando comparadas com estrelas de sequência principal. Aqui apresentamos as primeiras tentativas de selecionar uma amostra de candidatas a anãs LT usando os dados DES em conjunto com surveys no infraverelho próximo e médio. Nós analisamos cortes no espaço cor-cor e os testamos usando anãs MLT conhecidas e QSOs. Nós também desenvolvemos uma ferramenta de simulação que gera amostras sintéticas de anãs MLT, novamente para testar nossos critérios de seleção. Finalmente, descreveremos brevemente uma ferramenta simples de análise de verossimilhança para aperfeiçoar a amostra de anãs LT.

Keywords. brown dwarfs – stars: low-mass – surveys

1. Introduction

The search for substellar objects, with masses that bridge the gap between H-burning low mass stars and giant planets, has led to the identification of over a thousand of sources classified as being of LTY spectral types. For instance, the Dwarf Archives (http://dwarfarchives.org/) lists 1281 known LTY dwarfs up to 2012. The more recent compilation by J. Gagné (https://jgagneastro.wordpress.com/list-of-ultracool-dwarfs/) reaches over 1700 sources later than an L0. Brown Dwarfs are supposed to be among the most common objects in the Milky Way, but their very low masses and temperatures, and hence luminosities, also rank them among the hardest sources to detect. Deep photometric surveys covering infrared filters, such as the 2MASS (Skrutskie et al 2006), UKIDSS (Lawrence et al 2007), and WISE (Wright et al 2010) have been responsible for the systematic increase to the census of brown dwarfs experienced in recent years. Optical surveys are also useful for probing such cool objects, specially L dwarfs, as is the case of the SDSS (York et al 2000), and more recently, the Dark Energy Survey (DES; The Dark Energy Survey Collaboration 2005).

In this contribution, we describe our initial efforts towards: i) selecting a sample of LT dwarfs using DES photometry coupled with near and mid-infrared from VHS (Emerson et al 2004) and WISE, respectively. ii) assessing the contamination of such a sample, mostly by M dwarfs, high-redshift QSOs, and very red galaxies; iii) photometrically classifying our candidate sources.

Our ultimate goal is to use this relatively deep sample of LT dwarfs to better constrain the spatial distribution of these objects away from the immediate solar neighbourhood, estimating their scale height and scale length on the disk, and assessing any possible contribution by thick disk LT dwarfs.

2. The Data

We have used internal releases of the first and third year by the DES collaboration, Y1A1 and Y3A2, respectively. Y1A1 is described in detail by Drlica-Wagner et al (2017) and provides reliable magnitudes down to $\simeq$ 23 mag in gr, $\simeq$ 22.5 mag in i, $\simeq$ 22 mag in z, and $\simeq$ 20 mag Y over $\simeq$ 2000 sq. deg. Y3A2 covers the full 5.000 sq. deg expected for the survey and is currently being characterized in terms of depth, star-galaxy separation, and other issues.

With the goal of identifying LT candidates and performing their spectral classification, we added more photometric bands to our data. We matched our DES sources to those from two infrared surveys: VISTA Hemisphere Survey (VHS) and Wide-Field Infrared Survey Explorer (WISE). The VHS and WISE were chosen because, besides complementing the DES photometry with infrared bands, they have a large overlap area with DES. We also compiled samples of known LT dwarfs (from J. Gagné's compilation), M dwarfs (West et al 2011), and quasars (Flesch 2015) that fall in the DES footprint, and identified these sources in the DES catalogues. They are very useful to test and validate our selection criteria, and to quantify contamination.

3. LT Selection

We looked at the color distributions of known LT dwarfs together with the known contaminant sources. We also developed a code, which we call Galmod-BDs, that computes expected counts of LT dwarfs, both as a function of magnitude and colour, using empirically determined space densities, absolute magnitudes (and hence colours) as a function of spectral type, and a model of Galactic structure. Galmod-BDs also creates synthetic samples of MLT dwarfs, with true and observed magnitudes in izY(DES)+JHK(VHS)+W1W2W3(WISE) filters. The observed magnitudes are determined according to input uncertainty curves

for the filters and assuming Gaussian errors. The local space densities we use come from Marocco et al (2015) and references therein. The reference absolute magnitudes were empirically determined for the DES filters using the known MLT sources that fall in the DES Y1 and Y3 footprints. They have been cross-checked against estimates from Dupuy & Liu (2012) and Knapp et al (2004), and inconsistencies of the order of 0.1-0.2 mags were found, specially for izY, as the result of unaccounted for differences in the passbands.

After inspecting these distributions in colours, both of real and simulated sources, we were able to define a LT candidate selection based on cuts applied to the colour-colour diagrams. Figure 1 shows one of the main colour-colour planes we used and the selection adopted. We show both real and simulated LTs in the figure. The red dashed zone delimits our current colour selection. We estimated the completeness and purity of our selected sample, again for both real and artificial objects. We define completeness as c = (# of actual LT dwarfs selected as such) / (total # of actual LT dwarfs), and purity as p = (# of actual LT dwarfs selected as such) / (total # of selected LT dwarfs). Experiments with the latest simulated set yields values of $c = 0.94$ and $p = 0.64$ based on the colours alone.

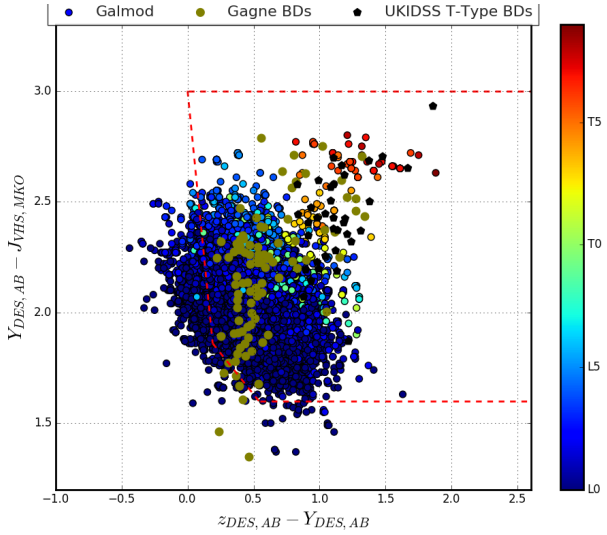

Figure 1. $Y(DES)-J(VHS)$ *vs.* $z-Y(DES)$ colour-colour diagram. The olive green circles come from Gagné's compilation and as measured by DES. The black hexagons are from UKIDSS (Burningham et al, 2010, MNRAS,406, 1885), converted from SDSS z and MKO Y and J. The slightly smaller circles are simulated LTs from Galmod-BDs (see text for a brief description of the code) and are colour coded according to their spectral type. The red dashed lines show our colour selection of LT dwarfs.

In brief, our approach to select the data is: i) use colour-colour cuts to find a sample that is complete in LT dwarfs, but that may be somewhat contaminated by galaxies, high-z QSOs and M dwarfs; ii) use the classification code described below to refine our sample in order to keep sources which are LT dwarfs and eliminate as many contaminants as possible. The final product will be a sample with high completeness and purity of LT dwarfs in DES+VHS+WISE data.

4. Classification Code

We have developed a simple algorithm that uses measured colours for the i-th source ($c_{ik}, k = 1, Ncols$) and their associated uncertainties ($\sigma_{c_{ik}}, k = 1, Ncols$) and compares them to reference colours ($c_{jk}, k = 1, Ncols$) from the j-th spectral type, this latter ranging from M1 up to T8. The reference colours we used are the same ones which were empirically determined and adopted by Galmod-BDs to predict LT counts and create synthetic MLT samples. With the measured and reference colours, we can build a Gaussian likelihood L_{ij} that the data for the i-th star come from the j-th model.

$$L_{ij} = \prod_{k}^{Ncols} \frac{1}{\sqrt{(2\pi)}\sigma_{c_{ik}}} \exp \frac{(c_{ik} - c_{jk})^2}{2\sigma^2_{c_{ik}}} \quad (1)$$

The product above is over all available $Ncols$ colours for each candidate LT source. Our algorithm currently finds the particular model that yields the largest likelihood value and tags each star to that model. We tested it against real MLTs of known spectral type and simulated sets. The accuracy depends on the number of colour indices available. This simple likelihood analysis is being used to further refine our colour selected sample. In particular, sources whose likelihood corresponds to colour deviations by 3σ or more from the reference values are discarded as non MLTs.

A more detailed description of the data, colour cuts, Galmod-BDs simulations, likelihood classification and modeling of the spatial distribution of LTs will be presented in a full journal paper (Carnero et al., in preparation).

Acknowledgements. MDP and BXS were supported by CNPq grant 473352/2013-3. MDP is also supported by CAPES Master fellowship. BXS is also supported by CNPq fellowship 304639/2013-3. The authors are grateful to the entire DES collaboration, specially the Milky-Way science working group, for all the support and useful discussions.

References

Burningham et al, 2010, MNRAS,406, 1885
The Dark Energy Survey Collaboration 2005, arXiv:astro-ph/0510346
Drlica-Wagner, A. et al. 2017, arXiv:1708.01531
Dupoy, T and Liu, M. 2012, ApJS, 201, 19
Emerson, J. P., Sutherland, W. J., McPherson, A. M., et al. 2004, The Messenger, 117, 27
Flesch E., 2015, PASA, 32, 10
Knapp, G. et al. 2004, AJ, 127, 3553
Lawrence, A., Warren, S. J., Almaini, O., et al. 2007, MNRAS, 379, 1599
Marocco, F. et al. 2015, MNRAS, 449, 3651
Skrutskie, M. F., Cutri, R. M., Stiening, R., et al. 2006, AJ, 131, 1163
West, A., et al. 2011, AJ, 141, 97
Wright, E. L., Eisenhardt, P. R. M., Mainzer, A. K., et al. 2010, AJ, 140, 1868
York, D. G., Adelman, J., Anderson, Jr., J. E., et al. 2000, AJ, 120, 1579

Boletim da Sociedade Astronômica Brasileira, **30**, no. 1, 103-104

Photometry and spectroscopy of A-type stars observed by the Kepler K2 Mission Campaign 8

J. M. Eidam[1], A. W. Pereira[1], M. Emilio[1], L. Andrade[1], M. C. Rabello-Soares[2], E. Janot-Pacheco[3] & J. Armstrong[4]

[1] Universidade Estadual de Ponta Grossa - e-mail: jessyeidam@gmail.com
[2] Universidade Federal de Minas Gerais
[3] IAG – Universidade de São Paulo
[4] Institute for Astronomy/University of Hawaii

Abstract. In this work we present the preliminary results of the analysis of eight A-type stars observed in the Galactic Pole by the Kepler K2 Mission during its Campaign 8. Frequency analysis of the eight light curves was made using the CLEANEST algorithm. In addition to the photometric data, ground spectroscopy was done at the OPD/LNA in October 2015 with the Zeiss Telescope (0.6m) and in August 2016 with the Perkin-Elmer Telescope (1.6m). Ground spectroscopic information enhances the data from the satellite's light curves, allowing for the characterization of the internal structure of the stars. Spectroscopy data were reduced using IRAF, and spectral characterization using Spectroscopy Made Easy (SME). In this work, we present preliminary results of this analysis. We show that a variable star, BD+10 102, has a period of 1.55 days (0.645 c/d) and can be classified as an A0/B9.5 star.

Resumo. Neste trabalho são apresentados resultados preliminares da análise de oito estrelas do tipo A observados no Pólo Galactico pela Missão Kepler K2 durante a campanha 8. A análise das frequencias das oito curvas de luz foi feita usando o algoritmo CLEANEST. Além dos dados fotométricos, espectroscopia de solo foi feita no OPD/LNA em outubro de 2015 com o telescópio Zeiss (0.6m) e em agosto de 2016 com o telescópio Perkin-Elmer (1.6m). Informações espectroscópicas de solo completam os dados das curvas de luz do satélite, permitindo a caracterização da estrutura interna das estrelas. Dados de espectroscopia foram reduzidos usando IRAF, e a caracterização espectral usando o Spectroscopy Made Easy (SME). Neste trabalho, apresentamos os resultados preliminares desta análise. Mostramos o estudo de uma estrela variável, BD+10 102, com um período de 1.55 dias (0.645 c/d) e que pôde ser classificada como uma estrela A0/B9.5.

Keywords. Stars: early-type – Stars: fundamental parameters – Techniques: photometric – Techniques: spectroscopic

1. Introduction

The primary objective of the Kepler Mission was monitoring more than 150 000 stars to transit-driven exoplanet detection in the Cygnus-Lyra region. After the loss of two reaction wheels, the spacecraft was refitted to observe the ecliptic plane, and renamed the K2 mission. Since then, it allows the scientific community to propose targets to be observed. Campaign 8 was observed between January and March 2016 and among the targets were eight A-type stars proposed by our group at the Galactic Pole. Pointing: RA: 16.3379975 degrees; Dec: 5.2623459 degrees; Roll: -157.3538761 degrees[1].

Figure 1 shows the distribution of our targets observed by Campaign 8, and figure 2 shows the light curve for one of our targets, BD+10 102 (or EPIC ID 220679442).

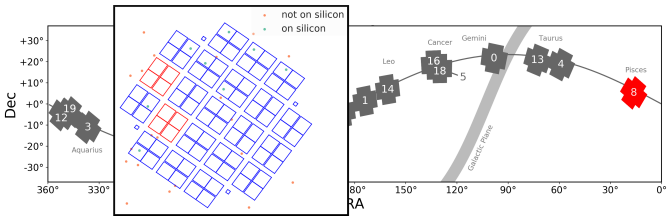

Figure 1. K2 campaign fields, with field 8 highlighted. Inset: Targets proposed for campaign 8. Green targets were observed, and red targets were discarded.

[1] https://keplerscience.arc.nasa.gov/

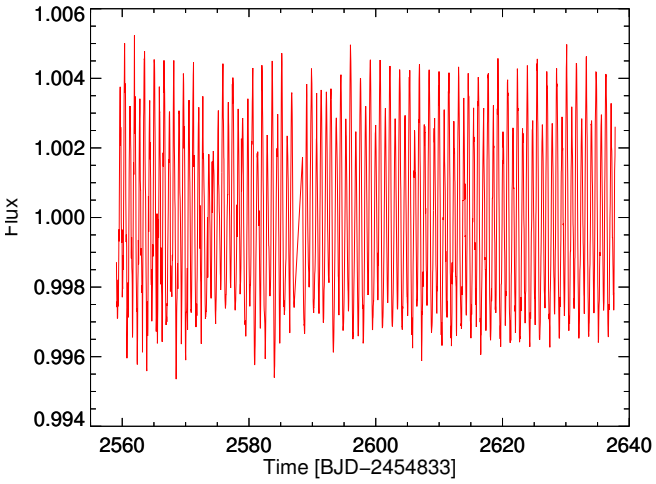

Figure 2. Corrected K2 light curve of target BD+10 102.

2. Methods

Frequency analysis of the eight light curves was made using the CLEANEST algorithm (Foster 1995).

In addition to photometric data, ground spectroscopy was obtained from the Observatório Pico dos Dias / Laboratório Nacional de Astrofísica (LNA) in October 2015 – before K2 observing – with the Zeiss Telescope (0.6m) and in August 2016 – after K2 observing – with the Perkin-Elmer Telescope (1.6m).

Spectroscopic data was reduced using IRAF, and spectral characterization was made using Spectroscopy Made Easy (SME) – an IDL software and a compiled external library that fits stellar spectra with synthetic ones (Valenti & Piskunov 1996; Piskunov & Valenti 2017).

Figures 3 and 4 show the spectra of one of the targets, BD+10 102, taken with the 1.6m telescope and centered respectively on 4400Åand 6300Å.

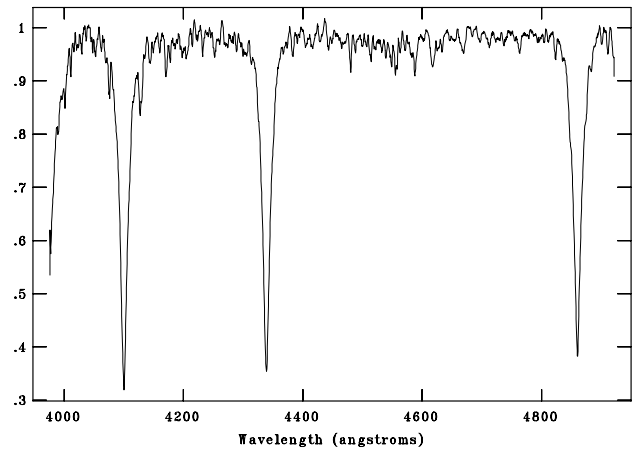

Figure 3. Spectrum in the blue region of C8 target BD+10 102 observed at the OPD/LNA in August 2016.

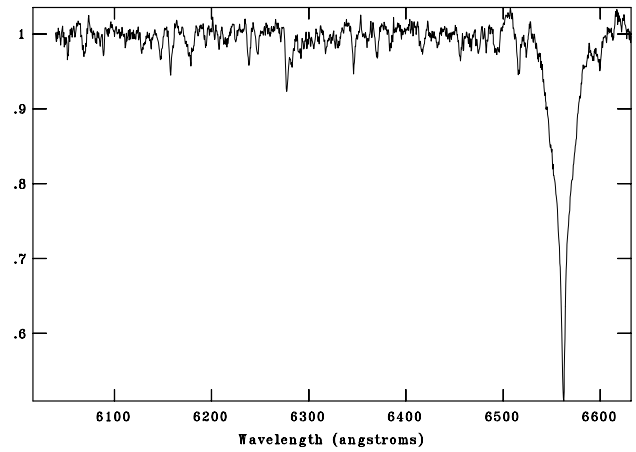

Figure 4. Spectrum in the red region of C8 target BD+10 102 observed at the OPD/LNA in August 2016.

The synthetic spectrum is calculated from the initial parameters provided by the user. For this, a list of input lines provided by the Vienna Atomic Line Database (VALD) is used, which is one of the requirements to operate spectral tuning in SME (Heiter et al. 2008). The global parameters are then varied internally and in different directions with the aid of interpolated atmospheric models for the parameter space to be determined.

We obtain from SME the following stellar parameters for each target: its effective temperature (Teff), surface gravity (logg), vsini, macro and micro velocity turbulence, radial velocity and metallicity. SME provides uncertainty values that are purely numerical and therefore do not properly represent the real uncertainties. Thus, we executed for each adjusted parameter 100 Monte Carlo simulations, randomly varying 5% of the best fit obtained with SME. We assume as uncertainty in the measures the value of 1σ in the dispersion of each parameter.

3. Results and conclusions

Performing the frequency analysis of the light curve for star BD+10 102, we determined its fundamental period as 1.55 days, or, in frequency, 0.645 cycles/day, as can be seen in figure 5.

From the values generated by SME, after passing through the Monte Carlo method, and based on the values for Teff and log g we could confirm BD+10 102 to be a A0/B9.5 star. We are currently finishing the analysis of the eight targets, and by finding their pulsation frequencies we hope to be able to classify any variabilities found.

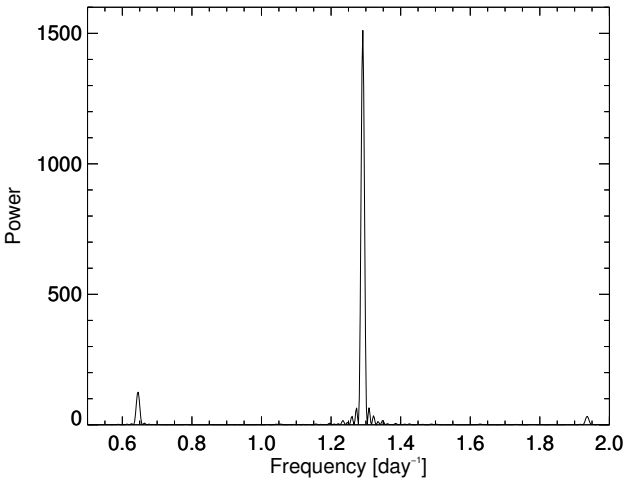

Figure 5. Frequency analysis of the light curve of star BD+10 102.

Acknowledgements. Based on observations made at the Observatório Pico dos Dias / LNA. This paper includes data collected by the Kepler mission.

References

Foster, G. 1995, AJ, 109, 1889
Heiter, U. et al. 2008, J.Phys.Conf.Ser., 130, 012011
Piskunov, N. & Valenti, J. A. 2017, A&A, 597, A16
Valenti, J. A. & Piskunov, N. 1996,A&AS, 118, 595

Boletim da Sociedade Astronômica Brasileira, **30**, no. 1, 105-106

The flickering of the dwarf nova OY Carinae in quiescence

W. Schlindwein[1], R. Baptista[1], E. Wojcikiewicz[1], & T. Ribeiro[2]

[1] Universidade Federal de Santa Catarina
e-mail: wagner.schlindwein@astro.ufsc.br, raybap@gmail.com, eduardowoj@gmail.com
[2] Universidade Federal de Sergipe
e-mail: tiago.astro@gmail.com

Abstract. We observed OY Car with the SOAR Telescope between 2014 February-April while the object was in its quiescent brightness state. Flickering curves were obtained by the 'Single' (high frequency) and 'Ensemble' (mostly low frequency) methods. We applied 3D eclipse mapping tecniques to the steady light and flickering components curves to map the surface brightness/flickering distribution of the accretion disc. The results show that most of the flickering originates in the circularization radius and along the gas stream trajectory (possibly caused by inhomogeneities or post-shock turbulence in the accretion flow), suggesting that matter is being deposited (and remains "frozen") at the circularization radius of a low viscosity accretion disc.

Resumo. Nós observamos OY Car com o Telescópio SOAR entre fevereiro-abril de 2014 quando o objeto estava no seu estado quiescente de brilho. Curvas de *flickering* foram obtidas pelos métodos 'Single' (altas frequências) e 'Ensemble' (dominado pelas baixas frequências). Aplicamos a técnica de mapeamento por eclipse 3D nas curvas de luz estacionária e da componente *flickering* para mapear a distribuição superficial de brilho/*flickering* do disco de acréscimo. Os resultados mostram que a maior parte do *flickering* se origina no raio de circularização e ao longo da trajetória do jorro de matéria (possivelmente causado por inomogeneidade ou turbulência pós-choque no jorro de acréscimo), sugerindo que a matéria está sendo depositada (e permanece "congelada") no raio de circularização de um disco de acréscimo de baixa viscosidade.

Keywords. Stars: dwarf novae – binaries: eclipsing – novae, cataclysmic variables

1. Introduction

OY Carinae is a short period dwarf nova ($P_{orb} \simeq 91$ min) of the SU UMa type. Its light curves show deep eclipses (~ 2.5 mag), which last ~ 9 min, as well as outbursts and superoutbursts on a days-months time scale.

Two models compete for the explanation of the causes of these outbursts. The disc instability model (DIM, Lasota 2001) attributes the outbursts to a thermal-viscous instability in the disc that causes it to cyclically transition between a cold, low viscosity state ($\alpha \sim 0.01$, quiescence) and a hot, high viscosity state ($\alpha \sim 0.1$, outburst). On the other hand, the mass transfer instability model (MTIM, Bath 1972) attributes the outbursts to the response of a disc with constant (and high) viscosity to sudden increases in the mass transfer rate from the secondary.

Flickering is an intrinsic brightness variation at time scales from seconds to tens of minutes seen in light curves of dwarf novae and all objects in which accretion occur (Warner 1995; Baptista & Bortoletto 2004, and their references). In dwarf novae, flickering may originate in (i) the region of the disc-stream impact (possibly caused by instability in the mass transfer or post-shock turbulence) (Warner & Nather 1971; Shu 1976), (ii) the innermost disc regions (possibly generated by unstable accetion onto the white dwarf or post-shock turbulence in the boundary layer)(Elsworth & James 1982; Bruch 1992), and (iii) the accretion disc itself (probably a consequence of magneto-hydrodynamic turbulence or magnetic reconnection events in the atmosphere of the disc) (Geertsema & Achterberg 1992; Kawaguchi et al. 2000; Baptista & Bortoletto 2004).

2. Analysis and results

OY Car was observed with SOI/SOAR in 2014 February-April when it was in the quiescent brightness state. The data cover 23 binary orbits. Individual light curves present $\sim 30\%$ variations in brightness and corresponding changes in the morphology of the orbital hump and eclipse that lead us to separate them into two distinct (high- and low-) brightness states. Flickering curves were obtained by the 'Single' (high frequency, Bruch 2000) and 'Ensemble' (mostly low frequency, Horne & Stiening 1985) methods. We used 3D eclipse mapping techniques to obtain the disc + edge brightness distributions of the steady light and the flickering components (e.g., Saito & Baptista 2016; Baptista et al. 2016). The results are shown in Fig. 1.

The steady light map of the low-state is dominated by contributions from the compact white dwarf and bright spot at disc rim, with very low disc emission. In the high-state map the accretion disc is brighter and larger, and the bright spot is fainter, possibly as a consequence of a larger mass transfer rate. Flickering maps of the low- and high-state are similar, with a central source and a bright spot component plus enhanced emission at the circularization radius, but the intensities are larger in the high-state. There is no clear disc flickering component, suggesting a low viscosity accretion disc (see, e.g., Baptista et al. 2016). The bright spot flickering is of low frequency, whereas the accretion disc has both high and low frequency flickering components.

3. Conclusion

Our study reveals that the flickering amplitude scales with brightness level. The bright spot flickering is of low frequency, whereas in the accretion disc we have flickering of both high and low frequencies. While there is almost no evidence of gas stream emission in the low-state steady light, this component appears clearly in the correspond flickering map, suggesting that the emission of this source is almost entirely in the form of flickering. The bright spot flickering has a relative amplitude of $\sim 20\%$. Most of the flickering originates in the circularization

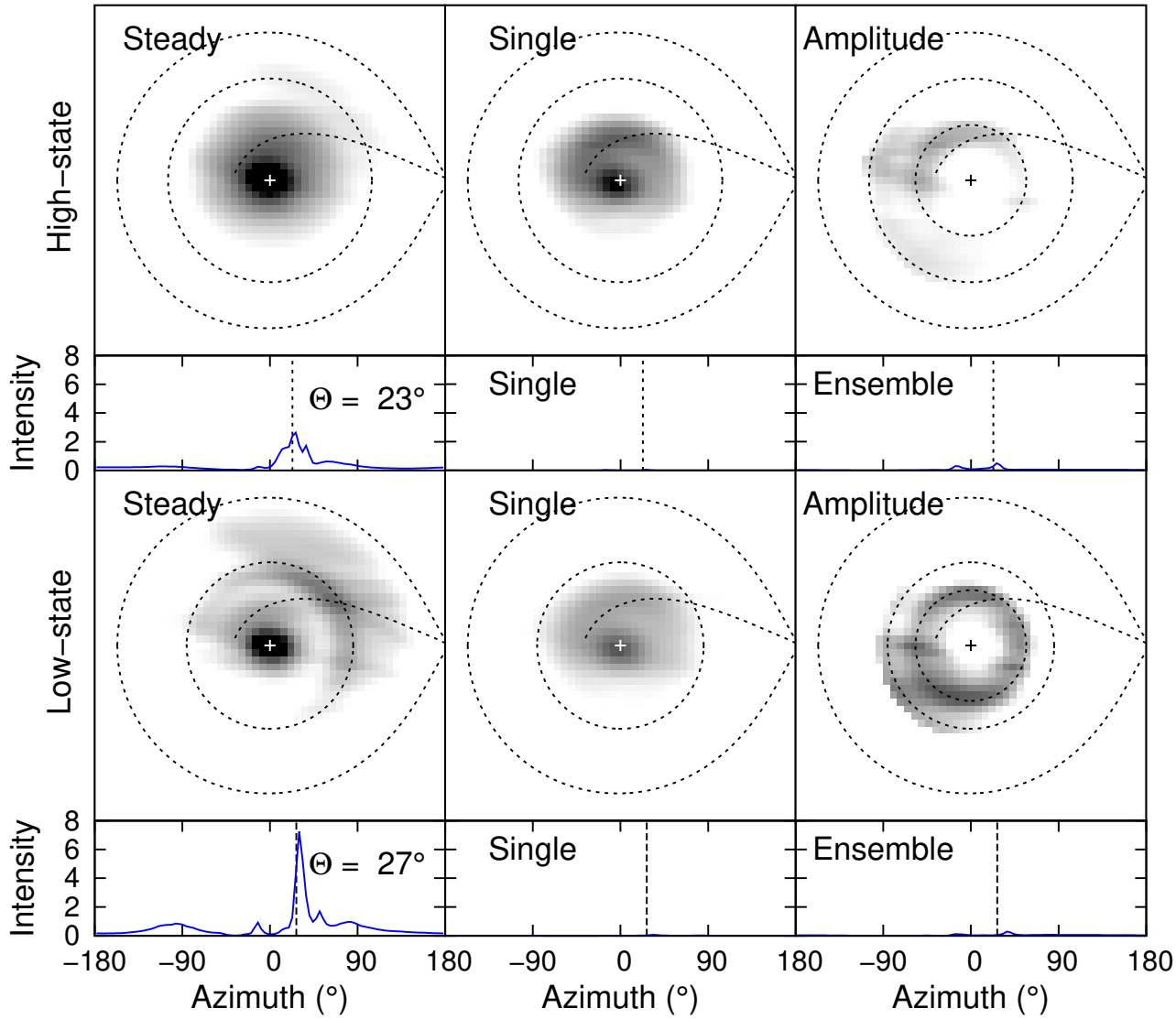

Figure 1. *Left-hand panels:* Steady light eclipse maps of the high- (top) and low-states (buttom) in logarithmic grayscale. Dashed lines shown the Roche lobe, the radius of the accretion disc, and the ballistic gas stream trajectory. Inset panels show the brightness distribution of the disc rim. The dotted line indicates the azimuthal position of the bright spot from the intersection of the ballistic gas stream trajectory with the disc rim. *Center panels:* Single flickering eclipse maps in logarithmic grayscale, and corresponding distribuition of the disc rim. *Right-hand panels:* Relative amplitude of the Single flickering with respect to the steady light in logarithmic grayscale, and Ensemble flickering distribuitions of the disc rim. An additional dashed line depicts the circularization radius.

radius and along the gas stream trajectory (possibly caused by inhomogeneities or post-shock turbulence in the accretion flow), suggesting that matter is being deposited (and remains "frozen") at the circularization radius of a low viscosity accretion disc.

Acknowledgements. We thank CNPq and CAPES for financial support through scholarships.

References

Baptista, R., & Bortoletto, A. 2004, AJ, 128, 411
Baptista, R., Borges, B. W., & Oliveira, A. S. 2016, MNRAS, 463, 3799
Bath, G. T. 1972, ApJ, 173, 121
Bruch, A. 1992, A&A, 266, 237
Bruch, A. 2000, A&A, 359, 998
Elsworth, Y. P., & James, J. F. 1982, MNRAS, 198, 889
Geertsema, G. T., & Achterberg, A. 1992, A&A, 255, 427
Horne, K., & Stiening, R. F. 1985, MNRAS, 216, 933
Kawaguchi, T., Mineshige, S., Machida, M., Matsumoto, R., & Shibata, K. 2000, PASJ, 52, L1
Lasota, J.-P. 2001, New A Rev., 45, 449
Saito, R. K., & Baptista, R. 2016, MNRAS, 457, 198
Shu, F. H. 1976, Structure and Evolution of Close Binary Systems, 73, 253
Warner, B., & Nather, R. E. 1971, MNRAS, 152, 219
Warner, B. 1995, Cataclysmic Variable Stars, Cambridge Astrophysics Series, 28

Boletim da Sociedade Astronômica Brasileira, **30**, no. 1, 107-108

Spectropolarimetry of AM Herculis with ESPaDOnS/CFHT

Yasmin Matos Amado[1], Cláudia Vilega Rodrigues[1], Eder Martioli[2], Antonio Pereyra[3], Karleyne M. G. Silva[4]

[1] Instituto Nacional de Pesquisas Espaciais - INPE e-mail: yasmin.amado@inpe.br
[2] Laboratório Nacional de Astrofísica - LNA
[3] Instituto Geofísico del Perú, Área Astronomía
[4] Gemini Observatory

Abstract. We present preliminary results on spectropolarimetry of AM Herculis using ESPaDOnS/CFHT. AM Her spectra presents variations of the emission lines along the orbital cycle. The polarimetric spectra of AM Her show continuum circular polarization up to 9% in the continuum and depolarization effect in the emission lines. Polarization measurements from a unpolarized standard star remain very close to 0% with errors within ±0.1%, showing that the instrumental polarization the instrument is very low and does not prevent measurements of the continuum polarization.

Resumo. Apresentamos os resultados preliminares de espectropolarimetria de AM Herculis e de uma estrela padrão utilizando o instrumento ESPaDOnS/CFHT. Os espectros de AM Her mostram variações das linhas de emissão ao longo do ciclo orbital. Seu espectro polarimétrico mostra depolarização nas linhas de emissão e polarização circular no contínuo de até 9%. As medidas de polarização da estrela padrão são muito próximas de 0% com erros dentro de 0,1%, mostrando que a polarização instrumental de ESPaDOnS/CFHT é muito pequena e não impede medidas de polarização no contínuo.

Keywords. Cataclysmic variables – Polarimetry

1. Introduction

Cataclysmic variables (CVs) with synchronized white dwarfs and harboring high magnetic field are called *polars*. In this type of CV, the highly magnetized white dwarf (primary) accretes material from its Roche lobe filling main sequence companion (secondary) through the inner Lagrangian point. The transferred material flows first through a stream and then is channeled via the magnetic field lines of the primary, creating an accretion column. Polarization variability is a usual characteristic in polars.

AM Her is the prototype of the polars. It has a 3.094 h orbital period (Dai et al., 2013) and a magnetic field of 14.5 MG (Bailey et al., 1991). We present flux and polarimetry spectra of AM Her, along with its radial velocity determined by the Hα line. Furthermore, results demonstrating that ESPaDOnS can measure polarimetry by comparing observations of AM Her and a unpolarized star.

2. Data and Preliminary Results

Data were acquired on 2015 August 28, using ESPaDOnS/CFHT, located on the summit of Mauna Kea in Hawaii. They consist of 16 flux spectra of AM Her and 12 of HD 202573, a null-polarization standard star. We used the OPERA[1] pipeline to reduce the data. Each polarimetric spectrum is calculated from the combination of four flux spectra.

2.1. Flux Spectra

The 16 spectra of AM Her were obtained during a complete orbital cycle. The average spectrum is shown in Figure 1. Some of the emission lines vary with orbital phase, as shown in Figure 2 where the Hα line presents variable profile with at least two components.

[1] http://wiki.lna.br/wiki/espectro

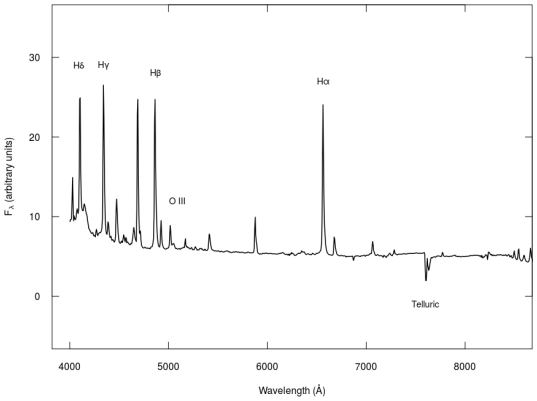

Figure 1. Average spectrum of AM Her, featuring some emission and telluric lines.

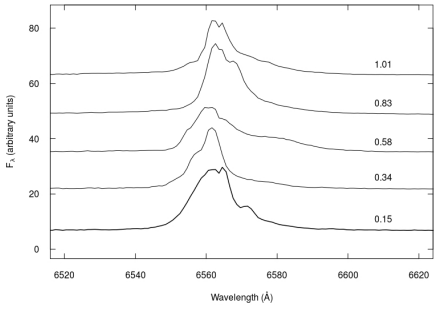

Figure 2. Hα emission line for five spectra at different orbital periods. The profile is composed of at least two variable components.

Using the Hα emission line (6563 Å), we obtained a preliminary radial velocity curve presenting a K semi-amplitude of 100 km/s (Figure 3) in good agreement with previous data (Kafka et al., 2006).

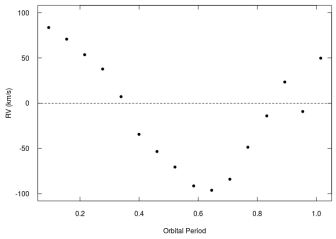

Figure 3. Radial velocity of the Hα emission line of AM Her.

2.2. Spectropolarimetry

Using a set of four flux spectra, we calculate 16 polarization spectra. Figure 4 presents four polarization spectra of AM Her, showing the variation of the continuum polarization at different orbital phases. Figure 5 shows nine polarimetric spectra around the Hα and HeI emission lines, where both present variable levels of depolarization for different orbital phases.

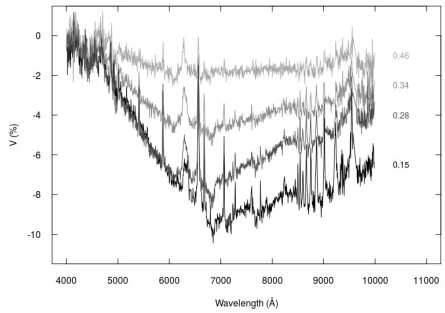

Figure 4. Polarization from AM Her in different orbital periods. Maximum polarization modulus in the continuum is 9%.

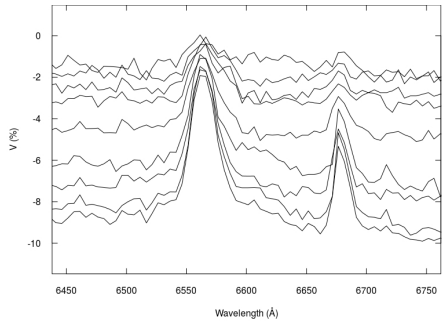

Figure 5. AM Her polarization in the spectral region containing Hα and HeI emission lines.

2.3. Standard Star

We also acquired data from a null polarization standard star, HD 202573. Figure 6 shows the spectrum of HD 202573 and a model spectrum for a G5 III star. It is striking the resemblance of the spectra, attesting the quality of the differential flux calibration of ESPaDOnS data using OPERA software.

ESPaDOnS data confirm null V polarization for HD202573 (Oudmaier et al., 2005). Figure 7 shows circular polarization spectra for both the standard star HD202573 and AM Her. The instrumental polarization of ESPaDOnS is very low, as can be seen from the polarization spectrum of the standard star, confirming the results from Pereyra et al. (2015).

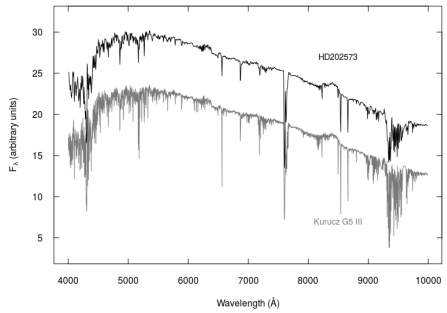

Figure 6. Black: flux spectrum of HD 202573 shifted by 10 units. Gray: a G5 III model from the Kurucz Atlas (2013)[3].

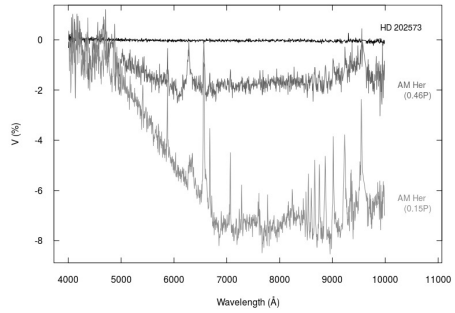

Figure 7. Circular polarization spectra for the standard star HD 202573 (black) which presents V $\approx$ 0%, in comparison with AM Her spectra on 0.15 and 0.46 of the orbital phases. These results show that the instrumental polarization is small and do not present measurements of the circular continuum polarization.

3. Conclusions

AM Her spectra show different profiles for emission lines depending on its orbital phase. The k semi-amplitude $\approx$ 100 km/s is consistent with previous results. The polarimetric spectra of AM Her show circular polarization up to 9% and depolarization in the Hα emission lines.

Furthermore, instrumental polarization of ESPaDOnS/CFHT is very low, therefore, continuum polarimetric measures are not significantly affected by the instrumental polarization.

Acknowledgements. We acknowledge FAPESP (2013/26258-4), CNPq (306701/2015-4) and CAPES. The Canada France Hawaii Telescope (CFHT) through an agreement between with the Laboratório Nacional de Astrofísica supported by the Ministério da Ciência, Tecnologia, Inovação e Comunicações.

References

Bailey, J., Ferrario, L., Wickramasinghe, D. T. 1991, MNRAS, 251, 37
Dai, Z., Qian, S., Li, L. 2013, ApJ,774, 153
Kafka, S., Honeycutt, R. K., Howell, S. B. 2006, AJ, 131, 2673
Oudmaijer, R. D., Davies, B., Vink, J. S., Drew, J. E. 2005, in Astronomical Polarimetry: Current Status and Future Directions, eds. A. Adamson, C. Aspin, C. J. Davis, & T. Fujiyoshi, ASP Conference Series, p.227
Pereyra, A., Rodrigues, C. V., Martioli, E. 2015, Measuring the continuum polarization with ESPaDOnS, A&A, 573, A133

Boletim da Sociedade Astronômica Brasileira, **30**, no. 1, 109-110

Calibration of $(B-V)_o$ with MILES stars

A. Milone[1], P. Sánchez-Blázquez[2], A. Vazdekis[3], C. Allende-Prieto[4], and A. Sansom[5]

[1] Instituto Nacional de Pesquisas Espaciais, Brazil, e-mail: andre.milone@inpe.br
[2] Universidad Autónoma de Madrid, Spain, e-mail: psanchezblazquez@gmail.com
[3] Instituto de Astrofísica de Canarias, Spain, e-mail: vazdekis@iac.es
[4] Universidad de La Laguna, Spain, e-mail: callende@iac.es
[5] University of Central, Lancashire, UK, e-mail: AESansom@uclan.ac.uk

Abstract. $(B-V)$ is one of the integrated properties of a stellar system that can help determining its light-weighted average age and metallicity. We have derived a set of empirical calibrations of the intrinsic colour $(B-V)_o$ as a function of T_{eff}, [Fe/H] and [α/Fe]. The photospheric parameters of MILES (Mid-resolution Isaac Newton Telescope Library of Empirical Spectra) stars have been homogeneously redetermined (approach to be shown in another work). The calibrations have been independently obtained for distinct spectral types (O-B, A, F-G-K and M), which have been split into up to five ranges in [Fe/H]. For M type only, the stars are divided in dwarfs and giants. $(B-V)_o$ has been directly measured by using the MILES fully calibrated stellar spectra with a typical error of 0.025 mag. In the current work, we just present the $(B-V)_o$ calibrations for F-G-K types, whose error in $(B-V)_o$ varies from 0.014 up to 0.022 mag. The next main goal is to self-consistently compute $(B-V)_o$ for semi-empirical simple stellar population models based on MILES.

Resumo. $(B-V)$ é uma das propriedades integradas de um sistema estelar que pode nos ajudar a determinar sua idade e metalicidade ponderadas em fluxo. Nós obtivemos um conjunto de calibrações empíricas para a cor intrínseca $(B-V)_o$ em função de T_{eff}, [Fe/H] and [α/Fe]. Os parâmetros fotosféricos das estrelas de MILES (Mid-resolution Isaac Newton Telescope Library of Empirical Spectra) foram redeterminados de modo homogêneo (metodologia a ser apresentada noutro trabalho). As calibrações foram derivadas de modo independente para tipos espectrais distintos (O-B, A, F-G-K and M), os quais foram divididos em até cinco intervalos de [Fe/H]. As estrelas foram separadas em anãs e gigantes para apenas o tipo M. $(B-V)_o$ foi medida com um erro típico de 0,025 mag diretamente nos espectros estelares MILES, os quais são inteiramente calibrados. No presente trabalho, nós somente apresentamos as calibrações de $(B-V)_o$ para os tipos F-G-K, cujo erro em $(B-V)_o$ varia desde 0,014 a 0,022 mag. O objetivo principal seguinte será calcular $(B-V)_o$ de modo autoconsistente para modelos semiempíricos de populações estelares simples com uso de MILES.

Keywords. catalogs – stars: fundamental parameters – stars: abundances

1. Introduction

The age and chemical abundances of a hypothetical simple stellar population (SSP) are imprinted in its integrated spectrum and photometric colours. Even in the case of more complex stellar systems such as a galaxy, those properties, or even their luminosity-weighted averages, can be extracted through a stellar population synthesis method. In fact, $(B-V)_o$ increases with mean age as well as with mean metallicity of the stellar component. here is also a dependence of this colour on the timescale of star formation history, because it is closely related to the mean age.

The $(B-V)_o$ integrated colour of semi-empirical SSP models can be computed from $(B-V)_o$ of all stellar evolutive stages defined over the isochrone of a given age and chemical composition ([M/H], [Fe/H], [α/Fe]). $(B-V)_o$ of each stage can be expressed as a function of the photospheric parameters T_{eff}, [Fe/H] and [α/Fe] through empirical calibrations. The precision of SSP model colour is, in fact, dominated by the calibration error acquired for the brightest stages in B and V bands. This self-consistent procedure aims to minimize the errors in the derivation of $(B-V)_o$ for a large variety of semi-empirical SSP models. This modelling of $(B-V)_o$ for SSPs will be useful to help deriving age, star formation history and metallicity of galaxies, when included in a full evolutionary stellar population synthesis.

2. Multi-parametric calibration of $(B-V)_o$

$(B-V)_o$ of MILES stars have been directly measured on the MILES spectra by applying the Johnson & Morgan (1953) filter transmissions (the Revised Yerkes Atlas System of Spectral Classification, MK) and a spectrophotometric calibration to Vega such that B=V=0.03 mag (Castelli & Kurucz 1994). The average systematic error of $(B-V)_o$ is about 0.025 mag when compared with different samples with stars in common (Sánchez-Blázquez et al. 2006).

Also taking into account $[M/H]$ of BaSTI scaled-solar and α-enhanced isochrones (Pietrinferni et al. 2004, 2006), we have divided the MILES stars into T_{eff} and [Fe/H] intervals.

T_{eff} ranges nearly resemble spectral types: $11000 \leq T_{eff} < 3600$ K (O-B types), $7000 \leq T_{eff} < 11000$ K (A type), $4750 \leq T_{eff} < 7000$ K (F-G-K types), and $3000 \leq T_{eff} < 4750$ K (M type). Only M type is split in dwarfs (log $g \geq 3.0$) and giants (log $g < 3.0$). Only F-G-K types have five [Fe/H] ranges: [Fe/H] < -1.0 (metal poor), $-1.0 \leq$ [Fe/H] < -0.2 (intermediate metal poor), $-0.2 \leq$ [Fe/H] $< +0.2$ (solar metallicity), $+0.2 \leq$ [Fe/H] $< +0.6$ (intermediate metal rich), and [Fe/H] $\geq +0.6$ (metal rich). O-B stars are not split in [Fe/H], A stars and M giants have both two [Fe/H] ranges ([Fe/H] < -0.2 and [Fe/H] ≤ -0.2), and M dwarfs with different [Fe/H] are dealt together.

T_{eff}, [Fe/H], log g, V_{micro} and [α/Fe] have been homogeneously determined through a full spectrum analysis of the MILES spectra ($\lambda\lambda$3544.1–7406.9 Å), whose details will be de-

scribed in an specific paper. We have just adopted the original MILES library (Sánchez-Blázquez et al. 2006).

$$(B-V)_o = a + b.\theta_{\rm eff} + c.\theta_{\rm eff}^2 + d.[{\rm Fe/H}] + e.[{\rm Fe/H}]^2 + f.[\alpha/{\rm Fe}] + d.[\alpha/{\rm Fe}]^2. \quad (1)$$

We have applied polynomial fits to calibrate $(B-V)_o$ as a function of $T_{\rm eff}$, [Fe/H] and [α/Fe], nearly similar to Alonso, Arribas & Martinez-Roger (1996). Eq. 1 shows the adopted multi-parametric 2$^{\rm nd}$ order polynomial function, where $\theta_{\rm eff}$ = 5040 K/$T_{\rm eff}$ (K). In order to derive the final dependence of $(B-V)_o$ with the terms of Eq. 1, we have added each term one by one based on the analysis of fit residuals as a function of each additional parameter. The base polynomial fit is $a+b.\theta_{\rm eff}+c.\theta_{\rm eff}^2$, and the inclusion of other terms was done following the sequence: [Fe/H], [Fe/H]^2, [α/Fe] and [α/Fe]^2. Each term is only included if the fit is improved based on the resulting *rms* and χ^2 and the error of the correspondent fitting parameter is smaller than its value. Alonso et al. (1996) derived for a sample of F-G-K dwarfs a *rms* of 0.039 mag through a similar multi-parametric fit by including the cross term $\theta_{\rm eff}$.[Fe/H], but without adding any dependence on [α/Fe] and without splitting the stars in ranges of [Fe/H].

We will also consider an additional sample of 205 stars, whose spectra were collected with the 2.5 m Isaac Newton Telescope (Observatorio del Roque de Los Muchachos, La Palma, Spain) in 2011, employing the same instrumental setup as MILES.

3. Results for F-G-K types

The best multi-parametric polynomial fits for F, G and K types ($4750 \le T_{\rm eff} < 7000$ K) and their five metallicity ranges have been derived (see Fig. 1). We have reached good agreement of our $(B-V)_o$ calibration for a sample of MILES F-G-K dwarfs against that calibration by Alonso et al. (1996), considering their same multi-parametric function with six terms and stellar parameters ranges. The derived fit rms are: 0.021 mag for the metal poor stars ($\chi^2 = 0.9815$), 0.015 mag for the intermediate metal poor stars ($\chi^2 = 0.9928$), 0.014 mag for the solar metallicity stars ($\chi^2 = 0.9943$), 0.019 mag for the intermediate metal rich stars ($\chi^2 = 0.9856$), and 0.022 mag for the metal rich stars ($\chi^2 = 0.9807$).

We have found a dependence of $(B-V)_o$ on [α/Fe] for intermediate metal poor, solar metallicity and intermediate metal rich stars. For instance, the resulting calibration *rms* for the solar metallicity stars, having just included a single linear term of [Fe/H], decreases from 0.017 mag down to 0.014 mag after adding both terms [α/Fe] and [α/Fe]^2. The relative errors of [α/Fe] fitting terms parameters are, respectively, about 12.5% and 20% in this case.

4. Summary

Our calibrations of $(B-V)_o$ for F-G-K types are quite reliable and provide an acceptable precision to compute this colour for a wide set of SSP models. We will present in a further work the $(B-V)_o$ calibrations for other spectral types as well as the whole set of $T_{\rm eff}$ calibrations as a function of $(B-V)_o$, [Fe/H] and [α/Fe] (already derived for F-G-K types only).

Acknowledgements. A. Milone thanks the Brazilian foundation CNPq/MCTIC (grant number 309562/2015-5). A. Vazdekis thanks the Spanish Ministry of Economy and Competitiveness (MINECO grant process AYA2016-77237-C3-1-P).

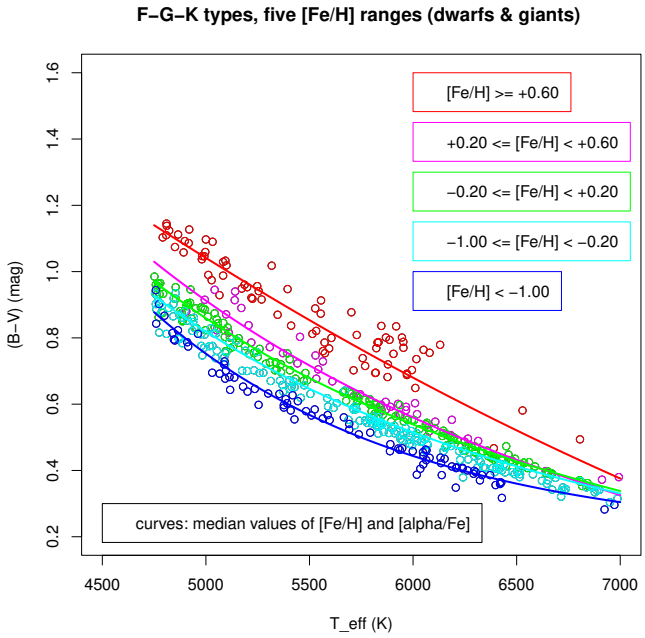

Figure 1. $(B-V)_o$ as a function of $T_{\rm eff}$ for F-G-K types over five [Fe/H] ranges. The colourful curves represent polynomial fits assuming median values of [Fe/H] and [α/Fe] of each subsample.

References

Alonso, A., Arribas, S., & Martinez-Roger, C. 1996, A&A, 313, 873
Castelli, F., & Kurucz, R. L. 1994, A&A, 281, 817
Johnson, H. L., & Morgan, W. W. 1953, ApJ, 117, 313
Pietrinferni, A., Cassisi, S., Salaris, M., & Castelli, F. 2004, ApJ, 612, 168
Pietrinferni, A., Cassisi, S., Salaris, M., & Castelli, F. 2006, ApJ, 642, 797
Sánchez-Blázquez, P., Peletier, R. F., Jimenez-Vicente, J., Cardiel, N., Cenarro, A. J., Falcón-Barroso, J., Gorgas, J., Selam, S., & Vazdekis, A. 2006, MNRAS, 371, 703

Boletim da Sociedade Astronômica Brasileira, **30**, no. 1, 111-112

Accretion processes in Herbig Ae/Be stars: the case of HD 261941

T. Moura, A. P. Sousa, & S. H. P. Alencar

[1] Universidade Federal de Minas Gerais. e-mail: tatiana@fisica.ufmg.br

Abstract. Young stars are born with circumstellar disks and the star-disk interaction is an important factor to understand the early evolution of such systems. The morphology and variability of emission lines that are formed in the circumstellar environment of young stellar objects can be used as tools to understand the physics of accretion/ejection processes. These processes are not well described in intermediate mass young stellar systems, called Herbig Ae/Be stars. Our goal is to identify signatures of magnetospheric accretion and ejection in the spectra of the Herbig Ae star HD 261941. This star is member of the young (∼ 3 Myr) open cluster NGC 2264 and was observed with the high resolution (R ∼ 47000) UVES/ESO spectrograph (4800 – 6800 Å) over 20 non-consecutive nights. We determined stellar parameters comparing the average observed spectra with synthetic spectra. We also analyzed Hα, Hβ, He I λ5875.7 emission line variability and modelled the Hα mean line profile, using the MHD model described by Lima et al. (2010). The disk-wind presents a strong contribution to the Hα profile in this star and we found signatures of magnetospheric accretion in the observed spectra.

Resumo. Estrelas jovens formam-se com discos circunstelares e a interação estrela-disco é um fator importante para entendermos a evolução desses sistemas. A morfologia e a variabilidade das linhas de emissão que se formam no ambiente circunstelar de objetos estelares jovens podem ser usadas como ferramentas para compreender a física dos processos de acreção/ejeção. Esses processos não são bem descritos em sistemas estelares jovens de massa intermediária, denominados estrelas Ae/Be de Herbig. Nosso objetivo é identificar sinais de acreção magnetosférica e ejeções na estrela Ae de Herbig HD 261941. Esta estrela é membro do aglomerado aberto jovem (∼ 3 Myr) NGC 2264 e foi observada com o espectrógrafo UVES/ESO de alta resolução (R ∼ 47000; 4800 – 6800 Å) por 20 noites não consecutivas. Determinamos os parâmetros estelares comparando os espectros observados médios com espectros sintéticos. Analisamos a variabilidade das linhas de emissão Hα, Hβ, He I λ 5875.7 e modelamos o perfil médio da linha Hα, usando o modelo MHD descrito por Lima et al. (2010). O vento de disco apresenta uma forte contribuição para o perfil Hα nesta estrela e encontramos características de acreção magnetosférica nos perfis observados.

Keywords. Herbig Ae/Be stars – accretion disk – magnetospheric accretion – disk winds – line profiles

1. Introduction

Herbig Ae/Be (HAeBe) stars are optically visible Pre-Main-Sequence (PMS) stars with masses ranging from 2 e 10 $M_\odot$. They present F2 to B0 spectral types, which correspond to effetive temperature between 7000-30000 K (Pogodin et al. 2015). HAeBe stars show both characteristics of high-mass systems (Testi et al. 1999), like the absence of a convective envelope, as well as characteristics of young low mass stars (Vink et al. 2002), such as emission lines with similar features. One of the main open issues in star formation is the difference between the formation mechanisms of low and high mass stars. Although it is well established that low mass stars accrete matter from the circumstellar disk through a magnetic field, the mechanism that leads to this accretion in stars of larger masses is still uncertain. The study of HAeBe stars is extremely important for the understanding of these mechanisms, since it is a bridge between the star formation of low and high mass stars. Despite the absence of convective envelopes in the HAeBe stars, a globally organized magnetic field has been measured in some of these systems (Hubrig et al. 2013). The magnetospheric accretion model should therefore be applicable to some HAeBe stars.

2. Circumstellar lines

We analyze spectra of the HD 261941 star that was observed during 20 nights between 04 December 2011 e 24 February 2012 with the UVES (VLT/ESO) spectrograph in the spectral range 4800-6800 Å with resolution of ∼ 47000.

Table 1. Parameters of the Mon-000631 system with their respective determination method.

Parameters	Value	Standard deviation	Methods/Code
T_{eff} (K)	8500	119	SME
log g	3.5	0.2	SME
$[Fe/H]$	0.0	0.07	SME
v_{rad} (km/s)	22	0.7	SME
$v \sin i$ (km/s)	120	2	BinMag4
Period (day)	3.3	1.7	width 10% Hα
$\dot{M}_{ac}$ ($M_\odot$/yr)	5.3 x 10^{-6}	2.2 x 10^{-6}	Flux Hα
mass ($M_\odot$)	2.03	0.04	ATON 2.0
Radius ($R_\odot$)	4.4	1.2	ATON 2.0
Age (Myr)	5.99	0.17	ATON 2.0

Synthetic photospheric spectra were computed using the SME (Valenti el al. 1998) and BinMag4 (Kochukhov 2007) codes, with the ATLAS9 atmosphere models (Kurucz 1993) and a spectral line list from the *Vienna Atomic Line Database* (*VALD*) (Kupka el al. 1999) to determine stellar parameters.

The best fit photospheric synthetic spectrum was subtracted from the observed spectra to obtain the circumstellar spectral contribution in this system. In Table 1 we list the stellar parameters determined from the spectral line synthesis and the mass accretion rate, obtained from modeling of the Hα circumstellar contribution.

We notice a strong variability in the intensity and morphology of the Hα, Hβ and He I lines (Figure 2). This variability is characteristic of young stars and can be used to analyse the dynamics of the accretion and outflow processes.

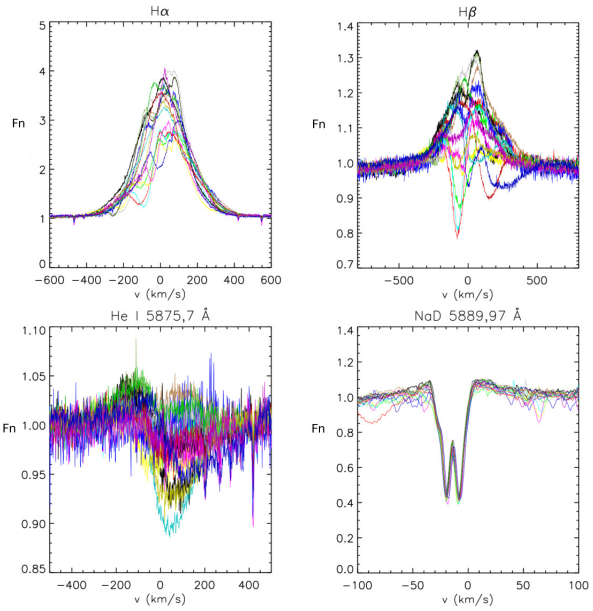

Figure 1. Circumstellar contributions of observed spectral lines. Fn represents the normalized flux.

The Hα line variability is most prominent in the blue, indicating variations due to winds (photons absorbed in regions where the gas has projected velocities on our line of sight traveling towards us). The Hβ line contains absorptions in the blue and red wings, thus indicating regions where the material is possibly being absorbed by the wind and the magnetosphere (redshifted absorptions correspond to photons absorbed in regions where the gas has projected velocities on our line of sight traveling away from us), respectively. The morphology of this line indicates that there is a possible magnetospheric accretion and outflow scenario. The He I λ5875,7 line presents a variable absorption throughout in the red wing, contributing to the magnetosphere accretion scenario.

3. Magnetospheric accretion and outflow model

The computational model used in this work was initially proposed by Hartmann et al. (1994) and complemented by Lima et al. (2010). The model allows the calculation of the Hα profile coming from an accreting magnetosphere radiatively coupled to a diskwind. Figure 3 shows results of the Hα line profile modeling and Table 2 summarizes the parameters of the best fit models.

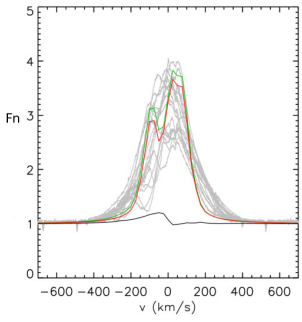

Figure 2. Computed models with only the magnetospheric accretion contribution (black), with only the diskwind contribution (red) and with both the magnetosphere and diskwind contributions (green). The parameters used in the three models are shown in Table 2. Fn represents the normalized flux.

Table 2. Parameters of the Mon-000631 system obtained from the best Hα line model: θ, lauching angle between the accretion disk and magnetic field lines; R_{do}, outer wind radius; R_{mi}, inner magnetosphere radius; R_{mo}, outer magnetosphere radius; T_{mag}, maximum magnetosphere temperature; T_{wind}, maximum disk wind temperature; and i, inclination of the system.

Parameters	Value
θ	33.42°
R_{do}	20 R_*
R_{mi}	2.0 R_*
R_{mo}	2.45 R_*
T_{mag}	7000 K
T_{wind}	7000 K
i	85°
B_* (*)	0.6 kG

(*) Dipole component of the magnetic field (B_*) was obtained from the best fits of $\dot{M}_{ac}$ e R_m ($R_m \propto [B_*^4/\dot{M}_{ac}^2]^{1/7}$; Bessolaz el al. 2008)

4. Conclusions

- The hybrid model of magneto-accretion plus disk wind can be applied to the Herbig Ae star HD 261941
- Main line formation sites: Hα - diskwind; Hβ - magnetosphere + disk wind; He I - hot spot + magnetosphere
- High mass accretion rate ($\sim$ 3,0 x 10^{-6} $M_\odot$/yr)

Acknowledgment

We thank finantial support from CAPES, FAPEMIG and CNPq

References

Bessolaz, N., Zanni, C., Ferreira, J., Keppens, R., & Bouvier, J. 2008, A&A, 478, 155
Hartmann, L., Hewett, R., & Calvet, N. 1994, APJ, 426, 669
Hubrig, S., Ilyin, I., Scholler, M., & Lo Curto, G. 2013, Astronomische Nachrichten, 334, 1093
Kochukhov. 2007, Synth3 (Phtsics of Magnetic Stars)
Kupka, F., Piskunov, N., Ryabchikona, T. A., Stempels, H. C., & Weiss, W. W. 1999, A&AS, 138, 119
Kurucz, R. 1993, ATLAS9 Stellar atmosphere Programs, 1993
Lima, G. H. R. A., Alencar, S. H. P., Calvet, N., Hartmann, L., & Muzerolle, J. 2010, A&A, 522, A104+
Pogodin, M. A., Cahuasqui, J. A., Drake, N. A., et al. 2015, in Astronomical Society of the Pacific Conference Series, Vol. 494, Physics and Evolution of Magnectic and Related Stars, ed. Y. Y. Balega, I. I. Romanyuk, & D. O. Kudryavtsev, 175
Romanova, M. M. & Owocki, S. P. 2015, SSR, 191, 339
Testi, L., Palla, F., & Natta, A. 1999, A&A, 342, 515
Valenti, J. A., Piskunov, N., & Johns-Krull, C. M. 1998, ApJ, 498, 851
Vink, J. S., Drew, J. E., Harries, T. J., & Oudmaijer, R. D. 2002, MNRAS, 337, 356

Boletim da Sociedade Astronômica Brasileira, **30**, no. 1, 113-114

The Be star α Col: a laboratory for the physics of circunstellar disks

A. C. Rubio[1], A. C. Carciofi[1], B. M. Mota[1], R. G. Vieira[1]

[1] Instituto de Astronomia, Geofísica e Ciências Atmosféricas (IAG/USP), e-mail: amanda.rubio@usp.br

Abstract. Be stars have been the target of several multi-technique and multi-spectral modelling works in the past years, in the framework of the Viscous Decretion Disk model (VDD). Although those results are very satisfying, there is a clear need to make multi-technique modelling, which fits one observable at a time, more robust. In this work we show the first results for a simultaneous fitting of all disk and stellar observables to a grid of HDUST models, using a Monte Carlo Markov Chain method, for the stable Be star α Col.

Resumo. Estrelas Be foram alvo de diversos trabalhos de modelagem multi-técnicas e multi-espectrais nos últimos anos, dentro do contexto do modelo do Disco de Decréscimo Viscoso (VDD). Apesar de satisfatórios, há uma clara necessidade de tornar a modelage multi-tecnica, que foca em um observável por vez, mais robusta. Nesse trabalho apresentamos os primeiros resultados para um ajuste simultâneo de observáveis tanto estelar quanto do disco à uma grade de modelos HDUST, utilizando um método de Monte Carlo em Cadeias de Markov, para a estrela Be estável α Col.

Keywords. Stars: individual: α Col – Stars: emission-line, Be

1. Introduction

Be stars are fast rotating, main sequence B stars that present a Keplerian decretion disk that causes excess emission of neutral hydrogen, among other changes in the spectrum. The model that best describes the physics of Be disks is the Viscous Decretion Disk model (VDD). In the VDD model, some mechanism accelerates stellar material so that it leaves the star and enters orbit. From this point onwards, turbulent viscosity redistributes the material, building the Be disk (see Rivinius et al. 2013 for a recent review on Be stars and the VDD). In order to test the VDD, multi-technique and multi-spectral modelling of stable Be stars have been made in the past decade, all with positive results (e.g., ζ Tauri – Carciofi et al. 2009, 48 Lib – Silaj et al. 2016 and β CMi – Klement et al. 2015). These works model stellar and disk parameters separately for each type of observation. In this work, we take the test one step further, simultaneously fitting all observables to a grid of HDUST models, using a Monte Carlo Markov Chain method. We present here our results for the stable Be star α Col.

2. Methodology

Analysis of polarimetric data indicate that α Col's disk has been relatively stable for the past couple of decades, a feature quite rare in Be stars, but that greatly simplifies the modelling procedure. An extensive data collection was the first step in the process. Next, we calculated a grid of models using the HDUST radiative transfer code (see Carciofi & Bjorkman 2006 and Carciofi & Bjorkman 2008). The preliminary grid consisted of 324 models, and the newest expanded grid consists of 1296 models, varying the parameters according to table 1. The stellar parameters varied were the mass, the oblatness and the fraction of hydrogen present in the nucleus, which corresponds to the time of life over the Main Sequence; the disk parameters were the base number density n_0, the radial density exponent n and the size of the disk, R_d. With the grid in hands, the analysis itself could begin.

Table 1. Disk and stellar parameters used to create the grid.

Stellar parameters	Values
$M[M_\odot]$	4.4, 4.9, 5, 6
R_{eq}/R_{pole}	1.07,1.33,1.51
H fraction	0.3,0.5,0.6
Disk parameters	**Values**
$\log n_0\ [cm^{-3}]$	12, 12.5, 13
n	2.0, 2.5, 3.0
$R_d\ [R_{eq}]$	10, 20, 30, 40

3. Markov chain Monte Carlo method

Our ultimate goal is to infer all disk and stellar parameters by finding the model that best fits all types of observations, but this cannot be accomplished in a straightforward way right from the start. The most reasonable method is to analyse a single observable first and add others continuously until the end goal is reached. We therefore began by studying the behaviour of the calculated grid of models with our observational SED data, from 0.115 μm to 6.3 cm. The great difficulty lies in determining how well the models fit the observational data and from that analysis, infer the most likely and best fit Be star parameters. Nowadays, the most practical and intelligent way to obtain probability density functions and correlations between many parameters in a sample with large dimensions is to use Bayesian inference methods, such as the Markov chain Monte Carlo (MCMC). To this end, we use the Python implementation of an MCMC method, the `emcee` code (Foreman-Mackey et al. 2013). The return of the `emcee` code is a corner plot where the PDFs of each parameter is presented on the main diagonal, while the intersection between a column and a row parameter gives their respective correlation map.

4. Results

We present here the resulting corner plot for the fitting of a grid of HDUST models to our observational SED data in the UV re-

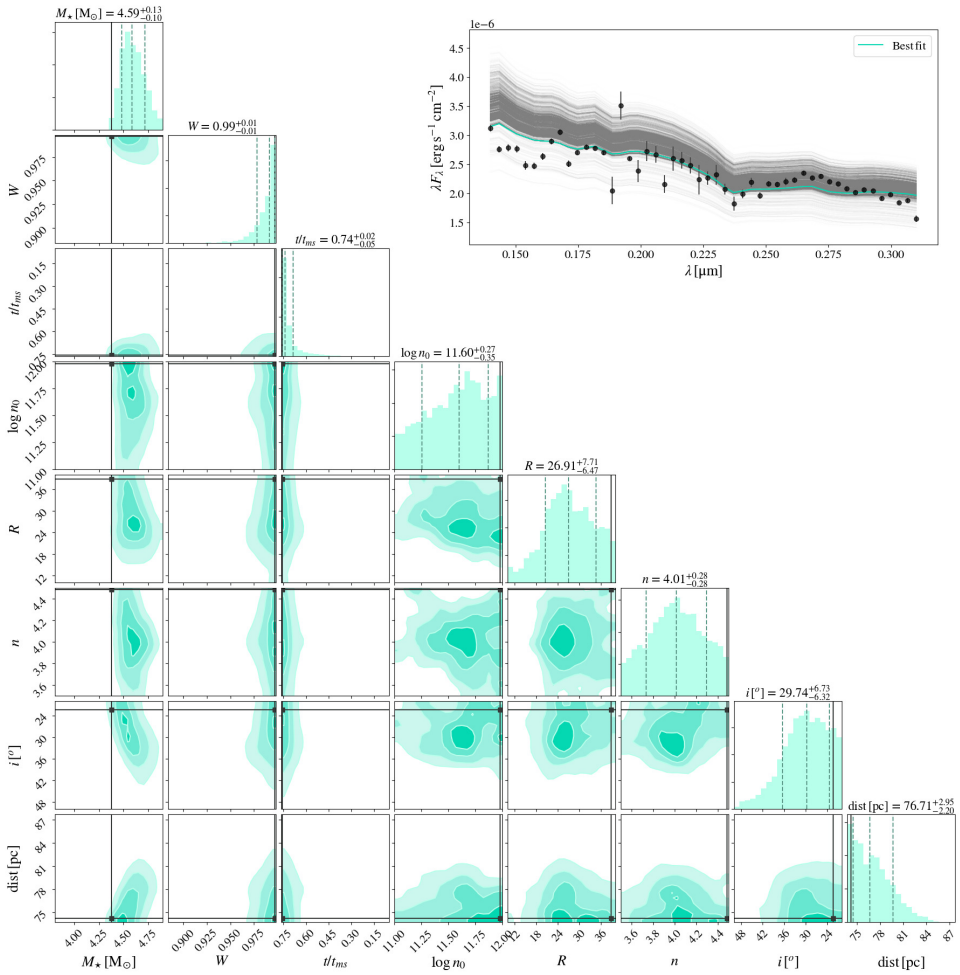

Figure 1. Corner plot for the UV part of the SED, from from 0.115 to 0.3 μm. The plot on the upper right is the observational IUE data (black dots) and a fraction of our models; the darker the line, the smaller the associated χ^2 of the fit to the data.

gion (from 0.115 to 0.3 μm), in Fig. 1. The sharpness of the PDFs are indicative of a good convergence of the results. Besides the parameters varied to build the grid, we also consider the inclination angle of the disk i and the distance of the Be star d in parsecs. In this case, since the grid is still under construction, we are probing a very small part of the SED, and most of the excess in the UV region comes from the central star, not the disk ((Vieira et al. 2015)). Therefore, the disk parameters n, n_0 and R are not as well defined as the stellar parameters, and neither is the disk inclination i. We can see in the PDF for t/t_{ms} that smaller values of H fraction in the nucleus need to be included in the grid, since the result forces the PDF very clearly towards the left. That is most likely forcing the distance parameter to smaller distances as well, to compensate the effect. It should be noted that result shown in Fig. 1 is not very well sampled yet, since the MCMC calculations take much longer once the number of steps and walkers are increased (see Foreman-Mackey et al. 2013 for more information on how these values impact results). More MCMC calculations and further grid expansion are already under way.

5. Final remarks

Multi-technique analysis of Be stars have been done in the past, always analysing each observable separately. Using Bayesian statistics, a grid of HDUST radiative transfer models, and taking advantage of years of observations by various missions, we intend to take the analysis further, by simultaneously probing both disk and stellar parameters using all observables for the stable Be star α Col. Inferring all parameters at once would be an even greater test for the VDD model and would positively cement it as the definitive model for describing the physics of a Be star disk. Preliminary results show the multi-technique analysis potential, being able to define well stellar parameters from just the UV region of the SED. Expansion of the grid to smaller values of H fraction is under way, as well as to the other regions of the SED and polarimetry. Better sampled MCMC calculations are also being worked on.

Acknowledgements. ACR acknowledges support from FAPESP grant 2017/08001-7.

References

Carciofi, A. C. & Bjorkman, J. E. 2006, ApJ, 639, 1081
Carciofi, A. C. & Bjorkman, J. E. 2008, ApJ, 684, 1374
Carciofi, A. C., Okazaki, A. T., Le Bouquin, J.-B., et al. 2009, A&A, 504, 915
Foreman-Mackey, D., Hogg, D. W., Lang, D., & Goodman, J. 2013, PASP, 125, 306
Klement, R., Carciofi, A. C., Rivinius, T., et al. 2015, A&A, 584, A85
Rivinius, T., Carciofi, A. C., & Martayan, C. 2013, A&A Rev., 21, 69
Silaj, J., Jones, C. E., Carciofi, A. C., et al. 2016, ApJ, 826, 81
Vieira, R. G., Carciofi, A. C., & Bjorkman, J. E. 2015, MNRAS, 454, 2107

Boletim da Sociedade Astronômica Brasileira, **30**, no. 1, 115-116

Study of variability and periodicity in white dwarf stars

Larissa A. Amaral, Alejandra D. Romero, & S. O. Kepler

[1] Departamento de Astronomia, Instituto de Física, UFRGS
e-mail: antunes.amaral@ufrgs.br, alejandra.romero@ufrgs.br, kepler@if.ufrgs.br

Abstract. We studied the photometric variability in white dwarfs, through the use of the Period04 program, in the periodicity search. A new ZZ Ceti was found with three pulsation periods. In magnetic white dwarves, due to their scale of variation being unknown and the lack of photometric data, no significant period was found.

Resumo. Nós estudamos a variabilidade fotométrica em anãs brancas, a través do uso do programa Period04, na busca por periodicidade. Foi achado uma nova ZZ Ceti com três períodos de pulsação. Nas anãs brancas magnéticas, devido a sua escala de variação ser desconhecida e a falta de dados fotométricos, não foi encontrado nenhum período significativo.

Keywords. white dwarfs – stars: variables: ZZ Ceti

1. Introduction

White dwarf stars are the final evolutionary state of stars with mass lower than ∼ 10 solar masses, corresponding to at least 95% of all stars in the Milky Way. The most common class of white dwarf is the one with hydrogen atmosphere. Those stars have photometric variability due to stellar pulsation when they cool to an effective temperature of ∼ 12000 K. In these case, they are called ZZ Ceti stars. About 4% of single white dwarfs have a magnetic fields (Kepler et al. 2013). The variability can be as a result of atmospheric spots, caused by the change of energy transport in the stellar atmosphere by the magnetic field.

2. Methodology

We present the firsts results using Period04 (Lenz et al. 2005) which calculates the Fourier transform (FT) from the light curve of each star, decomposing a function of time (a signal) into the frequencies that make it up, what will show the variability of each object and, if possible, determine the rotational period.

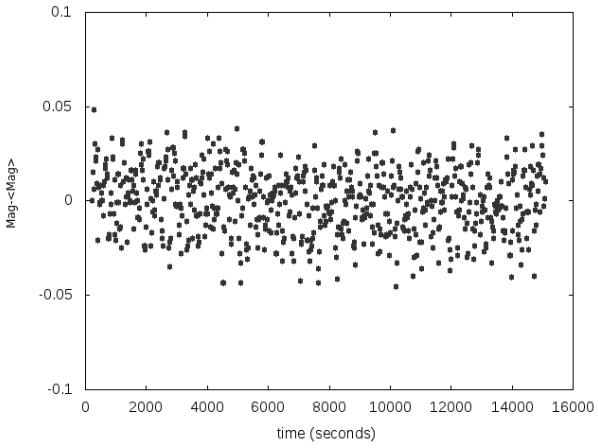

Figure 1. The light curve of the star ZZ Ceti J082804.63+094956.66, observed with SOAR telescope over 4 hours. The *x*-axis indicates time and the y-axis gives the measured magnitude minus the average magnitude <Mag>.

3. Results

3.1. J082804.63+094956.66

The light curve of the star observed with the telescope SOAR, displayed in figure 1, presents three main peaks in its Fourier transform, as well the pre-whitening process, displayed in figure 2, where the dashed line is 3 times the average value <*A*> of the amplitude of the peaks. The main peak gave us a period P_1 = (286.1 ± 0.2) s, the second peak P_2 = (196.39 ± 0.08) s and the third peak P_3 = (255.4 ± 0.3) s. That star is a new ZZ Ceti with effective temperature T_{eff} = (11560 ± 70)K and mass M = (0.73 ± 0.02)$M_\odot$.

3.2. J064532.74+280330.5

The same method used before was apply to a magnetic white dwarf. The light curve of this star, available in Mikulski Archive for Space Telescopes (MAST) from Kepler spacial mission, is shown in figure 3 and its FT in figure 4. However, in this case, we used the significance threshold as 5 times the average value <*A*> of the amplitude, because of the Kepler Satellite's rocket, when it is turned on to center the object again, causing a non-real variation in the light curve. None of the peaks correspond to a periodic variability.

4. Conclusion

A new star ZZ Ceti has been discovered with three pulsating periods. For magnetic white dwarfs, it was not possible to find pulsation variability, due to their scale of variation, that can vary from seconds to years, and of not having photometric data. We will apply the technique presented to other variable white dwarf stars observed with SOAR telescope and Observatório do Pico dos Dias (LNA) during the years 2016 and 2017, in order to determine their periodicities.

References

Kepler, S. O. et al. 2013, MNRAS, 429, 2934
Lenz P., Breger M. 2005, CoAst, 146, 53

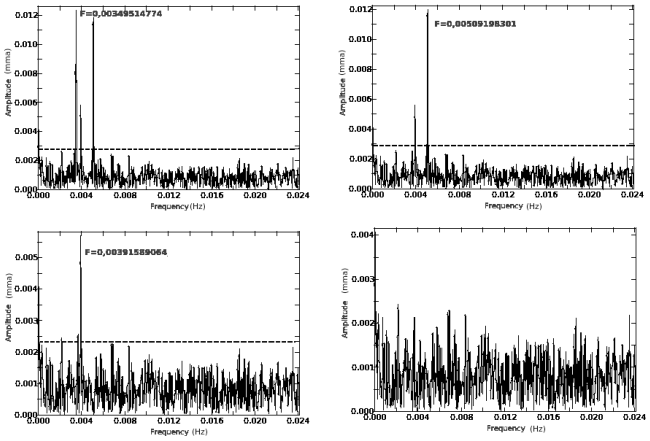

Figure 2. FT of the light curve of the star ZZ Ceti J082804.63+094956.66 with the three peaks, in decreasing amplitude order P_1 = (286.1 ± 0.2), P_2 = (196.39 ± 0.08) and P_3 = (255.4 ± 0.3) s, is shown in the top left image, as well the pre-whitening process in the others three images. The dashed line is the 3<A> significance threshold.

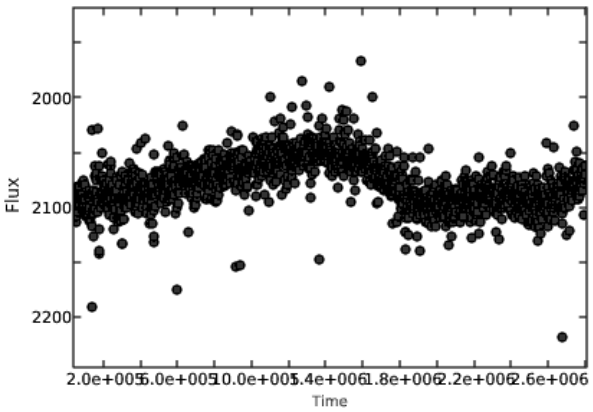

Figure 3. Light curve of magnetic white dwarf J064532.74+280330.5 available in Mikulski Archive for Space Telescopes (MAST) from Kepler spacial mission. The x-axis is time in seconds and the y-axis is the relative flux.

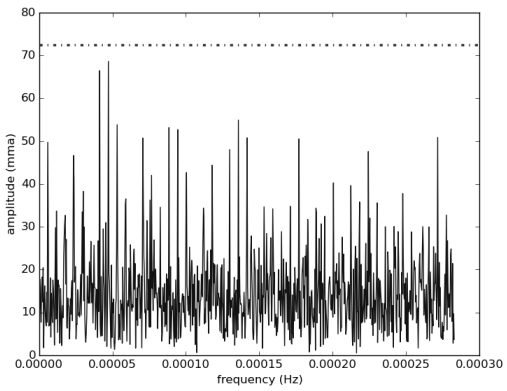

Figure 4. FT of magnetic white dwarf J064532.74+280330.5 The dashed line is the 5<A> significance threshold of the data.

Boletim da Sociedade Astronômica Brasileira, **30**, no. 1, 117-118

Photoionization models of nova V723 Cas

L. Takeda[1], M. Diaz[1], R. Campbell[2] & J. Lyke[2]

[1] Universidade de São Paulo, IAG, Departamento de Astronomia; e-mail: larissa.takeda@usp.br
[2] Keck Observatory

Abstract. We present modeling and analysis of the ejecta of nova V723 Cas based on diffraction-limited IR spectroscopic data from Keck-OSIRIS, with adaptive optics. The 3D photoionization models include the shell geometry taken from the observations and an anisotropic radiation field, composed by a spherical central source and an accretion disk. Our simulations indicate revised abundances $\log(N_{Al}/N_H) = -5.4$, $\log(N_{Ca}/N_H) = -6.4$ and $\log(N_{Si}/N_H) = -4.7$ in the shell. The total ejected mass was found as $M_{ej} = 1.1 \times 10^{-5}$ $M_\odot$ and the central source temperature and luminosity are $T = 280,000$ K and $L = 10^{38}$ erg/s.

Resumo. Nós apresentamos modelos e análises da ejeção da nova V723 Cas baseados em dados de espectroscopia no IV no limite de difração do Keck-OSIRIS, com óptica adaptativa. Os modelos de fotoionização 3D incluem a geometria do envelope, construída a partir das observações, e um campo anisotrópico de radiação, composto por uma fonte central esférica e um disco de acreção. Nossas simulações indicam os valores revisados de abundâncias $\log(N_{Al}/N_H) = -5.4$, $\log(N_{Ca}/N_H) = -6.4$ e $\log(N_{Si}/N_H) = -4.7$ no envelope. A massa total ejetada obtida é $M_{ej} = 1.1 \times 10^{-5} M_\odot$ e a temperatura e a luminosidade da fonte central são $T = 280,000$ K e $L = 10^{38}$ erg/s.

Keywords. novae, cataclysmic variables — stars: individual(V723 Cas) — accretion, accretion discs — stars: abundances

1. Introduction

V723 Cas is a classical nova, detected in 1995 (Hirosawa et al. 1995). It presented a slow magnitude decay, with $t_{3,V} = 173$ days (Ohshima et al. 1995), and the longest nuclear burning activity registered for novae. The X-rays observations suggested an extremely hot central source for this object (Ness et al. 2015), and the optical spectra indicated overabundance of neon (Iijima 2006). Along with these peculiarities, V723 Cas also presented spectral features consistent with a complex geometry shell that were later confirmed by spatially resolved spectroscopy in IR (Lyke & Campbell 2009). These observations were performed with Keck-OSIRIS near-infrared integral field spectrograph and an adaptive optics module from 2005 to 2008. Our models are mainly based on the 2008 data, when the nova was in the nebular stage.

2. Photoionization models

The Keck-OSIRIS data showed distinct shell morphologies for different emission lines, as shown in figure 1. Overall, the shell is formed by two main structures: an equatorial torus and polar nodules. For the [Si VI] 1.963μm and [Ca VIII] 2.321μm bands, the torus is more prominent, and for the [Al IX] 2.044μm, the polar emission is stronger. This anisotropy in the ionizing radiation field can be explained by the restoration of the accretion disk. Therefore, we have added a disk-shaped ionizing source to our models.

The fluxes and distances used in the models were taken from the Keck data and the temperature and luminosity of the central source were limited by the X-rays observations, with $2.8 \times 10^5 \leq T_{\rm eff} \leq 3.8 \times 10^5$ K and $5 \times 10^{36} \leq L \leq 2 \times 10^{38}$ erg/s (Ness et al. 2008). The abundances were obtained from optical (Iijima 2006) and IR spectra (Evans et al. 2003).

To perform our photoionization models, we used RAINY3D code (Moraes & Diaz 2011), which runs Cloudy (Ferland et al. 2013) as a subroutine. In RAINY3D we were able to include the complex 3D geometry of gas distribution observed in Keck data (torus + polar nodules + clumps) and the ionizing radiation field composed by both spherical and disk-shaped components.

3. Results

The 3D simulations indicate that V723 Cas central source achieved $L = 10^{38}$ erg/s and $T_{\rm eff} = 280,000$ K in 2008, higher values than the ones obtained with isotropic radiation field. These values are needed to reproduce the order of magnitude of the permitted line fluxes. Using the initial assumptions of Al, Si and Ca abundances, we could not reproduce the forbidden lines fluxes or the lines flux ratios. Therefore, we assumed that those abundances were underestimated, and we ran new models with higher values. The set of abundances that best fitted the observational fluxes are $\log(N_{Al}/N_H) = -5.4$, $\log(N_{Si}/N_H) = -4.7$ and $\log(N_{Ca}/N_H) = -6.4$. The line fluxes ratios for this model are displayed in table 1.

The resulting projection of each line emissivity is displayed in figure 2. For the H line, it is not possible to exactly compare the 2D observations to the modeled projection because of the line self-absorption in the cloud. For [Si VI] and [Ca VIII] lines, the ring and polar caps can be noticed in both observed images and model projections. For the [Al IX] line, there is a bright emission from the polar caps, that also is present in both model projection and observed image.

4. Conclusions

Our RAINY3D photoionization models based on Keck-OSIRIS data indicate that V723 Cas had an ionizing source with both spherical and disk components, with a substantial contribution the disk-like source being essential to match the 2d observations. A high temperature $280,000K$ central source is found for this nova and the total luminosity approaches the Eddington limit $L = 10^{38}$ erg/s. The models also suggest higher values for Al, Ca and Si abundances than previous literature findings, being $\log(N_{Al}/N_H) = -5.4$, $\log(N_{Ca}/N_H) = -6.4$ and $\log(N_{Si}/N_H) =$

Table 1. Integrated fluxes ratios for Al, Si and Ca lines in the best fit 3D model

	$F_{Si}/F_{Br\gamma}$	$F_{Al}/F_{Br\gamma}$	$F_{Ca}/F_{Br\gamma}$	$F_{He}/F_{Br\gamma}$	F_{Al}/F_{Si}	F_{Ca}/F_{Si}
Observed	1.2	1.4	6.8	0.4	1.2	5.9
Modeled	1.0	1.3	6.2	0.5	1.3	6.1

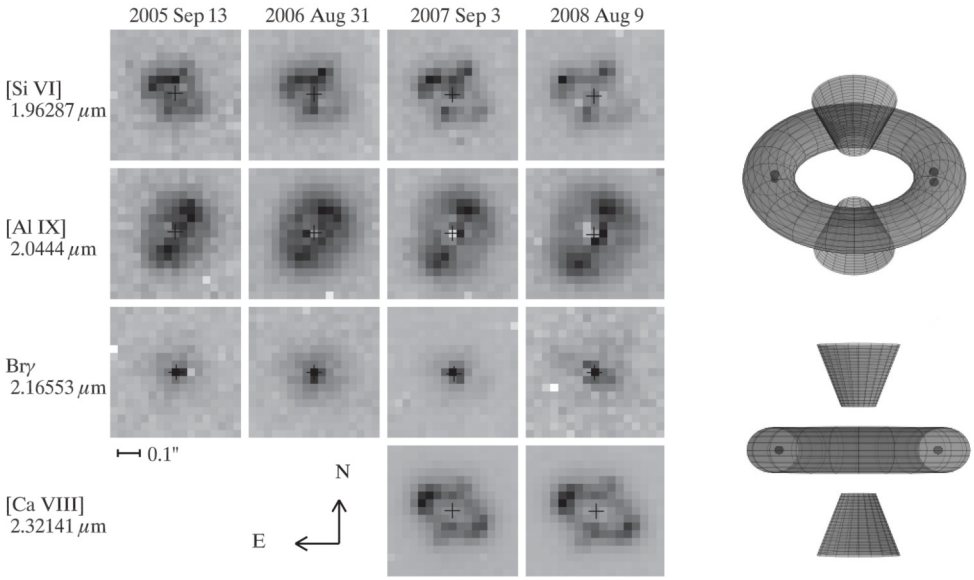

Figure 1. (a) Keck-OSIRIS data from 2005 to 2008 in 4 narrow bands (Lyke & Campbell 2009). The different morphologies from each narrow band are explained by an anisotropy of the ionizing radiation field. (b) 3D shell geometry used in RAINY3D models.

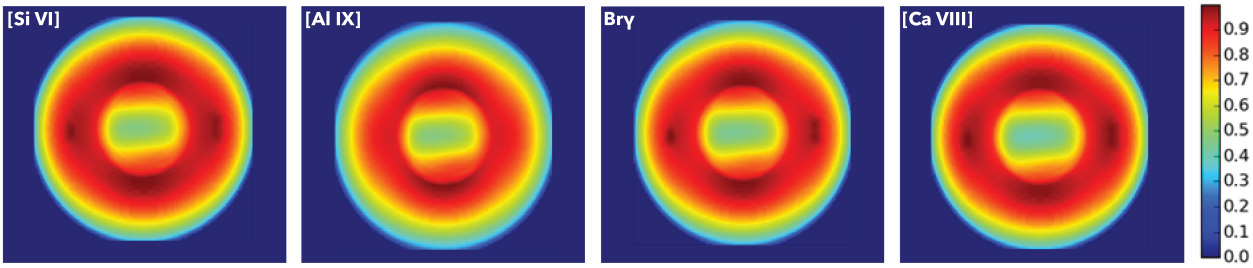

Figure 2. Best-fit model 2D surface brightness distributions.

−4.7. We estimated the total ejected shell mass in $M_{\rm shell} = 1.1 \times 10^{-5}\ M_{\odot}$.

Acknowledgements. We thank FAPESP for the support under grant 2014/10326-3 and CNPq funding under grant #305657.

References

Evans A. et al., AJ, 2003, vol. 126, p. 1981
Ferland G. J., Porter R. L., van Hoof P. A. M., Williams R. J. R., Abel N. P., Lykins M. L., Shaw G., Henney W. J., Stancil P. C., Rev. Mexicana Astron. Astrofis., 2013, vol. 49, p. 137
Hirosawa K., Yamamoto M., Nakano S., Kojima T., Iida M., Sugie A., Takahashi S., Williams G. V., IAU Circ., 1995, vol. 6213
Iijima T., A&A, 2006, vol. 451, p. 563
Lyke J. E. & Campbell R. D., AJ, 2009, vol. 138, p. 1090
Moraes M. & Diaz M., PASP, 2011, vol. 123, p. 844
Ness J.-U., Goranskij V. P., Page K. L., Osborne J., Schwarz G., The Astronomer's Telegram, 2015, vol. 8053
Ness J.-U., Schwarz G., Starrfield S., Osborne J. P., Page K. L., Beardmore A. P., Wagner R. M., Woodward C. E., AJ, 2008, vol. 135, p. 1328
Ohshima O. et al., IAU Circ., 1995, vol. 6214

Boletim da Sociedade Astronômica Brasileira, **30**, no. 1, 119-123

SOAR optical photometry of stellar clusters in the Magellanic Clouds: the VISCACHA survey

Francisco F. S. Maia[1,⋆], João F. C. Santos Jr.[1], Leandro Kerber[2,3], Bruno Dias[4], Eduardo Bica[5], Andres E. Piatti[6]

[1] UFMG, [2] IAG-USP, [3] UESC, [4] ESO, [5] IF-UFRGS, [6] UNC

Abstract. The VISCACHA Survey is an ongoing project based on deep, high quality photometric observations of low mass ($M < 10^4$ $M_\odot$) Magellanic Cloud star clusters located preferentially in the outermost regions of these galaxies, collected using the SOAR Adaptive Module Imager (SAMI). By homogeneously determining their astrophysical parameters (e.g. ages, metallicities, distances, masses, structural properties), the survey aims at investigating the interplay between the galactic environment and the clusters' evolution and at deriving the star formation history and chemical enrichment at the periphery of these galaxies. The survey's data processing and early results are presented.

Resumo. O levantamento VISCACHA é um projeto em andamento voltado para a obtenção de imagens profundas e de alta qualidade de aglomerados de baixa massa ($M < 10^4$ $M_\odot$) localizados preferencialmente nas regiões externas das Nuvens de Magalhães, coletadas utilizando o Módulo de Óptica Adaptativa do SOAR (SAMI). Através da determinação homogênea de seus parâmetros astrofísicos (e.g. idades, metalicidades, massas, propriedades estruturais), este levantamento busca investigar o papel do ambiente galáctico na evolução dos aglomerados estelares e derivar histórico de formação estelar e enriquecimento químico na periferia destas galáxias. Apresentamos o processamento dos dados e resultados preliminares.

Keywords. galaxies: star clusters: general – Magellanic Clouds

1. Introduction

The gravitational disturbances resulting from interactions between the Large Magellanic Cloud (LMC) and the Small Magellanic Cloud (SMC) and between these galaxies and the Milky Way are probably imprinted on the star formation history of these galaxies, as the strong tidal effects are known to trigger star formation across dwarf galaxies (Kennicutt et al. 1996). Gas dynamics simulations of galaxy collision and merging have shown that the properties of the tidally induced features such as the Magellanic Stream and Bridge can be used to gather information about the collision process and to infer on the past history of the colliding galaxies (Olson & Kwan 1990). When applied to model the Magellanic Clouds system, present-day simulations have been able to reproduce several of the observed features of the interacting galaxies such as shape, mass and the induced star formation rates. However, it is still not clear whether the Magellanic Clouds are on their first passage, or if they have been orbiting the Milky Way for longer times (e.g. Mastropietro et al. 2005; Diaz & Bekki 2012).

It is well known that the tidal forces have a direct impact over the dynamical evolution and dissolution of stellar clusters and that the intensity of these effects typically scale with galactocentric distances (Bastian et al. 2008). If the effects of the gravitational interactions in the Magellanic System are somewhat underlined on the structural, kinematical or on the spatial properties of their stellar clusters, the ones on the periphery of the LMC and SMC constitute an ideal sample to probe for the tidal effects arising from such interactions. Comparing these clusters properties at different galactocentric distances would allow unveiling the role of tidal forces over their evolution (e.g. Werchan & Zaritsky 2011; Glatt et al. 2011), while also mapping some LMC and SMC properties at projected distances usually not covered by previous surveys such as the *Magellanic Clouds Photometric Survey* (MCPS - Zaritsky et al. 1997) and the *Vista Magellanic Survey* (VMC - Cioni et al. 2011).

The VISCACHA (VIsible Soar photometry of star Clusters in tApii and Coxi HuguA[1]) survey will perform a comprehensive study of the outer regions of the Magellanic Clouds by collecting deep, high quality images of its stellar clusters using the SOAR telescope (4.1 m) Adaptive Module Imager (SAMI). A complete characterisation of these clusters, providing details of their structure, chemical composition, mass distribution and dynamical times, will serve as a basis for understanding both the local galactic properties at these largely unexplored regions and also how they influence clusters' evolution.

Photometric studies of Magellanic Clouds clusters are usually limited to those with the isochrone turn-off above the detection limits (Chiosi et al. 2006), which is directly related to the depth of the observations. Furthermore, crowding can also hamper the studies of many compact clusters, namely those immersed in rich backgrounds such as the bar (Maia et al. 2014). This bias the sample to massive, young to intermediate-aged clusters, while leaving the much more numerous low mass ones largely unexplored. When compared to other surveys on the Magellanic Clouds, the VISCACHA survey will reach significantly deeper than previous studies (largely based on the 2MASS, MCPS or the VMC surveys) reaching about $V \approx 24$ at $S/N \approx 0.1$, with better spatial resolution ($FWHM \approx 0.5''$) due to the employment of the adaptive optics system. Even thought HST studies (e.g. Glatt et al. 2008) are still unmatched by ground based photometry, the spatial coverage of the VISCACHA survey greatly surpass those, allowing for a larger cluster sample and a more complete understanding of these galaxies properties.

⋆ e-mail: ffsmaia@ufmg.br

[1] LMC and SMC names in the Tupi-Guarani language

1.1. Objectives

On a short term, the VISCACHA survey will deliver a high quality, homogeneous database of star clusters in the Magellanic Clouds, providing reliable physical parameters such as structure, distances, ages, metallicities, mass distributions as derived from a standardised data reduction and analysis processes. The effects of the local tidal field over their evolution will be quantified through analysis of their structural parameters, dynamical times, and position within the galactic system. Comparison of these results with stellar population models (e.g. van der Marel et al. 2009; Baumgardt et al. 2013) will provide important constraints to understand the evolution of the Magellanic Clouds.

Once a significative sample had been collected, an pioneering study of the star formation history and chemical enrichment on the periphery of these galaxies will be carried out, using the derived cluster parameters as probes of the local galactic properties (e.g. Piatti 2015; Piatti et al. 2018). Based on this expanded dataset, several aspects concerning the evolution of these galaxies will be revisited, such as spatial dependency of age-metallicity relationship (Dobbie et al. 2014), the "V" shape metallicity gradient found in the SMC (Dias et al. 2016), the 3D cluster distribution and the inclination of the LMC galactic disk.

Finally, our catalogues will be matched against other tables in the literature (e.g. MCPS, VMC, OGLE) comprising a more complete dataset that will serve as reference to future studies of star clusters in the Magellanic Clouds. All scientific results from the VISCACHA project, including catalogs, images and tables, will be compiled on an easily accessed on-line database for legacy value.

2. Data Handling

The SOAR Telescope Adaptive Module (SAM) is a ground-layer adaptive optics instrument using a Rayleigh laser guide star at ~7 km from the telescope. SAM was employed with its internal CCD detector, SAMI (4K× 4K CCD), set to a gain of 2.1 e^-/ADU and a readout noise of 4.7 e^- and binned to 2×2 factor, resulting in a plate scale of 0.091 arcsec/pixel with the detector covering a field-of-view of 3×3 arcmin on the sky. Peak performance of the system produce FWHM ~0.3 arcsec in the *I* band and ~0.4 arcsec in the *V* band, which still allows for adequate sampling of the point spread function (PSF), reaching a minimum size of ~3.3 pixels (at half maximum) in those occasions.

Photometric images with *BVI* filters were obtained for approximately 170 clusters[2] in the LMC, SMC and Bridge during the semesters of 2015A, 2015B, 2016B and 2017B as shown in Fig. 1. The catalogued clusters from Bica et al. (2008) are also shown as reference. The typical observing scheme included short and long exposures of each target with total integration times of 3×450s (*B*–band), 3×375s (*V*-band) and 3×560s (*I*–band).

The data were pre-reduced in a standard way in IRAF, being processed for bias subtraction and division by skyflats by use of the CCDRED package. Astrometric calibration was also performed with IRAF tasks (IMCOORDS package) using the 2MASS stars in the fields as astrometric references. See Fraga et al. (2013) for reduction and astrometric calibration details. The data reduction was also done using automated IRAF scripts designed to work on SAMI images that perform cosmic rays removal (CRUTIL package), images registration to a common frame and the subsequent mean stacking of the long exposures in each filter into a deeper mosaic (IMMATCH package).

[2] Eventually, 2006-2013 data acquired with the previous generation imager (SOI) will also be integrated in our database.

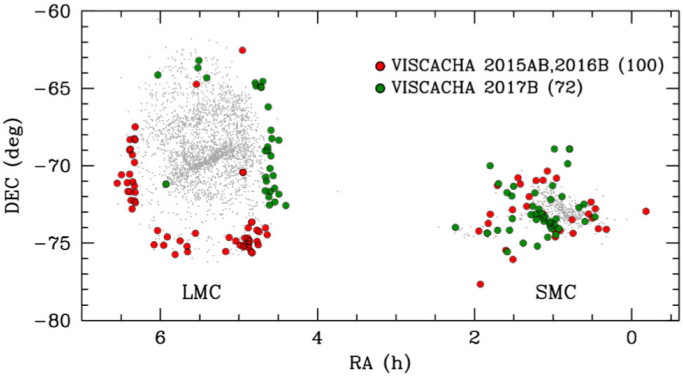

Figure 1. Present sample of VISCACHA clusters, including ~ 170 clusters observed through 2015-2016 (red circles) and planned for 2017 (green circles). The catalogued clusters in the Magellanic Clouds are shown in grey dots as a reference.

Photometry was done using a modified version of the Starfinder code (Diolaiti et al. 2000), which performs isoplanatic high resolution analysis of crowded fields by extracting an empirical PSF from the image and cross-correlating it with every signal detected above a defined threshold. The modifications were aimed mainly at automating the code, minimising the user intervention. Modelling of each image PSF was done by selecting 20 to 50 bright, unsaturated stars presenting no bright neighbour closer than 6 FWHM. This initial PSF was used to model and remove faint neighbours around the initially selected stars, which were then reprocessed to generate a definitive PSF, used to extract the photometry.

Calibration of the instrumental magnitudes was usually done using two populous Stetson (2000) photometric standard fields (e.g. SN1987A, NGC2298), observed at 3-4 different airmasses through each night. Individual solutions for each star in these fields were calculated in a two step process:

i) extinction correction based on the usual prescription for computing the extra-atmospheric magnitudes:

$$m_i - M_i = cte + e_i X_i \quad ; \tag{1}$$

ii) colour correction to account for subtle diferences in the passbands of the filters used:

$$m'_i - M_i = z_i + c_i(m'_i - m'_{i+1}) \quad ; \tag{2}$$

where m and M represent the instrumental and catalogue magnitudes, respectively, X the airmass and e, c and z the extinction, colour and the night zero-point coefficients, respectively. The subscript i denotes the band (B, V, I) and $m'_i = m_i - e_i X_i$ are the extra-atmospheric magnitudes.

Figure 2 shows the fit of eqs. 1 and 2 to determine the *V*–band extinction, zero-point and colour coefficients for stars in the NGC2818 and NGC2298 standard fields in the night of 22/02/2015. Extinction coefficients and uncertainties were determined from the average of the slopes found for each star while the colour and zero-point coefficients were found from a single fit using the extra-atmospheric magnitudes for all stars in the standard fields. The mean values and deviations of the determined coefficients through semesters 2015A−2016B is shown in Table 1. These values are in excellent agreement with those by Fraga et al. (2013).

The derived coefficients from the calibration process were used to invert the system of equations used in the fits leading to the calibration equations for deriving the calibrated magnitudes.

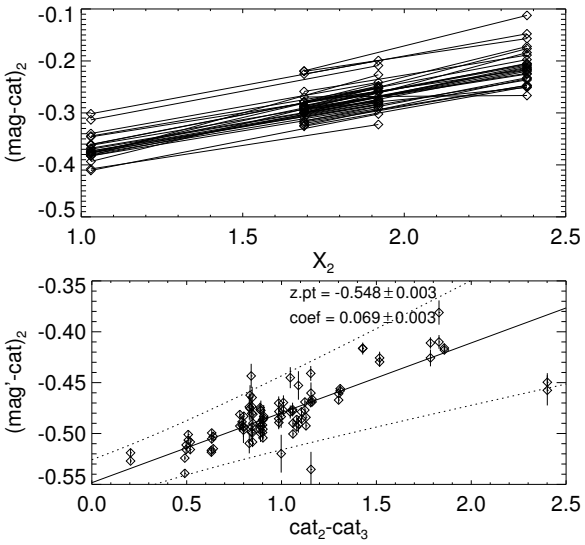

Figure 2. Fits in the V band to determine the extra-atmospheric magnitudes and the extinction coefficients (top) and the colour and zero-point coefficients (bottom) for the night of 22-02-2015, using the NGC2818 and NGC2298 standard fields.

Table 1. Mean calibration coefficients through 2015A−2016B

Coef.	B	V	I
e	0.177 ± 0.011	0.106 ± 0.006	0.022 ± 0.006
c	-0.193 ± 0.008	0.064 ± 0.005	-0.063 ± 0.005
z	24.862 ± 0.006	24.461 ± 0.005	24.418 ± 0.005

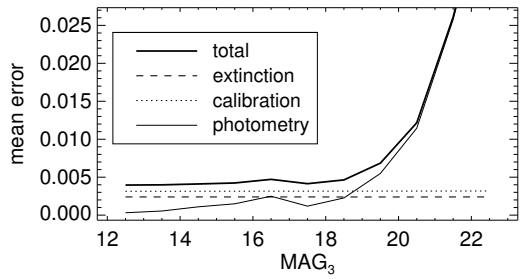

Figure 3. Photometric uncertainties as function of magnitude for the I band of cluster SL897, as arising from the photometry (thin line), extinction (dashed line) and colour calibration (dotted line). The total photometric uncertainty adopted for the calibrated magnitudes is also shown (solid line).

When applied to the standard stars themselves, the calibration returned average RMS uncertainties of about 0.03 mag in the B band and 0.02 mag in the V and I bands. Through these calibration equations, the errors of the derived coefficients z, e and c where properly propagated and added to the photometric uncertainties, as shown in Fig. 3 for the cluster SL897. It is clear that the magnitude uncertainties from the PSF photometry are dominated by those arising from the extinction and colour calibrations for most of the sampled magnitude range.

Artificial star tests were performed in each image of our sample in order to derive completeness levels as function of magnitude and position. The empirical PSF model image was used to artificially add stars with a fixed magnitude to the image in a homogeneous grid, with a fixed spacing of 6 FWHM between stars to prevent overlapping of the artificial stars wings. Several grids with slightly different positioning and with stellar magnitudes ranging from 14 to 24 were simulated, generating nearly 100 artificial images for each original one. Photometry was carried out

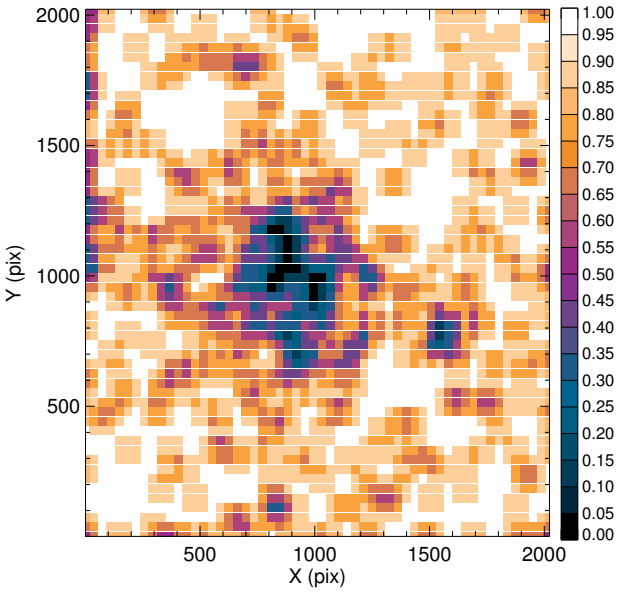

Figure 4. Completeness map for cluster SL897, constructed by artificially adding $V = 22$ stars over the original image in an uniform grid with 6 FWHM spacing, covering the entire image. Even though the average completeness over the image is 84%, near the center of the cluster it drops to approximately zero.

over the artificial images and the recovery fraction of the artificially added stars used to construct completeness maps, such as the one shown in Fig. 4 for cluster SL897 at $V = 22$. It can be seen that incompleteness can severely hamper the analysis of the low mass content of the cluster, as the local completeness value near the centre of cluster ($\lesssim 5\%$) fall much more rapidly than the overall field value ($\sim 84\%$).

3. Structural analysis

Structural analysis of the studied clusters are determined by fittings of King (1962) analytical function to the clusters' radial density profile. Profiles derived from both completeness corrected stellar counts and surface brightness are being used to derive several structural parameters such as the core radius (r_c), tidal radius (r_t), central surface brightness (μ_0) and integrated magnitudes. Surface brightness profiles are obtained directly from the calibrated images, by measuring the fluxes in anular rings around the cluster centre, which is defined by averaging the stellar positions around a preliminary visual radius. Stellar density profiles are constructed by counting stars in concentric rings around the determined centre and then correcting the counts by the average incompleteness in the ring. Figure 5 shows a fit of the King profile to the surface brightness of cluster SL897, and its derived parameters.

The clusters deprojected distances from the LMC dynamical centre are computed according to Elmegreen (1998) prescription, using the position angle and inclination of the LMC disc as given by van der Marel & Kallivayalil (2014) kinematic data. The sample can be separated in four groups at distinct locations, through the LMC outer regions, as it can be seen in Fig. 6. The relationship between their derived r_c, μ_0 and deprojected galactocentric distance is shown in Fig. 7, as function of their azimuthal position (color coded). It is clear that the clusters in the westernmost groups (towards the SMC) are larger and fainter than those in the eastern regions. We have also found that there is a larger spread in r_c for clusters located farther away from the centre, specially for those in the westernmost region, as their me-

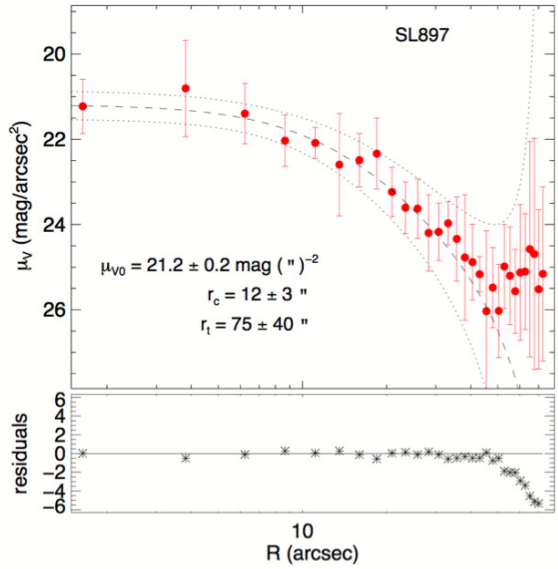

Figure 5. King fit to the surface brightness profile of cluster SL897 in the V band. The central surface brightness (μ_{V0}), core radius (r_c) and tidal radius (r_t) derived are shown.

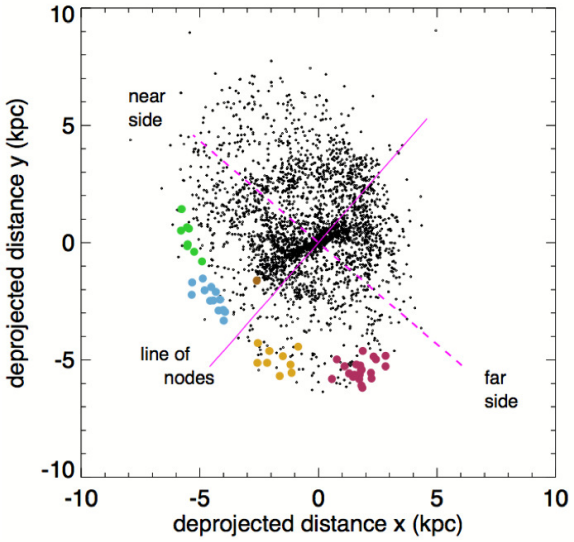

Figure 6. Deprojected distribution of LMC stellar clusters, overlaid against Bica et al. (2008) catalogue. Clusters are colour coded according to their azimuthal position in the outer LMC. The line of nodes, separating the closer and farther sides of the galaxy are also indicated.

dian core radius is larger than those of eastern clusters. Finally, comparison of our clusters tidal radius with those of clusters in the inner region of the LMC (Werchan & Zaritsky 2011) confirms that the latter are indeed smaller, pointing that tidal effects might be at action.

Further details on this structural analysis is presented by Santos Jr. et al. in this proceedings.

4. Colour-magnitude diagram analysis

Analysis of the photometric data was done by using the structural parameters to define a cluster and a field sample within each observed field. Then, a decontamination procedure (Maia et al. 2010) was applied to statistically probe and remove the most probable field contaminants from the cluster region, based

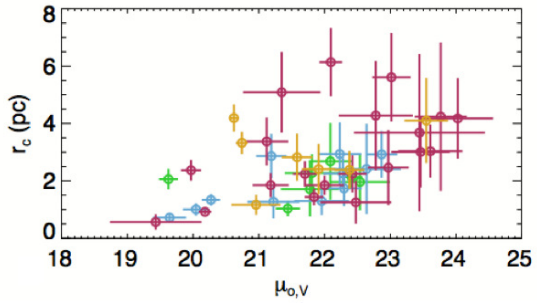

Figure 7. Relationship between the core radius and the central surface brightness. Clusters at different azimuthal regions are color coded as in Fig. 6.

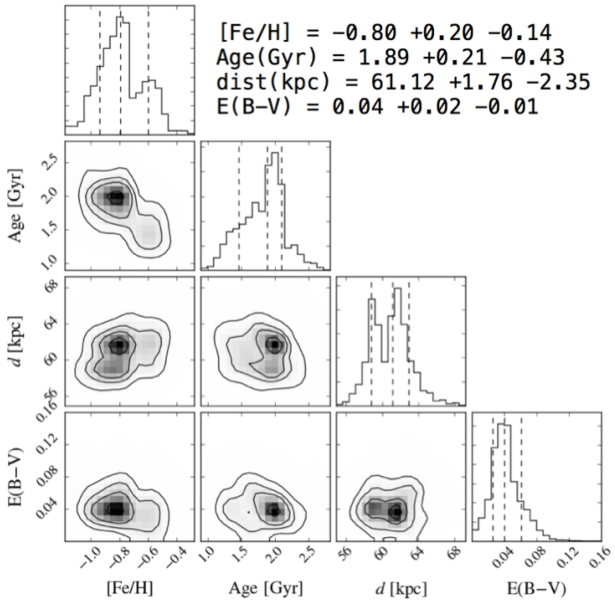

Figure 8. Posterior distribution for parameters derived K37 using a MCMC bayesian framework. The derived parameters and their uncertainties are also shown.

on both the positional and the photometric characteristics of the stars. The field decontaminated colour-magnitude diagrams (CMD) of the clusters were then used to derive their astrophysical parameters via the Markov-Chain Monte-Carlo technique in a bayesian framework. The likelihood function was derived using the PARSEC isochrones (Bressan et al. 2012) to build synthetic CMDs of simple stellar populations, spanning a wide range of parameters (e.g. Dias et al. 2014). Figure 8 shows the posterior distribution of the determined parameters for cluster K37. Typical uncertainties of the method are about 15 dex in metallicity, 10-20% in age, ~2 kpc in distance and ~0.02 mag in colour excess. Figure 9 shows the best model isochrone and the synthetic population superimposed over K37 decontaminated CMD.

Parameters resulting from the analysis of our previous SOI data (Dias et al. 2016) reveal that the age-metallicity gradients found for the outer clusters are not compatible with those of clusters in the main body of the galaxy (Fig. 10). Additionally, these gradients seems to change with the azimuthal position of the clusters around the periphery (i.e. bridge, west-halo, counter-bridge), indicating that they might have formed and evolved under different environmental conditions.

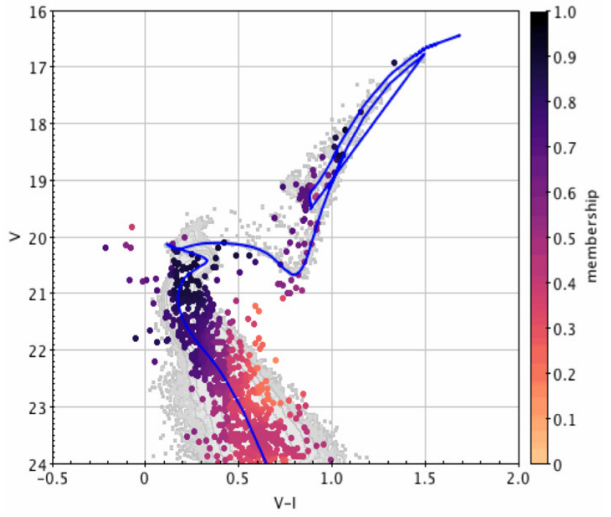

Figure 9. Best model isochrone (solid line) and synthetic population (gray dots) corresponding to the K37 cluster, superimposed over its field decontaminated CMD. The assigned stellar memberships are also shown.

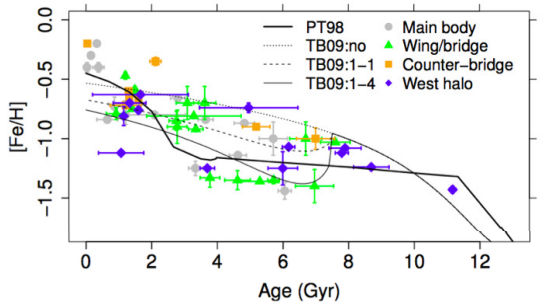

Figure 10. Age-metallicity relationship of SMC clusters, colour coded according to their azimuthal position within the galaxy. Theoretical models from Pagel & Tautvaisiene (1998, PT98) and Tsujimoto & Bekki (2009, TB09) are also shown. Adapted from Dias et al. (2016).

Further details on this CMD analysis is presented by Kerber et al. in this proceedings.

5. Conclusions and perspectives

The VISCACHA survey aims at producing a reference library of high-quality, homogeneously determined cluster parameters and information dedicated to the study of the Magellanic Clouds. With ~170 targets, the growing database is already one of the largest compilations of observed stellar clusters in these galaxies outskirts. Careful determination of the structural and astrophysical parameters of these clusters have shown that the tidal effects of Magellanic Clouds interactions are indeed imprinted both on the structure and on the chemistry of their outer clusters. A statistical interpretation of a larger dataset is bound to reveal interesting aspects of these galaxies dynamical evolution as well as their impact on their stellar clusters ecology.

Acknowledgements. We acknowledge CAPES and FAPESP for partial funding support.

References

Bastian N., Gieles M., Goodwin S. P., Trancho G., Smith L. J., Konstantopoulos I., Efremov Y., 2008, MNRAS, 389, 223
Baumgardt H., Parmentier G., Anders P., Grebel E. K., 2013, MNRAS, 430, 676
Bica E., Bonatto C., Dutra C. M., Santos J. F. C., 2008, MNRAS, 389, 678
Bressan A., Marigo P., Girardi L., Salasnich B., Dal Cero C., Rubele S., Nanni A., 2012, MNRAS, 427, 127
Chiosi E., Vallenari A., Held E. V., Rizzi L., Moretti A., 2006, A&A, 452, 179
Cioni M.-R. L., Clementini G., Girardi L., Guandalini R., Gullieuszik M., et al. 2011, A&A, 527, A116
Dias B., Kerber L., Barbuy B., Bica E., Ortolani S., 2016, A&A, 591, A11
Dias B., Kerber L. O., Barbuy B., Santiago B., Ortolani S., Balbinot E., 2014, A&A, 561, A106
Diaz J. D., Bekki K., 2012, ApJ, 750, 36
Diolaiti E., Bendinelli O., Bonaccini D., Close L., Currie D., Parmeggiani G., 2000, A&AS, 147, 335
Dobbie P. D., Cole A. A., Subramaniam A., Keller S., 2014, MNRAS, 442, 1680
Elmegreen D. M., 1998, Galaxies and galactic structure
Fraga L., Kunder A., Tokovinin A., 2013, AJ, 145, 165
Glatt K., Grebel E. K., Jordi K., Gallagher III J. S., Da Costa G., Clementini G., Tosi M., Harbeck D., Nota A., Sabbi E., Sirianni M., 2011, AJ, 142, 36
Glatt K., Grebel E. K., Sabbi E., Gallagher III J. S., Nota A., Sirianni M., Clementini G., Tosi M., Harbeck D., Koch A., Kayser A., Da Costa G., 2008, AJ, 136, 1703
Kennicutt Jr. R. C., Schweizer F., Barnes J. E., 1996, Galaxies: Interactions and Induced Star Formation
King I., 1962, AJ, 67, 471
Maia F. F. S., Corradi W. J. B., Santos Jr. J. F. C., 2010, MNRAS, 407, 1875
Maia F. F. S., Piatti A. E., Santos J. F. C., 2014, MNRAS, 437, 2005
Mastropietro C., Moore B., Mayer L., Wadsley J., Stadel J., 2005, MNRAS, 363, 509
Olson K. M., Kwan J., 1990, ApJ, 361, 426
Pagel B. E. J., Tautvaisiene G., 1998, MNRAS, 299, 535
Piatti A. E., 2015, MNRAS, 451, 3219
Piatti A. E., Cole A. A., Emptage B., 2018, MNRAS, 473, 105
Stetson P. B., 2000, PASP, 112, 925
Tsujimoto T., Bekki K., 2009, ApJ, 700, L69
van der Marel R. P., Kallivayalil N., 2014, ApJ, 781, 121
van der Marel R. P., Kallivayalil N., Besla G., 2009, in Van Loon J. T., Oliveira J. M., eds, The Magellanic System: Stars, Gas, and Galaxies Vol. 256 of IAU Symposium, Kinematical structure of the Magellanic System. pp 81–92
Werchan F., Zaritsky D., 2011, AJ, 142, 48
Zaritsky D., Harris J., Thompson I., 1997, AJ, 114, 1002

Boletim da Sociedade Astronômica Brasileira, **30**, no. 1, 124-125

Transition disk candidates in the NGC 2264 cluster – Disk diagnostics

A. P. Sousa[1] & S. H. P. Alencar[1,2]

[1] Departamento de Física, ICEx–UFMG, Belo Horizonte, MG, Brazil, e-mail: alana@fisica.ufmg.br
[2] Univ. Grenoble Alpes, IPAG, F-38000 Grenoble, France

Abstract. Disk holes are inferred from infrared observations of T Tauri stars, indicating the existence of a transitional phase between thick accreting disks and debris disks. Using data from the observational multiwavelength campaign CSI2264, we analyzed 410 stars belonging to NGC 2264 and found about 7% transition disk candidates. We characterized these star-disk systems using disk parameters and we compared them with star–disk systems with full disks and diskless. We were able to evaluate the influence of disk evolution on the observed disk characteristics.

Resumo. Buracos no disco de acreção são inferidos a partir de observações de estrelas T Tauri no infravermelho, indicando a existência de uma fase de transição entre disco espesso e disco de pedregulhos. Usando dados da campanha observacional CSI2264, analisamos 410 estrelas pertencentes a NGC 2264 e encontramos cerca de 7% de candidatas a disco de transição. Caracterizamos estes sistemas de disco–estrelas usando parâmetros de disco e comparando-os com sistemas disco-estrela com disco completo e sem disco. Avaliamos a influência da evolução do disco sobre as características de disco observadas.

Keywords. Stars: formation – Stars: variables: T Tauri – Accretion disk

1. Introduction

Young low mass stars ($\sim$ 1 Myr and $M \leq 2M_{\odot}$) are surrounded by a circumstellar disk from which they can still accrete. It is known that the disks are planet formation sites. Therefore understanding disk dissipation is essential to study how planets form.

The inner disk gas can be dissipated by accretion to the star through the stellar magnetic field, by photoevaporation from the central star high-energy radiation (Alexander et al. 2014; Owen 2016) and the disk material may also be driven out of the system through disk winds and jets (Pelletier & Pudritz 1992; Shu et al. 1994). The disk can also be consumed in the coagulation of grains and planets formation (Hollenbach et al. 2005).

Transition disks are systems with a hole in the inner disk and are characterized by a lack of emission, above the photospheric level, in NIR wavelengths and an emission excess like a thick disk in mid-infrared bands (Owen 2016). We searched for transitional disk candidates belonging to the young stellar cluster NGC 2264 ($\sim$ 3 Myr and d $\sim$ 760 pc; Dahm 2008) to characterize them in terms of their infrared excess. We fitted spectral energy distribution models to the data available for all the stars in our sample.

2. Observation

We used data from the *Coordinated Synoptic Investigation of NGC 2264* (CSI 2264) that was an international campaign which involved simultaneous and high-resolution observations (Cody et al. 2013), that included photometric data from the CoRoT satellite (40 days, 2011), *u* band from Megacam (CFHT). We also used photometric data from catalog surveys, such as near-infrared JHK_S from 2MASS, $UBVR_cI_c$ from Rebull et al. (2002), IRAC and MIPs data from the Spitzer Telescope and observations from the Wide-field Infrared Survey Explorer (WISE) performed at wavelengths 3.4, 4.6, 12.0 and 22 μm (Wright et al. 2010).

3. Results

3.1. SED model

Our sample of stars is composed of 410 T Tauri stars that were observed with both *Spitzer*/IRAC (Teixeira et al. 2012) and CFHT/Megacam (Venuti et al. 2014), to select the systems with the largest number of measured stellar, accretion and disk parameters.

We constructed SEDs (spectral energy distributions) of all these stars and modeled them with the Hyperion SED model[1] (Robitaille 2017). We found 28 transition disk candidates (stars with inner hole according to the SED modeling and that have 24 μm flux above photospheric level), 212 stars with a full disk and 170 diskless stars (see Figure 1). This number of transition disks ($\sim$ 7 % of the total of 410 stars that we analyzed) confirms that disk dispersal is rapid compared to disk lifetime as reported in the literature (Owen 2016).

3.2. Disk diagnostics

The $\alpha_{\rm IRAC}$ index (the slope of the SED between 3.6 μm and 8 μm (Teixeira et al. 2012)) allows a classification of inner disk evolution, as shown in Fig. 2. Transition disk candidates are generally located among anemic disk that corroborates the depletion of the dust in the inner disk. All the flat spectra and thick disk systems are indeed classified as full disks according to their SEDs and most of the naked photospheres correspond to the diskless SED systems.

A transition disk system has a hole in the inner disk, this hole is characterized by a lower quantity of dust compared to the outer part of the disk. Then, we expect that transition disks show little excess in NIR and some excess in MIR (Owen 2016). A way to check if our transition disk sample obeys this criteria is to build color-color diagrams comparing near and mid-infrared fluxes. In Fig. 3 we show K_S − [8.0] vs. K_S − [24] diagrams. We

[1] We using the version v1.1 of the modular sets of synthetic spectral energy distributions.

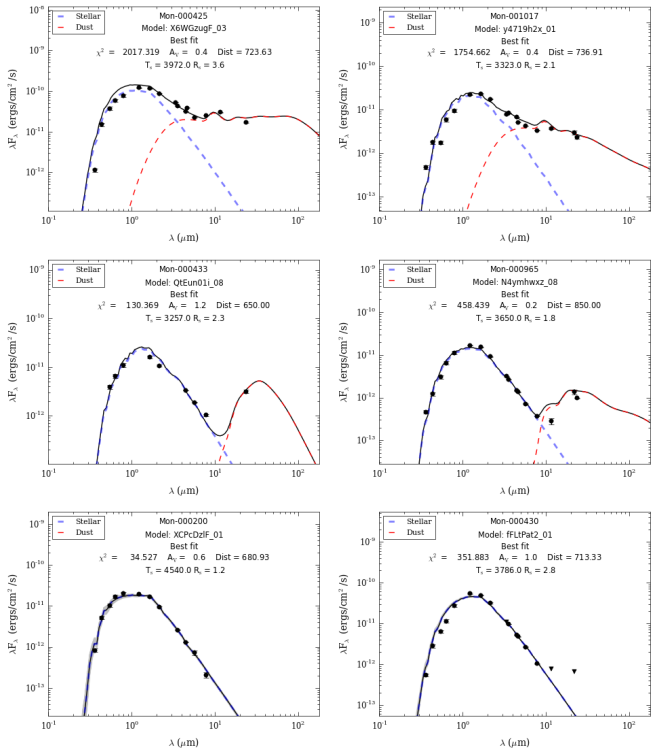

Figure 1. Examples of SEDs for systems with full disk (top), transition disk candidate (middle) and diskless stars (bottom). The circles show literature observed data from U to 24 mμ (Rebull et al. 2002; Wright et al. 2010). The black solid line is the best data fit (based on χ^2) of the Hyperion SED model and the dashed lines are stellar and dust emission components (Robitaille 2017, 2011).

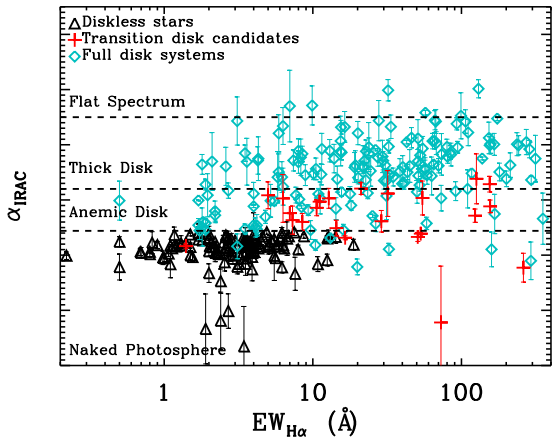

Figure 2. Slope of the spectral energy distribution from 3.6 μm to 8 μm from Teixeira et al. (2012) as a function of Hα equivalent width (Sousa et al. 2016; Dahm & Simon 2005).

can see that stars with full disks present excess above the photospheric emission in the inner and outer parts of the disk, while transition disks present emission in the outer disk as full disk systems but lower emission in the inner disk. Unfortunately, we do not have *Spitzer* data for the diskless stars, which we expect to show no excess emission at all wavelengths, as seen, e.g., in Owen (2016).

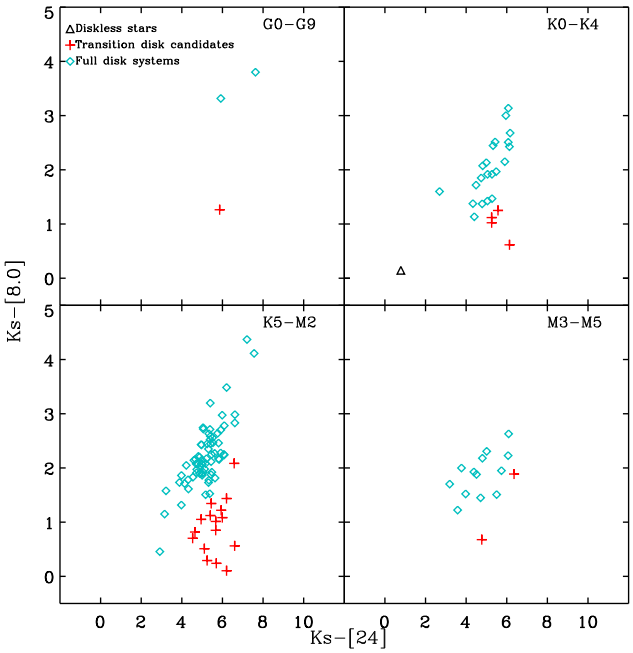

Figure 3. NIR and MIR color-color diagram for stars belonging to the NGC 2264 cluster.

4. Conclusions

- We modeled the SED of all our sample of 410 T Tauri stars and we found 212 full disk systems and 177 diskless stars. SED modeling also showed that 28 of the 410 T Tauri stars of the NGC 2264 that we analyzed presented inner disk holes. This represents 7 % of our sample and confirms that transition disks are a rapid phase of disk evolution.
- Transition disk candidates have dust in the inner disk similar to anemic disks, according to $\alpha_{\rm IRAC}$ classification as seen in the $\alpha_{\rm IRAC}$ analyze.
- In color-color diagram classification we can see two different populations: Stars with full disk have excess, above the photospheric emission, in the inner and outer parts of the disk, transition disk systems present weak dust emission in the inner disk, and present dust emission in the outer disk like a star with full disk.

Acknowledgements. The authors wish to thank Luisa Rebull for sharing with us the photometric data and CNPq, FAPEMIG and CAPES for their funding of this research.

References

Alexander, R. et al. 2014, Protostars and Planets VI, 475
Cody, A. M. et al. 2013, Astronomische Nachrichten, 334, 63
Dahm, S. E. 2008, The Young Cluster and Star Forming Region NGC 2264, ed. B. Reipurth, 966
Dahm, S. E. & Simon, T. 2005, AJ, 129, 829
Hollenbach, D., Gorti, U., Meyer, M., et al. 2005, ApJ, 631, 1180
Owen, J. E. 2016, PASA, 33, e005
Pelletier, G. & Pudritz, R. 1992, ApJ, 394, 117
Rebull, L. M., Makidon, R. B., Strom, S. E., et al. 2002, AJ, 123, 1528
Robitaille, T. P. 2011, A&A, 536, A79
Robitaille, T. P. 2017, A&A, 600, A11
Shu, F., Najita, J., Ostriker, E., et al. 1994, ApJ, 429
Sousa, A. P., Alencar, S. H. P., et al. 2016, A&A, 586, A47
Teixeira, P. S. et al. 2012, A&A, 540, A83
Venuti, L., Bouvier, J., Flaccomio, E., et al. 2014, A&A, 570, A82
Wright, E. L. et al. 2010, AJ, 140, 1868

Boletim da Sociedade Astronômica Brasileira, **30**, no. 1, 126-127

Fitting of King's model to young star clusters

José Lucas Lima Berretta & Annibal Hetem Jr.

[1] UFABC e-mail: jose.lucas@aluno.ufabc.edu.br

Abstract. It was done an analysis of a young cluster sample to investigate the cluster's inherent properties and the dynamical evolution of the stellar components. Particularly, the parameters from King's model measured for clusters. Using consolidated algorithms, as quicksort and genetic algorithm, we developed a series of programs in C++ to organize and plot graphicaly the data of each cluster to obtain the King's profile. With the parameters of the King's mode, we tried to compare them with each other and with the fractal parameter Q.

Resumo. Fez-se uma análise de uma amostra de aglomerados de estrelas jovens com o intuito de investigar as propriedades inerentes ao agrupamento e evolução dinâmica das componentes estelares. Em especial, os parâmetros oriundos dos modelos de King medidos para os clusters. Este projeto foi focado na exploração do tema, estudo sobre os parâmetros envolvidos em nossa análise e o desenvolvimento das rotinas numéricas para o tratamento e estudo dos dados. Com o uso de algoritmos consolidados como quicksort e algoritmo genético, desenvolvemos uma série de programas em C++ que organizaram e plotaram graficamente os dados de cada cluster para enfim obter o perfil de King da cada um. Com os parâmetros do modelo de King em mãos, buscamos comparar eles entre si e com o parâmetro fractal Q.

Keywords. Stars: pre-main sequence – ISM: clouds – Methods: data analysis

1. Introduction

A very significant measurement related to the cluster structure is given by the King's profile of each cluster, which parameter is used, in this study, to find a correlation between structural parameters and other properties found in the literature.

A young cluster sample was analyzed to investigate the inherent properties to the clustering and the dynamical evolution of each star component. In this case, the parameters obtained from the measured King's models for the clusters. In previous works, we have measured the superficial density and the core's radius for a set of clusters and the results were correlated with some other clusters properties (including fractal and geometrical parameters), which show that almost half of these groups has a relation with their parental cloud. These properties can bring us to conclusions about the formation of the clusters (hot or cold collapse), initial evolution and their expected dynamical galactic evolution (crossing time).

With the adjusted parameters from King's profile, we intend to advance to a lager number of clusters and expanded the studied galactic regions through samples at different bands of coordinates.

The analyzed parameters related to the clusters, are:

Core's Radius

Radius where the density is 50% of the central density

Central Brightness

How much brightness the cluster show in its center, this parameter is important in the King's model to relate with the rest of the cluster.

Q parameter

A fractal parameter obtained with the distribution of the stars inside the cluster, and is related with its evolution. This parameter were obtained at another study (Sampa-Hetem, poster 140).

2. Methodology

The study of the early stages of the star's clusters evolution is part of a bigger subject, which includes the comprehension of the cloud-gas to cluster-star transition. As long as the data volume is great, we established a flux to treat and control these data, and execute automatically all the calculations.

With the observational data, the intermediate parameters were calculated through the development and application of numerical routines. Formally, the parameters were obtained by fitting the function that approaches the King's profile for each cluster (Equation 1).

$$\Sigma(r) = \Sigma_{\circ}\left[1 + \left(\frac{r}{r_c}\right)^2\right]^{-\frac{3}{2}} \quad (1)$$

3. Results

Table 1 presents used data and the obtained results. Each row shows the data of each cluster, in the order: name, two columns of its coordinates, number of members, obtained central brightness and obtained core's radius.

3.1. King's Profile

Figure 1 shows us the fitted profile of some clusters. The blue points represents the histogram of the brightness on radius bands, and the red curve is the adjusted king's profile. The parameters to produce the profile were fitted by using genetic algorithm to find the best adjusted curve for the cluster.

3.2. Analysis

The obtained data about both parameters of King's model were correlated with each other and with the Q parameter of the corresponding cluster, as shown at Figure 2.

We can see some restricted regions of each graph, which boundaries are evidenced by the red lines, showing a pattern relation between the parameters. Therefore, there are exceptions of these patterns, which were highlighted with the star on the graph.

Table 1. Cluster data and results

Cluster	l(gal)	b(gal)	Nstars	$\Sigma_\circ$	r_c
Berkeley 86	76,7	1,28	86	7,1644	1,5423
Collinder 205	269	-1,8	177	9,9632	1,9770
Hogg 10	291	0,08	88	5,4948	3,6688
Hogg 22	339	-1,1	98	9,8459	1,7995
Lynga 14	341	-1,1	67	9,9255	1,3138
Markarian 38	12	-0,9	58	9,9649	1,9996
NGC 2244	206	-2,1	296	2,3279	8,8475
NGC 2264	203	2,18	293	1,3307	1,0473
NGC 2302	219	-3,1	70	9,8593	2,0464
NGC 2362	238	-5,5	132	9,6249	3,6776
NGC 2367	236	-3,8	61	9,9218	1,5288
NGC 2645	265	-2,9	104	9,7338	1,8813
NGC 2659	264	-1,7	220	5,8014	4,9636
NGC 3572	291	0,2	151	9,8978	2,1512
NGC 3590	291	-0,2	81	9,9711	1,4295
NGC 5606	315	0,99	99	3,9161	4,2335
NGC 6178	338	1,21	104	3,2920	19,9665
NGC 6530	6,08	-1,3	63	4,6007	1,8835
NGC 6604	18,2	1,69	90	4,0858	4,3548
NGC 6613	14,2	-1	135	9,8757	1,0854
Ruprecht 79	277	-0,8	175	2,9387	13,2255
Stock 13	291	1,6	67	5,3127	2,0034
Stock 16	306	0,06	141	3,0532	5,4898
Trumpler 18	291	-0,1	161	5,3186	3,6053
Trumpler 28	356	-0,3	74	5,5074	3,1733

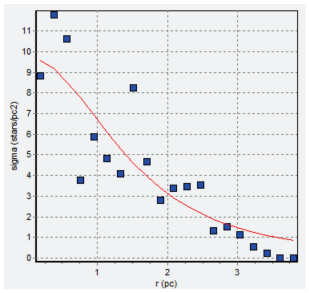

(a) NGC2244

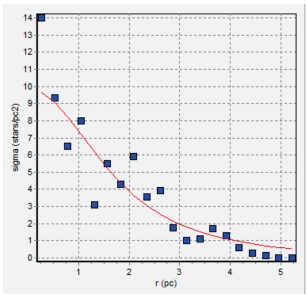

(b) NGC6613

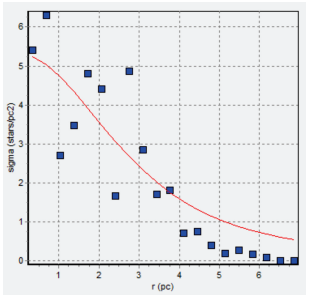

(c) Trumpler 18

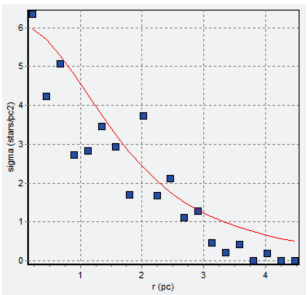

(d) Stock 13

Figure 1. Fitted King's model of 4 analyzed clusters

4. Conclusion

By using a series of numerical routines, it were obtained the central brightness and the core's radius value for each cluster of the sample, as shown. With these parameters, a comparative analysis was made correlating the obtained values and the Q parameter (Sampa-Hetem, poster 140).

In these correlations we can observe some prohibited regions and a tendency of each parameter on dependence to the others.

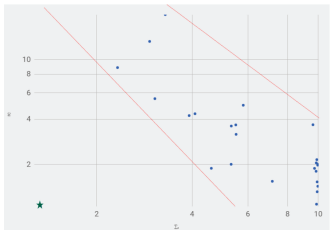

(a) $r_c \times \Sigma_\circ$

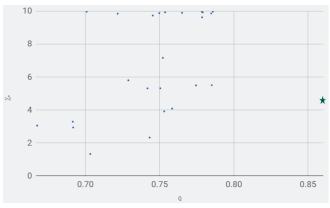

(b) $\Sigma_\circ \times Q$

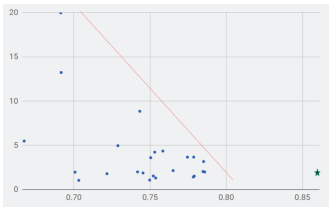

(c) $r_c \times Q$

Figure 2. Correlation between the parameters

References

Alfaro, E. J., González, M., 2016, MNRAS 456, 2900–2906
Dale, J. E., Ercolano, B., Bonnell, I. A., 2012, MNRAS, 424, 377
Dale, J. E., Ercolano, B., Bonnell, I. A., 2013, MNRAS, 430, 234
Davidge, T. J., 2017, ApJ 837:178
Elmegreen, B. G., Falgarone, E., 1996, ApJ, 471, 816.
Gieles, M., Portegies Zwart, S. F., 2011, MNRAS, 410, L6
Girichidis, P., Federrath, C., Allison, R., Banerjee, R., Klessen, R. S., 2012, MNRAS, 420, 3264
Gregorio-Hetem, J., 2008, "The Canis Major Star Formation Region", Handbook of Star Forming Regions Vol. II, Astronomical Society of the Pacific, Bo Reipurth, ed.
Gregorio-Hetem, J.; Hetem, A.; Santos-Silva, T.; Fernandes, B., 2015, "Statistical fractal analysis of 25 young star clusters". Monthly Notices of the Royal Astronomical Society, v. 448, p. 2504-2513
Hetem, A., Lépine, J. R. D., 1993, A&A 270, 451
Jaffa, S. E., Whitworth, A. P., Lomax, O., 2017, MNRAS 466, 1082–1092
Parker, R. J., Dale, J. E., 2013, MNRAS, 432-986
Parker, R. J., Dale, J. E., 2015, MNRAS 451, 3664–3670
Parker, R. J., Andersen M., 2014, MNRAS, 441, 784
Portegies Zwart, S. F., McMillan, S. L. W., Gieles, M., 2010, ARA&A 48, 431
Reid, M. J. et al., 2009, ApJ, 700, 137
Sánchez, N., Alfaro, E. J., 2009, ApJ 696-2086
Saurin T. A., Bica E., Bonatto C., 2012, MNRAS, 421, 3206
Schmeja S., Klessen R. S., 2006, A&A, 449, 151

Boletim da Sociedade Astronômica Brasileira, **30**, no. 1, 128-131

Intermediate-mass black holes in dwarf galaxies at high redshifts

Paramita Barai & Elisabete M. de Gouveia Dal Pino

[1] Instituto de Astronomia, Geofísica e Ciências Atmosféricas (IAG-USP), Universidade de São Paulo. e-mail: paramita.barai@iag.usp.br

Abstract. Black holes are mostly observed to be of stellar-mass or supermassive. By natural extension, there should be a population of Intermediate-Mass Black Holes (IMBHs: with mass between 100 to $10^6 M_\odot$) in the Universe; which has started to being observed currently. An exciting claim has been made recently by Silk (2017): that there are IMBHs in essentially all old Dwarf Galaxies. Early feedback by IMBHs in gas-rich dwarf galaxies at $z = 5 - 8$, can potentially solve multiple dwarf galaxy problems (e.g. core-cusp, number) within the Λ-cold-dark-matter cosmology. Here we perform cosmological hydrodynamical simulations to test the case for IMBHs in Dwarf Galaxies. Our simulations employ the 3D TreePM SPH code GADGET-3, and include metal cooling, star formation, chemical enrichment, supernova feedback, AGN accretion and feedback. We are simulating small $(2\ \mathrm{Mpc})^3$ cosmological volumes with periodic boundary conditions, starting from $z = 100$. Black Holes of mass $10^2 - 10^3 M_\odot$ are seeded inside halos when they reach a mass of $10^6 - 10^7 M_\odot$. The black holes grow by accretion of gas from their surroundings and by merger with other black holes, and consequently eject feedback energy. By analyzing the simulation output in post-processing, we study the growth of the first IMBHs, and quantify the impact of IMBHs on star formation.

Resumo. Os buracos negros são observados principalmente como sendo de massa estelar ou supermassivos. Assim, naturalmente, deve haver no Universo uma população de Buracos Negros de massa-intermediária (IMBHs, Intermediate-Mass Black Holes) com massas entre 100 a $10^6 M_\odot$, que de fato tem sido observada atualmente. Uma importante afirmação foi realizada recentemente por Silk (2017): a de que IMBHs estão presentes, essencialmente, em todas as galáxias anãs mais velhas. O feedback inicial de IMBHs em galáxias anãs ricas em gás (em $z = 5 - 8$) pode potencialmente resolver múltiplos problemas de galáxias anãs (por exemplo, core-cusp, número) dentro da cosmologia ΛCDM. Neste trabalho, realizamos simulações hidrodinâmicas cosmológicas para testar a presença de IMBHs em galáxias anãs. Nossas simulações empregam o uso do código 3D TreePM SPH GADGET-3, e incluem o resfriamento de metais, a formação de estrelas, o enriquecimento químico, o feedback de supernovas, e a acreção e o feedback em AGNs. Estamos simulando pequenos volumes cosmológicos de $(2Mpc)^3$ com condições de fronteira periódicas, a partir de $z = 100$. Buracos Negros com massas entre $10^2 - 10^3 M_{odot}$ são semeados dentro de halos quando estes atingem uma massa entre $10^6 - 10^7 M_\odot$. Os buracos negros crescem pela acreção de gás ao redor deles e por fusão com outros buracos negros que, conseqüentemente, ejetam energia por feedback. Ao analisar os dados das simulações no pós-processamento, estudamos o crescimento das primeiras IMBHs e quantificamos o impacto da IMBH na formação de estrelas.

Keywords. cosmology: theory – black holes – dwarf galaxies

1. Introduction

Black holes usually come in two flavours: stellar-mass ($M_{\rm BH} \leq 10 M_\odot$), and supermassive ($M_{\rm BH} \geq 10^6 M_\odot$). Naturally, there should be a population of Intermediate-Mass Black Holes (IMBHs) of masses between $100 - 10^6 M_\odot$. Analogous to supermassive BHs producing AGN feedback, the IMBHs should also have feedback. Energy radiated by BHs affect their host galaxies, and drives galactic outflows. In this work we focus on negative BH feedback effects where star-formation is quenched.

AGN feedback mechanism has recently started to been observed in low-mass galaxies. Investigating the presence of AGN in nearby dwarf galaxies using mid-infrared emission, Marleau et al. (2017) identified 303 candidates, of which 91% were subsequently confirmed as AGN by other methods. The stellar masses of these galaxies are estimated to be between $10^6 - 10^9 M_\odot$; and the black hole masses in the range $10^3 - 10^6 M_\odot$. Penny et al. (2017) presented observational evidence for AGN feedback in a sample of 69 quenched low-mass galaxies ($M_\star < 4 \times 10^9 M_\odot$); including 6 galaxies showing signatures of an active AGN preventing ongoing star-formation.

The concordance ΛCDM cosmological scenario of galaxy formation presents multiple challenges in the dwarf galaxy mass range: e.g. core-cusp, number of DGs. Recently, Silk (2017) made an exciting claim that the presence of IMBHs at the centers of essentially all old Dwarf Galaxies (DGs) can potentially solve the problems. Early feedback from these IMBHs output energy and affect the host gas-rich DGs at $z = 5 - 8$. This early feedback can quench star-formation, reduce the number of DGs, and impact the density profile at DG centers. Dashyan et al. (2017) studied the same problem analytically, and compared AGN versus SN feedback. They find a critical halo mass below which the central AGN can drive gas out of the host halo. This negative feedback effect of AGN is found to be more efficient than SN in the most massive DGs, where SN is not able to expel the gas.

In this work, we investigate the scenario that IMBHs are present at the centers of all dwarf galaxies, by performing cosmological hydrodynamical simulations. Our goals are to (i) test if IMBHs would grow at DG centers, and (ii) quantify the impact on star formation.

2. Numerical Method

We use a modified version of the TreePM (particle mesh) — SPH (smoothed particle hydrodynamics) code GADGET-3 (Springel , 2005).

Radiative cooling and heating is incorporated from Wiersma, Schaye & Smith (2009). Eleven element species (H, He, C, Ca, O, N, Ne, Mg, S, Si, Fe) are tracked. Star-formation is implemented following the multiphase effective sub-resolution model by Springel & Hernquist (2003). Stellar evolution and chem-

ical enrichment are computed for the 11 elements, and kinetic feedback from supernovae is included (Tornatore et al. , 2007).

2.1. BH Accretion and Feedback

BHs are collisionless sink particles (of mass $M_{\rm BH}$) in our simulations. A BH (of initial mass $M_{\rm BHseed}$) is seeded at the center of each galaxy more massive than a total mass $M_{\rm HaloMin}$, which does not contain a BH already. We test different values of minimum halo mass and seed BH mass in the range: $M_{\rm HaloMin} = (10^6 - 10^7)M_\odot$, and $M_{\rm BHseed} = (10^2 - 10^3)M_\odot$.

Gas is considered to accrete onto a BH according to the Bondi-Hoyle-Lyttleton accretion rate $\dot{M}_{\rm Bondi}$ (Hoyle & Lyttleton , 1939; Bondi , 1952), and is limited to the Eddington rate ($\dot{M}_{\rm Edd}$),

$$\dot{M}_{\rm BH} = \min\left(\dot{M}_{\rm Bondi}, \dot{M}_{\rm Edd}\right), \tag{1}$$

$$\dot{M}_{\rm Bondi} = \alpha \frac{4\pi G^2 M_{\rm BH}^2 \rho}{(c_s^2 + v^2)^{3/2}}, \tag{2}$$

where G is the gravitational constant, ρ is the gas density, c_s is the sound speed, and v is the velocity of the BH relative to the gas. We set $\alpha = 100$ as a numerical boost factor (Springel, Di Matteo & Hernquist , 2005). The Eddington luminosity is used to express the Eddington mass accretion rate,

$$L_{\rm Edd} = \frac{4\pi G M_{\rm BH} m_p c}{\sigma_T} = \epsilon_r \dot{M}_{\rm Edd} c^2, \tag{3}$$

where m_p is the mass of a proton, c is the speed of light, and σ_T is the Thomson scattering cross-section for an electron. A fraction of the accretion rest-mass energy is coupled to the surrounding gas as feedback energy:

$$\dot{E}_{\rm feed} = \epsilon_f \epsilon_r \dot{M}_{\rm BH} c^2. \tag{4}$$

Here ϵ_r is the radiative efficiency, and ϵ_f is the feedback efficiency. We adopt the mean value for radiatively efficient accretion onto a Schwarzschild BH (Shakura & Sunyaev , 1973): $\epsilon_r = 0.1$.

The BH feedback energy is distributed in the *kinetic* form (introduced in Barai et al. 2014, 2016). Surrounding gas is driven outward at a velocity v_w and mass outflow rate $\dot{M}_w$. Given energy conservation,

$$\frac{1}{2}\dot{M}_w v_w^2 = \dot{E}_{\rm feed}, \tag{5}$$

and using Eq. (4), the outflow rate can be expressed in terms of the BH accretion rate,

$$\dot{M}_w = 2\epsilon_f \epsilon_r \dot{M}_{\rm BH} \frac{c^2}{v_w^2}. \tag{6}$$

We use the values: $\epsilon_f = 0.05$, and $v_w = 2000$ km/s.

The implementation in the GADGET-3 code involves computing physical quantities by kernel-weighted smoothing over gas particles neighboring each BH. The kernel size, or the BH smoothing length $h_{\rm BH}$, is determined at each timestep by implicit solution of the equation,

$$\frac{4}{3}\pi h_{\rm BH}^3 \rho_{\rm BH} = M_{\rm ngb}, \tag{7}$$

where $\rho_{\rm BH}$ is the kernel estimate of the gas density at the position of the BH, and $M_{\rm ngb}$ is the mass of 200 neighboring gas particles.

In particular, the kinetic feedback energy from a BH is distributed to the surrounding gas lying inside a bi-cone volume. The slant height of each cone is $h_{\rm BH}$, and the half-opening angle is 45°. The cone-axis direction is considered as fixed for each BH, which is randomly assigned during a BH seeding. Gas particles lying within the bi-cone are tracked, and their total mass $M_{\rm gas}^{\rm vicinity}$ is computed. The probability for i-th gas particle within the bi-cone to be kicked is calculated:

$$p_i = \frac{\dot{M}_w \Delta t}{M_{\rm gas}^{\rm vicinity}}, \tag{8}$$

where Δt is the timestep, and $\dot{M}_w$ is the mass outflow rate obtained from Eq. (6). A random number x_i, uniformly distributed in the interval [0, 1], is drawn and compared with p_i. For $x_i < p_i$, the gas particle is given an AGN wind kick, such that its new velocity becomes:

$$\boldsymbol{v}_{\rm new} = \boldsymbol{v}_{\rm old} + v_w \hat{\boldsymbol{n}}. \tag{9}$$

The kick direction $\hat{n}$ is set radially outward from the BH.

We incorporate a scheme for BH *pinning*, or *BH advection algorithm* (also done in e.g., Schaye et al. 2015). Each BH is repositioned manually at each time-step to the center (minimum gravitational potential location) of its host galaxy. This is done in SPH simulations to correct for dynamical movements of BH particles wandering away from galaxy centers by numerical effects.

We consider that central BHs merge when their host galaxies merge during hierarchical structure formation. When two BH particles come near such that the distance between them is smaller than the smoothing length of either one, and their relative velocity is below the local sound speed, they are allowed to merge to form a single BH (Di Matteo et al. , 2012).

2.2. Simulations

We perform cosmological hydrodynamical simulations of small-sized boxes to probe dwarf galaxies at high redshifts. The initial condition at $z = 100$ is generated using the MUSIC[1] software (Hahn & Abel , 2011). A concordance flat ΛCDM model is used, with the cosmological parameters (Planck Collaboration (2015), results XIII): $\Omega_{M,0} = 0.3089, \Omega_{\Lambda,0} = 0.6911, \Omega_{B,0} = 0.0486, H_0 = 67.74$ km s^{-1} Mpc^{-1}.

The size of the cubic cosmological volume is $(2h^{-1}$ Mpc$)^3$ comoving. Hence the total mass of matter (dark matter + baryons) in the box is $6.86 \times 10^{11} h^{-1} M_\odot$. We use 256^3 dark matter and 256^3 gas particles in the initial condition. The dark matter particle mass is $m_{\rm DM} = 3.44 \times 10^4 h^{-1} M_\odot$, and the gas particle mass is $m_{\rm gas} = 6.43 \times 10^3 h^{-1} M_\odot$. The gravitational softening length is set to $L_{\rm soft} = 0.1 h^{-1}$ kpc comoving. Starting from $z = 100$, the box is subsequently evolved up to $z = 4$, with periodic boundary conditions.

We execute a series of 10 simulations, with characteristics listed in Table 1. All the 10 runs incorporate metal cooling, chemical enrichment, SF and SN feedback. The first run has no BH included, while the latter 9 explore different models of BH feedback.

Table 1. Simulation runs and parameters.

Run name	BH present	Min. Halo Mass for BH Seeding, $M_{\rm HaloMin}[M_\odot]$	Seed BH Mass, $M_{\rm BHseed}[M_\odot]$	BH kinetic feedback kick velocity v_w (km/s)
SN	No	–	–	–
BHs2h1e6	Yes	$h^{-1} \times 10^6$	10^2	2000
BHs2h7e7	Yes	$5h^{-1} \times 10^7$	10^2	2000
BHs3h1e7	Yes	1×10^7	10^3	2000
BHs3h2e7	Yes	2×10^7	10^3	2000
BHs3h3e7	Yes	3×10^7	10^3	2000
BHs3h4e7	Yes	4×10^7	10^3	2000
BHs3h4e7v5	Yes	4×10^7	10^3	5000
BHs3h5e7	Yes	5×10^7	10^3	2000
BHs4h4e7	Yes	4×10^7	10^4	2000

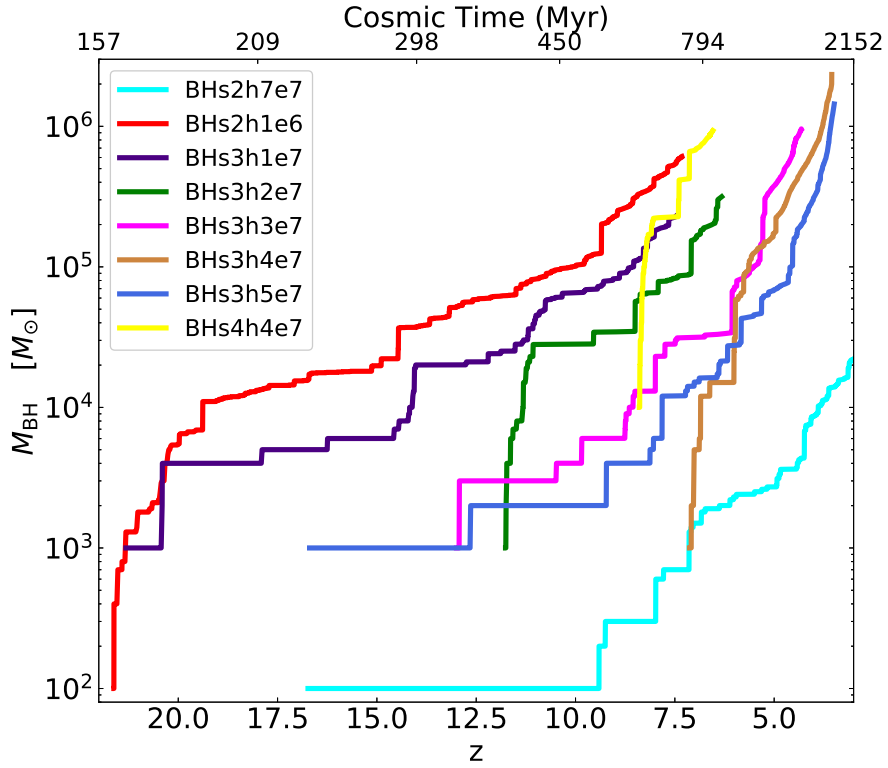

Figure 1. BH mass growth with redshift of the most-massive BH in each run. The different colours discriminate the runs.

3. Results and Discussion

3.1. Black Hole Accretion and Growth

We find that first BHs are seeded at different cosmic times depending on the value of minimum halo mass for BH seeding, $M_{\rm HaloMin}$. The seeding epoch varies between $z \sim 22$ to $z \sim 16$ in our simulations, when the first halos reach $M_{\rm halo} = h^{-1} \times 10^6 M_\odot$ to $M_{\rm halo} = 5 \times 10^7 M_\odot$. In the runs *BHs2h1e6*, *BHs2h7e7*, *BHs3h1e7* and *BHs3h5e7*, one of these first seeds grow to become the most-massive BH. However in runs *BHs3h2e7*, *BHs3h3e7*, *BHs3h4e7* and *BHs4h4e7*, the BH which becomes most-massive is seeded at later epochs $z \sim 11 - 7$. This variance in the seed epochs is because of the different BH growth modes.

The redshift evolution of the most-massive BH mass in the BH runs is plotted in Fig. 1. Each BH starts from an initial seed of $M_{\rm BH} = 10^2 M_\odot$ in the runs named *BHs2**, $10^3 M_\odot$ in the runs named *BHs3**, and $10^4 M_\odot$ in the runs named *BHs4**. The subsequent mass growth is due to merger with other BHs (revealed as vertical rises in $M_{\rm BH}$), and gas accretion (visualized as the positive-sloped regions of the $M_{\rm BH}$ versus z curve).

The final properties reached depends on the simulation. The most-massive BH, considering all the runs, has grown to $M_{\rm BH} = 2 \times 10^6 M_\odot$ at $z = 5$ in run *BHs3h4e7* (brown curve in Fig. 1).

3.2. Star Formation

Stars form in the simulation volume from cold dense gas. The Star Formation Rate Density (SFRD in units of $M_\odot yr^{-1} Mpc^{-3}$, counting stars forming in the whole simulation box) versus redshift of the simulation runs is displayed in Fig. 2. We take the *SN* run without BHs as the standard, and compare the *BH** runs with it to estimate the impact of BH feedback in star-formation.

The SFRD rises with time in the *SN* run (blue curve in Fig. 2) initially from $z \sim 15$, reaches a peak at $z \sim 4$ (the peak epoch

[1] MUSIC — Multi-scale Initial Conditions for Cosmological Simulations: https://bitbucket.org/ohahn/music

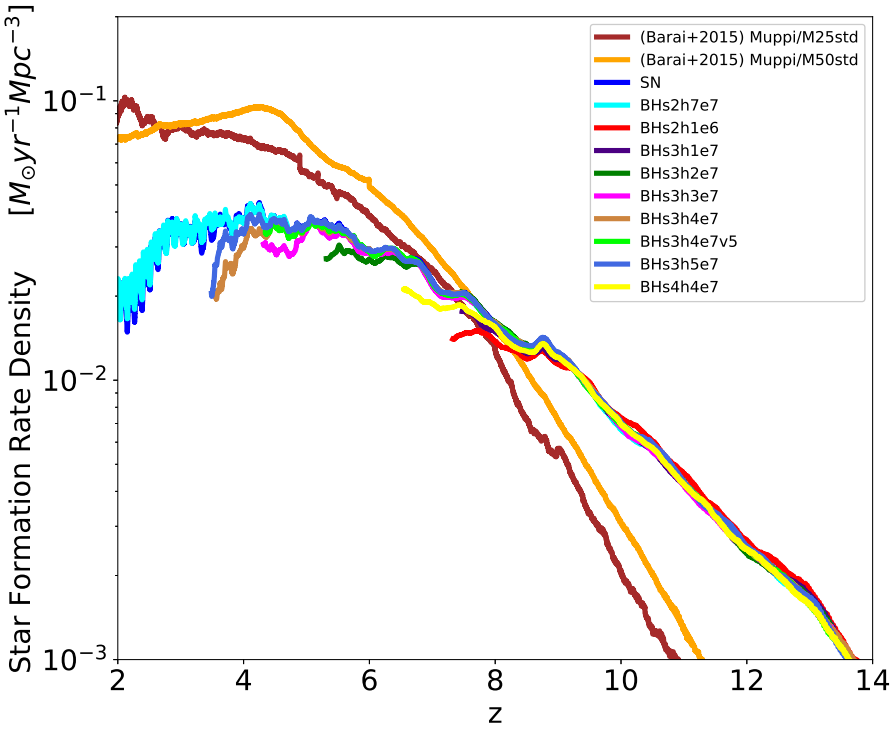

Figure 2. Total star formation rate density in simulation volume as a function of redshift.

of star-formation activity in the Universe), and decreases subsequently over $z \sim 4-2$. The SFRD in run *BHs2h7e7* (cyan curve) is almost similar to that in the run *SN*, because the BHs are too small there to generate enough feedback. A similar outcome happens in all the other runs at $z \geq 8$, when the BHs are too small.

The star-formation mostly occurs over an extended region at galaxy centers, where cosmic large-scale-structure gas inflows and cools. The presence of a BH quenches star formation by accreting some gas in, ejecting some gas out of the halo as outflows, and/or heating the gas.

The models suppress SF substantially from $z \sim 8$ onwards, when the BHs have grown massive and generate larger feedback energy. Thus, we find that BHs need to grow to $M_{\rm BH} > 10^5 M_\odot$, in order to suppress star-formation, even in these dwarf galaxies. BH feedback causes a reduction of SFR up to 5 times in the different runs.

The red curve (run *BHs2h1e6*) already quenches SF as early as $z \sim 8$. This is because the BH has already grown to $M_{\rm BH} \sim 5 \times 10^5 M_\odot$ at that epoch, more massive than all the other runs. As another example, the brown (run *BHs3h4e7*) and royal-blue (run *BHs3h5e7*) curves quench SF from $z \sim 4.5$ to $z \sim 3.5$. This is the epoch when the BH masses in these runs increase from $M_{\rm BH} = 10^5 M_\odot$ to $M_{\rm BH} = 10^6 M_\odot$.

4. Conclusions

We conclude that: (i) IMBHs at DG centers grow from $10^2 - 10^3 M_\odot$ to $10^5 - 10^6 M_\odot$ by $z \sim 4$ in a cosmological environment. These IMBHs in DGs can become the seeds of supermassive BHs (which grows to $M_{\rm BH} \sim 10^9 M_\odot$) in massive galaxies. (ii) Star formation is quenched when the BHs have grown to $M_{\rm BH} > 10^5 M_\odot$. We find a positive correlation between the mass growth BHs and the quenching of SF.

Acknowledgements. We are most grateful to Volker Springel for allowing us to use the GADGET-3 code. This work is supported by FAPESP (Jovem Pesquisador grant number 2016/01355-5). The numerical simulations were performed in the computing cluster GAPAE of the High Energy and Plasma Astrophysics group of IAG-USP.

References

Barai, P. et al. 2013, MNRAS, 430, 3213
Barai, P., Viel, M., Murante, G., Gaspari, M. & Borgani, S. 2014, MNRAS, 437, 1456
Barai, P., Monaco, P., Murante, G., Ragagnin, A. & Viel, M. 2015, MNRAS, 447, 266
Barai, P., Murante, G., Borgani, S., Gaspari, M., Granato, G. L., Monaco, P. & Ragone-Figueroa, C. 2016, MNRAS, 461, 1548
Bondi, H. 1952, MNRAS, 112, 195
Dashyan, G., Silk, J., Mamon, G. A., Dubois, Y. & Hartwig, T. 2017, eprint arXiv:1710.05900
Di Matteo, T., Khandai, N., DeGraf, C., Feng, Y., Croft, R. A. C., Lopez, J. & Springel, V. 2012, ApJ, 745, L29
Hahn, O. & Abel, T. 2011, MNRAS, 415, 2101
Hoyle, F. & Lyttleton, R. A. 1939, Proc. Cam. Phil. Soc., 35, 405
Marleau, F. R., Clancy, D., Habas, R. & Bianconi, M. 2017, A&A, 602, A28
Martin, C. L. 1999, ApJ, 513, 156
Penny, S. J. et al. 2017, submitted to MNRAS, eprint arXiv:1710.07568
Planck Collaboration; Ade, P. A. R. et al. 2016, A&A, 594, A13
Schaye, J. et al. 2015, MNRAS, 446, 521
Shakura, N. I. & Sunyaev, R. A. 1973, A&A, 24, 337
Silk, J. 2017, ApJ, 839, L13
Springel, V. & Hernquist, L. 2003, MNRAS, 339, 289
Springel, V. 2005, MNRAS, 364, 1105
Springel, V., Di Matteo, T. & Hernquist, L. 2005, MNRAS, 361, 776
Tornatore, L., Borgani, S., Dolag, K. & Matteucci, F. 2007, MNRAS, 382, 1050
Wiersma, R. P. C., Schaye, J. & Smith, B. D. 2009, MNRAS, 393, 99

Boletim da Sociedade Astronômica Brasileira, **30**, no. 1, 132-133

Chemical analysis of eight giant stars of the globular cluster NGC 6366

A. A. Puls & A. Alves Brito

[1] Instituto de Física, Universidade Federal do Rio Grande do Sul. e-mail: puls.arthur@gmail.com

Abstract. The metal-rich Galactic globular cluster NGC 6366 is the fifth closest to the Sun. We present a detailed chemical analysis of eight giant stars of NGC 6366, using high resolution and high quality spectra obtained at the VLT (8.2 m) and CFHT (3.6 m) telescopes. We attempted to characterize its chemistry and to search for evidence of multiple stellar populations. The atmospheric parameters were derived using the method of excitation and ionization equilibrium of Fe I and Fe II lines. None of the measured elements presents star-to-star variation greater than the uncertainties. We determined a mean [Fe/H] = −0.60 ± 0.03 for NGC 6366. The Na-O anticorrelation extension is short and no star-to-star variation in Al is found. The presence of second generation stars is not evident in NGC 6366.

Resumo. O aglomerado globular rico em metais NGC 6366 é o quinto mais próximo do Sol. Nós apresentamos uma análise química detalhada de oito estrelas gigantes de NGC 6366, usando espectros de alta resolução e alta qualidade obtidos nos telescópios VLT (8.2 m) e CFHT (3.6 m). Tentamos caracterizar sua composição química e procuramos por evidências de múltiplas populações estelares. Os parâmetros atmosféricos foram derivados usando o método de equilíbrio de ionização e excitação de linhas de Fe I e Fe II. Nenhum dos elementos medidos apresenta variação estrela-a-estrela maior que as incertezas. Nós determinamos o [Fe/H] médio igual a −0.60 ± 0.03 para NGC 6366. A extensão da anticorrelação Na-O é curta e nenhuma variação em Al foi encontrada. A presença de estrelas de segunda geração não é evidente em NGC 6366.

Keywords. stars: abundances – Galaxy: abundances – globular clusters: individual: NGC 6366

1. Introduction

Globular clusters (GCs) were, for many years, viewed as the prototypes of simple stellar populations, that is, all their stars would have the same age and metallicity in a first approximation. As of today, the consensus is that some of the light elements studied in GCs present star-to-star abundance variations. In this context, NGC 6366, one of the least massive Galactic GCs, is an interesting object to be investigated. It is the fifth closest GC according to the catalogue of Harris (1996, 2010 edition, 2010 edition), and its distance from the Sun is 3.5 kpc. Also, this GC still had no measurements based on high resolution spectra of chemical elements widely studied in the context of Galactic and GC chemical evolution, such as Al and Eu.

2. Data and Method

Our sample consists of eight bright giant stars observed with UVES@VLT (Dekker et al. 2000) and ESPaDOnS@CFHT, the former for a study of metal-rich Galactic GCs (Feltzing et al. 2009). ESPaDOnS data are reduced through the software Upena/Libre-Esprit pipeline, provided by the instrument team (Donati et al. 1997). The spectra have high resolution (R ≥ 40000) and high signal-to-noise ratio (S/N ≥ 60).

The stellar atmospheric parameters – effective temperature (T_{eff}), surface gravity (log g), metallicity ([Fe/H]), and microturbulent velocity (ξ_t), were obtained by photometric and spectroscopic methods.

The spectroscopic stellar parameters for each object were determined by traditional methods. Equivalent widths (EW) of Fe I and Fe II lines were measured by hand using IRAF *splot* task. For each star, a LTE 1D plane-parallel atmospheric model was created, and used as input in the *abfind* driver of MOOG. The effective temperature (T_{eff}) was found by excitation equilibrium of Fe I lines. Microturbulent velocity ξ_t was found removing trends between abundance of Fe I lines and reduced EW. The surface gravity log g was found by ionization equilibrium of Fe I and Fe II. Finally, the metallicity [Fe/H] was determined by equalizing the value used in the model and the value given by MOOG in the output. The adopted stellar parameters were found when all the conditions were satisfied simultaneously.

To obtain the abundance of elements with atomic number Z ≤ 28 we adopted EW measurements, except for Mn. For heavier elements and Mn, the spectral synthesis method was used.

3. Results

The mean heliocentric radial velocity for our sample is −121.2 ± 0.7 km s^{-1} (σ = 2.0 km s^{-1}), without outliers. The result is consistent with those found in the literature. From radial velocities, we assume cluster membership for all the eight stars.

The values found for T_{eff}, microturbulence and log g are typical for giant stars. As for metallicities, we found a mean [Fe/H] = −0.60 (σ = 0.08). The mean metallicity is consistent with that found by Johnson et al. (2016) and studies based upon low-resolution data.

As for the chemical abundances, the Na-O anti-correlation extension is short and no star-to-star variation in Al is found. The presence of second generation stars is not evident in NGC 6366. Among the species measured, no element present star-to-star abundance variations greater than mean uncertainties.

4. Conclusions

Our analysis confirms NGC 6366 as a metal-rich GC, with no internal [Fe/H] variation. None of the elements measured spread beyond uncertainties in NGC 6366. Being considered a GC with halo kinematics, NGC 6366 has a chemical abundance pattern which can be consistent with both the bulge and the α-rich, metal-rich halo. We have not found any unambiguously second generation star. It can be assumed that our entire sample, or at

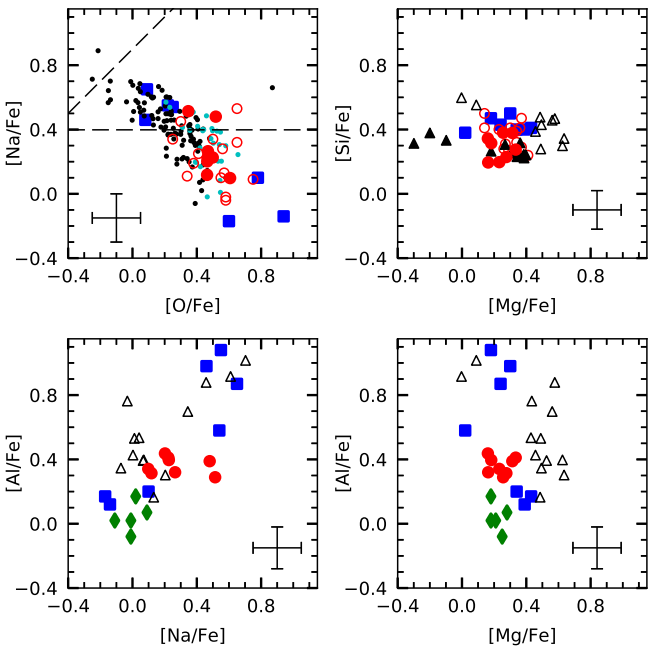

Figure 1. [X/Fe] abundance ratios for light elements. *Red filled circles*: this work. *Red open circles*: NGC 6366 from Johnson et al. (2016). *Blue squares*: NGC 6266 (Yong et al. 2014). *Green diamonds*: NGC 6558 (Barbuy et al. 2007). *Black dots*: 47 Tuc (Alves-Brito et al. 2005; Carretta et al. 2009a). *Cyan dots*: M 71 (Carretta et al. 2009a) *Black filled triangles*: NGC 2808 and *Black open triangles*: NGC 7078 (Carretta et al. 2009b) The error bars are typical for this work. The dashed lines are the borders between P, I and E components defined in Carretta et al. (2009a).

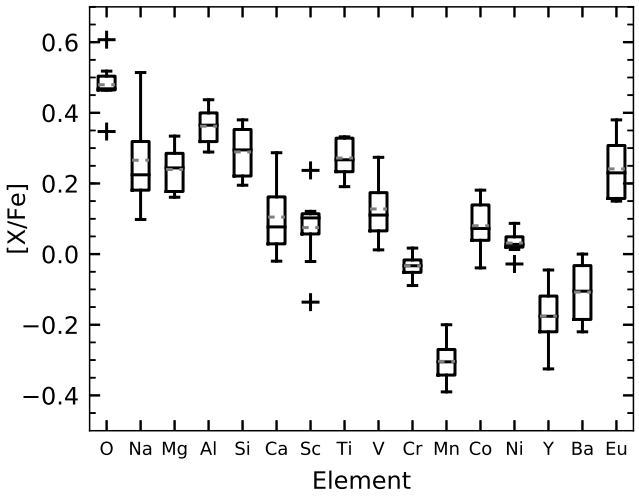

Figure 2. Star-to-star abundance spread for all elements measured in this work, except Fe. *Boxes*: the interquartile ranges (IQR). *Whiskers*: data inside 1.5*IQR limits. *Black horizontal lines*: medians. *Grey dashed lines*: means. *Crosses*: outliers.

least most of it, is from the first generation. If NGC 6366 contains a simple stellar population, which is possibly the case, it enters the list of Galactic GCs without detection of multiple populations, adding evidence that, at least in the Galaxy, such phenomenon occurs only in GCs brighter than $M_V \approx -7$.

Acknowledgements. Partial financial support for this research comes from BIC-UFRGS institutional program and CNPq. IRAF is distributed by the National Optical Astronomy Observatories, which are operated by the Association of Universities for Research in Astronomy, Inc., under cooperative agreement with the National Science Foundation. Based on observations collected at the European Organisation for Astronomical Research in the Southern Hemisphere under ESO programme 69.B-0467. Based on observations obtained at the Canada-France-Hawaii Telescope (CFHT) which is operated by the National Research Council of Canada, the Institut National des Sciences de l'Univers of the Centre National de la Recherche Scientique of France, and the University of Hawaii.

References

Alves-Brito, A., Barbuy, B., Ortolani, et al., 2005, A&A, 435, 657A
Barbuy, B., Zoccali, M., Ortolani, et al., 2007, AJ, 134, 1613B
Carretta, E., Bragaglia, A., Gratton, R. G., et al., 2009a, A&A, 505, 117C
Carretta, E., Bragaglia, A., Gratton, R. and Lucatello, S., 2009b, A&A, 505, 139C
Dekker, H., D'Odorico, S., Kaufer, A., et al., 2000, Proc. SPIE Vol. 4008, p. 534-545
Donati, J.-F., Semel, M., Carter, B. D., et al., 1997, MNRAS, 291, 658D
Feltzing, S., Primas, F. and Johnson, R. A., 2009, A&A, 493, 913F
Harris, W. E.,1996, AJ, 112, 1487
Johnson, C. I., Caldwell, N., Rich, R. M., et al., 2016, AJ, 152, 21J
Yong, D., Alves Brito, A., Da Costa, G. S., et al., 2014, MNRAS, 439, 2638Y

Boletim da Sociedade Astronômica Brasileira, **30**, no. 1, 134-135

Multiple stellar populations from HST UV Legacy Survey

In the moderately metal-rich Bulge globular clusters NGC 6304, NGC 6624 and NGC 6637

R. A. P. Oliveira[1], B. Barbuy[1], S. O. Souza[1], L. Kerber[1] & G. Piotto[2]

[1] Instituto de Astronomia, Geofísica e Ciências Atmosféricas (IAG - USP), São Paulo, Brasil
e-mail: rap.oliveira@usp.br, b.barbuy@iag.usp.br, stefano.souza@usp.br, lekerber@gmail.com
[2] Dipartimento di Fisica e Astronomia "Galileo Galilei", Università di Padova, Padua, Italy
e-mail: giampaolo.piotto@unipd.it

Abstract. In the last decade, the classical paradigm of the formation of globular clusters (GCs) as a single burst of star formation has been challenged by the discovery of multiple stellar population patterns, in a surprising variety and complexity. In particular, the UV-initiative Hubble project GO-13297 obtained photometric data for 57 GCs with the UV/blue WFC3/UVIS filters F275W, F336W and F438W. Combined with previous optical HST/ACS data in the filters F606W and F814W, it produces an unprecedent photometric database for GCs. NGC 6304, NGC 6624 and NGC 6637 have been selected from their location in the Galactic bulge, and metallicity values of $-0.65 \lesssim$ [Fe/H] $\lesssim -0.40$. The data analysis involves elaboration of multiband color-magnitude diagrams (CMDs), identification of the different generations of stars, application of statistical isochrone fitting techniques, in order to accurately determine distances, ages, reddening, fraction of stars in the first and second generations, and even variations in He, C, N and O abundances.

Resumo. Na última década, o paradigma clássico da formação dos GCs a partir de um único *burst* de formação estelar tem sido desafiado pela descoberta de padrões de múltiplas populações estelares, em uma variedade e complexidade surpreendentes. Em particular, o projeto do Hubble GO-13297 obteve dados fotométricos para 57 GCs com os filtros UV/azul F275W, F336W e F438W, da WFC3/UVIS. Combinados com dados anteriores no óptico, nos filtros F606W e F814W, produziu-se uma importante base de dados fotométricos para GCs. NGC 6304, NGC 6624 e NGC 6637 foram selecionados pela sua localização no bojo Galáctico e valores de metalicidade em $-0.65 \lesssim$ [Fe/H] $\lesssim -0.40$. A análise dos dados consiste na elaboração de CMDs multibandas, identificação das gerações de estrelas, aplicação de técnicas estatísticas de ajuste de isócronas, para a determinação precisa das distâncias, idades, avermelhamento, frações de estrelas na primeira e segunda gerações, e até mesmo variações nas abundâncias de He, C, N e O.

Keywords. globular clusters: individual: NGC 6304, NGC 6624, NGC 6637 – Hertzsprung-Russell and C-M diagrams

1. Introduction

Recent discoveries of multiple stellar populations (MPs) in GCs challenge the classical paradigm that they host a single stellar population, i.e., that their stars are homogeneous both in age and chemical composition. Since the pioneer work from Bedin et al. (2004), detecting two main sequences in the CMD of ω Cen, the MPs have been broadly explored, by photometric and spectroscopic means.

Metal-rich GCs are usually associated with the Galactic bulge, whereas the metal-poor ones ([Fe/H]<-1.5) are usually associated with the Galactic halo. These structures are thought to be formed in an initial collapse in the Galaxy, in slightly different timescales.

More precisely, the Bulge formed within a timescale of 0.3–0.5 Gyr, and its metallicity distribution function shows a bimodal distribution, with a classical metal-poor population and also a metal-rich population, probably a result of star formation induced by the Galactic bar. Considering only bulge GCs, there is a metallicity peak at [Fe/H] ~ -1.0 and a secondary peak at [Fe/H] ~ -0.5 (Bica et al. 2016).

The clusters in this sample present metallicity values of $-0.65 \lesssim$ [Fe/H] $\lesssim -0.40$, corresponding to this secondary peak. NGC 6304, NGC 6624 and NGC 6637 (M 69) are located in the Galactic bulge, with galactocentric distances lower than 2.3 kpc.

2. Data: GO-13297 HST program

A clear chemical enrichment is observed between the generations of stars: the first generation (1G) have compositions similar to the protogalactic cloud, and the following ones (2G, ...) can be depleted in C and O, and enhanced in N, Na, Al and He. In this scenario, the major candidate producers of 2G material are: supermassive stars, massive interacting binaries, fast-rotating massive stars, AGB and super-AGB stars (Renzini et al. 2015).

The data analyzed is part of the HST UV Legacy Survey project GO-13297, led by Giampaolo Piotto, intended to characterize the MPs, combining UV and optical filters. These UV filters, namely F275W, F336W and F438W, are very sensitive to C, N and O abundance variations, because the filter's bandpasses include the molecular bands of OH, NH, CN and CH (see Piotto et al. 2015, their Fig. 1).

3. Methods

3.1. Multiple stellar populations

This method was developed by Milone et al. (2017) and efficiently separate the MPs. It uses a CMD combination that maximizes the RGB broadening, and shows the horizontal distribution of stars, based on two envelopes, that limit the 4^{th} and 96^{th} percentiles on each magnitude bin (Fig. 1).

The first generation is expected to be C/O-rich and N-poor, hence faint in F275W/F438W and bright in F336W, whereas the

2G is expected to be the contrary. Defining a so-called *pseudo-color*, which adequately relates these three filters, we can maximize the separation 1G/2G:

$$C_{F275W,F336W,F438W} = (m_{F275W} - m_{F336W}) - (m_{F336W} - m_{F438W}) \quad (1)$$

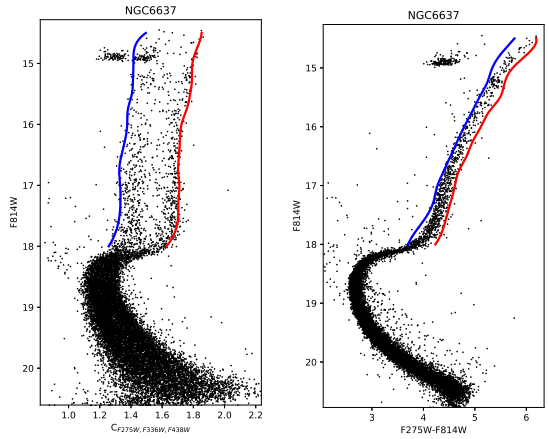

Figure 1. F814W vs. F275W-F814W or $C_{F275W,F336W,F438W}$ CMDs of NGC 6637. Red and blue solid lines are the 1G/2G envelopes.

To quantify the horizontal separation in RGB stars, the envelopes are verticalized computing for each star:

$$\Delta_{F275W,F814W} = W_{F275W,F814W} \cdot \frac{X_{red} - X}{X_{blue} - X_{red}} \quad (2)$$

$$\Delta_{C\,F275W,F336W,F438W} = W_C \cdot \frac{Y_{red} - Y}{Y_{blue} - Y_{red}} \quad (3)$$

where $X = (m_{F275W} - m_{F814W})$, Y is the pseudo-color and W are the RGB widths. The final plot ($\Delta_{C\,F275W,F336W,F438W}$ vs. $\Delta_{F275W,F814W}$), called *chromosome map* (CMap), is shown in Fig. 2 (Hess diagram and histogram rotated by 18°) .

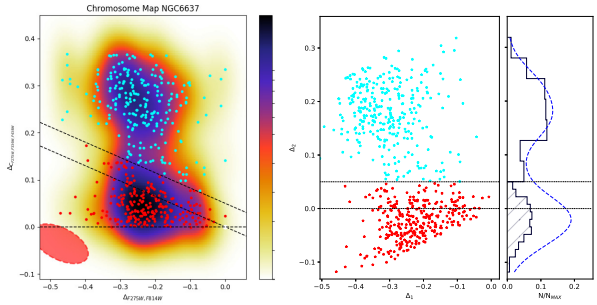

Figure 2. *(Left:)* CMap and the density map, showing two wells. *(Right:)* CMap rotated by 18° and its associated histogram.

3.2. Isochrone fitting

Our group developed a statistical tool in *Python*, based on the maximum likelihood considering the inserted ranges of the free parameters ([Fe/H], Y, Age, $E(B-V)$, $(m-M)_0$), in order to carry out the isochrone fitting, using BaSTI models (Pietrinferni et al. 2006). The likelihood function compares the magnitudes and colors of the observational and theoretical points, through:

$$L \propto \exp\left[-\frac{(m_{obs} - m_{iso})^2}{\sigma_{m,obs}}\right] \cdot \exp\left[-\frac{(C_{obs} - C_{iso})^2}{\sigma_{C,obs}}\right] \quad (4)$$

L_{total} (for each set of free parameters) is given by the product of all L's, or by $\sum \ln(L_i)$, and the maximim likelihood value corresponds to the best possible solution. In addition, the Markov chain Monte Carlo (MCMC) method is applied to analyze the distribution of solutions and derive the uncertainties (see S. O. Souza et al. in this volume).

4. Results (Isochrone fitting and uncertainties)

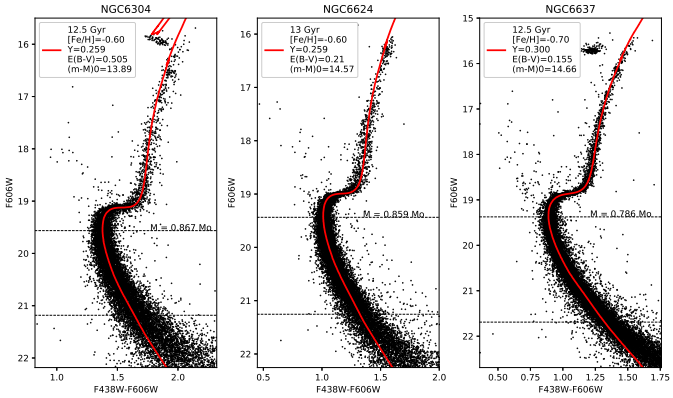

Figure 3. Best fits for NGC 6304, NGC 6624 and NGC 6637.

Table 1. Results from maximum likelihood and MCMC.

NGC	[Fe/H]	Y	Age	E(B-V)	$(m-M)_0$
6304	-0.60	0.259	$12.03^{+0.41}_{-0.29}$	$0.51^{+0.01}_{-0.01}$	$13.93^{+0.02}_{-0.04}$
6624	-0.60	0.259	$12.57^{+0.42}_{-0.26}$	$0.21^{+0.01}_{-0.01}$	$14.61^{+0.01}_{-0.03}$
6637	-0.70	0.300	$12.31^{+0.59}_{-0.45}$	$0.16^{+0.01}_{-0.01}$	$14.68^{+0.04}_{-0.03}$

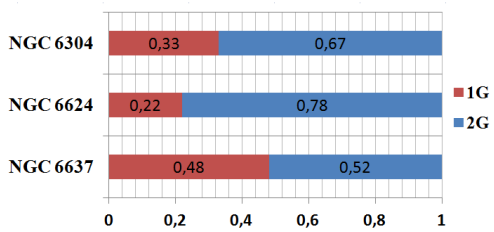

Figure 4. Results for the fractions of 1G and 2G stars.

5. Conclusions and perspectives

The results relative to MPs agree very well with Milone et al. (2017), and the results from isochrones fitting were self-consistent and compatible with the literature. Our solutions indicate a primordial helium for NGC 6304 and NGC 6624, but a helium enhancement for M 69. Additional constraints to He abundances and distances will be provided by the study of RR Lyrae. We are also improving a tool to combine the study of MPs and the statistical isochrone fitting.

Acknowledgements. The authors acknowledge support from CAPES, CNPq and FAPESP. Support for *Hubble Space Telescope* proposal GO-13297 was provided by NASA through grants from STScI.

References

Bedin, L. R., Piotto, G., Anderson, J. et al. 2004, ApJ, 605, L125
Bica, E., Ortolani, S. & Barbuy, B. 2016, PASA, 33, 28
Milone, A. P., Piotto, G., Renzini, A. et al. 2017, MNRAS, 464, 3636
Pietrinferni, A., Cassisi, S., Salaris, M. et al. 2006, ApJ, 642, 797
Piotto, G., Milone, A. P., Bedin, L. R. et al. 2015, AJ, 149, 91
Renzini, A., D'Antona, F., Cassisi, S. et al. 2015, MNRAS, 454, 4197

Boletim da Sociedade Astronômica Brasileira, **30**, no. 1, 136-137

Spectroscopy analysis of NGC 1952, NGC 2024 and NGC 6210

C. A. Rosa[1], M. Emilio[1], L. Andrade[1] & J. Armstrong[2]

[1] Universidade Estadual de Ponta Grossa; e-mail: carolalixandre@gmail.com
[2] Institute for Astronomy, University of Hawaii

Abstract. In this work, we present the study of spectra in the visible region of nebulae NGC 1952 and NGC 2024 using the Perkin-Elmer Telescope (1.6m) at the Observaório Astronômico do Pico dos Dias (OPD/LNA). The observations were done in March 2017. Spectral data were also obtained in visible and near-infrared regions of the nebula NGC 6210 with the Faulkes Telescope North (2m). Data were reduced using the software Image Reduction and Analysis Facility (IRAF). We identified atomic emission lines for argon, oxygen, carbon, iron, hydrogen, nitrogen, sulfur, neon and helium.

Resumo. Neste trabalho, apresentamos análises de espectros na região do visível das nebulosas NGC 1952 e NGC 2024, obtidos com o telescópio Perkin-Elmer (1.6m) no Observatório Astronômico do Pico dos Dias (OPD/LNA) em março de 2017. Dados espectrais também foram obtidos na região do visível e do infravermelho próximo da nebulosa NGC 6210 com o Faulkes Telescope North (2m). Os dados foram reduzidos com o software Image Reduction and Analysis Facility (IRAF). Nós identificamos linhas de emissão atômica para argônio, oxigênio, carbono, ferro, hidrogênio, nitrogênio, enxofre, neônio e hélio.

Keywords. Astrobiology– (ISM:) planetary nebulae: general – Line: identification

1. Introduction

We know how stars, nebulae, planetary atmospheres are made of due to spectroscopy. The known life forms in our planet are mainly constituted of carbon, hydrogen, oxygen, nitrogen and sulfur (CHONS) atoms. The presence of those elements in the interstellar medium as well as molecules is interesting for astrobiology, the science uniting astronomy and biology. Molecules consisted of CHONS atoms were already identified in nebulae, therefore the chemical composition of these objects is an interesting subject for study.

2. Methods

Spectral data of NGC 1952 (Crab Nebula) and NGC 2024 (Flame Nebula) were obtained at the Observatório Astronômico do Pico dos Dias (Laboratório Nacional de Astrofísica), using the Perkin-Elmer telescope (1.6m) coupled to the Cassegrain spectroscope, with a diffraction grid of 1200 *l*/mm and signal-to-noise ratio of ∼100. NGC 1952 was observed in two central wavelenghts, 4500Å (blue region) and 6563Å (red region), and NGC 2024 only in the red region.

We also collected spectral data for the planetary nebula NGC 6210 in the ultraviolet to infrared regions using the Faulkes Telescope North (2m) from the Las Cumbres Observatory (Hawaii, USA). The spectral profiles were processed and reduced using the software Image Reduction and Analysis Facility (IRAF).

3. Results and Discussion

We observed atomic emission lines in all of the nebulae spectra obtained. Using the *Catalog of Emission Lines in Astrophysical Objects* (Meinel, Avini & Stockton 1969) and the *Planetary Nebula Emission Lines Catalog* (Kaler, Shaw & Browning 1997) it was possible to identify the chemical element corresponding to each emission line.

3.1. NGC 1952

Atomic emission lines were identified in NGC 1952 for argon (4047.61Å) and oxygen (4358.4Å; 4503.88Å; 4696.34Å) in the blue region of the spectrum (figure 1).

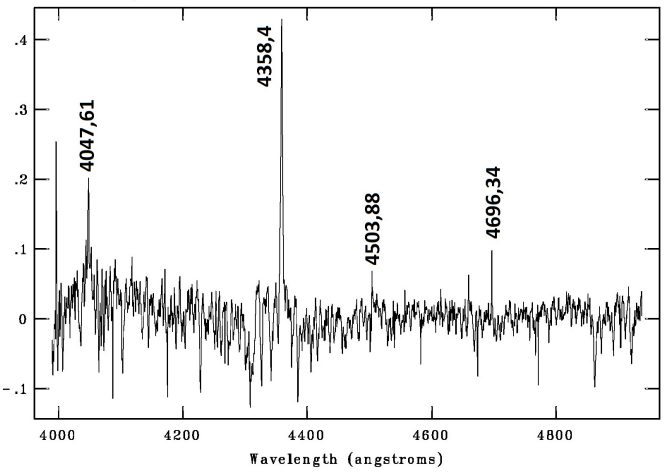

Figure 1. Spectrum of NGC 1952 (blue region).

We identified emission lines for oxygen (6299.54Å; 6362.99Å), carbon (6162.62Å), iron (6496.46Å), hydrogen (6563.97Å) and nitrogen (6575.98Å) in the red region (figure 2).

The literature also shows the presence of the same chemical elements identified in these spectra (Fesen & Kirshner 1977).

3.2. NGC 2024

We identified atomic emission lines for oxygen (6299.55Å), nitrogen (6548.74Å; 6583.99Å) hydrogen (6563.39Å) and sulfur (6717.55Å; 6731.61Å) in the red region of NGC 2024 (figure 3).

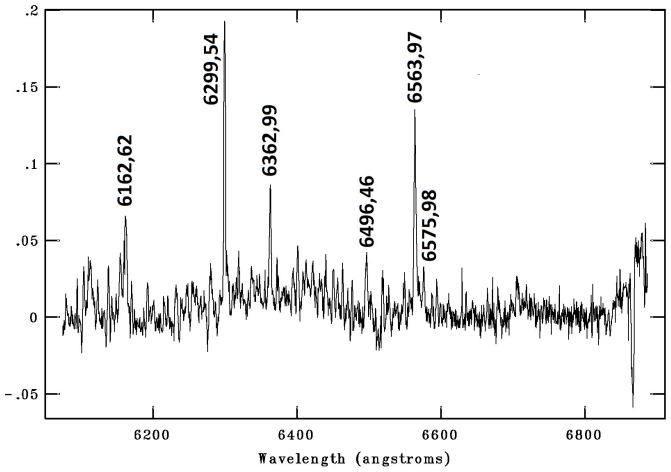

Figure 2. Spectrum of NGC 1952 (red region).

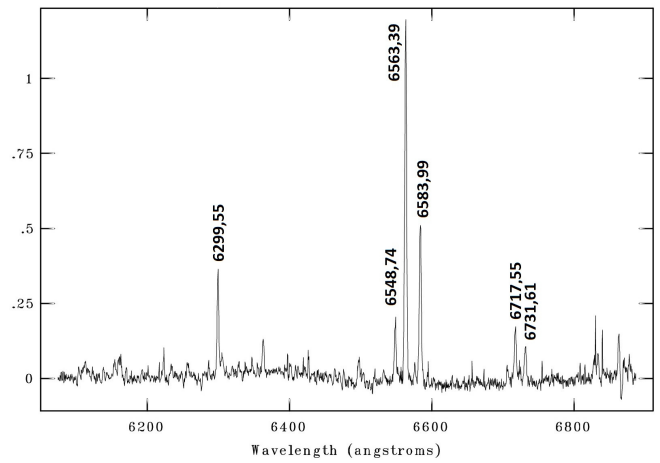

Figure 3. Spectrum of NGC 2024 (red region).

The tables found in the literature also points to the presence of these atomic emission lines (Balick 1976).

3.3. NGC 6210

We identified atomic emission lines for neon (3873.24Å; 3972.59Å), hydrogen (4106.63Å; 4343.68Å; 4865.32Å), oxygen (4963.42Å; 5011.16Å) in spectra on ultraviolet/blue region of NGC 6210 (figure 4). We also identified helium (5871.75Å), hydrogen (6557.94Å), argon (7131.01Å) and sulfur (9065.04Å; 9527.16Å) in the red/infrared regions of NGC 6210 (figure 5).

Pottasch, Salas & Roelling (2009) also found the same emission lines identified in this nebula.

4. Conclusions

We analyzed the spectroscopic data obtained for nebulae NGC 1952, NGC 2024 and NGC 6210 in OPD/LNA and the Las Cumbres Observatory. We identified emission lines in all of them. The essential atoms elements for life is present. Among them, carbon, hydrogen, oxygen, nitrogen and sulfur (CHONS).

Acknowledgements. This work is based on observations made at the Observatório do Pico dos Dias / LNA.

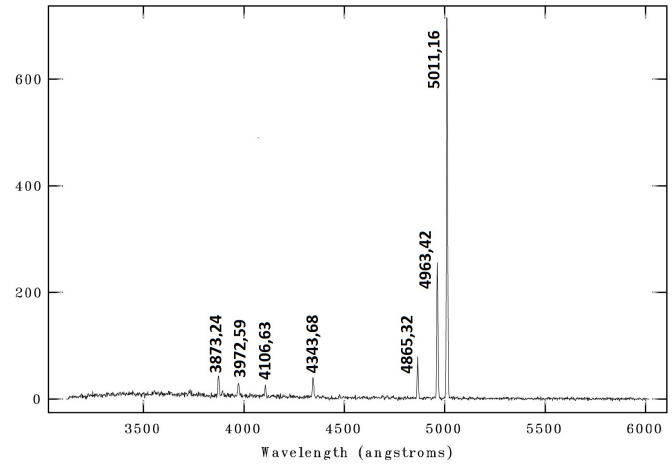

Figure 4. Spectrum of NGC 6210 (UV/blue region).

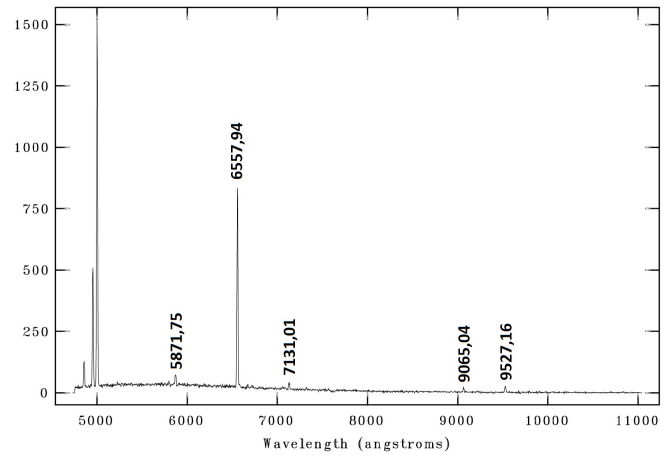

Figure 5. Spectrum of NGC 6210 (red/IR region).

References

Balick, B. 1976, The Astrophysical Journal, 208, 75.
Fesen, R. A.; Kirshner, R. P. 1977, Publications of Astronomical Society of the Pacific, 90, 32.
Kaler, J. B.; Shaw, R. A.; Browning, L. 1997, Publications of the Astronomical Society of the Pacific, 109, 289.
Meinel, A. B.; Avini, A. F.; Stockton, M. W. 1969, in Catalog of emission lines in Astrophysical Objects. Optical Sciences Center (Tucson: Arizona), 1.
Pottasch S. R.; Salas B.; Roelling T. L. 2009, Astronomy & Astrophysics, 499, 249.

Boletim da Sociedade Astronômica Brasileira, **30**, no. 1, 138-141

Stellar ages: combination of the Kinematical and Isochronal methods

F. Almeida-Fernandes[1] & H. J. Rocha-Pinto[2]

[1] Observatório do Valongo, Universidade Federal do Rio de Janeiro
e-mail: felipe11@astro.ufrj.br,felipefer42@gmail.com

Abstract. We have developed a method to estimate a probability density function (pdf) for the age of a star based on its spatial velocity. The fundaments of the method is the formalism of the velocity ellipsoid and the increase of the dispersion of stellar velocities with age. We show how this method can be used to infer properties of interest to study the evolution of the Galaxy, like the star formation history and the age-metallicity relation. We explain how the age pdf obtained by the kinematical method can be used as a prior pdf for the isochronal method, resulting in better constrained ages. In order to implement the isochronal method, we developed a python library to perform the calculations involving isochrones and evolutionary tracks: the EITApy code. To quantify the benefits of combining both methods, we simulated a sample of 10000 stars with known ages and analysed the results for different regions of the HR diagram. We show that for some groups, age uncertainties are 20% smaller. As an application of the method, we obtained the ages for the stars of the S4N survey and obtained its kinematical parameters using the orbital integrator galpy. The next step is to investigate how the relations between compositions and kinematical parameters with age can be explained in the context of the chemodynamical evolution of the Galaxy.

Resumo. Desenvolvemos um método para estimar uma função de densidade de probabilidade (pdf) para a idade de uma estrela com base em sua velocidade espacial. O método se fundamenta no formalismo do elipsoide de velocidades e no aumento da dispersão de velocidades com a idade. Mostramos que o método pode ser utilizado para inferir propriedades de interesse para o estudo da evolução da Galáxia, como o histórico de formação estelar e a relação idade–metalicidade. Descrevemos como a pdf de idade obtida pelo método cinemático pode ser utilizada como distribuição prior no método isocronal, resultando em idades melhor definidas. Para aplicar o método isocronal, desenvolvemos uma biblioteca em python que realiza os calculos numéricos envolvendo as isócronas e trajetórias evolutivas: o código EITApy. Para quantificar os benefícios da combinação dos dois métodos, simulamos uma amostra de 10000 estrelas com idades conhecidades e analisamos os resultados para diferentes regiões do diagrama HR. Mostramos que para alguns grupos, as incertezas são 20% menores. Aplicamos os métodos para as estrelas do levantamento S^{4}N, além de obter seus parâmetros cinemáticos utilizando o integrador orbital galpy. O próximo passo, será investigar como as relações entre composição química e parâmetros cinemáticos com a idade podem ser explicadas em um cenário de evolução quimiodinâmica da Galáxia.

Keywords. Stars: evolution – Stars: kinematics and dynamics – Stars: statistics

1. Introduction

The stellar composition and kinematics are a reflex of the interstellar medium properties at a given epoch, and the age allows us to place these properties in time. Ages are derived from properties that change with time in a way that can be predicted empirically and/or theoretically.

For studies that aim to understand the chemodynamical evolution of the Galaxy, it's of great importance to be able to derive precise ages for long lived stars. It's these stars that have been around since the formation of the Galaxy and will contain key informations about its state in different epochs. But when working with long lived stars, a new problem arises: these stars live this long because their internal evolution is slower, therefore, their observation properties change in slower rate, difficulting the inference of the ages.

In this work, we developed a method to derive a stellar age that is independent from its internal evolution, the Kinematical Method. We combined this method with the Isochronal Method, which consists of comparing the observed atmospheric parameters with those predicted by evolutionary models. We showed that it allows us to derive better constrained ages for late-type stars, which we expect will contribute to provide more data to understand the Galactic evolution. We also build the python module EITApy for the numerical calculations.

2. The Kinematical Method

The velocity dispersion of a group of stars increases with the age of the stars (Nordström et al. 2004). It causes the velocitie's probabilities to depend on age.

The Bayes theorem allows us to reverse this probability dependence and obtain the probability for the age, given the velocities. To simplify the analysis we use the formalism of the velocity ellipsoid:

$$v_1 = (U + U_\odot)\cos\ell_v + (V + V'_\odot)\sin\ell_v\,, \tag{1a}$$

$$v_2 = -(U + U_\odot)\sin\ell_v + (V + V'_\odot)\cos\ell_v\,, \tag{1b}$$

$$v_3 = W + W_\odot\,, \tag{1c}$$

The probabilities are then given by:

$$p(t|U,V,W) \propto p(v_1|t)\cdot p(v_2|t)\cdot p(v_3|t)\cdot p(t) \tag{2}$$

We use a flat prior $p(t)$ and model the velocity distributions as a gaussian which dispersion depends on the stellar age:

$$p(v_i|t) = \frac{1}{\sqrt{2\pi\sigma_i^2(t)}}\exp\left(-\frac{v_i^2(t)}{2\sigma_i^2(t)}\right) \tag{3}$$

The probabilities are then modelled by the velocities dispersions, the vertex deviation (ℓ_v), the asymmetric drift (considered in $V'_\odot(t)$) and the two other components of the Solar peculiar velocity. Figures 1 and 2 shows the relations fitted for these parameters as a function of age using data from the Geneva-Copenhagen survey (Casagrande et al. 2011).

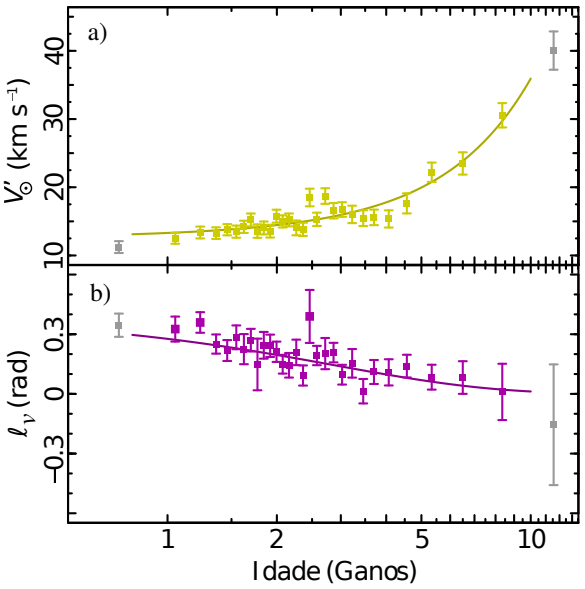

Figure 1. Relations fitted for $V'_\odot = 0.17t^2 + 0.63t + 12.5$ and $\ell_v(t) = 0.41\,\exp(-0.37t)$ using data from the Geneva-Copenhagen survey.

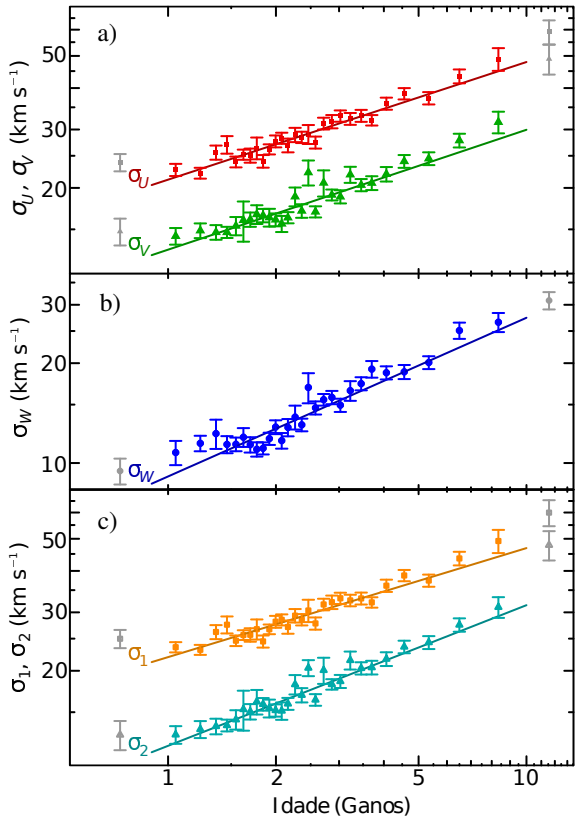

Figure 2. Power laws fitted for the velocity dispersions using data from the Geneva-Copenhagen survey: $\sigma_U = 21.2t^{0.35}$, $\sigma_V = 13.0t^{0.36}$, $\sigma_W = 9.1t^{0.48}$, $\sigma_1 = 22.0t^{0.33}$, $\sigma_2 = 11.9t^{0.42}$

3. Methodology

The Kinematical method described in the last section depends on how the stellar orbit changes with time, while the well established Isochronal Method is based on the internal evolution of the stars and the changes it causes on the observed atmospheric parameters. Therefore, both methods are physically independent. Despite the differences in physical causes and observables used, both methods follow a very similar statistical approach, and can be combined. The goal of this work is to test if this combination can be used to derive better defined ages.

Jørgensen & Lindegren (2005, hereafter J&L05) describe how the isochronal method can be used to derive a pdf for stellar ages through the calculation of what they call the G function and the prior age distribution $\phi(t)$:

$$f(t) \propto \phi(t)\, G(t) \tag{4}$$

The independence between both methods allows us to substitute the prior by the result of the Kinematical method, combining the information derived by the two methods.

$$\phi(t) \rightarrow p(t|U, V, W) \tag{5}$$

In order to calculate the G function, we developed a python module (called EITApy - **E**volutionary Tracks and **I**sochrones: **T**ools and **A**pplications) to perform the numerical calculations described in Equations 4, 5 and 11 of J&L05. The evolutionary tracks data, needed for Eq. 5 in J&L05, was obtained using the PARSEC tracks (Bressan et al. 2012).

To quantify the increase of precision and accuracy obtained by this combination of the methods, we used EITApy to synthesize a sample of 10,000 stars of known ages from the PARSEC tracks. For each star, the sampled values of age, metalicity and mass are used to interpolate the evolutionary tracks and generate the stellar effective temperature, bolometric magnitude and surface gravity (Figura 3). We have also simulated the stellar velocities following the distributions fitted in the last Section (Figura 4). Due to the statistical nature of the kinematical method, we have simulated 10 sets of spatial velocities for each simulated star; we do this to lessen the influence of eventual outliers.

We have also artificially divided the stars in 7 groups according to their position in the HR diagram. The isochronal method results in better defined ages for the stars in the regions where the space between isochrones is larger, therefore, we expect the benefits of combining both methods to also depend on the stellar position in the diagram. We analyse the results for the different groups to find which one benefits the most by the combination with the kinematical method, and also check if in some cases the isochronal method alone returns better results.

We have applied the methods for all the simulated stars considering two sets of observational uncertainties: $(\sigma_{T_{\rm eff}}, \sigma_{M_{\rm bol}}, \sigma_{\rm logg}, \sigma_Z) = (40, 0.1, 0.1, 0.0005)$ and $(120, 0.3, 0.3, 0.0015)$. After obtaining the posterior age pdf, we characterize individual ages using both the most-likely age ($t_{\rm ML}$) and the expected age ($t_{\rm E}$):

$$t_{\rm ML} = \arg\max_t f(t)\,, \tag{6a}$$

$$t_{\rm E} = \int_{-\infty}^{\infty} t\, f(t)\, {\rm d}t\,, \tag{6b}$$

We are working with both definitions because they suffer from two different bias: $t_{\rm ML}$ is skewed towards the extremes of the age interval (0 and 13.7 Gyrs) because of the truncation of the pdf imposed by the prior distribution; and $t_{\rm E}$ is skewed towards the center of the distribution because of the spread of the pdf. Therefore, obtaining the same conclusions using both ages means the results are more robust and less affected by the bias in the definitions.

The comparison between the ages obtained by the combined methods and only by the isochronal method is made through the distribution of differences between estimated age and real age. If the mean of the distribution is far from zero, it means the method is biased; and if the spread is too large, it means that lots of stars are having their ages underestimated.

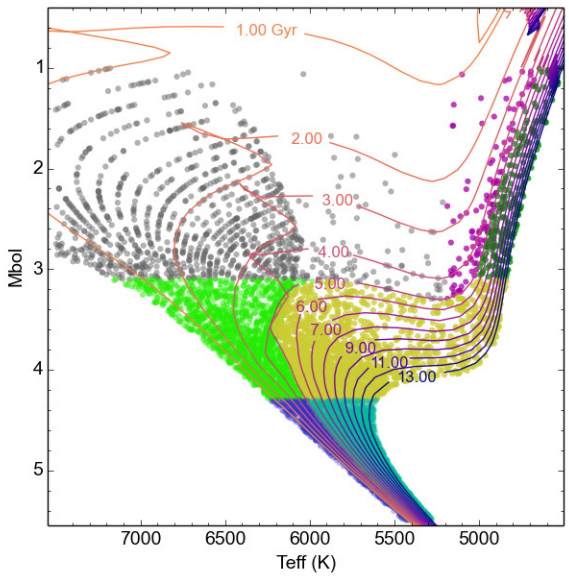

Figure 3. Distribution of the synthesized stars in the HR diagram. The different colors represent the 7 different groups to which the stars were assigned.

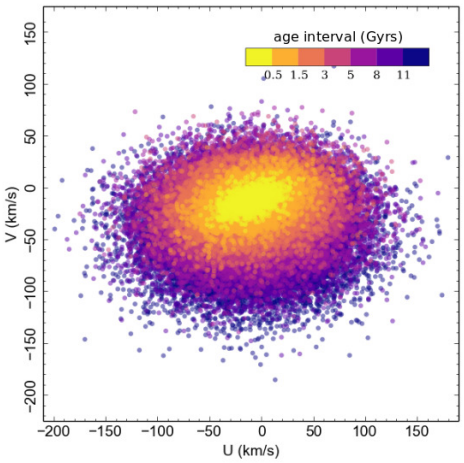

Figure 4. Distribution of the synthesized stars in the UV plane. The colors indicate different age intervals.

We also characterize the ages uncertainties using the spread of the pdf. In particular, we have defined the errors according to the ages of the 2.5% ($t_{2.5}$), 16% (t_{16}), 84% (t_{84}) and 97.5% ($t_{97.5}$) percentiles:

$$\delta_t = \frac{1}{4}\left[(t_{84} - t_{16}) + \frac{t_{97.5} - t_{2.5}}{2}\right], \quad (7)$$

this equation is designed to considerer both the spread closer to the median and at the tails, and its value is equal to 1σ for a normal distribution.

We have checked that our definition of δ_t can truly be used to compare the uncertainties between the combined method and the isochronal method by analysing the fraction of stars within $\pm 1\delta_t$, $\pm 2\delta_t$ and $\pm 3\delta_t$ from the real age.

4. Results

We characterize the distributions of differences between estimated age and calculated age through its mean and standard deviation. When comparing two different methods, the one who performs better is the one with the mean closer to zero and the smaller dispersion. We characterized these distributions considering our two defined ages (t_{ML} and t_E) and the two sets of observational uncertainties. The results are presented in Table 1.

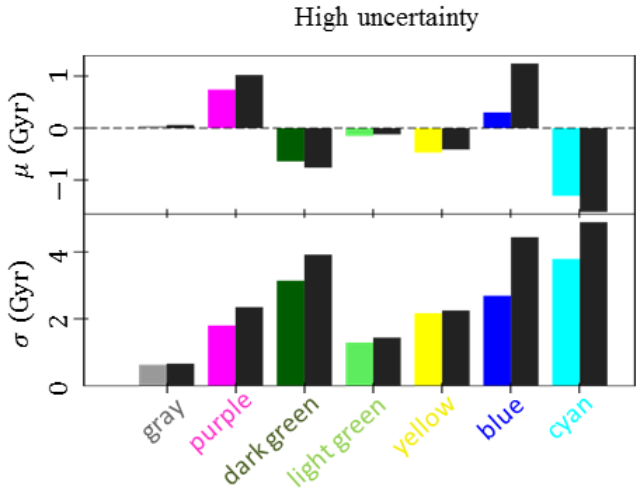

Figure 5. Characterizations of the distribution of differences between real age and estimated age (in the case of t_{ML} and high uncertainties), obtained by the combined method (groups colors) and isochronal method (dark gray)

It's clear that the two age definitions are affected by different age's bias. Both the combined and the isochronal method are, on average, more precise when considering the most likely age instead of the expected age: the mean of the distributions are closer to zero. Although, when considering accuracy, the expected age is the one that produce the best results, as for both methods the dispersion are systematically lower. This results hold true for both observational uncertainties scenarios and most of the groups.

Figure 5 displays the means and dispersions for the age's differences obtained by the combined method (groups colors) and isochronal method (dark gray), using t_{ML}, for the high uncertainty scenario. As we can see, the combined method systematically returns means that are closer to zero and smaller dispersions. It indicates that the combined method returns ages that are both more accurate and more precise. Although, it's important to notice that the p-value only allows us to reject the null hypotenuses (that both distributions are equivalent), with a 5% significance level, for the case of the light green, blue and cyan groups.

In general though, the differences obtained by the combined method are only significant in the cases of the blue and cyan groups: which corresponds to low mass stars that are at the main sequence or close to the turn off. In the other cases, the combined method either improves the ages by a small amount, or display no changes at all, which is also important, because in none of the considered scenarios the combined method returns results that are worse than the isochronal method alone. It means that the combined method can be applied to a sample containing both low mass main sequence stars and evolved stars, without having to worry if it is negatively effecting the ages of some stars.

The results obtained using t_E and it's average with t_{ML}, for the scenarios of low and high uncertainties are only displayed in Table 1. In all cases, the results are similar to what was discussed above. Considering that t_E and t_{ML} are affected by two different bias, obtaining the same results using both of them indicates that the our conclusion is robust, and the combined method in fact

Table 1. Characterization of the distribution of differences between the known simulated age and the estimated age by the combined method (index C) and the isochronal method (index I). Results are shown for both uncertainties scenarios (low and high) and for three age estimators: the most-likely age (t_{ML}), the expected age (t_E) and the average between them (t).

Group	Uncertainty	t_{MP}					t_E					t				
		μ_C	μ_I	σ_C	σ_I	p	μ_C	μ_I	σ_C	σ_I	p	μ_C	μ_I	σ_C	σ_I	p
Grey	Low	-0.01	-0.01	0.24	0.25	1.0e+00	0.03	0.03	0.24	0.24	8.6e-01	0.01	0.01	0.23	0.24	8.7e-01
	High	0.04	0.06	0.63	0.66	1.0e+00	0.16	0.15	0.66	0.71	2.5e-02	0.10	0.10	0.63	0.66	4.6e-01
Purple	Low	0.13	0.14	0.75	0.76	1.0e+00	0.48	0.51	0.83	0.89	9.7e-01	0.31	0.32	0.78	0.81	1.0e+00
	High	0.74	1.02	1.80	2.35	9.4e-01	2.19	2.67	1.49	1.55	2.1e-04	1.47	1.84	1.58	1.84	1.0e-01
Dark Green	Low	-0.13	-0.15	1.95	2.11	9.5e-01	-0.15	-0.16	1.66	1.74	9.7e-01	-0.14	-0.15	1.75	1.86	7.9e-01
	High	-0.64	-0.76	3.14	3.92	1.4e-01	-0.47	-0.65	2.25	2.44	1.0e-01	-0.56	-0.70	2.54	2.93	3.1e-01
Light Green	Low	0.01	-0.01	0.68	0.72	1.3e-01	0.05	0.01	0.58	0.62	1.0e-02	0.03	-0.00	0.61	0.65	4.4e-02
	High	-0.15	-0.12	1.29	1.44	2.3e-02	0.20	0.12	1.06	1.13	1.0e-04	0.03	0.00	1.14	1.23	1.2e-03
Yellow	Low	-0.03	-0.03	0.80	0.82	1.0e+00	-0.08	-0.08	0.76	0.78	1.0e+00	-0.06	-0.06	0.77	0.79	9.7e-01
	High	-0.47	-0.41	2.17	2.25	3.4e-01	-0.61	-0.79	1.73	1.82	1.2e-07	-0.54	-0.60	1.89	1.96	5.7e-03
Blue	Low	0.10	0.24	1.96	2.44	2.5e-07	0.86	0.96	1.57	1.75	3.8e-02	0.48	0.60	1.72	2.04	9.9e-04
	High	0.30	1.24	2.69	4.44	2.6e-38	1.88	2.57	1.81	1.95	4.3e-25	1.09	1.90	2.17	3.02	8.0e-26
Cyan	Low	-0.34	-0.34	2.47	2.68	2.8e-02	-0.70	-0.98	1.89	2.03	7.6e-13	-0.52	-0.66	2.13	2.29	3.8e-04
	High	-1.30	-1.61	3.79	4.89	3.4e-29	-1.38	-2.20	2.45	2.42	4.2e-65	-1.34	-1.91	3.02	3.37	6.9e-27

returns better results for the blue and cyan groups, no matter how you choose to characterize the age from the pdf.

5. Conclusions

We have developed a new method to derive an age pdf from the stellar spatial velocities. To do that, we calibrate the velocities distribution as a function of age using data from the GCS survey.

We show how this kinematical age pdf can be incorporated to the isochronal method, using more information to better constrain the stellar age.

In order to validate this combination, we have synthesized a sample of 10 000, with known ages and, applied to them the combined method and the isochronal method alone. The comparison of the results allows us to conclude that:

- The combined method considerably improves the precision and accuracy for the low mass stars that are at the main sequence or close to the turn off.
- The increase in accuracy and precision are more evident when observational uncertainties for the atmospheric parameters are higher.
- In none of the considered scenarios the combined method results in worse defined ages than the isochronal method alone. It's either better defined or statistically equivalent.

The low mass stars, that benefits the most by the combination of the isochronal and kinematical methods are also the best tracers of the Galactic evolution, due to their extended lifetime. Also, the high uncertainty scenario, in which the differences between the combined and isochronal method are greater, is the one that represents the quality of data in large surveys. It's these large surveys that contains enough stars for us to derive information about the chemodynamical evolution of the Galaxy. Therefore, combined with precise astrometric information from Gaia (for the determination of the spatial velocities), the method derived here has great potential to improve the age determinations for stars from surveys like RAVE (Steinmetz et al. 2006) and consequently allows for a better understanding of the chemodynamical evolution of our Galaxy.

References

Casagrande L., et al., 2011, A&A, 530, A138
Nordström B., et al., 2004, A&A, 418, 989
Jørgensen B. R. & Lindegren L., 2005, A&A, 436, 127
Bressan A., et al., 2012, MNRAS, 427, 127
Steinmetz M., et al., 2006, AJ, 132, 1645

Boletim da Sociedade Astronômica Brasileira, **30**, no. 1, 142-143

Low surface brightness star clusters of the Large Magellanic Cloud outer regions

João F. C. Santos Jr.[1,⋆], Francisco Maia[1], Leandro Kerber[2,3], Bruno Dias[4], Eduardo Bica[5], Andres E. Piatti[6]

[1] UFMG, [2] IAG-USP, [3] UESC, [4] ESO, [5] IF-UFRGS, [6] UNC

Abstract. *BVI*-band images obtained with instrument SAMI@SOAR for 56 Large Magellanic Cloud (LMC) outer disk star clusters – in the scope of the VISCACHA Survey – were analysed aiming at determining their structural parameters. Preliminary results show that the outer clusters' core radius is in average larger than that for inner clusters.

Resumo. Imagens nos filtros *BVI* obtidas com o instrumento SAMI@SOAR para 56 aglomerados de estrelas das regiões externas da Grande Nuvem de Magalhães – no escopo do projeto VISCACHA – foram analisadas com o objetivo de determinar seus parâmetros estruturais. Resultados preliminares mostram que o raio nuclear de aglomerados mais externos é em média maior que o dos aglomerados mais internos.

Keywords. galaxies: star clusters: general – Magellanic Clouds

1. Introduction

We are building a large photometric database of star clusters (SCs), mostly located in the outskirsts of the Magellanic Clouds, aiming at a comprehensive study of their properties in connection with the galaxies' evolution. This work focuses on 56 Large Magellanic Cloud (LMC) clusters, for which we have collected *BVI* images with SAMI@SOAR in the scope of the VISCACHA (VIsible Soar photometry of star Clusters in tApii and Coxi HuguA[†]) Survey. Results on structural parameters obtained from King model fittings to the clusters' surface brightness profiles (SBPs) are presented in this study. We intend to explore the significance of tidal effects from the Clouds and the Milky Way on the clusters' structure. A VISCACHA review is presented by Maia et al. in this proceedings.

2. Deprojected distance to the LMC center

SCs deprojected distances from the LMC dynamical center (α=5^h 19^m 31^s and δ= -69° 35′ 24″) were computed according to $d = s\left[1 + \sin^2(PA - \theta)\tan^2 i\right]^{1/2}$ (Elmegreen 1998), where s is the projected distance, PA is the position angle of the SC, θ is the position angle of the line of nodes and i the tilt of the LMC plane. The values of $\theta = 139°.1$ and $i = 34°$ were based on a model built from proper motion and radial velocities of the disk old population (van der Marel & Kallivayalil 2014). The sample SCs were separated in four groups at distinct locations (green, blue, yellow and red symbols) throughout the outer LMC (Fig. 1).

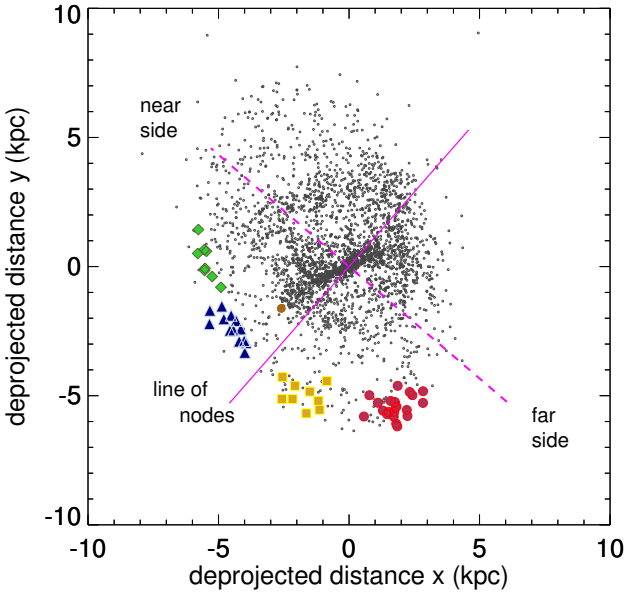

Figure 1. Deprojected distribution of LMC SCs. Black dots are clusters from Bica et al. (2008) catalogue. Colored symbols identify azimuthally distinct SC groups in our sample. The brown dot marks the control cluster SL 788. The line of nodes separating the closer and far away sides of the LMC are also indicated.

3. King model fit to surface brightness profiles (SBPs)

The SC center was determined iteratively by the average position of the stars within the SC visual radius. The SBPs were built from the calibrated V and I images in annular bins divided in eight sectors for which the flux median was calculated. The sky level, obtained from the whole image, was subtracted before the fitting procedure. Although the I band provide the best image quality compared to the V band, its enhanced background makes the resulting profiles noisier, therefore smaller uncertainties were achieved for the V band, which was preferred in this analysis.

The King model structural parameters central surface brightness ($\mu_\circ$), core radius (r_c) and tidal radius (r_t) were estimated by fitting the King (1962) model to the clusters' SBPs. The model fittings were performed from the cluster center to the limiting radius, where the flux of field stars starts to overcome the flux of the cluster stars. From the limiting radius outward, the flux was

⋆ e-mail: jsantos@fisica.ufmg.br

† Tupi-guarani names for the LMC and SMC

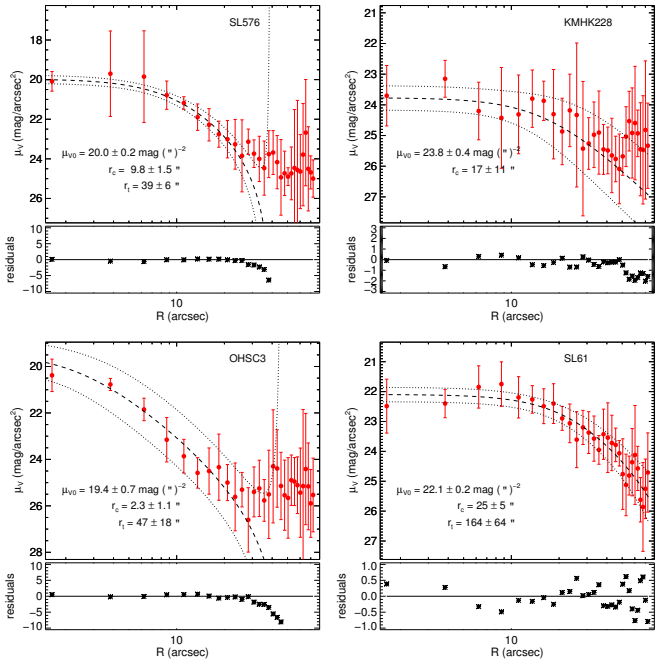

Figure 2. Selected King model fittings to SBPs. Top: The brightest (integrated M_V) cluster (left) and the faintest one (right) in our sample. Bottom: SCs with the smallest core radius (left) and the largest one (right).

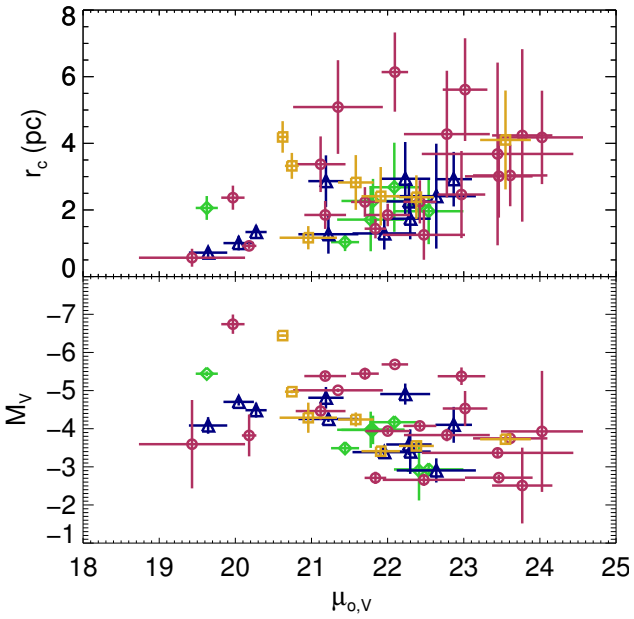

Figure 3. Distribution of core radius and integrated magnitude with the central surface brightness for the four SC groups.

used to compute the stellar background/foreground, which was then subtracted from the profile. For most of the clusters it was not possible to obtain r_t because field contamination dominates the outer profile. King model fittings are shown in Fig. 2.

SCs with large core radius tend to have lower central surface brightness and are fainter in integrated V light, as expected (Fig. 3). Fig. 4 shows that there is a large spread in r_c for SCs located at greater distances from the LMC center. More significantly, the two westernmost SC groups (red and yellow symbols) have median r_c and their dispersions above those for the eastern groups (blue and green).

4. Conclusions and perspectives

Although the SCs have deprojected distances to the LMC center that do not differ by more than 2 kpc, they are distributed azimuthally from east to southwest throughout ~130°, making different dynamical effects expected among the groups. Indeed, the westernmost SCs (red dots), that are closer to the SMC, seem to have r_c more scattered with relation to the other SCs. This group is also in the farther side of the LMC from us and contains the lowest surface brightness members of our sample. A comparison between r_t and r_c for our sample and that of inner SCs studied by Werchan & Zaritsky (2011) shows that, in average, the latter are smaller than most SCs in our sample, which may reflect tidal effects. In the near future, we will obtain age and metallicity for the sample and study their gradients in connection with the structural parameters. Such investigation shall provide new findings on the LMC cluster population more strongly affected by the interaction between the Clouds and may reveal interesting aspects of the galaxies' evolution.

Acknowledgements. We thank CAPES and FAPESP for support.

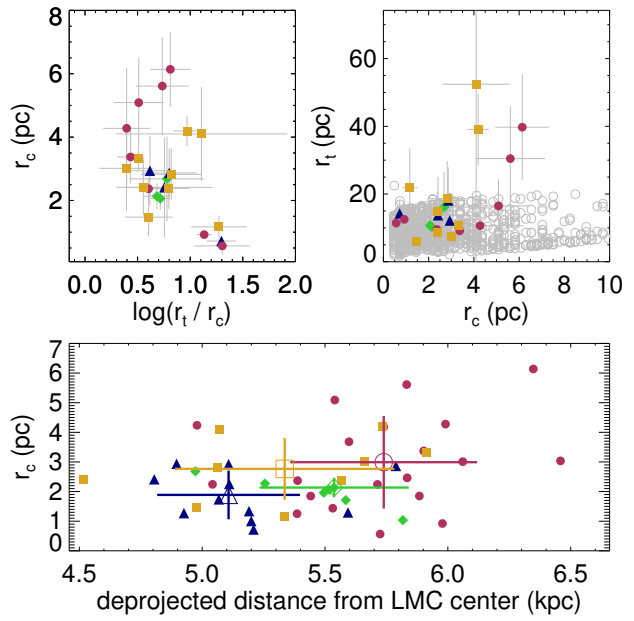

Figure 4. Top: Relations between core radius and tidal radius for our sample compared to that analysed by Werchan & Zaritsky (2011) (gray circles). Bottom: core radius vs deprojected distance from the LMC center for the four SC groups.

References

Elmegreen D. M., 1998, Galaxies & Galactic Structure, Prentice-Hall ed.
Elson R. A. W., Fall S. M., Freeman K. C., 1987, ApJ, 323, 54
Fraga L., Kunder A., Tokovinin A., 2013, AJ, 145, 165
King I., 1962, AJ, 67, 471
Stetson P. B., 2000, PASP 112, 925
van der Marel R. P., Kallivayalil N., 2014, ApJ 781, 121
Werchan F., Zaritsky D., 2011, AJ, 142, 48

Boletim da Sociedade Astronômica Brasileira, **30**, no. 1, 144-145

Deprojecting the metallicity and age gradients for the Magellanic Clouds using star clusters

P. Westera[1], B. L. Kerber[2,3], B. Dias[4], E. Bica[5], F. Maia[6] & J. F. C. Santos Jr[6]

[1] UFABC, e-mail: pieter.westera@ufabc.edu.br
[2] IAG-USP, e-mail: lekerber@gmail.com
[3] UESC, e-mail: lokerber@uesc.br
[4] ESO, e-mail: bdias@eso.org
[5] UFRGS, e-mail: 00006798@ufrgs.br
[6] UFMG, e-mail: kicage@gmail.com, e-mail: jsantos.ufmg@gmail.com

Abstract. We compile the most reliable age, metallicity and distance determinations of well-studied stellar clusters from the Magellanic Clouds available, including the new results from the VISCACHA Survey. Using these benchmark clusters, we determine the age-metallicity relations of the two galaxies, the one of the LMC we show as an example, as well as the age and metallicity gradients of the LMC measuring the clusters' galactocentric distances using two different methods: On the one hand the standard deprojection based on the assumption that the clusters lie in the galaxy's main plane, and on the other hand using the distances as determined from their colour-magnitude diagrams. The results lead to an improved understanding of the formation and evolution of the Magellanic System, and allow to evaluate the validity of the standard deprojection method.

Resumo. Fizemos uma compilação das determinações mais confiáveis disponíveis de idades, metalicidades e distâncias de aglomerados estelares bem estudados das Nuvens de Magalhães, incluindo resultados novos do levantamento VISCACHA. Usando estes aglomerados de referência, determinamos as relações idade-metalicidade das duas galáxias, aquela da LMC mostramos como exemplo, assim como os gradientes de idade e metalicidade da LMC medindo as distâncias galactocêntricas dos aglomerados usando dois métodos diferentes: Por um lado a deprojeção padrão baseada na suposição, de que os aglomerados se encontram no plano principal da galáxia, e por outro lado usando as distâncias determinadas a partir dos seus diagramas cor-magnitude. Os resultados levam a um melhor entendimento das formação e evolução do Sistema Magellânico, e permitem avaliar a validade do método de deprojeção padrão.

Keywords. Magellanic Clouds – Galaxies: star clusters: general – Galaxies: structure

1. Introduction

The Small and Large Magellanic Clouds (SMC and LMC) represent ideal laboratories to test galaxy evolution models and probe 3D galactic structure, being among the galaxies closest to us. Whereas the LMC is known to have a prominent disk, the structure of the SMC is more complicated, very elongated in the direction of the line of sight, a possible disk would appear nearly edge-on (van der Marel et al. 2002). Star clusters can be used to trace the age and metallicity of the stellar content, and gradients of these properties, i. e. in the galacto-centric directions, can give us indications of the formation and evolution of the Magellanic System. These gradients are often estimated using a standard deprojection based on the assumption that the clusters lie in the galaxies' main planes (Palma et al. 2015). However, in the Magellanic Clouds it is possible to properly determine the distances to the star clusters from their colour-magnitude diagrams and calculate the gradients without making simplifying assumptions about their distribution.

2. Method

We compiled the most reliable age, metallicity and distance determinations of well-studied stellar clusters from the Magellanic Clouds available, determined by means of isochrone fitting on colour- magnitude diagrams, and red giant spectroscopy. We also include new results from the VISCACHA survey (VIsible Soar photometry of star Clusters in tApii and Coxi HuguA, Kerber et al. 2018). Typical errors on the distance moduli range from 0.03 to 0.15. Our sample contains 85 SMC clusters, and 111 LMC clusters. We then used the distance determinations to determine their distribution in three dimensions.

After that, we determined the galaxies' age-metallicity relations and age gradients and, for the LMC, the metallicity gradients along different galacto-centric directions: the traditional projection along the line of sight onto the galactic plane, a, the projection perpendicular to the galactic plane, $R_{\rm LMC}$, the distance to the plane, $Z_{\rm LMC}$, and the true galacto-centric distance, R. For the orientation of the LMC plane, we used a position angle of the line of nodes of 145° and an inclination to the plane of the sky of 35.8° (Palma et al. 2015). For objects in the galactic plane, $a = R_{\rm LMC} = R$.

3. Results

We compare the age-metallicity relations of our sample clusters with analytical chemical evolution models of the Clouds from Pagel & Tautvaišiené (1998). They agree remarkably well for the LMC, as can be ssen in Fig. 1, and within the standard deviation for the SMC (not shown).

We then determined the 3D distribution of our sample clusters, and their metallicity and age gradients.

In order to calculate the gradients, we subdivided our LMC cluster sample in two populations: an old one, with ages over 10 Gyr, corresponding to a galaxy "halo", and a younger, "disk" population. We determined [Fe/H] - and log(*age*) gradients for both populations individually, as can be seen in Fig. 2 (in red and

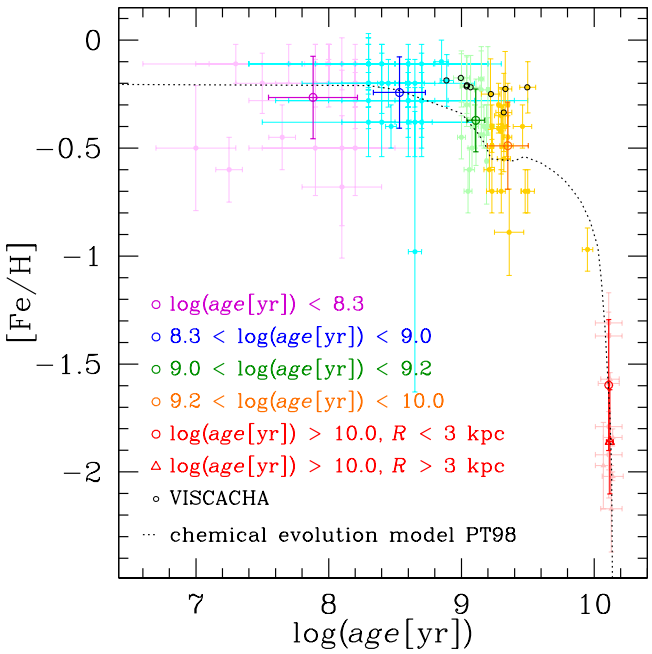

Figure 1. Age-metallicity relations of the Large Magellanic Cloud.

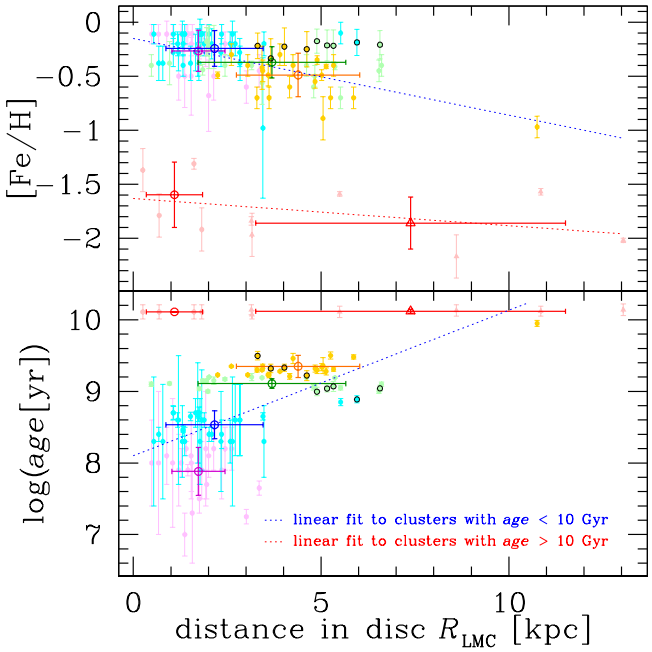

Figure 2. [Fe/H] and log(*age*) as projected perpendicularly onto the galaxy plane, the colours, symbols and error bars have the same meaning as in Fig. 1.

blue, respectively).
The cluster distributions and gradients in a and $R_{\rm LMC}$ are very similar, since they both represent projections onto the same plane, in similar directions, differing by 35.8°.
The younger population shows clear gradients in the usual senses, decreasing for [Fe/H] vs. $R_{\rm LMC}$ and increasing for log(*age*) vs. $R_{\rm LMC}$. The old, "halo", population shows no significant gradients, as expected for a galaxy component that has had plenty of time to relax and seen several close encounters with the Galaxy and the SMC.

Table 1. gradients of LMC cluster metallicities and ages.

	∇ [Fe/H] [dex/kpc]	∇ [Fe/H] [dex/kpc]	∇log(*age*) $\left[\mathrm{kpc}^{-1}\right]$
direction	< 10 Gyr	> 10 Gyr	< 10 Gyr
a	-0.052 ± 0.009	-0.022 ± 0.02	0.18 ± 0.03
$R_{\rm LMC}$	-0.054 ± 0.01	-0.025 ± 0.02	0.20 ± 0.03
$Z_{\rm LMC}$	-0.02 ± 0.02	0.14 ± 0.05	0.18 ± 0.06
R	-0.053 ± 0.01	-0.024 ± 0.02	0.21 ± 0.03

Perpendicular to the LMC plane, an age gradient can be seen in the young population but no metallicity gradient.
Surprisingly, calculating the clusters' true distances to the LMC center, R, did not yield significantly better results than using the projections a and $R_{\rm LMC}$. It will be interesting to see if this result persists, when more and more precise distance determinations will be available.
Table 1 shows the numerical values of the different gradients determined in this work.

4. Conclusions & Perspectives

To our surprise, a true deprojection of the positions of LMC star clusters with age, metallicity and distance determinations did not yield any significant improvement for the calculation of age - and metallicity gradients in relation to the traditional "deprojection" method, based on the assumption, that all clusters lie in the galaxy's main plane. If this is due to the limited size of our sample (i. e. selection effects) can only be evaluated using a more complete sample.
As next steps, we will apply isochrone fits to 100 clusters of the VISCACHA survey of Magellanic Cloud star cluster CMDs, ~ 60 in the LMC and ~ 30 in the SMC plus another 10 + 30 that will be observed this semester, in order to increase the sample for both the SMC and LMC, and obtain more statistically significant results, find the galaxies' main planes by adjusting planes to the cluster positions, and compare our results to other works. This way we'll be able to make a revelant contribution to the discussion about the Clouds' formation and evolution.

Acknowledgements. We thank CAPES and FAPESP for partial support.

References

Kerber, L. et al., 2018, in preparation
Pagel, B. E. J. & Tautvaišiené, G., 1998, MNRAS, 299, 535
Palma, T., Clariá, J. J., Geisler, D., Ahumada, A. V., 2015, ASP Conf. S., 491, 235
van der Marel, R. P., Alves, D. R., Hardy, E. & Suntzeff, N. B., 2002, AJ, 124, 2639

Boletim da Sociedade Astronômica Brasileira, **30**, no. 1, 146-147

A synthetic spectral stellar library of blue horizontal branch stars

Radi Melo Martins & Lucimara Martins

[1] Núcleo de Astrofísica Teórica — NAT e-mail: radimartins@gmail.com, lucimara.martins@cruzeirodosul.edu.br

Abstract. Blue Horizontal Branch (BHB) stars are stars that have gone through most of their evolutionary process, lost part of their outer layers, leaving a thin layer of H and the core burning He. This makes them very warm and blue, but old. We can find these stars in many stellar systems, and their presence may induce errors in determining the age of these objects. The technique of analysis of stellar populations using integrated spectra is a powerful tool in the study of galaxies, but models of stellar populations do not take into account BHB stars. Because of this, the presence of these stars induces a determination of younger ages than expected for these systems. In this project we are creating synthetic spectra for the stars of the Horizontal Branch (HB) that can be incorporated to the models of stellar populations used in spectral synthesis. We performed a careful research in the literature to determine the coverage of atmospheric parameters and chemical properties required to represent the HB of various stellar systems. These values are the base of the creation of the library. To generate the synthetic spectra we are using ATLAS9 atmosphere models and the spectral synthesis code SYNTHE. As a preliminary result, we noticed that the spectra of 14 observed HB stars, extracted from the MILES empirical spectral library, are better represented by spectra rich in He.

Resumo. As estrelas do Ramo Horizontal Azul (BHB) são estrelas que já passaram por quase todo seu processo evolutivo, perderam parte de sua camada externa, deixando uma fina camada de H e o núcleo queimando He. Isso faz com que elas sejam muito quentes e azuis, porém velhas. Podemos encontrar essas estrelas em muitos sistemas estelares, e sua presença pode induzir a erros na determinação da idade desses objetos. A técnica de análise de populações estelares utilizando espectros integrados é uma ferramenta poderosa no estudo de galáxias, mas modelos de populações estelares não levam em conta as estrelas BHB. Por causa disso, a presença dessas estrelas induz a uma determinação de idades mais jovens do que o esperado para esses sistemas. Neste projeto estamos criando espectros sintéticos para as estrelas do Ramo Horzontal (HB) que poderão ser incorporados aos modelos de populações estelares utilizados em sínteses espectrais. Realizamos uma pesquisa cuidadosa na bibliografia para determinar a cobertura de parâmetros atmosféricos e propriedades químicas necessárias para representar o HB de diversos sistemas estelares. Esses valores baseiam a criação da biblioteca de espectros. Para gerar os espectros sintéticos estamos utilizando modelos de atmosfera do ATLAS9 e o código de síntese espectral SYNTHE. Resultados preliminares mostram que o espectro observado de 14 estrelas do HB, retirados da biblioteca estelar empírica MILES, são melhor representados com espectros ricos em He.

Keywords. Stars: horizontal-branch, abundances, atmospheres

1. Introduction

Models of single stellar population have quickly become a fundamental tool in the study of both galactic and extragalactic populations (e.g. Percival & Salaris 2009; Kotulla et al. 2009; Coelho et al. 2007; Maraston 2005; Bruzual & Charlot 2003). Despite the increasing sophistication of the models used, there are still areas where models and methods could be improved and expanded. A key area in which simplifications are usually made is related to the Horizonltal Branch (HB). The presence of Extreme Horizontal Branch (EHB) stars in a stellar population directly affects the age inferred through spectroscopic adjustments with synthetic models of stellar populations (Schwartz 2004).

2. Objective

The main objective of this work is to construct a library of HB synthetic spectra, which can be created with any variation of atmospheric parameters desired for these stars so that they can later be included in the analyzes of the stellar populations.

3. The Horizontal Branch

After undergoing deep changes in its structure, in RGB, the star eventually re-balances and reaches the HB of the HR diagram. HB is populated as follows: if the star loses a lot of mass, only a thin layer of hydrogen will remain around the nucleus that is burning helium, resulting in a bluish coloration and higher temperature. This star will be further to the left in the HR diagram. A star that loses little mass will have a thick outer layer, resulting in a red coloration and a lower temperature. This star will be further to the right in the HR diagram. Figure 1 shows an example of HR diagram for the cluster M5, where many phases of stellar evolution are represented, including the HB.

Some chemical peculiarities may be related to the formation of these stars, in particular related to the abundance of He (D'Antona et al. 2002; D'Antona 2005; Lee et al. 2005).

4. Material and methods

The study of the distribution of atmospheric parameters and chemical peculiarities of the stars of HB and EHB can lead to a better understanding of the formation and evolution of these stars and the clusters that have them (Salgado et al. 2013). Through careful research in the literature we determined the coverage of atmospheric parameters and chemical properties necessary to represent the HB and EHB of various stellar systems.

To generate the synthetic spectra, ATLAS9 atmosphere models were used (Castelli & Kurucz 2004). The spectral synthesis code used to generate the spectra was SYNTHE (Kurucz & Avrett 1981).

To test the validity of the generated synthetic spectra and to evaluate their limitations, it was necessary to compare them with observed spectra of HB stars.

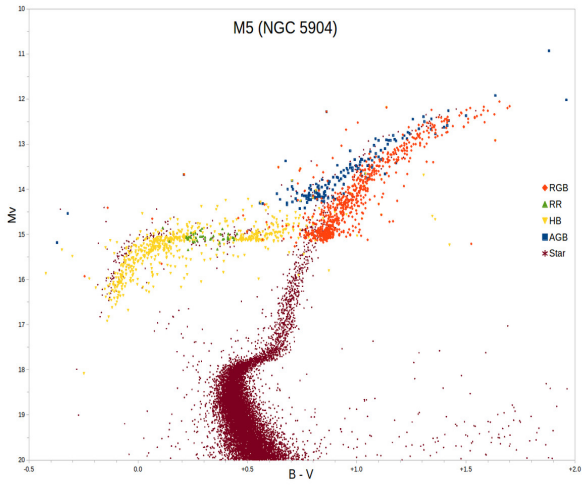

Figure 1. Example HR diagram, representing some stages of stellar evolution. Source:`http://www.wikiwand.com/en/Horizontal_branch`

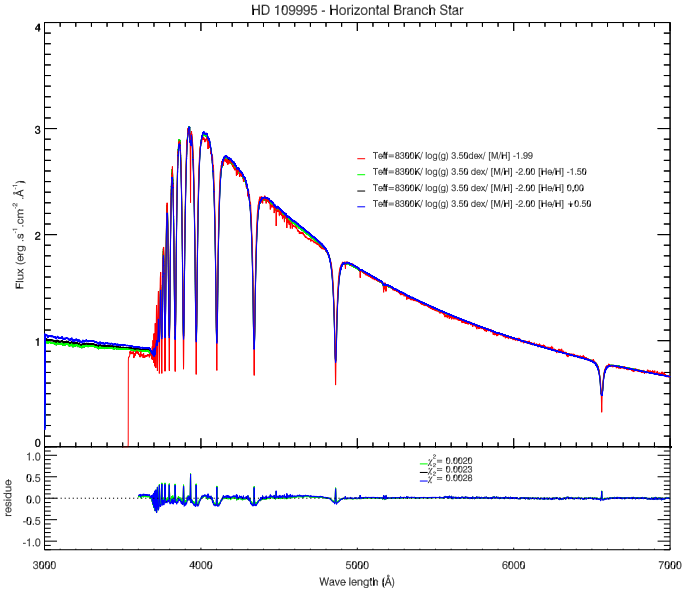

Figure 2. Adjustment of spectra model, to observed spectrum, with best approximation in abundance He sub-solar to HB stars.

Once the generated synthetic spectra have been tested and validated using observed spectra, the full library of synthetic spectra covering the entire range of parameters observed for HB and EHB will be created, forming the library. This library will be made available to the community and can be used to generate future SSPs that more fully consider HB and EHB.

5. Parcial Results

We looked in the MILES empirical stellar library for stars classified as HB to test our spectra. We found 14 out of about 1000 stars. Of the stars analyzed 10 were better fit with subsolar He abundance, 2 with super solar He abundance and 2 with solar. That means 85.72% of them are better adjusted by non-conventional He abundances. Figure 2 shows, as an example, the comparison between the observed spectra of HD109995 and models with different He abundances. Our library, therefore, will have different He abundances.

Acknowledgements. Capes e NAT-Unicsul.

References

Bruzual G., Charlot S., 2003, MNRAS, 344, 1000
Castelli F., Kurucz R. L., 2004, ArXiv Astrophysics e-prints
Coelho P., Bruzual G., Charlot S., Weiss A., Barbuy B., Ferguson J. W., 2007, MNRAS, 382, 498
D'Antona F., 2005, Highlights of Astronomy, 13, 156
D'Antona F., Caloi V., Montalbán J., Ventura P., Gratton R., 2002, A&A, 395, 69
Kotulla R., Fritze U., Weilbacher P., Anders P., 2009, MNRAS, 396, 462
Kurucz R. L., Avrett E. H., 1981, SAO Special Report, 391
Lee Y.-W., Ree C. H., Rich R. M., Deharveng J.-M., Sohn Y.-J., Rey S.-C., Yi S. K., Yoon S.-J., Bianchi L., Lee J.-W., Seibert M., Barlow T. A., Byun Y.-I., Donas J., Forster K., Friedman P. G., Heckman T. M., Jee M. J., Jelinsky P. N. e. a., 2005, ApJ, 619, L103
Maraston C., 2005, Monthly Notices of the Royal Astronomical Society, 362, 799
Percival S. M., Salaris M., 2009, ApJ, 703, 1123
Salgado C., Moni Bidin C., Villanova S., Geisler D., Catelan M., 2013, A&A, 559, A101
Schwartz M. J., 2004, PhD thesis, University of California, s Angeles, California, USA

Boletim da Sociedade Astronômica Brasileira, **30**, no. 1, 148-149

Modelling the formation of the galactic bulge

O. Cavichia[1] & M. Mollá[2]

[1] Instituto de Física e Química, Universidade Federal de Itajubá, Av. BPS, 1303, 37500-903, Itajubá-MG, Brazil e-mail: cavichia@unifei.edu.br
[2] Departamento de Investigación Básica, CIEMAT, Avda. Complutense 40, E-28040 Madrid, Spain e-mail: mercedes.molla@ciemat.es

Abstract. In this work we have assumed a Hernquist model with an inside-out formation for the Galactic bulge and, using a chemical evolution model, we were able obtain the bulge metallicity distribution function (MDF) for different radial regions. The preliminary results show that in the inner regions of the bulge the MDF has a higher fraction of metal poor stars, while this fraction is progressively diminished as moving outwards in the bulge. These results may explain the metallicity gradient observed in the Galactic bulge.

Resumo. Neste trabalho assumimos um modelo de Hernquist com uma formação interna-externa para o bojo Galáctico e, usando um modelo de evolução química, fomos capazes de obter a distribuição de metalicidades do bojo (MDF) para diferentes regiões radiais. Os resultados preliminares mostram que nas regiões internas do bojo a MDF apresenta uma fração maior de estrelas pobres em metais, enquanto que esta fração diminui movendo-se para as regiões externas do bojo. Estes resultados podem explicar o gradiente de metalicidades observado no bojo Galáctico.

Keywords. Galaxy: bulge – Galaxy: evolution – Galaxy: formation

1. Introduction

The Galactic bulge (GB) is the only galaxy bulge that can be resolved and can be studied with exquisite details. Hence, the bulge metallicity distribution function (MDF) can be traced for different regions within the bulge and can give us clues about the bulge formation scenario. Recently, observations (e.g. Zoccali et al. 2008, Rojas-Arriagada et al. 2014) have shown that the GB is composed of at least two components with different mean metallicities, and possibly different spatial distribution and kinematics. Zoccali et al. (2017) have demonstrated that the two components present a different spatial distribution, with the metal poor population being more centrally concentrated. There is no consensus in the literature regarding if this result point to a GB formation scenario formed by a bar instability or if the the GB formed from a spheroidal collapse. In this regarding, chemical evolution models (CEM) are important tools to understand the formation and evolution of the components of the Milky Way Galaxy (MWG) and other galaxies in the universe. The outputs generated by the CEM are compared with the observational data and the physics adopted is changed self-consistently until satisfactory results are achieved. Precisely, one of the most important constraints for CEM is the metallicity distribution function (MDF). In particular, the MDF of a region is sensible to the timescale that the region was formed.

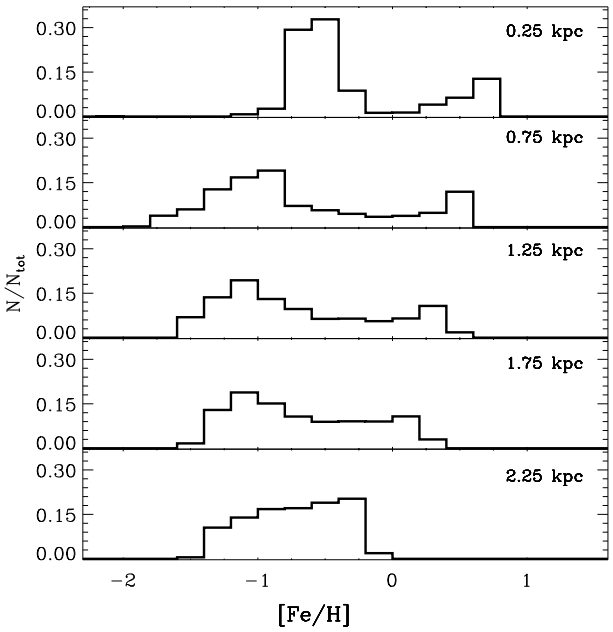

Figure 1. Fe/H] histograms for different regions in the GB (0.25, 0.75, 1.25, 1.75 and 2.25 kpc), as labeled in each panel. The theoretical MDFs represent those from giant GB stars, being the stellar abundances computed taking into account the stellar life-times from Padova isochrones.

2. Model and results

Our model is an update of the one from Mollá & Díaz (2005) and the GB is formed assuming an inside-out growth scenario where the accretion of metal-poor gas from the halo builds the spheroidal component and also the disc. The infall rate for each radial region is given in Mollá et al. (2016) and is obtained by imposing that after a Hubble time the system ends with a mass as observed for a Milky Way sized galaxy. In this work we have adopted the Hernquist mass model (Hernquist 1990) for the GB in order to constraint the scenario that formed the GB:

$$M(r) = M_{\rm b}\frac{r^2}{(r+a_{\rm b})^2}, \quad (1)$$

where $M_{\rm b}$ is the GB mass, adopted to be $1.85 \times 10^{10}{\rm M}_{\odot}$ (following Cavichia et al. et al. 2014) and the characteristic scale-length $a_{\rm b} = r_{\rm eff}(1+\sqrt{2})^{-1} = 0.124$ kpc using $r_{\rm eff} = 300$ pc

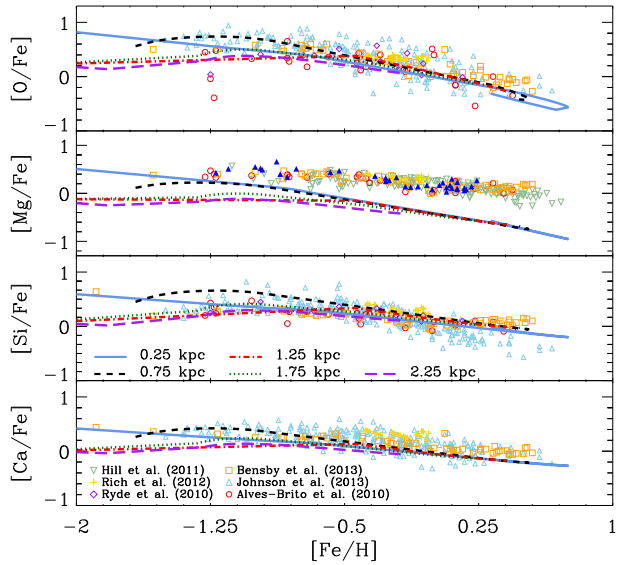

Figure 2. Comparison between the predictions of our model at different radial regions and the literature data for [α/Fe] where α stands for O, Mg, Si, and Ca, vs. [Fe/H]. The observational data for the bulge are labeled in the last panel (from top to bottom). The line codes of the models are as labeled in the third panel (from top to bottom). The observational data for the bulge are open circles from Alves-Brito et al. (2010), open squares from Bensby et al. (2013), open upside triangles from Johnson et al. (2013), open upside-down triangles from Hill et al. (2011), open stars from Rich et al. (2012), and open diamonds from Ryde et al. (2010).

(bulge half-light radius) from Wyse & Gilmore (1993). We divided the GB in five concentric regions, being the innermost a sphere of 0.25 kpc radius. The subsequent regions are spherical shells with external radii 0.75, 1.25, 1.75 and 2.25 kpc, each one 0.5 kpc wide. The Hernquist mass distribution is obtained allowing gas infalling first in the innermost spherical region and, when the mass distribution in that region resembles that from the Hernquist profile at the same radius, the infall ceases at this spherical region and begins at the following spherical shell. The total collapse-time scale to form the GB is 2 Gyr. The resulting GB metallicity distribution function (MDF) for each spherical region is shown in Fig. 1, represented by the [Fe/H] histograms. Double peak histograms are observed for each region, with exception of the outermost one, suggesting a GB composed by two populations with different mean metallicities. Probably in the outermost spherical shell there is an overlap between the disc and bulge population and the two component population is not observed. Nonetheless, it is evident in this figure the differences in the MDFs for each region. In the innermost one the fraction of the metal poor population is higher than the metal rich one. However, as moving further out to the other spherical shells, the fraction of metal poor stars decreases and the one from metal rich population increases. In spite of that, the positions of the peaks do not change considerably, considering the shells 0.75, 1.25 and 1.75 kpc. This results are in agreement with the most recent observations from Zoccali et al. (2017).

In Fig.2 it is shown [α/Fe] versus [Fe/H], where α stands for the α-elements: O, Mg, Si and Ca. Overall, our model is able to reproduce the observational data regarding the [O/Fe], [Si/Fe] and [Ca/Fe] abundance ratios. The [Ca/Fe] abundance ratio of Bensby et al. (2013) and Rich et al. (2012) are higher than the results of the model. In our case, we adopted the yields of O and Mg for high mass stars from Woosley & Weaver (1995) and it is known that these yields needed to be increased in order to reproduce the most recent data of the bulge (Cavichia et al. et al. 2014 and Mollá et al. et al. 2015). Interesting, the model predicts different [α/Fe] ratios for each spherical region, the ratio being higher at the innermost regions (0.25 and 0.75 kpc) and lower at the outermost regions, especially at low [Fe/H] abundances. Higher [α/Fe] ratios at low [Fe/H] indicate a fast enrichment by massive stars which explode as type II supernovae. On the other hand, at higher metallicities ([Fe/H]> -0.5 dex) the differences in [α/Fe] ratios of the models are less important, probably because at these metallicities the type Ia supernovae have enriched the interstellar medium.

3. Discussion

The results of Fig. 2 suggest that the spread in [α/Fe] ratios, as shown by the observational data at lower metallicities, may be the result of mixing stars from different radial locations within the GB. Since the differences are in the range of ~ 0.30 dex, it will be very difficult to detect this trend given the level of the uncertainties of the present observations. To confirm this possible gradient of [α/Fe] in the GB predicted by our models, more data with higher precision is needed, mainly for lower metallicities and galactocentric distances.

Acknowledgements. This work has made use of the computing facilities available at the Laboratory of Computational Astrophysics of the Universidade Federal de Itajubá (LAC-UNIFEI). The LAC-UNIFEI is maintained with grants from Capes, Cnpq and FAPEMIG. O.C. would like to thank CAPES and the PGF/UNIFEI.

References

Alves-Brito, A., Meléndez, J., Asplund, M., Ramírez, I., & Yong, D. 2010, A&A, 513, A35
Bensby, T., Yee, J. C., Feltzing, S., et al. 2013, A&A, 549, A147
Cavichia, O., Mollá, M., Costa, R. D. D., & Maciel, W. J. 2014, MNRAS, 437, 3688
Hernquist, L. 1990, ApJ, 356, 359
Hill, V., Lecureur, A., Gómez, A., et al. 2011, A&A, 534, A80
Johnson, C. I., Rich, R. M., Kobayashi, C., et al. 2013, ApJ, 765, 157
Mollá, M., & Díaz, A. I. 2005, MNRAS, 358, 521
Mollá, M., Cavichia, O., Gavilán, M., & Gibson, B. K. 2015, MNRAS, 451, 3693
Mollá, M., Díaz, Á. I., Gibson, B. K., Cavichia, O., & López-Sánchez, Á.-R. 2016, MNRAS, 462, 1329
Rich, R. M., Origlia, L., & Valenti, E. 2012, ApJ, 746, 59
Rojas-Arriagada, A., Recio-Blanco, A., Hill, V., et al. 2014, A&A, 569, A103
Ryde, N., Gustafsson, B., Edvardsson, B., et al. 2010, A&A, 509, A20
Woosley, S. E., & Weaver, T. A. 1995, ApJS, 101, 181
Wyse, R. F. G., & Gilmore, G. 1993, Galaxy Evolution. The Milky Way Perspective, 49, 209
Zoccali, M., Hill, V., Lecureur, A., et al. 2008, A&A, 486, 177
Zoccali, M., Vasquez, S., Gonzalez, O. A., et al. 2017, A&A, 599, A12

Boletim da Sociedade Astronômica Brasileira, **30**, no. 1, 150-151

TW Hydrae association membership analysis based on Gaia DR1

R. Teixeira[1], E.R. Gonoretzky[1], C. Ducourant[2], J.F. Le Campion[2], P.A.B. Galli[1], & A.G.O. Krone-Martins[3]

[1] Universidade de São Paulo, IAG, São Paulo, Brasil rama.teixeira@iag.usp.br e-mail: rama.teixeira@iag.usp.br
[2] Laboratoire d ' Astrophysique de Bordeaux, Université de Bordeaux, France
[3] Faculdade de Ciências, Universidade de Lisboa, Portugal

Abstract. Taking advantage of the positions of the first Gaia data release, GDR1, in 2016 and of others from the literature, we have calculated new proper motions for the stars traditionally investigated as members of the TW Hydrae association (TWA). In recent works we could notice the great sensibility that the membership and trace-back analysis present in relation to the proper motion data. As a consequence we felt motivated to review the proper motion data of these objects aiming to work with more accurate and realistic data based on the excellent positions of GDR1. The results presented below give a panorama of the significant differences that we have found between the proper motion here determined and those used in previous works.

Resumo. Aproveitando as posições Gaia publicadas no primeiro "data release", GDR1, em 2016 e outros dados encontrados na literatura, calculamos novos movimentos próprios para as estrelas que tradicionalmente são discutidas como membros ou não membros da Associação TW Hydrae. Em trabalhos recentes pudemos constatar a grande sensibilidade que a análise de pertinência e a determinação da idade por trace-back apresentam em relação aos dados de movimento próprio. Isso nos motivou a fazer uma revisão desses dados para esses objetos, no sentido de obter movimentos mais precisos e realistas com a utilização das excelentes posições do GDR1. Os resultados apresentados a seguir, dão um panorama das diferenças significativas que pudemos encontrar entre os movimentos aqui determinados e aqueles utilizados em trabalhos precedentes.

Keywords. Astrometry – Proper motion – Stellar association

1. Introduction

TW Hydrae is a very young ($\approx$ 8 million of years) and relatively nearby ($\approx$ 60pc) stellar association. With its approximately 30 known members, among them planetary systems, brown dwarfs, etc., this association is an excellent target to stellar evolutionary studies (Weinberger et al., 2013; Ducourant et al., 2014).

As a consequence of the new astrometric data reality due to the publication of the first data release of the Gaia spatial mission (Gaia Collaboration, 2016a,b), we have started a proper motion data review for those objects traditionally investigated as members of this association. It is precisely on these objects that many current works are based, including that by ourselves (Ducourant et al., 2014).

More accurate proper motions are fundamental to the membership analysis and to a more realistic trace-back age determination. The existent proper motion astrometric catalogs: PPMXL (Roser et al., 2010), SPM4 (Girard et al., 2011), UCAC4 (Zacharias et al., 2013), etc., even globally good, locally, they present many inconsistencies and could be very bad (Teixeira et al., 2014).

Thus, in possession of the Gaia positions and those from other catalogs we obtained the results partially resumed in Figures 1 and 2 below. In these figures we show the proper motion differences in both coordinates as obtained in this work in relation to those used (Table 3) by Ducourant et al. (2014). As we can see, for many stars we found proper motions significantly different. Of course, these differences have important consequences to the study of this association. In these figures, we show in red those star for which we have obtained distances in the phase space greater than 15 mas/yr.

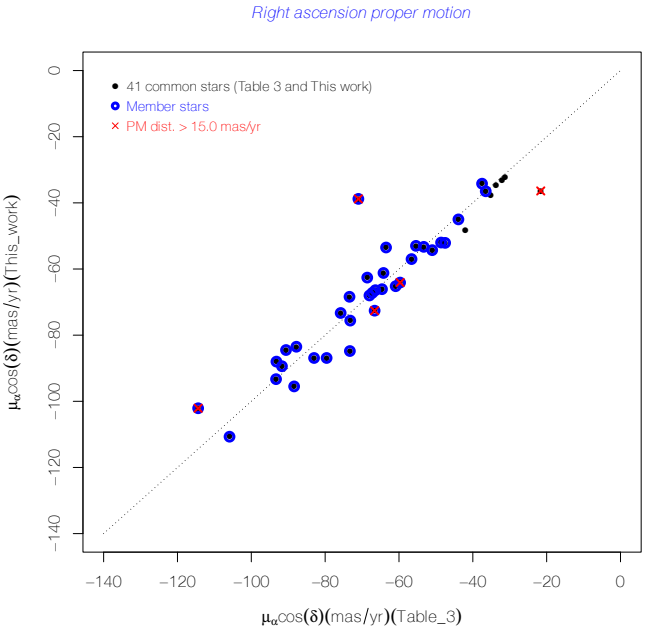

Figure 1. Comparison between the right ascension proper motions determined here and those used (Table 3) by Ducourant et al. (2014).

Acknowledgements. We are grateful to the French and Brazilian organisms COFECUB, FAPESP, CAPES and CNPq for financial support. This work has made use of data from the European Space Agency (ESA) mission *Gaia* (https://www.cosmos.esa.int/gaia), processed by the *Gaia* Data Processing and Analysis Consortium (DPAC, https://www.cosmos.esa.int/web/gaia/dpac/consortium). Funding for the DPAC has been provided by national institutions, in particular the institutions participating in the *Gaia* Multilateral Agreement.

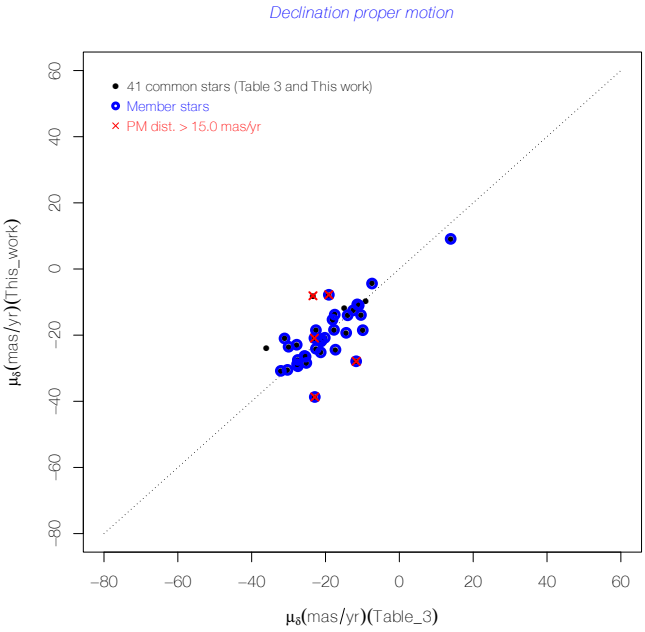

Figure 2. Comparison between the declination proper motions determined here and those used (Table 3) by Ducourant et al. (2014).

References

Ducourant C., Teixeira R., Chauvin G. et al. 2008, A&A, 477, L1-L4
Gaia Collaboration, 2016, A&A, 595, A1
Gaia Collaboration, 2016, A&A, 595, A2
Girard, T. M., van Altena, W. F., Zacharias, N. et al., 2011, AJ, 142, 15
Roeser S., Demleitner M. & Schilbach E., 2010, AJ, 139, 2440
Teixeira, R., Galli, P. A. B., Le Campion, et al., 2014, RMxAC, 43, 55
Weinberger A. J., Anglada-Escudé G. & Boss A. P. 2013, ApJ, 762, 118
Zacharias N., Finch C. T., Girard T. M. et al., 2013, AJ, 145, 44

Boletim da Sociedade Astronômica Brasileira, **30**, no. 1, 152-153

Multiple stellar populations from the HST UV Legacy Survey

in the moderately metal-poor Bulge globular clusters NGC 6717, NGC 6723 and NGC 6652

S. Souza[1], R. A. P. Oliveira[1], B. Barbuy[1], L. Kerber[1], & G. Piotto[2]

[1] Instituto de Astronomia, Geofísica e Ciências Atmosféricas — IAG-USP;
e-mail: stefano.souza@usp.br
[2] Università di Padova
e-mail: giampaolo.piotto@unipd.it

Abstract. In the present work we selected three Bulge globular clusters with blue (NGC 6717 and NGC 6723) and red (NGC 6652) horizontal branches, all of them moderately metal-poor ([Fe/H] ≈ -1.00). We analysed optical and ultraviolet images obtained in the UV-Legacy Survey programs GO-13297 and GO-10775 with the Hubble Space Telescope (HST). Color-magnitude diagrams (CMDs) for the globular clusters NGC 6717 ([Fe/H] = −1.26), NGC 6723 ([Fe/H] = −1.10) and NGC 6652 ([Fe/H] = −0.81) are built, applying the artificial colors. Using BaSTI stellar evolutionary models and statistical isochrone fits on the optical CMDs, we recovered the main physical parameters for each cluster. We also obtained evidence of multiple stellar populations in these clusters, through the so-called Chromosome Maps and they are of Type I.

Resumo. Neste trabalho selecionamos três aglomerados globulares do Bojo moderadamente pobres em metais ([Fe/H] ≈ -1.00) com ramo horizontal azul (NGC 6717 e NGC 6723) e vermelho (NGC 6652). Foram analisadas imagens do ótico e do ultravioleta (UV) obtidas nos programas GO-13297 e GO-10775 do UV-Legacy Survey com o *Hubble Space Telescope* (HST). Foram feitos diagramas cor-magnitude (CMDs) aplicando uma cor artificial que evidencia a presença de multiplas populações através do método chamado *Chromosome Map*. Com o auxilio do método de estatistico de máxima-verossimilhança e Cadeias de Markov - Monte Carlo foram determinados os parâmetros astrofísicos para cada aglomerado.

Keywords. Galaxy: bulge – Methods: statistical – globular clusters: individual: NGC 6652, NGC 6717 and NGC 6723

1. Introduction

Globular clusters (GCs) are physical systems of typically hundreds of thousands of stars that are being held together by gravity. Since they were formed during the first Gyrs of the universe they can be used as tracers of the early formation and evolution of the Milky Way. Among the GCs, those located in the most central and obscure Galactic structural component – the Bulge – are still the less studied ones. Furthermore, the Bulge GCs are probably the oldest objects of the Galaxy, especially those moderately metal-poor with blue horizontal branch (HB).

For a long time astronomers believed that GCs were made of only one stellar population (stars with the same age/chemical composition), but the Hubble Space Telescope provided evidence of more than one population in almost any GC. So the study of multiple stellar populations in GCs have been revolutionizing the understanding of the formation and evolution of stellar systems in general.

High-resolution spectroscopy have been demonstrated that there are significant chemical abundances variations from one stellar population to other, supporting the multiple population scenario. An appropriate choice and combination of UV filters is very sensitive to CNO variations, clearly splitting the multiple stellar population.

Color-magnitude diagrams (CMDs) combining optical and ultraviolet (UV) filters allow us to investigate the presence of multiple stellar populations in star clusters as well as their physical parameters such as age, metallicity, distance, reddening and helium abundance. In the present work we selected three bulge globular clusters with blue (NGC 6717 and NGC 6723) and red (NGC 6652) horizontal branches, all of them moderately metal-poor. This project consists to characterize the galactic GCs as in terms of astrophysical parameters as well in terms of multiple stellar populations.

2. HST Data

The data were obtained from HST by means the UV Legacy Survey (GO-13297, PI Piotto) and ACS GCs Treasury Program (GO-10775, PI Sarajedini) programs.

We used the UV filters (F275W, F336W, F438W) of the Wide Field Camera 3 (WFC3) and the optical filters (F606W, F814W) of the Wide Field Camera of Advanced Camera for Survey (WFC/ACS). A correlation for CNO elements abundances is clearly observed using the UVfilters (see Piotto et al. 2015, their Fig. 1).

3. Methods

Since the UV filters are very sensitive to the variations in the C, N and O abundances, they are very appropriate to detect the presence of multiple stellar populations within each GC. Using the so-called Chromossome map method (Milone et al. 2017) it is also possible to determine the fraction of stars in each stellar population. More details about this method can be found in the R.A.P Oliveira et al. contribution in this proceedings.

To characterize the ages, distances, reddening and helium abundance of the GCs in our sample we employed isochrones from BaSTI stellar evolutionay models (Pietrinferni et al. 2006). An isochrone contains a set of astrophysical parameters well defined, in this way it is an appropriate model to describe some

of the main properties of each GC. The isochrone fitting was made from the statistical method of Maximum Likelihood, it is the product between the color and magnitude gaussians distributions:

$$L = \prod_{obs=1}^{N} \prod_{Iso=1}^{1190} e^{-\frac{(color_{obs}-color_{Iso})^2}{\sigma^2_{color_{obs}}}} \times e^{-\frac{(Mag_{obs}-Mag_{Iso})^2}{\sigma^2_{Mag_{obs}}}}$$

where **obs** index represents the CMD information, N the number of observed stars and 1190 is the total points computed from BaSTI isochrones. For simplicity we adopt the $ln(L)_{MAX}$.

$$\mathcal{L} = \sum_{obs=1}^{N} \sum_{Iso=1}^{1190} -\frac{(color_{obs}-color_{Iso})^2}{\sigma^2_{color_{obs}}} - \frac{(Mag_{obs}-Mag_{Iso})^2}{\sigma^2_{Mag_{obs}}}$$

The final solutions were determined using a Markov-chain Monte Carlo (MCMC) algorithm (Foreman-Mackey et al. 2013).

4. Results

Through the rotation of Chromosome Map it is possible to obtain the fraction of stars of different populations. For NGC6717 the fraction of population 1 is higher than fraction of population 2 whereas for NGC6723 and NGC6652 population 2 is dominant (Fig. 1).

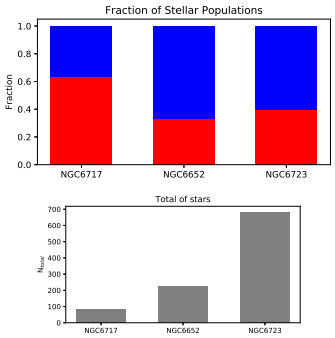

Figure 1. Results for multiple populations. The red bars represents the fraction of first population, the blue bars represents the second population and the grey bars represents the total number of stars.

The results from the isochrone fitting are presented on Fig 2 and Table 1.

Table 1. Results from Markov-Chain.

Parameters	NGC 6652	NGC 6717	NGC 6723
[Fe/H]	-0.70	-1.31	-1.01
Y	0.300	0.248	0.300
Age (Gyr)	$11.38^{0.44}_{0.37}$	$13.05^{0.34}_{0.37}$	$12.85^{0.70}_{0.70}$
E(B-V)	$0.11^{0.03}_{0.03}$	$0.06^{0.01}_{0.01}$	$0.24^{0.01}_{0.01}$
$(m-M)_0$	$14.85^{0.03}_{0.03}$	$14.42^{0.02}_{0.02}$	$14.18^{0.06}_{0.06}$

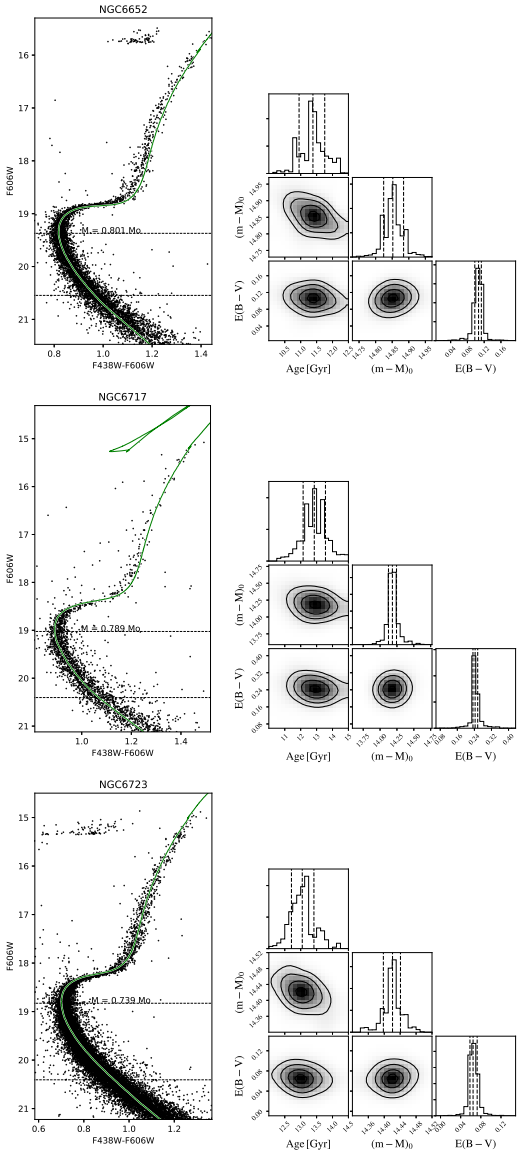

Figure 2. Results from the isochrone fitting. The left presents the best solutions, whereas the right panels show the corner plots with the 1d and 2d posterior probability distributions.

5. Conclusions

The preliminar results for the $ln(L)_{MAX}$ indicate a helium enhancement for the NGC6723 and NGC6652. These results are consistent with those from the Chromosome Map method.

Acknowledgements. São Paulo Research Foundation (FAPESP)

References

Piotto, G. et al. 2015, AJ, 149, 91
Milone, A. P. et al. 2017, MNRAS, 464, 3636
Pietrinferni, A., Cassisi, S., Salaris, M., Castelli, F. 2006, ApJ, 642, 797
Foreman-Mackey, D., Hogg, D. W., Lang, D., Goodman, J., 2013, PASP, 125, 306

Boletim da Sociedade Astronômica Brasileira, **30**, no. 1, 154-155

Fractal parameter algorithm for young star clusters

Sérgio Enzo Matsuda Sampa & Annibal Hetem Jr.

[1] Universidade Federal do ABC (UFABC) e-mail: sergio.sampa@aluno.ufabc.edu.br

Abstract. In previous works, we measured the fractal parameter Q for a set of clusters and the results were correlated with others clusters properties showing that almost half of these groups shows a relation between its parental cloud fractal dimension. In this study, it was analyzed a sample of young star clusters with the purpose of investigating inherent cluster properties and the stellar components dynamical evolution. Above all, the Q parameter measured for the clusters and its correlations with King's profile. These properties can take us to conclusions about the initial formation conditions of the clusters (hot or cold collapse), initial evolution (bonded or not) and its expected galactic dynamical evolution(crossing time). These studies can also provide information about the galaxy influence history on clusters and how they were affected by the passage through the structures. To analyze and study the data, it was necessary the development of numerical routines, done in C++, that organized and plotted the processed data.

Resumo. Em trabalhos anteriores, medimos o parâmetro fractal Q para um conjunto de clusters e os resultados foram correlacionados com outras propriedades dos clusters e mostram que quase metade desses grupos apresenta uma relação com a dimensão fractal de sua nuvem parental. Neste projeto foi feita a análise de uma amostra de aglomerados de estrelas jovens com o intuito de investigar as propriedades inerentes ao agrupamento e evolução dinâmica das componentes estelares. Em especial, o parâmetro Q medido para os clusters, e suas correlações com o perfil de King. Estas propriedades podem levar a conclusões sobre as condições iniciais de formação de clusters (colapso frio ou colapso quente), evolução inicial (ligada ou não) e sua evolução dinâmica galáctica esperada (tempo de cruzamento). Esses estudos também poderão nos dar informações sobre a história da influência da Galáxia sobre os clusters e como estes foram afetados por sua passagem pelas suas estruturas. Para o estudo e análise dos dados foi necessário o desenvolvimento de uma série de rotinas numéricas, realizado em C++, que organizaram e plotaram os dados tratados.

Keywords. Chaos – ISM: clouds – Methods: data analysis – Stars: pre-main sequence

1. Introduction

During the study of the characteristics of star formation clusters it is observed a wide scale of values and qualities (Lada & Lada 2003). Young star clusters can be found both in a large young star aggregate and in compacts concentrations of protostars embedded star formation regions. Considering ongoing models and star formation processes (Elmegreen 2011), it is evident the necessity of an investigation about the natural connection between these several scales of groups and agglomerates. Very likely, all these star formation processes might be related, despite the differences in scale.

In previous works (Gregorio-Hetem et al 2015, Fernandes et al. 2012), an analysis of a huge young star cluster sample was done in order to investigate intrinsic properties of the grouping and dynamical evolution of stellar components. In these studies, a special attention was given to the statistical parameter (Cartwright & Whitworth 2004), measured for the clusters, and its possible correlations with the fractal dimension estimated for the projected clouds (Hetem & Lépine 1993). These works demonstrate that more than 50% of the samples show substructures (or subgroups) that, once analyzed under a statistc and geometric view, exhibit a tendency to reproduce artificial simulations of stellar distributions (Lomax, Whitworth & Cartwright 2011).

The fractal geometry (or chaotic – not just random) of distributions of size and mass in interstellar gas relations have been evaluated for many studies (Hetem & Lépine 1993; Elmegreen & Falgarone 1996) and have been determinated by surveys of cloud imaging from literature.

2. Methodology

The parameter Q , which carries information about the cluster fractal structure, is a dimensionless quantity given by equation 1,

$$Q = \frac{\bar{m}}{\bar{s}} \tag{1}$$

where $\bar{m}$ and $\bar{s}$, normalized mean edge length and mean separation of points respectively, are statistical parameters that depend on the geometric distribution of data points (Cartwright & Whitworth 2004), as shown by equations 2 and 3.

$$\bar{m} = \frac{1}{(A_N N)^{1/2}} \sum_{i=1}^{N-i} m_i \tag{2}$$

A_N is the area of the smallest circle that contains all points (Megiddo 1983) and m_i is the length of edges in the minimum spanning tree (Gower & Ross 1969).

$$\bar{s} = \frac{1}{N(N-1)R_N} \sum_{i=1}^{N-i} \sum_{j=1+i}^{N} |\boldsymbol{r_i} - \boldsymbol{r_j}| \tag{3}$$

R_N is the radius of the smallest circle that contains all points and $\boldsymbol{r_i}$ and $\boldsymbol{r_j}$ are vector position of points.

3. Results

The parameters Q, $\bar{m}$ and $\bar{s}$ obtained through our numerical routines for the clusters are presented in table 1.

Table 1. Cluster data and results

Cluster	Q	$\bar{m}$	$\bar{s}$	Nstars
Berkeley 86	0.75218 ± 0.09924	0.68967 ± 0.08855	0.91690 ± 0.02788	86
Collinder 205	0.70082 ± 0.10329	0.66513 ± 0.09685	0.94907 ± 0.02166	177
Hogg 10	0.77455 ± 0.16803	0.69727 ± 0.14714	0.90022 ± 0.04527	88
Hogg 22	0.72174 ± 0.13335	0.69240 ± 0.12497	0.95934 ± 0.03791	98
Lynga 14	0.75372 ± 0.10793	0.70679 ± 0.09763	0.93774 ± 0.03538	67
Markarian 38	0.78586 ± 0.11486	0.69543 ± 0.09748	0.88493 ± 0.03667	58
NGC 2244	0.74330 ± 0.06030	0.67447 ± 0.05430	0.90740 ± 0.00912	296
NGC 2264	0.70326 ± 0.04399	0.65046 ± 0.04040	0.92492 ± 0.00690	293
NGC 2302	0.78474 ± 0.10397	0.65724 ± 0.08428	0.83752 ± 0.02788	70
NGC 2362	0.77863 ± 0.15075	0.64898 ± 0.12352	0.83349 ± 0.02957	132
NGC 2367	0.77900 ± 0.10365	0.64508 ± 0.08277	0.82809 ± 0.02917	61
NGC 2645	0.74542 ± 0.12376	0.65658 ± 0.10673	0.88083 ± 0.02978	104
NGC 2659	0.72893 ± 0.12101	0.68155 ± 0.11198	0.93499 ± 0.02223	220
NGC 3572	0.76514 ± 0.14664	0.69040 ± 0.13023	0.90233 ± 0.03056	151
NGC 3590	0.77843 ± 0.15229	0.75005 ± 0.14199	0.96354 ± 0.04756	81
NGC 5606	0.75310 ± 0.13636	0.66338 ± 0.11742	0.88087 ± 0.03359	99
NGC 6178	0.69149 ± 0.12146	0.69835 ± 0.12004	1.00993 ± 0.03655	104
NGC 6530	0.85984 ± 0.05765	0.64913 ± 0.04188	0.75494 ± 0.01379	63
NGC 6604	0.75843 ± 0.09169	0.68977 ± 0.08123	0.90947 ± 0.02487	90
NGC 6613	0.74977 ± 0.09400	0.68608 ± 0.08454	0.91505 ± 0.02117	135
Ruprecht 79	0.69175 ± 0.13663	0.64583 ± 0.12607	0.93363 ± 0.02806	175
Stock 13	0.74184 ± 0.11059	0.68719 ± 0.09898	0.92634 ± 0.03559	67
Stock 16	0.66747 ± 0.12311	0.64916 ± 0.11804	0.97258 ± 0.03007	141
Trumpler 18	0.75046 ± 0.12243	0.67824 ± 0.10907	0.90376 ± 0.02480	161
Trumpler 28	0.78515 ± 0.11149	0.66102 ± 0.09099	0.84191 ± 0.02935	74

An example of the minimum spanning tree and the smallest circle that contains all points for Colinder205 and NGC2244 is presented in figure 1.

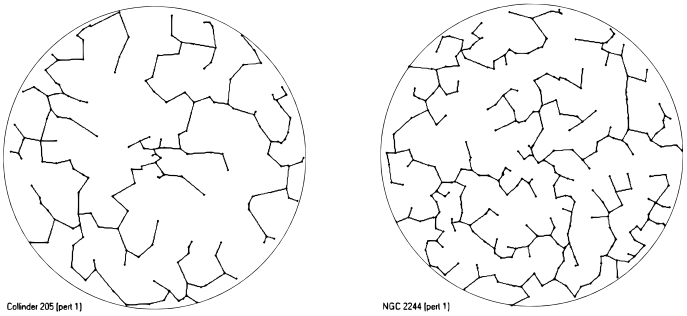

(a) Colinder205 (b) NGC2244

Figure 1. Graphic results for Colinder205 and NGC2244.

3.1. Analysis

The Q parameter, so as $\bar{m}$ and $\bar{s}$, were correlated with with the number of stars, Σ_0 and r_c in many ways.

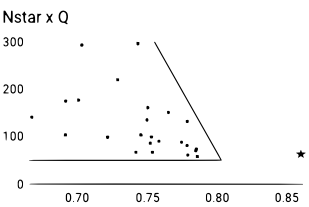

Figure 2. $N \times Q$

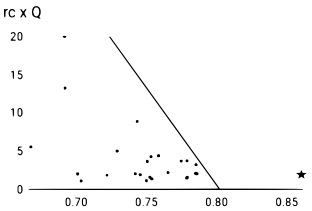

Figure 3. $r_c \times Q$

In graphs of figures 2 and 3 we can see a bottleneck tendency.

All three graphs, figure 2, 3 and 4, show forbidden regions, which boundaries are evidenced by the straight lines, showing a pattern relation between the parameters. However, there is an exception for these patterns, cluster NGC6530, illustrated as the star point. It happened due to a high value of Q, that is a consequence of a low value of $\bar{s}$.

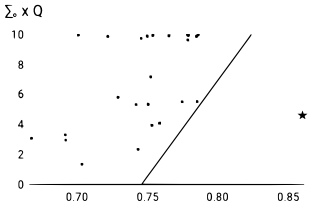

Figure 4. $\Sigma_0 \times Q$

4. Conclusion

By analyzing the obtained data in the present study and the data obtained from "Fitting of King's Model to Young Star Clusters", poster 118, it can be observed that the parameters for the clusters are somehow related, showing behaviours and forbidden regions. The cluster NGC6530 demonstrated a peculiar behaviour in every single relation made, extrapolating all the green lines, due to a low $\bar{s}$. In other words, either our model is not faithful with this cluster for some reason or this cluster have some particular characteristics that were not considered in this study.

References

Alfaro, E. J., &; González, M., 2016, MNRAS 456, 2900–2906
Cartwright &; Whitworth 2004
Dale, J. E., Ercolano, B., Bonnell, I. A., 2012, MNRAS, 424, 377
Dale, J. E., Ercolano, B., Bonnell, I. A., 2013, MNRAS, 430, 234
Davidge, T. J., 2017, ApJ 837:178
Elmegreen, B. G., 2011, EAS Publications Series, 51, 31
Elmegreen, B. G., Falgarone, E., 1996, ApJ, 471, 816.
Fernandes, B. Gregorio-Hetem, J.; Hetem, A. 2012, "Probing the anomalous extinction of four young star clusters: the use of colour-excess, main-sequence fitting and fractal analysis". A&;A, v. 541, p. A95.
Gieles, M., &; Portegies Zwart, S. F., 2011, MNRAS, 410, L6
Girichidis, P., Federrath, C., Allison, R., Banerjee, R., Klessen, R. S., 2012, MNRAS, 420, 3264
Gower, J.C., Ross, G.J.S., 1969, Appl. Stat., 18, 54
Gregorio-Hetem, J., 2008, "The Canis Major Star Formation Region", Handbook of Star Forming Regions Vol. II, Astronomical Society of the Pacific, Bo Reipurth, ed.
Gregorio-Hetem, J.; Hetem, A.; Santos-Silva, T.; Fernandes, B., 2015, "Statistical fractal analysis of 25 young star clusters". Monthly Notices of the Royal Astronomical Society, v. 448, p. 2504-2513
Hetem, A. &; Lépine, J. R. D., 1993, A&;A 270, 451
Annibal Hetem,. The Search for Parameters and Solutions: Applying Genetic Algorithms on Astronomy and Engineering. In: Shangce Gao. (Org.). Bio-Inspired Computational Algorithms and Their Applications. 1ed.Rijeka, Croatia: InTech, 2012, v. 1, p. 161-186.
Jaffa, S. E., Whitworth, A. P., Lomax, O., 2017, MNRAS 466, 1082–1092
Lada, C. J., &; Lada, E. A. 2003, ARA&;A, 41, 57
Lomax, O., Whitworth, P., &; Cartwright, A. 2011, MNRAS, 412-627
Parker, R. J., &; Dale, J. E., 2013, MNRAS, 432-986
Parker, R. J., &; Dale, J. E., 2015, MNRAS 451, 3664–3670
Parker, R. J., Andersen M., 2014, MNRAS, 441, 784
Portegies Zwart, S. F., McMillan, S. L. W., Gieles, M., 2010, ARA&;A 48, 431
Schmeja &; Klessen (2006)
Walker, D. L., Longmore, S. N., Bastian, N., Kruijssen, J. M. D., Rathborne, J. M., Galván-Madrid, R., Liu, H. B., 2016, MNRAS 457, 4536.

Boletim da Sociedade Astronômica Brasileira, **30**, no. 1, 156-157

Synthetic photometry for J-PLUS and S-PLUS and the multiple populations in globular clusters

Vinicius Branco[1], Paula R. T. Coelho[1], Ana Chies Santos[2] and Maria Luiza L. Dantas[1]

[1] Institute of Astronomy, Geophysics and Atmospheric Sciences (USP)
e-mail: vinicius.branco.silva@usp.br, pcoelho@usp.br, maria.luiza.dantas@usp.br
[2] Institute of Physics (UFRGS). e-mail: ana.chies@ufrgs.br

Abstract. The question of multiple populations in galactic globular clusters (GCs) is a matter of intense study and research nowadays. In recent years, both photometric and spectroscopic studies show that GCs are not the simple stellar populations we once believed they were: we observe stars with different abundance patterns in a same cluster. This work consists in developing a Python code which allows one to study isochrones (stellar evolution prescriptions) in magnitudes and colors as they will be observed from the surveys J-PLUS and S-PLUS. As multiple populations in GCs can be represented as a superposition of isochrones with different abundances and ages, this code will allows us to study the combination of filters in J-PLUS and S-PLUS which better highlight the existence of multipopulations.

Resumo. A questão das populações múltiplas em aglomerados globulares galácticos (GCs) é uma questão de intenso estudo e pesquisa nos dias de hoje. Nos últimos anos, evidências por estudos de fotometria e espectroscopia mostram que GCs não são as populações estelares simples conhecíamos: observamos estrelas com diferentes padrões de abundância em um mesmo aglomerado. Este trabalho consiste em desenvolver um código Python que permite estudar isócronas (prescrições de evolução estelar) em magnitudes e cores, pois serão observados a partir das pesquisas J-PLUS e S-PLUS. Como múltiplas populações em CGs podem ser representadas como uma superposição de isocronos com diferentes abundâncias e idades, o código nos permitirá estudar a combinação de filtros em J-PLUS e S-PLUS que melhor destaca a existência de multipopulações.

Keywords. globular clusters: general – Hertzsprung-Russell and C-M diagrams – Astrochemistry

1. Introduction

Globular clusters (GC) are systems of hundreds of thousand of stars born out of a common molecular cloud and mass distribution according to a initial mass function. Historically they were considered to be Simple Stellar Population (SSP) – all stars being chemically homogeneous and coeval – being represented by a single isochrone on the Color-Magnitude Diagram (CMD). However, recent studies have shown, that GCs of the Galaxy are constituted by multiple stellar population, e.g. the Main Sequence (MS) of the NGC 2808 (Fig. 1), whereas it's needed more than one isochrone to represent the system (Piotto et al. 2007; Milone et al. 2012). The S-PLUS (Southern Photometric Local Universe Survey) is a project inspired by the J-PLUS survey, which consists of observations in 12 filters covering the optical range from 3.000 to 11.000 Å, being 5 broad bands (similar to that of the SLOAN, 'ugriz') and 7 narrow bands. The assertive combination of its filters may show how differences in the chemical abundances of the stars affects the CMD.

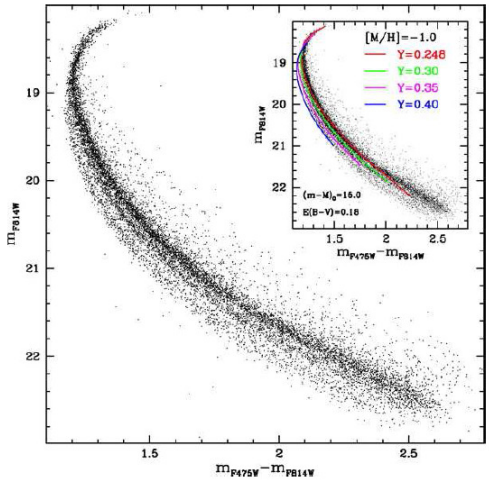

Figure 1. Four isochrones, with variation of the Helium abundance and same metallicity, to represent the apparent branches in the MS of the Globular Cluster NGC 2808 (Piotto et al. 2007).

2. Objectives

This work consists in creating a code in Python that simulate synthetic photometry based on the stellar library BaSeL (Westera et al. 2002), convolving it with all the S-PLUS filters. By selecting the stars over an isochrone of interest from BaSTI (Pietrinferni et al. 2006), we could convert the stellar parameters from the theoretical plane to the observational plane, i.e., the CMD. The main goal of this work is to understand how a population of stars with variations in Helium and abundances of C, N, O, and Na (commonly found in multiple populations in GCs) affect the CMD for different GC metallicities.

3. Metodology

First, all the stars in BaSeL were convolved with the S-PLUS filters using the PySynPhot[1] package for Python in order to obtain their integrated flux on each filter. Then the stars were selected based on their location ($\log T_{eff} \times \log g$) in the Hertzsprung-Russell Diagram (HRD) in comparison with an isochrone of interest from BaSTI (Fig. 2). Here, we used the GCs M15

[1] http://pysynphot.readthedocs.io/en/latest/

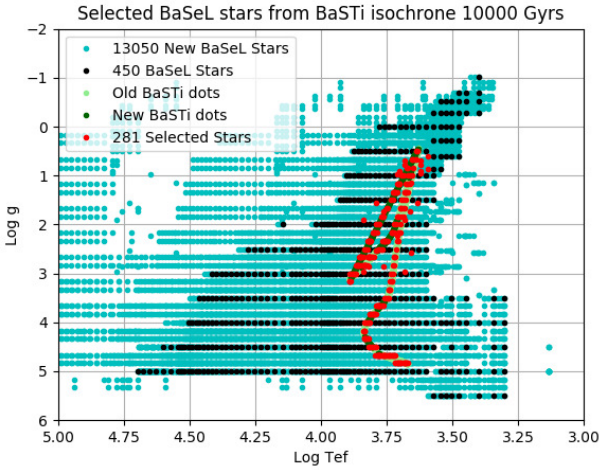

Figure 2. HR-Diagram showing all BaSeL original stars in black, the new interpolated stars in cyan, the BaSTI α-enhanced isochrone of 10 Gyrs, [Fe/H] = −2.14, in lightgreen and its interpolated points in dark-green. The selected stars are represented in red and vary depending on the used isochrone of reference.

([Fe/H] = −2.30) and 47 Tuc ([Fe/H] = −0.70) as reference (Bonatto et al. 2017).

The data points from the BaSeL were interpolated in order to have a finer grid of points in the HR. Values of integrated flux on each filter were found by 2D linear interpolation in T_{eff} and $\log g$. After the stars were selected, the fluxes were converted to the ABMAG system of magnitudes and the CMD produced as observed by Bonatto et al. (2017), whereas the Color is defined as (F0410 - F0660) and Magnitude as (F0410).

4. Results and Discussion

As seen on Fig. 1, it is expected that with the increasing variation of the Helium abundance one should find an increasing magnitude. This is reproduced on the panels (a) and (b) from Fig. 3, for both metallities, [Fe/H] = −0.70 and [Fe/H] = −2.14, where in blue is the α-enhanced population and the color gradient in red is the population with Helium abundance. Regarding variations in the light-elements abundance (CNONa), it is also verified on the panels (c) and (d), from Fig. 3 that the magnitude is increased (reducing brightness). Fig. 4 shows two populations with difference in both Helium and ligh-elements abundances. The same effect in the CMD is observed, like the other cases.

5. Conclusions and Perspectives

Out code manage to illustrate how the variation in the abundances of Helium and CNONa affects the CMD by lowering the brightness of the population of stars and that Multiple Populations of stars in GC may be represented by more than one isochrone, reflecting the discrepancy in their chemical abundances, as expected from the literature. These are preliminary results and the code needs improvement on the selection of stars and a better 2D interpolation of the CMD would highlight the difference between the populations. We plan to expand the study using other stellar libraries besides BaSeL. A comparison with Bonatto et al. (2017) work for the M15 case will show if this results are consistent with observations.

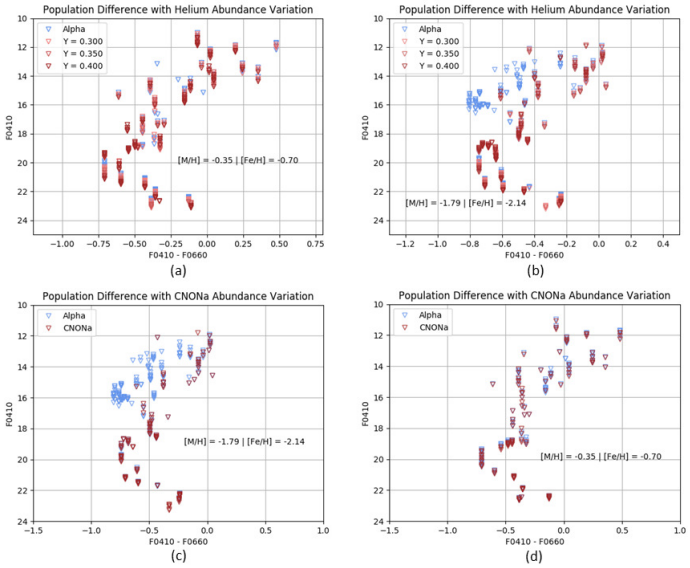

Figure 3. Populations of stars in different abundances variations in the CMD for two different metallicities: [Fe/H] = −0.70 and [Fe/H] = −2.14. (a) and (b) shows the effects of the variation in the Helium abundance for two different metallicities. (c) and (d) shows the effects of the variation of light-elements (CNONa) for two different metallicities.

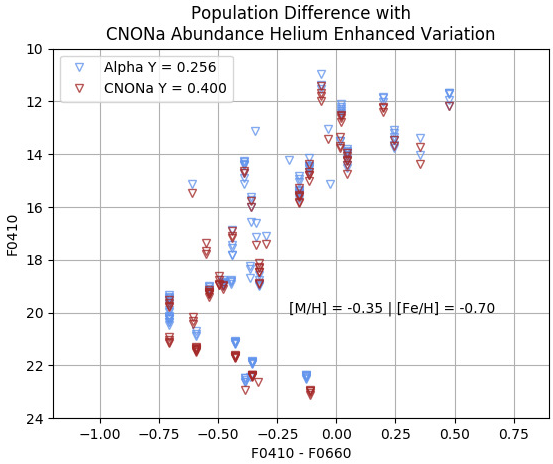

Figure 4. CMD of a population with [Fe/H] = −0.70 and both variations in Helium and light-elements, as expected in observations such as in Fig. 1

References

Bonatto, C., et al. 2017, A&A.
Milone A. P., et al. 2012 ApJ, vol. 745, p. 27.
Piotto, C., et al. 2007, AJL, vol. 661, p. L53.
Pietrinferni, A., et al. 2006, ApJ, vol. 642, p. 797.
Westera, P., et al. 2002, A&A, vol. 381, p. 524.

Boletim da Sociedade Astronômica Brasileira, **30**, no. 1, 158-159

S-PLUS, J-PLUS and J-PAS in the search for planetary nebulae

L. A. Gutiérrez-Soto[1], D. R. Gonçalves[1], S. Akras[2], A. Cortesi[3], S. Daflon[2], A. Ederoclite[4], M. Borges Fernandes[2], C. Mendes de Oliveira[3], C. B. Pereira[2], K. Viironen[4] & S-PLUS, J-PLUS and J-PAS collaborations

[1] Observatório do Valongo, Universidade Federal do Rio de Janeiro, Rio de Janeiro, Brazil
[2] Observatório Nacional - Ministério da Ciência, Tecnologia, Inovações e Comunicações, Brazil
[3] IAG - Universidade de São Paulo, Brazil
[4] Centro de Estudios de Física del Cosmos de Aragón, Pza. San Juan 1, E-44001, Teruel, Spain

Abstract. From the approximately 3,000 planetary nebulae (PNe) discovered in our Galaxy, only 14 are found to be members of the halo. Moreover, a systematic search for halo PNe was never done. We have developed tools to identify PNe in the Javalambre-Physics of the Accelerating Universe Astrophysical Survey (J-PAS) and related surveys, S-PLUS and J-PLUS, taking advantage of their great combination of narrow- and broad-band filters. The spectra of several classes of emission-line objects, which were convolved to the three photometric systems, were applied to the principal component analysis in order to find the most adequate combinations of colour to discriminate halo PNe from other objects. Here we propose colour-colour diagrams, based on these spectra. The diagrams separate halo PN candidates from other sources that resemble PNe (symbiotic stars; star-forming galaxies; cataclysmic variables; QSOs and extragalactic H II regions). We include, in our preliminary results, the photometry of a couple of halo PNe actually observed by the J-PLUS survey. Altogether, we show it is possible to discriminate halo PNe from other sources using different techniques which enclose important spectral nebular features.

Resumo. Das aproximadamente 3000 nebulosas planetárias (NPs) descobertos em nosso Galáxia, apenas 14 são membros do halo. Além disso, uma busca sistemática de NPs do halo nunca foi feita. Desenvolvemos ferramentas para detectar essas fontes no Javalambre-Physics of the Accelerating Universe Astrophysical Survey (J-PAS) e nos surveys, S-PLUS e J-PLUS, aproveitando sua ótima combinação de filtros estreitos e largos. Os espectros de vários tipos de objetos com linhas de emissão, que foram convolvidos para os três sistemas fotométricos, foram utilizados com a análise de componentes principais para encontrar as combinações de cor mais adequadas para discriminar NPs do halo de outros objetos. Aqui propomos novos diagramas cor-cor, que separam as NPs de outras fontes com linhas (estrelas simbióticas, galáxias formadoras de estrelas, variáveis cataclísmicas, QSOs e regiões H II extragalácticas). Incluímos em nossos resultados, a fotometria de um par de NPs observadas por J-PLUS. Ao todo, mostramos que é possível discriminar NPs de outras fontes usando diferentes técnicas que envolvem importantes características espectrais.

Keywords. Galaxy: halo – planetary nebulae – ISM: lines and bands

1. Motivation

Planetary nebulae (PNe) are a kind of emission line nebula that represent a short phase of the stellar evolution of low- and intermediate-mass stars ($0.8M_{\odot}$ - $8.0M_{\odot}$). During the unstable AGB phase, stars eject their outer layers into the interstellar medium resulting in an enrichment in heavy elements. Approximately, 3,000 PNe have been identified in our Galaxy (Parker et al. 2012). Of these, only fourteen objects are located in the Galactic halo (Otsuka et al. 2015). Halo PNe are interesting objects because they provide important information about the evolution of old and low-mass stars of in the halo, and allow the early chemical conditions of the Galaxy to be studied.

A number of new Galactic PNe were identified in the equatorial plane (Viironen et al. 2009) by using the $(r' - \mathrm{H}\alpha)$ vs $(r' - i')$ colour-colour diagram in the Isaac Newton Telescope (INT) Photometric Hα Survey of the Northern Galactic Plane (IPHAS; Drew et al. 2005). The multi-filter J-PAS, J-PLUS[1] and S-PLUS[2] surveys are more suitable surveys for searching PNe in the direction of Galactic halo. The combination of narrow- and broad-band filters in these surveys (in total, 56, 12 and 12, respectively) allow us to identify objects with prominent emission lines. We use the principal component analysis (PCA) to search for the most adequate combination of colours that distinguish halo PNe from their contaminants. Several colour–colour diagrams have been generated and explored in order to separate halo PNe from other emission line objects.

[1] The Javalambre-Photometric Local Universe Survey
[2] The Southern Photometric Local Universe Survey

2. Results

The synthetic magnitudes of various classes of objects were calculated for the filters in the three surveys, using available observed spectra, and a set of photo-ionization models for halo PNe. The spectra of PNe: DdDm-1, NGC 242 and MWC 574 were taken from Kwitter & Henry (1998), Kwitter et al. (2003) and Pereira & Miranda (2007), respectively, while the spectra of PNe H 4-1 and PNG 135.9+55.9 were obtained from the SDSS. The spectra of the rest of the objects: cataclysmic variables (CVs), star-forming galaxies and quasistellar objects (QSOs) with different redshift ranges are also from SDSS. Galactic disk symbiotic stars (SySts) were taken from Munari & Zwitter (2002) and IPHAS (Rodríguez-Flores et al. 2014), while the extragalactic SySts in IC10, NGC 185 and in NGC 205 were gathered from Gonçalves et al. (2015). Finally, H II regions in NGC 55 (Magrini et al. 2017) are also included in this analysis.

Fig. 1 displays the S-PLUS colour-colour diagram (J0515 – J0660) vs (J0515 – J0861). Halo PNe with strong Hα emission are placed at the upper left. The J-PLUS colour-colour diagram (J0660 – gSDSS) vs (J0660 – rSDSS) is presented in Fig. 2. Note that the known PNe: H 4-1 and PNG135.9+55.9 (blue and green circles with errorbars, respectively) observed in the J-PLUS survey, during the phase of the data science verification, are located

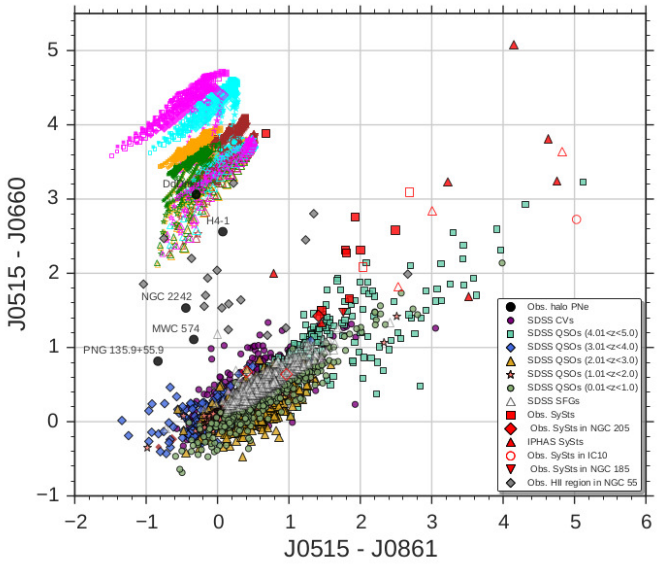

Figure 1. The S-PLUS colour-colour diagram (J0515-J0660) vs (J0660-J0861). Families of cloudy modelled halo PNe (the pink, cyan, orange, green and brown symbols) spanning a range of halo PN properties are included. These models represent different sets of nebular abundances, with densities of 6000 cm^{-3} (filled symbols) and 3000 cm^{-3} (empty symbols), for a spherically symmetric nebula of 2.7″ in radius, at a distance of 10 kpc. Central star black-body effective temperatures and luminosities are from 50×10^3 to 250×10^3 K, in steps 10×10^3 K; and 0.5, 1.0, 5.0 and 10×10^3 $L_\odot$. The rest of the symbols are as follows: halo PNe (black circles); QSOs with redshift in the range from 0.01 to 1.0 (light green circles); 1.01 to 2.0 (light orange stars); 2.01 to 3.0 (light orange triangles); 3.01 to 4.0 (light blue diamonds); and 4.01 to 5.0 (green boxes), CVs (violet circles); star-forming galaxies (black, open triangles); symbiotic stars (red boxes); extragalactic symbiotic stars (red diamonds); symbiotic stars from IPHAS (red triangles); extragalactic H II region (gray diamonds).

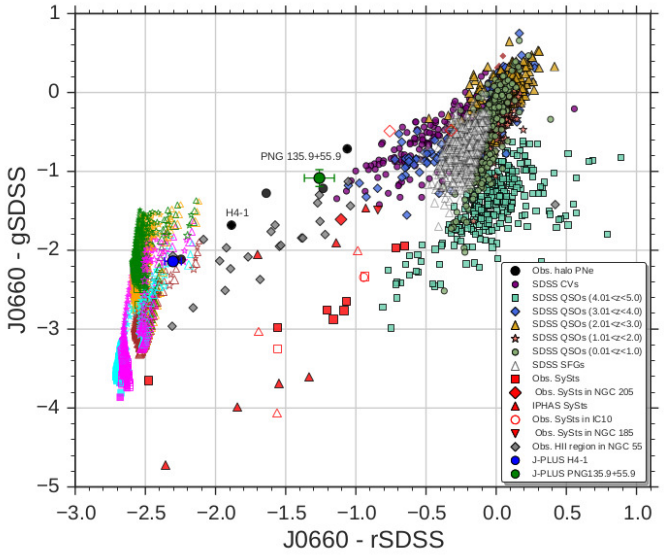

Figure 2. The J-PLUS colour-colour diagram (J0660 – gSDSS) vs (J0660 – rSDSS). The blue and green symbols with errorbars are the J-PLUS observations for H 4-1 and PNG 135.9+55.9 respectively. The rest of the symbols are the same as in Fig. 1.

very close to the regime where halo PNe are expected. The J-PAS colour-colour diagram (J4200 – J5001) vs. (J4200 – J8400) is shown in Fig. 3. The J4200 - J5001 colour is prominent for modelled and some observed halo PNe, due to the strong [O III] emission. The halo PNe MWC 574 and PNG135.9+55.9 are found at the bottom side of the diagram in the regime of QSOs. This may be associated with the very low O abundance in these PNe (e. g. Sandin et al. 2010), which results in a J4200 – J5001 colour index close to zero. A combination of colours from narrow- and broad-band filters seems to be efficient in the identification of PNe.

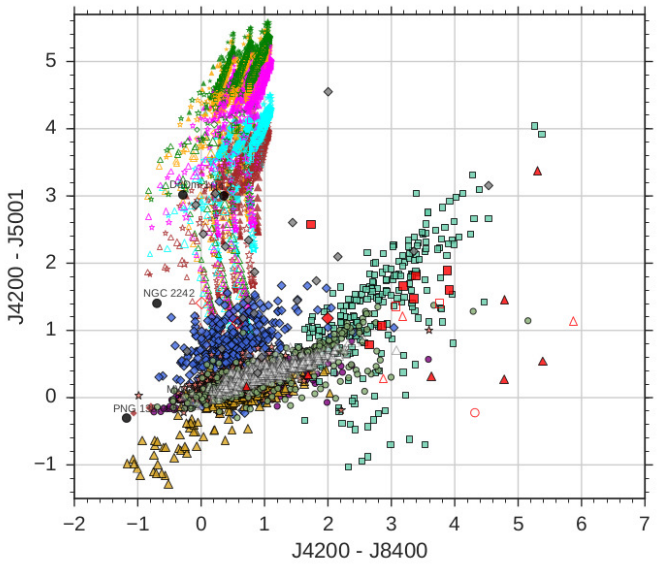

Figure 3. The J-PAS colour-colour diagram (J4200 – J5001) vs (J4200 – J8400). The symbols are the same as in Fig. 1.

Acknowledgements. LAGS, DRG and SA acknowledge the support of CAPES and CNPq.

References

Drew, J. E., Greimel, R., Irwin, M. J., et al. 2005, MNRAS, 362, 753
Gonçalves, D. R., Magrini, L., de la Rosa, I. G., & Akras, S. 2015, MNRAS, 447, 993
Kwitter, K. B., & Henry, R. B. C. 1998, ApJ, 493, 247
Kwitter, K. B., Henry, R. B. C., & Milingo, J. B. 2003, PASP, 115, 80
Magrini, L., Gonçalves, D. R., & Vajgel, B. 2017, MNRAS, 464, 739
Munari, U., & Zwitter, T. 2002, A&A, 383, 188
Otsuka, M., Hyung, S., & Tajitsu, A. 2015, ApJS, 217, 22
Parker, Q. A., Cohen, M., Stupar, M., et al. 2012, MNRAS, 427, 3016
Pereira, C.-B., & Miranda, L.-F. 2007, A&A, 467, 1249
Rodríguez-Flores, E. R., Corradi, R. L. M., Mampaso, A., et al. 2014, A&A, 567, A49
Sandin, C., Jacob, R., Schönberner, D., Steffen, M., & Roth, M. M. 2010, A&A, 512, A18
Viironen, K., Mampaso, A., Corradi, R. L. M., et al. 2009, A&A, 502, 113

Boletim da Sociedade Astronômica Brasileira, **30**, no. 1, 160-161

Tracing the Galactic bar through dense molecular cores with broad emission spectra

Shaila Akhter[1,2,7], Maria R. Cunningham[1], Lisa Harvey-Smith[2,1], Mohammad Ali Nawaz[3], Paul A. Jones[1], Cormac Purcell[4,5], Andrew Walsh[6], Elisabete M. de Gouveia Dal Pino[7], D. Falceta-Gonçalves[3]

[1] School of Physics, University of New South Wales, NSW 2052, Australia e-mail: s.akhter@unsw.edu.au
[2] CSIRO Astronomy and Space Science, PO Box 76, Epping, NSW 1710, Australia
[3] Escola de Artes, Ciências e Humanidades, Universidade de São Paulo, Rua Arlindo Bettio, 1000, SP 03828-000, Brazil
[4] Department of Physics & Astronomy, Faculty of Science and Engineering, Macquarie University, NSW 2109, Australia
[5] Sydney Institute for Astronomy (SiFA), School of Physics, The University of Sydney, NSW 2006, Australia
[6] International Centre for Radio Astronomy Research, Curtin University, GPO Box U1987, Perth, WA 6845, Australia
[7] Instituto de Astronomia, Geofísica e Ciencias Atmosfericas - Universidade de São Paulo, São Paulo, Brazil

Abstract. We find 14 dense molecular regions with $NH_3(1,1)$ transition line from the H_2O Southern Galactic Plane Survey (HOPS) exhibiting broad emission spectra (with observed velocity widths between 19.8 and 47.6 km/s). These clumps are clustered at $l \approx 5.4°, -5.4°$ and $-10°$. Cluster-1 and Cluster-2 have inverse symmetry with respect to the Galactic centre and are rotating in a non-circular x-1 orbit. We predict them as the indicator of Galactic Bar potential. Cluster-3 with 2 clumps are undergoing high-mass star formation.

Resumo. Encontramos 14 regioes moleculares densas com linha de transicão $NH_3(1,1)$ do H_2O Southern Galactic Plane Survey (HOPS) exibindo amplos espectros de emissão (com larguras de velocidade observadas entre 19,8 e 47,6 km/s). Esses aglomerados são agrupados em $l \approx 5.4°, -5.4°$ e $-10°$. Cluster-1 e Cluster-2 tem simetria inversa em relacão ao centro galactico e estão rolando em uma orbita x-1 não-circular. Nos os predizemos como o indicador do potencial da Barra Galãctica. Cluster-3 com 2 aglomerados estão passando por formacão de estrelas de alta massa.

Keywords. Stars: formation – ISM: clouds – Galaxy: kinematics and dynamics

1. Introduction

Study of high-mass star formation helps us to understand the evolution of our Galaxy, its surrounding ISM and shape of the Universe. From literature we know that our Galaxy has a central rotating bar (e.g., Sormani & Magorrian 2015). This has been suggested since the 1970's, from the large non-circular kinematics of HI and CO lines in the inner Galaxy (e.g., Peters 1975) and was confirmed two decades later with evidences (e.g., Binney et al. 1997). The understanding of the formation of this bar can help us to solve the mystery of star formation, evolution of the Galaxy, gas infall in the vicinity of the Galactic centre, disk accretion and the non-circular motion of the gases near the Galactic centre.

In this research, we used $NH_3(1,1)$ from the HOPS as the primary tracer of dense molecular cores. NH_3 is a very good tracer for colder and denser gas (Walsh et al. 2011) because: 1) it has a high critical density ($\rho_c \sim 10^4 cm^{-3}$, Ho & Townes 1983) and 2) unlike many other tracers, it is protected from being frozen out to dust in the cold temperature (Bergin & Langer 1997). We then compared NH_3 spectra with other tracers available from the HOPS. This study will aid in the understanding of the dynamics of the molecular clouds in the Galactic bar. All the results, analysis and discussion of this proceeding are in Akhter et al. (2018).

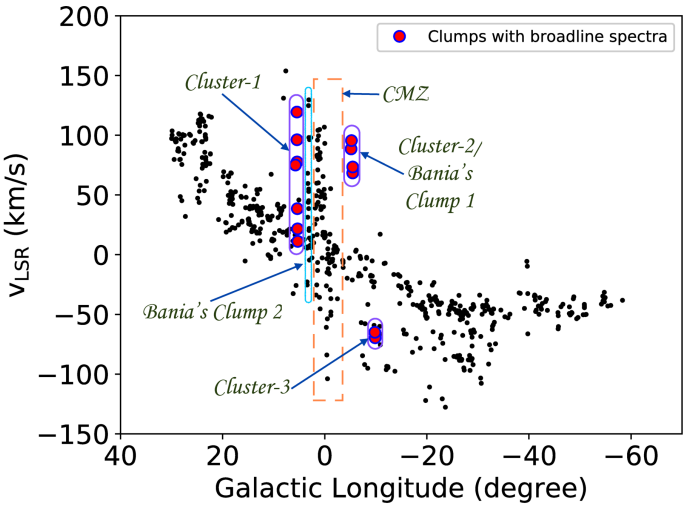

Figure 1. The $l - v$ diagram of all the clumps found in the entire HOPS region with $NH_3(1,1)$ transition line. The three clusters of 14 clumps with broad emission spectra are shown with 'red solid circles with blue edge'. The 'orange dotted box' shows the CMZ and the 'sky-blue oval box' shows *Bania's Clump 2* (Bania 1977) to put all these features into perspective.

2. Data

We used data from HOPS (Walsh et al. 2011) - a survey of selected frequencies between 19.5−27.5 GHz with the 22 m Mopra Radio Telescope. The survey covered one third of the Galactic plane, 100° in Galactic longitude $30° \leqslant l \leqslant 290°$ (through $l = 0°$) and 1° in Galactic latitude $|b| \leqslant 0.5°$. The average beam size was $\sim$ 2 arc-min (2.4′ to 1.7′) with a velocity coverage of ±200 kms^{-1}. We used the 3D position-position-velocity data cubes of the molecular transition lines $NH_3(1,1)$, (2,2), (3,3),

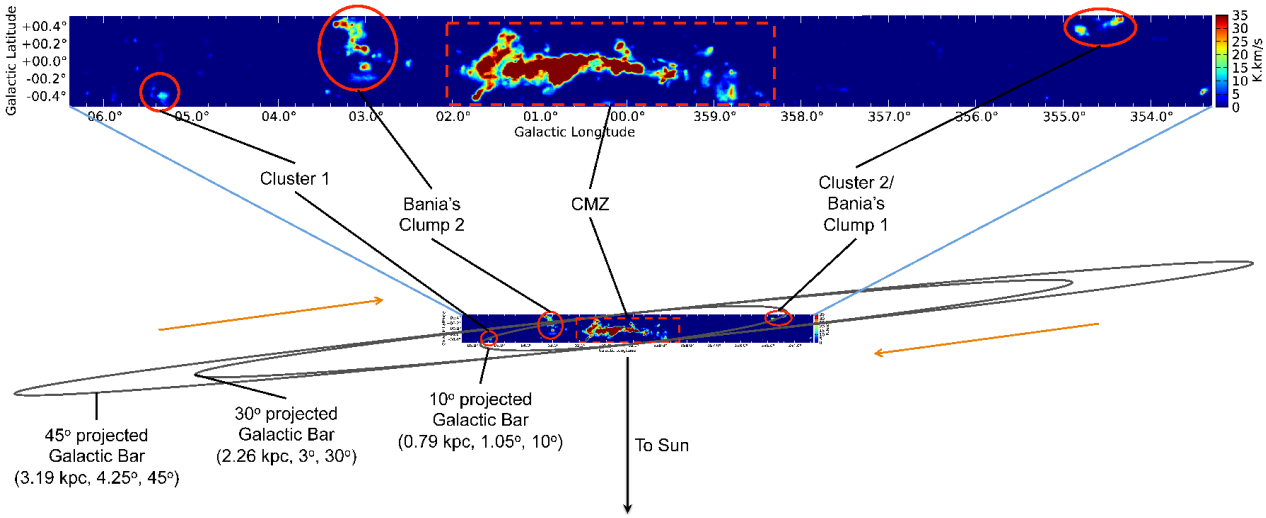

Figure 2. *Top:* $NH_3(1,1)$ integrated emission data from the HOPS; *Bottom:* A geometrical Galactic model showing Cluster-1 and Cluster-2 in relation to the Galactic bar potential. Three apparent projected galactic bars with respect to different bar parameters are shown ('black outlined' ellipses). This Figure is adapted from Akhter et al. (2018).

(6,6), $HC_3N(3-2)$, H_2O maser emission and the radio recombination line H69α. Because the CMZ is dominated by dense molecular gas with large velocity dispersion and high temperatures (Morris & Serabyn 1996), to avoid inexplicability, we did not use the data from the HOPS region $-2.7^\circ < l < 3.9^\circ$ that contains the CMZ.

3. Analysis and Results

To find clumps (regions of dense molecular gas which may form stars), we used FELLWALKER, a clump finding algorithm from the STARLINK-CUPID package (Berry 2015) on 2D position-position images (integrated over velocity) of the $NH_3(1,1)$ line. We identified 496 candidate star forming clumps in $-60^\circ \leqslant l \leqslant -2.7^\circ$ & $3.9^\circ \leqslant l \leqslant 30^\circ$. We then used 3D data cubes to find averaged spectra over each clump. Among these, 14 clumps exhibit broad observed linewidths ($\sim 19.8 - 47.6$ kms^{-1}) with all five hyperfine components blended. Here, we analyse these clumps.

Figure 1 shows $l - v$ diagram of these broad emission line clumps. These clumps are clustered in three positions and we refer them as Cluster-1, Cluster-2 and Cluster-3. A multimolecular line comparison exhibits the same line broadening for other tracers as well (where detected emission). We did not detect any $NH_3(6,6)$ emission in the current working region of HOPS. *Cluster-1 and Cluster-2:* Clumps in these clusters have anomalous and positive central velocities with large velocity dispersion (Figure 1) and approximately equal angular distance from the Galactic centre (i.e., $|l| = 5.5^\circ \pm 0.1^\circ$). We detect $NH_3(1,1)$, (2,2), (3,3), and $HC_3N(3-2)$ lines in the clumps and no H_2O maser emission and H69α. *Cluster-3* is quite different from Cluster-1 and Cluster-2. The clumps in the Cluster-3 have negative velocities and are at $l \approx -10^\circ$. Other than detecting $NH_3(1,1)$, (2,2), (3,3), and $HC_3N(3-2)$ lines in the two clumps, we also detect H_2O maser emission and H69α in one of the clumps.

We measured observed velocity widths, velocity center and antenna temperature for all the clumps with Gaussian model fitting. We also performed Ammonia model fitting on these clumps for $NH_3(1,1)$, (2,2), (3,3) lines, measured their intrinsic velocity widths and estimated their rotational temperature using equation from Menten & Alcolea (1995) considering the system is optically thin and in LTE.

4. Discussion and Conclusion

We found that Cluster-1 and Cluster-2 have: **a)** No visible sign of star formation; **b)** High rotational temperatures for NH_3 (2,2)/(1,1) and (3,3)/(1,1); **c)** High Spearman's rank-order correlation between cloud positions and their spectral parameters; **d)** Relative positions w.r.t. the Galactic Bar (Figure 2); **e)** Appear as two vertical features (i.e., regions with a large velocity range within a small longitude range, indicating clumps lying on the dust lane shocks Sormani & Magorrian 2015) in the $l - v$ diagram. We suggest that *these two clusters are associated with the shocked dust-lane and are affected by dynamics of the Galactic bar potential.* This scenario gives explanation for their line broadening and high velocity dispersion.

Clumps in Cluster-3 are undergoing high-mass star formation. The clumpiness in the three clusters might result from molecular clouds undergoing heating & cooling processes (Baba et al. 2010).

Acknowledgements. Authors use observations from Mopra radio telescope — a part of the Australia Telescope National Facility, managed by CSIRO, funded by the Australian Government. SA acknowledges the hospitality of IAG-USP & USP-Leste, where she concluded this work. MAN acknowledges support from FAPESP (2015/25126-2) grant, EMGDP and DAFG from FAPESP (2013/10559-5) grant, EMGDP from CNPq (306598/2009-4) grant.

References

Akhter S. et al. 2018, MNRAS, submitted.
Baba J., Saitoh T. R., Wada K., 2010, PASJ, 62, 1413
Bania T. M., 1977, ApJ, 216, 381
Bergin, E. A., & Langer, W. D. 1997, ApJ, 486, 316
Berry, D. S. 2015, Astronomy and Computing, 10, 22
Binney, J., Gerhard, O., & Spergel, D. 1997, MNRAS, 288, 365
Ho P. T. P. & Townes C. H., 1983, ARA&A, 21, 239
Menten, K., Alcolea, J., 1995, ApJ 448, 416
Morris, M., & Serabyn, E. 1996, ARA&A, 34, 645
Peters, W. L., III 1975, ApJ, 195, 617
Walsh, A. J., Breen, S. L., Britton, T., et al. 2011, MNRAS, 416, 1764
Sormani M. C., Magorrian J., 2015, MNRAS, 446, 4186

Boletim da Sociedade Astronômica Brasileira, **30**, no. 1, 162-165

Compact galaxies? : ask the Illustris simulation!

I. G. de la Rosa[1], N. Caon[1] & B. T. Dullo[2]

[1] Instituto de Astrofisica de Canarias, Spain. e-mail: irosa@iac.es
[2] Universidad Complutense de Madrid, Spain.

Abstract. Compact galaxies, known to be abundant in the past, some 10 billion years ago, are generally thought to be almost extinct in the present Universe. In a previous statistical study, we ratified that, instead of vanishing, the majority of them have survived, hidden by stellar disks or halos. Recent hydrodynamical cosmological simulations, like Illustris, not only produce realistic galaxies, but also enclose a sufficiently large volume to include some of the rarest specimens, like the compact galaxies. By tracking the evolution of the simulated systems we have followed the fate of the high-redshift compact galaxies. As already observed, the compact galaxies at $z = 2$ survive to $z = 0$ embedded in accreted halos or disks. We also compare two simulated galaxies hosting compact cores, yet accreting either a disk or a spheroidal halo.

Resumo. As galáxias compactas, abundantes no passado, cerca de 10 bilhões de anos atrás, encontram-se quase extintas no universo presente. Em um estudo estatístico anterior, ratificamos que, em vez de desaparecer, a maioria delas sobreviveu, escondidas por discos estelares ou halos. As recentes simulações cosmológicas hidrodinâmicas, como Illustris, não apenas produzem galáxias realistas, mas também incluem um volume suficientemente grande para incluir alguns dos espécimes mais raros, como as galáxias compactas. Neste estudo seguimos a evolução das galáxias compactas simuladas. Neste estudo confirmamos que, as galáxias compactas a redshift 2 sobrevivem na actualidade embutidas em halos ou discos. Comparamos também duas galáxias simuladas que possuem núcleos compactos, ainda que uma delas acrescentou um disco enquanto a outra um halo esferoidal.

Keywords. Galaxy: evolution – Cosmology: miscellaneous – Techniques: miscellaneous

1. Introduction

Numerical Simulations still suffer from a bad image in some observational astrophysical communities. Yet, it is worth emphasizing that numerical simulations are a must, rather than a luxury, for studying the non-linear growth of structures in the Universe. In the *pre-computer era* (1940-50), scientists and engineers commented: *God would not be so unkind as to make the equations of nature nonlinear*, frustrated after realizing that nature is essentially non-linear and, consequently out of the reach of their analitical tools. Today, numerical simulations are the theoretical tool of choice to study the formation and evolution of galaxies.

Cosmological hydrodynamic simulations, like Illustris (Vogelsberger et al. 2014; Nelson et al. 2015) or EAGLE (Schaye et al. 2015), produce a realistic morphological mixture of galaxies, which follow scaling relations not explicitly imposed by the postulated physical mechanisms. Additionally, the Illustris cosmological co-moving volume $(106.5\ \mathrm{Mpc})^3$ is large enough to include rare galaxies.

Simulations allow one to track the galaxy evolution along a wide redshift range from 47 to 0 by means of the merger tree which connect galaxies at different redshifts. This makes simulations a useful tool to assist astronomers on the theoretical interpretation of their results. In the present study, we have used the Illustris simulation to shed light on the unsolved mystery of the red nugget's fate.

More than nine Gyrs ago, at $z = 1.5$, a massive galaxy census would result in roughly 40 % disks, 15 % extended spheroids, 25 % compact spheroids and some 20 % peculiars (e.g. Peth et al. 2016). A compact spheroid encloses a mass comparable to the Milky Way, within a small volume (typically the size of a bulge). At $z = 1.5$, the compact spheroids are divided into 1/4 blue (star-forming) and 3/4 red (quiescent). For short, the high-redshift massive quiescent compact galaxies have been nicknamed *red-nuggets*. On average, 200 red nuggets were found in each Illustris volume $(106.5\ \mathrm{Mpc})^3$ at $z = 1.5$. In the present day universe, a similar census of massive galaxies gives 30% disks, 65% extended spheroids and 5% peculiar morphologies (Buitrago et al. 2013). Strikingly, red nuggets are virtually absent (e.g. Trujillo et al. 2009; Taylor et al. 2010).

The predominant interpretation of this extinction problem postulates that red nuggets ended up in the centres of present day massive ellipticals after the growth of an extended stellar halo through disipationless minor mergers (Hopkins et al. 2009; Bezanson et al. 2009). An alternative view links red nuggets to the bulges of the present day massive disk galaxies (e.g. Graham, Dullo & Savorgnan 2015), showing that bulges and red nuggets are structurally similar. In this scenario, red nuggets would have *survived* hidden by stellar disks. In a further study, de la Rosa et al. (2016) showed that both channels are possible and roughly 50 % of the massive galaxies hosting red nugget-like cores show disks. Additionally, the number density of red nugget-like cores hosted by present day galaxies is comparable to that of red nuggets at $z = 1.5$, giving more weight to the hypothesis of their survival.

The question we pose to the Illustris simulation is, do all individual compact cores survive from $z = 1.5$ to $z = 0.0$? By tracking the red nugget's descendants along the merger trees, the simulation allows us to watch the 2D or 3D stellar halo construction around the surviving compact core. We are particularly interested on understanding the growth of a disk around a red nugget, so we will carry out a detailed monitoring of two alternative examples, a disk and a spheroidal galaxy.

2. The Data

In de la Rosa et al. (2016), photometric bulge+disk (B+D) decomposition was used to carry out a segregated study of the bulge, herein called *core*. We use the compactness criterion devised by van Dokkum et al. (2015), $R_{eff} < 2.0$ kpc

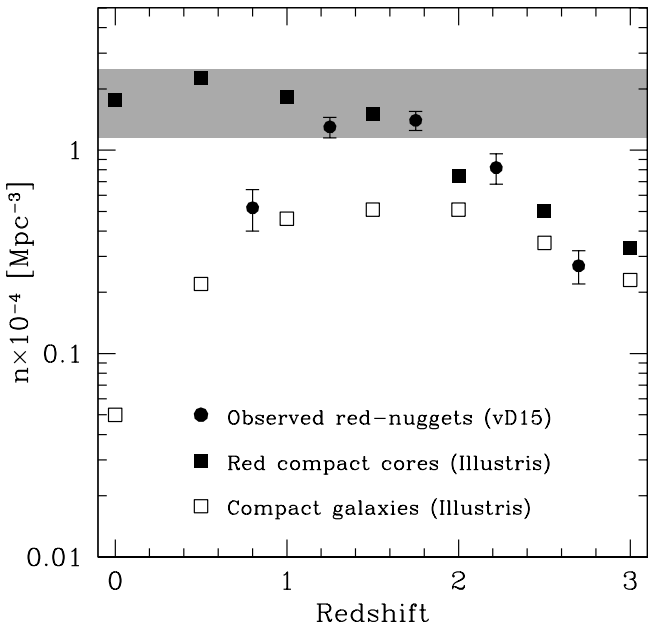

Figure 1. Number density evolution of observed red nuggets (van Dokkum et al. 2015) and Illustris red compact cores (solid circles and squares). The discrepancy between observations and simulations, at redshifts $\lesssim 1.5$, are attributed to the fact that observations compute full galaxies (instead of their cores), which are hardly compact at low redshifts, as seen by the density of Illustris compact galaxies (open squares).

$\times (M_\star/10^{11} M_\odot)$ to compare the number density of *compact* red nuggets at z≈1.5 with that of present day *compact* cores. A constant number density would fit the expectations of the red nugget survival hypothesis, as it was found by de la Rosa et al. (2016), using SDSS galaxies. Illustris simulation allows tracking the compact core number density along the full $z = 3$ to 0 redshift range. B+D decomposition has always been a laborious task. A kinematic, rather than photometric B+D decomposition has shown to be more suited for Illustris galaxies by Bottrell et al. (2017). Using Illustris data for 6,762 galaxies with $\log M_\star > 10$ we have measured the compacity of their cores, $\log(M_\star/R_{eff})_{core}$, discovering that it shows a perfect correlation with the parameter $\log\Sigma_{1kpc}$, the stellar mass density in the central 1 kpc of the galaxy. This parameter, introduced by Cheung et al. (2012), is easily computable in simulated galaxies and makes a perfect proxy for the core compacity. As shown above, for van Dokkum et al. (2015) a core can be classified as compact when its compacity $\log(M_\star/R_{eff})_{core}$ exceeds 10.7. Our calculations (to be published) show that this condition is equivalent to $\log\Sigma_{1kpc} > 9.15$.

3. Results

In the present study, the Illustris data are used to shed light on two different controversies. On one side, the disagreement on the evolution of the number density of compact galaxies. On the other side, the poorly understood process of disk formation around a compact core.

3.1. Number density

As discussed in Section 1, red nuggets are considered as virtually extinc in the present universe (e.g. Trujillo et al. 2009; van der Wel et al. 2014; van Dokkum et al. 2015). However, other studies, using low redshift samples, disagree on that results (An updated summary in Charbonnier et al. 2017). In the present study, we test the possibility that this discrepancy could be attributable to the questionable use of compacity measurements of full galaxies. As galaxies evolve and external accretion proceeds, full galaxies see their general compacity declining to the point that, at $z = 0$ virtually no full galaxy satisfies the strict compactness criteria. Galaxy cores, on the contrary, can keep their compacity intact, despite the progressive assembly of an accreted halo.

We have carried out compacity measurements on both the core and the full galaxy of Illustris samples at redshifts ranging from 3 to 0. Following van Dokkum et al. (2015) criterion, a *compact full galaxy* must fulfil $\log M_\star > 10.6$ and $\log(M_\star/R_{eff}) > 10.7$. A *compact core*, as shown in Section 2, must comply with $\log\Sigma_{1kpc} > 9.15$. We have used the star formation rate (SFR) Illustris information to seggregate quiescent from actively star forming galaxies. Only cores hosted by quiescent (red) galaxies are accounted. As shown in Figure 1, the number density evolution of both red compact cores and compact full galaxies are compared to van Dokkum et al. (2015) observations. Observed and simulated galaxies reasonably match down to redshift ≈ 2. There, the compact full galaxy number density declines, as expected by the accretion. The Illustris red compact core density grows along with that of the red nuggets up to a peak at redshift ≈ 1.5. At lower redshifts, when the red nuggets have likely accreted a diffuse halo, the number of both observed and simulated full compact galaxies (even those hosting a hidden red nugget) drops drastically. Oppositely, the Illustris compact core number density is kept relatively constant around the red nugget peak value, at z≈1.5, supporting the hypothesis of their survival to the present day universe.

3.2. Disk formation

We have selected examples of two simulated galaxies which host a compact core, but differ on their morphology. Galaxy id=138414 shows a disk and id=233087 (ids at $z = 0$) show a spheroidal morphology. Our purpose is to find out the processes responsible for their alternative developments. To this end, we have collected the evolution of several structural parameters, which allow us to follow the galaxy assembling. Those parameters, shown in Figures 2 and 3 include: (a) the star formation rate (SFR) and central super massive black hole (SMBH) accretion rate; (b) the gas and star masses; (c) the *in-situ* and *ex-situ* stellar masses, which refer to stars formed respectively in the present galaxy or in an external one, but later accreted; (d) bulge-to-total (B/T) ratio, where high (B/T) corresponds to spheroidal-like morphologies; (e) the stellar mass density in the central 1 kpc, the $\log\Sigma_{1kpc}$ parameter introduced by Cheung et al. (2012) and (f) the SMBH mass.

As seen in Figure 2, the disk galaxy exhibits two main phases: a *compact-core* phase, ranging from z ≈ 3.3 to z ≈ 2.5 and an *accretion* phase lasting to $z \lesssim 0.5$. The *compact-core* phase is triggered by a major merger (1:1), which contributes to the formation of the bulk of the galaxy's stellar mass, with both gas and ex-situ (ready formed) stars (panel-c). Gas from the merger (panel-b) is converted into in-stu stars (panel-c) by means of the intense star formation rate, which peaks at 250 $M_\odot$/yr (panel-a). There are evidences of cold gas driven to the galaxy center, where an intense star formation burst creates a compact core and feeds the SMBH. Evidences that cold gas was driven to the galaxy center are seen in the enhanced SMBH ac-

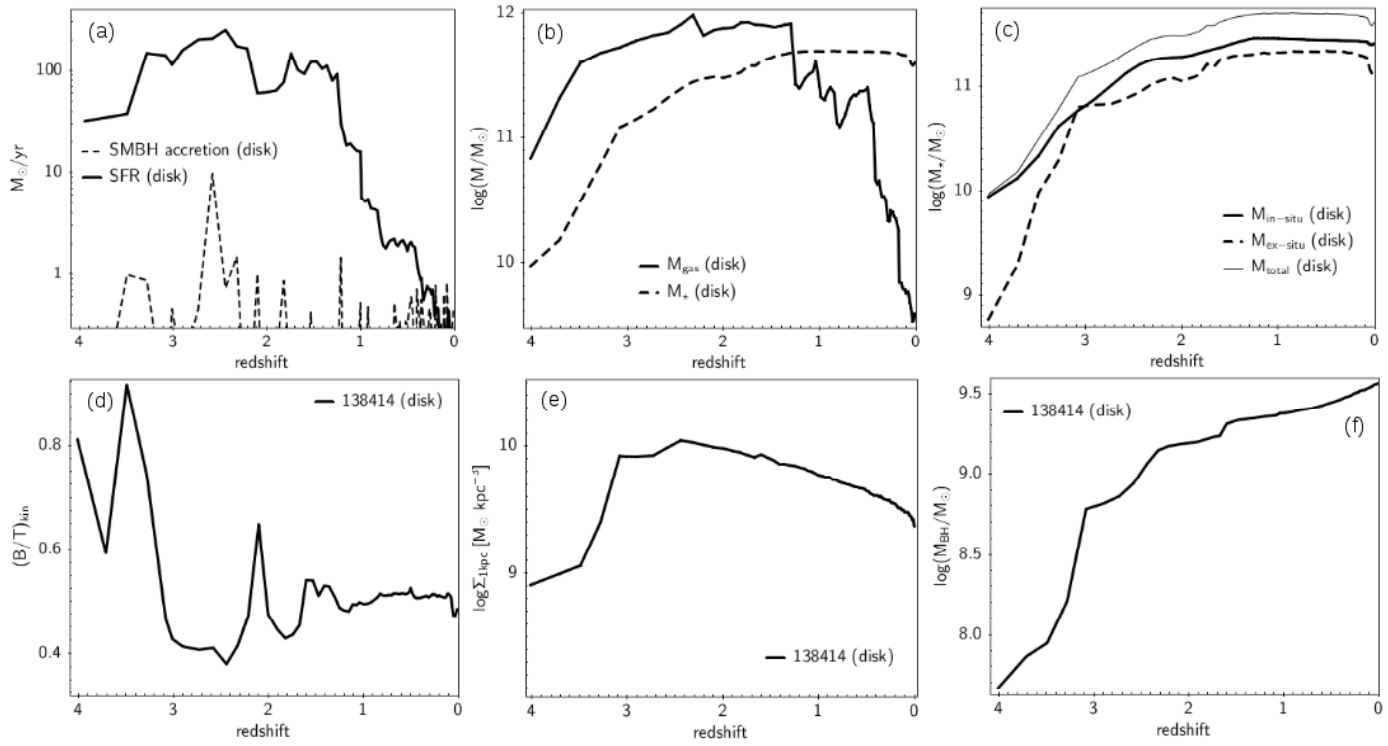

Figure 2. Parameter evolution from $z = 4$ to 0 for the simulated disk-like galaxy. See main text for parameter explanation and their evolution interpretation.

cretion (panel-a), SMBH mass increase (panel-f) and rapid central density increase (panel-e), which creates a compact core, surviving to $z = 0$, albeit with a decreasing compacity. At the beginning of this phase, the galaxy becomes morphologically very spheroidal-like (high (B/T)), although it rapidly changes to very disk-like (panel-d). This morphology is reminiscent of the high redshift disks reported by the observations (e.g. Davari et al. 2017). The subsequent accretion phase is characterized by the assembly of the external galaxy, via gas-rich mergers, generally minor, which only marginally affect the central core. Even one particular merger at $z = 1.7$, which attains a 1:4 mass ratio, equally shows mild effects on the central galaxy core.

The spheroidal galaxy, shown in Figure 3 also exhibits two main phases: a *compact-core* phase, from z≈3 to z≈2 and a subsequent *accretion* phase. A major gas-rich merger starting at z≈3 contributes few ex-situ stars (panel-c), but a large gas mass (panel-b), which is efficiently converted into in-situ stars (panel-c) via a high star formation rate, peaking at more than 350 $M_\odot$/yr (panel-a). As a consequence of that event, gas is funneled to the galaxy center to produce an intense star formation burst, which creates a compact core (panel-e) and feeds the SMBH (panels-a and -f). As in the disk galaxy, the compact core survives to $z = 0$, with slightly decreasing compacity. The accretion phase is characterized by gas-poor minor mergers, which are unable to replenish the depleted galaxy gas. As a result of feedback mechanisms, AGN and SN, star formation is rapidly quenched after z≈2 (panel-a) and in-situ stellar mass stops its growth (panel-c). Only a gas-rich merger at $z = 0.8$, contributes ex-situ stars (panel-c) and shows other minor effects on the external galaxy halo, but none on its central core. Along this phase, the galaxy shows an steady (B/T) growth, which changes its morphology from disk-like to the spheroidal one observed at $z = 0$. As seen above, both galaxies share a similar initial *compact-core* phase, but diverge on the *accretion* phase, key to the formation of the external galaxy parts. We can track the disk formation of the simulated galaxies and even follow the orbits of the satellites originating the minor mergers. In a preliminary study, shown in Figure 4, we follow the orbits of three satellites. Their orbits are not random, but they follow coordinated movements, which contribute to the angular momentum build-up. This observation, which deserves a deeper study, reinforces the connections found between the angular momentum of the entire DM halo and that of the baryonic component, particularly for spiral galaxies (e.g. Teklu et al. 2015).

It is worth mentioning that, although the selected Illustris disk galaxy is very massive, with $M_\star \approx 4.1\ 10^{11} M_\odot$, rather than being an eccentric simulation outcome, it is comparable to the more than fifty superluminous spiral galaxies found by Ogle et al. (2016) in the SDSS.

References

Bezanson, R., van Dokkum, P. G., Tal, T., Marchesini, D., Kriek, M., Franx, M., Coppi, P., 2009, ApJ, 697, 1290
Buitrago, F., Trujillo, I., Conselice, C. J., Häussler, B., 2013, MNRAS, 428, 1460
Bottrell, C., Torrey, P., Simard, L., Ellison, S. L., 2017, MNRAS, 467, 2879
Charbonnier, A., Huertas-Company, M., Gonçalves, T. S. et al., 2017, MNRAS, 469, 4523
Cheung, E., Faber, S. M., Koo, D. C. et al., 2012, ApJ, 760, 131
Davari, R. H., Ho, L. C., Mobasher, B., Canalizo, G., 2017, ApJ, 836, 75
de la Rosa I. G., La Barbera F., Ferreras I. et al., 2016, MNRAS, 457, 1916
Graham, A. W., Dullo, B. T., Savorgnan, G. A. D., 2015, ApJ, 804, 32
Hopkins, P. F., Bundy, K., Murray, N., Quataert, E., Lauer, T. R., Ma, C.-P., 2009, MNRAS, 398, 898
Nelson, D., Pillepich, A., Genel, S. et al., 2015, A&C, 13, 12
Peth, M. A., Lotz, J. M., Freeman, P. E. et al., 2016, MNRAS, 458, 963
Ogle, P. M., Lanz, L., Nader, C., Helou, G., 2016, ApJ, 817, 1090
Schaye, J., Crain, R.A., Bower, R.G. et al., 2015, MNRAS, 446, 521
Teklu, A. F., Remus, R-S., Dolag, K. et al., 2015, ApJ, 812, 29
Trujillo, I., Cenarro, A. J., de Lorenzo-Cáceres, A. et al., 2009, ApJ, 692, L118
Taylor, E. N., Franx, M., Glazebrook, K. et al., 2010, ApJ, 720, 723
van der Wel, A., Franx, M., van Dokkum, P. G. et al. 2014, ApJ, 788, 28

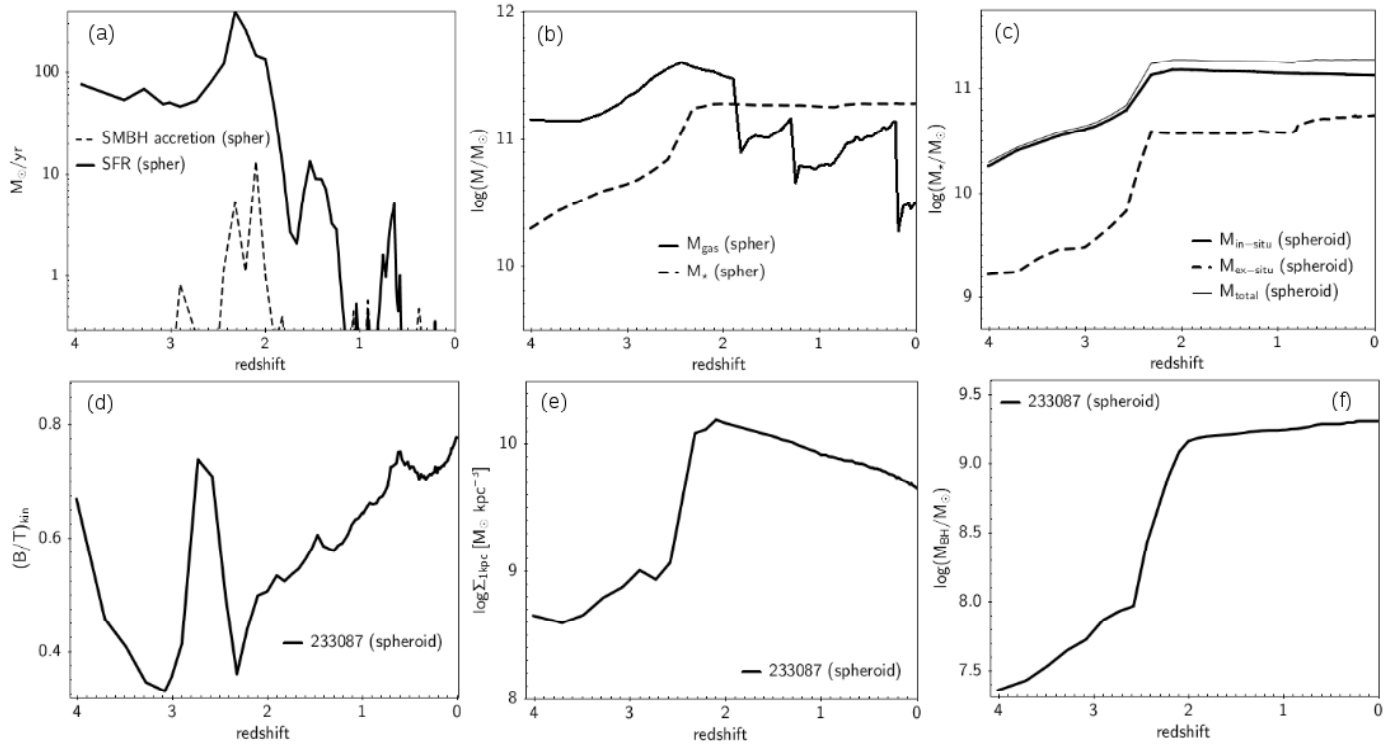

Figure 3. Parameter evolution from $z = 4$ to 0 for the simulated spheroidal galaxy. See main text for parameter explanation and their evolution interpretation.

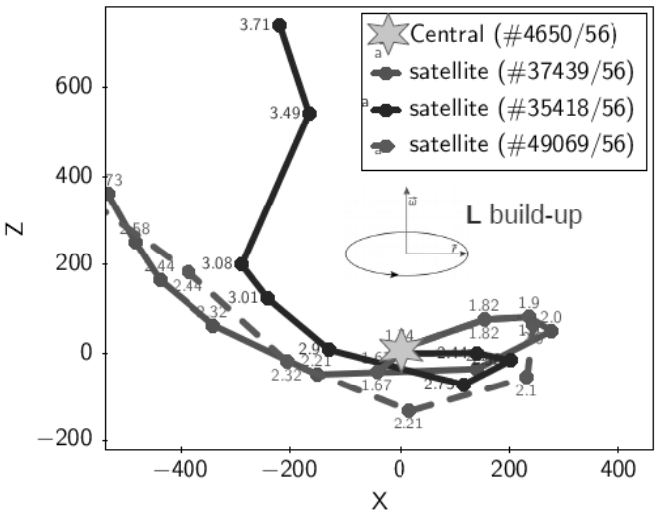

Figure 4. The disk construction around the central compact core results from the coordinated orbits of the accreted fragments, which contribute to the angular momentum build-up. Three fragments are shown in this figure.

van Dokkum, P. G., Nelson, E. J., Franx, M. et al., 2015, ApJ, 813, 23
Vogelsberger, M., Genel, S., Springel, V. et al., 2014, Nature, 509, 177

Boletim da Sociedade Astronômica Brasileira, **30**, no. 1, 166-167

Separation of stars and quasars in multispectral images of J-PAS, J-PLUS, S-PLUS and ALHAMBRA

L. M. I. Nakazono[1], C. M. de Oliveira[1], N. S. T. Hirata[2], J. E. Steiner[1], A. Molino[1], & W. Schoenel[1] and the S-PLUS collaboration

[1] Instituto de Astronomia, Geofísica e Ciências Atmosféricas da USP, São Paulo, Brasil.
e-mail: lilianne.nakazono@usp.br
[2] Instituto de Matemática e Estatística da USP, São Paulo, Brasil.

Abstract. In order to classify stars and quasars from the data collected by J-PAS and other multi-band surveys, we elaborated a method that essentially consists in Principal Component Analysis (PCA), which was primarily applied on ALHAMBRA database. This database contains images in 20 different bands of a small area of the northern sky. We obtained some graphical results that show different regions of stars and quasars densities, allowing us to classify 79 quasar candidates in the studied area. A procedure to measure the redshift of each object is employed using thousands of known quasars by simulating the 20 bands of ALHAMBRA from the SDSS spectra of these quasars. We tested this procedure on the known QSOs of ALHAMBRA, and it returned 65.15% of the redshifts at the second decimal place. 16 out of the 79 QSO candidates had their redshift estimated within STD < 0.1.

Resumo. Para classificar estrelas e quasares de dados coletados pelo J-PAS e outros *surveys*, elaboramos um método baseado em Análise de Componentes Principais que foi aplicado, primordialmente, aos dados do ALHAMBRA. Estes dados referem-se a imagens em 20 dferentes bandas de uma pequena área do hemisfério norte. Obtivemos resultados gráficos que mostram diferentes regiões de densidade para estrelas e quasares, permitindo-nos classificar 79 candidatos a quasar. Para estimar o redshift destes candidatos, foi aplicado um método usando milhares de espectros de quasares conhecidos do SDSS, convoluídos nos filtros do ALHAMBRA. Testamos este método nos QSOs conhecidos do ALHAMBRA, retornando 65.15% dos redshifts na segunda casa decimal. Dos 79 candidatos a quasar, 16 tiveram seus redshifts estimados com STD < 0.1.

Keywords. quasars: general – methods: statistical

1. Introduction

Elaborating a method based only on multi-band photometry to separate point-like objects into stars or quasars (QSOs) allow us to possibly find QSOs not cataloged. Finding new QSOs and determining their redshifts is a crucial first step for understanding the physics of QSOs and their environments and for using them as tracers of large scale structure. In order to devise a method to accomplish such a goal, we applied Principal Component Analysis (PCA) on 8 ALHAMBRA fields (Moles et al., 2008), for which images in 20 optical and 3 NIR bands are available, covering 3 square degrees. We sampled stars from ALHAMBRA, i.e., point sources at a high confidence level (Molino et al., 2014), but some of them could be misclassified QSOs. In addition, we have 198 known QSOs identified in the ALHAMBRA fields (Matute et al., 2012). Both samples have objects with magnitudes 17 < F814W < 21. Our objective is to find new QSOs and determine their redshifts, by using approximately 90k sloan spectra convolved with the ALHAMBRA filters.

2. Principal Component Analysis

The PCA was applied on 10 parameters, which were chosen based on their contrasting behaviours for QSOs and stars. Those parameters are: standard deviation (STD), skewness and kurtosis of the residuals from linear regression applied on the SED, slope of that linear regression, Hα, Hβ, D4000, J − H, H − KS and J − F954W. Plotting two different principal components, one against the other, shows two different locus for QSOs and stars as seen in Figure 1. In order to disregard the real stars on our data, we selected the objects above the dashed line in top panel of Figure 1 and applied PCA again, obtaining the bottom panel of the same figure. Therefore, we estimated in Section 3 the redshift for all the objects in bottom panel of the Figure 1 to get the best QSO candidates.

3. Redshift estimation

Unlike QSOs, stars are not receding by the cosmological expansion, so their stellar spectra are not affected by redshift. Therefore estimating the redshifts of our QSO candidates allows us to confirm their classification. For redshift determination, we elaborated the method described for each QSO candidate:

1. Get the residuals from the linear regression to the 18-band SED of each known QSO from SDSS and of the QSO candidate from ALHAMBRA
2. Calculate the root mean square error to each QSO from SDSS:

$$RMSE = \sqrt{\frac{\sum (x_i - y_i)^2}{n}}, \quad (1)$$

   which x_i is the residual i from ALHAMBRA and y_i is the residual i from SDSS, $i = 1, ..., n$.
3. Estimate redshift by the median of the 10 spectroscopic redshifts with lowest RMSE

We only selected objects with estimated redshift higher than 0.1 to ensure that our list of QSO candidates is not contaminated by any stars.

The standard deviation of the 10 spectroscopic redshifts with lowest RMSE give us an idea of how well estimated is our redshift. Objects with STD much greater than zero have no reliable

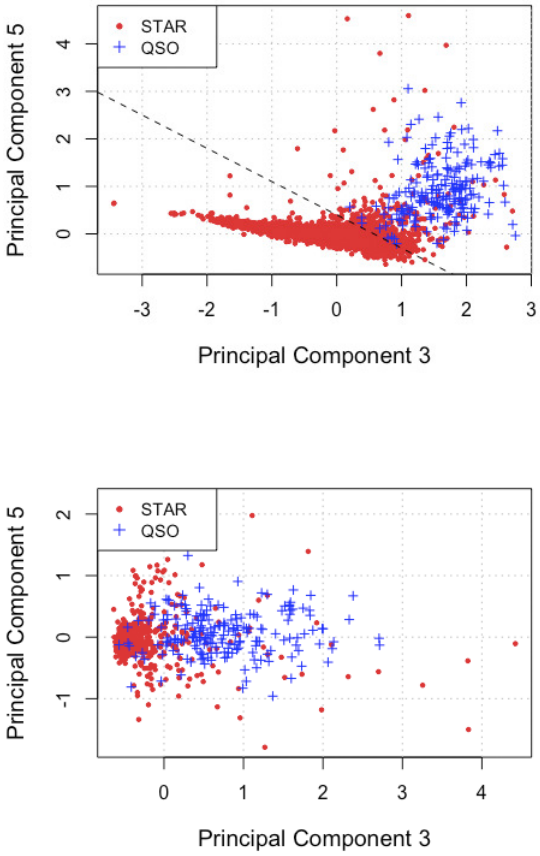

Figure 1. Principal Component 5 versus Principal Component 3, where blue crosses represents known QSOs and red filled circles represents stars. The top panel represents the first run of PCA, while the bottom panel represents the PCA applied only on the objects above the dashed line in top panel.

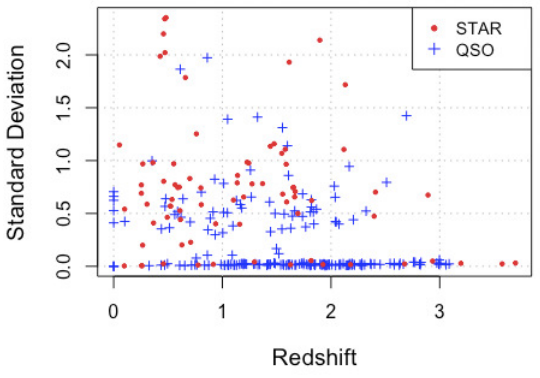

Figure 2. Standard deviation versus estimated redshift, where blue crosses represents known QSOs and red filled circles represents stars, or, actually, candidates of QSO.

estimation. We have 79 QSO candidates, which only 16 have STD ≈ 0 (Figure 2).

Figure 3 shows that most of the redshifts of known QSOs were estimated with low error. Precisely, 65.16% of those QSOs had their redshift estimated at the second decimal place. It increases to 88.89% when considering those with STD ≈ 0.

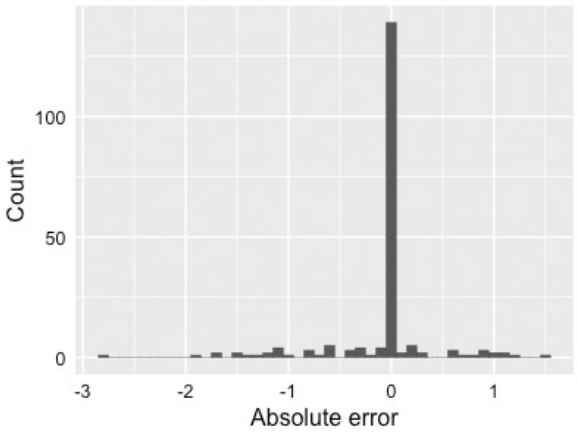

Figure 3. Distribution of the difference between estimated redshift and spectroscopic redshift for the known QSOs

4. Conclusions

We have found 79 QSO candidates by applying PCA on some defined parameters. Accordingly, the PCA seems a great tool to find new quasars among stars only using photometric data. Our method to estimate redshift returned 65.15% of known QSOs' spectroscopic redshift at the second decimal place, leading us to accept that this method can be useful. Finally, 16 of our QSO candidates had their redshift well determined (STD < 0.1). They are on fields 2, 3, 4, 6 and 7 with 15'x15' area from ALHAMBRA. We intend to observe the spectra of those objects to ensure that our results are correct.

References

Moles, M., et al., 2008, AJ, 136, 1325.
Molino, A., Benítez, M., Moles, M., et al., 2014, MNRAS, 441, 2891.
Matute, I., et al., 2012, A&A, 542, A20.

Boletim da Sociedade Astronômica Brasileira, **30**, no. 1, 168-169

Detecting extragalactic globular clusters in early-type galaxies in J-PLUS images

D. Brito Silva[1], P. R. T. Coelho[1], & A. L. Chies Santos[2]

[1] Instituto de Astronomia, Geofísica e Ciências Atmosféricas, Universidade de São Paulo.
e-mail: danielle.brito.silva@usp.br, e-mail: pcoelho@usp.br
[2] Instituto de Física, Universidade Federal do Rio Grande do Sul.
e-mail: ana.chies@ufrgs.br

Abstract. J-PLUS and S-PLUS are photometric surveys that can revolutionize the study of extragalactic globular clusters (GC). These objects will not be detected *a priori* by the data reduction pipeline of the surveys. In order to fill this gap, here we present a study for developing a pipeline to detect GC candidates, exploring methods for galaxy subtraction as well as objects selection. In our preliminary runs, the number of detected globular clusters candidates in NGC1023 is 188 ± 20 and the number of GC candidates in NGC3384 and M105 is 93 ± 15.

Resumo. J-PLUS e S-PLUS são surveys fotométricos que podem revolucionar o estudo de aglomerados globulares extragalácticos (AG). Esses objetos não serão detectados *a priori* pela pipeline de redução de dados dos surveys. Para suprir tal carência, neste trabalho apresentamos um estudo para desenvolver uma pipeline para detectar candidatos a AG, explorando métodos para subtração de galáxias, bem como seleção de objetos. Nesse estudo preliminar, o número de candidatos a aglomerados globulares detectados na NGC 1023 foi 188 ± 20 e o número de candidatos a AG na NGC3384 e na M105 foi 93 ± 15.

Keywords. Galaxies: star clusters: general

1. Introduction

Globular Clusters are found in most galaxies and are among the oldest radiant objects in the universe (Larsen 2001). The study of these objects is a powerful way to recover the history of galaxy formation and evolution.

J-PLUS (http://jplus.cefca.es) and S-PLUS (http://splus.iag.usp.br) are photometric surveys that together will observe about 15 000 square degrees of the sky. However, globular clusters will not be detected *a priori* by the data reduction pipeline of J-PLUS and S-PLUS. Therefore, being capable of detect GC in an automatized and efficient way is important to explore all the potential of the surveys for GC studies.

Here we show our preliminary results on detecting extragalactic GC in a semi-automatized way.

2. Developing the pipeline

We started working on J-PLUS images of the galaxies NGC1023 (S0), NGC3384(S0) and M105(E1) interactively. Due to the fact that NGC3384 and M105 appear very close to each other in the images, we worked with it as a single system.

J-PLUS (as well as S-PLUS) data are composed of observations in 5 broad-band filters based on SDSS filters plus 7 narrow-band filters that cover the major stellar indices from 3 700 to 9 000 Å. The galaxies were observed using the JAST/T80 telescope (diameter of 80 cm) and T80Cam (pixel scale of 0.55"/pixel).

With the aim of detecting point-like objects inlaid in the extended galaxy halo light, we first removed the smooth galaxy light profiles from the individual images. To execute this step we performed numerous tests with different software, among them: CHEFs (Jimènez-Teja & Benìtez 2012), ELLIPSE (Tody 1993) and ISOFIT (Ciambur 2015); in order to establish optimal input parameters. An example of a residual image after subtracting the bright galaxies of the field is presented in Fig. 1.

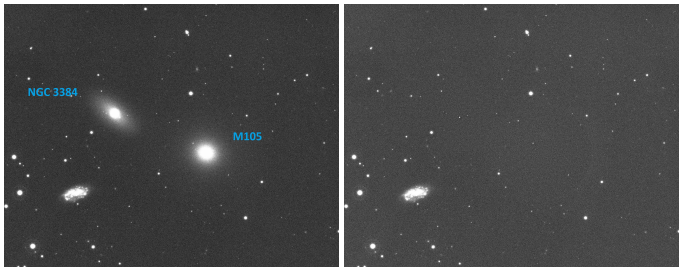

Figure 1. Left: NGC3384 and M105. Right: Residual image of NGC3384 and M105.

From the best residual images obtained using ISOFIT, the detection of point-like objects was performed using SExtractor (Bertin & Arnouts 1996). In order to select GC candidates, we adapted part of the methodology presented in Cho et al. (2016) and Kartha et al. (2014). We adopted criteria based on magnitude, color, data quality and shape. We started working on the detected objects of *g* and *i* bands.

The *i* band magnitude selection was $i \geq 18.9$ mag, because considering the distances of the galaxies (about 11 Mpc; Kartha et al. 2014, Bergond et al. 2006), objects brighter then this value would likely be ultra compact dwarfs (Kartha et al. 2014). The color range adopted was $0.65 \leq (g\text{-}i) \leq 1.3$ mag, as also presented by Kartha et al. (2014).

As a data quality criteria, we selected only objects with the SExtractor parameter *FLAGS* < 4 with the aim of excluding objects that are close to the edge of the images. We also selected only objects with a S/N > 5 relation by setting *MAGERR_ISO* < 0.2 mag (Cho et al. 2016) as shown in Fig. 2.

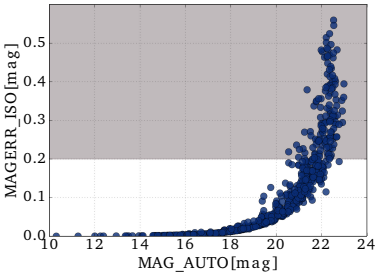

Figure 2. *MAGERR_ISO* adopted for NGC1023. Objects in gray regions were excluded.

Considering the shape of the detected objects, we required our GC candidates to be compact, so we were interested in objects with *CLASS_STAR* > 0.5. We also set limits for *FWHM* to select faint point-like sources (Cho et al. 2016). These criteria are illustrated in Fig. 3.

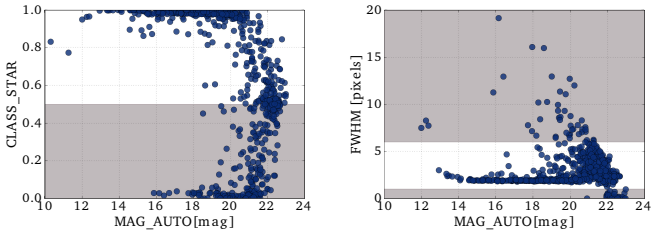

Figure 3. Left: *CLASS_STAR* adopted for NGC1023. Right: *FWHM* adopted for NGC1023. Objects in gray regions were excluded.

The remaining objects of this selection were considered to be the GC candidates of the *g* and *i* bands. In order to select the GC candidates of the other bands, we matched the positions of the GC candidates of *g* and *i* bands with the detected objects of the extra bands within a matching radius of 2 arcsec. As a sanity check, we also applied the selection of data quality and shape on the data of the new catalogs. By the end of the process, we obtained a catalog of GC candidates for each band and dataset.

3. Results

In these preliminary runs, we detected 188 ± 20 GC candidates in NGC1023, and 93 ± 15 GC candidates in NGC3384 and M105.

The numbers of detected GC candidates were compared to what is reported in literature for HST/ACS and VLT data (Cortesi et al. 2016; Bergond et al. 2006), as illustrated in Fig. 4. We are currently comparing the coordinates of the objects we detected with information found in published catalogs. We matched the position of about 20 % of the candidates within a matching radius of 2 arcsec.

Possible reasons for the different number of detections between our images and literature are currently being investigated. That can be at least partially explained by different magnitude limits, the large pixel size of the CCD used in J-PLUS (0.55"/pixel), and the relatively bad weather condition of some of our observing nights.

4. Conclusions and Perspectives

Our pipeline is able to partially retrieve the GC candidates, in comparison to studies reported in literature. Those literature

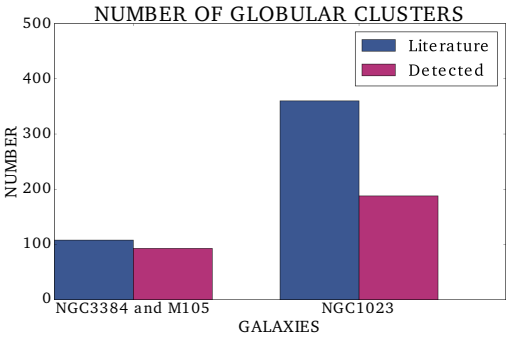

Figure 4. Comparison between our detection and literature.

studies were performed with better observing conditions and higher spatial resolutions, as such we consider that our preliminary partial match already illustrates the capabilities of J-PLUS for GC studies.

We plan to expand this work in the following ways:

1) Improve our methodology, exploring other software and criteria to increase the number of matches.

2) Apply what we have learned interactively to more datasets.

3) Automatize the methodology presented in this work, either making it available as a `python` script or as a scientific workflow like a script in Apache Taverna, a platform which has already being used for astronomical applications (see Benson & Walton 2009).

Acknowledgements. We thank FAPESP 2017/00204-6 for the financial support provided for the current project.

References

Benson, K. M., Walton, N. A. 2009, Memorie della Società Astronomica Italiana, 80, 574
Bergond, G., Zepf, S. E.,Romanowsky, A. J., Sharples, R. M., Rhode, K. L. 2006, A&A, 448, 155
Bertin, E., Arnouts,S. 1996, A&AS, 117, 393
Cho, H., Blakeslee, J. P., Chies-Santos, A. L., Jee, M. J., Jensen, J. B., Peng, E. W., Lee, Y.-W. 2016, ApJ, 822, 95
Ciambur, B. C. 2015, ApJ, 810, 120
Cortesi, A. et al. 2016, MNRAS, 456, 2611
Jimènez-Teja, Y., Benìtez, N. 2012,ApJ, 745,150
Kartha, S. S., Forbes, D. A., Spitler, L. R., Romanowsky, A. J., Arnold, J. A., Brodie, J. P. 2014, MNRAS, 437, 273
Larsen, S. S. 2001, AJ, 122, 1782
Tody, D. 1993, Astronomical Society of the Pacific Conference Series, 52, 173

Boletim da Sociedade Astronômica Brasileira, **30**, no. 1, 170-171

The role of environment on the formation of clumpy starburst galaxies

Santana-Silva, L., Gonçalves, T. S., Rigucinni, L., & Charbonnier, A.

[1] Federal University of Rio de Janeiro, Valongo Observatory e-mail: luidhy@astro.ufrj.br

Abstract. The study of galaxies at high redshift is challenging due to observational limitations, but investigations on how these objects form is of fundamental importance to understand the evolution of star formation processes throughout the history of the universe. Objects at $2 \leq z \leq 3$ present high star formation rates (up to $\sim 100\ M_{\odot}yr^{-1}$ and above) and irregular clumpy morphologies. The classical scenario for galaxy formation from the collapse of gas onto a dark matter halo and subsequent gradual cooling cannot explain these properties and more complex scenarios become necessary, such as cooling flows and galaxy mergers. In that sense, we are currently analyzing a sample of low-redshift galaxies ($z \sim 0.2$) with SFR and morphologies similar to those found in the distant universe (the Lyman break analog sample - LBAs). Here, we show preliminary results of our observations of 13 LBAs to identify possible relations between the environment and other properties of these galaxies. To this end we obtain deep ($r \sim 25.5$) images using the DECam, on the Blanco telescope, in four bands (*ugri*), yielding photometric redshifts with uncertainties of $dz(1+z)^{-1} \sim 0.07$. We will calculate environmental densities around the LBAs and compare these values with other star-forming galaxies of similar stellar masses in order to understand the impact of environmental properties on the intense star formation activity in these galaxies.

Resumo. O estudo de galáxias em alto redshift é um desafio devido a limitações observacionais, mas investigar como esses objetos são formados é de vital importância para entender a evolução do processo de formação estelar ao longo da história do universo. Objetos em $2 \leq z \leq 3$ apresentam elevada formação estelar ($\sim 100\ M_{\odot}yr^{-1}$ ou maior) e morfologia irregular. O cenário clássico para a formação de galáxias no qual o gás colapsa em um halo de matéria escura e sofre um processo gradual de resfriamento não consegue explicar todas propriedades observadas em galáxias do universo distante e cenários mais complexos são necessários, como cooling flows e fusão de galáxias. Nesse contexto, estamos analisando uma amostra de galáxias em baixo redshift ($z \sim 0.2$) com SFR e morfologia similares àquelas observadas no universo distante. Aqui são apresentados resultados preliminares das observações de 13 LBAs para identificar possíveis relações entre o ambiente dessas galáxias. Para isso foram obtidas imagens profundas ($r \sim 25.5$) usando a DECam, no telescópio Blanco, em quatro bandas (*ugri*), permitindo obter redshifts fotométricos com incertezas de $dz(1+z)^{-1} \sim 0.07$.

Keywords. Galaxies:starbursts — Galaxies:evolution

1. Introduction

Current models of galaxy formation and evolution describe galaxies in the local universe but fail to explain features in galaxies at high redshift ($2 \leq z \leq 3$) (Baugh 2006). In that sense, more complex scenarios are necessary to explain the observed properties in these galaxies, such as cold flows and galaxy mergers. The Cold-Flow model is an attempt to explain the high star formation rates in the distant universe by assuming that the transport of gas in the halo direction happens by cold fillament gas (Dekel et al. 2009). The cold gas in the filaments may be responsible for feed the halo. These filaments originate in regions outside the halo and keep the gas at high densities and are then fragmentend into smaller parts that move toward the center of the halo (Bournaud et al. 2008). Alternatively Di Matteo et al. (2007) propose that the star formation intensity can also be attributed to the occurrence of fusions and interactions between galaxies, found that the merger rate is higher at high redshift (Conselice 2006; Lee et al. 2006).

Galaxy clusters are a useful tool to investigate how the galaxy properties can change with the environment (Kelkar et al. 2017; Dressler 1980). Previous studies (e.g., Adelberger et al. 2005) analyzing the correlation function of Lyman break galaxies found that low-mass galaxy companions would be necessary to explain the large total masses of the halos inhabited by those objects. On the other hand a sample of local galaxies that share the same features with galaxies in the distant universe can be used as a tool to understand how these galaxies are formed.

2. Sample and Data

Lyman break analogs (LBAs) comprise a sample of local galaxies ($z \sim 0.2$) proposed by Heckman et al. (2005).These objects show metallicities, gas fractions, morphologies and attenuation values similar to those found in main-sequence galaxies at high redshift ($2 \leqslant z \leqslant 3$) (Hoopes et al. 2007; Basu-Zych et al. 2009; Overzier et al. 2010, 2011; Gonçalves et al. 2010, 2014) Our main goal in this work is to evaluate the effects of the environment (if any) on the formation of these objects. Our data was obtained using the DECam (Dark Energy Camera), installed on Blanco telescope. We observed 12 fields, one around each LBA in the sample in four photometric bands (*ugri*). This sample constitutes the ELBA survey (Environment of Lyman Break Analogs galaxies survey). We got very deep images in magnitude (22.7 in the *i* band for a 10σ detection). Table 1 presents a comparison between the detection limit for galaxies for ELBA and DES data (Drlica-Wagner et al. 2017) .

Table 1. Comparison of magnitudes limits between ELBA and Dark Energy Survey data

Filters	$ELBA_{10\sigma}$	$DES_{10\sigma}$
u	22.1	——
g	23.7	23.4
r	23.2	23.2
i	22.7	22.5

3. Results: photometric redshifts

In order to obtain photometric redshift measurements we apply LePhare (Ilbert et al. 2006) on the four photometric bands available on ELBA survey. By using a set of CFHTLS templates, we perform SED fitting for each source present in the survey. Figures 1 and 2 show the reliability of our photometric redshift measurements. Our typical uncertainty is $dz(1+z)^{-1} \sim 0.04$, similar with other surveys that use four photometric bands, such as the Dark Energy Survey (Sánchez et al. 2014).

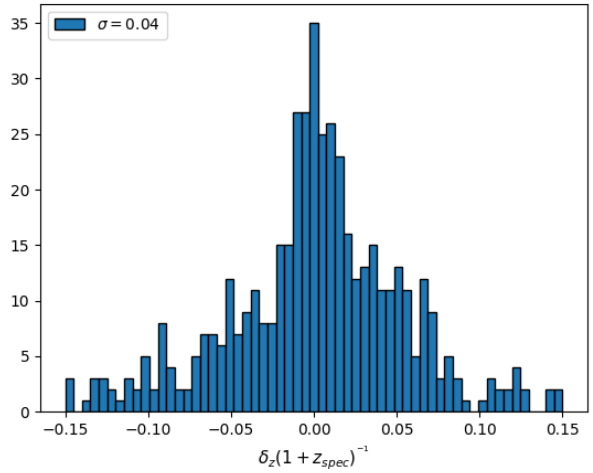

Figure 1. Distribution of differences between photometric and spectroscopic redshifts in the ELBA survey, when available. We conclude that, in general, $dz(1+z)^{-1} \sim 0.04$

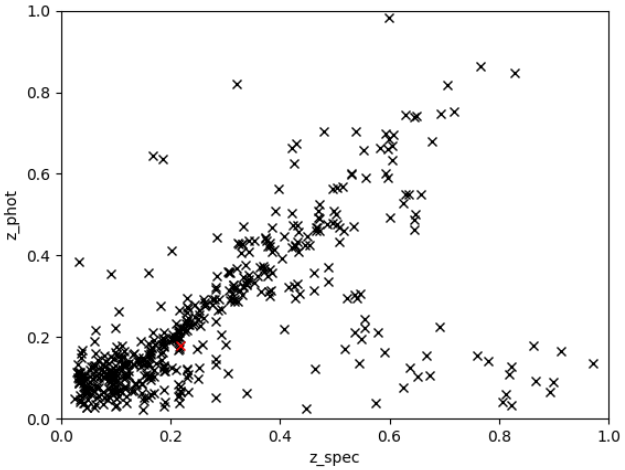

Figure 2. Comparison between z_{phot} and z_{spec} for the ELBA survey. The catastrophic photo-z rate is 20%.

4. Conclusions

In this work present preliminary results for the ELBA survey (Santana-Silva et al., in prep.). Our first analyses show that this is a deep and wide sample of galaxies, and the availability of u-band is particularly advantageous for low-z studies. Photometric redshifts are in good agreement with expected values, allowing for a good determination of the environment of objects in the sample. This will allow for a complete characterization of the effects of the environment on the formation of dense, compact star-forming galaxies.

References

Adelberger, K. L., Steidel, C. C., Pettini, M., et al. 2005, ApJ, 619, 697
Baugh, C. M. 2006, Reports on Progress in Physics, 69, 3101
Basu-Zych, A. R., Schiminovich, D., Heinis, S., et al. 2009, ApJ, 699, 1307
Bournaud, F., Duc, P.-A., & Emsellem, E. 2008, MNRAS, 389, L8
Conselice, C. J. 2006, ApJ, 638, 686
Dekel, A., Birnboim, Y., Engel, G., et al. 2009, Nature, 457, 451
Di Matteo, P., Combes, F., Melchior, A.-L., & Semelin, B. 2007, A&A, 468, 61
Dressler, A. 1980, ApJ, 236, 351
Drlica-Wagner, A., Sevilla-Noarbe, I., Rykoff, E. S., et al. 2017, arXiv:1708.01531
Gonçalves, T. S., Basu-Zych, A., Overzier, R., et al. 2010, ApJ, 724, 1373
Gonçalves, T. S., Basu-Zych, A., Overzier, R. A., Pérez, L., & Martin, D. C. 2014, MNRAS, 442, 1429
Heckman, T. M., Hoopes, C. G., Seibert, M., et al. 2005, ApJ, 619, L35
Hoopes, C. G., Heckman, T. M., Salim, S., et al. 2007, ApJS, 173, 441
Ilbert, O., et al. 2006, A&A, 457, 841
Kelkar, K., Gray, M. E., Aragón-Salamanca, A., et al. 2017, MNRAS, 469, 4551
Lee, K.-S., Giavalisco, M., Gnedin, O. Y., et al. 2006, ApJ, 642, 63
Overzier, R. A., Heckman, T. M., Schiminovich, D., et al. 2010, ApJ, 710, 979
Overzier, R. A., Heckman, T. M., Wang, J., et al. 2011, ApJ, 726, L7
Sánchez, C., Carrasco Kind, M., Lin, H., et al. 2014, MNRAS, 445, 1482

Boletim da Sociedade Astronômica Brasileira, **30**, no. 1, 172-173

Peculiar ring galaxies: morphology and properties.

G. Silva[1], H. Monteiro[1], M. Faúndez-Abans[2], M. de Oliveira-Abans[2], Paulo C. R. Poppe[3] & Vera A. F. Martin[3].

[1] UNIFEI– IFQ;-e-mail: giuanafisica@gmail.com; e-mail: hektor.monteiro@gmail.com
[2] MCTIC/Laboratório Nacional de Astrofísica – Brasil;e-mail: max@lna.br; e-mail: mabans@lna.br
[3] UEFS – Departamento de Física/Observatório Astronômico Antares – Brasil; e-mail: paulopoppe@gmail.com;e-mail: vmartin@uefs.br

Abstract. In this work we investigate a possible relation between visual morphology of the peculiar ringed galaxies and their photometric properties. Ringed galaxies are usually classified into five main types: Polar, Hoag, Elliptical, Irregular and Centrally Smooth Rings. We perform a reclassification of a sample of objects according to the proposed subcategories using up to date images. The images of each object have been analyzed independently by 10 trained volunteers. We also obtained from the literature all available data that could aid in the classifcation process as well as in determining photometric properties. For this, we obtained 2MASS, DSS2, WISE and GALEX photometry as well as redshifts from the NED database. From these data we investigate relationships in the color-color and redshift color diagrams to probe relations with the morphology.

Resumo. Neste trabalho investigamos uma possível relação entre a morfologia das galáxias peculiares aneladas e suas propriedades. Originalmente foi proposta na literatura uma classificação visual das galáxias aneladas, dividindo-as em cinco tipos principais: Polar, Hoag, Aneis Elípticos, Irregulares e Centralmente suaves. Partindo de imagens usadas previamente e incluindo novas imagens refizemos a classificação visual dos objetos segundo as subcategorias propostas, com exceção das polares, por serem já bem definidas. As imagens dos objetos, foram analisadas independentemente por 10 voluntários (treinados), afim de se ter um levantamento estatístico da classificação visual. Com a morfologia dos grupos definida obtivemos também da literatura todos os dados disponíveis que pudessem auxiliar em sua classificação, em particular a partir de diagramas cor-cor. Para tanto obtivemos dados de fotometria do 2MASS, DSS2 , WISE e GALEX. Coletamos também a partir da base de dados NED os redshifts. A partir destes dados investigamos as relações nos diagramas cor-cor e cor redshift para sondar relações com a morfologia.

Keywords. Ringed Galaxy – Morphology – Photometry

1. Introduction

The study of peculiar interactive galaxies is important for understanding the exotic nature of these objects. The present research proposal focuses on the relationship between morphological categories of “Peculiar Ringed Galaxies” and their observational properties in different spectral bands. The objects of study belong to Arp Madore’s "Catalog of Peculiar Galaxies and Associations of the Southern Hemisphere" Arp & Madore (1986), which presents 25 morphological categories supposedly originated by processes of “collisions”, “fusions” or results of “effects of tipe”. In the article ("On the morphology of peculiar ring galaxies"), they divided the mofological types into five main classes, which could have subclasses. In this work, we analyze the classes: Elliptic ring, Hoag and Centrally smooth since the polar ones are established.

The peculiar ringed galaxies are poorly studied, possibly due to difficulties in obtaining observational data and the complexity of numerical simulations. In order to improve our understanding of these objects, we collected data from several databases covering ultraviolet to infrared bands. The objects of the present sample are of the local universe, however many objects in the sample lack data such as: redshift, distance, major and minor axis, mass and spectra. Most of the data comes from surveys of the entire sky. We intend, therefore, to determine if details of the interactive nature of the objects can be inferred from the data and if these point to the specific morphological classes, determined visually.

2. Methodology

The initial database contained 486 objects that were analyzed by a group of ten instructed volunteers, with the objective of making the visual morphological classification. The images used came from four missions 2MASS, WISE, SDSS and GALEX (Figure 1), thus giving information of near and far infrared, visible and ultraviolet. The images were manipulated to highlight structures in the various filters. From these missions, we use the public photometric data in order to verify if there is a relation between the visually determined morphologies and the photometric properties, the spatial distribution of the objects and their geometric parameters.

3. Results

As a result of the visual classification, 314 objects were divided into six morphological classes (Figure 1). In the graphs below we see some of the obtained relations of color indices, the spatial distribution and the geometric parameters.

4. Conclusion

Based on the integrated photometry data of the GALEX, 2MASS and WISE spectral bands obtained from VizieR and NED / NASA, a clear distinction between the visually determined morphological classes and possible details of the interactive process that formed each can not be inferred. One of the reasons may be the dominance of the object’s bulge in integrated photometry. However, the six exposed classes reveal interesting and peculiar structures that need more detailed studies with observations

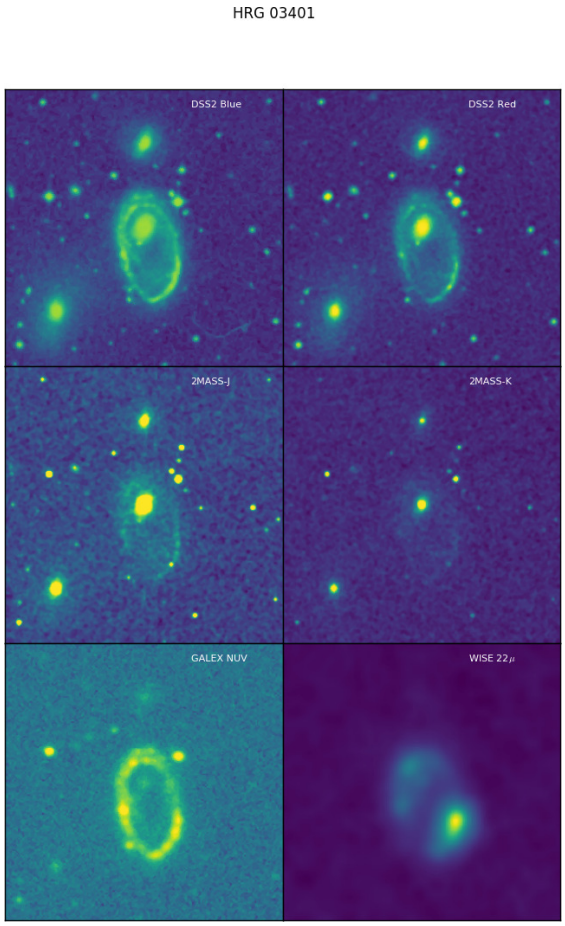

Figure 1. Mosaic with examples of the analyzed images seeking to reveal structures and to understand the morphology.

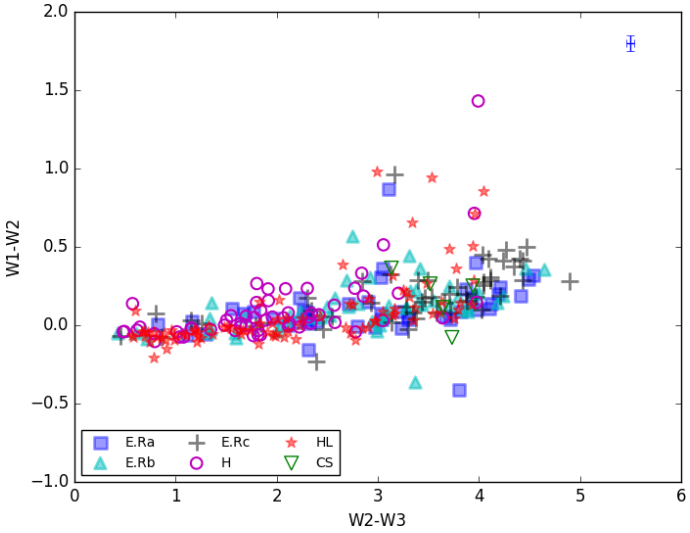

Figure 2. Distribution of the morphological types in the WISE color-color diagram. The purpose of this chart is to determine if there is a separation between classes and to allow the comparison of the normal objects with the peculiar ones. The diagram is related to the one of @@@ incluir a referencia do artgo.

and numerical simulations that may allow to distinguish between possible relevant physical phenomena that lead to the formation of each class.

Acknowledgements. FAPEMIG for the masters scholarship started on 08/2016.

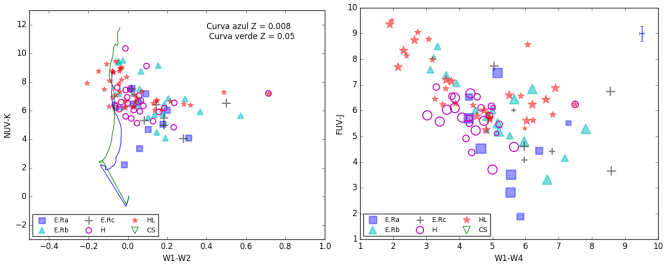

Figure 3. Left:We present the color-color diagrams, independent of the distance of the objects. The lines refer to models of "Single Stellar Poputation" obtained from the group of Padova (http://pleiadi.pd.astro.it/). Right:Color-color diagram of Fuv-J versus W3-W4. Point size is related to weather object nucleus appear in the GALEX image.

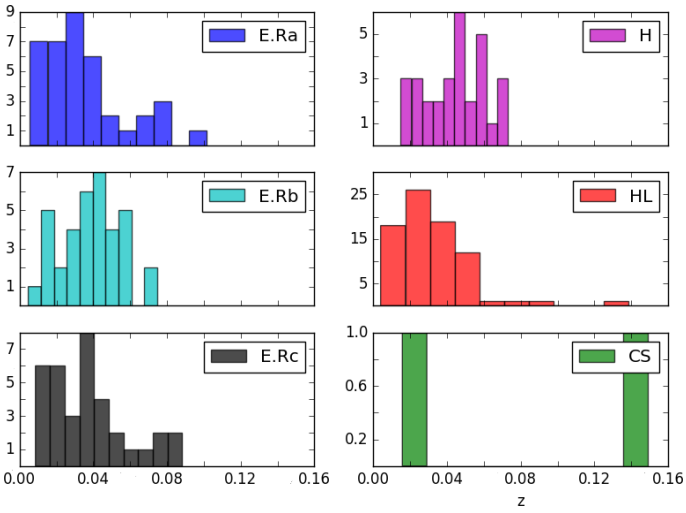

Figure 4. Distribution of morphological types by redshift.

References

Arp, H. C., Madore, B. F. 1986, Catalogue of Southern Peculiar Galaxies and Associations, Vol I, Positions and Descriptions, Clarke-Irwin, Toronto.
Faundez-Abans, M., de Oliveira-Abans, M. 1998, On the morphology of peculiar ring galaxies, AAS, 129, p.357-361.
Wright, E. L. 2010, AJ, 140, art. id. 1868
Freitas-Lemes, P. 2014, Análise espectrofotométrica de candidatas a galáxias com anel polar, PhD Thesis: UniVaP

Boletim da Sociedade Astronômica Brasileira, **30**, no. 1, 174-175

Star-forming clumps in Lyman break analogs

J. M. Santos-Junior[1,2], T. S. Gonçalves[1], L. L. S. Guedes[2]

[1] Observatório do Valongo, Universidade Federal do Rio de Janeiro, Rio de Janeiro, Brazil
[2] Fundação Planetário da Cidade do Rio de Janeiro, Rio de Janeiro, Brazil

Abstract. In this work we analize a sample of near galaxies (z ∼ 0.2) with behavior analogous to the distant galaxies. The study of clumps in this galaxies, provides information on structures, radial velocity mapping and deviations from the star formation law for main-sequence star-forming galaxies. In addition, we investigate the physical processes that regulate star formation in this galaxies these galaxies and extrapolate the results to nearby and distant starbursts galaxies. We describe the clump identification process, the parameters that characterize them and present some results, such as: clumps are dominated by the velocity dispersion, presenting a small velocity shear; the star formation rate within clumps is more efficient than the surrounding interstellar medium by a factor of 2, and approximately 50% of the clump virial mass is composed of molecular gas.

Resumo. Neste trabalho analisamos uma amostra de galáxias próximas (z ∼ 0,2) com comportamento análogo a galáxias no Universo distante. O estudo dos nódulos (*clumps*) dessas galáxias fornece informações sobre estruturas, mapeamento de velocidade radial e desvios da lei de formação estelar para galáxias da sequência principal. Além disso, buscamos compreender os processos físicos que regulam a formação de estrelas nessas galáxias e na tentativa de extrapolar os resultados para as galáxias *Starbursts*, próximas e distantes. Neste trabalho descrevemos o processo de identificação dos *clumps*, os parâmetros que os caracterizam e apresentamos alguns resultados, tais como: os aglomerados são dominados pela dispersão de velocidade, apresentando um pequeno gradiente de velocidades; a taxa de formação estelar dentro dos *clumps* é mais eficiente do que o meio interestelar ao redor por um fator 2 e estimamos que aproximadamente 50% da massa virial é composta de gás molecular.

Keywords. galaxies: formation — galaxies: ISM — galaxies: starburst

1. Motivation

We know today that there is a significant increase in the density of star formation at large redshifts (z ∼ 2) relative to that observed in the local universe (Madau & Dickson 2014). However, due to the low spatial resolution obtained with the observations, the intrinsic properties of the distant objects are still not fully understood. This galaxies show irregular morphologies (Law et al. 2007) and clump structures (Bournaud et al. 2015). Usually, in the Local Universe, this clumps are observed in irregular dwarf galaxies, however, at high redshift, they are commonly found in disk galaxies. The most plausible alternative for the study of distant main sequence galaxies are the so-called Lyman-break analogs (LBAs). These objects, with the median redshift of z ∼ 0.2 were initially selected by ultraviolet luminosity ($L_{FUV} > 10^{10.3} L_{\odot}$) and surface brightness ($L_{UFV} > 10^{9} L_{\odot} kpc^{-2}$) using the Galaxy Evolution Explorer (GALEX). They present characteristics very similar to the high redshift star-forming, such as their masses, SFR, metallicity, (Heckman et al. 2005, Hoopes et al. 2007), morphology (Overzier et al. 2009, 2010), kinematics (Gonçalves et al. 2010) and molecular gas reservoirs (Gonçalves et al. 2014). In addition, observations in the ultraviolet and optical also show typical characteristics of high resdhift star-forming galaxies, such as massive star formation clumps, evidences for outflows, mergers and interactions . There for, LBAs are the best laboratories to study the physical processes associated with star formation in the early universe, with the advantage of higher spatial resolution and signal-to-noise ratios. The standard cosmological model, with $H_0 = 70 kms^{-1} Mpc^{-1}$, $\Omega_m = 0.30$ and $\Omega_\Delta = 0.70$, was adopted for all analyses and calculations in this work.

2. Sample

Our sample consists of 17 LBA observed with the OSIRIS integral field unit, attached to the Keck II telescope (Larkin 2006), using adaptive optics, resulting in an angular resolution of approximately 50 mas, corresponding to structures with physical dimension of 200 pc for these distances. The spectral resolution is R ∼ 3800. The observations were centered on the Paschen-α (Paα) emission line (rest wavelength 1875.1 nm). A more detailed description of the observations, as well as the discussion of the properties of objects in our sample, can be found in Hoopes et al.(2007), Overzier et al.(2009, 2010) and Gonçalves et al.(2010, 2014).

3. Clump properties

In this work, we apply the FellWalker method of the CUPID package found in Starlink's astronomical analysis and processing software (Currie 2013) to select the clumps in each Pa-α image. We also obtain the velocity dispersion (σ) distribution and compare the velocity shear (v_c) and dispersion between host galaxies and clumps. In our sample the typical value for our clumps is ∼ 70 km s^{-1} (Figure 1).

Using the velocity dispersion and clump dimensions, and assuming clumps are virialized, we infer virial masses for each one.

We obtain a relation between the star formation rate and the gas mass for the host galaxies and the clumps, to estimate the depletion time of these objects.

The relation for clumps is given by:

$$\log \frac{SFR}{[M_{\odot} \mathrm{yr}^{-1}]} = 1.16 \log \frac{M_{\mathrm{gas}}}{[M_{\odot}]} - 8.96 \quad (1)$$

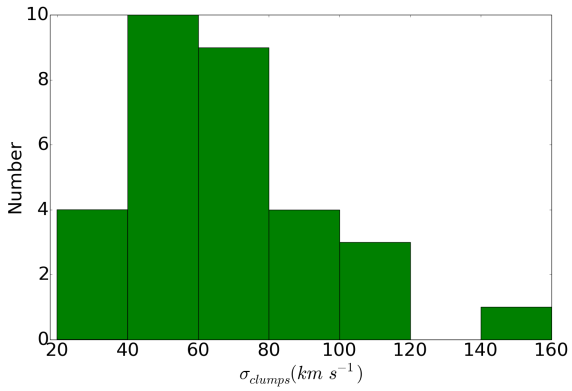

Figure 1. Distribution of the velocity dispersion of the 31 clumps. The typical value for our clumps is $\sim$ 70 km s^{-1}

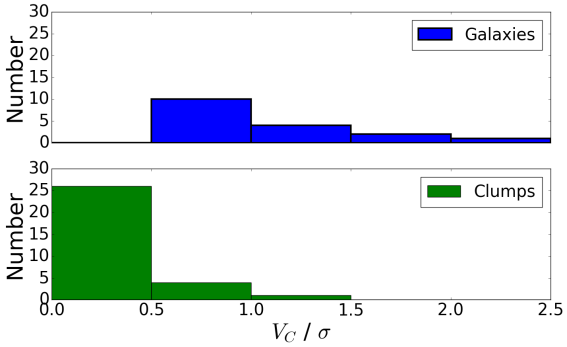

Figure 2. Distribution of v_c/σ for host galaxies and clumps. The clumps are dispersion dominated, showing little velocity shear and a strong random component;

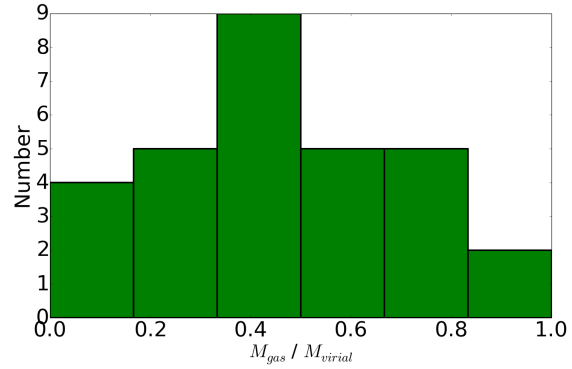

Figure 3. Distribution of the ratio between the circular velocity and the velocity dispersion, for host galaxies and clumps. We estimate that approximately 50 % of the viral mass in clumps is composed by molecular gas. The remaining is probably dominated by stars.

Using a Schmidt-Kennicut equation, Genzel et al. (2010) found a relation for the molecular gas with almost the same angular coefficient value (1.17). Time calculated was 0.3 Gyr for galaxies and 0.23 Gyr for clumps.

4. Results

Star formation within the clumps is more efficient than in the surrounding interstellar medium by a factor of 1.3. The clumps are dominated by velocity dispersion with a little velocity shear. Assuming these clumps are in dynamic equilibrium, we estimated that approximately 50 % of the virial mass in clumps is

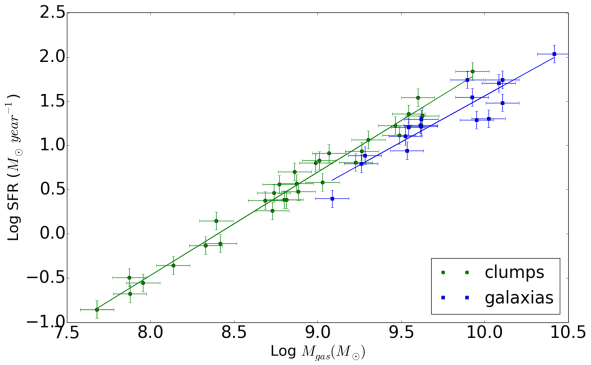

Figure 4. Main sequence of galaxies and clumps. The star formation rate on clumps is higher than the environment around them.

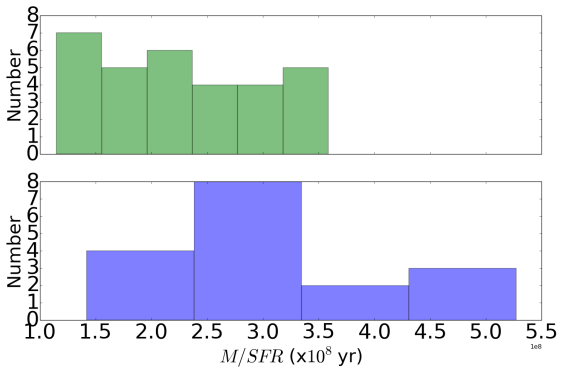

Figure 5. Distribution of depletion time of galaxies (blue) and clumps (green). The star formation rate is more efficient in clumps than the insterstellar medium by a factor of 1.3.

composed by gas. The remaining is probably dominated by stars. We intend to examine the stellar mass distribution in these galaxies in order to verify this hypothesis.

References

Bournaud, F., Daddi, E., Weiß, A., et al. 2015, A&A, 575, A56
Currie, M. J. 2013, in Astronomical Data Analysis Software and Systems XXII, edited by D. N. Friedel, vol. 475 of ASP Conf. Ser., 341
Genzel, R., Tacconi, L.J., Gracia-Carpio, J. et al. 2010, MNRAS, 407, 2091G
Gonçalves, T. S., Basu-Zych, A., Overzier, R., et al. 2010, ApJ, 724, 1373
Gonçalves, T. S., Basu-Zych, A., Overzier, R., et al. 2014, MNRAS, 442, 1492G
Heckman, T., Hoopes, C.G., Seibert, M. et al. 2005, ApJ, 619, L35
Hoopes, C. G., Heckman, T. M., Salim, S., et al. 2007, ApJS, 173, 441
Kennicutt, R. C., Jr. 1998, ApJ, 498, 541
Law, D. R., Steidel, C. C., Erb, D. K., et al. 2007, ApJ, 669, 929
Madau, P., & Dickson, M. 2014, ARA&A, 52, 415
Overzier, R., Heckman, T., Tremonti, C., et al. 2009, ApJ, 706, 203
Overzier, R., Heckman, T., Schiminovich, D. et al. 2010, ApJ, 710, 979

Boletim da Sociedade Astronômica Brasileira, **30**, no. 1, 176-177

Panchromatic stellar populations in early type galaxies: NGC 1052

L. G. Dahmer-Hahn[1], R. Riffel[1], J. E. Steiner[2], T. Storchi-Bergmann[1], R. A. Riffel[3], R. B. Menezes[2], T. V. Ricci[4], & M. R. Diniz[3]

[1] Departamento de Astronomia, Instituto de Física, Universidade Federal do Rio Grande do Sul, CP 15051, 91501-970, Porto Alegre, RS, Brazil. e-mail: dahmer.hahn@ufrgs.br, e-mail: riffel@ufrgs.br, e-mail: thaisa@ufrgs.br
[2] Instituto de Astronomia, Geofísica e Ciências Atmosféricas, Universidade de São Paulo, 05508-900, São Paulo, Brasil. e-mail: joao.steiner@iag.usp.br, e-mail: roberto.menezes@iag.usp.br
[3] Departamento de Física, Centro de Ciências Naturais e Exatas, Universidade Federal de Santa Maria, 97105-900, Santa Maria, RS, Brazil. e-mail: rogemar@ufsm.br, e-mail: diniz.mr@gmail.com
[4] Universidade Federal da Fronteira Sul, Campus Cerro Largo, RS 97900-000, Brasil. e-mail: tiago.ricci@uffs.edu.br

Abstract. We map the gas excitation and kinematics, and the stellar population properties of the elliptical NGC 1052 both in the optical and in the J and K Near Infrared bands. Emission-line flux distributions reveal, beside a rotation component, two double peaked regions along the radio jet. The flux-ratios show extended LINER emission throughout the 5.0 × 3.0" optical field of view. These regions are found to be compatible with inflows/outflows. Principal component analysis (PCA) reveal an unresolved broad line region centered at the nucleus, consistent with a low luminosity active galactic nucleus (LLAGN). This scenario is found to be compatible with a X-ray source located in the same point. In the near infrared, the emission lines are much weaker, with only the [FeII] and H_2 lines displaying extended emission. Also, for the first time in the literature, we combine optical and NIR datacubes and perform stellar population synthesis. By using the optical alone, we find only contribution from old stellar populations. When adding the NIR, in the other hand, we detect a featureless continuum in the nucleus, associated with the LLAGN and compatible with the PCA results.

Resumo. Nós mapeamos a excitação e a cinemática do gás, além das propriedades da população estelar da galáxia elíptica NGC 1052, tanto no óptico quanto nas bandas infravermelhas J e K. As distribuições de fluxos das linhas de emissão revelam, além de uma componente de rotação, duas regiões com duplo pico ao longo do jato em rádio. As razões de fluxo mostram emissão LINER extendida ao longo do campo de visão óptico de 5.0 × 3.0". Estas regiões são compatíveis com *inflows/outflows*. Análise das componentes principais revela uma linha larga não resolvida centrada no núcleo, consistente com um núcleo ativo de baixa luminosidade. Este cenário é compatível com uma fonte em raios-X localizada no mesmo ponto. No infravermelho próximo, as linhas de emissão são muito mais fracas, com apenas as linhas de [FeII] e H_2 apresentando emissão extendida. Pela primeira vez na literatura, nós combinamos dados ópticos e infravermelhos e realizamos síntese de população estelar. Usando apenas dados ópticos, nós encontramos apenas contribuição de populações velhas. Por outro lado, ao incluir dados infravermelhos, nós detectamos um *featureless continuum* no núcleo, associado com o núcleo ativo e compatível com os resultados PCA.

Keywords. Galaxies: stellar content – Galaxies: elliptical and lenticular, cD – Galaxies: active

1. Introduction

NGC 1052 is an E4 galaxy located in the constellation Cetus, the nearest radio-loud AGN. On radio wavelengths, it displays two jets with slightly different orientations (Wrobel 1984, Fey & Charlot 1997). It also has AGN properties reported in X-rays (Kadler et al. 2004), with emissions from an absorbed power law, various jet-related emissions and an extended region, also aligned with the radio synchrotron jet-emission. Also, in the optical, both Barth et al. (1999) and Sugai et al. (2005) found a broad line region in the Hydrogen emission lines.

Regarding the stellar population of NGC 1052, Fernández-Ontiveros et al. (2011) found 15 compact sources exhibiting Hα luminosities an order of magnitude above the estimate for an evolved population of extreme horizontal branch stars. Their Hα equivalent widths and optical-to-NIR spectral energy distributions are consistent with them being young stellar clusters aged <7 Myr. According to them, this is probably related with the merger event that occurred ~1 Gyr ago (van Gorkom et al. 1986)

2. Data

The optical data was obtained with Gemini South Multi Object Spectrograph (GMOS) on Integral Field Unit (IFU) mode. Near Infrared (NIR) data was obtained using the Near-Infrared Integral Field Spectrometer (NIFS) from Gemini North. Both data were reduced using Gemini IRAF package, which included trimming of the images, flat fielding, sky subtraction, wavelength and s-distortion calibrations and remotion of the telluric absorptions.

3. Results and Discussion

To study the stellar population, we used the STARLIGHT code (Cid Fernandes et al. 2004, 2005), who fits the observed spectrum with Simple Stellar Populations (SSPs) in different proportions. To reproduce extragalactic dust, we used the Calzetti et al. (2000) reddening law. As a library of models, we used the Röck et al. (2016) library. This library was chosen because it covers a wavelength range from 3500 to 50000 Å. Also, the high resolution it offers on the NIR is essential for a proper classification of the stellar population (Dahmer-Hahn et al. 2017, submitted).

By using the optical alone, STARLIGHT found only old stellar populations. This result was already expected, since NGC 1052 is an elliptical galaxy whose last major merging event happened ~ 1Gyr ago. On the other hand, when using only NIR data, we found high (>90%) intermediate populations on the whole

cube but the nucleus. However, these populations came along a high (>1.0) extinction, which is in contrast with other results, that found that dust extinction in elliptical galaxies is negligible (Padilla & Strauss 2008). The divergence between optical and NIR results was already reported by (Dahmer-Hahn et al. 2017, submitted), which found that stellar population synthesis in the NIR, as long as the dust extinction cannot be constrained by other methods, produce unreliable results.

For an improved characterization of the stellar population, we combined optical and NIR data in a panchromatic, spatially resolved datacube. For the full optical+NIR spectral range, the code was able to detect a Featureless Continuum (FC) in the nucleus of the galaxy.

After subtracting the stellar population, we fitted the emission lines with Gauss-Hermite polynomials. All emission lines displayed nearly identical profiles, with an emission peak in the nucleus and two double-peaked regions located along the radio jets, suggesting regions with a kinematic component that deviates from the gas rotation. Since they are located along the radio jet, they are probably generated by inflows/outflows.

Also, the kinematics of the gas is decoupled from the kinematics of the stars, presenting different inclinations. This result has already been reported by Dopita et al. (2015), and implies different origins for the gas and the stars.

We also followed Steiner et al. (2009) and used Principal Component Analysis (PCA) on the optical datacube to disentangle the main emissions from the datacube. The eigenvector 1, as expected, reflects the emission from the stellar continuum and the gas that is spread along the galaxy. Eigenvector 2, on the other hand, reflects a punctual emission centered in the nucleus, co-spatial with the obscured AGN detected in X-rays. On this eigenvector, it is possible to see a correlation between the emission-line fluxes and the stellar absorptions of FeI λ5270 and NaD λ5893. As pointed out by Ricci, Steiner & Menezes (2014), this is an indicative of a power-law, since a featureless continuum decreases the equivalent width of the stellar lines on the nuclear region. This result is in direct agreement with the Featureless Continuum detected by the panchromatic synthesis. These two results together can be taken as strong evidence of the LLAGN behind the broad lines detected by Barth et al. (1999), Sugai et al. (2005) and eigenvector 2 of the PCA.

Also, eigenvectors 3 and 6 find components oriented along the radio jets. While eigenvector 3 seems to be a kinematic component (e.g. inflows/outflows), eigenvector 6 resembles a ionization cone.

The NIR emission lines, on the other hand, are much weaker if compared to the optical ones, with only Paβ, [FeII] λ12570Åand H_2 λ21218Åabove the signal-to-noise threshold. From these three lines, only [FeII]λ12570Å and $H_2\lambda$21218Å display extended emission, with Paβ having only nuclear emission.

4. Final Remarks

We present here, for the first time, panchromatic spatially resolved data of the elliptical galaxy NGC 1052. We mapped the stellar population and emission lines. Our main results can be summarized as follows:

- When using the optical alone, STARLIGHT finds only contributions from old stellar populations. On the other hand, when adding the NIR to the synthesis, the code is able to detect a featureless continuum in the nucleus.
- Optical emission line fluxes reveal a rotation component and two double peaked regions located along the radio jets, probably generated by inflows/outflows.
- The stellar and gas rotations are decoupled, implying different origins for the stars and the gas.
- PCA find a broad Hα component centered in the nucleus, co-spatial with a Featureless Continuum. It also detects two components associated with the radio jets.
- Near Infrared emission lines are much weaker, with only [FeII] λ12570Å and H_2 λ21218Å displaying extended emission.

Acknowledgements. LGDH agradece ao CNPq

References

Barth A. J., Filippenko A. V., Moran E. C., 1999, ApJ, 515, L61
Calzetti D., Armus L., Bohlin R. C., Kinney A. L., Koornneef J., Storchi-Bergmann T., 2000, ApJ, 533, 682
Cid Fernandes R., Gu Q., Melnick J., Terlevich E., Terlevich R., Kunth D., Rodrigues Lacerda R., Joguet B., 2004, MNRAS, 355, 273
Cid Fernandes R., Mateus A., Sodré L., Stasińska G., Gomes J. M., 2005, MNRAS, 358, 363
Dopita M. A., et al., 2015, ApJ, 801, 42
Fernández-Ontiveros J. A., López-Sanjuan C., Montes M., Prieto M. A., Acosta-Pulido J. A., 2011, MNRAS, 411, L21
Fey A. L., Charlot P., 1997, ApJS, 111, 95
Kadler M., Kerp J., Ros E., Falcke H., Pogge R. W., Zensus J. A., 2004, A&A, 420, 467
Padilla N. D., Strauss M. A., 2008, MNRAS, 388, 1321
Röck B., Vazdekis A., Ricciardelli E., Peletier R. F., Knapen J. H., Falcón-Barroso J., 2016, A&A, 589, A73
Ricci T. V., Steiner J. E., Menezes R. B., 2014a, MNRAS, 440, 2419
Steiner J. E., Menezes R. B., Ricci T. V., Oliveira A. S., 2009, MNRAS, 395, 64
Sugai H., Malkan M. A., 2000, ApJ, 529, 219
van Gorkom J. H., Knapp G. R., Raimond E., Faber S. M., Gallagher J. S., 1986, AJ, 91, 791
Wrobel J. M., 1984, ApJ, 284, 531

Boletim da Sociedade Astronômica Brasileira, **30**, no. 1, 178-179

Measuring the gas reservoir for star formation in high redshift galaxies

Natália Nogueira-Maia & Thiago S. Gonçalves

[1] Observatório do Valongo, Universidade Federal do Rio de Janeiro, e-mail: natalia12@astro.ufrj.br, tsg@astro.ufrj.br

Abstract. Star formation occurs from the collapse of cold giant molecular gas clouds present in the interstellar medium. The physical properties of these clouds can be altered by several factors, such as metallicity, density and temperature of the gas itself. On one hand, low metallicities yield lower dust abundances which allow for the destruction of CO molecules by UV radiation; on the other hand, dense and turbulent gas excites the CO molecules, increasing line luminosities. High redshift galaxies are metal poor and have high gas densities, making the determination of total molecular gas from CO luminosities challenging. In this work, we estimate dust emission and CO luminosities for a sample of starburst galaxies at low redshift in order to provide estimates and verify the feasibility of testing these measurements for galaxies of different stellar masses and gas phase metallicities. Finally, we compare our estimates with real data already available from sub-millimetre observatories, and discuss future endeavors for fainter objects in our sample.

Resumo. A formação de estrelas ocorre a partir do colapso de gigantes nuvens de gás molecular frio presentes no meio interestelar. As propriedades físicas dessas nuvens podem ser alteradas por diversos fatores, como a metalicidade, densidade e temperatura do próprio gás. Por um lado, baixas metalicidades significam menores abundâncias de poeira, o que permite a destruição de moléculas de CO pela radiação UV, diminuindo a luminosidade de sua linha; Por outro lado, gás denso e turbulento excita as moléculas de CO, aumentando sua luminosidade. Galáxias em alto redshift são pobres em metal e possuem alta densidade de gás, tornando a determinação do gás molecular total através das luminosidades de CO desafiadora. Neste trabalho, estimamos a emissão de poeira e as luminosidades de CO através de dados reais de taxa de formação estelar para uma amostra de galáxias starburst em baixo redshift, a fim de verificar a viabilidade em testar essas medidas para galáxias de diferentes massas estelares e metalicidades. Finalmente, comparamos nossas estimativas com dados reais já disponíveis de observatórios sub-milimétricos e discutimos perspectivas futuras para objetos mais fracos em nossa amostra.

Keywords. Galaxies: starburst – Galaxies: ISM

1. Introduction

Star formation occurs from the collapse of giant molecular clouds present in the interstellar medium (ISM).

We know the comoving star formation density in the Universe peaked approximately 10 Gyr ago, at z ≈ 2 (Madau & Dickinson (2014)).

Galaxies at this epoch were typically more metal-poor and had higher densities that their counterparts in the local universe.

Because of the large distances involved, it is easier to study similar objects in the local universe, where we can obtain more detailed data about relevant physical parameters: the Lyman-Break Analogs (LBAs), star forming galaxies (SFGs) with redshift 0.1 - 0.3 (Heckman et al. (2005), Hoopes et al. (2007), Basu-Zych et al. (2007), Basu-Zych et al. (2009), Gonçalves et al. (2010), Gonçalves et al. (2014), Overzier et al. (2010), Overzier et al. (2011)) with same physical properties as those at high redshift, such as stellar mass, metallicity, dust extinction, star formation rate (SFR), physical size and gas velocity dispersion.

2. Data & Methodology

We have selected 30 LBAs from SDSS and GALEX, based on luminosity ($L_{FUV} > 10^{10.3} L_{\odot}$) and surface brightness ($I_{FUV} > 10^{9} L_{\odot}\ kpc^{2}$) at low redshift ($z < 0.3$) (Heckman et al. (2005), Hoopes et al. (2007)).

In this work, we attempt to understand how ISM conditions influence the determination of the molecular gas reservoir of these objects by using two methods: CO luminosity and dust emission.

2.1. CO Luminosity

Since hydrogen molecules do not hold any permanent dipole moment, they are virtually undetectable at low temperatures. Instead, we use CO as a molecular gas tracer, the second most abundant molecule in a gas cloud (Bolatto et al. (2013)). The rotational transitions of CO molecules emit radiation in a fairly transparent atmospheric window.

$$M(H_2) = \alpha_{CO} L'_{CO} \tag{1}$$

The α_{CO} $[M_{\odot}\ (K\ km\ s^{-1} pc^{2})^{-1}]$ value was determined through dynamic mass measurements to be 4.6 in the Milky Way (Solomon & Barrett (1991), Gonçalves et al. (2014)). However, in extreme environments such as starburst galaxies, this value can be as low as 0.8 (Downes & Solomon (1998)), because of high temperature and velocity dispersion of the gas that collisionally excites CO molecules.

On the other hand, low metallicity environments present lower dust shielding and a higher level of photodissociation of CO molecules by FUV radiation. The result is an increase of the α_{CO} value with a decrease in metallicity (Gonçalves et al. (2014)).

LBAs are, at the same time, dense and metal-poor, rendering the determination of α_{CO} imprecise. In this work, we estimate CO fluxes correcting for metallicity effects according to Genzel et al. (2012),

$$\log(\alpha_{CO}) = -1.3(12 + \log(O/H)) + 12 \tag{2}$$

in order to provide a baseline for future observations.

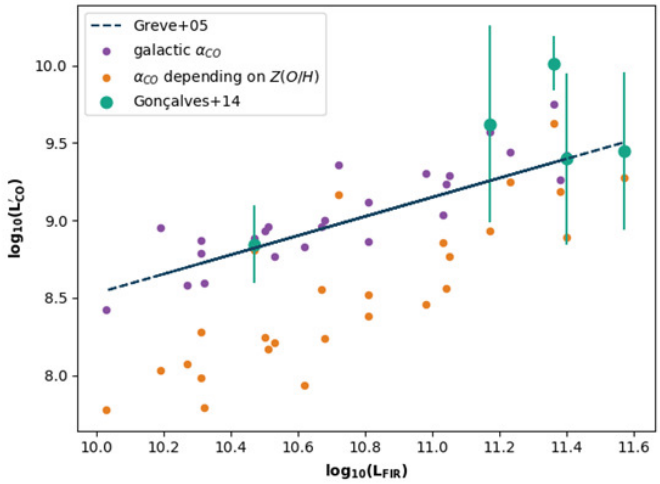

Figure 1. Relation between Far Infrared and CO line luminosities

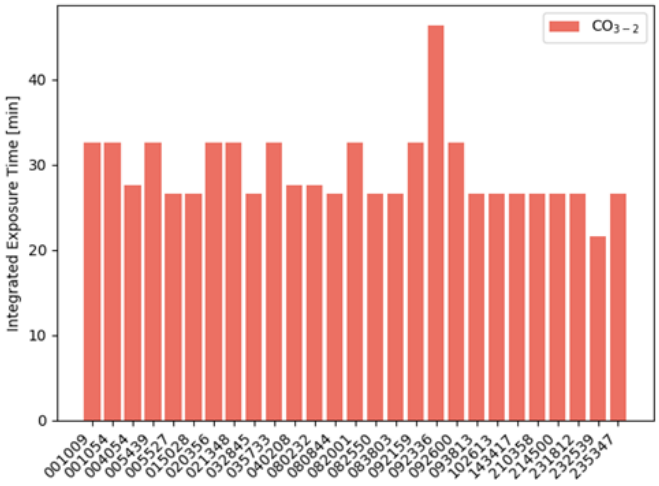

Figure 2. Time estimations with ALMA

2.2. Dust Emission

Stars heat up the dust grains in the ISM causing them to emit radiation in the far infrared (FIR). Additionally, since the amount of dust depends on the amount of gas in the ISM, we can define, approximately,

$$L_{\nu_{850\mu m}} = M_{ISM}\alpha_{850\mu m} \quad (3)$$

where $\alpha_{850\mu m} = 1.0 \pm 0.23 \times 10^{20}$ $[erg\ s^{-1}Hz^{-1}M_{\odot}^{-1}]$ as observationally determined by Scoville et al. (2014). This, of course, assumes a constant gas-to-dust ratio for all galaxies.

In metal-poor galaxies we expect dust to be relatively depleted, decreasing the FIR thermal emission. Here, we correct $\alpha_{850\mu m}$ by metallicity according to Groves et al. (2015), and estimate fluxes for all galaxies in our sample.

3. Partial Results

The galactic value of $\alpha_{CO} = 4.6\ [M_{\odot}\ (K\ km\ s^1 pc^2)^1]$ predicts CO luminosities that match estimates based on the far infrared (e.g. Greve et al. (2005)). However, assuming the conversion factor varies as a function of metallicity, the estimates are decreased by a factor of 5 for metal-poor objects. This allows for a verifiable prediction of the metallicity dependence of α_{CO} [figure 1].

In order to test these hypotheses, we calculate the amount of time needed to observe each galaxy, observing simultaneously the dust continuum and CO line emission.

As seen in figure 2, using ALMA, we would need approximately 30 minutes for each object, for a total of 12 hours. This means that ALMA is the only telescope on Earth capable of completing this project.

4. Future Perspectives

We expect to compare our estimates with actual observations by sub-mm observatories, in order to assess whether metallicity corrections alone are enough to determine gas masses in metal-poor starburst galaxies.

Acknowledgements. NNM and TSG would like to thank CNPq and UFRJ for financing this project, through the Scientific Initiation (IC) fund.

References

Basu-Zych, A. R., Schiminovich, D., Johnson, B. D., et al. 2007, ApJS, 173, 457
Basu-Zych, A. R., Gonçalves, T. S., Overzier, R., et al. 2009, ApJ, 699, L118
Bolatto, A. D., Wolfire, M., & Leroy, A. K. 2013, ARA&A, 51, 207
Downes, D., & Solomon, P. M. 1998, ApJ, 507, 615
Genzel, R., Tacconi, L. J., Combes, F., et al. 2012, ApJ, 746, 69
Greve, T. R., Bertoldi, F., Smail, I., et al. 2005, MNRAS, 359, 1165
Groves, B. A., Schinnerer, E., Leroy, A., et al. 2015, ApJ, 799, 96
Gonçalves, T. S., Basu-Zych, A., Overzier, R., et al. 2010, ApJ, 724, 1373
Gonçalves, T. S., Basu-Zych, A., Overzier, R. A., Pérez, L., & Martin, D. C. 2014, MNRAS, 442, 1429
Heckman, T. M., Hoopes, C. G., Seibert, M., et al. 2005, ApJ, 619, L35
Hoopes, C. G., Heckman, T. M., Salim, S., et al. 2007, ApJS, 173, 441
Madau, P., & Dickinson, M. 2014, ARA&A, 52, 415
Overzier, R. A., Heckman, T. M., Schiminovich, D., et al. 2010, ApJ, 710, 979
Overzier, R. A., Heckman, T. M., Wang, J., et al. 2011, ApJ, 726, L7
Scoville, N., Aussel, H., Sheth, K., et al. 2014, ApJ, 783, 84
Solomon, P. M., & Barrett, J. W. 1991, Dynamics of Galaxies and Their Molecular Cloud Distributions, 146, 235

Boletim da Sociedade Astronômica Brasileira, **30**, no. 1, 180-181

Improving galaxy morphology with machine learning

P. H. Barchi[1], R. Sautter[1], F. G. da Costa[2], T. C. Moura[1], D. H. Stalder[1], Rosa, R.R.[1], e R.R. de Carvalho[1]

[1] National Institute for Space Research (INPE), São José dos Campos, SP, Brazil
e-mail: paulobarchi@gmail.com
[2] University of São Paulo (USP), São Carlos, SP, Brazil

Abstract. This work presents a new non-parametric approach to study galaxy morphology and application of machine learning experiments aiming to distinguish ellipticals (E) and spirals (Sp). We measure morphology with the following parameters: concentration (C), asymmetry (A), smoothness (S), entropy (H) and gradient pattern analysis parameter (GA). The dataset used for supervised learning experiments consists of 48,145 objects, with 44,760 galaxies labeled as Sp and 3,385 as E. The results are evaluated with metrics like precision ($P = TP/(TP + FP)$) and recall ($R = (TP/(TP + FN)$) for each galaxy class. Overall Accuracy ($OA = (TP + TN)/(TP + TN + FP + FN)$) is also presented for each experiment. In general, Decision Tress (DTs) have the best results and all supervised methods have over 97% of OA. The result of this ongoing research have potential to provide unbiased morphological classifications for hundreds of thousands of galaxies.

Resumo. Este trabalho apresenta avanços em morfologia de galáxias não-paramétrica e experimentos realizados com métodos de aprendizado de máquina sobre resultados de classificação de galáxias em elípticas (E) e espirais (Sp) com métricas morfológicas: concentração (C), métrica de assimetria (A), *smoothness* (S), entropia (H) e parâmetro de análise de padrão de gradiente (GA). O conjunto de dados utilizado para os experimentos com aprendizado supervisionado consiste de 48,145 objetos, com 44,760 galáxias rotuladas como Sp e 3,385 como E. Os resultados foram avaliados com precisão ($P = TP/(TP+FP)$), cobertura ($R = (TP/(TP+FN)$) para cada classe de galáxia considerada. Acurácia geral ($OA = (TP + TN)/(TP + TN + FP + FN)$) também é apresentada para cada experimento. No geral, as árvores de decisão apresentaram os melhores resultados e todos os métodos supervisionados atingiram mais de 97% de OA. O resultado desta pesquisa, ainda em desenvolvimento, tem potencial para fornecer classificação morfológica objetiva para centenas de milhares de galáxias.

Keywords. Galaxy Morphology – Computational Science – Machine Learning

1. Introduction

Astronomy has become an extremely data-rich enterprise with the advancement of new technologies in recent decades. New telescopes and instruments on board of satellites provide massive datasets. In view of their voluminous size, much of these data are never looked at, and therefore the potential extraction of information from these collected data is only partially accomplished, even though many answers of the contemporary science critically depend on the processing of such large amount of data (1; 2).

One of the key aspects of any extragalactic investigation is the definition of an unbiased sample that includes reliable morphological types. Galaxy morphological properties result from not only the internal formation and evolution processes but also from the interaction with the environment. Galaxies in groups or clusters may have diverse evolutionary paths compared to the isolated ones, which is clearly reflected in their morphology. Therefore, classification of galaxies into a meaningful taxonomy system is of paramount importance for galaxy formation and evolution studies.

Several attempts to objectively measure galaxy morphology have been tried. The most used system is based on Concentration, Asymmetry, Smoothness, Gini and M20 (CASGM), presented in (3; 4). The general rule for using a certain parameter to describe galaxy morphology is that it maximises the distinction between early and late type systems and minimize seeing effects. Such a parametrisation answers two immediate needs. First, to reproduce human classification by positioning the galaxies in the space of these parameters and second to establish a galaxy morphometry system that seeks structures in the quantitative morphology parameter space that may yield clues on the physical reasons for the formation and evolution of galaxies.

The main purpose of this investigation is to answer the question "How to morphologically classify galaxies using GalaxyZoo (12) classification, non-parametric features and Machine Learning methods?". The general schema of this work is represented in Figure 1.We present the first steps towards improving galaxy morphology with Machine Learning (ML). The dataset used for supervised learning experiments consists of 48,145 objects after preprocessing, with 44,760 galaxies labeled as Sp and 3,385 as E. The preprocessing removed 3,611 objects with missing data for one of the features, C. We used as features of the dataset the best morphological parameters from each type to classify galaxies: concentration (5), asymmetry (6), smoothness (S) (7; 8), entropy (9) and gradient pattern analysis parameter (10; 11).

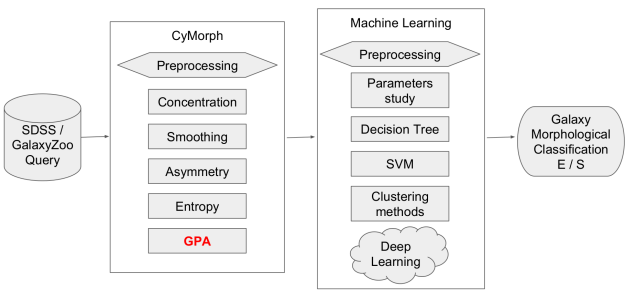

Figure 1. General schema proposed to morphologically classify galaxies into early and late-type.

2. Non-parametric Galaxy Morphology

Among the possible configurations of metrics, we focus on the five parameters that, in principle, better describe the morphology of a galaxy: 1) Concentration (C) - is given by the ratio of the circular radii containing 65% and 25% of the Petrosian flux of the galaxy, respectively, $C = log(R_{65\%}/R_{25\%})$; 2) Asymmetry (A) - is measured by the correlation between an image and its π-rotated variant. We adopted the prescription introduced by (13), where $A = 1 - r(Im, Im^{\pi})$. In this equation, Im represents the original image, Im^{π} is the rotated (by π radians) corresponding image, and r indicates the Pearson correlation coefficient; 3) Smoothness (S) - is measured by the correlation between an image and its smoothed variant. We estimated smoothness as $S = 1 - r(Im, Im^{F})$, where Im is the original image and Im^{F} is its smoothed version; 4) Entropy (H) - is the Shannon entropy, namely the average amount of information resulting from a stochastic process - the clumpiest an image is the larger is its entropy; and 5) GPA - technique to separate early from late-type galaxies by the second moment of gradient from images All these parameters measured, except GPA, are already described in more detail in (13) and references therein. All these quantities are measured within a package named CyMorph, write in Cython (a C-extension for Python).

3. Data Mining in Galaxy Morphology

CyMorph presents a consistent non-parametric morphology system, which can achieve better classification results if a data mining process is employed to gather the best information from the group of metrics with Machine Learning (ML) methods. Basically, ML can be divided into Supervised and Unsupervised Learning. Supervised Learning (SL) is a learning process guided by some form of supervision to build a classification model. For this, the dataset must be divided into train, validating and model testing set. Unsupervised Learning (UL), differs from SL because has no supervision, i.e., there is no model to guide the learning process.

Different configurations for supervised (Support Vector Machine – SVM, and Decision Tree – DT) and unsupervised learning methods (K-means and Agglomerative Hierarchical Clustering – AHC) were tested.

Support Vector Machines (SVM) constructs the optimal hyperplane that will divide the target classes. An optimal hyperplane is the one that maximizes the separation margins between the classes, providing a unique solution for the problem (15).

Decision Tree (DT) is a supervised machine learning method to classification and regression. The goal here is to create a model which predicts the classification by learning simple decision rules inferred from the dataset (16).

One of the more general-purpose clustering methods (non-supervised machine learning), K-means finds clusters of similar sizes, flat geometry, not many clusters, and accepts specification of clusters (17).

4. Concluding Remarks

Morphology is a key ingredient in the process of selecting a sample of galaxies for studying the physical mechanisms responsible for shaping the galaxies as we observe today. Also, considering that the following decades will be dominated by photometric (image) rather than spectroscopic data (e.g. LSST, Pan-STARRS, etc.), it is critical to have robust measurements that capture the essential morphological information and avoid redundancy.

In general, DTs have the best results, considering CN as the most important feature to separate galaxies into spiral and elliptical (responsible attribute for the first decision in all DTs). The Grid Search applied in the supervised methods optimized the OA. Due to the unbalance in the dataset (44760 galaxies labeled as S and 3385 as E), none experiment reached Kappa index (κ) of 0,9, although the interval $0,8 \leq \kappa \leq 1$ is considered of excellent concordance. The recall was also affected by this unbalance. However, all supervised methods have over 97% of OA.

The research from (14) presented here shows satisfactory preliminary results for separating early from late-type galaxies with non-parametric morphology features improved by data mining. The result of this ongoing research have potential to provide unbiased morphological classification for hundreds of thousands of galaxies.

References

Feigelson, E. D., & Babu, J. (Eds.). 2006, Statistical challenges in astronomy (Springer Science & Business Media)

Zaïane, O. R. 1999, Introduction to data mining (University of Alberta)

Conselice, C.J. and Bershady, M.A. and Jangren, A. 2000, The Astrophysical Journal, 886-910, 529, doi:10.1086/308300

Lotz, J. M. and Primack, J. and Madau, P. 2004, The Astronomical Journal, 1, 128, 163

Kent, S.M. 1985, The Astrophysical Journal. Supplement Series, 59, 115

Abraham, R.G., Bergh, S.V.D., Glazebrook, K., Ellis, R.S., Santiago, B.X., Surma, P. and Griffiths, R.E. 1996, The Astrophysical journal. Supplement series. Chicago. 107, 1, 1.

Lotz, J.M., Primack, J. and Madau, P. 2004, The Astronomical Journal, 128, 1, 163

Hamming, R.W., 1998. Digital Filters (3rd ed.). Courier Dover Publications.

Bishop, C., 2007. Pattern Recognition and Machine Learning (Springer, New York)

Rosa, R.R., Sharma, A.S. & Valdivia, J.A. 1999, International Journal of Modern Physics C, 10, 1, 147

Baroni, M.P.M.A., Rosa, R.R., da Silva, A.F., Pepe, I., Roman, L.S., Ramos, F.M., Ahuja, R., Persson, C. & Veje, E. 2006, Microelectronics Journal, 37, 4, 290

Willett, K. W., Lintott, C. J., Bamford, S. P., Masters, K. L., Simmons, B. D., Casteels, K. R., ... & Melvin, T. 2013, Monthly Notices of the Royal Astronomical Society, 435, 4, 2835

Ferrari, F., de Carvalho, R. R., & Trevisan, M. 2015, The Astrophysical Journal, 814, 1, 55

Barchi, P. H. and Sautter, R. & da Costa, F. G. & Moura, T. C. & Stalder, D. H. & Rosa, R. R. & de Carvalho, R. R. 2016, Journal of Computational Interdisciplinary Sciences, 7, 3, 114–120.

Hearst, M. A., Dumais, S. T., Osuna, E., Platt, J., & Scholkopf, B. 1998, IEEE Intelligent Systems and their Applications, 13, 4, 18.

Quinlan, J. R. 1986, Machine learning, 1, 1, 81

Hartigan, J. A., & Wong, M. A. 1979, Journal of the Royal Statistical Society. Series C (Applied Statistics), 28, 1, 100

Boletim da Sociedade Astronômica Brasileira, **30**, no. 1, 182-183

Origin of high ionization lines in active galaxy nuclei

Yaherlyn Diaz[1] & Alberto Rodríguez-Ardila[1,2]

[1] Instituto Nacional de Pesquisas Espaciais (INPE), São José dos Campos — SP.
e-mail: yaherlyn.ramirez1@inpe.br
[2] ILaboratorio Nacional de Astrofísica, Itajubá - MG
e-mail: aardila@lna.br

Abstract. We present strong evidence that the photoionization by radiation from the central engine cannot explain the emision of Coronal lines observed in Active Galactic Nuclei. Aparently, models accounting for both photoionization and shocks were required to explain both the continuum and NLR spectrum, including the CLs, observed in the spectra of active galaxies

Resumo. Apresentamos provas contundentes de que a fotoionização pela radiação emitida pelo mecanismo central não explica a emissão de linhas coronais observada em Galáxias de nucleos ativos. Aparentemente, modelos que consideram a fotoionização e os choques são necessarios para explicar o continuo e o espectro da NLR, particularmente, as linhas coronais, observadas nos espectros das galáxias ativas.

Keywords. Galaxies: active – Galaxies: Seyfert – Infrared: galaxies

1. Introduction

Active galactic nuclei (AGNs) present, in their spectra, lines of high ionization or coronal lines (CLs). Due to the potential necessary for its production (> 100 eV), the CLs trace a part of the ionizing continuum which is not always directly accessible from observations due to galactic absorption. It is known that CLs are generally emitted in compact regions near the central source, but the physical conditions of the gas and the mechanisms associated with its production are under discussion. In this work we analyze the most internal parsecs of a sample of 4 nearby active galaxies with prominent coronal emission to study the physical mechanisms responsible for the production of CLs. For this purpose, observations of high angular resolution (∼ 0.1"/px) collected with integral field spectroscopy and adaptive optics allowed the study of the spatial distribution of the high ionization gas and model the reasons [Si VI]/Brγ, [S IX]/Paβ, [Ca VIII]/Brγ and [S VIII]/Paβ using Cloudy. The width, shape of the profiles and position of the centroid lines are additional diagnostics used to determine the contribution of energy processes such as outflows and shocks between the jets and the NLR gas.

2. Observations

For this work, we use galaxies with multiwavelength data, because this allows a more complete analysis of the physics associated to the gas. In addition, we select objects with evidence of the presence of outflows and extended coronal emission.

- 4 AGNs: NGC1068, NGC1386, NGC4151 and ESO428-G014
- Observations with AO using NIFS/Gemini and SINFONI/VLT
- High-quality spectroscopic data spatially resolved at smaller scales of 0.15"/pixel, that translate to a angular scale of 15"/pix.

Visual inspection of Fig.1 shows that the region emitting [Si VI]λ1.963μm and Brγ for ESO428-G14 is highly inhomogeneus and elongated along the NE-SW direction. Fig. 2 shows

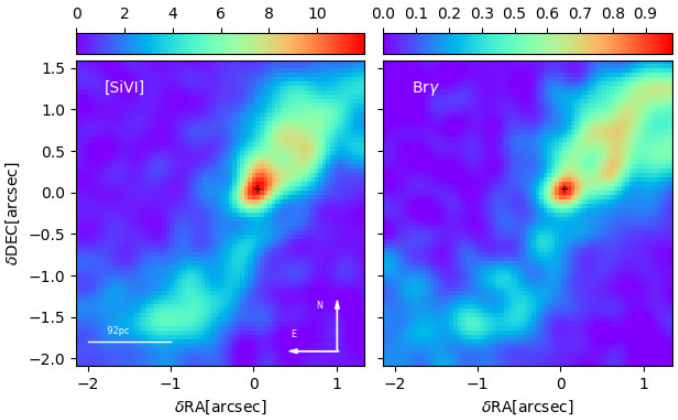

Figure 1. Flux distribution map of [Si VI]λ1.962μm and Brγ for ESO428-G14. The color bar indicates the values of integrated flux in units of 10^{-17} erg cm^{-2} s^{-1}. The orientation and spatial scale are the same for all panels.

the flux map of NGC1386. It can be seen that [Si VI]λ1.963μm is displayin one prominent region of emission. It is characterized by a blob of ∼1" in radius, centred at the AGN and slightly elongated in the N-S direction. The brightest region of this component is highly elongated in the N-S direction, with a size of ∼1.2"×0.6".

3. Kinematics of the CLs

It can be seen in 4 and 3 that [Si VI] is significatively broader than Brγ. Moreover, high-velocity clouds are observed at distances of up to ∼100pc from the centre and coincident with regions of strong radio emission, suggesting outflowing gas, probably due to interaction of the radio-jet with the interstellar medium (ISM).

4. Photoionization models

Cloudy models were employed (Ferland et al., 1998). A luminosity of L_{bol} = 2.9 × 10^{42} erg/s (NGC1386) and L_{bol} =

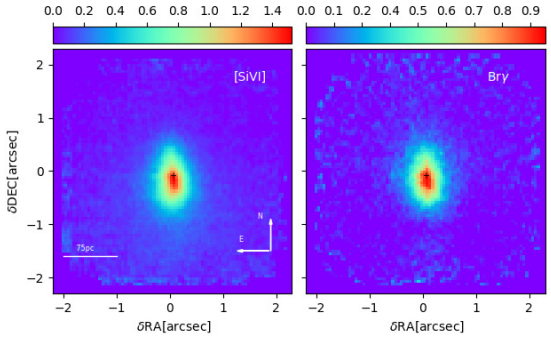

Figure 2. Flux distribution map of [Si VI]λ1.963μm and Brγ for NGC1386. The color bar indicates the values of integrated flux in units of 10^{-17} erg cm^{-2} s^{-1}. The orientation and spatial scale are the same for all panels.

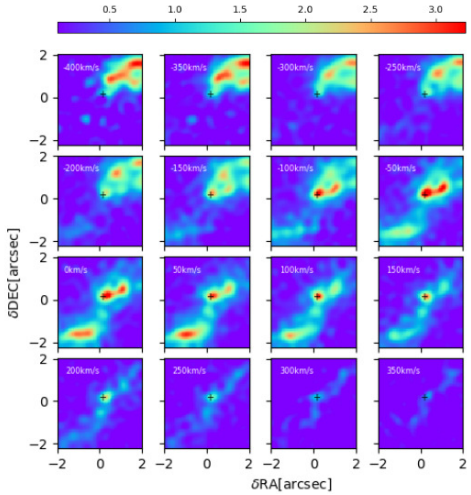

Figure 3. Channel maps derived for Brγ for ESO428-G14. A velocity bin of 50km/s is used to slice the datacube. The color bar indicates the values of integrated flux in units of 10^{-17} erg cm^{-2} s^{-1}.

10.6×10^{42} erg/s (ESO428-G14) for the central source was assumed. The density varies from n_H=500 cm^{-3} to 10^5 cm^{-3}. Solar metallicity was employed. Notice that the observed line ratios

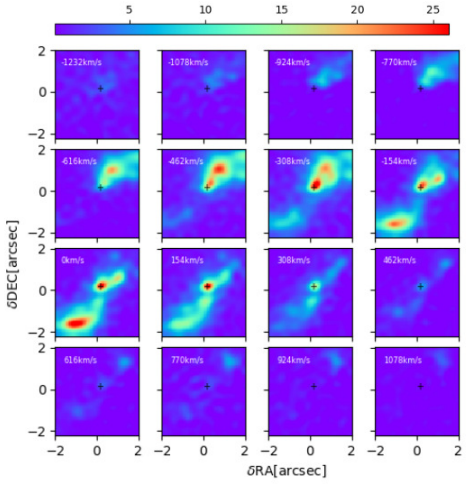

Figure 4. Channel maps derived for [Si VI] 1.963μm for ESO428-G14. A velocity bin of 154km/s is used to slice the datacube. The color bar indicates the values of integrated flux in units of 10^{-17} erg cm^{-2} s^{-1}.

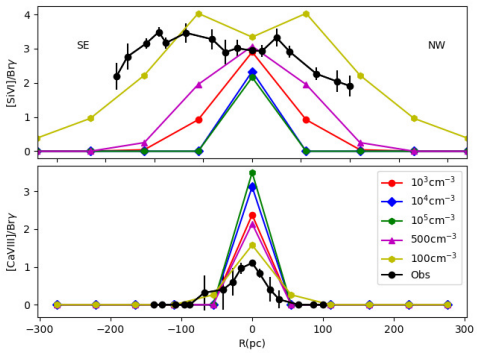

Figure 5. Predicted emission lines ratios [Si VI]/Brγ (upper panel) and [Ca VIII]/Brγ (bottom panel) for clouds with different densities (10^3cm^3 red, 10^4cm^3 blue, 10^3cm^5 green and 500cm^3 purple) for ESO428-G14. The full circles are the observed line ratios.

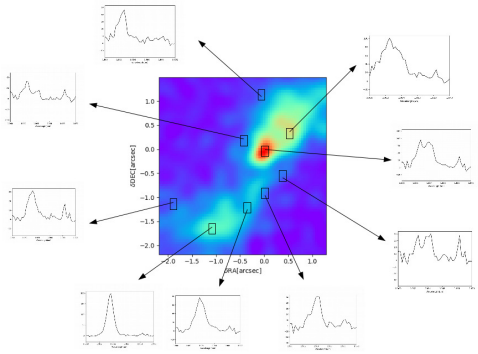

Figure 6. [Si VI] emission-line profiles for ESO428-G14. The spectra were extracted from different spatial regions of ~0.25×0.25 arcsec^2. [Si VI] emission display a very intricate profile, with multiple components and strong variations in their form and width from region to region.

for the extended gas cannot be reproduced by photoionizacion by the central source.

5. Morphology and extension of the CLR

The CLs of ESO4028-G14 display very intricate profiles, with multiple components and strong variations in their form and width from region to region. As an example, Fig. 6 shows the [Si VI] line profiles of spectra extracted from different spatial regions ~0.2"×0.2".

6. Conclusions

- For [Si VI] and Brγ in NGC1386 the light distribution is compact and clearly resolved.
- For ESO428-G14 [Si VI] is emitted by gas with a wide range of velocities, both positives and negatives, reaching values as high as ~ 1000 km/s and ~ −1000 km/s. The gas in the central regions (~ 0.5 arcsec) is more turbulent, emitting at practically all the observed velocities.
- Our observations cannot be explained solely as due to photoionization by radiation from the central engine.

References

Ferland, G. J., Korista, K. T., Verner, D. A., Ferguson, J. W., Kingdon, J. B., & Verner, E. M. 1998, PASP, 110, 761

Boletim da Sociedade Astronômica Brasileira, **30**, no. 1, 184-185

Star formation vs AGN black hole feedback in the evolution of galaxy outflows

W. Clavijo-Bohórquez[1], E. M. de Gouveia Dal Pino[1], C. Melioli[1]

[1] Instituto de Astronomía, Geofísica y ciências Atmosfericas (IAG)
e-mail: weclavijob@usp.br, dalpino@iag.usp.br, claudio.melioli@iag.usp.br

Abstract. Large scale, weakly collimated outflows occur in most galaxies. In complex systems, where (SF) coexists with an active galactic nucleus (AGN) it is unclear whether the SF, the AGN, or both are driving the outflows which frequently exhibit persistent high-speed cold structures. In this work we perform 3D-HD and MHD numerical simulations of the formation of these outflows considering both the feedback from the AGN wind with an opening angle of 0 and 10 supernovae (SNe) type I and II explosions. Magnetic fields are introduced too in the system because they may help to prevent the evaporation of such structures in the ISM and galactic wind. The results indicate that the inclusion of both magnetic fields and an AGN wind substantially affect the evolution of these systems and may account for high speed features, though not cold enough.

Resumo. Fluxo de material de grande escala, fracamente colimado, ocorrem na maioria das galáxias. Em sistemas complexos, onde formação estelar (SF) coexiste com um núcleo galáctico ativo (AGN), não está claro se o SF, o AGN, ou ambos estão produzindo esses fluxos de material que freqüentemente exibem estruturas persistentes densas e frias de alta velocidade. Neste trabalho, realizamos simulações numéricas hydrodynamicas e magneto-hydrodynamicas tri-dimensionais, da formação desses fluxos considerando tanto o feedback do vento AGN com um ângulo de abertura de 0 e 10, como de regiões de SF com explosões de supernova (SNe) tipo I e II. Campos magnéticos com orientações horizontais e verticais ao plano do disco são introduzidos no sistema ja que se pensa que podem ajudar a evitar a evaporação de tais estruturas no ISM e vento galáctico. Os resultados indicam que a inclusão de campos magnéticos e um vento AGN-jet afetam substancialmente a evolução desses sistemas e podem dar conta de estruturas de alta velocidade, embora não suficientemente frias.

Keywords. ISM: jets and outflows

1. Introduction

Outflows in galaxies are ubiquitus in the universe. In Seyferts galaxies and others the mechanism that accelerates the observed dense cool estructures between 10 and 10 km/s ($0.1c$) above the kpc scales is still a mistery. The energy and momentum feedback sources that can be responsable for these structures can be provided by radiation pressure released by gas accretion onto the central engine and by the SMBH in the center of the active galaxy (AGN wind) and/or by star formation (SF wind). Both mechanisms can be responsible for the transference of momentum and energy that carry out these clumps and clouds to kiloparsec scales. Recently observations of these outflows together with the statistical analysis of the produced data (Tombesi 2013) report a possible unified model treating them as single collimated structures covering a wide range of parametres in ionization, velocity, column density and distances from the nucleus. Some models which include magneto-centrifugal and radiation mechanisms are invoqued to explain these phenomena. Recently HD simulations (Melioli and de Gouveia Dal Pino 2015) that include feedback of winds produced by SF and by AGN-jets show that the system is almost insensitive to the passage of the collimated jet, but its presence is necessary to accelerate plasma structures to the observed velocities $\sim$ 10 km/s, and a steady flux of gas can be generated by intense SF only. Nevertheless the introduction of magnetic fields can to play an important role in the evolution of these outflows, as well as in the evolution of plasma accretion rates and the SF region. In the next, we will analize how magnetic fields perpendicular and paralell to the disc can participate in the feedback and we will compare them with previous results (Melioli and de Gouveia Dal Pino 2015) that didn't include magnetic fields.

2. Numerical model

Initial setup: we consider a model for the galaxy which includes a stellar bulge and a three-phase gas disk initially in hydrostatic equilibrium with the gravitational potential given by the dark matter halo and the bulge. The setup is appropriate for a Seyfert galaxy.

Mass and energy injection: we consider mass and energy injection by Supernovae type I and II (SNI - SNII), and a jet driven by the supermassive black hole (SMBH). The injected mass for the SNI is 10 MBH/yr and the luminosity injected by SNII is 3×10 erg/s over 300 Myr. The SMBH injects a constant luminosity (1×10 erg/s), non-relativistic collimated outflow with a speed 0.07c above and below the disk.

3. HD Model: comparison between star-formation-driven wind and the black hole Jet feedbacks

The overall evolution of the ISM of the Galaxy is almost insensitive to the passage of the narrow SMBH jet, but it is able to speed up the velocity of a very small fraction of the ISM gas that is swept by the surrounding SF-wind. The highest velocities reached are comparable to those observed in Seyfert galaxies and Ultraluminous Infrared galaxies (e.g. Melioli & de Gouveia Dal Pino 2015; Tombesi et al. 2016). Nevertheless, these high speed fetures are too hot to explain the high-speed cold clumps that are also observed in these galaxies. We find that the very small

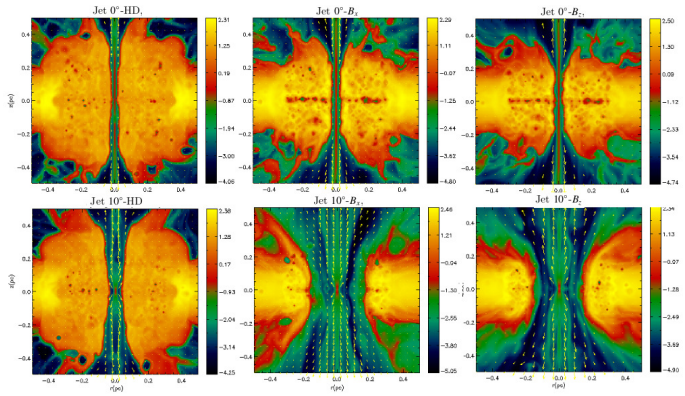

Figure 1. Edge on logaritmic gas density (cm^{-3}) after t = 5 Myr of evolution. Top and bottom diagrams are 0 and 10 models respectively.Left diagrams are hydrodynamical; middle diagrams have an initial horizontal magnetic field (B_x); and right have vertical magnetic field (B_z). The arrows shows the velocity field (v_x, v_z)

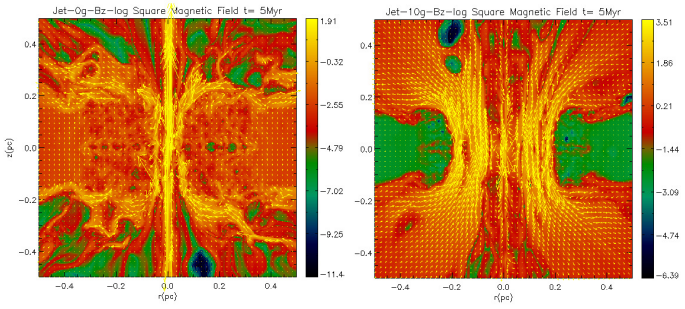

Figure 2. Edge-on logarithmic magnetic pressure (erg/cm^3) for models Jet 0-Bz (left) and Jet 10-Bz (right). The arrows show the magnetic field vector (B_x, B_z) in the plane.

fraction of gas that is accelerated to velocities of ∼ 10 km/s has densities between 10 and 10 cm (see Fig. 4) .

4. MHD Models

We now explore how the presence of a magnetic field in the gas with an initially $\beta = 300$ and a SMBH jet with an opening angle of 10° may affect the feedback. Figure 1 shows two-dimensional cuts (2D) of the density distribution of 6 models (HD and MHD). The results of our simulations show some important conclusions:

1. The magnetic field decreases the average temperature of the system preserving more cold structures because a fraction of energy released by the SN explosions used to heat the ISM gas is transferred to the magnetic field. (see Fig. 3 bottom left)
2. The SMBH outflow with an opening angle of 10 (Jet-10 model in Fig. 1, bottom left) clearly helps to accelerate more low density plasma increasing the velocity by one order of magnitude from 10 to 10 km/s (compare bottom left and top left in Fig. 4).
3. The comparison of MHD and HD-models with same jet-opening angle clearly shows that the presence of $\boldsymbol{B}$ helps to enhance the average outflow velocity (see Fig. 3 middle panel left and Fig. 4). This because of the combination of several effects that include the extra acceleration effect due to magnetic pressure gradient and tension forces and the less expanded (colder) surrounding ISM in the magnetized models.

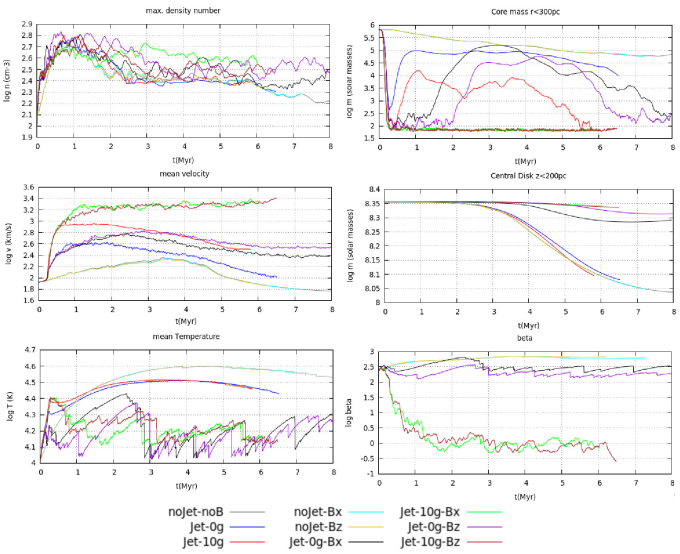

Figure 3. Logarithmic mean values for velocity (left-middle), central disc mass (right middle), thermal pressure (bottom-left), beta (bottom-right), central core mass (top-right). The max. number density (top-left) is the maximum value of density in one cell over all the cells in the system.

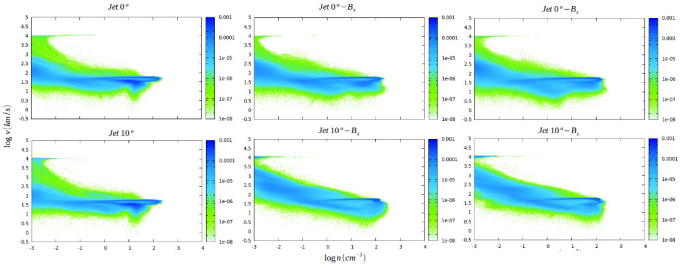

Figure 4. Two dimensional histogram of the vertical velocity (km/s) vs. density (cm) calculated considering every cell whithin the whole simulated system for all the models at a time $t = 5$ Myr. The color bar indicates the cell number normalized to the total number.

4. The combination of the effects of the SMBH jet and the magnetic fields together are not enough to drive the formation of high speed cold features in kpc scales expected from observations. (Fig. 4)
5. The inclusion of the magnetic field in the 10 jet model, helps to open a broader channel in the central region when compared with the HD 10 case, where the channel is confined by the thermal pressure of the gas heated by SN explosions. In fact the evolution of gas surrounding the core region ($r \leq 300$ pc, $| z | \leq 200$ pc), shows the removal of plasma in the central region that could accrete onto the SMBH possibly inhibiting the active phase of the galaxy (Fig. 3 top-right).

References

Tombesi F., et al, 2013, MNRAS 430, 1102-1117
Melioli, C., de Gouveia Dal Pino, 2015, E. M., ApJ, 812, 90

Boletim da Sociedade Astronômica Brasileira, **30**, no. 1, 186-187

Structure and Dynamics of the Fornax Cluster

Davi Dias Barbosa[1], Hugo Vicente Capelato[1], & Tatiana Ferraz Laganá[1]

[1] Núcleo de Astrofísica Teórica, Universidade Cruzeiro do Sul, São Paulo, Brazil e-mail: davidiasbass@hotmail.com e-mail: hugo.capelato@cruzeirodosul.edu.br e-mail: tatiana.lagana@cruzeirodosul.edu.br

Abstract. We study the distribution in the phase space in the cluster of the galaxies of the Fornax to determine their structure and dynamic state.

Resumo. Estudamos a distribuição no espaço de fase das galáxias do aglomerado de Fornax para determinar sua estrutura e estado dinâmico.

Keywords. Galaxies: clusters: individual: Fornax – Galaxies: clusters: intracluster medium – X-rays: galaxies: clusters – Galaxies: kinematics and dynamics

1. Introduction

Groups and clusters of galaxies are large galactic structures believed to be formed from smaller structures and may be considered the largest ones in the universe. In the hierarchical scenario of structure formation, clusters are the last structures to be formed whereas groups of galaxies appear as intermediate structures formed in earlier times. The Fornax cluster, despite its apparent state of relaxation, is known to be packed full of substructures (Drinkwater et al., 2001), some still in course of relaxation (Iodice et al., 2016, 2017). We studied the phase space distribution of the galaxies of the Fornax cluster to determine their structure and dynamic state. Although the system has been studied in detail in the past, new spectroscopic data as well as new results obtained from deep X-ray observations show evidence of intense activity in the region.

2. Methodology

Optical data came from the HyperLeda database (http://leda.univ-lyon1.fr). We obtained a representative sample of the distribution of galaxies in an 8 degree region around the central galaxy NGC1399 (Fig. 1). The velocity distribution of the system was analyzed through the statistical methods provided by the ROSTAT routines package. By making an iterated use of the gap distribution of data and theirs probabilities (both given by ROSTAT), we arrived to a representative sample of Fornax cluster galaxies within the redshift interval $600 < cz < 2400$ km.s^{-1} with mean velocity (bi-weighted) $\overline{cz}$= 1469 km.s^{-1} ($\overline{z}$= 0.004900), and velocity dispersion (bi-weighted) σ_{cz} = 403 km.s^{-1} (see Fig. 2) Spectral X-ray data from XMM-Newton satellite were also included in our study, in order to obtain temperature and metallicities maps of the cluster central region (Figs. 4 and 5).

3. Results and Conclusions

As a first attempt to understand the overall cluster kinematic and dynamics, was divided the entire region into 6 rings of velocities sorted in distance from NGC1399. Then for each ring we calculated the mean velocity and velocity dispersion. As it can be seen the velocity distribution do not vary significantly as we move away from the cluster center (Fig. 3).

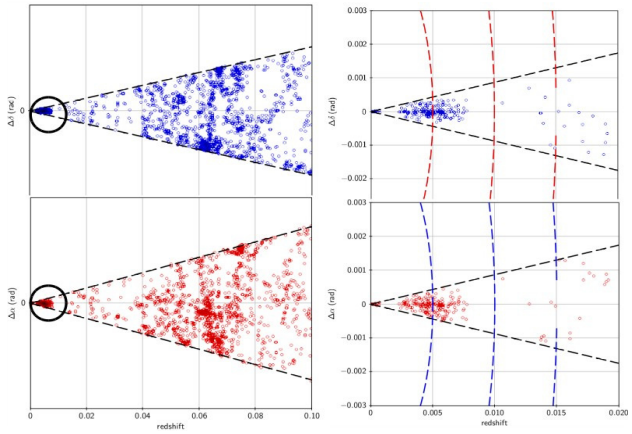

Figure 1. Cone diagrams of the 8° region showing the field of Fornax in depth up to redshift $z = 0.10$. The left panel displays the entire sample, whereas the right panel shows a zoom of the circled region on the left panel.

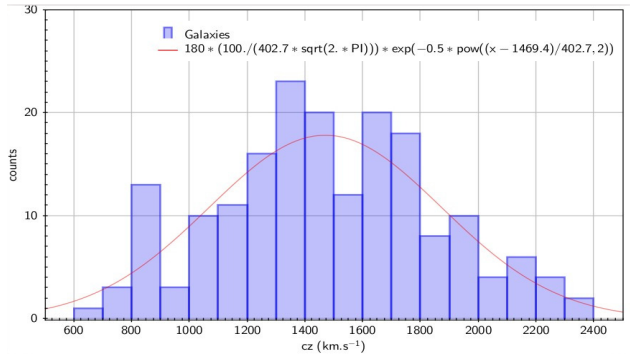

Figure 2. The velocity histogram of the Fornax cluster sample of galaxies. Superposed is a Gaussian profile with parameters given the ROSTAT bi-weighted estimators (see text).

To resolve structures in temperature and metallicity, the X-ray data were divided into small regions from which spectra can be extracted. The 2D maps were made in a grid, where each pixel; is 512 × 512 XMM EPIC physical pixels, i.e., each cell

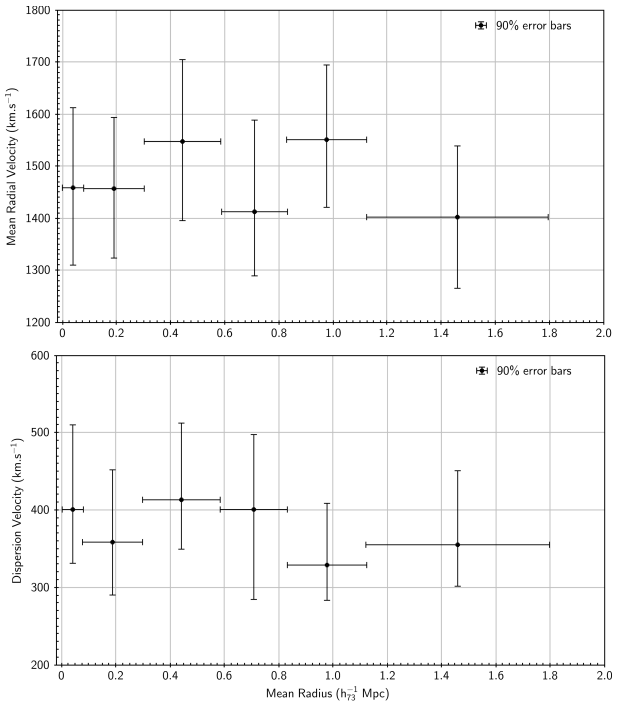

Figure 3. Bi-weighted estimates of mean radial velocities (*upper panel*) and velocity dispersion (*bottom panel*) for 6 concentric rings centered on NGC1399. Error bars are 90% confidence.

grid is 25.6 arcsec × 25.6 arcsec. In each pixel we performed a spectral fit to determine the temperature and metallicity simultaneously (Laganá et al., 2015). The results are shown in Fig. 4 and 5 below.

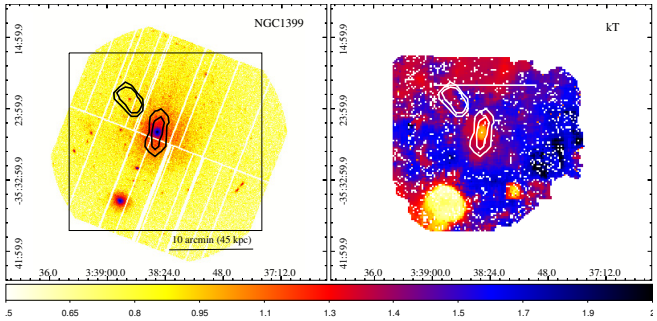

Figure 4. Maps of the X-emission (left) and of temperature distribution (right). Most of the emission in concentrated around the central galaxy NGC1399. Temperatures are lower in the central region, suggesting the cluster to be classified as Cool Core.

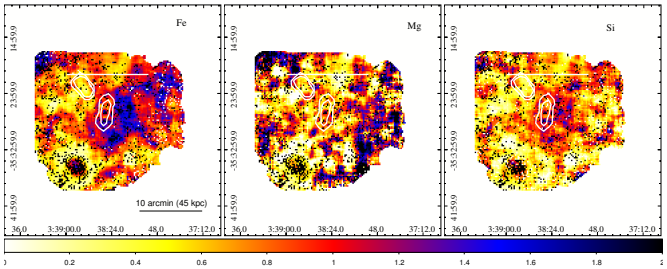

Figure 5. The map of Fe abundances (*left*), Mg (*middle*), and Si (*right*). The high Fe concentration is correlated with the distribution of galaxies in the central region of the system.

These figures suggest that in the neighborhood of NGC1399 the intra cluster gas is highly inhomogeneous both in temperature as in its chemical abundances, a situation which is reminiscent of that of the NCG4325 group (cf. Lagana et al., 2015). We have tried to correlate these inhomogeneities to the distribution and kinematics of the galaxies in the central region of Fornax. With this aim we calculated the adaptative map of the local velocity dispersion of galaxies as described by Biviano et al. (1996). The result is shown in Fig. 6 together with the contours of the regions with Fe abundance excess (the blue spots of Fig. 5, left panel). As it can be seen, the “hotter" regions in the galaxy distribution coincides with the regions with excess of Fe abundances suggesting a possible correlation.

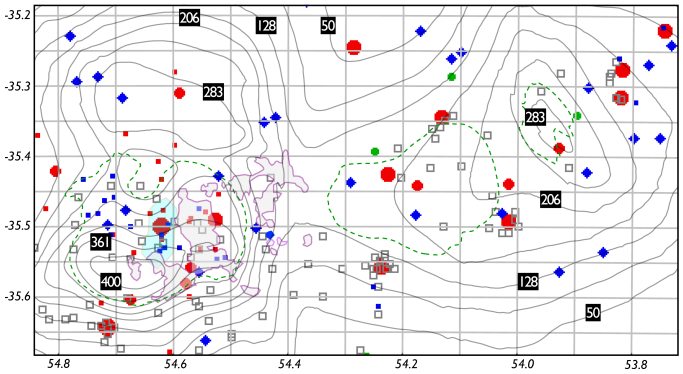

Figure 6. Isocontours of local velocity dispersion (km.s^{-1}; black continuous lines) superimposed to the map of galaxy positions of the central region of the Fornax, their diameters being proportional to the B-magnitude of the galaxy (*red points*: galaxies kinematically belonging to the cluster; *blue points*: galaxies with no redshift measurement; *open squares*: globular clusters). The *dashed lines* give the boundaries of regions for which the velocity dispersion map is significant at a 3-σ confidence level. The *purple* shaded region are the regions in excess of Fe abundances (see Fig. 5) whereas the *green* shaded region, which includes NGC1399, is the region where an excess of non-thermal radio emission has been detected (Killeen et al. 1988).

References

Beers, T. C. et al. 1990, AJ, 100, 32
Biviano, A. et al. 1996, A&A, 311, 95
Drinkwater, M. J. et al. 2001, ApJL, 548, L139
Iodice, E. et al. 2016, ApJ, 820, 42
Iodice, E. et al. 2017, ApJ, 839, 21
Killen, N. E. B. et al. 1988, ApJ, 325, 180
Laganá, T. et al. 2015, A&A, 573, 16

Boletim da Sociedade Astronômica Brasileira, **30**, no. 1, 188-189

Probing PAH molecules in luminous infrared galaxies

Y. Martins[1], K. Menéndez-Delmestre[1] and L. Riguccini[1]

[1] Valongo Observatory - Federal University of Rio de Janeiro, Brazil e-mail: yanna11@astro.ufrj.br

Abstract. A significant fraction of the infrared (IR) emission in star-forming galaxies corresponds to dust-reprocessed emission arising from complex molecules known as Polycyclic Aromatic Hydrocarbons (PAHs). PAHs are excited by ultraviolet (UV) photons and detected in the mid-IR due to their vibrational transitions. Detailed study of PAH transitions can give us insights into the radiation field within deeply dust-embedded mid-IR emitting regions. We explore the molecular complexity of PAH-emitting galaxies in the nearby universe by exploiting archival mid-IR spectra from the Infrared Spectrograph (IRS) on board the Spitzer Telescope. We focus our study on Luminous Infrared Galaxies (LIRGs; $10^{11}L_{\odot} \leq L_{IR} < 10^{12}L_{\odot}$), from the Great Observatories All-Sky LIRG Survey (GOALS). GOALS surveyed 180 low redshift ($z \leq 0.088$) LIRGs with a wide range of properties, including systems dominated by an AGN (Active Galactic Nucleus), starbursts, as well as systems in varying stages of galaxy interaction. We use the PAHFIT routine and the NASA Ames PAH IR database (PAHdb) to decompose the observed PAH features and characterize the underlying PAH population in terms of size, composition and charge. Following this approach, we will be capable of identifying how much of the IR emission in LIRGs is provided by PAHs and elucidate on how molecularly-rich these environments are. We here present preliminary results for a pilot sample of 20 LIRGs. This represents the first attempt to link the star formation history of LIRGs to the breakdown of their PAH emission.

Resumo. Uma fração significativa da emissão em infravermelho em galáxias com formação estelar correspondem a emissão por reprocessamento da poeira resultante de moléculas complexas conhecidas como Hidrocarbonetos Policíclicos Aromáticos. Os PAHs são excitados por fótons no ultravioleta e detectados no IR-médio devido a suas transições vibracionais. Estudos detalhados de transições dos PAHs podem nos dar o conhecimento do campo de radiação em regiões emissoras no IR-médio. Nesse projeto, nós exploramos a complexidade molecular de galáxias no universo local através de espectros em IR-médio do *Infrared Spectrograph* a bordo do Telescópio Espacial Spitzer. Nós focamos nosso estudo em Galáxias Luminosas no Infravermelho (LIRGs; $10^{11}L_{\odot} \leq L_{IR} < 10^{12}L_{\odot}$), do *Great Observatories All-Sky LIRG Survey*. GOALS inspecionou 180 LIRGs de baixo redshift ($z \leq 0.088$) com uma grande variedade de propriedades, incluindo sistemas dominados por AGNs, starbursts, assim como sistemas em diversos estágios de interação entre galáxias. Nós usamos a rotina PAHFIT e NASA PAHdb para decompor as bandas observadas dos PAHs e caracterizar essa população de moléculas em termos de tamanho, composição e carga. Como resultado, somos capazes de identificar o quanto da emissão em IR em LIRGs é provida pelos PAHs e elucidar o quão molecularmente rico esses ambientes são. Aqui, apresentamos nossos resultados para uma amostra piloto de 20 LIRGs. Esse projeto representa a primeira tentativa de inferir propriedades globais de galáxias, como caracterizar seu campo de radiação quanto a presença de AGNs, a partir de características específicas dos PAHs, como seu tamanho, carga e composição.

Keywords. Galaxies: star formation – Galaxies: ISM – Infrared: galaxies

1. Introduction

Luminous infrared galaxies are rare in the local universe, but become abundant at $z \geq 1$ (Casey et al. 2014). Although many works have studied this galaxy population, there are still important questions regarding their nature that have not yet been answered: what is the source of their luminosities and what mechanisms are responsible for their energy? AGNs and intense starbursts are used as energy origin of this particular type of galaxies. However, there is a consensus that LIRGs are dusty galaxies, where most part ($\sim 90\%$) of the UV radiation emitted by the stars and/or AGNs is absorbed by grains and re-emitted in IR (e.g., Armus et al. 2009).

Up to 20% of the IR emission in star-forming galaxies is in the form of broad emission bands at 6.2, 7.7, 8.6, 11.3, and 12.7 μm (Spoon et al. 2004) arising from the excitation of PAHs. It has been shown that the ratio between different PAH features can be used to constrain the size (i.e., number of carbon atoms) and ionization state of these molecules (Draine & Li 2001), while the ratio between PAH emission and dust continuum can be used as a measure of the relative contribution of an AGN (Menéndez-Delmestre et al. 2009).

Spitzer/IRS spectra of low resolution are ideal to study the PAHs features and silicate absorption at 9.7 and 18 μm (Spoon et al. 2004). The GOALS (Armus et al. 2009) database combines imaging and spectroscopy of a sample of 201 (U)LIRGs selected from the IRAS Revised Bright Galaxy Sample (Sanders et al. 2003). GOALS was created to characterize the observed diversity in properties in a statistically-significant sample of LIRGs. In the IR, the survey is mainly comprised of Spitzer data.

2. Methodology and Results

To analyze the PAH transitions in the mid-IR, we used low resolution spectra from Spitzer/IRS. The 20 LIRGs that comprise our pilot sample are selected following these two criteria: 1) they need to have low-resolution IRS spectroscopy covering the wavelength range where the main PAH features appear (i.e., $\sim$ 6 - 14 μm) and 2) they have the lowest redshifts from the GOALS sample ($z < 0.00298$).

The IRS spectra of our pilot sample[1] have been fit using the method described by Smith et al. (2007; PAHFIT). PAHFIT is an IDL-routine to decompose the low-resolution mid-IR spectra of galaxies with significant dust and PAH emission. It models the spectra by combining the contributions from (1) a stellar continuum, (2) dust continua at different temperatures, (3)

[1] http://irsa.ipac.caltech.edu/data/GOALS/galaxies.html

resolved PAH band emission, (3) emission lines and (4) dust-extinction models (i.e., simple, fully-mixed or screen). We show our PAHFIT results for NGC 5653 in Figure 1.

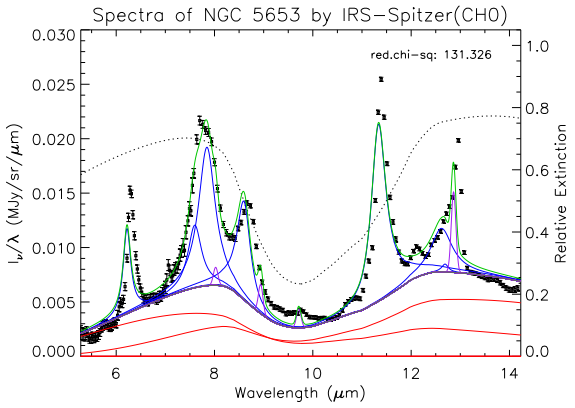

Figure 1. Decomposition of the spectrum for NGC 5653 with PAHFIT. In red, dust continua at different temperatures (200 K and 300 K); in gray, the sum of stellar and dust continua; in blue, the dust features atributed to PAHs; in purple, the atomic lines; in green, the PAHFIT model; the black dotted line represents the extinction model.

One of the results we obtain from the PAHFIT analysis is the relative contribution from dust components at different temperatures. The distribution of dust temperatures for our sample is shown in Figure 2, were each galaxy is represented by several dust temperature components. The global distribution displays a general bimodality, with hotter dust associated with the shorter-wavelength IRS channel and warmer dust associated to the longer wavelenght. Although this correspondance between dust temperature and wavelength is expected, we find that there is a tendency for a greater portion of our sample (65%) to be represented by hotter dust. This may be an indication that AGN have a greater contribution to the mid-IR emission in these galaxies when compared to the very small grain (VSG) continuum, associated to star forming regions and responsible for the warm dust continuum at $\lambda > 14$ μm (Petric et al. 2011).

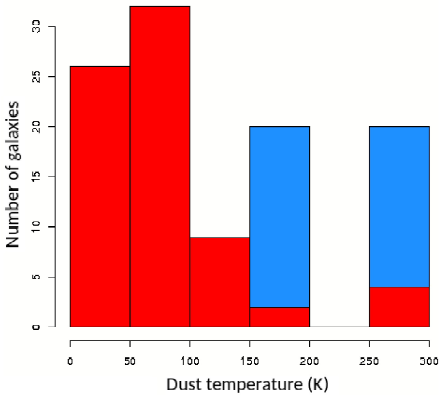

Figure 2. Dust temperature distribution for the galaxies of our LIRG sample. In red, the PAHFIT results based on the IRS longer-wavelength channel, 14-36 μm; in blue, those from the shorter-wavelength channel, 5-14 μm.

We aim break down the PAH emission into different subclasses (charge, size and type) running the PAHdb tools (Boersma et al. 2014; Bauschlicher et al. 2010) on our IRS spectra. About 700 spectra of a great variety of PAHs are present in this database. For the majority of molecules, the spectra were calculated for neutral and singly-ionized states; the spectra of multiply-ionized states are provided only for a few select molecules. PAHs composed only by carbon and hydrogen atoms (so-called "pure PAHs") comprise the majority of molecules in the database. However, PAHs with nitrogen, oxygen, silicon and other metals can also be found.

Figure 3 shows the fit obtained with PAHdb for the LIRG ESO 221-IG010, considering PAHs with no silicon, magnesium, iron, but with up to 2 atoms of oxygen and 2 of nitrogen. This type of characterization allow us to explore in details the astrochemichal richness of these galaxies.

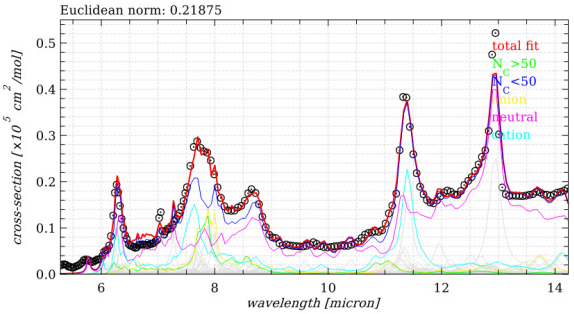

Figure 3. PAHdb decomposition for the ESO 221-IG010 spectrum (black circles) between 5-14 μm: PAHs with a carbon number less than 50 (blue curve) and greater than 50 (green curve); negatively charged (yellow curve), positively charged (cyan curve) and neutral PAHs (magenta curve). The combined contribution of these molecules is represented by the red curve.

References

Armus, L. et al. 2007, The Astrophysical Journal, 656, 148
Armus, L. et al. 2009, Publications of the Astronomical Society of Pacific, 121, 559
Bauschlicher Jr., C. W. et al. 2010, The Astrophysical Journal Supplement Series, 189, 341
Boersma, C. et al. 2014, The Astrophysical Journal Supplement Series, 211, 8
Casey, C. M. et al. 2014, The Astrophysical Journal, 796, 95
Draine, B. T. & Li, A., 2001, The Astrophysical Journal, 554, 778
Menéndez-Delmestre, K. et al. 2009, The Astrophysical Journal, 699, 667
Petric, A. O. et al. 2011, The Astrophysical Journal, 730, 28
Sanders, D. B. et al. 2003, The Astronomical Journal, 126, 1607
Smith, J. D. T. et al. 2007, The Astrophysical Journal, 656, 770
Spoon, H. W. W. et al. 2009, The Astrophysical Journal Supplement Series, 154, 184

Boletim da Sociedade Astronômica Brasileira, **30**, no. 1, 190-191

Polycyclic aromatic nitrogen heterocycles in starburst-dominated galaxies

C. M. Canelo[1], A. C. S. Friaça[1], & D. A. Sales[2]

[1] Departamento de Astronomia, Instituto de Astronomia, Geofísica e Ciências Atmosféricas, Universidade de São Paulo, São Paulo, Brazil e-mail: carla.canelo@usp.br
[2] Instituto de Matemática, Estatística e Física, Universidade Federal do Rio Grande, Rio Grande do Sul, Brazil

Abstract. Analyses of the polycyclic aromatic hydrocarbon (PAH) features profiles, especially the 6.2 and 7.7 μm features, could indicate the presence of nitrogen incorporated to their rings. For this work, 155 galaxies (starburst-dominated, in general), extracted from the Spitzer/IRS ATLAS project, have their 6.2 μm profiles fitted and distributed into the Peeters' classes. 67% of these galaxies were classified as class A objects which have only been explained by carbon replaced by nitrogen into the aromatic rings. Therefore, these spectra suggest a significant presence of PANHs (polyciclic aromatic nitrogen heterocycles) in the astrophysical environments of these galaxies that could be related to their starburst-dominated emission. To compare and complement these findings the same procedure is been applied to the 7.7 and 8.6 μm features.

Resumo. Análises dos perfis de bandas de hidrocarboneto policíclico aromático (PAH), especialmente as características de 6.2 e 7.7 μm, podem indicar a presença de nitrogênio incorporado aos seus anéis. Para este trabalho, 155 galáxias (*starburst-dominated*, em geral), extraídas do Spitzer/IRS ATLAS project, tiveram seus perfis de 6.2 μm ajustados e distribuídos nas classes de Peeters. 67% destas galáxias foram classificadas como objetos classe A, que só foram explicados pelo carbono substituído por nitrogênio nos anéis aromáticos. Portanto, esses espectros sugerem uma presença significativa de PANHs (heterociclos policíclicos aromáticos nitrogenados) nos ambientes astrofísicos dessas galáxias que poderia estar relacionada à emissão dominada por *starbursts*. Para comparar e complementar essas descobertas, o mesmo procedimento foi aplicado aos perfis de 7.7 e 8.6 μm.

Keywords. infrared: galaxies – ISM: molecules – astrobiology

1. Introduction

Analyses of the polycyclic aromatic hydrocarbon (PAH) feature profiles could indicate the presence of nitrogen incorporated to their rings. For this work, 155 starburst-dominated galaxies extracted from the Spitzer/IRS ATLAS project (Hernán-Caballero & Hatziminaoglou 2011) have their 6.2, 7.7 and 8.6 μm profiles fitted allowing the separation of the sources into the Peeters' A, B and C classes (Peeters et al. 2002). Currently class A sources, corresponding to a central wavelength near 6.22 μm, seems only to be explained by polycyclic aromatic nitrogen heterocycles (PANH, Hudgins, Bauschlicher & Allamandola 2005), whereas class B may represent a mix between PAHs and PANHs emissions. PANHs could provide the missing link between the abundant PAHs chemistry at the interstellar medium and the nucleobases that compose all living beings.

Since 6.2 and 7.7 μm bands are both caused by the CC stretching vibrational mode, they are connected to each other in some cases, mainly for class A (van Diedenhoven et al. 2004). This association could furnish another strategy for deriving the variations of the 6.2 μm band in an indirect way. It is also possible to use the 8.6 μm band (CH mode) to compare the results.

2. Methods

Our main goal is to verify the presence of PANH molecules in starburst-dominated galaxies using the 6.2, 7.7 and 8.6 μm PAH bands. Firstly, the spectral contributions of the silicate absorption and the line emissions were subtracted from the spectra using PAHFIT (Smith et al. 2007). The continuum was fitted with a spline following the same method of Peeters et al. (2017) and was also subtracted from the spectra.

Table 1. Profile peak positions for each Peeters' classes.

Class	6.2 μm	7.7 μm	8.6 μm
A	< 6.23	~ 7.6	< 8.6
B	$6.23 < \lambda < 6.29$	~ 7.8	> 8.6
C	> 6.29	~ 8.22	——

We constructed a python based script to estimate the profile features through the submodule scipy.optmize.curve_fit. The separation of the sources into the classes followed the Tab.1. The 7.7 μm band presents both 7.6 and 7.8 μm features and we used their flux ratio to distinguish between classes A and B (for class A, $F_{7.6}/F_{7.8}>1$).

3. Results

Considering the 6.2 μm band, 67% of 155 galaxies were classified as class A, 31% were as class B and 2% as class C (Fig. 1, Canelo et al. submitted). Therefore, these spectra suggest a significant presence of PANHs in the ISM of the galaxies which could be related to their starburst-dominated emission. These results could also indicate another reservoir of nitrogen in the Universe, with density and temperature conditions different from those of gas phase and ices.

The class A objects are the most common in the Universe, as Pino et al. (2008) have already noticed. And we can see a correlation along the bands in some galaxies: more than one profile was classified as class A. This is more evident for the 6.2 and 7.7 μm bands, as expected because of the same CC vibrational mode. On the other hand, the 8.6 μm band is less connected than

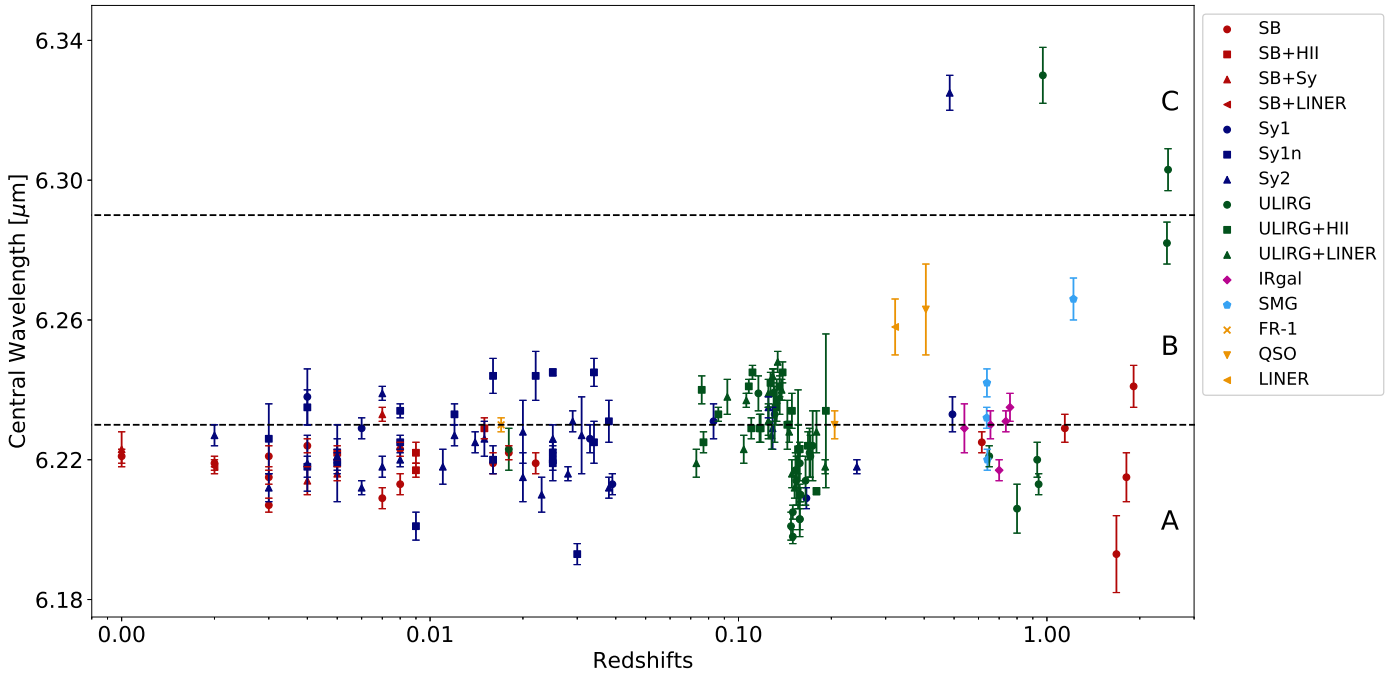

Figure 1. Distribution of the central wavelengths of the 6.2 μm band according to the redshift of the galaxies (Canelo et al. submitted). The dashed lines are the limits among the Peeters' classes, indicated also by A, B or C letter. Acronyms: AGN — Active Galactic Nucleus, FR — Fanaroff-Riley galaxy, HII — HII region, IRgal — Infrared galaxy, LINER — Low-Ionization Nuclear Emission-line Region, QSO — Quasi-Stellar Object, SB — Starburst galaxy, SMG — Submillimeter Galaxy, Sy — Seyfert galaxy, ULIRG — Ultra-Luminous Infrared Galaxy.

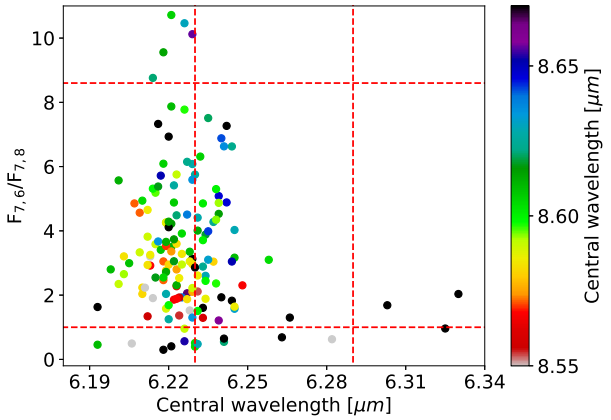

Figure 2. Colormap comparing the separation of the sources into the Peeters' class for the three analyzed PAH bands. The dashed lines are the limits among the Peeters' classes.

the others. Fig. 2 shows the comparison of the Peeters' classes separation for the 6.2 μm band and the preliminary results of the 7.7 and 8.6 μm bands.

4. Conclusions and perspectives

This study suggests that the ubiquity of PANHs could indicate that they are responsible for an important fraction of the mid-infrared emission, especially for the 6.2 μm band. These findings also give support to the idea of their contribution to the origins of life on Earth and elsewhere, since they could form nucleobase-type structures in the ISM (Elsila et al. 2006; Parker et al. 2015).

From an astrochemical perspective, metallicity and cosmic abundance variations may also be significant in ways not currently understood. Computational capabilities together with experimental measurements need to be further addressed to better determine PANHs vibration frequencies mainly in the galaxy environment.

Acknowledgements. Special acknowledgements to CAPES (Comissão de Aperfeiçoamento de Pessoal do Nível Superior) and CNPq (Conselho Nacional de Desenvolvimento Científico e Tecnológico) for the financial support.

References

Canelo, C. M. et al., 2018, MNRAS, 475, 3746
Elsila, J. E. et al., 2006, Meteoritics and Planetary Science, 41, 785
Hernán-Caballero, A. & Hatziminaoglou, E., 2011, MNRAS, 414, 500
Hudgins, D. M., Bauschlicher, C. W. & Allamandola, L. J., 2005, ApJ, 632, 316
Parker, D. S. N. et al., 2015, ApJ, 803, 53
Peeters, E. et al., 2002, 390, 1089
Peeters, E. et al., 2017, ApJ, 836, 198
Pino, T. et al., 2008, A&A, 490, 665
Smith, J. D. T. et al., 2007, ApJ, 656, 770
van Diedenhoven, B. et al., 2004, ApJ, 611, 928

Boletim da Sociedade Astronômica Brasileira, **30**, no. 1, 192-193

Chromodynamical analysis of lenticular galaxies using globular clusters and planetary nebulae

E. Zanatta[1], A. Cortesi[2], & A.L. Chies-Santos[1]

[1] Departamento de Astronomia, Instituto de Fisica, Universidade Federal do Rio Grande do Sul, Porto Alegre, R.S., Brazil
e-mail: emiliojbzanatta@ufrgs.com, ana.chies@ufrgs.br
[2] Departamento de Astronomia, Instituto de Astronomia, Geofisica e Ciencias Atmosfericas da USP, Cidade Universitaria, CEP:05508900, Sao Paulo, SP, Brazil
e-mail: aricorte@googlemail.com

Abstract. Lenticular galaxies are suggested as a transitional morphology between elliptical and spiral galaxies. Therefore, the study of their evolution can shed light on galaxy evolution in a global way. We studied the kinematics of the globular cluster (GC) systems of three lenticular galaxies: NGC 2768, NGC 3115 and NGC 7457, using kinematics from planetary nebulae (PNe). We show that all galaxies have GCs that can be found in both spheroid and disk components. Moreover, we find that there is great variety in the kinematics of the GC systems in each galaxy, showcasing that the formation and evolution of these galaxies is also varied.

Resumo. Galáxias lenticulares são consideradas como uma morfologia de transição entre galáxias elípticas e espirais. Portanto, o estudo de sua evolução pode nos ajudar a entender evolução de galáxias de forma global. Nós estudamos a cinemática dos aglomerados globulares (GC) de três galáxias lenticulares: NGC 2768, NGC 3115 e NGC 7457, usando a cinemática advinda de nebulosas planetárias (PNe). Mostramos que todas as galáxias possuem GCs que podem ser encontrados tanto nos componentes de disco ou esferoidais. Ainda, encontramos que existe grande variedade na cinemática de sistemas de GCs em cada galáxia, demonstrando que a formação e evolução destas galáxias é também variada.

Keywords. Galaxies: evolution - Galaxies: formation - Galaxies: kinematics and dynamics

1. Introduction

Outer halo kinematics can be used to study the evolution of galaxies, being generally obtained through spectroscopy of its gas content. In S0 galaxies, however, the fraction of undisturbed H1 gas available is usually not enough to obtain the kinematics of an entire galaxy. Thankfully, the study of kinematics of S0 galaxies through discrete tracers, such as GCs and PNe, has shown very promising results (Coccato et al. 2009; Cortesi et al. 2011; Brodie et al. 2004). Using the method developed in Cortesi et al.(2011; 2016) and PNe kinematics from Cortesi et al. (2013), the galaxies NGC 1023 (Cortesi et al. 2016), NGC 2768, NGC 3115 and NGC 7457 had their GC systems studied through kinematics, colours and probabilities to belong to spheroidal or disk components of their host galaxies.

The GC samples used in this analysis, both spectroscopic and photometric, come from the SLUGGS Survey (Brodie et al. 2004; Forbes et al. 2017). The PNe samples were obtained using the PN.S instrument (Douglas et al. 2002; Coccato et al. 2009; Cortesi et al. 2011) and their kinematics obtained from Cortesi et al. (2013).

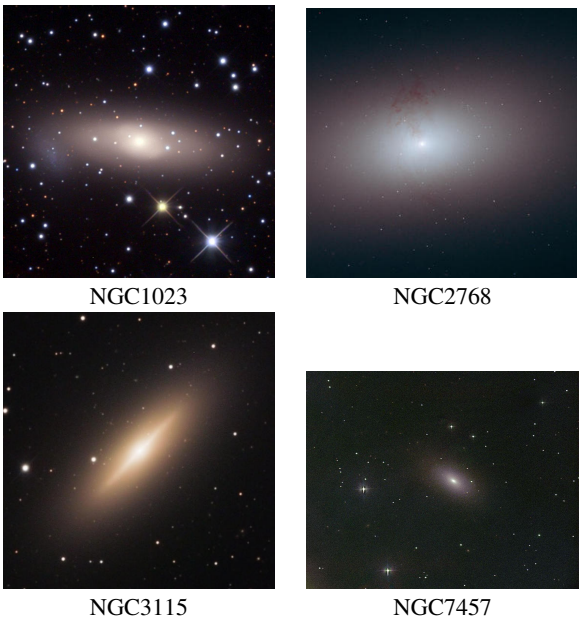

Figure 1. Galaxies present in this work and Cortesi et al.(2016) Cortesi et al. (2016).

2. Spheroid-Disk Decomposition

Using GALFIT (Peng et al. 2002) and K-band images from 2MASS, we decompose the galaxy light into an spheroidal and disk component. Dividing the spheroidal model from the total model of a given galaxy light, we obtain an *f-map*. The *f-map* is used to get preliminary probabilities f_i for each GC to belong to the host galaxy spheroid region, given the flux at an aperture of 3 pixels around its position.

3. Maximum Likelihood Analysis

Following the model described in Cortesi et al. (2016) we can estimate the best kinematic parameters for GCs using MLE and a Gaussian kinematic model with parameters $\theta_1 = (V, \sigma)$. In such model, the individual GC velocities, v_i, are projections of the

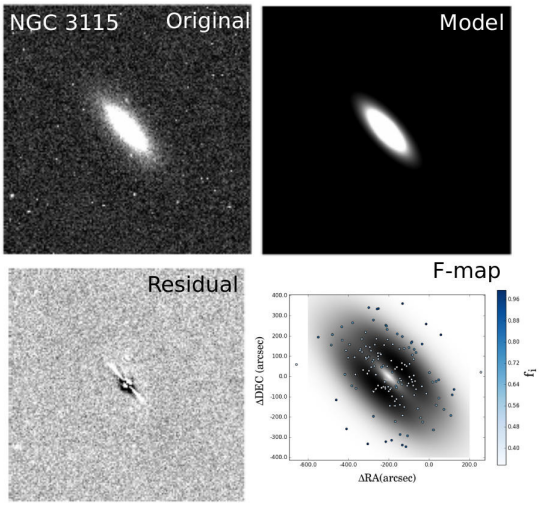

Figure 2. GALFIT model for NGC 3115 with associated F-map with GCs overplotted.

rotational velocity V, which is part of the line-of-sight velocity $V_{\rm los}$:

$$V_{\rm los} = V_{\rm sys} - V\sin(i)\cos(\phi). \quad (1)$$

Therefore, for the associated dispersion velocity σ, we have:

$$F(v_i;\theta_1) \propto exp\left[-\frac{(v_i - V_{\rm los}(V))^2}{2\sigma^2}\right]. \quad (2)$$

In Cortesi et al.(2013), PNe kinematics for a set of galaxies, including NGC 2768, NGC 3115 and NGC7457, were obtained using MLE and a *two-component* model, accounting for disk and spheroid kinematics, given by:

$$\mathcal{L}(v_i;\theta_2) \propto \frac{f_i}{\sigma_{\rm sph}}\exp\left[-\frac{v_i^2}{2\sigma_{sph}^2}\right] + \frac{1-f_i}{\sigma_{\rm los}}\exp\left[-\frac{(v_i - V_{\rm los})^2}{2\sigma_{\rm los}^2}\right], \quad (3)$$

Where $\theta_2 = (V, \sigma_{\rm los}, \sigma_{\rm sph})$. Assuming the PNe as tracers of the host galaxy overall stellar kinematics, we employ the later model to the velocities of GCs, obtaining thus the likelihood of each GC to be associated with disk or spheroidal components of the host galaxy, or to not be associated with the host galaxy.

4. Results

- Expansion of the work done in Cortesi et al. (2016) for three more galaxies, showcasing the diversity of GC systems properties in lenticular galaxies.
- We detected evidences of GCs remnants of a minor merger in NGC 3115
- NGC 2768 red and blue GCs have distinct kinematics.
- We found an unusual proportion of GCs associated with the disk in NGC 7457.
- Overall, GCs colours and their probabilities of being associated with the host galaxies' components were not correlated.
- **Future prospects:** Addition of more galaxies and refinement of the statistical method.

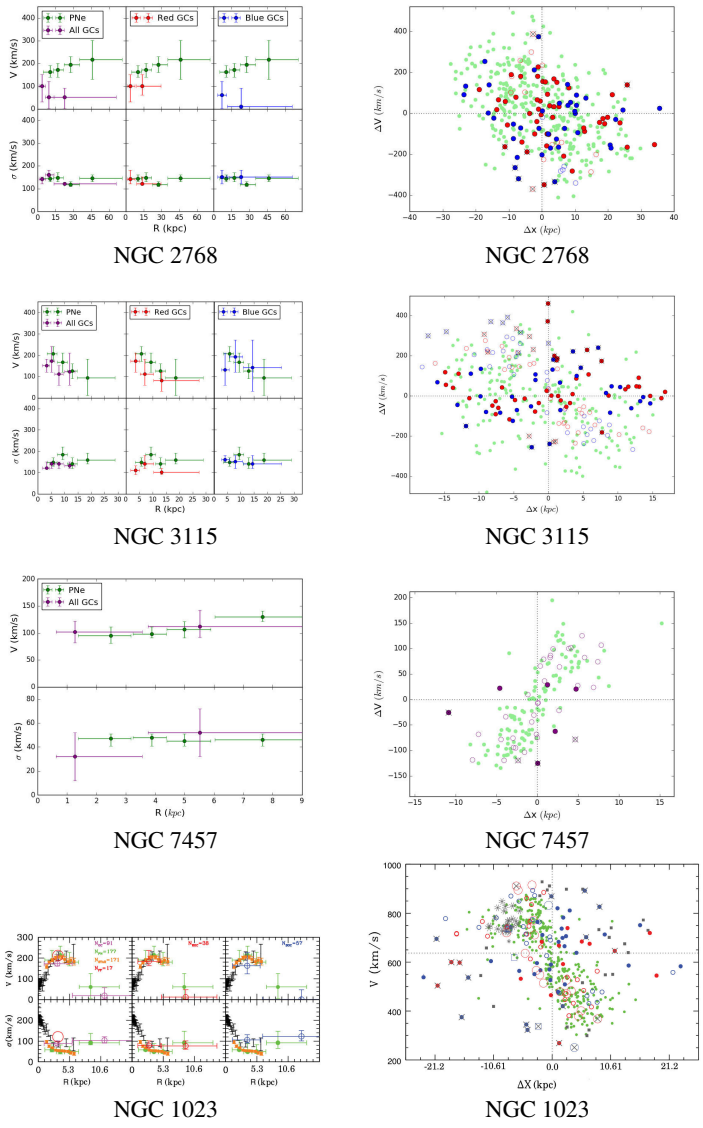

Figure 3. Left: Rotation curves and σ for GCs and PNe. Right: Velocities versus positions along the host galaxy major axis for GCs and PNe. NGC 1023 analysis taken from Cortesi et al. (2016) for comparison.

References

Brodie, J. P., et al. 2014, ApJ, 796, 52
Coccato, L., et al. 2009, MNRAS, 394, 1249
Cortesi, A., et al. 2011, MNRAS, 414, 642
Cortesi, A., et al. 2013, MNRAS, 432, 1010
Cortesi, A., et al. 2016, MNRAS, 456, 2611
Douglas, N. G., et al. 2002, PASP, 114, 1234
Forbes, D. A., et al. 2017, AJ, 153, 114.
Peng, C. Y., et al. 2002, AJ, 124, 266

Boletim da Sociedade Astronômica Brasileira, **30**, no. 1, 194-195

Quenching or bursting?

Physical processes in green valley galaxies and the star formation acceleration

T. S. Gonçalves[1], D. C. Martin[2], J. P. Nogueira-Cavalcante[1,3], K. Menéndez-Delmestre[1] & K. Sheth[4]

[1] Observatório do Valongo, Universidade Federal do Rio de Janeiro e-mail: tsg@astro.ufrj.br
[2] California Institute of Technology
[3] Observatório Nacional (ON/MCTI)
[4] NASA

Abstract. One of the main open questions in contemporary astrophysics is how galaxies quench star formation. The observed color bimodality is a strong indication that galaxies do not passively exhaust their gas reservoirs, instead requiring an active process that shuts down star formation over short timescales. In this work we show recent results by our group measuring quenching timescales of galaxies in different epochs and of different types, supporting the idea that some processes are more efficient for quenching star formation. We also present a new technique combining spectroscopic and photometric indices that allows for a measurement of the time derivative of the star-formation rate, i.e. the star formation acceleration. Finally we discuss the implications of this measurement, comparing for example the quenching timescales of galaxies with and without AGN activity.

Resumo. Uma das principais questões em aberto na astrofísica contemporânea é como galáxias param de formar estrelas. A bimodalidade em cores observada é um dos principais indícios de que galáxias não esgotam seus reservatórios de gás passivamente, mas requerem um processo ativo que acabe com a formação estelar em escalas de tempo curtas. Neste trabalho apresentamos resultados de nosso grupo medindo escalas de tempo de cessação de formação estelar em galáxias de diversos tipos e épocas, dando suporte à ideia de que alguns processos são mais eficientes para tal cessação. Também apresentamos uma nova técnica que combina índices espectroscópicos e fotométricos que nos permitem medir a derivada temporal da taxa de formação estelar, ou seja, a aceleração da formação estelar. Finalmente, discutimos aplicações práticas desta medida, usando como exemplo uma comparação entre galáxias com e sem núcleos ativos.

Keywords. galaxies: evolution – galaxies: stellar content – galaxies: structure

1. Introduction

A key problem in galaxy evolution is how galaxies stop forming stars. The bimodality in the color distribution of galaxies (e.g., Strateva et al. 2001; Baldry et al. 2004) indicates the process of star formation quenching – and the conversion of star-forming galaxies into passively evolving objects – happens relatively quickly. How fast is that transition, and what physical processes are associated with it? In order to understand such processes, one must study galaxies with intermediate colors, assumed to be undergoing quenching – the green valley.

2. Evolution with redshift

Using spectral indices (the break at 4000Å and the H_δ absorption) and stellar population synthesis models, Martin et al. (2007) have determined that galaxies in the green valley at low redshift ($z \sim 0.1$) stop forming stars typically in less than 1 Gyr. Following the same methodology, Gonçalves et al. (2012) have determined that when the universe was half its current age ($z \sim 0.8$), galaxies quenched faster – typically in less than 500 Myr – and the transition would occur for more massive objects. Therefore, the red sequence forms in a top-down manner: the massive end was created first (and quickly), and the low-mass end forms later and more slowly (Figure 1).

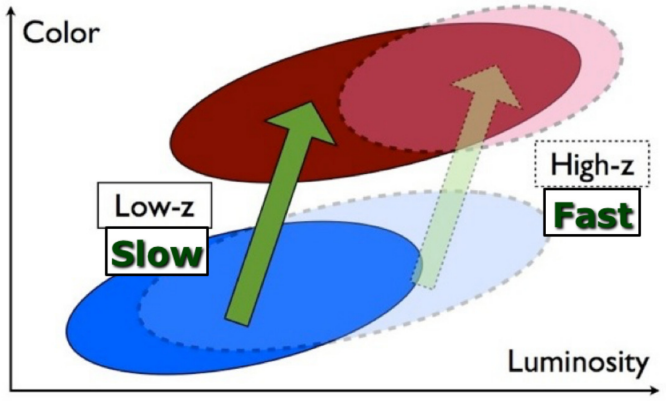

Figure 1. Summary of results in Gonçalves et al. (2012). Massive galaxies quench at earlier times, and at a faster pace.

3. Quenching timescales as a function of morphology

More recently, we have analyzed quenching timescales independently according to galaxy morphology. Our results indicate that spirals in the green valley are quenching more slowly than ellipticals (Nogueira-Cavalcante et al. 2018). In particular, barred spirals, which are clearly undergoing secular evolution without any strong external influences, are the slowest to quench their star formation. Major mergers, on the other hand, are the fastest to stop forming stars (Figure 2).

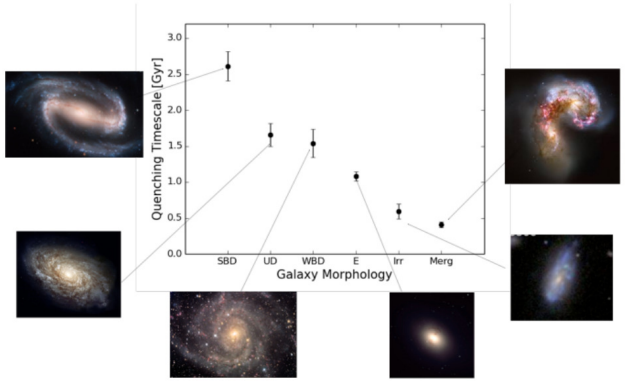

Figure 2. Quenching timescales as a function of galaxy morphology. Disk galaxies quench slowly, and barred galaxies are the slowest to quench, indicating the inefficiency of secular processes in stopping star formation. From Nogueira-Cavalcante et al. (2018).

4. Star formation acceleration

We have now improved our methodology in order to measure not only quenching timescales, but also the rate at which star formation rates are increasing or decreasing – the star formation acceleration (SFA, Martin et al. 2017). A combined analysis of stellar population synthesis models and cosmological simulations can yield a number of photometric (UV and optical) and spectral measurements (again, the 4000Å break and H_δ absorption) capable of recovering the instantaneous SFA of individual galaxies with remarkable accuracy (Figure 3). Our results show that the most massive galaxies in the green valley are bursting instead of quenching, through mergers with gas-rich satellites. Another result is that AGN hosts are quenching faster – a result that would be expected assuming AGN are capable of heating and/or expelling the gas from the galaxy (Figure 4).

Acknowledgements. TSG would like to thank CNPq for financial support through Productivity in Research grant 306968/2014-2.

References

Baldry, I. K., Glazebrook, K., Brinkmann, J., et al. 2004, ApJ, 600, 681
Gonçalves,T. S., Martin, D. C., Menéndez-Delmestre, K., Wyder, T., Koekomoer, A. 2012, ApJ, 759, 67
Martin, D. C., Wyder, T., Schiminovich, D. et al. 2007, ApJS, 173, 342
Martin, D. C., Gonçalves, T. S., Darvish, B., Seibert, M., Schiminovich, D. 2017,ApJ, 842, 20
Nogueira-Cavalcante, J. P., Gonçalves, T. S., Menéndez-Delmestre, K., Sheth, K. 2017, MNRAS, 473, 1346
Strateva, I., Ivezić, v., Knapp, G. R., et al. 2001, AJ, 122, 1861

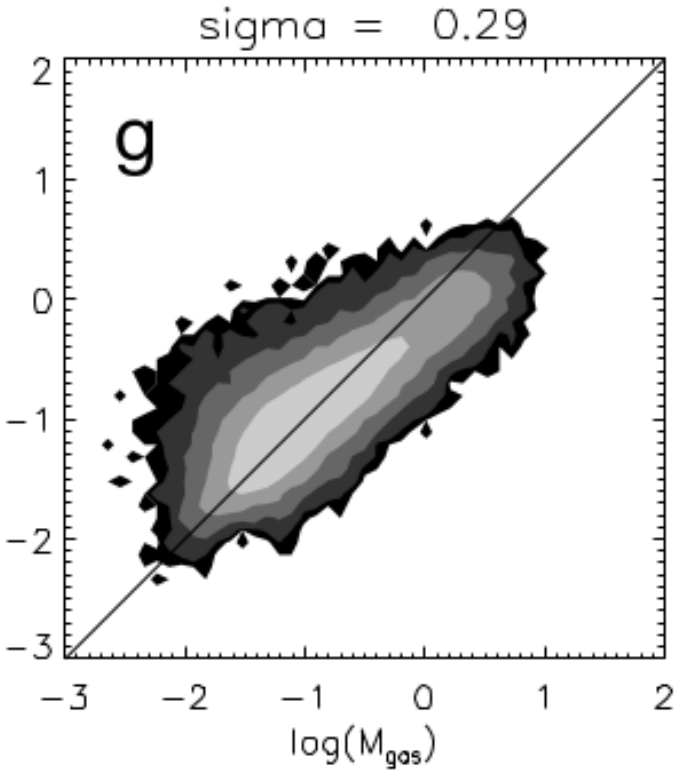

Figure 3. Results for SFA from linear regression as a function of simulation input. SFA of simulated galaxies is recovered with great accuracy. From Martin et al. (2017).

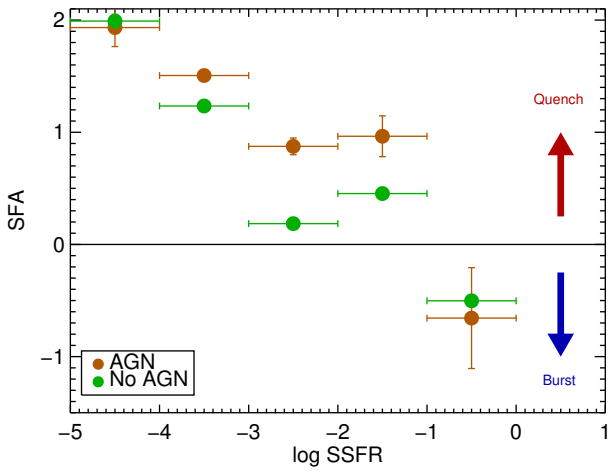

Figure 4. SFA of galaxies with (brown) and without (green) AGN. AGN hosts are quenching more strongly. From Martin et al. (2017).

Boletim da Sociedade Astronômica Brasileira, **30**, no. 1, 196-197

A morphological view of the Green Valley

C. de Sá Freitas e T. S. Gonçalves

[1] Observatório do Valongo, Ladeira Pedro Antônio, RJ
e-mail: camila14@astro.ufrj.br
e-mail: tsg@astro.ufrj.br

Abstract. In this work we study the population of the galaxies that lie in the transition region between the blue cloud and the red sequence, known as the Green Valley, and investigate which physical processes are responsible for quenching star formation in these objects. In particular, we measure the timescale in which this transition occurs and how it relates to the morphological type of the galaxies, in an attempt to determine whether the morphological transformation is associated with more violent processes. To do this, we use a sample of Sloan Digital Sky Survey (SDSS) galaxies combined with the morphological analysis performed by the Galaxy Zoo Project. Our methodology consists of analyzing spectra in order to measure a combination of photometric and spectroscopic indices — more specifically the 4000 Angstrom break and the H-delta absorption — and evaluate the age of the stellar population and recent star formation activity. Preliminary results indicate that, effectively, elliptical galaxies, which probably have undergone processes of interactions and merges, are quenching their star formation more rapidly. In the future, we will determine how this distinction depends on cosmological time, by comparing results from different redshifts.

Resumo. Nesse trabalho nós estudamos a população de galáxias que se encontra na região de transição entre a nuvem azul e a sequência vermelha, conhecida como vale verde, e investigamos quais processos físicos são responsáveis pela cessação de formação estelar destes objetos. Em particular, medimos a escala de tempo na qual essa transição ocorre e como ela está relacionada com o tipo morfológico das galáxias com o objetivo de tentar determinar se a transformação morfológica está associada a processos mais violentos. Para isso, utilizamos uma amostra de galáxias do Sloan Digital Sky Survey (SDSS) em conjunto com a análise morfológica realizada pelo Galaxy Zoo Project. Nossa metodologia consiste em analisar espectros para medir uma combinação de índices fotométricos e espectroscópicos - mais especificamente a ruptura de 4000 angstrom e a absorção de Hδ - e avaliar a idade da população estelar e a recente atividade de formação de estrelas. Resultados preliminares indicam que, efetivamente, galáxias elípticas, que provavelmente sofreram processos de interação e colisão, estão cessando sua formação estelar mais rapidamente. No futuro, determinaremos se esta diferença depende da época cosmológica, comparando resultados de redshifts diferentes.

Keywords. galaxies: evolution

1. Introduction

It has long been known that the bimodality in the color-magnitude diagram (CMD) separates two populations of galaxies (Figure 1): the blue cloud and the red sequence. The population of the former is mostly young, gas-rich, and with a high star formation rate (SFR), while the latter is characterized by a population of passive old gas-poor galaxies. In this work, we study the population of the galaxies that lie in the transition region between, known as the green valley (e.g. Martin et al., 2007; Wyder et al., 2007; Gonçalves et al. 2012) and investigate which physical processes are responsible for quenching star formation in these objects. More specifically, we ask: are quenching timescales related to galaxy morphology?

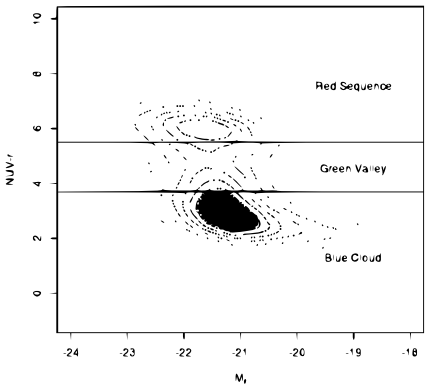

Figure 1. The color-magnitude diagram for a sample of approximately 59.000 galaxies, classified or as spirals or as ellipticals with 80% of confidence by the Galaxy Zoo Project. The lines indicate the empirical region of the green-valley for this work.

2. Metodology

We use a sample of Sloan Digital Sky Survey galaxies (Alam et al. 2015) of the local universe combined with the analysis performed by the Galaxy Zoo Project with 80% confidence of the morphological classification (Lintott et al. 2011), as can be seen in Figure 2. Our methodology consists of analyzing spectra in order to measure a combination of photometric and spectroscopic indices — more specifically the 4000 Angstrom break and the Hδ absorption — and evaluate the age of the stellar population and recent star formation activity (Martin et al., 2007, Gonçalves et al. 2012, Nogueira-Cavalcante et al, 2017).

2.1. Star Formation Histories

We use the same simplifying hypotheses used by Gonçalves et al. 2012 and Martin et al., 2007 (Figure 3a):

1. Galaxies only move towards redder colors;
2. $\mathrm{SFR}(t) = \begin{cases} \mathrm{SFR}(t=0), & \text{if } t < t_0 \\ \mathrm{SFR}(t=0)e^{-\gamma t}, & \text{if } t > t_0 \end{cases}$

Kauffmann et al. (2003) showed that the $D_n(4000)$ and Hδ,A indices trace a well-defined region in a diagram, where the ex-

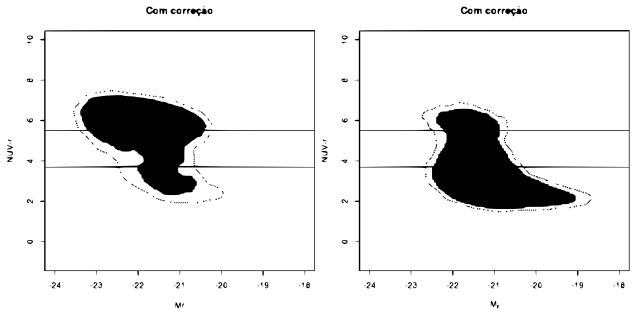

Figure 2. Left: The color-magnitude diagram for the sub-sample of ellipticals, with approximately 14.000 galaxies; Right: The color-magnitude diagram for the sub-sample of spirals, with approximately 45.000 galaxies.

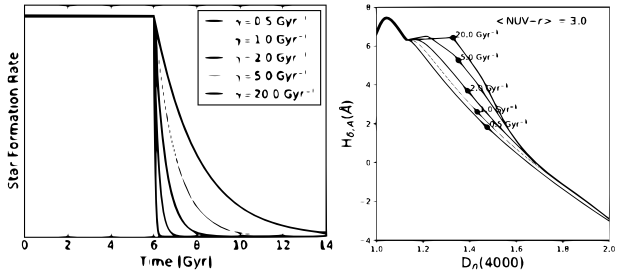

Figure 3. Left: Star formation rate as a function of time for five different SFHs with exponential decay. Hδ,A $\times$; Right: $D_n(4000)$ planes the same five SFH models. The black dots represent the Hδ,A and $D_n(4000)$ values for a given SFH model and NUV–r colour. Plots from Nogueira-Cavalcante et al. (2007)

act position of a galaxy depends strongly of its star formation history, as can be seen in the Figure 3b.

2.2. Spectral Parameters

We use the same definition used by Gonçalves et al. (2012) for the two indices (figura 4):

- $D_n(4000)$ is defined as the ratioof the average flux density Fν in the bands 3850–3950 and 4000–4100 Å, following the definition of Balogh et al. (1999);
- Hδ,A is the absorption equivalent width; the continuum is defined by fitting a straight line through the average flux density between 4041.60 and 4079.75 Å, on one end, and 4128.50 and 4161.00 Å, on the other:

$$H\delta, A = \sum_{\lambda=4083.5}^{4122.25} \left(1 - \frac{F_\nu}{F_{\nu,cont}}\right) \quad (1)$$

3. What is next

The next steps for our work will be the analysis of our sample at the plane Hδ,A $\times$ $D_n(4000)$ and compare with the models for different values for γ (as shown in the Figure 3). For this, we need to separate our sample in narrower color ranges (Figure 5).

Next, will be to determine gamma values according to morphology, in order to compare our results with previous works that measured quenching time-scaltes for local redshift (Schawinskiet al., 2014) and for higher redshifts (Nogueira-Cavalcante et al., 2017). Our final goal is to understand what processes may cause faster or slower quenching in each.

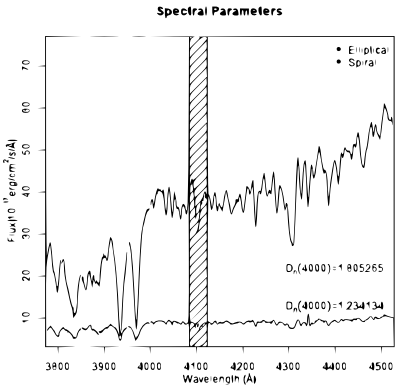

Figure 4. Two example spectra of galaxies in the sample, illustrating the determination of the aforementioned spectral indices: The gray-shaded areas indicates the bandpasses over which the Dn(4000) index is measured and the hatched area shows the Hδ,A bandpass

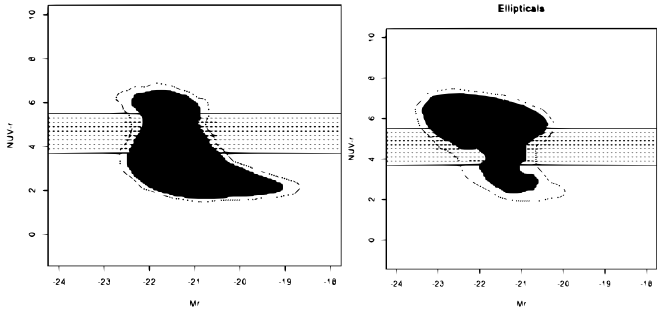

Figure 5. Green valley according to morfology: sample of ellipticals at left, and sample of spirals at right. The dashed lines indicate the bands of colours.

References

Alam, S. et al. 2015, ApJS, 219, 12..
Calzetti, D. et al. 1994, ApJ, 429, 582;
Gonçalves, T. et al. 2012, ApJ, 759, 67;
Kauffmann, G. et al. 2003, MNRAS, 341, 33;
Lintott, C. et al. 2011, MNRAS, 410, 166;
Martin, C. et al. 2007, ApJS, 173, 342;
Nogueira-Cavalcante, J. P. et al. 2017, MNRAS, 000, 1;
Schawinski, K. et al. 2014, MNRAS, 440, 889;

Boletim da Sociedade Astronômica Brasileira, **30**, no. 1, 198-199

Stellar metallicity gradients in simulated disc galaxies

Patricia B. Tissera[1] & Rubens E. G. Machado[2]

[1] Departamento de Ciencias Fisicas, Universidad Andres Bello, Av. Republica 220, Santiago, Chile.
[2] Universidade Tecnológica Federal do Paraná, Rua Sete de Setembro 3165, 80230-901 Curitiba, Brazil.
e-mail: rubensmachado@utfpr.edu.br

Abstract. Stellar metallicity gradients provide information on the assembly of disc galaxies, on star formation processes and on chemical evolution. The evolution of the gradients over time also holds clues on dynamical processes, such as migration, which could mix stars a posteriori affecting the distribution of chemical elements in the stellar components. We aim to investigate the metallicity gradients of the whole stellar populations in the disc component of simulated galaxies in a cosmological context. For low-redshift galaxies, we explore the dependence of the stellar metallicity gradients on stellar ages, sizes, and mass of the stellar discs. We also focus on exploring their evolution since $z = 1$. We analyse simulated disc galaxies from a cosmological hydrodynamical simulation which includes chemical evolution and a physically motivated supernova feedback. We compare our simulated galaxies to results from the CALIFA survey. We find that the simulated stellar discs have metallicity profiles with slopes in global agreement with observations. As a function of redshift, we detect a mild evolution in the metallicity gradients, in the sense of slopes becoming flatter since $z = 1$.

Resumo. Gradientes de metalicidade estelar proporcionam informações sobre a formação de galáxias, sobre processos de formação estelar e sobre evolução química. A evolução temporal dos gradientes também traz pistas sobre processos dinâmicos, como migração, que pode misturar as estrelas a posteriori, afetando a distribuição de elementos químicos na componente estelar. Nosso objetivo é o estudo dos gradientes de metalicidade de todas as populações estelares dos discos de galáxias simuladas em um contexto cosmológico. Para galáxias em baixo redshift, exploramos a dependência dos gradientes com idades, massas e tamanhos do disco estelar. Também exploramos sua evolução desde $z = 1$. Analisamos galáxias simuladas provenientes de uma simulação cosmológica hidrodinâmica que inclui evolução química e um feedback de supernovas fisicamente motivado. Comparamos nossas galáxias simuladas com resultados do survey CALIFA. Encontramos que os discos estelares simulados apresentam gradientes globalmente em acordo com as observações. Em função do redshift, detectamos uma evolução suave dos gradientes, no sentido de se tornarem mais planos desde $z = 1$.

Keywords. Galaxies: abundances – Galaxies: evolution – Galaxies: stellar content – Methods: numerical

1. Introduction and Methods

The chemical abundances of stars hold relevant information to understand the history of galaxy assembly. Both observational and theoretical results indicate the presence of metallicity gradients, whose origins may be linked to the effects of gas inflows and outflows that regulate chemical abundances and star formation activity (e.g. Chiappini et al. 2001; Mollá & Díaz 2005; Gibson et al. 2013; Mott et al. 2013).

We analyse the stellar populations of galaxies whose gas has been studied by Tissera et al. (2016). The disc galaxies were selected from a cosmological simulation that was carried out with a version of the code GADGET-3, an update of GADGET-2 Springel (2005). This version includes treatments of chemical enrichment, a multiphase model for the ISM, metal-dependent radiative cooling, stochastic star formation, and the supernova feedback scheme of Scannapieco et al. (2005, 2006). Th initial conditions of the simulation are consistent with the concordance cosmology with $\Omega_\Lambda = 0.7$, $\Omega_m = 0.3$, $\Omega_b = 0.04$, the normalization of the power spectrum of $\sigma_8 = 0.9$ and Hubble constant of $H_0 = 100h\,\mathrm{km\,s^{-1}\,Mpc^{-1}}$, with $h = 0.7$. The simulation volume is a box of 14 Mpc (comoving) side, resolved with 2×230^3 initial particles.

2. Results

An illustrative example of one massive galaxy from the simulation is given in Fig. 1. For the disc component, it shows the projected stellar mass density, the oxygen abundace of the stars and the ages of stars.

We find that the simulated stellar discs have metallicity profiles with slopes in global agreement with observations. Low-mass galaxies tend to have a larger variety of slopes. The stellar metallicity gradients correlate with the half-mass radius more strongly than with stellar mass. Fig. 2 shows the gradients obtained from the galaxies in our simulation compared to the observational results of the CALIFA survey (Sánchez-Blázquez et al. 2014). They were measured with the region $[0.5–1.0]r_{\mathrm{eff}}$. In the lower panel, the gradients are normalized by the effective radius of each galaxy.

As a function of redshift, we detect a mild evolution in the metallicity gradients, in the sense of slopes becoming flatter. Fig. 3 shows the evolution of the metallicity gradients since $z \sim 1.5$, comparing our simulation results with observational estimates of the Milky Way Maciel et al. (2003). We also resort to an archaeological estimation of metallicity gradients in the simulation. This is done by defining mono-age stellar populations within the $z \sim 0$ snapshot of the simulation. For further details, see Tissera et al. (2016, 2017).

Acknowledgements. REGM acknowledges support from CNPq.

References

Chiappini, C., Matteucci, F., & Romano, D. 2001, ApJ, 554, 1044
Gibson, B. K., et al. 2013, A&A, 554, A47
González Delgado, R. M., García-Benito, R., Pérez, E., et al. 2015, A&A, 581, A103

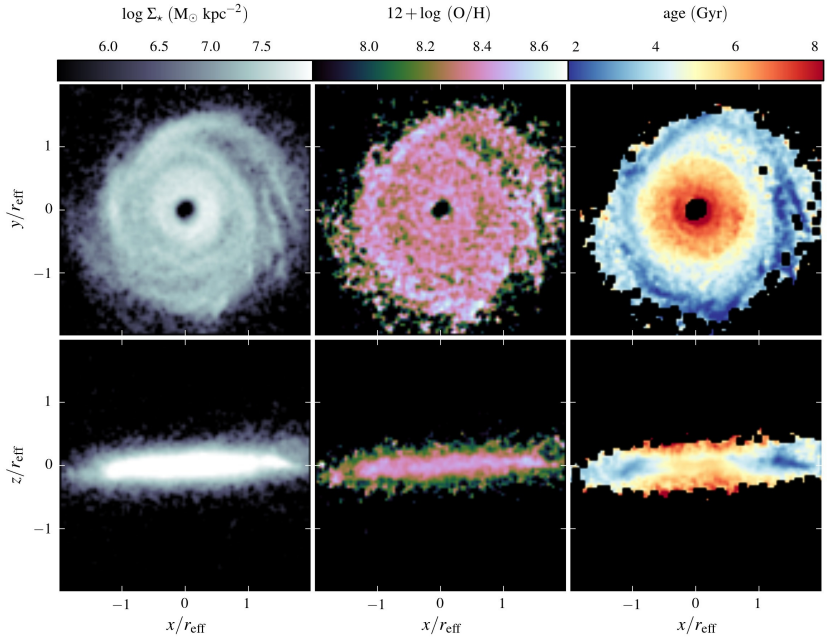

Figure 1. Example of a galaxy from our cosmological simulation, showing only the stellar disc component. The panels display the projected surface density, the oxygen abundance, and the ages of stars, each viewed both face-on and edge-on.

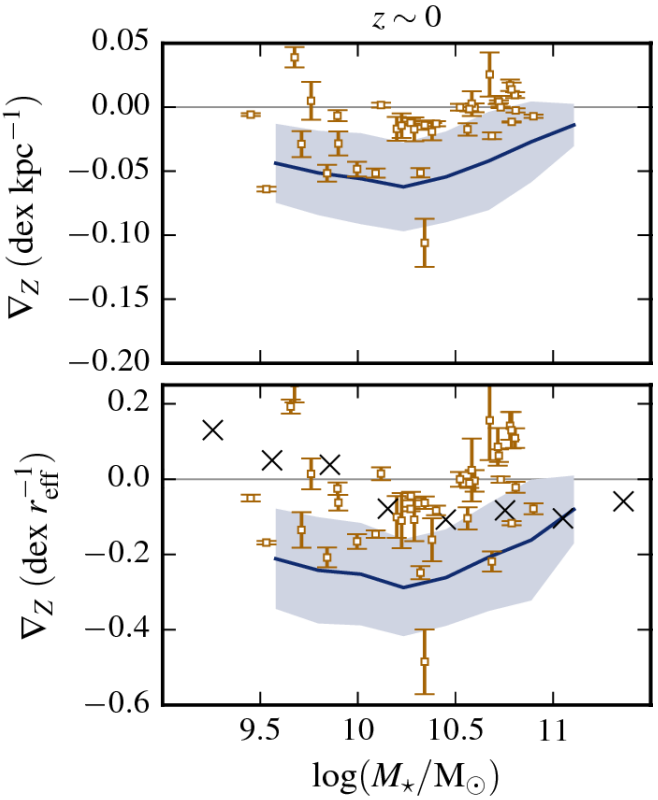

Figure 2. Metallicity gradients as a function os stellar mass, at redshift $z \sim 0$. The simulation means and dispersions are given by the solid lines with shaded areas. The yellow points are the observational results from the CALIFA survey Sánchez-Blázquez et al. (2014). The crosses in the lower panel are from González Delgado et al. (2015). In the lower panel, the gradients are normalized by the effective radius of each galaxy.

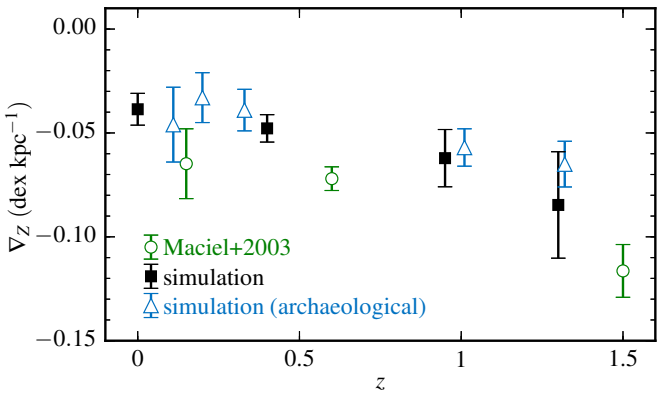

Figure 3. Evolution of the metallicity gradients. The green circles are estimates of the Milky Way from Maciel et al. (2003). The black squares are the gradients as a function of redshift from our simulations. The blue triangles are the archaeological gradients from the simulation.

Maciel, W. J., Costa, R. D. D., & Uchida, M. M. M. 2003, A&A, 397, 667
Mollá, M. & Díaz, A. I. 2005, MNRAS, 358, 521
Mott, A., Spitoni, E., & Matteucci, F. 2013, MNRAS, 435, 2918
Sánchez-Blázquez, P., Rosales-Ortega, F. F., Méndez-Abreu, J., et al. 2014, A&A, 570, A6
Scannapieco, C., Tissera, P. B., White, S. D. M., & Springel, V. 2005, MNRAS, 364, 552
Scannapieco, C., Tissera, P. B., White, S. D. M., & Springel, V. 2006, MNRAS, 371, 1125
Springel, V. 2005, MNRAS, 364, 1105
Tissera, P. B., Machado, R. E. G., Sanchez-Blazquez, P., et al. 2016, A&A, 592, A93
Tissera, P. B., Machado, R. E. G., Vilchez, J. M., et al. 2017, A&A, 604, A118
Tissera, P. B., et al. 2016, MNRAS, 456, 2982

Boletim da Sociedade Astronômica Brasileira, **30**, no. 1, 200-204

The BINGO Telescope: a new 21 cm window for exploring the Dark Universe and other astrophysics

C.A. Wuensche[1] on behalf of BINGO collaboration

[1] Divisão de Astrofísica, Instituto Nacional de Pesquisas Espaciais, São José dos Campos, SP, Brazil
e-mail: ca.wuensche@inpe.br

Abstract. BAO (Baryon Acoustic Oscillations) are arguably one of the best probes to explore the young Universe and can contribute critically to the understanding of the Dark Energy properties. BINGO is a radio telescope designed to make the first BAO measurement in the radio waveband (∼ 1 GHz) and is currently being constructed by a consortium including Brazil, United Kingdom, Switzerland, Uruguay and China. It will use a technique known as Intensity Mapping, measuring the 21 cm Hydrogen hyperfine transition for that. BINGO will operate in the frequency range 0.96 – 1.26 GHz, which corresponds to a redshift range z = 0.13 – 0.48, targeting an epoch where dark energy started dominating the Universe dynamics. It will be built in a low-intensity RFI site in Paraíba, Brazil, and its innovative design contains no moving parts and careful combination of two 40 m dishes, a focal plane containing 50 horns and receivers operating at total system noise temperature of ∼ 50 K. Such a design intends to achieve competitive results through an excellent polarization performance and very low sidelobe levels required for intensity mapping. Receiver and horn prototypes, as well as dishes and structure structure, are either under fabrication or executive design and construction in Brazil. The beginning of operation is scheduled for the second semester of 2019.

Resumo. BAO (do inglês, Baryon Acoustic Oscillations) são uma das melhores sondas para explorar o jovem Universo e podem contribuir criticamente para a compreensão das propriedades da Energia Escura. O BINGO é um radio telescópio projetado por um consórcio, incluindo Brasil, Reino Unido, Suíça, Uruguai e China, para fazer a primeira medição de BAO na faixa de rádio (∼ 1 GHz). Ele usará uma técnica conhecida como Mapeamento de Intensidade para medir a transição de 21 cm do hidrogênio. O BINGO funcionará na faixa de frequência de 0,96 – 1,26 GHz, correspondente ao intervalo de *redshift* z = 0,13 – 0,48, quando a energia escura já domina a dinâmica do Universo. O BINGO será construído em um sítio com baixo nível de radiointerferência na Paraíba, nordeste do Brasil, e deve obter resultados competitivos através de um projeto inovador, sem partes móveis, com duas parábolas de 40 m, um plano focal contendo 50 cornetas e receptores que funcionam em uma temperatura de ruído de ∼ 50 K. Esse projeto proporcionará um excelente desempenho de polarização e os níveis de contaminação nos lóbulos laterais necessários para o mapeamento de intensidade. A responsabilidade de fabricaçã dos receptores, cornetas, parábolas e a construção da estrutura é da parte brasileira. O início de operação está previsto para o segundo semestre de 2019.

Keywords. Cosmological parameters – Baryon Acoustic Oscillations

1. Introduction

One of the main cosmological challenges in the 21st century is the explanation of the cosmic acceleration, first unequivocally inferred in 1998 by two independent groups measuring supernovae of type I (Perlmutter et al., 1998; Riess et al., 1998). In combination with other observations, such as the Cosmic Microwave Background (CMB), there is little doubt about the existence of such a component and the main focus of observational cosmology is now to try to determine its detailed properties. Among the various programs to measure those properties, the study of Baryonic Acoustic Oscillations (BAO) is recognized as one of the most powerful probes of the properties of dark energy (e.g. Albrecht et al. 2006). The radio band provides a unique and complementary observational window for the understanding of dark energy via the redshifted 21 cm neutral hydrogen emission line from distant galaxies.

BAOs are a signature in the matter distribution from the recombination epoch (see Fig. 1). Note that BAO show up in the distribution of galaxies at redshifts less than that of the epoch of reionization ($z \lesssim 5$). In the context of the standard cosmological model, the so-called ΛCDM model, BAOs manifest themselves as a small but detectable excess of galaxies with separations of order of 150 Mpc.h^{-1} This excess is the imprint of the acoustic oscillations generated during CMB times and its linear scale is known from basic physics. Consequently, a measure of its angular scale can be used to determine the distance up to a given redshift.

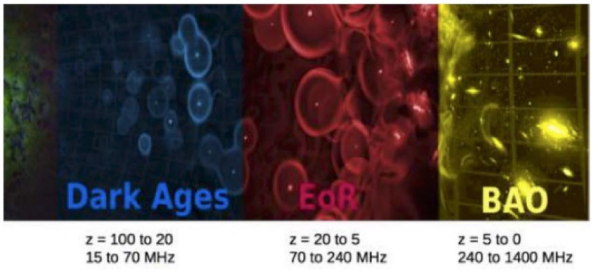

Figure 1. Late history of the Universe and the radio frequency of observation of the 21 cm line. The BAO epoch, well after reionization, will be the target of the BINGO telescope. In this epoch dark energy is dominating the expansion of the universe and it is possible to probe it.

The BINGO (**B**AO **I**n **N**eutral **G**as **O**bservations) telescope is a proposed new instrument designed specifically for observing such a signal and to provide a new insight into the Universe at $z \lesssim 0.5$ with a dedicated instrument. The optical project consists of a compact, two 40-m diameter, static dishes with an exceptionally wide field-of-view (15 deg.) and very sensitive op-

tics. The chosen technique for BAO observations is known as Intensity Mapping (e.g., Peterson et al. 2006). The main scientific goal for BINGO is to claim the first BAO detection in the radio band, mapping the 3D distribution of HI, yielding a fundamental contribution to the study of dark energy, with observations spanning several years.

The BINGO consortium is composed by Universidade de São Paulo and Instituto Nacional de Pesquisas Espaciais (Brazil), University of Manchester and University College London (United Kingdom), ETH Zürich (Switzerland) and Universidad de La República (Uruguay). An earlier version of the BINGO telescope concept is described in a paper by R. Battye and collaborators (Battye et al., 2013) and a comprehensive analysis of foregrounds and 1/f noise that can limit the BINGO performance was published by A. Bigot-Sazy and collaborators (Bigot-Sazy et al., 2015).

The structure of this paper includes this Introduction, followed by a description of the science motivation in Section 2. Section 3 will briefly describe BINGO design. The current status of the project will be summarized in Section 4, and will be followed by the Concluding Remarks, in Section 5

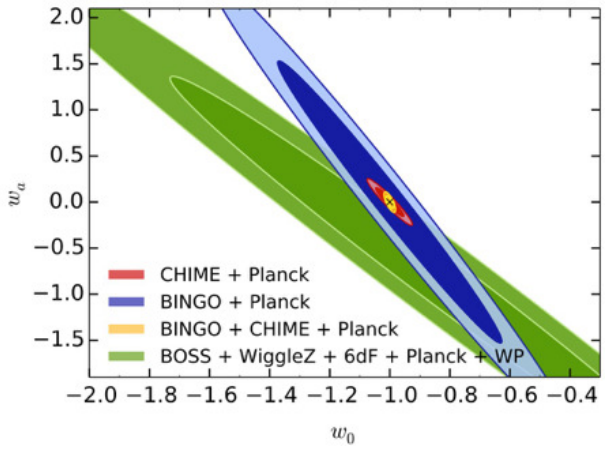

Figure 2. Constraints on Dark Energy equation of state, including forecasts from CHIME and BINGO. Note the tight error elipse obtained with combined radio data (BAO from CHIME and BINGO + Planck).

2. The science

Constraints on various existing dark energy models (see, e.g., Wang et al. 2005, 2007; Feng et al. 2008; Micheletti, Abdalla & Wang 2009; He et al. 2009; Abdalla et al. 2010; He et al. 2011) coming from BAO, such as those performed by Eisenstein and collaborators and Costa and collaborators (Eisenstein, 2005; Anderson et al., 2014) since BAOs provide precision distance measurements up to high redshifts ($z \gtrsim 1$). These will allow the degeneracies between cosmological parameters inferred from the cosmic microwave background to be broken, constraining most extensions to the standard cosmological model which are usually degenerate with the Hubble constant.

Measurements of the distribution of galaxies using observations in the radio region of the electromagnetic spectrum are based on the physics of the 21 cm (HI) line, which is a fundamental product of neutral hydrogen. HI redshift data allow us to construct a unique three dimensional map of the mass distribution, providing a different view when compared to the maps obtained with optical telescopes.

BAO measurements can be used to calculate the likelihoods for cosmological parameters given different cosmological input data. Fig. 2 shows the joint constraints for the equation-of-state of the dark energy with w_0 and w_a (1^{st} time derivative of w_0) given for various data sets. The constraints were computed using the Fisher Matrix code described in Bull et al. (2015). It clearly shows the improvement obtained with the combination of the intensity mapping experiments BINGO and CHIME (Newburgh et al., 2014), compared to the current constraints given by the combination of the results of the CMB experiments Planck (Ade et al., 2014, 2016) and WMAP (polarizations; Bennett et al. 2013), with the optical galaxy surveys (BOSS; Anderson et al. 2013; Tojeiro et al. 2014), WiggleZ (Kazin et al., 2014) and 6dF (Beutler et al., 2011).

Furthermore, tight constraints can be made with radio data alone (BAO plus Planck), providing a completely independent measurement from optical surveys. The improvement in going from the red to yellow contours is due to having two independent measurements at different redshifts, showing the importance of BINGO. We have made estimates of the projected errors of the dark energy parameters assuming that all the other cosmological parameters are fixed. For constant w, the measurement would lead to an accuracy on w of $\lesssim 8\%$ with BINGO experiment alone, including different types of foregrounds (Olivari et al., 2017). BINGO will be competitive with and complementary to optical surveys, which will likely be limited by different systematic errors.

2.1. HI intensity mapping

The standard approach to probing Large Scale Structure (LSS) is to perform a large redshift survey, to measure positions and redshifts of a large number of galaxies and use them to infer their density contrasts, using galaxies as tracers of the underlying total matter distribution. The natural tracer at radio wavelengths is the 21 cm line of neutral hydrogen, but the volume emissivity associated with this line is low, meaning that detecting individual galaxies at $z \sim 1$ requires a very substantial collecting area.

A number of approaches have been proposed to conduct intensity mapping surveys using an interferometer array rather than a single dish (see, for instance, Baker et al. 2011; Pober et al. 2012; van Bemmel et al. 2012). This approach can have a number of advantages, but it also requires complicated, and hence expensive, electronics to make the correlations. Using a single moderate sized telescope with an ultra stable receiver system is the lowest cost approach to intensity mapping measurements of BAO at $z \lesssim 0.5$ (see, e.g., Battye et al. 2013). BINGO will be the first telescope in the world operating in its frequency range whose goal is to study BAO with 21 cm intensity mapping. Its innovative idea is to use a telescope with broad beam operating at low frequencies to carry out intensity mapping (Peterson et al., 2006; Loeb et al., 2008; Masui et al., 2013; Battye et al., 2013) and hence measure the overall integrated HI brightness temperature of a very large number of galaxies, used together as a LSS tracer.

The main difficulty is that the HI signal is typically $\sim 100\,\mu$K whereas the foreground continuum emission from the Galaxy is $\sim$ 1 K with spatial fluctuations $\sim$ 100 mK. Fortunately, the integrated 21 cm emission exhibits characteristic variations as a function of frequency whereas the continuum emission has a very smooth spectrum. While there is a clear-cut statistical signature that allows for the two signals to be separated, the instrument used to distinguish the HI contribution from the foregrounds will need to be carefully designed in particular to avoid systematic effects that can result in leakage of the continuum background into the HI signal.

3. The instrument

Detecting signals of $\sim 100\,\mu K$ with a receiver of standard performance implies that every pixel in our intensity map requires an accumulated integration time larger than 1 day over the course of the observing campaign, which is expected to last at least 3 – 4 years. The total integration time can be built up by many returns to the same patch of sky but between these returns the receiver gains need to be highly alike and achieving this stability is a major design concern. The relative strength of the foreground, which is partially linearly polarized and concentrated towards the Galactic plane, means that the observations need to be made with a clean beam with low sidelobe levels and very good polarization purity. The general concept for the BINGO instrument is described in Battye et al. (2013) and updated in Battye et al. (2016).

A declination strip of $\sim 15°$, centered at $\delta \sim -15°$ aims at minimizing the Galactic foreground contamination and will be the optimal choice for the BINGO survey. The need to clearly resolve structures of angular sizes corresponding to a linear scale of around 150 Mpc at BINGO's chosen redshift range implies that the required angular resolution has to be $\sim 0°.75$.

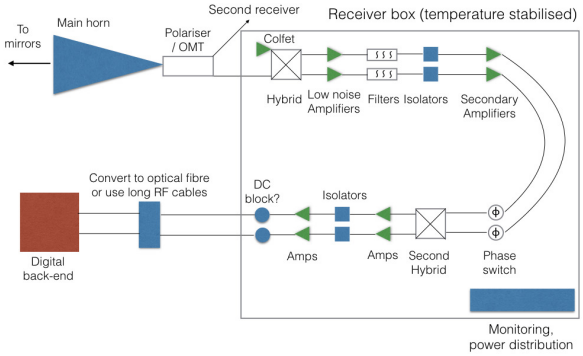

Figure 3. A block diagram of the main components of the BINGO correlation receiver. The correlation is achieved by means of the hybrids, which in this case will be waveguide magic tees. It is expected the low noise amplifiers will achieve a system temperature of $\lesssim 50\ K$.

3.1. The optics

The current optical design consists of two compact parabolic mirrors, with $\sim$ 40 m diameter, which gives a wider field-of-view (15°), lower sidelobe levels and improved polarization performance. The configuration under investigation considers a primary dish slightly tilted in relationship to the ground, while the second will hang from a vertical structure, iluminating uniformly the horn array. Since the mean wavelength of operation is 0.3 m, the surface profile of the telescope mirrors should have an *rms* error $\lesssim$ 15 mm to achieve maximum efficiency.

The gain of the telescope beams associated with the feedhorns at the edge of the array are less than 1 dB lower compared with those from the feedhorns at the centre and the edge beams are almost circular. The number of feedhorns in the array could in principle be more than 100, but the project will use 50 horns, completely covering a 15° strip of the sky every 24 hours

The guiding principle in the design of BINGO is to have components as simple as possible to minimize costs. Moreover, since there will be no moving parts, design, operation and instrument modeling will also be simpler than doing the same tasks for a conventional telescope. Another key advantage of a simple design is that it can be built quickly, allowing for results within a competitive science time window.

3.2. Receivers and feedhorns

Each receiver chain contains a correlation system, as shown in fig. 3, operating with uncooled amplifiers. The ambient temperature receivers will have a total system noise temperature of $\lesssim 50$ K and will operate in the frequency range 0.96 – 1.26 GHz. This corresponds to a redshift range of $z = 0.13 - 0.48$, long after the reionization era. After a year of observation BINGO should achieve a one degree pixel noise of 60 μK in a single 1 MHz frequency channel. The current plan is to use uncooled amplifiers because of their relatively good performance at these low frequencies and relatively low cost. The sky background and spillover will contribute up to 10 K and thus a cryogenically cooled receiver would give only a modest improvement in noise but with much more cost and complication. An additional benefit of receivers operating at ambient temperature is low maintenance given that cryogenics require constant attention that would be expensive to provide in a remote site.

BINGO will use specially designed conical corrugated feedhorns to illuminate the secondary mirror of the telescope. These need to be corrugated in order to provide the required low sidelobes coupled with very good polarization performance. Because of the large focal ratio needed to provide the required wide field of view, the feedhorns must be large with $\sim$ 1.7 m in diameter and $\sim$ 4.9 m in length. Their electromagnetic design is well understood and the challenge is to manufacture them at low cost and to minimize their weight due to the uncommon size. The mechanical project was done in Brazil. It consists of "4-like" profiles which will be curved into 127 circular sections, assembled together to make the horns. Also, it will receive an external layer of foam to ensure a better thermal stability during operation. A prototype is currently under construction and should be delivered by early January 2018. Details of the horns can be found in Fig. 4.

3.3. Site selection

The requirements for the telescope site are the following: a) a low Radio Frequency Interference (RFI) environment, distant for large cities or windmills; b) a topography that can easily support the two mirror design; c) easy access for researchers and technical staff; d) no planning/environmental restrictions on building a telescope structure; and e) a clear view of the South Galactic Pole for the reference feedhorns, in practice meaning a latitude south of $\sim 30°$. Recently, requirement e) was abandoned mostly due to budget constraints.

Uruguay was originally considered to host the telescope, and two cities were investigated: Minas de Corrales and Arerunguá. Budget concerns led to another site selection campaign in Brazilian areas. After a few months of procurement, including two regional centers of INPE, two sites were found in the west of Paraíba, a state located in the northeastern part of Brazil. Besides being very clean in terms of RFI, the local topography and support from a federal university with several campii spread around the western area of the state, made them the preferable sites. The construction is planned to start in early 2018. RFI measurements taken in Vão do Gato and Serra do Urubu (both in Paraíba) and

Figure 4. Top: Horn blueprint, with details on the corrugation. Center: Horn front view, green rings are machined and contain sockets for suspension rings. Bottow: Throat of the horn already assembled and coated with alodyne.

airplane routes covering the state of Paraíba, with the twot dot indicating the nominal sites marked are shown in Fig. 5.

4. Current status

BINGO systems are under planning or construction since July 2017. Horns are being fabricated and prototypes should be tested at the Laboratory of Integration and Tests of satellites (LIT), at INPE, starting mid January 2018. Transitions, polarimeters, magic tees and the receiver are already designed; fabrication of receivers and transitions should start at the end of 2017, subject to details of importation of components. Testing of amplifiers and other receiver components, as well as the initial steps of receiver assembly have already started at INPE.

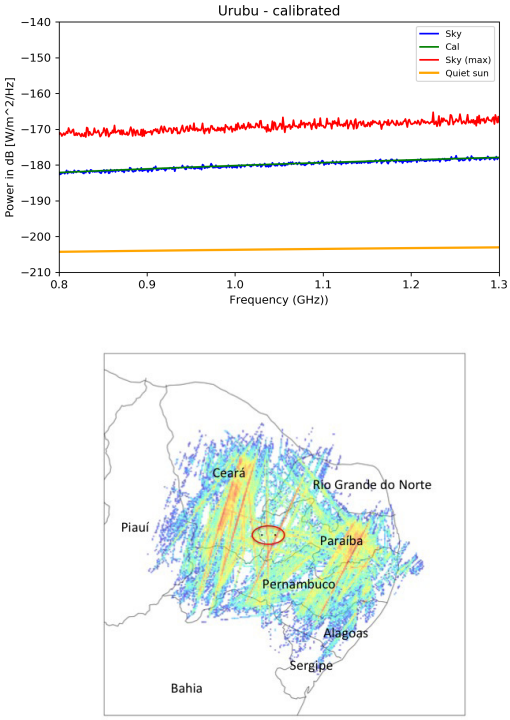

Figure 5. Top: RFI calibrated measurements in Serra do Urubu (right). Note the absence of any clear RFI signal. Bottom: Heat map of airplane routes covering the potential BINGO sites. Best sites are the two black dots in the center. The data runs from August 22 to September 15, 2017.

The current available funding is about US$ 3.0 million, dedicated to the construction of the telescope. Total cost of BINGO is estimated to be around US$ 4.2 million, the difference of US$ 1.2 million being for site preparation and structure construction. Current BINGO's competitors are FAST (Five-hundred-meter Aperture Spherical Telescope; FAST 2017) and CHIME (Canadian Hydrogen Intensity Mapping Experiment; CHIME 2017).

FAST main scientific goals involve hydrogen intensity mapping, fast radio bursts, pulsar timing, detection of interstellar molecules and interstellar communication signals. Midia references state that FAST will not be fully operational before late 2019, with three years needed to calibrate the various instruments. Once it is, it will likely require hundreds of radio astronomers. Problems with RFI produced by local tourists' visitation and also by its own actuators are current issues that may prevent FAST to operate at full capacity for a longer time.

Chime will also pursue the same major scientific goals as BINGO and FAST. Alike BINGO, it will have no moving parts but, instead of conventional mirrors and horns, it is based upon 20-m $\times$ 100-m long cylindrical mirrors and phased array beams. In addition to BAO and fast radio bursts, CHIME may also contribute to gravitational waves studies. It has entered operation in September 2017 and is able to monitor about 50% of the sky per observing day.

Fig. 6 shows the redshift space mapped by BINGO, FAST and CHIME, superimposed with current optical surveys.

5. Final remarks

BINGO is an innovative project to measure BAOs in the redshift interval $0.12 \leq z \leq 0.48$, at radio wavelenghts. The mea-

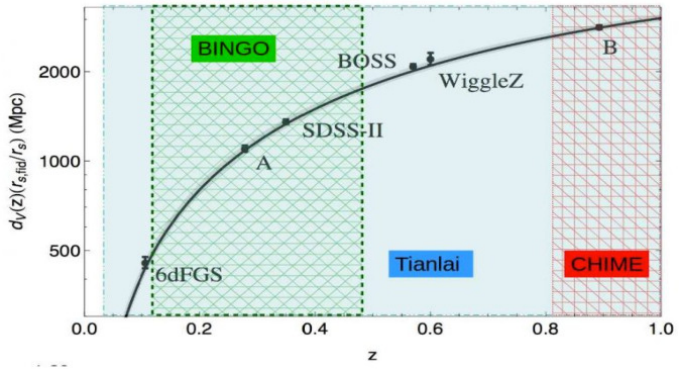

Figure 6. A version of the Hubble diagram including BINGO, FAST and CHIME, as well as other optical surveys such as SDSS, 6dFGS, BOSS and WiggleZ. Note the complementary coverage in redshift between BINGO and CHIME. Tianlai (FAST) will encompass both surveys from BINGO and CHIME.

sured signal is produced by the redshifted 21 cm line from neutral hydrogen, through a technique known as intensity mapping. BINGO will provide independent cosmological data and will probe the same redshift interval as the most important optical BAO surveys, but with different systematics. It is currently being constructed in Brazil, and will located in Paraíba, Northeastern Brazil, with the local support of the Universidade Federal de Campina Grande.

Scheduled to operate for at least 4 years, BINGO will provide high quality data, covering a wide range of scientific areas from Cosmology to Galactic science. With an upgrade to the digital backend, BINGO may also be able to detect a number of Fast Radio Bursts (FRBs) of which only ~ three dozens have been currently detected so far and whose origin is unknown.

The Bingo Collaboration can be found at http://www.bingo.telescope.org.

Acknowledgements. C.A.W. acknowledges a CNPq Grant 313.597/2014-6.

References

Abdalla, E., Abramo L. R. & de Souza, J. C. C. 1010, Phys. Rev. D, 82, 023508
Ade, P. et al. 2014, Planck Collaboration, A&A, 571, A16
Ade, P. et al. 2016, Planck Collaboration, A&A, 594, A13
Albrecht, A. et al. 2006, DETF report, astro-ph/0609591
Anderson, L., Aubourg, E., Bailey, S., et al. 2013, MNRAS, 427, 3435
Anderson, L., Aubourg, E., Bailey, S., et al. 2014, MNRAS, 441, 24
Baker, T., Ferreira, P. G., Skordis, C. & Zuntz, J. 2011, Phys. Rev. D, 84, 124018
Battye, R. A., Browne, I. W. A., Dickinson, C., et al. 2013, MNRAS, 434, 1239
Battye, R. et al. 2016, Proceedings of Recontres de Moriond, La Thuille, arXiv/1610.06826
Bennett, C. L. et al. 2013, WMAP Collaboration, ApJSS, 208, 20
Beutler, F., Blake, C., Colless, M. et al. 2011, MNRAS, 416, 3017
Bigot-Sazy, M.-A. et al. 2015, MNRAS, 454, 3240
Bull, P., et al. 2015, ApJ, 803, id. 21
Eisenstein, D. J. 2005, New Astronomy Reviews, 49, 7
Feng, C., Wang, B., Abdalla, E. and Su, R. K. 2008, Phys. Lett. B 665, 111
He, J. H., Wang, B. and Abdalla, E. 2009, Phys. Lett. B, 671, 139
He, J. H., Wang, B. and Abdalla, E. 2011, Phys. Rev. D, 83, id. 063515
Kazin, E. A., Koda, J., Blake, C., et al. 2014, MNRAS 441, 3524
Loeb, A., & Wyithe, S. 2008, Phys. Rev. Lett. 100, 161301
Masui, K. W., Switzer, E. R., Banavar, N. et al. 2013, MNRAS, 434, 46
Micheletti, S., Abdalla, E., & Wang, B. 2009, Phys. Rev. D, 79, id. 123506
Newburgh, L. B., et al., 2014, CHIME Collaboration, Proc. SPIE, Vol 9145, id. 91454V
Olivari, L. et al., MNRAS, submitted (Aug 2017)
Perlmutter, S. et al. 1998, Supernova Cosmology Project Collaboration, Nature 391, 51
Peterson, J. B., Bandura, K. & Pen, U. L. 2006, Moriond Cosmology Proceedings, astro-ph/0606104
Pober, J. C., Parsons, A. R., DeBoer, D. R., et al. 2012, AJ, 145, id. 65
Riess, A. G., et al. 1998, Supernova Search Team Collaboration, AJ, 116, 1009
The FAST Telescope. URL:http://fast.bao.ac.cn/en/FAST.html. Accessed: September 09, 2017
The CHIME telescope. URL:http://chime-experiment.ca/. Accessed: September 09, 2017
Tojeiro, R., Ross, A. J., Burden, A., et al. 2014, MNRAS, 440, 2222
van Bemmel, I.M., van Ardenne, A., de Vaate, J. G. B., et al. 2012, Proceedings of the meeting "Resolving The Sky - Radio Interferometry: Past, Present and Future", arXiv/1208.6180
Wang, B., Gong, Y. G., Abdalla, E. 2005, Phys. Lett. B, 624, 141
Wang, B., Zang, J., Lin, C. Y., Abdalla, E., Micheletti, S. 2007, Nucl. Phys. B, 778, 69

Boletim da Sociedade Astronômica Brasileira, **30**, no. 1, 205-206

The BINGO telescope: instrument description

M. W. Peel[1] on behalf of the BINGO collaboration

[1] Departamento de Física Matematica, Instituto de Física, Universidade de São Paulo, Rua do Matão 1371, São Paulo, Brazil, e-mail: email@mikepeel.net

Abstract. BINGO is a novel 40m-class telescope to be built in South America to observe Baryon Acoustic Oscillations through a new technique called Intensity Mapping, using the 21 cm Hydrogen line to statistically detect galaxies at different distances to measure dark energy. The transit telescope uses two large mirrors in a compact range configuration, ith a large focal plane of 50 horns, each 1.8 m wide and 4.7 m in length. These feed into room-temperature receivers with effective system temperatures around 50 K to record the very faint BAO signals.

Resumo. BINGO é um novo telescópio de 40 m que está sendo construído na América do Sul para observar as oscilações acústicas de bários (BAO). A partir de uma nova técnica, Mapeamento de Intensidade (Intensity Mapping) e usando a linha de hidrogênio 21 cm, será possível detectar estatisticamente galáxias em diferentes distâncias e medir a energia escura. Este telescópio utiliza dois grandes espelhos em uma configuração de alcance compacto, com um grande plano focal de 50 cornetas, cada qual medindo 1,8 m de largura e 4,7 m de comprimento. Estes alimentam os receptores, que estão em temperatura ambiente, com temperaturas efetivas do sistema em torno de 50 K para registrar os sinais BAO muito fracos.

Keywords. Telescopes – Instrumentation: miscellaneous

1. Telescope design

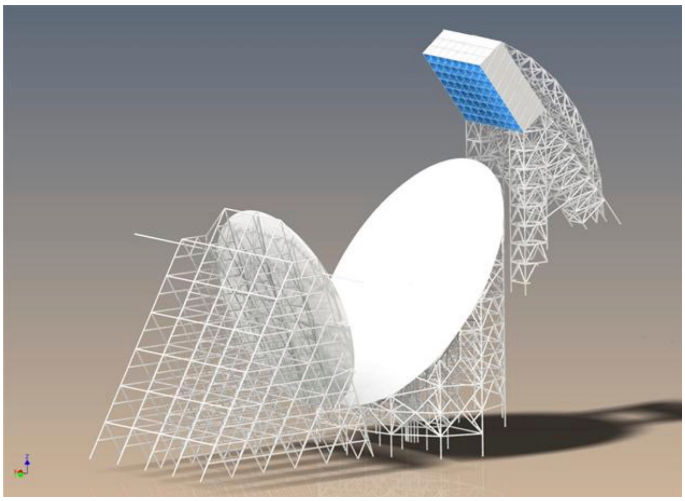

Figure 1. The preliminary BINGO telescope design

The BINGO telescope design is as simple as possible. It is a transit telescope to use the Earth's rotation to map the sky, with a Compact Range Antenna design to have a large number of horns, which under-illuminate the mirrors to have clean beams with low sidelobes. The design is commonly used by Cosmic Microwave Background telescopes, but this will be the first telescope of this design on a scale of tens of metres.

BINGO will map a $15 \times 360\cos(15\,\mathrm{deg})$ degree region of the sky at 960–1260 MHz with a resolution of 40 arcminute. This means that the mirrors have to be around 40 metres across. They will be wire mesh rather than solid surfaces, and the static design drastically reduces the cost compared to a movable telescope. For more background information on BINGO see Battye et al. (2012, 2013, 2016); Dickinson et al. (2014).

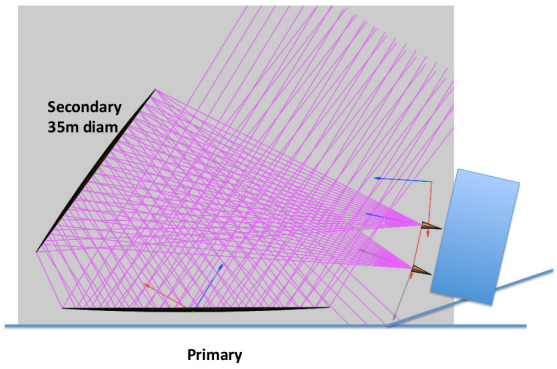

Figure 2. A schematic representation of the telescope

2. Horns

To illuminate the mirrors correctly at these frequencies, the horns have to be very large: 1.8 m in diameter, and 4.7 metres long. The horns have corrugations so that they are sensitive to the wide frequency range. These requirements mean that traditional manufacturing methods (machining from a solid piece of metal, or bending sheet metal) is very expensive or impractical.

Instead, the horns are being constructed as a series of rings, each of which are made from a shaped profile of one large and one small ring, which are bent into a circle and welded in place.

A series of these rings are made with different sizes, and are then attached to each other to build up the whole of the horn. The first and last rings are machined, and are used to mount the horn into the focal plane structure.

The completed horns will be tested at INPE's horn testing facility to make sure that they very low loss (~0.1dB), work at all frequencies, and have clean beams that match well with the mirrors.

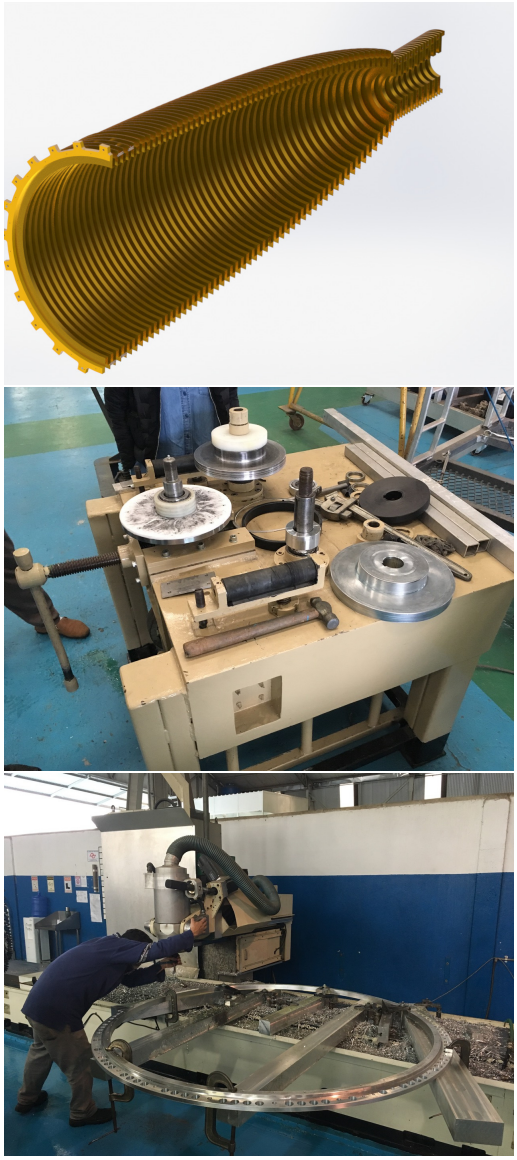

Figure 3. *Top*: A cut-away diagram of a horn. *Middle*: Bending part of a horn profile. *Bottom*: Machining the first ring of the horn.

3. Waveguide components

After the horns, a number of waveguide transitions, a polariser, and a magic tee convert the signal into one that can be amplified by a receiver. The polariser takes the signal from the horn and splits it into two polarisations, which are then processed separately but recombined for the final sky maps (to reduce the thermal noise by $\sqrt{2}$).

The magic tee takes the signal from the sky as well as a reference signal (provided here by a colfet, a reversed low-noise amplifier). The two outputs are then the combination of the two input signals, but with different phases.

4. Receiver modules

The receiver modules will be pseudo-correlation receivers, which are often used in CMB experiments (such as the Planck satellite). These provide very stable amplification: the input signal is split between two arms, amplified, and then recombined to cancel out 1/f fluctuations from the amplifiers. Additionally, phase switches between the arms alternate the output signals

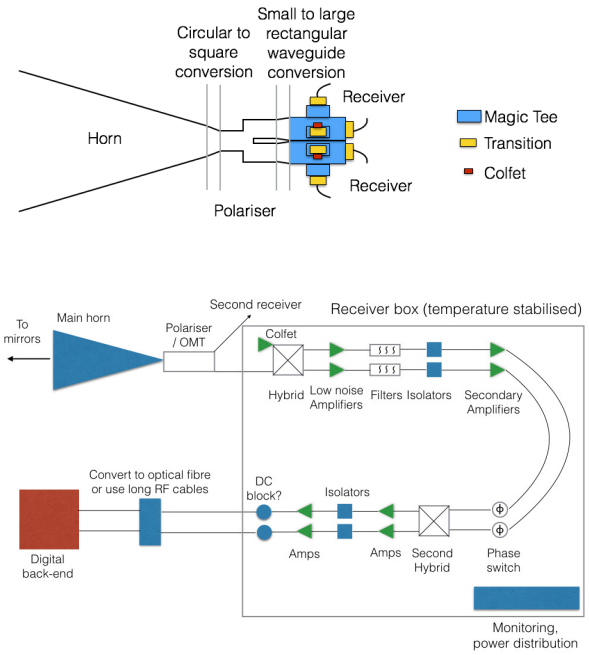

Figure 4. *Top*: Waveguide components. Magic tees are blue, coax transitions yellow, colfets red. *Bottom*: A schematic of the receiver components.

so later-stage 1/f noise can also be removed. The receiver will operate at room temperature, but will be temperature stabilised to minimise signal fluctuations. It will use off-the-shelf components as much as possible. Custom-built filters will define the receiver band and remove out-of-band interference (particularly from mobile phones, which are just below the BINGO frequency band). The digital back-end will digitise the signal and use Fourier Transforms to output spectra, which will then be used in the BINGO pipeline to produce maps at each frequency, and the cosmological results.

Acknowledgements. BINGO is a collaboration between the University of Manchester (UK), Universidade de São Paulo (Brazil), INPE (Brazil), Universidad de la Republica (Uruguay), ETH Zurich (Switzerland), IAS Paris (France), University College London (UK), Cardiff University (UK) and Yangzhou University (China). The BINGO project is funded by grant #2014/07885-0, São Paulo Research Foundation (FAPESP). Mike Peel has a FAPESP Young Investigator fellowship, grant #2015/19936-1, São Paulo Research Foundation (FAPESP)

References

Battye R. et al. 2012, Proceedings of Moriond Cosmology 2012, arXiv:1209.1041
Battye R. et al. 2013, MNRAS, 434, 1239
Battye R. et al. 2016, Proceedings of Recontres de Moriond, arXiv:1610.06826
Dickinson C. et al. (2014), Proceedings of Recontres de Moriond, arXiv:1405.7936

Boletim da Sociedade Astronômica Brasileira, **30**, no. 1, 207-210

On the topology of microlensing events of Earth-Sun fraction mass systems

L. de Almeida[1] & J.-D. Jr. do Nascimento[1]

[1] Federal University of Rio Grande do Norte, Natal, RN, Brazil e-mail: dealmeida.l@fisica.ufrn.br

Abstract. In this work, we analyze the topology of microlensing events that generate light curves in which it would be possible to detect Earth-mass planets around Solar-mass stars. We used the semi-analytical method of solving the lens equation to generate light curves and compare them with pre-defined synthetic models by varying all the parameters of the event. We propose the parametrization of two of these parameters: the smallest apparent distance between the source star and the lens (impact parameter μ_0); and the angle between the source path and the lens system arbitrary axis (impact angle α). Our parametrization aims to force the path of the source to pass through the region of interest of the event, thus increasing the probability of detection of a low mass planet. We focused on simulating systems with mass fraction and semi-major axis similar to the Sun-Earth system.

Resumo. Neste trabalho, nós analisamos a topologia de eventos de microlentes gravitacionais que produzem curvas de luz em que a detecção de planetas com a massa similar à da Terra é possível. Usamos o método semi-analítico de resolução da equação da lente para gerar curvas de luz e compara-las com modelos sintéticos pré-definidos, variando todos os parâmetos do evento. Propomos a parametrização de dois desses parâmetros: a menor distância entre o trajeto da estrela fonte e a lente principal (parâmetro de impacto μ_0); e o angulo que o caminho da fonte faz com o eixo relativo do sistema (ângulo de impacto α). Nossa parametrização força o caminho da fonte à passar pela região de interesse do evento em que seria possível a detecção de planetas de baixa massa, aumentando a probabilidade de detecção de planetas com a massa da Terra. Nos focamos em simular sistemas com a fração de massa e semi-eixo maior similares ao sistema Sol-Terra. Apresentamos as topologias e as implicações da nossa parametrização na busca por planetas em eventos de microlentes gravitacionais.

Keywords. Gravitational lensing: micro – Planets and satellites: detection – Methods: data analysis.

1. Introduction

In the last decade, the number of discovered exoplanets has grown exponentially, mainly due to the detections from the transit and radial velocity techniques. These discoveries show us that, giant planets orbiting very close to their stars, are the common types of exoplanets to be discovered. In contrast, the gravitational microlensing technique has the sensitivity to detect low-mass planets in orbits from 0.5 to 10 AU Gould et al. (2014). Because it depends only on the combined gravitational field of the star-planet, this technique can detect planets in faint stars, which would be difficult for other techniques that depends on the star's light. The observational surveys Microlensing Planet Search (MPS) (Rhie 1999) and Microlensing Observations in Astrophysics (MOA) (Rhie et al. 2000; Sumi et al. 2003) demonstrated for the first time that sensibility and even showed the capability of microlensing technique to discover Earth-mass planets around 1AU in binary systems. As discussed by Albrow et al. (2001); Gaudi et al. (2002), more than 77% of exoplanetary systems discovered with microlensing techniques shows planets with masses lower than Jupiter mass and with semi-major axis between 1.5 and 4 AU. These results are consistent with the fact that massive planets far away from their central stars are easier to be detected with microlensing method (Sumi et al 2006; Han 2006). In this context, (Paczynski 1986) shows that detection is function of the impact parameter μ_0 and the impact angle α. Here, in this study we propose a parametrization of the source's path to force it to cross the Caustic Region Of INterest (CROIN) (Penny 2014). This give advantage to the detections of Earth-like planets around Solar-like stars by microlensing events. We explore the caustic topology for events with a semi-major axis of about 1AU and with the lens at half distance away from the center of our galaxy. We present light curves where it is possible conducted an analysis of the μ_0 and α variation as a function of fixed parameters in the lens-planet apparent separation. We constructed a model to simulate our system based on a semi-analytical method for solving the binary lens equation take into account the source, lenses, caustic and critic curves. We used part of this approach to obtain the results published in Almeida & do Nascimento (2018).

2. The microlensing event

A gravitational microlensing event occurs when a star in the foreground (lens) passes near the line of sight of a background star (source) and get their light bend from the original path. This bending of the light generates a relative magnification of the source and if the system source-lens have relative movements, a characteristic light curve is produced. The deflection of the light by a single star can be express by $\alpha = \frac{4GM}{c^2 r}$, where α is the deflection angle, M é the lens mass, G is the universal gravitational constant, c is the speed of light and r is the apparent distance between the source and the lens. If we establish D_S as the distance between the observer and the source and D_L as the distance between the observer and the lens, we can write the distance between the source and lens as $(D_S - D_L)$, and we can derive the well know equation of the Einstein Radius

$$\theta_E = \sqrt{\frac{4GM}{c^2}\frac{D_S - D_L}{D_L - D_S}}. \quad (1)$$

The Eq. 1 holds for sources and lens that are aligned. Introducing the small distance β between the source and the lens, we can derive the lens equation for the single lens case

as $\beta = \theta - \frac{\theta_E^2}{\theta}$ which is the well known lens equation for the single lens case, and it can be easily solved as a second degree polynomial.

2.1. Formalism

For the 2 lenses case, we can rewrite β, originally written for single lens case, in cartesian coordinates and multiple lenses as

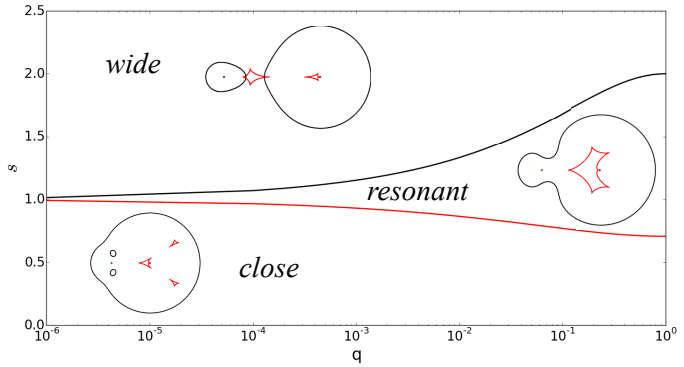

Figure 1. Different topologies dependent on s and q.

$$x_s = x - \sum \frac{m_i(x - x_i)}{(x - x_i)^2 + (y - y_i)^2}, \tag{2}$$

$$y_s = y - \sum \frac{m_i(y - y_i)}{(x - x_i)^2 + (y - y_i)^2}, \tag{3}$$

where m_i is the ith mass fraction of the ith lens of the system. x_s and y_s are the cartesian positions of the source. x_i and y_i are the lens position of the ith lens. Here we are using the complex notation to denote the lens equation for the two lenses (Witt H. J 1990; Witt & Mao 1995) case, representing a host star and their planet as

$$\omega = z - \frac{\varepsilon_1}{\bar{z} + \bar{z_1}} - \frac{\varepsilon_2}{\bar{z} + \bar{z_2}}. \tag{4}$$

In the above equation, ε_1 and ε_2 are the lenses masses, with $\varepsilon_1 + \varepsilon_2 = 1$. The parameter z is the images positions complex solutions set. The ω is the relative position of the source at a specific time. $\bar{z_1}$ and $\bar{z_2}$ are the lenses positions complex conjugate.

2.2. The semi-analytic method

Technically, to solve a lens equation with $n = 2$, it is necessary to invert a 5th order polynomial and solve it to find the polynomial roots. To accomplish this task we developed a model that uses a semi-analytic method to find polynomial coefficients and solutions (Witt H. J 1990). For the case where the source is not close enough to the caustic-crossing region, we used the point source magnification method to solve and obtain the light curve. In this case, the point source magnification uses the Jacobian determinant give by

$$J = \frac{\partial\omega}{\partial z}\frac{\partial\bar{\omega}}{\partial\bar{z}} - \frac{\partial\omega}{\partial\bar{z}}\frac{\partial\bar{\omega}}{\partial z} = 1 - \left|\frac{\partial w}{\partial\bar{z}}\right|^2, \tag{5}$$

where

$$\frac{\partial w}{\partial\bar{z}} = \frac{\varepsilon_1}{(\bar{z} + \bar{z_1})^2} - \frac{\varepsilon_2}{(\bar{z} + \bar{z_2})^2}. \tag{6}$$

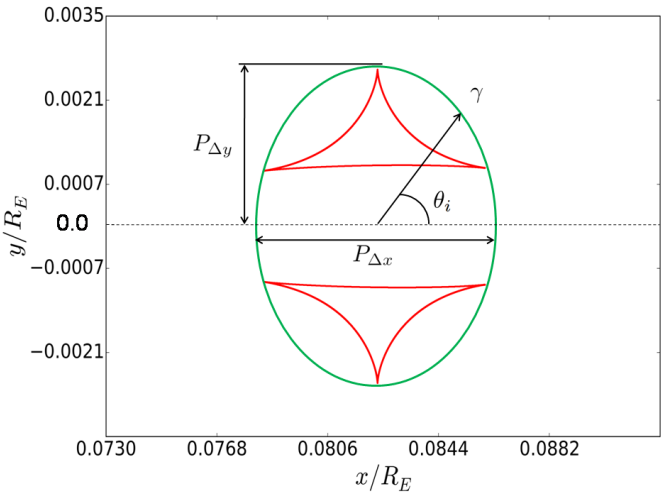

Figure 2. Planetary caustic in detail with $q = 3.003467 \times 10^{-6}$, $s = 0.9597E_R$, $\mu_0 = 0.0082E_R$. The green ellipse is the influence area defined by the Eq. 14

The Jacobian gives us the ratio between a given transformation and its original basis. Thus, To determine a relation between the images and their source, we need to compute the inverse of the Jacobian as $A = \frac{1}{|J|}$.

3. Earth-mass like systems topology

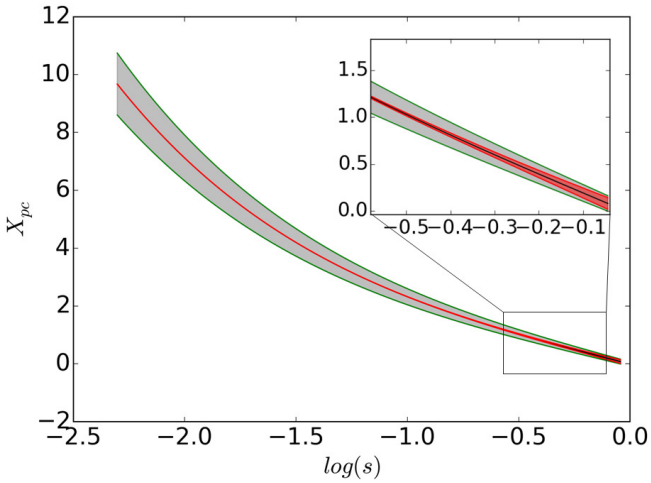

Figure 3. Plot of X_{pc} dependent on $\log s$ for our wanted system with $q = 3.003467 \times 10^{-6}$ and $0.95969 > s > 0.1$. The gray region is $2P_{\Delta y}$ and the red region is $P_{\Delta x}$ (both times by 20 for better visualization)

Caustics modeling and microlensing critical event curves depends fundamentally on the apparent semi-major axis s between the lenses, i.e., the host lens and the planet. Here we used Einstein radius units R_E, and the mass fraction as $q = M_2/M_1$, where M_2 stands for the planet mass and M_1 for the host star mass, and by definition $M_1 + M_2 = 1$. The source's path is defined by 2 parameters, the impact parameter μ_0 and the impact angle α. The impact parameter μ_0 represents the closest distance between the source and the host lens at the time t_0.

In general, binary systems caustics produce topology close, resonant and wide (Schneider & Weiss 1987; Erdl & Schneider

1993), and with limits varying as a function of s and q, as shown in the Fig. 1. For this case, the impact angle α is the angle between the source trajectory and the x-axis of to the system. For the 2 lenses case, the system lies in the x-axis.

For systems like our Sun-Earth system, in terms of Earth-Sun mass ratio, we find $q = 3 \times 10^{-6}$ and $s = 0.95969$, whereas the $M_1 = M_\odot$ and $1R_E = 1.0420AU$. In such a system, a planet orbiting a major-semi axis of $1AU$ it would lie at the Einstein Ring limit. Nevertheless, we cannot ignore possible values of $s < 1AU$ due to the fact that for this systems the major-semi axis is the projected separation between the planet and its host star. By considering systems with $q = 3 \times 10^{-6}$ and s independent, only two topologies can be obtained, they are wide or close. As presented by (Erdl & Schneider 1993), systems with such a wide topology satisfy the condition

$$s > \sqrt{\frac{(1+q^{\frac{1}{3}})^3}{1+q}}. \tag{7}$$

For the interval $0.1R_E < s < 0.95969$, our system can only be closed. Thus, to adjust the μ_0 and α parameters in an efficient way, we need to know the position of the planetary caustic as a function of the s variation.

By analyzing the Fig. 1, we can conclude that a system with an Earth-Sun mass ratio can only be within a wide topology if $s > 1.0217R_E$. On the other hand, as our system can only assume $0.1R_E < s < 0.95969$, we can discard the wide topology for systems like our own. Thus, to use microlensing path parametrization for Earth-like exoplanet detections around solar mass stars it is necessary a deep analysis of the close topology case.

3.1. Closed topology case

The closed topology is formed by three caustics. A central caustic close to the primary lens and two identical planetary caustics on the system axis and opposite side of the planet. For a light curve of a source that passes close the central caustic and on the same side as the planet, we will only detect the main lens signature. Following results from Erdl & Schneider (1993), we can define the topology system as closed when the condition below is satisfied

$$\frac{q}{(1+q)^2} < s^{-8}\left(\frac{1-s^4}{3}\right)^3. \tag{8}$$

In the above equation, for $q = 3 \times 10^{-6}$, a system like our Sun-Earth system can only be close if $s < 0.9893$. In order to set the region of influence, we need at this point, to define the planetary caustic characteristics for closed systems. Considering x as the position of the planetary caustic, that can be determined through the following equation (Han 2006)

$$X_{pc} = \frac{1}{1+q}\left(s - \frac{1-q}{s}\right), \tag{9}$$

where X_{pc} is the separation between primary lens and the center of the planetary caustic. The Eq. 9 makes clear that the smaller s, the larger the value of X_{pc}. By using this position X_{pc} we were able to parametrize some geometrical proprieties of the system and also to set the dependency of the source's path with the localization of the influence region around the planetary caustic. We can also link the position X_{pc} of the planetary caustic center with the impact parameter μ_0 by the following equation

$$\mu_0 = \frac{\left|s^2+q-1\right| \cdot |\tan(\alpha)|}{|q+1| \cdot |s| \cdot \sqrt{\tan(\alpha)^2+1}}. \tag{10}$$

To better describe the entire region of interest we need to described geometrically the entire area containing the planetary caustic. For that, following the geometry of the problem, we found values for $P_{\Delta x}$ and $P_{\Delta x}$, (Fig. 2) written below

$$P_{\Delta x} = \frac{3}{2}s^3\sqrt{3}\sqrt{q}, \tag{11}$$

$$P_{\Delta y} = 2\frac{\sqrt{q}}{s\sqrt{s^2+1}}. \tag{12}$$

The size of the influence area, which contains the planetary caustic, can be defined through an ellipse area πab, with $a = P_{\Delta x}/2$ and $b = P_{\Delta y}$. Thus, the influence area that defines the region containing the planetary caustic is

$$A = \pi\frac{P_{\Delta x}}{2}P_{\Delta y}. \tag{13}$$

Entering the Eqs. 11 and 12 into the Eq. 13, we determined the area size A that contains the planetary caustic as presented by the green ellipse in the Fig. 2, and now as a function of q and s

$$A = \frac{\gamma^2\pi s^2\sqrt{3}q}{\sqrt{s^2+1}}, \tag{14}$$

where γ is a scalar factor for the size of the area which contains the planetary caustic. For the particular case of γ equal to 1, Fig. 2, such area fits perfectly the planetary caustic.

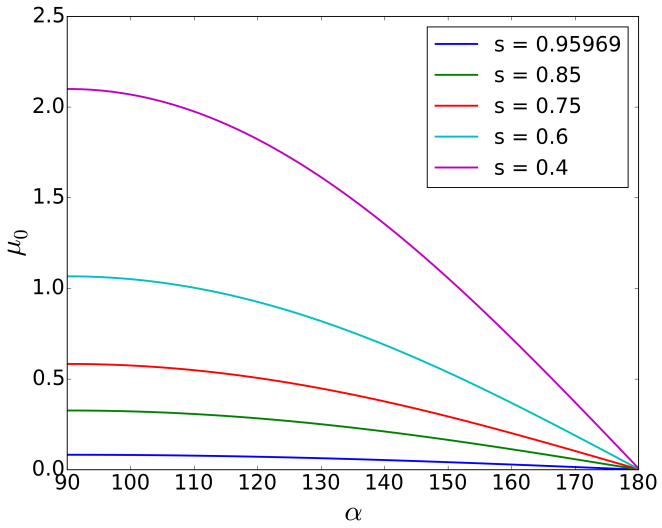

Figure 4. Evolution of the impact angle α when different initial mu_0 is set for $s = 0.95969, 0.85, 0.75, 0.6$ e 0.4.

By analyzing the Fig. 3 we find that, for systems with close topology, the distance X_{pc} increases as s decreases. We can also see, based on Eqs. 11 and 12, that $P_{\Delta x}$ drastically decreases and $P_{\Delta y}$ increase when s approaches the origin. The Eq. 14 leads to the conclusion that the area of the planetary caustic overall decreases when s approaches the origin. Thus, even with X_{pc} getting bigger when s decreases, the total area it is not enough for any possible detection. The Fig. 3 leads to the conclusion that $2P_{\Delta y}$ and $P_{\Delta x}$ approaches to the same value when s approaches to 1.

To link the source path with the *Caustic Region Of INfluence* (CROIN)(Penny 2014), we define all the points on the ellipse using the Eqs. 11 and 12 as

$$X_{ip} = \gamma P_{\Delta x} cos(\theta_i) + X_{pc}, \quad (15)$$

$$Y_{ip} = \gamma P_{\Delta y} sin(\theta_i). \quad (16)$$

If we evolve θ_i from 0 to 2π in the equations above, we define the perimeter of the ellipse of area A, for the close topology case. Now, we can define the parameterization of the source path to the close topology case by the next equation

$$\mu_i = \frac{\left|tan(\alpha)X_{ip} - Y_{ip}\right|}{\sqrt{\tan(\alpha)^2 + 1}}. \quad (17)$$

By setting $\gamma = 1$, and varying α from 0 to 2π, we got all values of μ_0 from the Eq. 17 with the path of the source always passing by the planetary caustic vicinity. Thus, to explore all the possible light curves for our Earth-Sun model, we need to vary γ, α and θ_i.

Fig. 4 presents the evolution of the impact angle α when different initial μ_0 is set to $s = 0.95969$, 0.85, 0.75, 0.6 and 0.4. We can see in all cases that the impact parameter μ_0 must be smaller than the position of the planetary caustic or else the path of the source will not pass through the region of influence.

From the Fig. 4 and relative Eq. 10 we see that, as α approaches 90 (perpendicular to the lens axis) the value of μ_0 increases. That happens because, in order to the source's path to cross the interest region in X_{pc}, μ_0 need to be 0 so that $\alpha = 2\pi$ and if the path is perpendicular, with $\alpha = \pi/2$, then μ_0 must be set to the value of X_{pc}.

4. SUMMARY AND DISCUSSION

We analyzed a set of simulations constructed to search Earth-like exoplanet around solar mass stars. Our simulations involved a parameter search on Sun-Earth models created using the semi-analytical method.

We find that all solutions involving closed topologies are not degenerated and since we are searching only around the region of interest, computationally, the speed-up factor depends directly on the fraction between the R_E area and the area that contains the planetary caustic from Eq. 14. For a system with mass fraction and semi-major axis apparent similar to our Sun-Earth system and $t_E = 90$ days, we find that the planetary deviation takes about 1 day and can be observed by high cadence surveys, such as LSST (first light planned to 2019) and WFIRST (planed to be launched in 2024). We find that Sun-Earth analogue observed system will present a close topology (for semi-major axis close to 1 AU) with doubled identical caustics on the other side of the planet. We also concluded that the ellipse around the planetary caustic decreases exponentially as s increases. We find that if the semi-major axis is equal to 1 AU, then the deviation of the light curve from the single-lens case will last for about one day (for $t_E = 90$ days). The new values for X_{ip} and Y_{ip} are implemented within the new parametrization of $\alpha(\mu_0)$ and can easily be integrated in the parameters search with γ dictating the evolution of α once we have defined a fixed μ_0.

Acknowledgements. We thank the University of Rio Grande do Norte and CAPES for the financial support.

References

Albrow, M. D., et al. 2001, Limits on the Abundance of Galactic Planets From 5 Years of PLANET Observations, Astrophys. J. Lett., 556, L113
Alcock, C., Allsman, R. A., Axelrod, T. S., et al. 1995, Physical Review Letters, 74, 2867
L. de Almeida & J.-D. Jr. do Nascimento, 2018, submitted, Microlensing path parametrization for Earth-like Exoplanet detections around Solar mass Stars.
Bennett, D. P., & Rhie, S. H. 1996, apj, 472, 660
Bozza, V. 2000, aap, 359, 1
Einstein, A. 1936, Science, 84, 506
Erdl, H., & Schneider, P. 1993, aap, 268, 453
Gaudi, B. S., et al. 2002, Microlensing Constraints on the Frequency of Jupiter-Mass Companions: Analysis of 5 Years of PLANET Photometry, Astrophys. J., 566, 463
Gould, A., Udalski, A., Shin, I.-G., et al. 2014, Science, 345, 46
Griest, K., Lehner, M. J., Cieplak, A. M., & Jain, B. 2011, Physical Review Letters, 107, 231101
Hamadache, C., Le Guillou, L., Tisserand, P., et al. 2006, aap, 454, 185
Han, C., Gould, A. 1995, ApJ, 447, 53
Han, C. 2006, ApJ, 638, 1080
Liebes, S. 1964, Physical Review, 133, 835
Mao, S., & Paczynski, B. 1991, apjl, 374, L37
Paczynski, B. 1986, ApJ, 304, 1
Penny, M. T. 2014, apj, 790, 142
Rhie, S. H. 1999, arXiv:astro-ph/9909433
Rhie, S. H. et al. 2000, On Planetary Companions to the MACHO 98-BLG-35 Microlens Star, Astrophys. J., 533, 378
Schneider, P., & Weiss, A. 1987, aap, 171, 49
Sumi, T., Abe, F., Bond, I. A., et al. 2003, ApJ, 591, 204
Sumi, T., et al. 2006, Microlensing Optical Depth toward the Galactic Bulge Using Bright Sources from OGLE-II, Astrophys. J., 636, 240
Witt H. J., 1990, Astronomy and Astrophysics (ISSN 0004-6361)
Witt, J., Mao, S., 1995, ApJ, 447, 105

Boletim da Sociedade Astronômica Brasileira, **30**, no. 1, 211-214

Systems Enginnering applied to spectroscopy of the ELTs

The Conceptual Design phase of GMACS

D. M. Faes[1], A. Souza[2,3], D. R. Bortoletto[3], & M. C. P. Almeida[4]

[1] Instituto de Astronomia, Geofísica e Ciências Atmosféricas (IAG/USP)
e-mail: daniel.gmt@iag.usp.br
[2] Universidade Federal de Minas Gerais (UFMG)
[3] Instituto Mauá de Tecnologia (IMT)
[4] Universidade do Vale do Paraíba (UniVap)

Abstract. An important tool for the development of the next generation of extremely large telescopes (ELTs) is the Systems Engineering (SE). GMACS is the first-generation multi-object spectrograph working at visible wavelengths for the Giant Magellan Telescope (GMT). The aim is to discuss the application of SE in ground-based astronomy for multi-object spectrographs. For this, it is presented the SE of the GMACS spectrograph, currently on its Conceptual Design phase. SE provide means to assist the management of complex projects, and in the case of GMACS, to ensure its success when in operation, maximizing the scientific potential of GMT.

Resumo. Uma ferramenta importante para o desenvolvimento da próxima geração de telescópios extremamente grandes (ELTs) é a Engenharia de Sistemas (SE). O GMACS é o espectrógrafo multi-objeto de primeira geração trabalhando em comprimentos de onda visíveis para o Telescópio Gigante de Magalhães (GMT). O objetivo é discutir a aplicação de SE em astronomia de solo para espectrógrafos de objetos múltiplos. Para isso, é apresentado o SE do espectrografo GMACS, atualmente em sua fase de Design Conceitual. SE oferece meios para auxiliar o gerenciamento de projetos complexos e no caso do GMACS, para garantir seu sucesso quando em operação, maximizando o potencial científico da GMT.

Keywords. Instrumentation: miscellaneous – Techniques: spectrographs – Telescopes

1. Introduction

The development of innovative scientific instrumentation has a number of challenges, involving its design, construction and long-term operation. Astronomy is no exception. An important tool for the development of the next generation of extremely large telescopes (ELTs) is the Systems Engineering (SE).

Multi-Object Spectroscopy (MOS) is one of the most demanding observational techniques in astronomy. The ELTs provide unique windows for scientific discoveries using MOS techniques. Good summaries of the science cases for MOS using the ELTs can be found in Colless (2006), Neichel et al. (2006), and Evans et al. (2015).

In this context, it was proposed the *Giant Magellan Telescope Multi-object Astronomical and Cosmological Spectrograph* (GMACS). GMACS is a multi-object spectrograph working at visible wavelengths for the GMT. See DePoy et al. (2014) for a project status overview.

In Section 2 we present what is Systems Engineering and its importance for projects such as the ELTs. Section 3 containts a brief discussion of the challenges involved in the development of instrumentation for the ELTs, with emphasis in spectrographs. The Systems Engineering processes of the GMACS Conceptual Design phase are described in Section 4. Our final remarks are in Section 5.

2. Systems Engineering

Systems Engineering (SE) proposes a series of methodologies and practices to ensure the successful development and operation of systems. Historically, many of the SE processes application were in the aerospace industry and the defence industry (INCOSE 2015). However, nowadays SE has a broader scope of applications (e.g., Product-SE, Enterprise-SE, Service-SE, etc). For a discussion of the impact of SE in ground-based observatories, see Swart and Meiring (2003).

Some of the reasons that led to the implementation of SE methodology in complex projects are: (i) Limited product effectiveness; (ii) Results often unrelated to the actual needs; (iii) Serious delays in schedules; (iv) Excessive costs; (v) Bad development directions; (vi) Need for unification or standardization of practices created in different fields.

The early implementation of SE practices aims to guarantee a good understand of the needs and requirements of the system from concept to disposal. SE design methodology will widely consider the system life cycle, the needs of the final users and mitigate risks as early as possible by working closely with specialized engineers.

Figure 1 shows the effectiveness of the application of SE throughout a project. This pattern has been observed in different projects from different domains.

3. Spectroscopy of the ELTs

The increasing cost of ground-based astronomy with the size of the telescope apertures, coupled with increased technical complexity are important reasons for observatories to seek the support of SE practices. Table 1 contains data from the survey of van Belle et al. (2004), as well as GMT as a representative case of the cost of an ELT.

In a very brief way, the main goal of the ELTs it to take spectra of targets that otherwise are only visible through images, like primordial (high-redshift) galaxies. Also, ELTs are the ideal

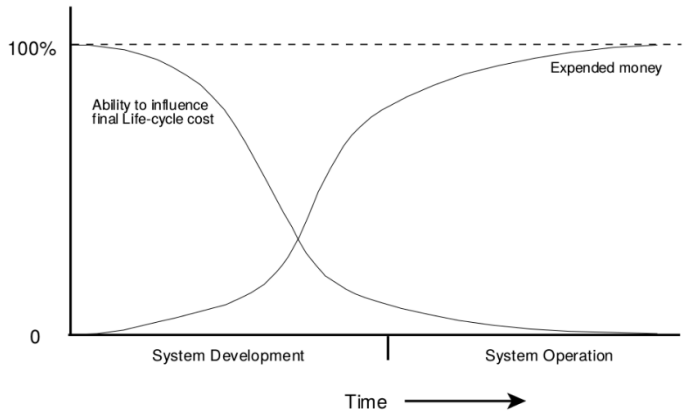

Figure 1. Declining ability to influence final system cost throughout a project (credit: Swart and Meiring 2003).

Table 1. Comparison of telescope projects. Costs are approximated and based on the buying power of the US dollar in 2000.

Telescope	Diameter	Start	First light	Cost
Magellan	(2x) 6.5m	1994	2002	$135.4M
Keck II	10m	1991	1996	$85.9M
Keck I	10m	1985	1993	$139.1M
MMT	6.5m	1979	2000	$49.4M
GMT	28m	2007	2024	$1.000M

Table 2. Comparison of the plate scale and a 10 arcmin image image of different telescopes aperture sizes and same effective f-number = 16.5 (approx. values).

Diameter (m)	Plate scale (”/mm)	Size of 10’ (mm)
3	4.0	150
10	1.3	450
30	0.4	1350

tools to obtain high cadence of observations in transient events, such as transit of exoplanets. However, the construction of instrumentation for these and other MOS goals has a number of challenges. Here we list the needs of ELT spectrographs that should be addressed in a systemic way.

Scale up to keep FoV

One of the main difficulties in the construction of spectrographs for ELTs is the physical size of the optics. By construction, the working f-number of reflector telescopes do not change considerably with its size. This means that the physical size of the generated images grows linearly with the diameter of the telescope. Table 2 contains typical values for telescopes with f-number $\approx$ 16. For ELTs covering a reasonable wide field of view, one can expect images that are more than one meter in size!

Competitive resolution and spectral coverage

When the resolution of the generated spectra is considered, there is a similar impact. The main factor controlling the spectral resolution in terms of the size of the optics is the ratio between the diameters of the collimator and the telescope (Allington-Smith 2007). Because it is very difficult to create large lenses, in first order the resolution of a given spectrograph is inversely proportional to the diameter of the telescope.

High mechanical stability

The size of the optics generate large instruments. Spectrographs in Cassegrain focus will need real-time mechanical actuators to correct mechanical flexure with gravity vector changes. This is true for GMACS, which will stand at the bottom of the telescope mount, and also to spectrographs in Nasmyth focus that need to rotate accordingly to the observed field. The total mass of the instruments increase the chances of inaccurate flexure corrections that can greatly degrade the efficiency and quality of the generated spectra.

Integration with AO capabilities

The integration with adaptive optics resources simultaneously serves to identify and observe weak targets as well as it is an effective mechanism to increase the resolution of the generated spectra. The area of the primary ELT mirrors generate additional deflections for adaptive optics corrections, especially if it is considered multiple targets or a large field of view.

High throughput

It seems to be a simple requirement, but high transparency is a challenge in a large system (which often uses internal mirrors to reduce its volume) and is still integrated into an adaptive optics system.

4. GMACS as a subsystem of the GMT

As mentioned in Section 2, SE methodology aims to address any issues of the project as early as possible. We describe here this methodology in more details, focusing in describing its tailored version as applied to GMACS.

The GMT System Engineering Framework defines the project hierarchy, overall scope of each project phase and highlights the common artifacts recommended to be used when implementing requirements flow-down, interface definition, risk analysis, planning, decision analysis and cost estimates (Maiten et al. 2012).

GMT recommends this approach to all instrumentation groups. Similarly to GMACS, a novel systems engineering approach is being applied to the *GMT-CfA Large Earth Finder* (G-CLEF) Podgorski et al. (2014).

Top-down approach

The Top-down approach covers managerial and design practices. It is a way of managing and designing the project so that engineers can address first architectural aspects of the project without focus in detail. As more information becomes available, details will be addressed in the design. To start this SE seeks to capture all subsystems necessary, for that a PBS (Product Breakdown Structured) is developed together with engineers. The PBS will help manage the group, plan activities, organize the flow-down of requirements from system to subsystem.

Traceability of requirements and requirements flow-down

The requirements flow-down at GMACS is responsibility of the system engineer with the support of specialized engineers and astronomers. It starts from the identification of scientific cases, operational aspects and constrains imposed by the observatory. From these, the first flow-down are written and the initial re-

quirements that will guide the technical team captured. The Traceability from all identified aspects and the derived requirements are managed by the system engineer, using specific tools. The traceability of the requirements allows the system engineer, to be prepare to estimate the impact of changes, to know better the scope of the project, to justify decisions, besides estimate cost and schedule.

Record of decisions, knowledge management

From the initial flown down of requirements many concepts are possible and the experience of the group and research are important to make decisions that will reduce the possibilities and narrow down those to the most likely options. The system engineers at GMACS oversees those decisions and participates to make sure the complete life-cycle is considered, instead of only performance and cost. All decisions are documented as Thread-off or technical notes from templates developed by SE team.

Cost and schedule estimates

System engineering applied to cost and schedules estimates will consider the entire systems life cycle (development, fabrication, integration, validation, commissioning, operation, upgrade and disposal), in addition to social and environmental aspects that may influence in some stage of the system life-cycle.

Making long term estimates, is matter addressed statistically by SE tools. In the GMACS case, to deal with the possibilities and uncertainty of the six remaining phases until first light, the risk analysis will be used as input for the estimation tools.

Risk management

Risk Management of the project allows the SE to identify technical and strategic risks and plan mitigation that can be applied in early stages. When applied at conceptual design, such as GMACS, the awareness of the risks allows to mitigate most of them during the tread-off and decision process. For GMACS, the expectation at the end of the conceptual design is to have all risks from the red area (Figure 2), moved to yellow and green, meaning that the risk will be much more manageable.

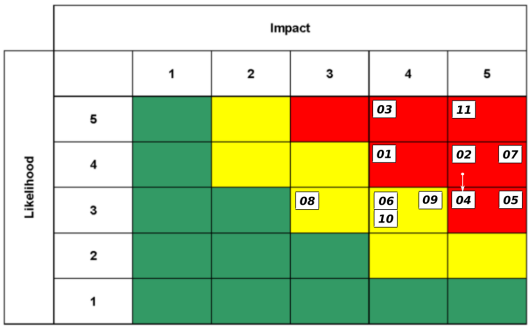

Figure 2. Example of risk matrix to identify and visualize the evolution of the risks. The higher the likelihood, more probable is its occurrence; the higher the impact, the greater the (negative) consequence in the project.

GMACS uses the same approach for risk management as GMT, only adapted for scaled reasons, at metrics for cost and schedule impacts and likelihood. Following that approach, all risks are classified as technical, cost, schedule and have the impacted requirement traced to it.

Interfaces

Interface is one of the most challenging aspects that SE deals with. It requires communication, organization, discipline and knowledge of the overall aspects of the system, its subsystems, operation and environment. For a conceptual design like GMACS, top-down approach and bottom-up approach need to be combined to consider all interfaces. Top-down allows the identification of interfaces from a wide point of view, considering observatory aspects, such as operation, facility instruments and AIT. Bottom-up complements by allowing the identification of interfaces that depends of subsystems solutions. In order to coordinate both approaches, good practices of requirements traceability and knowledge management need to be followed, which includes good communication between all stakeholders that SE needs to be prepared to facilitate.

5. Final Remarks

This work addresses the objectives of SE in complex systems and how SE is proposed in the GMACS project. This is contextualized within SE processes for GMT, and the focus is on the challenges of the multi-object spectroscopy technique for the ELTs need to overcome. From a broader perspective, it is pointed out how SE methods can assist the development of complex projects and maximize the scientific potential of big experiments, such as the ELTs.

Acknowledgements. DMF acknowledges support from FAPESP grants 2011/51680-6 and 2016/16844-1.

References

Allington-Smith, J. R. (2007). Strategies for spectroscopy on Extremely Large Telescopes - I. Image slicing. *MNRAS*, 376:1099–1108.

Colless, M. (2006). Wide-field spectroscopy and ELT science. In Whitelock, P., Dennefeld, M., and Leibundgut, B., editors, *The Scientific Requirements for Extremely Large Telescopes*, volume 232 of *IAU Symposium*, pages 204–208.

DePoy, D. L., Allen, R., Li, T., Marshall, J. L., Papovich, C., Prochaska, T., and Shectman, S. (2014). An update on the wide field, multi-object, moderate-resolution, spectrograph for the Giant Magellan Telescope. In *Ground-based and Airborne Instrumentation for Astronomy V*, volume 9147 of *Proc. SPIE*, page 914720.

Evans, C., Puech, M., Afonso, J., Almaini, O., Amram, P., Aussel, H., Barbuy, B., Basden, A., Bastian, N., Battaglia, G., Biller, B., Bonifacio, P., Bouché, N., Bunker, A., Caffau, E., Charlot, S., Cirasuolo, M., Clenet, Y., Combes, F., Conselice, C., Contini, T., Cuby, J.-G., Dalton, G., Davies, B., de Koter, A., Disseau, K., Dunlop, J., Epinat, B., Fiore, F., Feltzing, S., Ferguson, A., Flores, H., Fontana, A., Fusco, T., Gadotti, D., Gallazzi, A., Gallego, J., Giallongo, E., Gonçalves, T., Gratadour, D., Guenther, E., Hammer, F., Hill, V., Huertas-Company, M., Ibata, R., Kaper, L., Korn, A., Larsen, S., Le Fèvre, O., Lemasle, B., Maraston, C., Mei, S., Mellier, Y., Morris, S., Östlin, G., Paumard, T., Pello, R., Pentericci, L., Peroux, C., Petitjean, P., Rodrigues, M., Rodríguez-Muñoz, L., Rouan, D., Sana, H., Schaerer, D., Telles, E., Trager, S., Tresse, L., Welikala, N., Zibetti, S., and Ziegler, B. (2015). The Science Case for Multi-Object Spectroscopy on the European ELT. *ArXiv e-prints*.

INCOSE (2015). *Systems Engineering Handbook: A Guide for System Life Cycle Processes and Activities*. John Wiley and Sons, Inc, Hoboken, NJ, USA, 4.0 edition.

Maiten, J., Johns, M., Trancho, G., Sawyer, D., and Mady, P. (2012). Systems engineering implementation in the preliminary design phase of the Giant Magellan Telescope. In *Modeling, Systems Engineering, and Project Management for Astronomy V*, volume 8449 of *Proc. SPIE*, page 844906.

Neichel, B., Conan, J.-M., Fusco, T., Gendron, E., Puech, M., Rousset, G., and Hammer, F. (2006). ELTs adaptive optics for multi-objects 3D spectroscopy: key parameters and design rules. In *Society of Photo-Optical Instrumentation Engineers (SPIE) Conference Series*, volume 6272 of *Proc. SPIE*, page 62721X.

Podgorski, W., Bean, J., Bergner, H., Chun, M.-Y., Crane, J., Evans, I., Evans, J., Furesz, G., Guzman, D., Kim, K.-M., McCracken, K., Mueller, M., Norton, T., Park, C., Park, S., Plummer, D., Szentgyorgyi, A., Uomoto, A., and Yuk, I.-S. (2014). A novel systems engineering approach to the design of a precision radial velocity spectrograph: the GMT-Consortium Large Earth Finder (G-CLEF). In *Ground-based and Airborne Instrumentation for Astronomy V*, volume 9147 of *Proc. SPIE*, page 91478W.

Swart, G. P. and Meiring, J. G. (2003). Why systems engineering on telescopes? In Oschmann, J. M. and Stepp, L. M., editors, *Large Ground-based Telescopes*, volume 4837 of *Proc. SPIE*, pages 166–177.

van Belle, G. T., Meinel, A. B., and Meinel, M. P. (2004). The scaling relationship between telescope cost and aperture size for very large telescopes. page 563.

Boletim da Sociedade Astronômica Brasileira, **30**, no. 1, 215-216

SAMplus: Adaptive Optics in optical wavelengths at SOAR

D. M. Faes[1], A. Tokovinin[2], T. Vieria[1], A. Mello[3], M. Domingues[1], A. Souza[4,5], & M. C. P. Almeida[6]

[1] Instituto de Astronomia, Geofísica e Ciências Atmosféricas (IAG/USP)
e-mail: moser@usp.br
[2] Cerro Tololo Inter-American Observatory (CTIO)
[3] Universidade Tecnológica Federal do Paraná (UTFPR)
[4] Universidade Federal de Minas Gerais (UFMG)
[5] Instituto Mauá de Tecnologia (IMT)
[6] Universidade do Vale do Paraíba (UniVap)

Abstract. SAM is a laser-assisted AO module, designed to compensate ground-layer atmospheric turbulence at SOAR telescope. SAMplus is a project to upgrade SAM, focused on enhancing its performance at visible wavelengths. Such capabilities can be fully integrated with the latest SOAR instrumentation. This will open new research opportunities for various areas of Astronomy, both in spectroscopic as in imaging modes.

Resumo. SAM é um módulo AO assistido por laser, projetado para compensar a turbulência atmosférica da camada de solo no telescópio SOAR. O SAMplus é um projeto para atualizar o SAM focado em melhorar seu desempenho em comprimentos de onda visíveis. Tais recursos podem ser totalmente integrados com a última instrumentação SOAR. Isso abrirá novas oportunidades de pesquisa para várias áreas da Astronomia, tanto em modos espectroscópicos quanto em modos de imagem.

Keywords. Instrumentation: adaptive optics – Techniques: high angular resolution

1. Introduction

Adaptive Optics (AO) is an technique that substantially improve the optical performance of ground-based telescopes. So far, most of AO technologies were implemented for small on-sky Field of View (FoV) and/or to be applied over Infra-Red (IR) wavelengths.

Recently, a new access to AO came to the Brazilian community through SAM, the SOAR Adaptive Module (Tokovinin et al. 2016). SAM is a laser-assisted AO module, designed to compensate ground-layer atmospheric turbulence in near-IR and **visible wavelengths over a relative large FoV** (3×3 arcmin^2).

SAM was designed in early 2000's, based on the bimorph Deformable Mirrors (DM) technology that has considerable limitations (Madec 2012). SAM is in regular science operations since 2014. From the experience of these operations and theoretical considerations, it is clear that SAM's performance could be improved by an higher-order correction of the incoming wavefront.

SAMplus is a project addressed to the SOAR community to upgrade SAM focused on enhancing its performance at visible wavelengths. Science with AO in the visible offers a very broad perspective both in spectroscopic as in imaging modes (see Close 2016 for a review).

Some science cases of SAMplus: (i) LSST follow-up observations; (ii) Nuclei of galaxies; (iii) Young stars and star-forming regions; (iv) Compact nebulae; (v) Gravitational arcs and multiple lensed quasar systems; (vi) Globular clusters and multiple stars.

2. The SAMplus

The current AO technology allows to increase the turbulence correction order by using the same SAM's Nd:YAG laser flux more efficiently. The current version of SAM has a bimorph DM with 60 actuators. We propose for SAMplus a voice coil DM with 241 actuators and a corresponding new Wave-Front Sensor (WFS) and Real-Time Computer (RTC).

To illustrate SAMplus performance, a series of simulations were performed with the proposed 241 actuators DM and a 16x16 Shack-Hartman sensor. The typical seeing in SOAR site is 0.77 arcsec FWHM **at 500 nm** wavelength. Currently SAM improves the FWEHM resolution to 0.53 arcsec, and after the upgrade it is expected to deliver images with 0.39 arcsec – and up to 0.26 arcsec FWHM under good seeing conditions (Fig. 1).

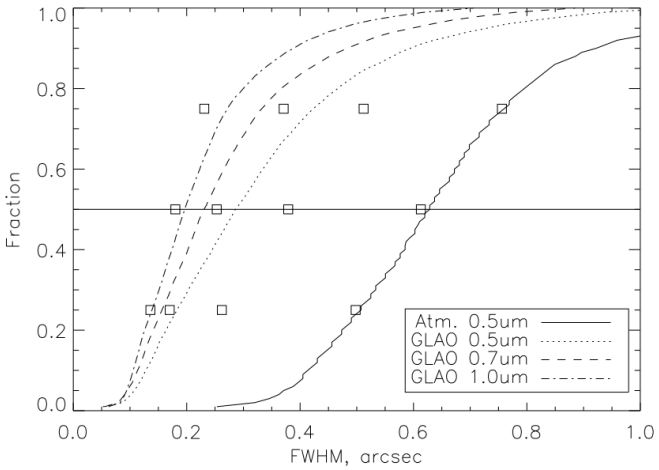

Figure 1. Cumulative distributions of FWHM resolution in the SAMplus. The squares depict performance for the good, median, and poor turbulence profiles computed previously for the current SAM parameters.

The most important aspect of the SAMplus project is the investigation of three critical AO components: (i) the specifications of the new DM (actuators settling time, pitch and stroke), within a physical size compatible with SAM optics; (ii) the def-

inition of the detector camera for the WFS. A detector with substrate gating can eliminate the need of the current Pockels-cell shutter, simplifying the WFS subsystem and increasing the detected flux; and (iii) the WFS optical strategy, making the choice between Pyramid vs. Shack-Hartman configurations.

3. Project Management and tools

SAMplus has Dr. A. Tokovinin as PI, Dr. D. Faes as Co-PI. It is sponsored by FAPESP, IAG/USP and SOAR direction. Most of workforce, as well as the prototyping activities, will be under the responsibility of the group of Astronomical Instrumentation of IAG/USP.

The project is divided in four phases: (i) Conceptual Design; (ii) Preliminary Design; (iii) Laboratory integration; and (iv) Telescope integration. At the end of each phase it is planned a revision by an external committee.

A number of questions must be addressed in order to establish the best characteristic of the upgrade beyond the investigation of critical AO components. To assist this, some Systems Engineering (SE) processes are being applied in a customized way to the demands of the project. The main processes SE employed are: (i) interface configuration documentation, (ii) requirements management and (iii) risk management. The technical notes are written in a standardized way as *System Design Notes* and then properly classified.

The idea is to develop the upgrade in the IAG/USP laboratories, replicating the interfaced SAM components locally. Once the new system is ready, it will be transported to Chile and integrated with SAM with the minimum down-time as possible. The project is expected to be completed by the end of 2020.

4. Final remarks

SAMplus is a project to enhance SOAR AO performance at visible wavelengths. The project is based on a more efficient use of the UV laser system available in the SAM with the replacement of more modern adaptive optics components.

SAMplus operations can be fully integrated with the latest SOAR instrumentation. Beyond the obvious case of direct imaging, SAMplus will be integrated with SIFS (SOAR Integral Field Spectrograph), Fabry-Perot, and the future SAMOS (SOAR Multi-object Spectrograph).

Extending the possibility of doing AO to the *R*, *V* and *B* bands will allow investigations for multiple areas of Astronomy where angular resolution information is critical. In spectroscopy, important diagnostic lines lie at visible wavelengths, such as Hα/[NII] as well as Hβ/[OIII], that will be greatly impacted by SAMplus.

These new capabilities of optical AO over a large FoV puts SOAR in an unique position as observatory facility, opening new research opportunities for various areas of Astronomy.

Acknowledgements. DMF acknowledges support from FAPESP grants 2011/51680-6 and 2016/16844-1.

References

Close, L. M. (2016). A review of astronomical science with visible light adaptive optics. In *Adaptive Optics Systems V*, volume 9909 of *Proc. SPIE*, page 99091E.

Madec, P.-Y. (2012). Overview of deformable mirror technologies for adaptive optics and astronomy. In *Adaptive Optics Systems III*, volume 8447 of *Proc. SPIE*, page 844705.

Tokovinin, A., Cantarutti, R., Tighe, R., Schurter, P., Martinez, M., Thomas, S., and van der Bliek, N. (2016). SOAR Adaptive Module (SAM): Seeing Improvement with a UV Laser. *PASP*, 128(12):125003.

Boletim da Sociedade Astronômica Brasileira, **30**, no. 1, 217-217

SPAnet: the São Paulo Astronomy Network

Laerte Sodré Jr.[1]

[1] Universidade de São Paulo, Instituto de Astronomia, Geofísica e Ciências Atmosféricas, Depto. de Astronomia
R. do Matão 1226, C. Universitária, 05508-090. São Paulo, Brazil. e-mail: laerte.sodre@iag.usp.br

Abstract. We present a brief description of the SPAnet, São Paulo Astronomy Network, an organization aiming to foster activities in Astronomy in the State of São Paulo.

Resumo. Fazemos uma breve apresentação da SPAnet, a Rede Paulista de Astronomia, uma organização informal com o objetivo de impulsionar as atividades em Astronomia no Estado de São Paulo.

Keywords. Sociology of Astronomy: networking

1. Introduction

The State of São Paulo has a strong activity in Astronomy, with more than a hundred people acting in research, teaching and/or outreach. Thanks to FAPESP- Fundação de Apoio à Pesquisa do Estado de São Paulo- many scientific resources are available for the astronomical comunity in the state. Our community has good collaboration links with colleagues from other states and from abroad, and many researchers participate in several international projects. Additionaly, several groups in São Paulo have been successfull to get competitive telescope time in facilities like ESO or ALMA. Our scientific interests covers a wide range, from minor bodies in the Solar System to cosmology, and we have a significant participation in the development of astronomical instrumentation in Brazil.

During 2014/2015 FAPESP approved three large projects (worth more than R$160 million) leaded by researchers from IAG/USP, the largest astronomical institution in the state and in the country. These projects will support the participation of São Paulo researchers in the Giant Magellan Telescope (GMT), in the Large Latin-American Millimeter Array (LLAMA), and in the ASTRI MINI-ARRAY, a precursor of the Cherenkov Telescope Array.

To assure the best use of this money, FAPESP asked me, as Director of IAG in that occasion, to create instrumentation laboratories (electronics, mechanics, optics) with resources from the institutional technical reserve of these projects. These laboratories are already operational and, in principle, available for the community of the State of São Paulo.

Another requirement from FAPESP was actions to promote the connectivity of the Astronomy in the state to optimize the resources available and to increase the visibility of our science. This is actually the main objective of the *São Paulo Astronomy Network* - SPAnet.

2. The SPAnet

The SPAnet was created in a workshop at FAPESP on March 16th, 2017. Its main objective is to promote networking in Astronomy within the State of São Paulo: connections are necessary to foster new ideas and initiatives by sharing relevant information as well as new opportunities and activities. Examples of successful scientific networks include the International Centre for Theoretical Physics South American Institute for Fundamental Research, ICTP-SAIFIR[1], at UNESP, and NOVA, the Netherlands Research School for Astronomy[2].

This has been done by an email list, a website[3] and through workshops. These workshops aim to gather people working on a certain subject to a) promote the mutual knowledge of the people involved, b) know what has been done in the area and c) to discuss actions that help the development of the area. The workshops have been organized by post-docs working in the area. Although the prime target of these workshops are scientists, students and post-docs of the State of São Paulo, people from elsewhere are welcome. We had already a workshop on radio-astronomy[4]. Currently another one, on galaxy clusters, is bein organized and others (deep learning, time series) are being planed.

An important aspect of SPAnet is that it has no money and any activity should be supported by the projects, institutions and/or individuals.

Currently SPAnet is being coordinated by a steering committee with Adriana Valio (Mackenzie), João Braga (INPE), Cláudia Mendes de Oliveira (USP), Gustavo de Araújo Rojas (UFSCar), Lucimara Pires Martins (UNICSUL) and Laerte Sodré Jr. (USP).

[1] http://www.ictp-saifr.org/
[2] http://nova-astronomy.nl
[3] http://www.spanet.iag.usp.br/
[4] http://www.radioastronomia.net/pt/

Boletim da Sociedade Astronômica Brasileira, **30**, no. 1, 218-219

The United Nations Open Universe Initiative

and the Brazilian Science Data Center (BSDC)

Ulisses Barres de Almeida[1]

[1] Centro Brasileiro de Pesquisas Fisicas (CBPF), Rua Dr. Xavier Sigaud 150, 22290-180 URCA, Rio de Janeiro, Brazil e-mail: ulisses@cbpf.br

Abstract. Space-science related activities and access to astronomical facilities and data can offer a cost-effective, entry-level path for capacity building and science and technology education. In 2016, the government of Italy, working together with the Italian Space Agency (ASI), proposed the "Open Universe" Initiative, under the auspices of the Committee on the Peaceful Uses of Outer Space. The Initiative, which is included in the preparation for UNISPACE+50, has the main objective of promoting and facilitating visibility, free accessibility and easy utilisation of astronomical data collected by space-based and ground-based facilities among everybody in the world. In this report we will describe the Open Universe Initiative at its current status and its related activities currently in course in Brazil.

Resumo. Atividades associadas às Ciêcias Espaciais, e o acesso a facilidades astronômicas e dados, podem oferecer um modelo de entrada efetivo e sustentável para desenvolvimento de capacidades e educação em ciência e tecnologia. Em 2016, o governo italiano, trabalhando junto com a Agência Espacial Italiana (ASI), propuseram a Iniciativa "Open Universe", sob os auspícios do Comitê para os Usos Pacíficos do Espaço Exterior (COPUOS). A Iniciativa, a qual está incluída nas preparaçcões para o UNISPACE+50, tem o objetivo principal de promover e facilitar a visibilidade, o acesso livre e a fácil utilizaçcão de dados astronômicos coletados por facilidades terrestres e espaciais, a cidadãos do mundo todo. Neste breve documento, descreveremos a Iniciativa Open Universe em seu estado atual e as atividades a ela relacionadas atualmente em curso no Brasil.

Keywords. Astronomical databases: miscellaneous – Standards – Virtual observatory tools

1. Introduction

"Open Universe" is an initiative under the auspices of the Committee on the Peaceful Uses of Outer Space (COPUOS) that aims at stimulating a dramatic increase in the availability and usability of space science data, extending the potential of scientific discovery to new participants in all parts of the world. Originally proposed by Italy[1], the initiative is carried out in cooperation with the United Nations Office for Outer Space Affairs (UNOOSA), as part of the activities in preparation for UNISPACE+50 – the 2018 conference that will define a comprehensive United Nations Space2030 agenda for the contribution of space to the UN Sustainable Development Goals.

Open Universe seeks to trigger a major evolution of current space science data availability, fostering the publication of all existing open space science data in a way that is easily discoverable and immediately usable, thus responding to the growing global demand for transparency.

To this aim, the Office for Outer Space Affairs and the Open Universe Initiative will work towards enhancing and completing the on-line availability and visibility of astronomical and space science data, following existing data standards and developing additional ones whenever necessary. Additionally, they will work to promote the development of software tools for science, education and outreach, with the objective to further the cultural and knowledge progress of society, with particular attention to emerging and developing countries, such as Brazil.

[1] Cf. COPUOS document A/AC.102/2016/CRP.6

2. Space Science and Data Transparency

Much has already been done to offer open access to scientific data, but further efforts are necessary to consolidate and expand services, in order to promote substantial data-driven increase in technical and science training, education and discovery. A pre-condition for such process is that it must aim at leading to a broader level of transparency of space science data, across a large user base, from specialists to the citizen-scientist, supported by a wide initiative of international cooperation among space science providers.

In fact, most of data in scientific research is generated with public money, with an approximate 15 Billion Euros being invested every year for the sector of space science alone, according to data from 2016 by the Secure World Foundation (1). This alone justifies the application of new transparency criteria that will ensure that the benefits of the space sector will reach all citizens, increasing the amount of knowledge extracted from the existing data and democratising access to information across the world and among all nations.

Open data policies can be implemented in ways that benefit not only the user, but ensure a science reward for the provider, increasing its impact and the overall return for the investment on the generation of the scientific data. This has the potential of reinforcing the importance of the facilities that generate data, guaranteeing in turn continued funding and future operation.

When talking about transparency in space science data, one must consider the open access to high level calibrated data products like images, spectra, etc., which are readily usable by all, be it for purposes of efficient research and data mining by the scientists, or application to educational purposes, or even increasing discoverability by the citizen scientist.

In this regard, internet technologies are key, and represent an unprecedented two-way channel of communication across the globe, between producers and users of data. For this reason, transparent data must also be web-ready, and the availability of data products must be accompanied by the development of appropriate interfaces and software tools for mining, visualisation and efficient utilisation of this data by all sectors.

3. The Open Universe Workshop

With the purpose of drawing recommendations for the Open Universe Initiative, the United Nations, together with the Government of Italy, organised, between the 20 and 22 November 2017, at the headquarters of UNOOSA in Vienna, a Workshop on the Open Universe Initiative. An official report, along with a set of recommendations for the General Assembly of COPUOS is being currently prepared.[2]

The Workshop, in the context of the preparations for UNISPACE+50, had the following main objectives:

- Review the status of current initiatives in space science with regard to data sharing and data availability;
- Promote the universal adoption of established good practices and standards in the field of astronomy and planetary science, of the FAIR principles in data sharing (Findable, Accessible, Interoperable, and Reusable), aiming at enabling transparent access and use of science-ready high-level data (2);
- Discuss the long-term sustainability of astronomy and space science data archives as an enabler for the robust provision and preservation of high-level science-ready data;
- Examine the opportunities for education and capacity-building in the field of space-science data, with special attention to emerging and developing countries; and
- Discuss coordination of international efforts of providers of space science data according to a set of criteria on ease of access, quality, robustness, transparency, completeness and timeliness.

4. A web portal for the Open Universe Initiative

As a first contribution to the Initiative, the Italian Space Agency (ASI) is developing a prototype Open Universe portal, that is a multi-discipline (astrophysics, planetary sciences, cosmic-ray and atmospheric physics) web site where a large number of space science data sets, analysis tools, bibliography and general information services, provided by many on-line space science data archives, can be found next to each other.

The ASI web portal, which is accessible at www.openuniverse.asi.it, can be though of as a sort of virtual "shopping mall" dedicated to space science data, where professional scientists and common citizens alike can go, call on the many "shops" (data archive sites, each identified by its own brand) offering different services and data products. In this way, they can use the results to learn about space science or perform scientific analyses, while the software that is running behind the portal communicates with all components, in an attempt to adapt to the user's needs.

[2] A preliminary recommendations document is available online or from the UNOOSA website under the following reference code A/AC.105/2017/CRP.22

5. Open Universe and related activities in Brazil

Brazil is an active participant in the Open Universe Initiative, since its first proposals, through the institutional support of the Brazilian Space Agency (AEB) and activities under development at the Brazilian Center for Research in Physics (CBPF). In particular, we cite the Brazilian Science Data Center (BSDC), a novel data center initiative under development at CBPF since 2016 (3). The BSDC is built, from the start, over the concepts and ideas proposed by the Open Universe Initiative, as a virtual interface for data access, visualisation and mining in astrophysics and space science, based on Virtual Observatory Tools and Protocols. It has been focused from the start on topics related to Extragalactic Astrophysics and in particular blazars and active galactic nuclei (AGN) science.

Although it is a multi-messenger archival and data interface, the BSDC is focusing in activities to resurface some datasets which are either unavailable or hard to access. One of these is very-high-energy (VHE) gamma-ray data, for which no comprehensive online repository is available, due to restrictive data sharing policies in the field. We are working at the moment in a project to publish the full legacy AGN catalogue and standardised high-level data products for the VERITAS Collaboration, as a pathfinder project before extending the initiative to ther data providers in the field.

A similar effort is being undertaken regarding AGN optical polarimetry data. In this case, much data is freely available online, but the lack of standards in data provision among different providers, lack of compliance to VO standards and protocols and poor repository infrastructure make these data hard to find and use. We are currently working with some data providers in this field, and across the globe, to create the first centralised repository for AGN high-level optical polarimetry data, developing standards, protocols and data interfaces whenever it is necessary, for the homogeneous provision, integration and publication of as much new and past data as possible.

The BSDC online interface is expected to be launched early next year and will be accessible via the following address: www.bsdc.cbpf.br.

Acknowledgements. I thank Paolo Giommi, Andy Pollock and Massimo De Angelis for numerous discussions and exchanges about the Open Universe Initiative. The Brazilian participation in the Open Universe Initiative has the institutional support of the Brazilian Center for Research in Physics (CBPF), the Brazilian Space Agency (AEB). The BSDC has been partly funded by FAPERJ, under the thematic project 110.148/2013.

References

Secure World Foundation 2016. UNOOSA High Level Forum of Dubai, http://www.unoosa.org/oosa/en/ourwork/hlf/2016/first-hlf-meeting.html.

Wilkinson, M.D. et al. 2016. *The FAIR Guiding Principles for scientific data management and stewardship*, Sci. Data 3:160018.

Barres de Almeida, U, et al. 2017. *The Brazilian Science Data Center (BSDC)*, arXiv:1702.06828.

Boletim da Sociedade Astronômica Brasileira, **30**, no. 1, 220-221

HEURISTIKA

Implementing a multi-purpose optimization code

João Luiz Kohl-Moreira

[1] Observatório Nacional, e-mail: kohl@on.br

Abstract. **HEURISTIKA** is a Java-based system aimed to solve highly complex, non-linear problems of any sort, sustained in evolutionary algorithms assumptions. It introduces different aspects and functionalities caught in the specialized literature. It is intended to integrate heuristic methods to solve complex numerical and ODE problems, optimization, classification and control processes and all problems which involve impractical exhausting solutions. In the course of its development, the author made use of analogies and metaphors found in ordinary life concepts.

Resumo. **HEURISTIKA** é um sistema baseado no Java objetivada na solução de problemas altamente complexos e não lineares, com base nas premissas dos algoritmos evolutivos. Ele introduz os mais diferentes aspectos e funcionalidades recolhidos na literatura especializada. Pretende-se integrar métodos heurísticos para resolver problemas numéricos e problemas como Equações Diferenciais Ordinárias, otimização, classificação e processos de controle, além de problemas que envolvem soluções exaustivas intratáveis. No curso de seu desenvolvimento, o autor fez uso de analogias e metáforas encontradas na vida comum.

Keywords. Methods: numerical

1. Introduction

Heuristic methods have multi-purpose applications. They may be numerical, differential, logical, neural, multi branches (classifying algorithms) and so on. They may even be algorithms. **HEURISTIKA** is intended to cover all the existing heuristic methods (or ready to be extended to) such that package's mere instantiation could implement specific applications.

The author considers some analogy with processes occurring in nature — and society —, especially the processes governing the Darwin observations and theory exposed in his framework "On the Origin of Species by Means of Natural Selection" (Darwin 1859). As pointed out by uncounted texts about genetic and evolutionary algorithms (see, i.e., Goldberg (1989) for details) the primary goal of this kind of algorithms application is to find solutions for puzzling numerical, differential or integral equations, process optimizations, filtering, learning algorithms and so on, all being considered under an optimization process.

To accomplish these goals the author has developed algorithms considering aspects found in common-life concepts. In the next Section some of these aspects are introduced.

2. Concepts Running in **HEURISTIKA**

Random walk: a process that generates "beings" having the concerned characteristics of the problem in study whose parameters cover as much as possible the domain of its the function(s). The parameters values are randomly distributed.

Selection: environment, or evolutive pressure. In nature, selection is done by simply mate extinction. It can occur by starvation, hunt, exhaustion, or illness. The sum of all these causes is called evolutive pressure. In algorithmic development, we can define a kind of evolutive pressure inspired in nature and according to the particular application.

World: where the kind of payoff is defined; a set of conditions that defines on what the "organisms" should adapt. An example of world is a differential equation to be solved. "Organisms" should adapt in the sense that the neighbourhood of the roots of the equation means the best adaptation.

Population: environment or **tribe**, or even **clan**. Organisms, depending on their nature, may have different ways of replication, in the sense of Dawkins (2006) description. It can be numeric, bit exchange, string compositions etc. As in real life, after replication or crossing-over, the news being may be submitted to a **mutation**. Depending on the genotype codification a mutation may be a bit inversion, or, in the case of numeric 'world', an addition of, or multiplication by a number, under the numeric domain conditions.

Clock: or time machine. Every life environment takes a certain number of generations, otherwise evolution won't take effect. In algorithm context each generation is linked to the concept of iteration. Then, clock, reflecting a certain number of generations is built on the same basis as the iteration context.

Genesis: The natural process of life is very long and yet not completely understood and described. If we want to start a process of some evolutive process, establishing the beginning of the course with beings already evolved to its operational stage from scratch needs some bridge (or a metaphor, or myth) to step over all the long and unfinished back evolution process. 'Genesis,' the chapter of the Bible may be a good metaphor.

Armageddon: or stopping criteria. The main aim of numerical calculations is to reach to some final results, the solution. In natural conditions, there is no ending in the environment evolution, unless the given species reaches to a deadlock in the environment it lives and gets extinct, or a hecatomb comes over. I called this process "HarMeggido" the Hebrew word for the Gospel's "Armageddon", the biblical ending of human race, and the collecting of the "elected" ones by God to go with Him to paradise. By analogy, when the process reach some condition to stop, the "elected" organisms are collected to serve as a solution to the problem.

Migration / Colonization: In nature and human social environment migration happens all the time. We may simulate it in a multicore CPU computer calculations using **HEURISTIKA**. It may be by transferring the best-qualified beings from a process running in a machine to another "society," running in the neighborhood. It may be the worst individuals, too. In the former case I use to call it "invasion" and in the latter one, "immigration". In human societies it may happens that the immigration process ends by being very efficient and gives beings that will dominate the "new" society, which, in real world, uses to be the case for the so-called "New World".

Taboo: Some characteristics of primitive (and actual) societies may be models to the conditions that a heuristic method will run. It is well acknowledged that primitive societies ran under the set of rules of Totem-and-taboo (Freud 1913). The most conspicuous of the Totem-and-taboo rules is the incest prohibition. This rule most likely origin, according to Freud, is derived from the very primitive human groups, at initial stages, when they were similar to apes actual group formation, where, in most of them, only the dominant male (father) has rights of reproduction.

Infanticide & Œdipus: Here we have a mix of conditions whose metaphors may be extracted from Mother Nature or human mythology. We know that the male of some animal species uses to kill cubs no matter they are or are not its own offsprings. This is the case of the polar white bear. To avoid it, the mother-bear flees with her cub away from the father view. Furthermore, from human mythology there are countless clues that infanticide was a common practise in old societies. The biblical myth of Abraham in the sacrifice of his first-born is one of them. Even the most sacred moment of Christianity, the Jesus Christ crucifixion (sacrifice of God's Son), may be seen as a clue of this practice (Freud 1913, p. 153). On the other hand, we have Œdipus Rex: the Sophocles Greek tragedy where he, the son, ends by killing his father Laius and marrying his mother Jocasta, giving birth to Antigone, Eteocles, and Polyneices. Apart from the nefarious consequences (including the childhood phase of the feeling of castration), from the system point of view, one could say that Œdipus represents the infanticide's revenge. Anyway, in **HEURISTIKA**, if the flag of infanticide is set, the child's genotype is faced to the father's. If it happens to be less adapted, infanticide takes place, otherwise, is Œdipus that is going to run.

Xenophoby (anti-entropy): Rejection of "ill-formed" beings or foreigners is seen in many animal groups in nature and human societies. But, only with diversity we have at least an expectation to find the very best solution in optimization processes. One of the best diversity estimators is the Shannon entropy (Shannon 1948). Following our metaphoric attempts, we state that in **HEURISTIKA** all is done to follow the Second Law of Thermodynamics: entropy must to increase. Entropy of a population is evaluated in the following way. One makes a histogram $H(F)$, where F is the fitness for every being in population. The bin of this histogram is chosen such that $b = 1/m$, for $m \leq N$, the number of beings in the population. The histogram is normalized, such that $p_i = H_i/N$, $\sum_i p_i = 1$, and $p_i \leq 1$. Then

$$S = \frac{\sum_{i=1}^{m} p_i \ln p_i}{\ln m}.$$

From the above expression, $0 \leq S \leq 1$.

Epidemy and Pandemy: Nowadays epidemy is a process almost exclusive to humankind or in environments where human handles. There is a condition on which an epidemy happens. It suffices the epidemical agent find a free way to circulate. Its chances increase every time a particular imbalance in the environment comes over. If the environment is massively populated by just one species, diversity is severely compromised. Here one finds ideal conditions for epidemy to happens. There are they who sustain the thesis on which the humanity itself is an epidemic on earth. A way to measure this imbalance is to determine the entropy of the environment.

Cockfight: Inspired in the infamous practice of cockfight, for roosters instinctively attack competitors to death, in **HEURISTIKA**, if the hennery-flag is set, the population is considered as a hennery and all 'beings' with similar genotypes are taken as 'roosters' that go to a cockfight, and only the best one survives. The criterium for 'similarity' is done by the custom.

Leucocytes It is well known that the immunologic system of superior beings on earth has got a mechanism that destroys all aberrant new cell that has just been created in the process of renewing of dead ones. This task is made by the leucocytes, the "white globules", which are present in the blood. The concept of leucocytes in **HEURISTIKA** is useful for some conditions, e.g. highly non-linear equations where different function values take to huge ranges, compromising the evaluation of the fitness.

Late genesis The final aim of the processes of extermination and declining number in population is to let conditions for the population to renew itself. In **HEURISTIKA**, any time the population can renew itself, the process of a random walk is retaken, and new beings appear by a 'self-generation' process. One may reason that this is an artificial process, not having a parallel in nature. Nevertheless, given the vast complexity of nature, one can conceive this process of 'late-genesis' as being immigration coming from randomly distributed populations in the neighborhood.

References

Darwin, C. 1859, On the Origin of Species: By Means of Natural Selection (P.F. Collier & Son)

Dawkins, R. 2006, The selfish Gene (Oxford University Press)

Freud, S. 1913, Totem and Taboo (Routledge & Kegan Paul)

Goldberg, D. E. 1989, Genetics Algorithms in Search, Optimization, and Machine Learning (Addison-Wesley Publishing Company)

Shannon, C. 1948, Bell System Technical Journal, 27, 379

Boletim da Sociedade Astronômica Brasileira, **30**, no. 1, 222-225

Gamma-ray Emission Properties of Four Bright *Fermi*-LAT AGNs: Implications on Emission Processes

Pankaj Kushwaha[1], Atreyee Sinha[2], Ranjeev Misra[2], K. P. Singh[3], & E. M. de Gouveia Dal Pino[1]

[1] Department of Astronomy (IAG-USP), University of Sao Paulo, Sao Paulo 05508-090, Brazil
e-mail: pankaj.kushwaha@iag.usp.br
[2] Inter-University Center for Astronomy and Astrophysics, Pune 411007, India
[3] Department of Astronomy & Astrophysics, Tata Institute of Fundamental Research, Mumbai 400005, India

Abstract. The X-ray/Ultraviolet/Optical emission from radio-quiet AGNs, black hole binaries, and other compact sources, in general, follow a lognormal flux distribution, a linear rms-flux relation, and a (broken) power-law power spectral densities (PSDs). These characteristics are normally attributed to the multiplicative combination of fluctuations in the accretion disk. Similar features have been inferred for some well-observed blazars in different energy bands, but a systematic study over a long duration is still missing. Using a continuous gamma-ray light curves over 3-days cadence from August 2008 – October 2015, we present the first systematic study of these features in four sources: the FR I radio galaxy NGC 1275 and three blazars- Mrk 421, B2 1520+31 and PKS 1510-089. For all, except Mrk 421, the flux spans 2 orders of magnitude. For blazars, a log-normal profile describes the flux histograms better compared to a Gaussian, while none is favored for NGC 1275, the only non blazar source, suggesting a complex distribution. Regardless of flux histogram profile, the rms-flux relation is linear for all with PSDs being consistent with a power-law shot noise spectrum despite hints of breaks. The inferred results are consistent with the properties of unresolved magnetic reconnection sites, as inferred in the X-ray emission from the whole Solar disk and the statistical characteristics of magnetic reconnection based minijets-in-a-jet model. The results, thus, suggest a strong jet-accretion-disk coupling with energy input from the central source being distributed over a wide range in time and energy by the reconnection process depending on the geometry and local physical conditions.

Resumo. A emissão de raios-X/Ultravioleta/Óptica de AGNs radio-silenciosas, binários de buracos negros e outras fontes compactas, em geral, seguem uma distribuição de fluxo lognormal, uma relação linear rms-fluxo e um poder de lei de poder (quebrado) densidades espectrales (PSDs). Essas características são normalmente atribuídas à combinação multiplicativa de flutuações no disco de acreção. Características semelhantes foram inferidas para alguns blazers bem observados em diferentes faixas de energia, mas um estudo sistemático durante uma longa duração ainda está faltando. Usando curvas de luz de raios-gama contínuas ao longo de 3 dias cadência de agosto de 2008 - outubro de 2015, apresentamos o primeiro estudo sistemático dessas características em quatro fontes: a FR I radio galáxia NGC 1275 e três blazars - Mrk 421, B2 1520+31 e PKS 1510-089. Para todos, exceto Mrk 421, o fluxo abrange 2 ordens de grandeza. Para blazars, um perfil log-normal descreve os histogramas de fluxo melhor em comparação com um gaussiano, enquanto nenhum é favorecido para o NGC 1275, a única fonte não é blazar, sugerindo um distribuição complexa. Independentemente do perfil do histograma do fluxo, a relação rms-flux é linear para todos com PSDs consistentes com um espectro de barulho de tiro de lei de poder, apesar das dicas de quebras. Os resultados inferidos são consistentes com as propriedades das regiões de reconexão magnética não resolvidos, como inferido na emissão de raios-X de todo o disco solar e Características estatísticas do modelo minijets-in-a-jet baseado na reconexão magnética. Os resultados, portanto, sugerem um forte acoplamento de disco de acúmulo de jato com entrada de energia da fonte central sendo distribuída em uma ampla gama de tempo e energia pelo processo de reconexão dependendo da geometria e das condições físicas locais.

Keywords. gamma rays: galaxies – radiation mechanisms: non-thermal – galaxies: active – galaxies: jets – acceleration of particles

1. Introduction

Active Galactic Nuclei (AGNs) represent the class of astrophysical galaxies powered by accretion onto a super massive black hole (SMBH). Historically divided empirically based on observational properties, primarily on features in the radio and optical bands, they exhibit a huge and wide range of characteristics in different energy bands spectrally, temporally, and spatially (Tadhunter 2008). They emit high and rapidly variable emission across the entire observable electromagnetic spectrum and constitute the largest fraction of sources in any extra-galactic surveys. At γ-ray energies covered by the Fermi-LAT (Large Area Telescope), they constitute $\gtrsim 50\%$ of the total population in the latest LAT source catalog (3FGL; Acero et al. 2015) and $> 75\%$ above 10 GeV (3FHL; Ajello et al. 2017).

One of the defining characteristics of accretion-powered sources is the high, rapid, and energy-dependent brightness variability (Scaringi et al. 2015; Uttley et al. 2005; Vaughan et al. 2003). Extensive investigation of X-rays emission from compact sources such as luminous AGNs (most being radio-quiet), galactic black hole binaries (GXBs) and micro quasars show remarkable phenomenology in statistical properties of emission, characterized by a log-normal flux distribution, a linear scaling of intrinsic variability with flux (rms-flux), and a (broken) power-law power spectral density (PSD; Uttley et al. 2005; Vaughan et al. 2003, and references therein). Similar characteristics have been found in (optical/Ultraviolet/X-ray) emission from other non-compact accreting sources like young stellar objects, white dwarfs, and cataclysmic variables (Scaringi et al. 2015, and references therein). These remarkable similarities of emission features across the mass scale have been used to claim that the physics of accretion is universal and is independent of the accretor physical attributes. The most accepted explanation of such scale-free features is the multiplicative combination of fluctuations in the accretion disk (Uttley et al. 2005; Lyubarskii 1997).

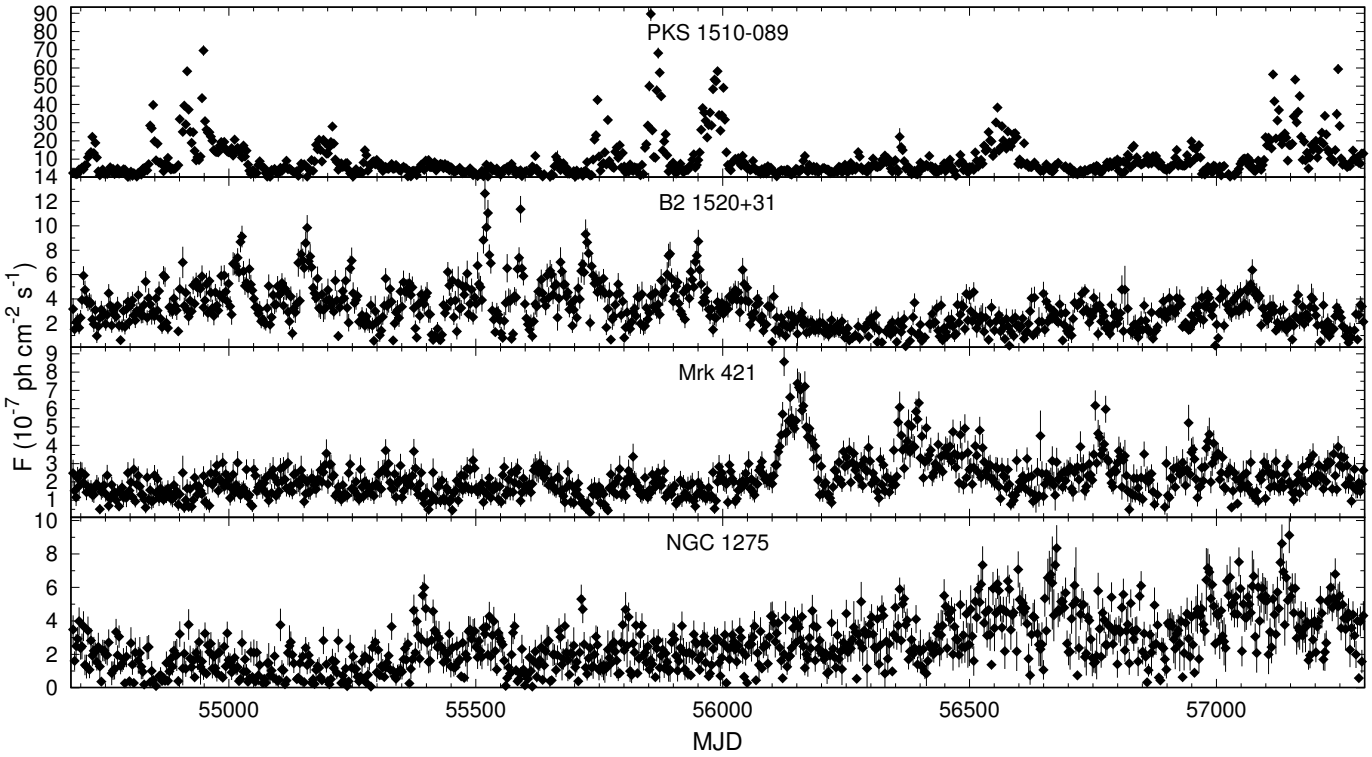

Figure 1. 3-days binned, 0.1-300 GeV *Fermi*-LAT γ-ray light curve of radio-galaxy NGC 1275 and three blazars: PKS 1510-089, B2 1520+32 and Mrk 421 from August 5, 2008 to October 5, 2015.

Presence of magnetic field, even sub-dominant, can substantially modify the characteristics of a system by introducing multiple scales of coupling and directions. In fact, the X-ray emission from the whole Solar disk exhibits all the above mentioned statistical features (Zhang 2007) but the variability here is the result of magnetic reconnection process (Aschwanden et al. 2017). This makes the uniqueness claim ambiguous in the magnetized accretion-powered sources like blazars and radio galaxies, the sources considered in this study (e.g. Kadowaki et al. 2015; de Gouveia dal Pino & Lazarian 2005, magnetic reconnection scenario for non-blazars sources). In these sources, the dominant emission is non-thermal and is believed be produced within the relativistic jets. But, being accretion-powered and magnetized, study of these systems offer a potential way to explore the accretion-disk-jet connection and relative roles of particles and magnetic field. In addition, a comparative study of physical process in other astrophysical sources which exhibit similar statistical features may further provide a broader insights into the jet processes. Here, we present some of the main results and summary of our work published in Kushwaha et al. (2017).

2. Data

We have used 7 years of LAT γ-ray data from August 5, 2008, to October 5, 2015, of four bright AGNs: radio-galaxy NGC 1275, and three blazars Mrk 421, B2 1520+31 and PKS 1510-089 to investigate the statistical features at γ-rays. These are the only AGNs which have a near continuous detection in the LAT on a shortest possible, uniformly binned timescale of 3-days. The choice of bin-duration is a compromise between maximizing the data length for PSDs and rms-flux estimation while, at the same time, avoiding significant non-detections which can bias the histograms. The extracted light curve is shown in Figure 1 and the details of work and data reduction method are published in the Kushwaha et al. (2017).

3. Analysis and Results

We have investigated the statistical properties: flux distribution, PSDs and the rms-flux relation which are used to study the accretion-powered sources, for the first time at γ-ray energies. For highly variable source, a histogram is a unique tool to search for the presence of scales in the data domain while PSD in the temporal domain. Figure 2 shows the γ-ray flux histograms generated following Knuth method (Knuth 2006). We have fitted the histograms with a log-normal and a Gaussian profile and the fit statistics is reported in the Figure label, favoring a log-normal for blazars and a Gaussian for NGC 1275.

Figure 3 shows the PSD of the two sources and the best fit power-law and broken power-law curve to the data with the fit statistics in the respective labels. The PSDs are estimated following the method of Gilfanov & Arefiev (2005) while the error bars are estimated via simulating 1000 light curves using the method of Timmer & Koenig (1995). The fit favors a broken power-law over power-law interpretation with similar inferences for the other two sources: Mrk 421 and B2 1520+31 (but see §4)

In figure 4, we present the shows intrinsic variability as the function of source flux for NGC 1275 and PKS 1510-089, estimated using a sequence of 50 data per rms point from the observed light curve. The error on the rms is calculated via simulating 1000 light curves as done for the PSD followed by their sampling as per the observed light curve and then estimating the variance (Vaughan et al. 2003). The best fitted linear curves with slope values are given in the figure labels. Similar linear relation holds for the other two sources with slope consistent with the NGC 1275 value.

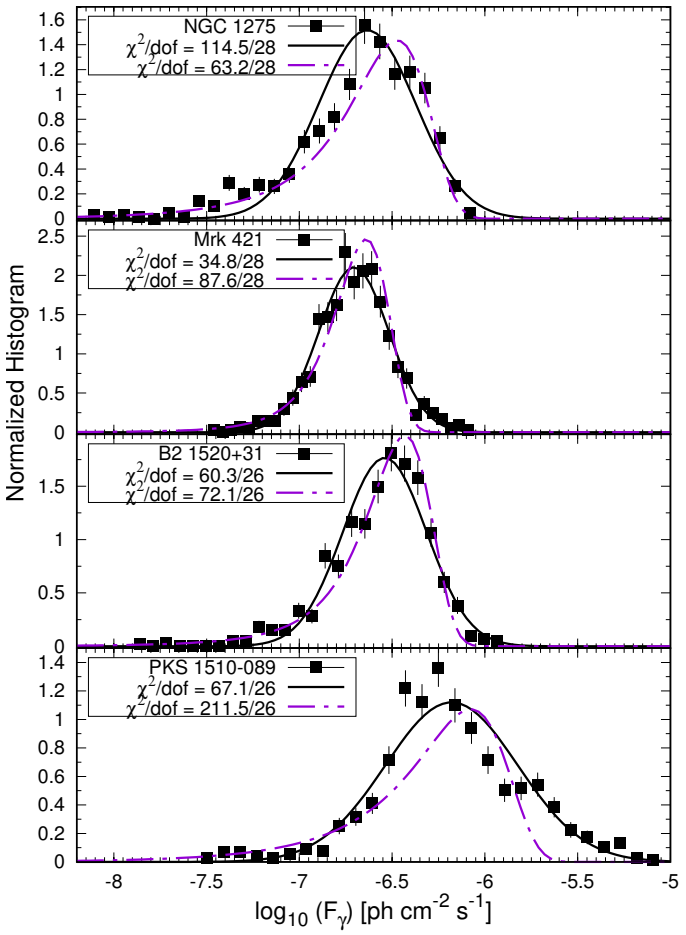

Figure 2. Flux histogram estimated using the Knuth method. The solid and the dashed- dotted curves are, respectively, the best fit log-normal and Gaussian to the histograms (dof = degree of freedom, see §3)

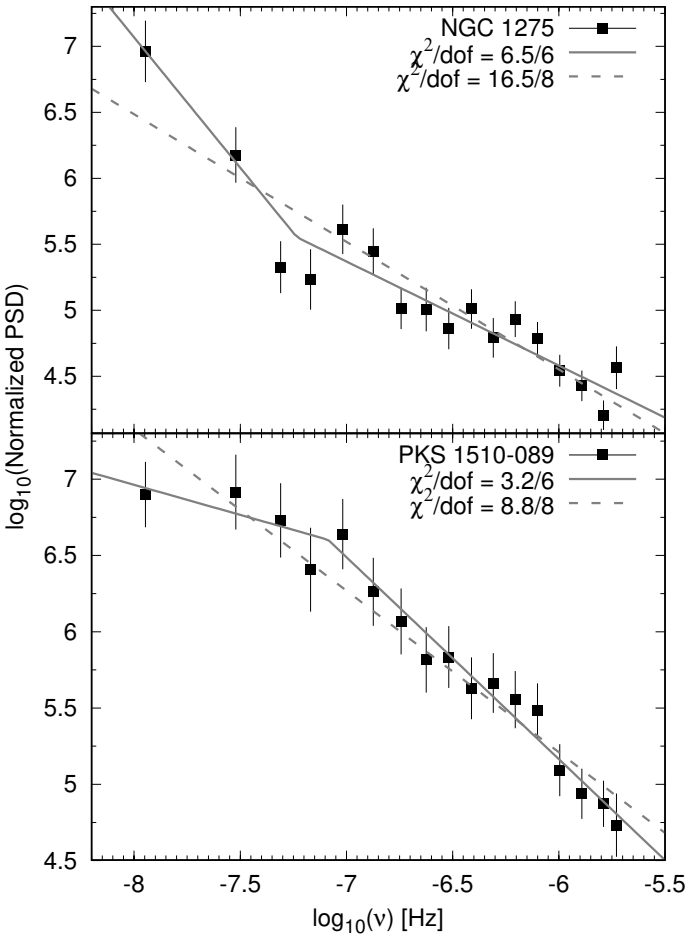

Figure 3. Gamma-ray PSD of radio-galaxy NGC 1275 and blazar PKS 1510-089. The dashed and solid curves are, respectively, the best fit power-law and broken power-law fit to the data (see §3).

4. Discussion

Variability, spectrally and temporally, is one of the few potential tools available to study rapidly variable sources which are beyond the resolution limit of any of the modern observing facilities. Among highly variable astrophysical sources, accretion-powered sources are the most prominent and have been explored extensively in different energy bands, especially at X-rays energies (Scaringi et al. 2015; Uttley et al. 2005; Gilfanov & Arefiev 2005; Vaughan et al. 2003). The temporal investigations have found some hallmark statistical features exhibited by these sources: a log-normal flux distribution with a linear relation with intrinsic variation (rms) and a shot nose PSD. These features have been claimed to be an imprint of a multiplicative combination of fluctuations in the accretion-disk. Here, we investigate these features, for the first time at γ-ray energies to gain insights into jet-disk connection and jet processes.

The systematic investigation reveals many interesting results with broad implications on the jet processes. In the flux domain, all the histogram show a prominent peak with extremes separated by $\gtrsim 2$ order of magnitudes except for Mrk 421. The width of the distribution around the peak is similar for all though there is a huge tail at the lower energy end (Kushwaha et al. 2017). The fit results for histograms, mentioned in labels of Fig. 2 show that a log-normal profile is favored for blazars while a Gaussian is favored for the sole non-blazar source NGC 1275. However, an in-depth statistical analysis by Kushwaha et al. (2017) has shown that neither of the distributions adequately describes the

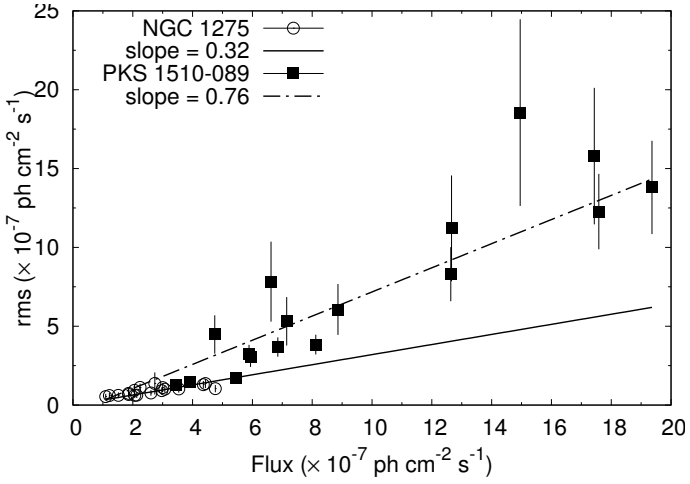

Figure 4. Intrinsic variability (RMS) as a function of source flux. The dashed-dotted solid line represents the best linear fit to the radio-galaxy NGC 1275 and blazar PKS 1510-089 with best file slope in the label (see §3).

NGC 1275 histogram. Surprisingly, the rms-flux relation is linear for all and so is the variance with respect to source flux state except for PKS 1510-089 (see Fig. 4). The linearity of rms-flux relation is contrary to the inferences from other accretion powered sources e.g. radio-quiet AGNs, BXBs, YSOs, CV etc. where lognormality is argued for the linear rms-flux relation and

is attributed to the multiplicative combination of the fluctuations in the accretion disk. In the Fourier domain, the PSDs exhibit a shot noise spectra (see Fig. 3), typical of accretion powered sources. Though a broken power-law fit seems to provide a better description of the PSD, the quality of data suggests breaks at many frequencies for the single broken power-law, while we have reported only the one which resulted in lowest χ^2 statistics. Thus, the nature of the best fit suggests that a more in-depth analysis is needed to statistically claim the presence of breaks within the considered duration if any.

The inferred results are broadly consistent with the statistical properties of the magnetic reconnection powered minijets-in-a-jet model (Giannios et al. 2009; Biteau & Giebels 2012; Clausen-Brown & Lyutikov 2012). In this model, emission from identical but randomly oriented emission regions follows Pareto distribution (Zaliapin et al. 2005). It predicts a huge range of histogram profiles, from a power-law in case of a single emission region to one that can be interpreted as the log-normal in case of contribution from large number of emission regions with a linear rms-flux relation for all (Biteau & Giebels 2012), as inferred for the γ-ray emission here (skewed or log-normal). The inferences are also consistent with the statistics of some of the physical quantities associated with the X-ray emission from the whole Solar disk and coronal mass ejections (CMEs) (Zhang 2007), both of which are known to be the result of magnetic reconnection. The results, combined with the highly magnetized nature of these sources suggest that magnetic reconnection is the dominant process responsible for powering the jet emission. Within this, the skewed distribution of NGC 1275 suggests that fewer regions are contributing to the emission in comparison with blazars. Since the central compact source is the main source of power, the inferences suggest that the magnetic reconnection may be a result of fluctuations in the accretion disk and/or it could be intrinsic to the jet as a result of non-linear dissipative processes within it. Another possibility could be that it is an imprint of magnetic reconnection in the corona, the likely location of the jet base, as argued in de Gouveia dal Pino & Lazarian (2005) for sources having non-boosted emission (Kadowaki et al. 2015). The latter scenario is interesting in the sense that if these imprints flow down the relativistic jet, the overall radiative output will be boosted and the boosting will also makes it appear as if more regions are contributing to the emission, thereby shifting the histogram profile closer to the log-normal, as is the case with blazars. It should be noted that a boosting factor of $\sim$ 10 can produce flux similar to the blazars.

5. Summary

Investigation of characteristics like flux distribution, rms-flux relation, and PSD at γ-ray energies which are used to characterize accretion-powered source show broadly similar yet interesting results. We find that the flux distribution exhibit complex shape with log-normal being favored over Gaussian for blazars but none for NGC 1275. Irrespective of the flux distribution, the rms-flux relation is linear for all and the PSDs are typical of accretion-powered sources i.e. shot noise profile. The linearity of rms-flux relation irrespective of the histogram profile disfavors a strong accretion disk contribution as generally claimed for accretion-powered sources, though there may be contributions. Instead, the features are consistent with the statistical properties of magnetic reconnection powered minijets-in-a-jet model and some characteristics of the quantities associated with the Sun like X-ray emission from whole Solar disk and CMEs, thereby favoring magnetic reconnection as the source powering relativistic jets. This is also consistent with the general emission characteristics of these sources such as a non-thermal broadband spectrum and the rapid variability. The analysis suggests that magnetic reconnection may be an imprint of accretion disk fluctuations on the jet or effect of dynamics within the jet and/or could be an imprint of the corona.

Acknowledgements. PK is supported by grants from the Brazilian agency FAPESP 2015/13933-0. EMGDP also acknowledges support from FAPESP (2013/10559-5) and CNPq (306598/2009-4) grants.

References

Acero, F., Ackermann, M., Ajello, M., et al. 2015, ApJS, 218, 23
Ajello, M., Atwood, W. B., Baldini, L., et al. 2017, ApJS, 232, 18
Aschwanden, M. J., Caspi, A., Cohen, C. M. S., et al. 2017, ApJ, 836, 17
Biteau, J., & Giebels, B. 2012, A&A, 548, A123
Clausen-Brown, E., & Lyutikov, M. 2012, MNRAS, 426, 1374
de Gouveia dal Pino, E. M., & Lazarian, A. 2005, A&A, 441, 845
Giannios, D., Uzdensky, D. A., & Begelman, M. C. 2009, MNRAS, 395, L29
Gilfanov, M., & Arefiev, V. 2005, arXiv:astro-ph/0501215
Kadowaki, L. H. S., de Gouveia Dal Pino, E. M., & Singh, C. B. 2015, ApJ, 802, 113
Knuth, K. H. 2006, arXiv:physics/0605197
Kushwaha, P., Chandra, S., Misra, R., et al. 2016, ApJ, 822, L13
Kushwaha, P., Sinha, A., Misra, R., Singh, K. P., & de Gouveia Dal Pino, E. M. 2017, ApJ, 849, 138
Lyubarskii, Y. E. 1997, MNRAS, 292, 679
Scaringi, S., Maccarone, T. J., Kording, E., et al. 2015, Science Advances, 1, e1500686
Tadhunter, C. 2008, New A Rev., 52, 227
Timmer, J., & Koenig, M. 1995, A&A, 300, 707
Uttley, P., McHardy, I. M., & Vaughan, S. 2005, MNRAS, 359, 345
Vaughan, S., Edelson, R., Warwick, R. S., & Uttley, P. 2003, MNRAS, 345, 1271
Zaliapin, I. V., Kagan, Y. Y., & Schoenberg, F. P. 2005, Pure and Applied Geophysics, 162, 1187
Zhang, S. N. 2007, Highlights of Astronomy, 14, 41

Boletim da Sociedade Astronômica Brasileira, **30**, no. 1, 226-227

Bayesian Analysis of CCDM models

J. F. de Jesus[1,2], R. Valentim[3], & F. Andrade-Oliveira[4]

[1] Universidade Estadual Paulista (UNESP), Câmpus Experimental de Itapeva, Itapeva, SP. e-mail: jfjesus@itapeva.unesp.br
[2] Universidade Estadual Paulista (UNESP), Faculdade de Engenharia, Guaratinguetá, Dept. de Física e Química, Guaratinguetá, SP
[3] Dept. de Física, ICAQF — Unifesp. e-mail: r.valentim@gmail.com
[4] Institute of Cosmology and Gravitation, University of Portsmouth, UK. e-mail: felipe.oliveira@port.ac.uk

Abstract. This work tests six different spatially flat models for Creation of Cold Dark Matter (CCDM) using three statistical criteria, in light of SNe Ia data: Akaike Information Criterion (AIC) (Akaike 1974), Bayesian Information Criterion (BIC) and Bayesian Evidence (BE) (Hobson et al. 2010). These criteria allow to compare models considering goodness of fit and number of free parameters, penalizing excess of complexity. We find that JO model is slightly favoured over LJO/ΛCDM model, however, neither of these, nor $\Gamma = 3\alpha H_0$ model can be discarded from the current analysis. Three other scenarios are discarded either because poor fitting or because of the excess of free parameters.

Resumo. Este trabalho testa seis modelos planos para Criação de Matéria Escura Fria (CCDMs em inglês) usando três critérios estatísticos diferentes, à luz de dados de SNe Ia: Akaike Critério de Informação (AIC) (Akaike 1974), Critério Bayesian de Informação (BIC) e Evidência Bayesian (BE) (Hobson et al. 2010). Estes critérios permitem comparar modelos considerando a qualidade do ajuste e o número de parâmetros e o excesso de complexidade. Encontramos que o modelo JO é levemente favorável em relação ao modelo LJO/ΛCDM, entretanto nenhum deles pode ser descartado nem o modelo $\Gamma = 3H_0$ nesta análise. Três outros cenários são descartados por causa da qualidade do ajuste e do excesso de parâmetros. O método de aumento da Evidência Bayesian na re-parametrização em ordem de reduzir a degenerescência dos parâmetros também é desenvolvida.

Keywords. Cosmology: observations – dark matter – cosmological parameters

1. Creation of Cold Dark Matter (CCDM) Models

Considering the process of matter creation, we have a source term at the level of the Einstein's Field Equations:

$$\frac{\dot{\rho}_{dm}}{\rho_{dm}} + 3\frac{\dot{a}}{a} = \Gamma, \tag{1}$$

where Γ is creation of dark matter ratio in units of s^{-1}. The creation of CDM is related with negative pressure p_c, by assuming an "adiabatic" creation, i.e., the entropy per particle as constant. Adiabatic regime is a hypothesis in which only the source of entropy grows up with the creation of matter from Universe. Explicitly the expression is:

$$\dot{\sigma} = \frac{\Psi}{nT}\left(\beta - \frac{\rho + p}{n}\right) \tag{2}$$

where σ is entropy per particle, Ψ is the numerical rate of creation of particles, n is the density of particles, T is temperature and β emerges like an assumption of creation pressure:

$$p_c = -\frac{\beta\Psi}{\Theta} \tag{3}$$

where $\Theta = 3H$ is the expansion rate of the mass and $H \equiv \dot{a}/a$. So, in case $\dot{\sigma} = 0$, as was assumed, we found $\beta = \frac{\rho+p}{n}$, so the creation pressure is given by:

$$p_c = -\frac{\rho + p}{\Theta}\frac{\Psi}{n} = -(\rho + p)\frac{\Gamma}{3H}. \tag{4}$$

We can see that the dynamics of the Universe is directly affected by the rate of creation of cold dark matter.

Table 1. Model parameters and priors. Concerning background equations, M_1 (LJO) is indistinguishable with ΛCDM.

Model	Creation rate	Reference
M_0	$\Gamma = \frac{3\alpha H_0^2}{H}$	Jesus & Andrade-Oliveira (2016) (JO)
M_1	$\Gamma = 3\alpha\frac{\rho_{c0}}{\rho_{dm}}H$	Lima et al. (2010) (LJO)
M_2	$\Gamma = 3\alpha H_0$	Graef et al. (2014)
M_3	$\Gamma = 3\beta H$	–
M_4	$\Gamma = 3\alpha H_0\left(\frac{H_0}{H}\right)^n$	–
M_5	$\Gamma = 3\alpha\frac{H_0^2}{H} + 3\beta H$	Graef et al. (2014)

2. Models

The models studies here are briefly described on Table 1.

In all models analysed here we have taken into account the contribution of baryons. The baryon density was assumed to be a fixed parameter, given by Planck satellite as $\Omega_b = 0.049$. The flat universe was chosen as indicated by CMB and preferred by inflation hypothesis, then: $\Omega_k \equiv 0$.

3. Methodology

Our methodology involved Bayesian model selection. The likelihood function is a main ingredient in this kind of analysis, other important aspect is the Ockham's razor principle. Next we summarise the model selection criteria used here.

Table 2. Results of the model selection analysis for the different models.

Model	χ^2_{min}	χ^2_ν	ν	ΔAIC	ΔBIC	V_P	$\ln B_{i0}$
$M_0 : \Gamma = \frac{3\alpha H_0^2}{H}$	562.251	0.97107	1	0	0	1	0
$M_1 : \Gamma = 3\alpha \frac{\rho_{c0}}{\rho_{dm}} H$	562.227	0.97103	1	-0.024	-0.024	1	0.043
$M_2 : \Gamma = 3\alpha H_0$	563.131	0.97259	1	0.880	0.880	1	0.155
$M_3 : \Gamma = 3\beta H$	566.936	0.97916	1	4.685	4.685	1	0.955
$M_4 : \Gamma = 3\alpha H_0 \left(\frac{H_0}{H}\right)^n$	562.220	0.97270	2	1.969	6.332	20	0.921
$M_5 : \Gamma = 3\alpha \frac{H_0^2}{H} + 3\beta H$	562.213	0.97269	2	1.962	6.325	20	1.463

3.1. Akaike Information Criterion

Akaike Information Criterion (AIC) provides a relative measure of the quality of models to describe a given data set. This tool emerges from the Information Theory (Akaike, 1974).

$$\mathrm{AIC} = -2\ln \mathcal{L}_{max} + 2p. \quad (5)$$

where $\mathcal{L}_{max}$ is the maximum likelihood and p is the number of free parameters of the model. In our case, we have: $\mathcal{L} = \mathcal{N}\exp\left(-\frac{\chi^2}{2}\right)$, where $\mathcal{N}$ is a normalisation constant. So, in our case, the AIC is given by

$$\mathrm{AIC} = \chi^2_{min} - 2\ln \mathcal{N} + 2p. \quad (6)$$

3.2. Bayesian Information Criterion

Bayesian Information Criterion (BIC) (Schwarz, 1978) is an interesting manner to compare different models with different number of parameters. BIC penalises models in agreement with Occham's razor principle: simple models, which equally describe the phenomenon, are preferred over complex models.

$$\mathrm{BIC} = -2\ln \mathcal{L}_{max} + p\ln N. \quad (7)$$

where N is number of data, $\mathcal{L}_{max}$ is maximum likelihood function and p is number of free parameters. In our case, BIC is given by:

$$\mathrm{BIC} = \chi^2_{min} - 2\ln \mathcal{N} + p\ln N. \quad (8)$$

3.3. Bayesian Evidence

Bayesian Evidence (BE) emerges from Bayes' theorem and it is the integral of the posterior in all parameter space.

$$B_{ij} = \frac{E(M_j)}{E(M_i)}. \quad (9)$$

The Bayesian Evidence is the most complete criterion used here, as it contains information of the full posterior and is in agreement with the Occham's razor. BIC is an useful approximation of BE, as BE usually is hard to obtain.

3.4. Models selections and matter creation

AIC, BIC and BE are calculated for all models studied here. The results are in Table 2.

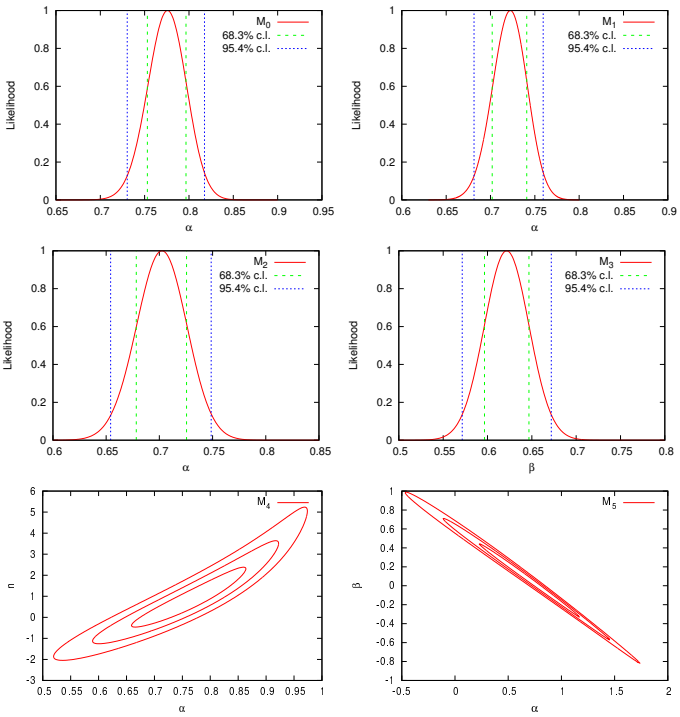

Figure 1. The results of our statistical analysis, with constraints from SNe Union 2.1 data (**?**). **Panels (a)-(d)** Likelihoods for the parameters on each indicated model, M_0-M_3, including 68.3% and 95.4% confidence levels. **Panels (e)-(f)** Contours for 68.3%, 95.4% and 99.7% confidence intervals for each indicated model, M_4 and M_5.

4. Conclusion

We have compared 6 spatially flat CCDM models, including one that is degenerate with the ΛCDM model. The JO model is slightly favoured over ΛCDM in the Bayesian evidence, however, ΛCDM and $\Gamma = 3\alpha H_0$ can not be discarded from this analysis. Models M_3 and M_4 are moderately weak and M_5 can certainly be discarded with the current parameterization. At this point, it is important to mention that JO model is equivalent to the late phase. Further investigations of CCDM models may include spatial curvature, other background data and the evolution of density perturbations.

5. Acknowledgements

The authors wish to thank A. C. C. Guimarães for very helpful discussions. FAO is supported by CNPq-Brazil through a fellowship within the program Science without Borders, J. F. Jesus is supported by Fundação de Amparo à Pesquisa do Estado de São Paulo - FAPESP (Processes no. 2013/26258-4 and 2017/05859-0) and R. Valentim has been supported by Fundação de Amparo à Pesquisa do Estado de São Paulo - FAPESP (Processes no. 2013/26258-4 and 2016/09831-0).

References

Akaike, H. 1974, Transactions on Automatic Control, 19, no. 6
Graef, L. L., Costa, F. E. M., & Lima, J. A. S. 2014, Phys. Lett. B, 728, 400
Hobson, M. P., Jaffe, A. H., Liddle, A. R., Mukherjee, P., Parkinson, D. (eds.) 2010, Bayesian Methods in Cosmology, (New York: Cambridge University Press)
Jesus, J. F., & Andrade-Oliveira, F. 2016, JCAP, 1601, 014
Lima, J. A. S., Jesus, J. F., & Andrade-Oliveira, F., 2010, JCAP, 1011, 027
G. Schwarz, G. 1978, Ann. Stat., 5, 461.

Boletim da Sociedade Astronômica Brasileira, **30**, no. 1, 228-229

Neutrinos emission models with two temperatures for SN1987A

R. Valentim[1], J. E. Horvath[2], & E. M. Rangel[3]

[1] ICAQF/Unifesp. e-mail: r.valentim@gmail.com
[2] Instituto de Astronomia, Geofísica e Ciências Atmosféricas, Universidade de São Paulo. e-mail: foton@astro.iag.usp.br
[3] Enegebras

Abstract. The neutrino burst (νs) from SN1987A that were detected in several experiments around the world in February 1987 and is now the subject of discussions and reanalyses. All the events that were detected (total ~ 25) in the following experiments: Kamiokande II (KII) ~ 12, Irvine-Michigan-Brookhaven (IMB) ~ 8 and Baksan ~ 5. The importance of the νs is that they have an imporntant role in the cooling process of the renmant neutron star (NS), therefore, 99% of the energy of the collapse is lost in the first few seconds, and through the possibility of seeing the internal structure of the NS at the initial instants of its birth. This work proposes to analyze models with two temperatures, which presuppose two neutrino outbursts with time intervals of ~ 5 s between them. The motivation of the proposal is to distribute the data in relation to the time of arrival, which explains the existence of a time gap between two distinct groups of νs, where the second group would come from a form center of Strange Quark Matter (SQM). This hypothesis was the motivation to use *Bayesian Information Criterion* (BIC) that was tested by different models with two temperatures.

Resumo. O surto de neutrinos (νs) da SN1987A que foram detectados num total de eventos detectados foi de aproximadamente 25 nos seguintes experimentos: Kamiokande II (KII) ~ 12, Irvine-Michigan-Brookhaven (IMB) ~ 8 e Baksan ~ 5. A importância dos νs está no papel que eles desempenham no processo de resfriamento da Estrela de Nêutrons (EN) remanescente pois, 99% da energia do colapso é perdida na emissão de νs nos primeiros segundos, e através dos νs é possível "enxergar" a estrutura interna da EN nos instantes iniciais do seu nascimento. Este trabalho propõe analisar modelos com duas temperaturas, que pressupõe dois surtos de neutrinos com intervalo temporal de ~ 5 s entre eles. A motivação da proposta passa pela distribuição dos dados em relação ao tempo de chegada, o que explicita a existência de um hiato temporal entre dois grupos distintos de νs, onde o segundo grupo seria proveniente de um cenário de formação de Strange Quark Matter (SQM). Em nosso trabalho anterior mostramos ser mais provável a existência de dois surtos e apresentaremos os resultados preliminares desses modelos de emissão com duas temperaturas.

Keywords. neutrinos — SN1987A — Astrostatistics

1. Introduction

The explosion of the Supernova 1987A (SN1987A) was perhaps the most extraordinary astronomical event ever observed by man. In addition to the optical observation that made evident the occurrence of the event, signature of the νs burst in large detectors around the world were clearly observed and correlated over time (Bionta et al., 1987; Hirata et al., 1987; Alekseev et al., 1987). In all, 25 events were observed distributed in the experiments of Kamiokande II (KII) — Japan, Irvine-Michigan-Brookhaven (IMB) — USA and Baksan — USSR. The compilation of events observed by these three experiments can be seen in Figure 1 which shows energy versus arrival time for each event. Valentim, Horvath & Rangel (2017) have shown that the strong evidence of two bursts of νs, this hypothesis was proposed by Benvenuto & Horvath (1989), is more likely than only one. The model proposed by us presupposes a temporal gap that according to likelihood function suggested by Loredo & Lamb (2002). These bursts would be of different physical nature: $t_1 \sim 2$ s via deleptonization mechanism in a *prompt* scenario and $t_2 \sim 3$ s after of temporal gap ~ 5 s, in a deleptonization scenarios of the strange proto-star.

2. Statistical Methodology and Models

Statistical Methodology was adopted in this analysis derived likelihood function proposed by Loredo & Lamb (2002). The emission, propagation and detection of neutrinos on the KII, IMB and Baksan were modeled considering the parameters like efficiency curves and energy limits of detection. This approach allowed to estimate important parameters from compact object renmant: emission temperature and radii.

$$\mathcal{L}(\mathcal{P}) = \exp\left[-f\int_T dt\int d\boldsymbol{n}\int \bar{\eta}(\boldsymbol{n},\epsilon)R(\boldsymbol{n},\epsilon,t_i)\right] \times \prod_{i=1}^{Nd} e^{R_{\rm eff}(t_i)\tau}\left[B_i + \int d\boldsymbol{n}\int d\epsilon\mathcal{L}_i(\boldsymbol{n},\epsilon)R(\boldsymbol{n},\epsilon,t_i)\right]. \quad (1)$$

Where f is the fraction time life of detector, τ is dead time, $\bar{\eta}(\boldsymbol{n},\epsilon)$ efficiency's curve of each detector, B_i is the noise's rate integrated on time, $\mathcal{L}(\boldsymbol{n},\epsilon)$ weight function and $R(\boldsymbol{n},\epsilon,t_i)$ is the rate of events measured.

2.1. Models

Now the models proposed by us with two temperatures are presented, these ideas were based on Benvenuto & Horvath (1989). Figure 1 shows clearly for us that the dataset has two different set of data (from the site http://www.astrosurf.com):

i. Two Constant Temperatures (TCT)

This model two constant temperatures were proposed, the temporal gap between them was $(tp + \tau_1)$ 3.10 s. The motivation is to propose a simple model with low parameters number.

ii.Two Exponential Temperatures (TET)

This model has a great physical motivation because the cooling process could have happened through exponential decays, one to each temperature T_1 e T_2) independently. The duration

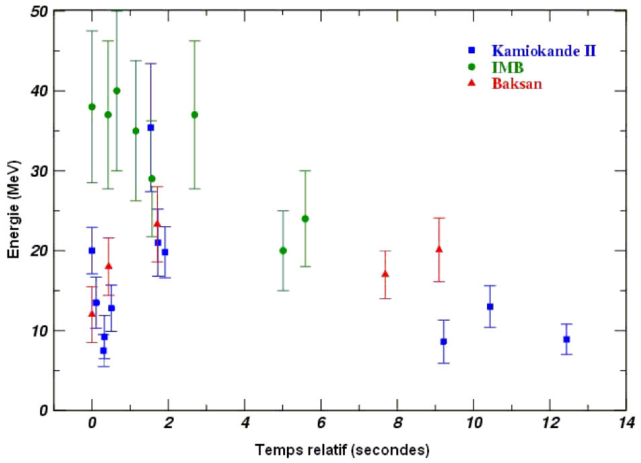

Figure 1. All events observed for different detectors: KII (∼ 12), IMB (∼ 8) and Baksan (∼ 5). Each one has a distinct efficiency curve and observed events in different range of energy.

time for each burst in theses models are: τ_1 and τ_2 and the time interval (t_p) between them is ∼ 5.00 s.

iii. Two Step Temperatures (TST)

The model proposes two steps temperatures T_1 and T_2. The bursts' times are: (T_1) first burst and T_2 for the second burst and are separated to t_p. The physical motivation that this model proposes that the cooling time is free.

3. Results

The results of the models calculated from the likelihood function (eq. 1) are shown in the table below. The parameter α is related to the radius of the neutrinosphere (km). At the temperature of t_1 is relative to the first neutrino burst, the TET model shows a higher temperature (∼ 3.90 MeV) compared to the TCT model which provided ∼ 3.30 MeV and TST with ∼ 3.60 MeV. The temperature of second burst, for the TET (∼ 3.12 MeV) model, is close value to theoretically proposed by Benvenuto & Horvath (1989), which was the values were for TST model with ∼ 2.52 MeV which is a value within the predicted by the theoretical and TCT ∼ 0.30 MeV which was a very low value, which suggests an imprecise description of the phenomenon. The relative time to the temporal gap, the TET model obtained ∼ 5.00 s in relation to ∼ 3.00 s for TCT models (which is the shortest time estimated) and ∼ 4.50 s for TST that is close to the value suggested by the data (see figure 1). For the decay time of the first burst (τ_1), the TET model provided ∼ 9.10 s which is a relatively long time since the burst has approximately 3 s. The TCT model provided a very short time (∼ 0.10 s) and TST a very close time to the ∼ 2.70 s from data. In relation to the time of the second burst (τ_2), the value of the TET model extends to ∼ 28.00 s in relation to the longest time for TCT and the most reasonable time for TST to be ∼ 8.00 s. These models had been tested by BIC for two models combinations: TET versus TCT with ∼ 29 is the strong evidence in favor of the first model. TST versus TET outcomed with ∼ 4 this is a weak evidence in favor TST. Finally, it was tested TST versus TCT with strong evidence in favor TST (∼ 28).

4. Conclusions

Valentim, Horvath & Rangel (2017) suggested temperature's models for the existence of two neutrinos' bursts. This work tested the model two temperature exponential decay (TET), two step temperatures (TST) and two constant temperatures models. BIC test showed that two step temperatures model is the most probable among them. Our theoretical investigation proposed new and more complex models, it suggests better description of the neutrinos emission on the newborn proto-neutron star remnant from SN1987A. This work showed TET described better the values of temperature but this model is not the most probable. The extension of this work is to analyse database under *Support Vector Machine* point of view, this tool allows to separe two set of data from bursts.

Table 1. Models for the neutrino cooling temperature. These models have two componentes of temperature, neutrinosphere radius, time of temporal gap and time of cooling.

Parameters	TCT	TET	TST
α	1.50	2.90	1.50
Radius (km)	15.0	29.0	15.0
T_1 (MeV)	3.30	3.90	3.60
T_2 (MeV)	0.30	3.12	2.52
t_p (s)	3.00	5.00	4.50
τ_1 (s)	0.10	9.10	2.70
τ_2 (s)	28.00	20.10	8.00

Acknowledgements. We are grateful to the *Fundação de Amparo à Pesquisa do Estado de São Paulo* (FAPESP) for supporting and financing this research through the Tematic Project *Matéria Super Densa no Universo*, process no. 2013/26258-4 and Regular Project *Populações de Estrelas de Nêutrons: ferramentas estatísticas bayesianas*, process no. 2016/09831-0.

References

Alekseev, E.N., et al. 1987, Soviet Journal of Experimental and Theoretical Physics Letters, 45, 589
Benvenuto, O. G. & Horvath, J. E. 1989, Phys. Rev. Lett., 63, 716
Bionta, R. M., Blewitt, G., Bratton, C. B., Casper, D., Ciocio, A. 1987, Phys. Rev. Lett., 58, 1494
Hirata, K., et al. 1987, Phys. Rev. Lett., 58, 1490
Loredo, T. J., & Lamb, D. Q. 2002, Phys. Rev. D, 65, a.id. 063002
Valentim, R., Horvath, J. E., & Rangel, E. M. 2017, astro-ph/1706.07824

Boletim da Sociedade Astronômica Brasileira, **30**, no. 1, 230-231

Bayesian correction of $H(z)$ data uncertainties

J. F. Jesus[1,2], Tiago M. Gregório[1], Felipe A. Oliveira[3,4], R. Valentim[5], & Carlos A. O. Matos[1]

[1] Universidade Estadual Paulista (UNESP), Câmpus Experimental de Itapeva, Itapeva, SP
[2] Universidade Estadual Paulista (UNESP), Faculdade de Engenharia, Guaratinguetá, Departamento de Física e Química, Guaratinguetá, SP
[3] Universidade Estadual Paulista (UNESP), Instituto de Física Teórica, São Paulo, SP
[4] Laboratório Interinstitucional de e-Astronomia - LIneA, Rio de Janeiro, RJ
[5] Departamento de Física, Instituto de Ciências Ambientais, Químicas e Farmacêuticas - ICAQF, Universidade Federal de São Paulo (UNIFESP), Unidade José Alencar, Diadema, SP

Abstract. We compile 41 $H(z)$ data from literature and use them to constrain OΛCDM and flat ΛCDM parameters. We show that the available $H(z)$ suffers from uncertainties overestimation and propose a Bayesian method to reduce them. As a result of this method, using $H(z)$ only, we find, in the context of OΛCDM, $H_0 = 69.5 \pm 2.5\,\mathrm{km\,s^{-1}Mpc^{-1}}$, $\Omega_m = 0.242 \pm 0.036$ and $\Omega_\Lambda = 0.68 \pm 0.14$. In the context of flat ΛCDM model, we have found $H_0 = 70.4 \pm 1.2\,\mathrm{km\,s^{-1}Mpc^{-1}}$ and $\Omega_m = 0.256 \pm 0.014$. This corresponds to an uncertainty reduction of up to $\approx 30\%$ when compared to the uncorrected analysis in both cases.

Resumo. Compilamos 41 dados de $H(z)$ da literatura e os usamos para vincular os parâmetros de OΛCDM e ΛCDM. Mostramos que os dados de $H(z)$ disponíveis sofrem de superestimação das incertezas e propomos um método bayesiano para reduzi-las. Como resultado, usando apenas $H(z)$, encontramos, no contexto do OΛCDM, $H_0 = 69,5 \pm 2,5\,\mathrm{km\,s^{-1}Mpc^{-1}}$, $\Omega_m = 0,242 \pm 0,036$ e $\Omega_\Lambda = 0,68 \pm 0,14$. No contexto do modelo ΛCDM plano, encontramos $H_0 = 70,4 \pm 1,2\,\mathrm{km\,s^{-1}Mpc^{-1}}$ e $\Omega_m = 0,256 \pm 0,014$. Isso corresponde a uma redução das incertezas de até $\approx 30\%$ em comparação com a análise sem correção em ambos os casos.

Keywords. Cosmology: observations – dark energy – dark matter

1. Cosmic Dynamics of ΛCDM Model

By considering an homogeneous and isotropic FRW geometry (with $c = 1$) and inserting it in the Einstein Field Equations, with baryons, cold dark matter and cosmological constant, we may write for the expansion rate

$$H(z) = H_0 \left[\Omega_m(1+z)^3 + (1-\Omega_m-\Omega_\Lambda)(1+z)^2 + \Omega_\Lambda\right]^{\frac{1}{2}} \qquad (1)$$

where $\Omega_i = \frac{\rho_i}{\rho_c}$ are parameter densities and we have used the normalization condition $\Omega_m + \Omega_\Lambda + \Omega_k = 1$. The standard, concordance flat ΛCDM model has $\Omega_k = 0$.

2. $H(z)$ data

Hubble parameter data are inferred from differential ages, BAO and LRG, not depending on any background cosmological models. The data we work here are a combination of two compilations: Sharov & Vorontsova (2014) and Moresco et al. (2016). By combining both datasets, we arrive at 41 $H(z)$ data. From these data, we perform a χ^2 analysis by minimizing the χ^2 function of free parameters:

$$\chi^2 = \sum_{i=1}^{41} \left[\frac{H_0 E(z_i, \Omega_m, \Omega_\Lambda) - H_i}{\sigma_{Hi}}\right]^2 \qquad (2)$$

where $E(z) \equiv \frac{H(z)}{H_0}$ and $H(z)$ is given by Eq. (1).

3. Data analysis and goodness of fit

In order to find the constraints over the free parameters $(H_0, \Omega_m, \Omega_\Lambda)$, we have sampled the likelihood $\mathscr{L} \propto e^{-\chi^2/2}$ through Monte Carlo Markov Chain (MCMC) analysis. We have used the so called Affine Invariant MCMC Ensemble Sampler by Goodman & Weare (2010), which was implemented in Python language with the emcee software by Foreman-Mackey et al. (2013). From this analysis, we find the red confidence contours on Fig. 1 and find $\chi^2_\nu \equiv \chi^2_{min}/\nu = 0.488$ for OΛCDM.

As it is well known (Bevington & Robinson 2003; Vuolo 1996), the expected value of χ^2_ν from its probability distribution is $\chi^2_\nu = 1$. Values very far from this are unlikely. High χ^2_ν values may indicate underestimation of uncertainties or poor fitting of the model, while low values of χ^2_ν indicate, in general, overestimation of uncertainties.

We calculate the cdf for χ^2_ν and find the probability of obtaining χ^2_ν as low as 0.488 for $\nu = 38$, $P(\chi^2_\nu < 0.488) = 0.3342\%$. It indicates a very low and unlikely χ^2 value, which, in turn, from Eq. (2) indicates overestimated $H(z)$ uncertainties.

4. $H(z)$ uncertainties correction

Following Hogg et al. (2010), we have considered the likelihood as a generative model for the data. It is a parameterized statistical procedure to reasonably generate the given data. Here, we consider the σ_i to be all overestimated by a constant factor f, thus, $\sigma_{i,true} = f\sigma_i$. For O$\Lambda$CDM, then, our set of free parameters now is $\theta = (H_0, \Omega_m, \Omega_\Lambda, f)$, to be constrained from the likelihood:

$$\ln \mathscr{L} = -\frac{1}{2}\sum_{i=1}^{n}\left\{\frac{[H_i - H(z_i, H_0, \Omega_m, \Omega_\Lambda)]^2}{f^2\sigma^2_{Hi}} + \ln(2\pi f^2 \sigma^2_{Hi})\right\} \qquad (3)$$

By doing the same procedure of last section, now with the additional parameter f, we find the constraints shown on Fig. 1 (black lines).

From Fig. 1, we may see the difference in the parameter space when we introduce the f parameter. The parameter constraints are shown on Table 1.

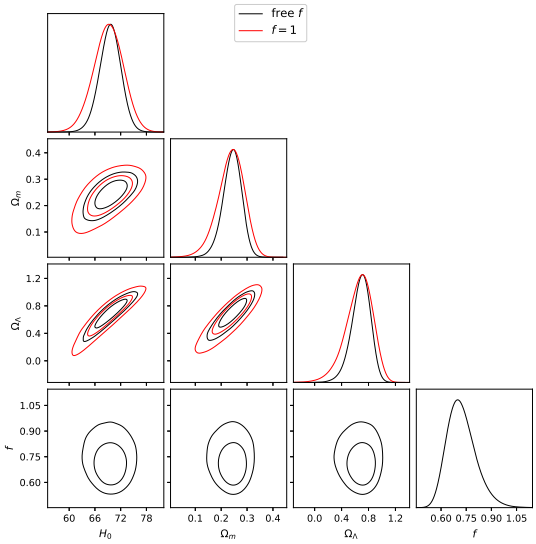

Figure 1. OΛCDM model, with contours for 68.3% and 95.4% confidence intervals. H_0 in km/s/Mpc.

Table 1. Mean values of parameters of OΛCDM model from $H(z)$ data, without uncertainties correction and with uncertainties correction factor f. Uncertainties correspond to 68% c.l.

Parameter	Uncorrected	Corrected
H_0	69.1 ± 3.5	69.5 ± 2.5
Ω_m	0.237 ± 0.051	0.242 ± 0.036
Ω_Λ	0.66 ± 0.20	0.68 ± 0.14
f	–	$0.723^{+0.084}_{-0.085}$

On Table 1, we may see the parameters uncertainties reduction. An interesting feature we may see from Fig. 1 is that the f parameter is much uncorrelated to cosmological parameters.

4.1. Flat ΛCDM

We have also analysed flat ΛCDM model. The results of this analysis may be seen on Fig. 2 and Table 2.

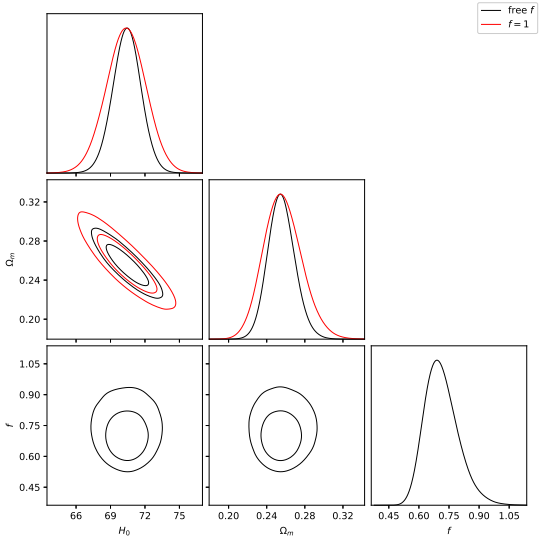

Figure 2. Flat ΛCDM model, with contours for 68.3% and 95.4% confidence intervals. H_0 in km/s/Mpc.

Table 2. Mean values of parameters of flat ΛCDM model from $H(z)$ data, without uncertainties correction and with uncertainties correction factor f. Uncertainties correspond to 68% c.l.

Parameter	Uncorrected	Corrected
H_0	70.3 ± 1.7	70.4 ± 1.2
Ω_m	0.257 ± 0.020	0.256 ± 0.014
f	–	0.714 ± 0.082

The H_0 uncertainty is reduced from 1.7 to 1.2, Ω_m uncertainty has reduced from 0.020 to 0.014.

5. Discussion and Conclusion

With 34 $H(z)$ data, Sharov & Vorontsova (2014) find a more stringent result, namely, $H_0 = 70.26 \pm 0.32$, $\Omega_m = 0.276^{+0.009}_{-0.008}$ and $\Omega_\Lambda = 0.769 \pm 0.029$. However, they have combined $H(z)$ data with SNe Ia and BAO data, which is beyond the scope of our present work, but our value is compatible at 1σ c.l.

Moresco *et al.* have used their compilation of 30 $H(z)$+H_0 to constrain the transition redshift from deceleration to acceleration, in the context of ΛCDM $\left(z_t = \left[\frac{2\Omega_\Lambda}{\Omega_m}\right]^{1/3} - 1\right)$. They have found $z_t = 0.64^{+0.11}_{-0.07}$. By using our 41 $H(z)$ data, we find $z_t = 0.77 \pm 0.22$ without correction and $z_t = 0.78 \pm 0.15$ with the f correction.

We have developed a promising method to reestimate uncertainties.

Acknowledgements. J. F. Jesus is supported by Fundação de Amparo à Pesquisa do Estado de São Paulo - FAPESP (Processes no. 2013/26258-4 and 2017/05859-0). TMG is supported by Unesp (Pró Talentos grant), FAO is supported by **CNPq-Brazil through a fellowship within the program Science without Borders**, R. Valentim is supported by Fundação de Amparo à Pesquisa do Estado de São Paulo - FAPESP (Processes no. 2013/26258-4 and 2016/09831-0).

References

Bevington P. R., & Robinson D. K. 2003, in Data Reduction and Error Analysis for the Physical Sciences, McGraw-Hill Book Company
Foreman-Mackey, D., et al. 2013, PASP, 125, 306
Goodman, J., & Weare, J. 2010, Comm. App. Math. Comp. Sci., 5, 65
Hogg, D. W., Bovy, J., & Lang, D. 2008, arXiv:1008.4686 [astro-ph.IM]
Moresco M., et al. 2016, JCAP, 1605, 014
Sharov, G. S., & Vorontsova, E. G. 2014, JCAP, 1410, 057
Vuolo, J. H. 1996, in Fundamentos da Teoria de Erros, (São Paulo: Edgard Blücher)

Boletim da Sociedade Astronômica Brasileira, **30**, no. 1, 232-233

Searching for High Redshift Quasars with S-PLUS, J-PLUS and J-PAS

Rodrigo Magalhães[1,2], Murilo Marinello[2], Roderik Overzier[2], L. Raul Abramo[3], Claudia Mendes de Oliveira[4], & Silvia Bonoli[5]

[1] UFRJ, Rio de Janeiro, Brazil e-mail: rod.magalhaes@ufrj.br
[2] Observatório Nacional, Rio de Janeiro, Brazil
[3] USP/IF, São Paulo, Brazil
[4] USP/IAG, São Paulo, Brazil
[5] CEFCA, Teruel, Spain

Abstract. The study of galaxies and the intergalactic medium (IGM) in the early universe remains one of the greatest challenges in astrophysics. Quasars (QSOs) are among the most luminous objects in the universe and their study allows us to understand the formation process of supermassive black holes and their relation to massive galaxy evolution and their environment. Moreover, QSOs at redshifts as high as $z \sim 6-8$ (i.e., within the first Gyr of the Universe) are crucial for assessing the ionization state of the IGM and to determine the role that QSOs played in reionization. The objective of this work is to determine the optimal color selection criteria for finding new QSOs at high redshifts in the ~8500 square degree areas covered by each of the upcoming S-PLUS, J-PLUS and J-PAS optical sky surveys combining them with near-IR data. For this, we are building a large library of synthetic QSO photometry based on QSO spectra previously found in the Sloan Digital Sky Survey. In this contribution, we will present our selection strategy and preliminary results based on the first observations from J-PLUS.

Resumo. O estudo das galáxias e do meio intergaláctico (IGM) no universo inicial permanece sendo um dos maiores desafios da astrofísica. Os quasares (QSOs) estão entre os objetos mais luminosos do universo e seu estudo nos permite compreender o processo de formação de buracos negros supermassivos e sua relação com a evolução de galáxias massivas e seus ambientes. Além disso, QSOs em redshifts tão altos quanto $z \sim 6-8$ (isto é, dentro do primeiro Gyr do universo) são cruciais para avaliar o estado de ionização do IGM e determinar o papel que os QSOs desempenharam na reionização. O objetivo desse trabalho é determinar os melhores critérios de seleção de cores para encontrar novos QSOs em alto redshift na área de aproximadamente 8500 deg^2 abrangida por cada um dos novos surveys ópticos S-PLUS, J-PLUS e J-PAS combinados com dados de infra-vermelho próximo. Para isso, nós estamos construindo uma grande biblioteca de fotometria sintética baseada em espectros de QSOs anteriormente encontrados no Sloan Digital Sky Survey (SDSS). Nesse trabalho apresentamos os primeiros passos na construção dessa biblioteca, bem como uma comparação entre fotometrias simuladas e fotometrias obtidas para uma amostra de quasares observados no J-PLUS.

Keywords. Surveys – Galaxies:active – Black hole physics

1. Introduction

Quasars (QSOs) are the most luminous point sources in the Universe. They are powered by active supermassive black holes (SMBHs) that are accreting matter in the center of massive galaxies, and are thus very important tracers of the formation and evolution of SMBHs in relation to their host galaxies (Rees 1984). High redshift QSOs are particularly interesting, as they allow us to investigate the structure of the early Universe. Observations indicate that the epoch at $z \sim 6-8$ marks the end of the cosmic reionization period. Studying QSOs at these high redshifts is also important to infer their overall contribution to the reionization epoch and constrain its duration (e.g. Fan et al. 2006; Carilli et al. 2010; Eilers et al. 2017).

2. Searching for quasars at high redshift

The simplest, most common way of finding high redshift QSOs consists of three major steps: (1) building photometric criteria based on previously found objects or templates, (2) matching photometric observations to these criteria, and (3) performing follow-up imaging and spectroscopy to confirm that the objects are genuine QSOs and determine their redshifts. Building the selection criteria demands information about the cosmology, the typical spectral properties of QSOs at a given redshift, and information about the IGM. Even with well defined criteria, the search is problematic because the highest redshift QSOs are very rare and the selection suffers from contamination primarely due to cool stars. However, having the availability of a number of narrow and medium-band filters will increase the level of accuracy of the selection.

3. The S-PLUS, J-PLUS and J-PAS surveys

The Javalambre-Photometric Local Universe Survey (J-PLUS; Cenarro et al., in prep., Vilella-Rojo et al. 2015) and the Southern-Photometric Local Universe Survey (S-PLUS; Mendes de Oliveira et al., in prep.) each aim to map a ~8000 deg^2 area of the northern and southern sky using new dedicated 0.8m robotic telescopes in Javalambre (Spain) and Cerro Tololo (Chile), respectively. These two surveys use the same set of 12 broad, intermediate and narrow band optical filters. A third survey, the Javalambre Physics of the Accelerating Universe Astrophysical Survey (J-PAS; e.g. Mejía-Narváez et al. 2017) will also cover at least 8000 deg^2 using an unprecedented system of 56 narrow band filters in the optical and a wide-field camera mounted on a 2.5m telescope.

4. Predictions for quasar selection

We predict the expected colors and magnitudes of high redshift QSOs based on synthetic photometry derived from QSO spectra

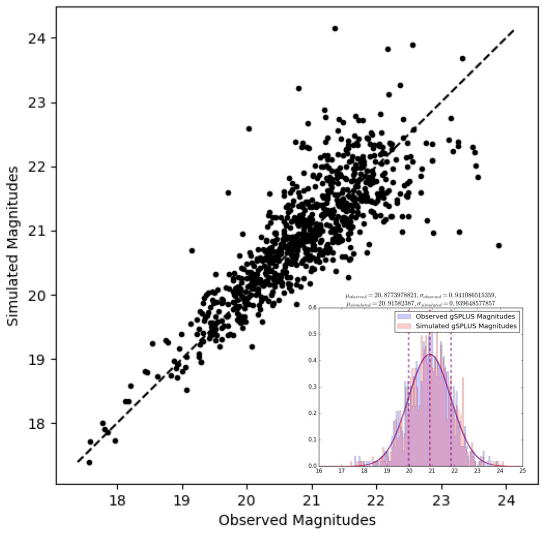

Figure 1. Comparison of the synthetic and real photometry in the g-band for QSOs detected in SDSS and J-PLUS.

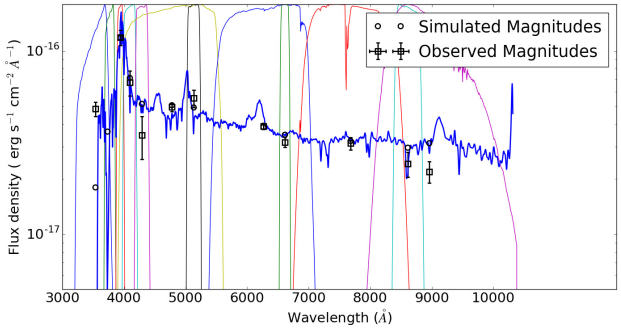

Figure 2. SDSS spectrum of a QSO at $z = 2.24$ and the S/J-PLUS filter system. Circles indicate the synthetic photometry for each filter derived from the spectrum, while squares indicate the actual magnitudes taken from the science verification J-PLUS data. The QSO has a strong *Lyα* emission line that falls into the F0395 filter at this redshift.

convolved with the S-PLUS, J-PLUS and J-PAS filter curves. To test how well our synthetic photometry matches with the actual quality of the data expected, we perform a comparison between our synthetic photometry derived from the spectra of $\sim$ 800 known QSOs in common between the SDSS spectroscopic survey and the first $\sim$ 60 deg^2 of data from J-PLUS. The result is shown in Fig. 1 for the synthetic (from SDSS spectra) and observed (from J-PLUS photometry) g-band magnitudes of the QSOs.

We also show an example of a QSO that can be identified on the basis of its strong emission lines falling in one or several of the S-PLUS/J-PLUS narrow-band filters for specific redshifts (in this case a QSO at $z \approx 2.2$ observed by both the SDSS and J-PLUS; Fig. 2). The synthetic and real J-PLUS photometry are indicated.

In order to test the feasibility of selecting even higher redshift QSOs, we have constructed a test sample of QSO spectra based on 100 of the brightest QSOs at $3.1 < z < 3.2$ from the Sloan Digital Sky Survey (SDSS) DR12 catalog, and built color-color diagrams as follows: (i) We slide the spectra through the redshift range of $5.0 < z < 7.5$ with steps of 0.1. Because we use

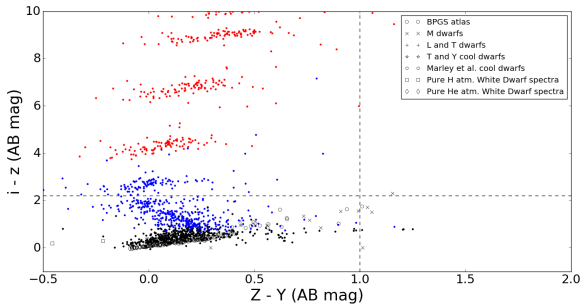

Figure 3. The $(z - Y)$ versus $(i - z)$ color-color diagram. Black points indicate QSOs at $z < 5.5$, blue points indicate QSOs at $5.5 < z < 6.0$ and red points indicate QSOs at $6.0 < z < 6.5$.

relatively low redshift QSOs as our model templates, we set any flux below 1216Å to zero, as expected at these high redshifts. (ii) We convolve the redshifted templates with the S-PLUS, J-PLUS, J-PAS and VISTA near-IR filters curves. (iii) We construct color-color diagrams, e.g., $(Y - J)$ versus $(Z - Y)$ for $6 < z < 7.5$ and $(Z - Y)$ versus $(i - z)$ for $5 < z < 6.5$, and identify the typical colors expected as a function of redshift. We also include galactic stars in order to study the contamination. The preliminary results are shown in Fig. 3. As expected, the high redshift QSOs clearly stand out from such a color-color diagram, although it remains to be checked to what depth we can effectively search for such objects.

5. Future work

The next steps for this project will be to determine the limiting depths of the photometry in each band expected for the future surveys, and then to obtain reliable criteria for selecting QSOs at the different redshifts. We will also determine the redshifts for which bright emission lines will fall in the narrow band filters, and how to select them from the data. The ultimate goal of this work will be to find new high redshift QSOs in S-PLUS, J-PLUS and J-PAS.

Acknowledgements. This project is part of the Iniciação Cientifica of student RM, funded through CNPq (459040/2014-6). CMdO acknowledges funding from FAPESP (2009/54202-8).

References

Carilli, C. L., Wang, R., Fan, X., et al. 2010, ApJ, 714, 834
Eilers, A.-C., Davies, F. B., Hennawi, J. F., et al. 2017, ApJ, 840, 24
Fan, X., Strauss, M. A., Becker, R. H., et al. 2006, AJ, 132, 117
Mejía-Narváez, A., Bruzual, G., Magris, C. G., et al. 2017, MNRAS, 471, 4722
Rees, M. J. 1984, ARA&A, 22, 471
Vilella-Rojo, G., Viironen, K., López-Sanjuan, C., et al. 2015, A&A, 580, A47

Boletim da Sociedade Astronômica Brasileira, **30**, no. 1, 234-235

Can Soft Gamma-Ray Repeaters and Anomalous X-Ray Pulsars be described as white dwarfs?

S. V. Borges[1], C. V. Rodrigues[2], J. G. Coelho[2] M. Malheiro[1], e R. Lima[3]

[1] Instituto Tecnológico de Aeronáutica (ITA) e-mail: villanovaborges@gmail.com
[2] Instituto Nacional de Pesquisas Espaciais (INPE)
[3] Universidade do Estado de Santa Catarina (UDESC)

Abstract. The Soft Gamma Repeaters (SGR) and Anomalous X-Ray Pulsars (AXP) are widely interpreted as magnetars, neutron stars having a huge magnetic field in the range 10^{13} to 10^{15} G, greater than the critical limit imposed by quantum mechanics. Because of that, other interpretations are also studied, among them is the massive white-dwarf model. We present a study of the three SGR/AXP that have detected optical counterparts to verify whether that emission is consistent with a white-dwarf origin. Adopting a hot spot at the surface to explain the optical variability observed, the required dimension of this hot spot is around 1 to 5 % of the white dwarf radius, which supports the white dwarf model for those SGR/AXPs. Besides, the white-dwarf temperatures estimated for 4U 0142+61 and SGR 0501+4516 are also consistent with the white-dwarf hypothesis.

Resumo. As fontes *Soft Gamma Repeaters* (SGR) e *Anomalous X-Ray Pulsars* (AXP) são interpretadas pela maioria da comunidade científica como magnetares, estrelas de nêutron com um alto campo magnético da ordem de 10^{13} até 10^{15} G, acima do limite crítico imposto pela mecânica quântica. Dessa forma, outras interpretações são sugeridas, entre elas o modelo de anãs brancas massivas. Nós apresentamos um estudo de três fontes SGR/AXP que possuem contrapartida óptica, de forma a verificar se tal contrapartida é consistente com a emissão de uma anã branca. Adotando uma mancha quente para explicar a variabilidade observada no óptico, a dimensão encontrada para tal mancha é de 1 a 5 % do raio da anã branca, o que suporta um modelo de anãs brancas para tais SGR/AXPs. Além disso, as temperaturas estimada para 4U 0142+61 e SGR 0501+4516 também são consistentes com a hipótese de anãs brancas.

Keywords. Accretion, accretion disks – Stars: magnetars – white dwarfs

1. Introduction

Supposing that the SGR/AXPs can be interpreted as rotation-powered neutron pulsars, the inferred magnetic field is in the range of 10^{13} G to 10^{15} G. On the other hand, because of the larger inertia moment, the magnetic field needed to explain the observational properties of the SGR/AXPs as white dwarfs (WD) is in the range of 10^{7} G to 10^{9} G, within the observed range of values for magnetic field in isolated WD (Ferrario, 2015). A further explanation of the WD model can be found in Malheiro et al. (2012) and Coelho & Malheiro (2014) .

Besides that, three sources have pulsed optical counterparts, which is unexpected for isolated neutron stars. For that reason, we tried to explain the observed optical counterpart in a WD context. We verify if a hot spot model could simulate the variability observed and we also estimate the WD temperature.

2. Methodology

We focus on verify how plausible is the interpretation of SGR/AXP as WD. To explain the pulsed optical emission, we suppose that the flux in the phase of minimum brightness is caused by the WD photosphere, with no contribution from the hot spot, it is possible to estimate the WD temperature value by knowing the WD radius. In addition, to explain the pulsed optical emission, we consider a hot spot in the WD surface. The relation between the temperature of the hot spot and the WD mass is calculated assuming an accretion scenario using Aizu (1973). We adopt the mass and radius for massive WDs from Coelho (2017). The distance and the hydrogen column density N(H) for the two AXP's are from Durant & van Kerkwijk (2006) and for the SGR these values are from Camero et al. (2014).

Table 1. Limiting values of temperature for 1E 1048.1-5937

WD radius (km)	4250	1050
WD mass ($M_{\odot}$)	1.27	1.39
Spot's temperature (keV)	58.5	420.5
WD temperature (K)	3.2×10^5	5.9×10^6

We apply the above methodology for the three SGR/AXP that have pulsed optical emission. They are SGR 0501+4516, 4U 0142+61 and 1E 1048.1-5937.

3. Results

According to Dhillon et al. (2009), the mean magnitude for 1E 1048.1-5937 in the i' band is 25.3 mag and the pulsed fraction is 52 ± 15%. For SGR 0501+4516, these values are respectively 24.4 mag and approximately 80% (Dhillon et al., 2011). And for 4U 0142+61, 27.3 mag and 58 ± 16% (Dhillon et al., 2005). The values of the white dwarf temperature obtained for the two limiting values of radii for each one of the three SGR/AXP can be seen in tables 1, 2 and 3.

Besides, Figures 1, 2 and 3 show the size of the accretion region as a percentage of the WD radius for different values of WD mass for these three SGR/AXPs.

4. Discussion and conclusions

We estimate WD temperatures around 100,000 K for 4U 0142+61 and SGR 0501+4516. This is in agreement with the WD hypothesis, since WD can be as hot as 200,000 K, as,

Table 2. Limiting values of temperature for SGR 0501+4516

WD radius (km)	4550	1040
WD mass ($M_\odot$)	1.17	1.39
Spot's temperature (KeV)	76.9	415.5
WD temperature (K)	2.1×10^4	2.5×10^5

Table 3. Limiting values of temperature for 4U 0142+61

WD radius (km)	4250	1040
WD mass ($M_\odot$)	1.30	1.39
Spot's temperature (KeV)	84.5	415.5
WD temperature (K)	8.0×10^4	1.9×10^6

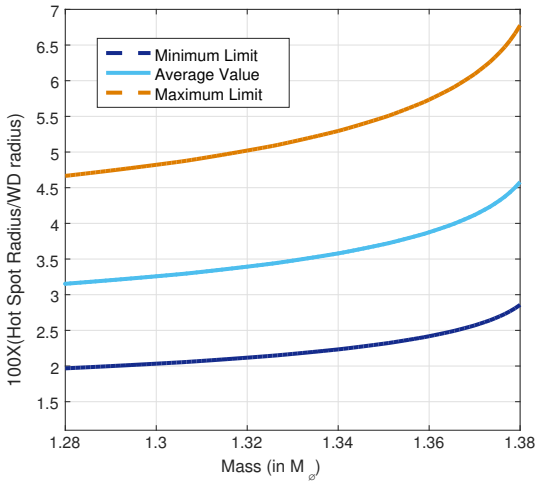

Figure 1. Size of the accretion region for 1E 1048.1-5937 as a percentage of the WD radius for different values of WD mass

for instance, H1505+65 (Werner & Ranch,2015). On the other hand, the white dwarf model for 1E 1048.1-5937 results in a temperature in the range 300,000 to 6,000,000 K, discarding this model for this source. The required dimension of the hot spot is around 1 to 5 % of the white dwarf radius to 4U 0142+61 and SGR 0501+4516. These results support the white dwarf model for some SGR/AXP.

Acknowledgements. PIBIC/CNPq 136119/2014-0, 127044/2015-9, 114537/2016-0; Fapesp 2013/15088-0, 2016/20059-8 and 2013/26258-4; CNPq 306701/2015-4; PROAP/Capes.

References

Aizu, K., 1973, 49, 1184-1194
Camero A. et al, MNRAS, 2014, 438, 3291
Coelho, J. G. et al., 2017, private communication
Coelho, J.G. & Malheiro, M., PASJ, 2014, 66, 14
Durant, M., & van Kerkwijk, ApJ, 2006, 650, 1070
Dhillon et al, MNRAS, 2005, 363, 609
Dhillon et al., 2009, MNRAS, 394, L112
Dhillon et al, MNRAS, 2011, 416, L16
Ferrario, L. et al, Space ScienceReviews, 2015, 191, p. 111–169
Malheiro, M. et al., PASJ, 2012, 64, 56
Mereghetti, 2013, Brazilian Journal of Physics, 43, 356
Werner, K.; Rauch, 2015, T. A & A, 584, A19

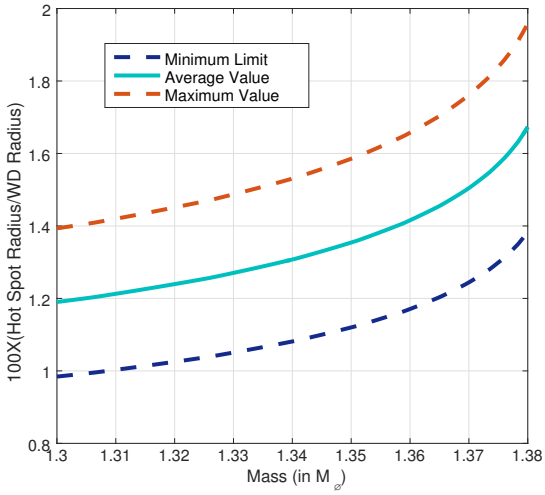

Figure 2. Size of the accretion region for SGR 0501+4516 as a percentage of the WD radius for different values of WD mass

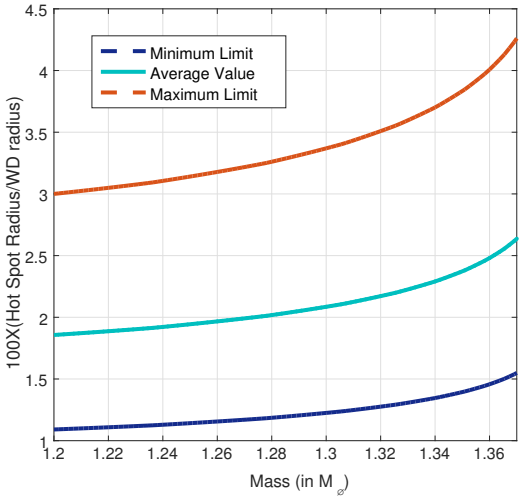

Figure 3. Size of the accretion region for 4U 0142+61 as a percentage of the WD radius for different values of WD mass

Boletim da Sociedade Astronômica Brasileira, **30**, no. 1, 236-238

Diffuse InterGalactic Magnetic Fields and Constraints for the CTA and ASTRI MINI-ARRAY Observations

S. A. Faria, P. Barai, & E. M. G. Dal Pino

[1] Instituto de Astronomia, Geofísica e Ciências Atmosféricas, Universidade de São Pauloe-mail: stela.faria@usp.br

Abstract. Primordial magnetic fields are amplified by turbulent dynamo effects, as well as by the processes of formation and evolution of stars in the Interstellar Medium (ISM). At the same time, galactic outflow streams are generated by the energetic feedback from stars and supernovae (SN) explosion, along with large-scale dynamic events (e.g. galaxy mergers and tidal interactions between galaxies). In massive galaxies, energetic winds are also produced by accretion of gas in central supermassive black holes, and resulting in the feedback from Active Nuclei of Galaxies (AGN). The magnetic fields in the ISM are pushed out by strong galactic outflows over time, magnetically enriching the InterGalactic Medium (IGM) at larger cosmological distances. These magnetic fields permeate the turbulent IGM, and can influence the formation of structures on large scales. The origin of the large-scale diffuse InterGalactic Magnetic Fields (IGMFs) is not known. IGMFs could be: generated primordially in the early Universe, or produced locally in galaxies and efficiently transported by galactic outflows to fill a significant volume fraction of the IGM . For the second case, the contribution of SN-driven versus AGN-driven outflows in the transport of magnetic fields is also unknown. The properties of the magnetic fields are very difficult to measure directly, especially in the low density diffuse regions of the IGM. The objectives of this study are: to investigate the origin of the IGMFs, compute the contributions of galactic outflows (driven by SN versus AGN) in the advection of magnetic fields from the galaxies to the IGM; explore the evolution of IGMFs through cosmic times. We will combine numerical simulation results with gamma ray observations (current and future observations made by CTA and its precursor - ASTRI MINI-ARRAY).

Resumo. Os campos magnéticos primordiais são amplificados por efeitos dínamo turbulentos, bem como por processos de formação e evolução estelar no meio Interestelar. Ao mesmo tempo, fluxos de saída galácticos são gerados pelo feedback energético de vários processos: estrelas, evolução estelar e explosão de supernovas (SN), juntamente com eventos dinâmicos de grande escala, por exemplo fusões de galáxias e interações de maré entre galáxias. Em galáxias maciças, ventos energéticos também são produzidos por acreção de gás em buracos negros supermassivos centrais e resultando no feedback de Núcleos Ativos de Galáxias (AGN). Os campos magnéticos na galáxia ISM são arrastados por fortes saídas galácticas com o tempo, enriquecendo magneticamente o Meio intergaláctico (IGM) em distâncias cosmológicas maiores, Esses campos magnéticos permeiam o IGM turbulento e podem influenciar a formação da estrutura em grande escala. Os campos magnéticos também afetam a propagação de raios cósmicos e raios gama produzidos por AGN e rajadas de raios gama em distâncias cosmológicas. A origem dos campos magnéticos InterGaláticos difusos de larga escala (IGMFs) não é conhecida, podendo ser: gerados de maneira a preencher o espaço primordial, ou produzidos localmente em galáxias e transportados de forma eficientemente por saídas galácticas para preencher uma fração volumétrica significativa do IGM. Para o segundo caso, a contribuição de saídas SN-driven versus AGN-driven no transporte de campos magnéticos também é desconhecida. As propriedades do campo magnético são muito difíceis de medir diretamente, especialmente nas regiões difusas de baixa densidade do IGM; que este projeto pretende esclarecer. Tendo como objetivos: - Investigar a origem dos IGMFs, computando as contribuições das saídas galácticas (movidas por SN versus AGN) na advecção de campos magnéticos das galáxias ao IGM. - Explorar a evolução dos IGMFs através de épocas cósmicas. - Restrinjir a força e o fator de preenchimento dos campos magnéticos cósmicos, combinando resultados de simulação numérica com observações de raios gama (observações atuais e futuras feitas pelo CTA e seu precursor - ASTRI MINI-ARRAY).

Keywords. AGN Feedback – SN Feedback – IGM – Magnetic Field

1. Introduction

The InterGalactic Medium (IGM) is the region that comprises the baryonic material existing between galaxies, which is the dominant component of this type of matter in the Universe. Galaxies are formed in the high-density regions of the IGM (Mo et al. 2010).

Observational studies find that diffuse large-scale magnetic fields exist in the IGM. Diffuse magnetic fields are fields immersed in a medium where the density is smaller than that within the galaxies (e.g., the intergalactic medium). The origin and evolution of cosmic magnetic fields, their intensity and structure in the intergalactic space, their first appearance in young galaxies, and their dynamical importance in the evolution of galaxies remain largely unknown (Beck 2012). Magnetic fields of higher intensity (order of μG) are observed in galaxies and galaxy clusters. This can be explained by the amplification of primordial magnetic fields. Although widely accepted, the existence of primordial magnetic fields is still the subject of several questions, most importantly its origin.

Some widely accepted theories are that primordial magnetic fields were generated during the Big Bang or during the early cosmological phases of the Universe (e.g. Thorne 1967; Enqvist 1998). These primordial fields are amplified by converting the rotational kinetic energy of gas into magnetic energy, with the conservation of magnetic helicity according to the dynamo phenomena, a process known as the "turbulent dynamo" (Roberts & Stix 1971; Eraso 2009). Magnetic fields in galaxies are dragged out of the Interstellar Medium (ISM) by powerful galactic outflows generated by local processes like star-formation, stellar evolution, Supernova (SN) explosion, and Active Galactic Nuclei (AGN) accretion. Global processes like galaxy mergers and tidal interactions between galaxies also develop galactic outflows, which as well enrich the IGM with magnetic fields.

This research aims to investigate the origin of the InterGalactic Magnetic Fields (IGMFs) by computing the contributions of SN *versus* AGN driven galactic outflows in the advection of magnetic fields from the galaxies to the IGM. The magnetic fields in the intergalactic medium are expected to vary with cosmic epoch. This project will explore the evolution of the IGMFs through cosmic times, as well estimate the amplitude and the filling factor of the cosmic magnetic fields.

2. Numerical Method

We analysed cosmological hydrodynamical simulations (e.g. Barai et al. 2013), performed using the code GADGET-3. The cosmological volume is a $(2Mpc)^3$ box, undergoing Hubble expansion, and evolved with periodic boundary conditions.

The GADGET code (Springel 2005) calculates gravitational forces between matter using an N-body collisionless method, in particular it uses a hierarchical Tree algorithm (optionally in combination with a particle grid scheme for long-range forces). GADGET allows the gas dynamics to be optionally included. It represents fluids by Smoothed Particles Hydrodynamics (SPH), employing the Lagrangian SPH numerical formalism.

The GADGET cosmological simulation gives as output these quantities for the SPH gas particle: position, velocity, radius ($R_{comoving}$), density (ρ_{gas}), mass ($M_{gaspart}$), specific internal energy (u_{int}).

3. Analysis

We perform post-processing analyses for gas flows around simulated galaxies. Our main assumption is that there is equipartition of energy between the thermal energy of gas and the magnetic energy. The magnetic field can then be obtained according to Eq. 1. The methodology used to calculate the magnetic field B (following (Barai 2008)) is:

$$u = \frac{u_E}{2} = \frac{B^2}{8\pi} \tag{1}$$

where u is the energy density of the magnetic field, u_E is the energy density of the gas particles and B is the magnetic field.

The output data generated by GADGET includes u_{int} of the gas particles. This u_{int} must first be converted to u, for which we use Eq. 2.

$$u = \frac{u_{int} \times M_{gaspart}}{V} \tag{2}$$

where V is the gas particle volume. Particles are considered to be spherical in shape, so the volume is calculated according to Eq. 3.

$$V = \frac{4\pi R^3_{physical}}{3} \tag{3}$$

where $R_{physical}$ is the physical radius of the gas particles.

The cosmological simulation represents an Universe undergoing Hubble expansion. This means that as the Big Bang (early Universe) is approached, matter particles were closer together. And with the passage of time, matter particles fly away from each other according to the Hubble rate. Therefore a distance correction must be made while performing our analyses, to take into account the actual physical distance. The relevant equation here is of the comoving distance, equation (4).

$$R_{physical} = \frac{R_{comoving}}{1+z} \tag{4}$$

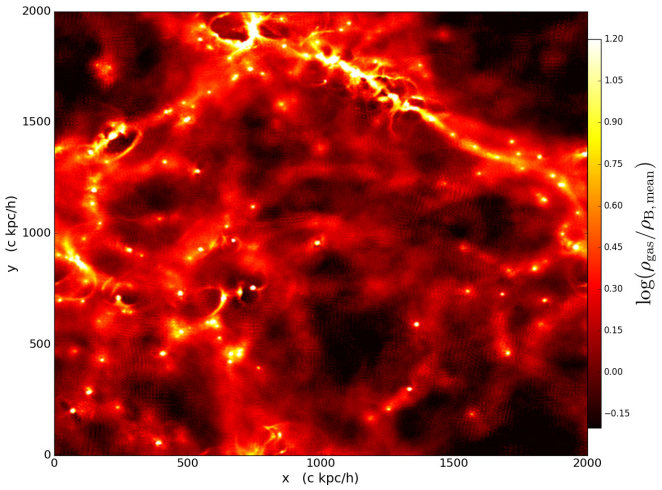

Figure 1. Projected 2D maps of the gas overdensity.

where $R_{comoving}$ is the comoving distance and z is the redshift.

Another parameter that has also been calculated is the overdensity of the gas particles δ, which is obtained through the Eq. 5.

$$\delta = \frac{\rho_{gas}}{<\rho_B>} \tag{5}$$

where ρ_{gas} is the density of the gas particles and $<\rho_B>$ the average density of the Universe. According to the ΛCDM cosmological model, the mean density of the Universe is obtained using Eq.6

$$<\rho_B> = \Omega_{B,0} \times \rho_{crit} = \frac{\Omega_{B,0} 3H_0^2}{8\pi G} \tag{6}$$

An input parameter for the GADGET cosmological simulations is the Star Formation Threshold Density (SFTD). It is the limiting density dividing the cosmic gas into regions where the star formation occurs (inside galaxies, where the density is higher) and the environment where it does not occur (IGM, where the density is lower). We convert this threshold from number density to mass density using Eq. 7

$$\rho_{SFTD} = \frac{n_{SF} \times M_{hydrogen}}{<\rho_B>(1+z)^3} \tag{7}$$

where ρ_{SFTD} is the threshold density of star formation, and n_{SF} is the corresponding number density. Our simulations use a value $n_{SF} = 0,13cm^{-3}$ (Barai et al. 2013). In this way, $\rho_{SFTD} = 1.200298 \times 10^3$. is obtained.

4. Simulation Results

Using the analysis methods, the following figures were obtained for the magnetic field in the $(2Mpc)^3$ cosmological volume at the cosmic epoch $z = 6.5$:

Figure 1 shows the projected 2D map of the gas overdensity in the whole $(2Mpc)^3$ volume. Here it is possible to note the intergalactic medium (dark and red regions) which is gas at low densities. Together the galaxies and clusters of galaxies are also visible (yellow and white filaments) as the high density regions.

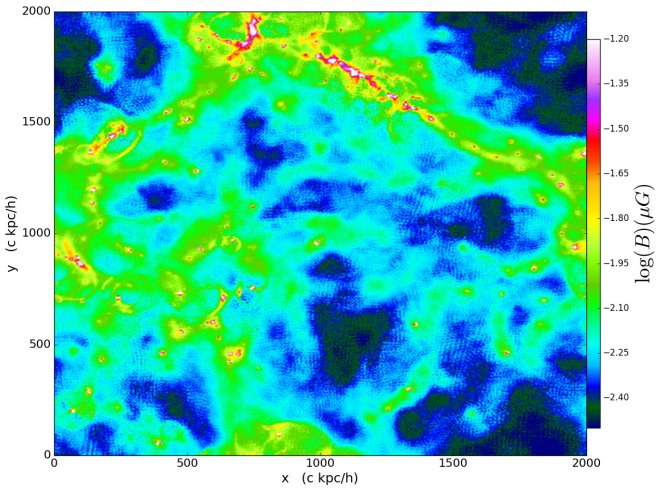

Figure 2. Projected 2D maps of the magnetic field.

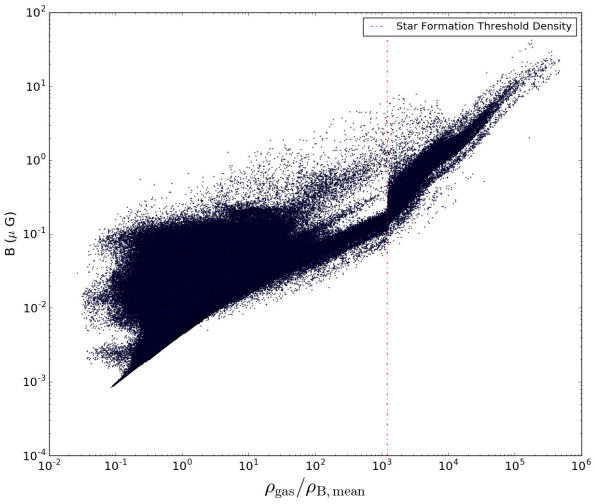

Figure 3. Diagrams of correlation of magnetic field with overdensity.

The magnetic field was calculated using the equipartition of energy (Eq. 1). Thus, as expected, it is possible to note that the magnetic field is distributed in the cosmological volume according to the concentration of matter (Figure 2). In other words, the magnetic field is larger in the high-density galaxies, and smaller in the low-density IGM.

Figure 3 and Figure 4 shows the relation between different properties of the cosmic gas in the whole $(2Mpc)^3$ volume.

Then, it is possible to analyze the correlation between the properties.

In the Figure 3 and 4, the limiting overdensity of 10^3 divides all the cosmic gas into two regions. In the right side is possible to see a high-density region, where the highest probability of star formation occurs (inside the galaxies), while on the left side it encounters the low density region, which represents mainly the IGM.

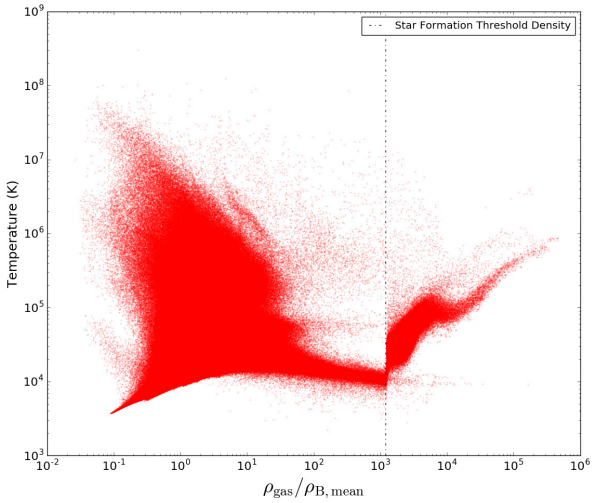

Figure 4. Diagrams of correlation of temperature with overdensity, respectively.

5. Conclusion

From the partial results, we conclude that the Magnetic field has a positive correlation with the overdensity in the IGM (Figure 3) and inside the galaxies.

In figure 4, a positive correlation is noted in the temperature inside the galaxies. Outside in the IGM, it is possible to note that most of the gas has low temperatures. A small fraction of IGM gas is heated up due to shocks.

So, it is noted that the magnetic field is frozen to the density of matter, thus having a higher magnetic field concentration in the regions of filaments of galaxies.

Acknowledgements. SAF thanks her advisor, for the dedication dedicated to the elaboration of this work, and Fapesp, for the financial assistance given to the realization of the project.

References

Mo, H., Van den Bosch, F., & White, S. 2010, Galaxy formation and evolution, Cambridge University Press.
Beck, R. 2012, Magnetic fields in galaxies, Space Science Reviews, 166
Thorne, K. S. 1967, ApJ, 148, 51
Enqvist, K. 1998, International Journal of Modern Physics D, 7, 331
Roberts, P. H., & Stix, M. 1971, The turbulent dynamo. NCAR, Boulder, Co.
Eraso, G. A. G. 2009, Estudos numéricos do dínamo Solar (Doctoral dissertation, Universidade de São Paulo).
Barai, P., Viel, M., Borgani, S., Tescari, E., et al. 2013, MNRAS, 430, 3213
Springel, V. 2005, MNRAS, 364, 1105
Barai, P. 2008, ApJL, 682, L17.
Marinacci, F., Vogelsberger, M., Pakmor, R., Torrey, P., et al. 2017, arXiv:1707.03396

Boletim da Sociedade Astronômica Brasileira, **30**, no. 1, 239-240

The FLASK code: beyond lognormal models of cosmological fields

Henrique S. Xavier[1,2], Filipe B. Abdalla[1], & Benjamin Joachimi[1]

[1] University College London (UK)
[2] University of Sao Paulo (Brazil) e-mail: hsxavier@if.usp.br

Abstract. It is common in cosmology to model either the matter density or the weak lensing convergence as lognormal fields; however, jointly modelling them is impossible. We propose two ways of overcoming this limitation: distorting the fields' power spectra; or obtaining the convergence from a line-of-sight integration of the lognormal density. The latter results in an analytical prediction for the skewness of the convergence distribution. We present the code FLASK, which creates tomographic realisations on the sphere of an arbitrary number of correlated lognormal fields, and show that it works for clustering and lensing with sub-per-cent accuracy over relevant angular scales and redshift ranges.

Resumo. É comum na cosmologia modelar a densidade da matéria ou a convergência de lentes fracas como campos lognormais; porém, a modelagem conjunta desses dois campos é impossível. Nós propomos duas formas de superar essa limitação: distorcendo os espectros de potência dos campos ou integrando a densidade lognormal sobre a linha de visada. A última abordagem também resulta em uma previsão analítica para a obliquidade da distribuição de convergência. Apresentamos o código FLASK, que gera realizações tomográficas na esfera de um número arbitrário de campos lognormais correlacionados, e mostramos que ele pode criar simulações conjuntas de distribuição de galáxias e lentes com precisão de sub-percentagem nas escalas angulares e intervalos de *redshift* relevantes.

Keywords. methods: statistical – gravitational lensing: weak – large-scale structure of Universe

1. Lognormal limitations

A lognormal random variable X is derived from a standard (zero mean, unit variance) Gaussian variable Z through the formula:

$$X = e^{\mu+\sigma Z} - \lambda. \tag{1}$$

Lognormals are better models to the density and convergence distributions than Gaussians because: They have a hard lower limit ($X \geq -\lambda$); and they have long tails at high values.

If two Gaussian variables Z_1 and Z_2 that have covariance ξ_g are used to generate lognormal variables X_1 and X_2, the covariance of the lognormal variables will be:

$$\xi_{ln} = (\langle X_1\rangle + \lambda_1)(\langle X_2\rangle + \lambda_2)(e^{\xi_g} - 1), \tag{2}$$

where $\langle X_i\rangle$ is the mean of X_i. Therefore, the relation between the Pearson correlation coefficients ρ_g and ρ_{ln} of the Gaussian and lognormal variables is given by Fig. 1. We notice that the correlation between lognormal variables is limited to a interval smaller than $[-1, +1]$. This happens because the relation between two lognormal variables with different skewnesses is non-linear.

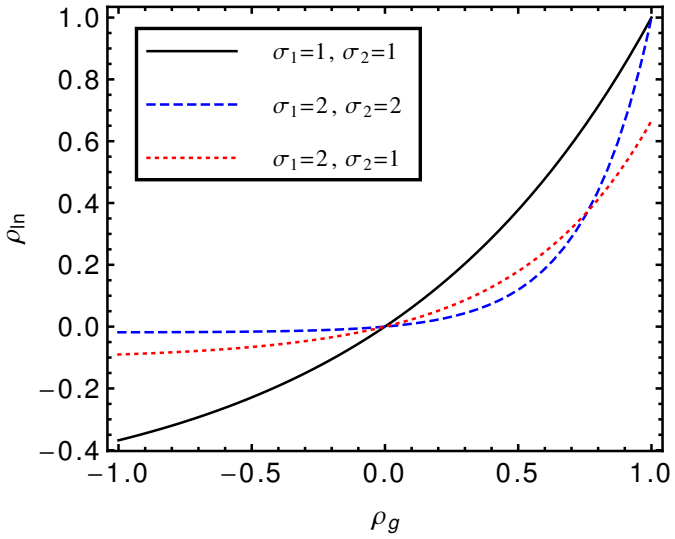

Figure 1. Relationship between the correlation ρ_g of two Gaussian variables and the correlation ρ_{ln} of their associated lognormal variables.

2. Consequences in cosmology

The limitations presented in Sec. 1 do not affect independent simulations of density nor of convergence. However, this is not the case for their joint simulations, in which the covariance matrices that describe the fields – given by their auto and cross power spectra – are unattainable by lognormal variables: as Fig. 2 shows, the amount of distortion that would have to be applied to the angular power spectra to make them lognormal compliant can be significantly large.

This happens because the relation between density and convergence enforces that both cannot be lognormals at the same time. The convergence κ at a line of sight (LoS) $\boldsymbol{\theta}$ for sources at redshift z_s is given by a weighted integral of the matter density contrast δ:

$$\kappa(\boldsymbol{\theta}, z_s) = \int_0^{z_s} K(z, z_s)\delta(\boldsymbol{\theta}, z)\mathrm{d}z. \tag{3}$$

While a sum of Gaussian variables is also a Gaussian variable, a sum (or integral) of lognormal variables is *not* a lognormal variable. Enforcing a power spectra derived from Eq. 3 at the same time one enforces all distributions to be lognormals is like enforcing two different angles for a triangle with equal sides. Therefore, one must either adopt different power spectra or different distributions.

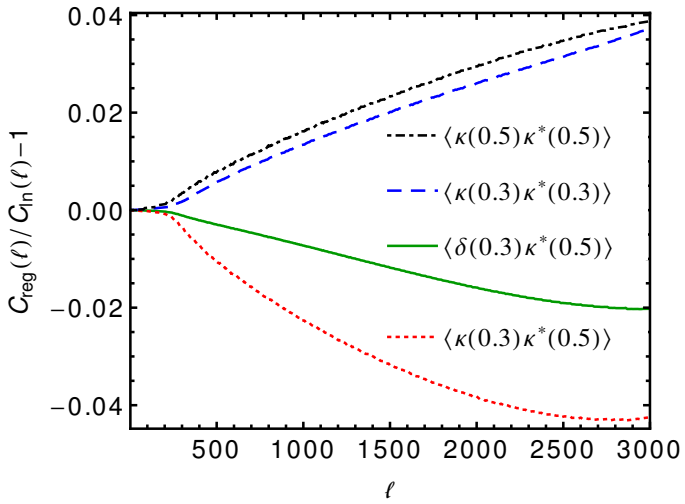

Figure 2. Fractional differences between the original angular power spectra $C^{ij}_{\rm ln}(\ell)$ and the regularised one $C^{ij}_{\rm reg}(\ell)$ when modelling density and convergence at three redshift bins.

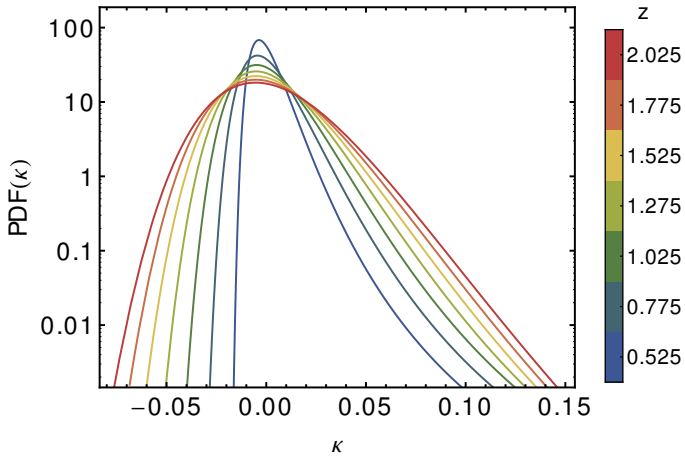

Figure 3. Distributions for the convergence obtained from lognormal density LoS integration, for various redshifts.

3. A different convergence PDF

Instead of assuming κ to be lognormal, one can compute it by LoS integration of the lognormal density field. The resulting distribution is shown as a function of redshift in Fig. 3.

The convergences obtained from density LoS integration should follow the theoretical $C^{ij}(\ell)$s exactly. Due to the approximation of the integral by a sum, however, they will slightly diverge in a predictable way. Fig. 4 shows that we can perfectly predict this deviation and that we can reproduce the true convergence power spectra up to one per cent on the relevant redshift ranges and angular scales.

Finally, this lognormal density LoS integration approach can be used to compute an analytic prediction for the skewness of the convergence distribution:

$$\mathrm{Skew}[\kappa(z_{\rm s})] = \frac{1}{\mathrm{Var}^{3/2}[\kappa(z_{\rm s})]} \iiint_0^{z_{\rm s}} K(z_1,z_{\rm s})K(z_2,z_{\rm s})K(z_3,z_{\rm s})\cdot$$
$$[3\xi_{\delta\delta}(z_1,z_2)\xi_{\delta\delta}(z_2,z_3) + \xi_{\delta\delta}(z_1,z_2)\xi_{\delta\delta}(z_2,z_3)\xi_{\delta\delta}(z_3,z_1)]\mathrm{d}z_1\mathrm{d}z_2\mathrm{d}z_3, \quad (4)$$

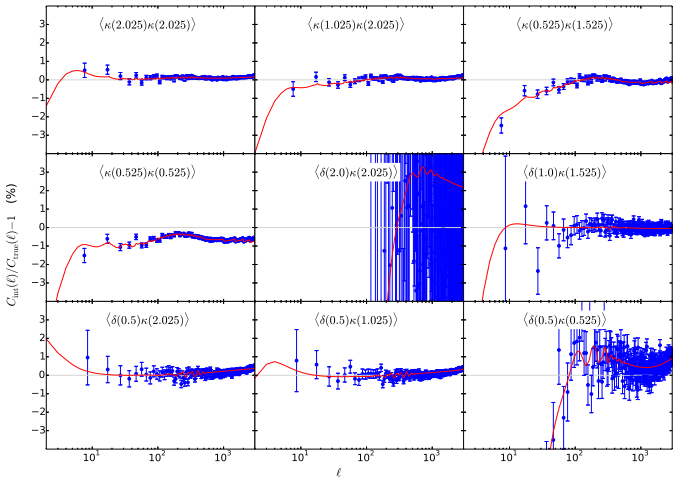

Figure 4. Fractional difference between the convergence $C(\ell)$ computed as a LoS Riemann sum of the simulated density, $C_{\rm int}(\ell)$, and the true one, $C_{\rm true}(\ell)$. The red curves show the theoretical expectation given the numerical approximations, and the blue data points show the average of 1000 independent simulations. The first four (last five) subplots show the results for convergence–convergence (density–convergence) power spectra. The density was simulated in 40 redshift bins of width $\Delta z = 0.05$.

where $\xi_{\delta\delta}(z,z') = \langle\delta(\boldsymbol{\theta},z)\delta(\boldsymbol{\theta},z')\rangle$ is the matter density contrast LoS correlation function.

4. The FLASK simulation code

The open-source, parallel simulation code FLASK[1] discretizes the universe around the observer into many redshift shells, each described by a HEALPIX map, and generates Gaussian or lognormal (or sum of lognormals) realisations of an arbitrary number of correlated fields on these shells (e.g. multiple galaxy populations, convergence, shear and CMB temperature maps). Effects such as magnification bias, redshift space distortions and intrinsic alignments can be included by providing to FLASK the appropriate input $C^{ij}(\ell)$s. Density tracers can be Poisson sampled and have ellipticities assigned to them. FLASK can output full-sky HEALPIX maps and catalogues.

Acknowledgements. HSX acknowledges FAPESP for the financial support.

References

Xavier H. S., Abdalla F. B., Joachimi, B. 2016, MNRAS 459, 3693

[1] `http://www.astro.iag.usp.br/~flask`

Boletim da Sociedade Astronômica Brasileira, **30**, no. 1, 241-242

The ISM properties of massive dusty obscured during the reionization

J. H. B. Santos & G. B. Lima Neto

[1] Instituto de Astronomia, Geofísica e Ciências Atmosféricas da Universidade de São Paulo, São Paulo, SP
e-mail: jullian.santos@usp.br

Abstract. In this work we investigate the ISM properties of dusty obscured galaxies during their first billion year evolution. We used the chemodynamic model from Friaça & Terlevich (1998) to simulate, in galactic scale, the hydrodynamic and chemical evolution of the stellar mass and dust. We take into account the grain growth/depletion in the ISM both by accretion and destruction in SNe events. We couple to the model a radiative transfer interface to calculate the IR SED, based on Bruzal & Charlot (2003) spectro-photometric library. We find that our model takes about 1.5 Gyr to reach the A1689-zD1 SFR, 0.03 Gyr the M_*, 0.1 Gyr to M_{dust}, and 0.1 Gyr the L_{IR}. Our analysis can be employed to constrain the time scale for the formation of the first galaxies.

Resumo. Neste trabalho foram investigadas as propriedades do meio interestelar de galáxias obscurecidas por poeira durante os primeiros bilhões de anos de sua evolução. Para tanto, foi usado o modelo quimiodinâmico de evolução de galáxias de Friaça & Terlevich (1998) para simular em escala galáctica a evolução hidrodinâmica, química, da massa estelar e da de poeira. A interação da poeira no meio interestelar (por acréscimo e choque de supernovas) também foi considerada. Acoplado ao modelo está uma interface de transferência radiativa, que, com a biblioteca espectro-fotométrica de Bruzal & Charlot (2003), para calcular a SED resultante no infravermelho. Foram calculados a massa estelar, a massa de poeira, a taxa de formação estelar e a SED para uma galáxia análoga a A1689-zD1 em $z \sim 7.5$. No modelo, a galáxia leva aproximadamente 1.5 Ga para a alcançar a SFR, M_{dust} e L_{IR} de A1689-zD1 em, respectivamente, 0.03 Ga, 0.1 Ga e 0.1 Ga. Esta análise é importante para estabelecer vínculos na escala de tempo necessária para a formação das primeiras galáxias do Universo.

Keywords. Galaxies: ISM – Galaxies: high-redshift – dust, extinction

1. Introduction

Dust obscured galaxies are crucial objects to understand galaxy evolution during the height of their formation. They have a high amount of dust accumulated in intense star-forming episodes (i.e. a starburst) and it is possible that almost all normal and massive galaxies in the local Universe have experienced this phase during their growth. In particular, ultraluminous infrared galaxies, ULIRGs, are associated with starbursts, AGNs, and morphological evolution around $z \sim 2$–2.5, Yan et al. (2007).

Even beyond, in the reionization era ($z \gtrsim 6$), galaxies with strong infrared emission and dust-to-gas ratio have been found, Strandet et al. (2017), bringing new challenges to the galaxy evolution theories. Since dust is composed by metals (such as C, O, Si, Mg, and Fe), the galaxy have first to be chemically enriched by generations of stars and supernovae.

2. Simulation

In this work we investigate the properties of the ISM of high-redshift starburst galaxies (BGs) with the aid of a chemodynamic model described in Friaça & Terlevich (1998). It is a semi-analytic multi-zonal model that couples hydrodynamics, star formation, and chemical evolution of a spheroid galaxy. The galaxy is constituted by three components: gas, stars and a dark matter (DM) halo. The stellar mass and DM distributions follow, respectively, the King and NFW profiles. We assumed a Salpeter IMF and Schmidt star formation law with $n_{\rm sf} = 1/2$ index Larson (1974). The gas inicial composition is $X = 0.76$, $Y = 0.24$ and $Z = 0$. The initial temperature is assumed to be $T_0 = 10^4$ K and gas density profile the same as DM. The galaxy is initially composed only by gas and DM with mass a ratio $M_h/M_G = 6$.

Para cópias, contate: J. H. B. Santos

The dust grains are composed by graphite, amorphous carbon, PAHs, and silicon. Dust is produced in AGBs stellar winds, SNIa and Core-Collapsed SNe (CCSNe), each one with a different dust formation law (following Dwek 1998, formulation). We used the Gioannini et al. (2016) formulation for grain accretion in the ISM. The complete dust model is described by Guimarães & Friaça (2005). The model is coupled to a radiative transfer interface to calculate the panchromatic SED, based on Bruzual & Charlot (2003) spectro-photometric library and in Guimarães & Friaça (2005) dust model.

We simulated a fiducial galaxy with $2.0 \times 10^{11} M_\odot$ initial gas mass. This value was set to represent an intermediate value between the dusty obscured galaxies A1689-zD1, at $z \sim 7.5$ Knudsen et al. (2016), ADFS-27, a HyLIRG at $z \sim 6$ Riechers et al. (2017) and SPT-S 0311-5823.4 $z \sim 7$ Strandet et al. (2017).

3. Results

Fig. 1 shows the evolution of the stellar, dust and gas mass for the first 3 Gyr of the fiducial galaxy. The collapse of the primordial gas feeds the star formation, but SNe feedback drives a galactic outflow, beginning to quench the star formation in ~ 0.4 Gyr. After ~ 1.0 Gyr the stellar mass reach a plateau. The growth of dust mass initially follows the stellar mass growth, but at ~ 1.0 Gyr, the dust mass decrease due to the gas mass loss in outflows and to the decrease of CCSNe.

Fig. 2 shows the metallicity-dust mass relation. The metallicity is given by the mass ratio Fe/H divided by the solar mass ratio ($Fe_\odot/H_\odot$). During the starburst phase, the total dust mass follows the metallicity, but at [Fe/H] ~ 0.3, the dust mass reaches a plateau with $\sim 2 \times 10^8 M_\odot$ due to the decrease of CCSNe rate and to the dust mass lost in outflows.

Fig. 3 shows the simulated SED for the first 1 Gyr of the galaxy evolution. Due to the UV emission of young star and dust

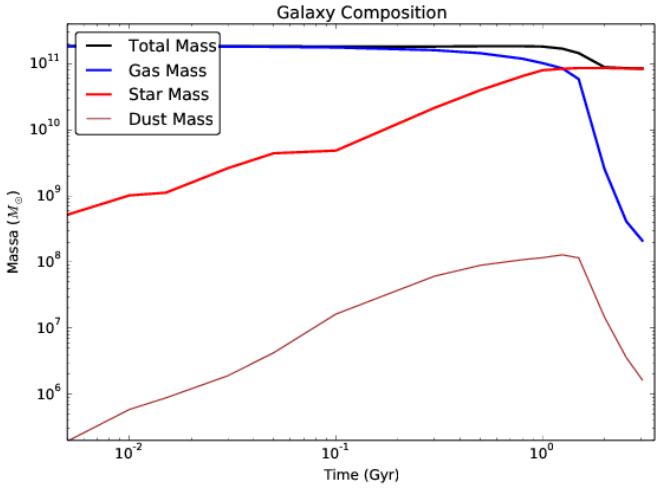

Figure 1. Evolution of barionic galactic components for the fiducial galaxy. Dust, stars, gas and the total mass.

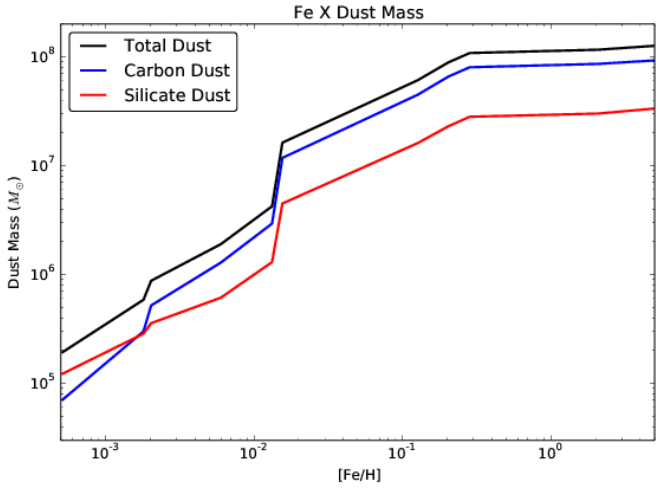

Figure 2. Metallicity × dust mass relation for the fiducial galaxy. The metallicity is given by [Fe/H] mass ratio.

mass produced mainly in CCSNe, after 0.1 Gyr the galaxy has strong FIR emission and in 0.3 Gyr the emission reaches a peak. The UV and visible components of the SED may be overestimated due to the lack of molecular clouds in the model.

Knudsen et al. (2016) estimated for A1689-zD1 a SFR $12 M_\odot$ yr^{-1}, $\log(M_*/M_\odot) = 9.4$, $\log(M_{dust}/M_\odot) = 7.2$ and $L_{IR} = 1.8 \times 10^{11} L_\odot$. Our model matches this values after the time:

- SFR $12.2 M_\odot$ a^{-1} after 1.5 Gyr;
- $\log(M_*/M_\odot) = 9.4$ after 0.03 Gyr;
- $\log(M_{dust}/M_\odot) = 7.0$ after 0.1 Gyr; and
- $L_{IR} = 1.5 \times 10^{11}$ $L_\odot$ after 0.1 Gyr

of galactic evolution. We believe that either A1689-zD1 has a very long star formation history or it is in the final stage of a very strong starburst.

4. Conclusion

In this section we summarize our main conclusions:

- Outflows quench the star formation after only ∼ 1 Gyr.
- The [Fe/H] X Dust relation reaches a plateau in [Fe/H] ∼ 0.3.

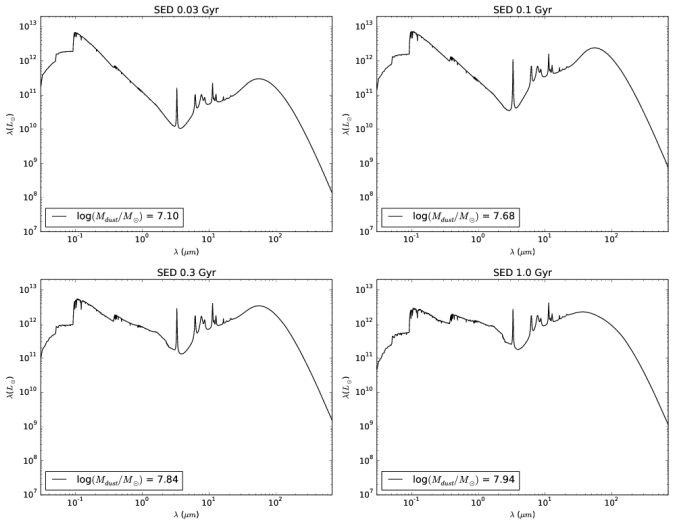

Figure 3. Simulated SED for the fiducial galaxy from 0.03 Ga to 1 Ga. The UV emission may be overestimated due to the lack of molecular clouds.

- In our simulations IR emission is strong at ∼ 0.1 Gyr and reaches the peak at 0.3 Gyr.
- The simulation recovers the stellar and dust masses of A1689-zD1 in less the 0.1 Gyr.

We find that the time needed to form a obscured galaxy is ∼ 0.1 Gyr and A1689-zD1 could be in the later phase of a starburst.

References

Bruzual, G., & Charlot, S. 2003, MNRAS, 344, 4, 1000
Dwek, E. 1998, ApJ, 501, 663
Friaça, A. C. S., & R. J. Terlevich., R. J. 1998, MNRAS, 298, 399
Gioannini, L., Matteucci, F., Vladilo G. & Calura F. (2016), MNRAS, 464, 985
Guimarães, M. C. & Friaça, A. C. S. 2005, Efeitos da Presença de Poeira na Emissão de Galáxias a Altos e Baixos Redshifts, Tese de Doutorado, São Paulo
Knudsen, K. K., Watson, D., Frayer, D., Christensen, L., A., Gallazzi, A., Michalowski, M. J., Richard, J., & ZavalaJ. 2016, 466, 138
Larson, R. B. 1974, MNRAS, 166, 585
Riechers, D. A., et al. 2017, ApJ, 850, 1, 1
Strandet, M. L., et al. 2017, ApJ, 842, 2
Yan et al. 2007, ApJ, 658, 778

Boletim da Sociedade Astronômica Brasileira, **30**, no. 1, 243-244

On the multifractality in GW150914 gravitational wave

Mackson M. F. Nepomuceno[1], Daniel B. de Freitas[2] & José R. de Medeiros[3]

[1] Departamento de Ciência e Tecnologia, Universidade Federal Rural do Rio Grande do Norte-UFERSA, Campus Caraúbas, Rio Grande do Norte, Brazil
[2] Departamento de Física, Universidade Federal do Ceará, Caixa Postal 6030, Campus do Pici, 60455-900 Fortaleza, Ceará, Brazil
[3] Departamento de Física Teórica e Experimental, Universidade Federal do Rio Grande do Norte-UFRN, Rio Grande do Norte, Brazil

Abstract. We analyze the data of the GW150914 gravitational wave signals detected by LIGO through the lens of multifractal formalism using the MFDMA method, as well as shuffled and surrogate procedures. We identified two regimes of multifractality in the strain measure of the time serie by examining long memory and the presence of nonlinearities. The moment used to divide the serie into two parts separates these two regimes and can be interpreted as the moment of collision between the black holes.

Resumo. Analisamos os dados do sinal de onda gravitacional GW150914 detectado pelo LIGO a partir do ponto de vista do formalismo multifractal usando o método MFDMA, bem como os procedimentos *shuffled e surrogate. Identificamos dois regimes de multifractalidade nas medidas da série temporal de deformação relativa examinando memória de longo prazo e presença de não linearidades. O momento usado para dividir a série em duas partes separam estes dois regimes e pode ser interpretado como o momemnto da colisão entre os buracos negros.*

Keywords. Gravitational waves – Multifractal analysis

1. Introduction

In February 11, 2016, data on the first direct observation of gravitational waves (hereafter, GWs) from a binary black hole merger was published, opening up new avenues for studying the universe beyond the analysis of electromagnetic waves (Abbott et al. 2016a; Aasi et al. 2015; Abbott et al. 2016c). The GW150914 signal was generated from the merger of two black holes with masses of $29^{+4}_{-4}M_{\odot}$ and $36^{+5}_{-4}M_{\odot}$. The event was observed by the two advanced LIGO (Aasi et al. 2015) detectors with a statistical significance of 5.1σ. The GW150914 data used here are within the range of 32 seconds around the event and have a measurement frequency of 4096Hz and will be considered a time-seres of strain measures.

2. Multifractal analysis

Since the end of the last century, several works, including de Freitas et al. (2016, 2017); Mali (2016); Norouzzadeh et al. (2007); Tanna & Pathak (2014), have applied multifractal analyses to time series. MFDMA with a backward-moving average ($\theta = 0$) has been found to yield parameters with better alignments with the numerically calculated parameters, and this is the method employed in this work. Additionally, this value of θ has been demonstrated to achieve the best performance (Eghdami et al. 2017; de Freitas et al. 2017; Gu & Zhou 2010). Tha analysis presented here is in accordance with the MFDMA procedure described by Gu & Zhou (2010).

3. Results and discussion

3.1. Shuflled and surrogate procedure

To investigate each type of multifractality, two methods, the shuffling and surrogate methods, are commonly used. These methods essentially consist of modifying the original sample to eliminate the source of the multifractality. The shuffling method randomizes the position of the data in the series to destroy the memory of the series and hence the long-term correlation. Applying an MFDMA to shuffled series will result in monofractal behavior, i.e., $h(2) \sim 0.5$ and $\Delta\alpha \sim 0$, if the series presents multifractality only due to long-term correlations. This procedure does not affect the other source of multifractality. Separately, the surrogate procedure generates a series via a Fourier transform, preserving amplitudes but randomizing the phases, and then performs an inverse Fourier transform. This eliminates non-linearities in the series but does not affect the long-range correlations; thus, the generalized Hurst exponent of

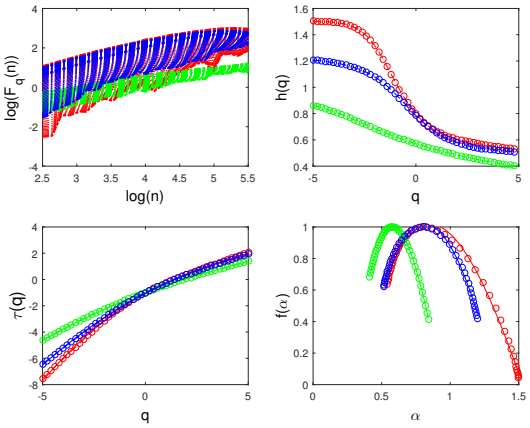

Figure 1. Multifractal analysis of the full data from GW150914 (`H1data`). The top-left panel shows the fluctuation function versus the multi-scale behavior in a log-log diagram. The original series is in red, the shuffled series is in green, and the upper and lower limits correspond to $q = 5$ and $q = -5$, respectively, while the bold in the middle corresponds to $q = 0$. Dependences on the q_{th} moment of the generalized Hurst exponent, h(q), and the multifractal scaling exponent, $\tau(q)$, are shown in the top-right and bottom-left panels, respectively. The multifractal spectrum is shown in the bottom-right panel.

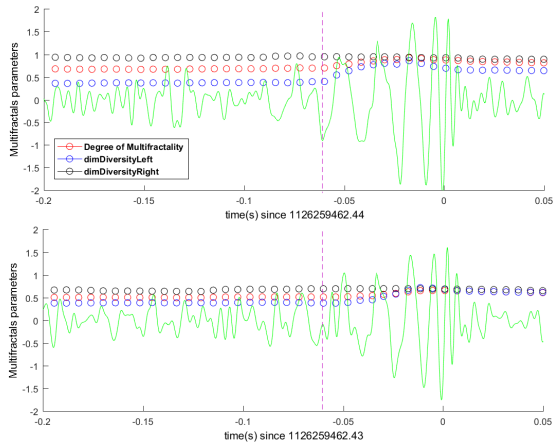

Figure 2. Point-to-point multifractal analysis for the GW150914 time series from Livingston (bottom panel) and Hanford (top panel; shifted and inverted (Abbott et al. 2016a)), illustrated in green. Red circles represent the degree of multifractality ($\Delta\alpha$) calculated in the time series up to that point; likewise, blue and black circles represent the left side diversity $f(\alpha)_{max} - f(\alpha)^{left}_{min}$ and right side diversity $f(\alpha)_{max} - f(\alpha)^{right}_{min}$, respectively. The vertical lines represent $t = -0.06s$, the time point at which the time series are divided.

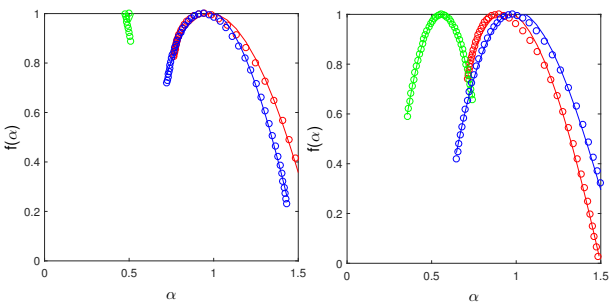

Figure 3. The multifractal spectrum of the first (left panel) and second (right panel) parts of the GW150914 time series are in red. The results of the application of the shuffled and surrogate methods are in green and blue, respectively.

surrogate series will not exhibit a dependence on q. The results of the MFDMA application in GW1509814 data are presented in Figure 1 and point to a multifractal behavior for this time-series. Neither shuffled nor surrogate procedures can be destroy the multifractality, indicating that the two sources are present.

The investigation point-to-point shown in Figure 2 indicate an elevation on left side diversity parameter. The division of the division of the original series into two sub-series at this point allows identification of two multifractals regimes indicated in Figure 3. In this figure we can see the multifractal spectra for the first (left panel) and second (right panel) parts of the orginal series. The shuffled procedure succeeds in destroying the multifractality in the first part, but not in the second. Therefore, both types are present in the second part.

We can associate the memory present in the oscillatory behavior as being the of long-term memory. In the second part, this behavior remains, but it is accompanied by a widening in the tails of the distribution of the strain measurements due to the increase in the gravitational wave amplitude. As this increase only occurs due to the collision of the black holes, the time used to divide the sub-series can be interpreted as the beginning of the merger phase.

4. Conclusions

The statistical approach proposed in this study highlights the scenario opened by detection of the first GWs. We summarize the main results in three points: i) characterize the fractal dynamics of the signals, identifying their multifractal sources; ii) find the moment of the beginning of merger phase in black hole coalescence system, and; iii) determine the empirical relationship between the variation in left side diversity and chirp mass as an additional way for estimating this latter parameter. The methodology applied here may serve as a standard procedure for future analyses of gravitational waves.

Acknowledgements. DBdeF acknowledges financial support from the Brazilian agency CNPq-PQ2 (grant No. 306007/2015-0). Research activities of the Astronomy Observational and the Astrostatistics Board of the Federal University of Rio Grande do Norte and Federal University of Ceará are supported by continuous grants from the Brazilian agency CNPq. We also acknowledge financial support from INCT INEspaço/CNPq/MCT.

References

Aasi, J., Abbott, B. P., Abbott, R., et al. 2015, Classical and Quantum Gravity, 32, 074001.
Abbott, B. P., Abbott, R., Abbott, T. D., et al. 2016, Physical Review Letters, 116, 061102
Abbott, B. P., Abbott, R., Abbott, T. D., et al. 2016, Physical Review Letters, 116, 131103
de Freitas, D. B., Nepomuceno, M. M. F., de Moraes Junior, P. R. V., et al. 2016, ApJ, 831, 87
de Freitas, D. B., Nepomuceno, M. M. F., Gomes de Souza, M., et al. 2017, ApJ, 843, 103
Eghdami, I., Panahi, H., & Movahed, S. M. S. 2017, arXiv:1704.08599
Gu, G.-F., & Zhou, W.-X. 2010, Phys. Rev. E, 82, 011136
Mali, P. 2016, Journal of Statistical Mechanics: Theory and Experiment, 1, 013201
Norouzzadeh, P., Dullaert, W., & Rahmani, B. 2007, Physica A Statistical Mechanics and its Applications, 380, 333
Tanna, H. J., & Pathak, K. N. 2014, Ap&SS, 350, 47

Boletim da Sociedade Astronômica Brasileira, **30**, no. 1, 245-246

Combined fit of spectrum and composition data as measured by the Pierre Auger Observatory

C. Ventura[1] for the Pierre Auger Collaboration[2]

[1] Observatório do Valongo, Universidade Federal do Rio de Janeiro, e-mail: cvizcarra@astro.ufrj.br
[2] Av. San Martín Norte 304, 5613 Malargüe, Argentina

Abstract. We present a combined fit of a simple astrophysical model of ultra-high energy cosmic rays UHECR sources to both the energy spectrum and composition data measured by the Pierre Auger Observatory. The fit has been performed for energies above 5×10^{18} eV, i.e. the region of the all-particle spectrum above the so-called "ankle" feature. The astrophysical model we adopted consists of identical sources uniformly distributed in a comoving volume, where nuclei are accelerated through a rigidity-dependent mechanism. The fit results suggest sources characterized by relatively low maximum injection energies, hard spectra and heavy chemical composition.

Resumo. Apresentamos um ajuste combinado de um modelo astrofísico simples de fontes UHECR de raios cósmicos de energia ultra alta tanto para o espectro de energia como para os dados de composição medidos pelo Observatório Pierre Auger. O ajuste foi realizado para energias acima de 5×10^{18} eV, ou seja, a região do espectro de todas as partículas acima do chamado recurso de "tornozelo". O modelo astrofísico que adotamos consiste em fontes idênticas uniformemente distribuídas em um volume comovente, onde os núcleos são acelerados através de um mecanismo dependente da rigidez. Os resultados de ajuste sugerem fontes caracterizadas por energias de injeção máximas relativamente baixas, espectros duros e composição química pesada.

Keywords. cosmic ray experiments - cosmic rays - composition

1. Introduction

The origin of UHECRs, particles reaching the Earth with energies over 10^{18} eV up to 10^{20} eV and beyond, is still unknown. Nevertheless, a general consensus has emerged that the most energetic cosmic rays are extragalactic, with the transition between galactic and extragalactic cosmic rays taking place somewhere between 10^{17} and a few times 10^{18} eV. The flux of cosmic rays above 10^{18} eV is of the order of 1 km^{-2} yr^{-1} . Therefore, very large arrays of particle detectors are needed to study them; the largest such array is the Pierre Auger Observatory in Argentina.

The propagation of such particles across cosmological distances can affect their observed energy spectrum and mass composition in nontrivial ways.

In this work, we attempt to simultaneously reproduce both the Auger spectrum and X_{max} data with a simplified model of UHECR sources, characterized by: sources accelerate different amounts of nuclei; injection of five representative stable nuclei: Hydrogen (H), Helium (He), Nitrogen (N), Silicon (Si) and Iron (Fe), which are approximately equally spaced in lnA; power-law spectrum with rigidity-dependent broken exponential cutoff

$$\frac{dN_{inj,i}}{dE} = \begin{cases} J_o a_i (E/E_o)^{-\gamma}, & \frac{E}{Z_i} < R_{cut} \\ J_o a_i (E/E_o)^{-\gamma} \exp[1 - E/(Z_i R_{cut})] & E/Z_i > R_{cut} \end{cases} \quad (1)$$

where J_o is a normalization factor, $E_o = 10^{18}$ eV, and Z_i is the atomic number of the $i-th$ injected nuclide, whose fraction in the sources, a_i, is normalized in such a way that $\sum_i a_i = 1$. This model is not able to reproduce the data measured over the entire energy range.

2. The data set and the simulations

The data we fit in this work consist of the SD event distribution in 15 bins of 0.1 of $\log_{10}$(E/eV), ($18.7 \leq \log 10$ (E/eV) ≤ 20.2) and X_{max} distributions (in bins of 20 g/cm^2).

Table 1. The parameter values obtained for the first and second minimum.

reference model (SPG - EPOS-LHC)	main minimum best fit	average	2nd minimum best fit	average
$\mathcal{L}_o$ [10^{44} erg Mpc^{-3} yr^{-1}]	4.99		9.46 (from $E_{min} = 10^{15}$eV)	
γ	$0.96^{+0.08}_{-0.13}$	0.93 ± 0.12	2.04 ± 0.01	$2.05^{+0.02}_{-0.04}$
$\log_{10}(R_{cut}/V)$	$18.68^{+0.02}_{-0.04}$	18.66±0.04	19.88±0.02	19.86±0.06
f_H(%)	0.0	$12.5^{+19.4}_{-12.5}$	0.0	$3.3^{+5.2}_{-3.3}$
f_{He}(%)	67.3	$58.6^{+13.5}_{-12.6}$	0.0	$3.6^{+3.6}_{-3.6}$
f_N(%)	28.1	$24.6^{+8.9}_{-9.1}$	79.8	$72.1^{+9.3}_{-10.6}$
f_{Si}(%)	4.6	$4.2^{+1.3}_{-1.3}$	20.2	$20.9^{+4.0}_{-3.91}$
f_{Fe}(%)	0.0		0.0	

The free parameters of the fit are: the injection normalization factor J_o, the injection spectral index γ, the cutoff rigidity R_{cut} , and the element fractions at injection (four free parameters a_H, a_{He}, a_N, a_{Si}; the fifth is bound by a_{Fe}=1-a_H-a_{He}-a_N-a_{Si}).

Main and second local minimum parameters for the reference model. Errors on best-fit spectral parameters are computed from the interval $D \leq D_{min} + 1$.

The best fit obtained occurs for $\gamma \approx 1$, low maximum rigidity around $R_{cut} = 10^{18.5}$ V, a hard spectrum and a composition dominated by Helium and heavier elements.

There is also a second relative minimum, which appears less extended, around the pair $\gamma = 2.04$ and $\log_{10}$ (R_{cut}/V)=19.88.

3. Fit results

Top: simulated energy spectrum of UHECRs (multiplied by E^3) at the top of the Earth's atmosphere with the best-fit parameters and the local minimum at $\gamma \approx 2$, along with Auger data points.

Bottom: average and standard deviation of the X_{max} distribution as predicted (assuming EPOS-LHC UHECR-air interactions) for the model (brown) versus pure H (red), He (grey), N (green) and Fe (blue), dashed lines. Only the energy range where the brown lines are solid is included in the fit.

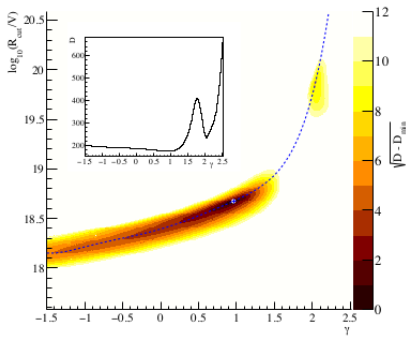

Figure 1. Deviance $\sqrt{D - D_{min}}$, as function of γ and $\log_{10}(R_{cut}/V)$. The dot indicates the position of the best minimum, while the dashed line connects the relative minima of D (valley line).

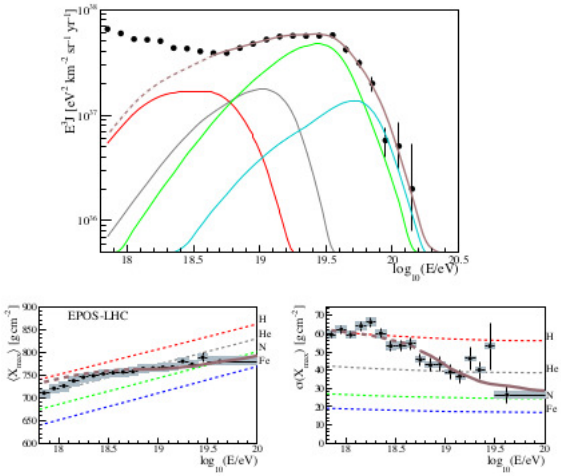

Figure 2. The best-fit parameters for the reference model

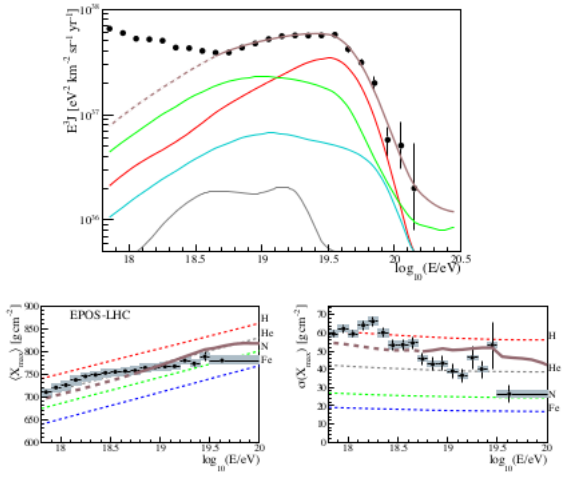

Figure 3. Same as figure 2 at the local minimum at $\gamma = 2.04$, EPOS-LHC UHECR-air interactions.

4. Propagation models

It can be seen that the relationship between γ and R_{cut} and the position of the second local minimum are very similar from one model to another, but the position of the best fit within the 'valley' and the height of the 'ridge' between the two local minima are strongly model-dependent.

To study the effects of uncertainties in the simulations of UHECR propagation, we repeated the fit using the combinations

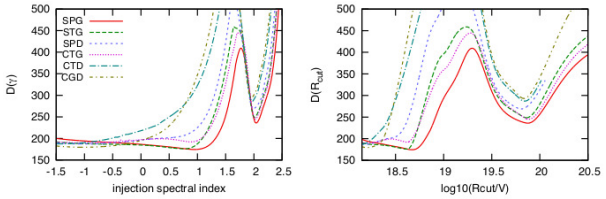

Figure 4. D for each value of γ (first panel) and R_{cut} (second panel) for each propagation model, where the other parameters are chosen so as to minimize D.

Table 2. Best-fit parameters and 68% uncertainties for the various propagation models we used (see table 3). For the CTG model we report the two main local minima.

model	γ	$\log_{10}(R_{cut}/V)$	D	D(J)	D(X_{max})
SPG	$+0.96^{+0.08}_{-0.13}$	$18.68^{+0.02}_{-0.04}$	174.3	13.2	161.1
STG	$+0.77^{+0.07}_{-0.13}$	$18.62^{+0.02}_{-0.04}$	175.9	18.8	157.1
SPD	$-1.02^{+0.31}_{-0.26}$	$18.19^{+0.04}_{-0.03}$	187.0	8.4	178.6
CTG	$-1.03^{+0.35}_{-0.30}$	$18.21^{+0.05}_{-0.04}$	189.7	8.3	181.4
	$+0.87^{+0.08}_{-0.06}$	$18.62_{\pm 0.02}$	191.9	29.2	162.7
CTD	$-1.47^{+0.28}_{*}$	$18.15^{+0.03}_{-0.01}$	187.3	8.8	178.5
CGD	$-1.01^{+0.26}_{-0.28}$	$18.21_{\pm 0.03}$	179.5	7.9	171.6

*This interval extends all the way down to -1.5, the lowest value of γ we considered.

Table 3. The propagation models used (see Ref. (5))

	MC code	$\sigma_{\text{photodisint}}$	EBL model
SPG	SimProp	PSB	Gilmore 2012
STG	SimProp	TALYS	Gilmore 2012
SPD	SimProp	PSB	Domínguez 2011
CTG	CRPropa	TALYS	Gilmore 2012
CTD	CRPropa	TALYS	Domínguez 2011
CGD	CRPropa	Geant4	Domínguez 2011

of Monte Carlo propagation code, photo-disintegration cross sections and EBL spectrum listed in the tables that represent Best-fit parameters and 68% uncertainties for the various propagation models.

5. Conclusions

In this work we have shown that, within given hypotheses on propagation and interaction at Earth, Auger data can bind the physical parameters of the sources in the simple astrophysical model considered.

However several different hypotheses (i.e. atmospheric interaction and choices of photo-disintegration cross sections) can be made with resulting source parameters well outside the statistical uncertainties of the fit. Better models of UHECR-air hadronic interactions, or photo-disintegration cross sections and branching ratios would help reduce these uncertainties.

References

Pierre Auger collaboration. 2017, Journal of Cosmology and Astroparticle Physics, 04, 038.
Pierre Auger collaboration. 2012, Astrophys. J. Suppl. 203, 34.
Pierre Auger collaboration. 2014, Phys. Rev. D90, 122005.
Pierre Auger collaboration. 2013, Journal of Cosmology and Astroparticle Physics, 1302, 026.
R. Alves Batista, D. Boncioli, A. di Matteo, A. van Vliet and D. Walz. 2015, Effects of uncertainties in simulations of extragalactic UHECR propagation, using CRPropa and SimProp, JCAP 1510, 063.

Boletim da Sociedade Astronômica Brasileira, **30**, no. 1, 247-248

Studies of cosmic ray acceleration in relativistic MHD jets

Tania E. Medina Torrejón[1], Elisabete de Gouveia Dal Pino[2], Greg Kowal[3], Yosuke Mizuno[4], Chandra Singh[2] and Luis Kadowaki[2]

[1] Instituto de Física, Universidade de São Paulo. e-mail: temttm@if.usp.br
[2] Instituto de Astronomia Geofísica e Ciências Atmosféricas, Universidade de São Paulo. e-mail: dalpino@iag.usp.br, e-mail: csingh@iag.usp.br, e-mail: luis.kadowaki@iag.usp.br
[3] Escola de Artes, Ciências e Humanidades, Universidade de São Paulo. e-mail: grzegorz.kowal@usp.br
[4] Institute of Astronomy, National Tsing-Hua University e-mail: mizuno@phys.nthu.edu.tw

Abstract. Here, we explore the acceleration of high energy (HE) particles in the jet launching area, where the relativistic plasma is probably magnetically dominated. We perform a three-dimensional MHD relativistic simulation of a magnetized jet with initial helical magnetic field subject to the current-driven kink instability. We then inject thousands of test particles in the reconnected magnetic field regions of the jet and follow their trajectories as well as the evolution of their kinetic energy. Preliminary results show that the latter grows exponentially with time, as expected in Fermi acceleration.

Resumo. Aqui, exploramos a aceleração de partículas de alta energia (HE) na área de lançamento de jatos, onde o plasma relativista provavelmente é dominado magneticamente. Realizamos uma simulação relativista MHD tridimensional de um jato magnetizado com o campo magnético helicoidal inicial sujeito à instabilidade da torção gerada pela corrente. Em seguida, injetamos milhares de partículas de teste nas regiões de campo magnético reconectadas do jato e seguimos suas trajetórias, bem como a evolução de sua energia cinética. Os resultados preliminares mostram que o último cresce exponencialmente com o tempo, conforme esperado na aceleração de Fermi.

Keywords. acceleration of particles – magnetic reconnection – instabilities – magnetohydrodynamics (MHD) – methods: numerical

1. Introduction

Very HE cosmic rays (CRs) are believed to be accelerated in the nuclear region or along the relativistic jets of compact sources like Galactic Black Hole binaries (GBHBs), active galactic nuclei (AGNs) or gamma ray bursts (GRBs). We here investigate the acceleration of CRs by magnetic reconnection in relativistic magnetized tower jets where the acceleration can be very important. In shocks (Bell 2013), the particles confined between the upstream and downstream flows of the velocity discontinuity undergo a first-order Fermi acceleration. De Gouveia Dal Pino & Lazarian (2005) demonstrated that a similar mechanism would occur when particles are trapped between the two converging magnetic flux tubes moving to each other in a current sheet with the reconnection velocity V_R. 3D numerical simulations of the trajectories of 10,000 particles injected with thermal energies in different MHD domains of fast magnetic reconnection have confirmed the efficiency of this acceleration mechanism and the predictions of de Gouveia Dal Pino and Lazarian (2005) model (Kowal, de Gouveia Dal Pino & Lazarian 2011, 2012, de Gouveia Dal Pino & Kowal 2015). Furthermore, these studies have been able to determine numerically the particle acceleration rate by magnetic reconnection as a function of the particle energy (Khiali, de Gouveia Dal Pino & del Valle 2015; del Valle, de Gouveia Dal Pino & Kowal 2016). This acceleration mechanism may be a dominating process in a wide range of astrophysical environments and currently there is extensive study in the literature applied to different classes of objects. This includes, relativistic jets and their sources (e.g., Giannios 2010; Sironi and Spitkovsky 2014; Uzdesnky 2011; Singh, Mizuno & de Gouveia Dal Pino 2016, de Gouveia Dal Pino et al. 2016, Kadowaki et al. 2015; Singh et al. 2015; Khiali et al. 2015a, b; Khiali & de Gouveia Dal Pino 2015) - especially in magnetically dominated regions where shocks may be absent or faint (de Gouveia Dal Pino & Kowal 2015).

Astrophysical relativistic jets are associated with several kinds of astrophysics systems like AGNs, microquasars and GRBs. Very near the source the relativistic jets are probable magnetically dominated. Jets with strong helical or toroidal fields are subject to current driven kink instability, this strongly distorts may disrupt the jet and may trigger magnetic reconnection (Singh, Mizuno, de Gouveia Dal Pino 2016). In this work, we will investigate the acceleration of particles by magnetic reconnection driven by current drive kink instabily in relativistic jets.

2. Methodology

In order to study particle acceleration in relativistic jets, we performed special relativistic magnetohydrodynamics (SRMHD) simulations using the tree-dimensional (3D) general relativistic MHD code RAISHIN (Mizuno et al. 2006, 2012). The code setup for spatial development of CD kink instability is similar to the initial parameters used in Singh et al. (2016), that is, a jet rotating with an inicial angular velocity $\Omega_0 = 2$ and initial helical magnetic field. The simulation grid is periodic along the axial z-direction. The grid is in Cartesian (x, y, z) coordinates with box of size $6L \times 6L \times 6L$, the grid resolution is the same in all directions with $\Delta L = L/40$. The x & y boundaries, $x = y = \pm 3L$ are set us outflow boundaries. After the development of the plasma configuration in the jet simulation with density, velocity and magnetic field profiles, we injected test particles at a given snapshot as in Figure 1 ($t = 50$ in code units which is given by L/c) and integrated their trajectories using the GACCEL code (Kowal et al. 2011, 2012) which solves the equation of motion $\mathrm{d}(\gamma m \boldsymbol{u})/\mathrm{d}t = q[(\boldsymbol{u} - \boldsymbol{v}) \times \boldsymbol{B}]$ for each charged particle, where $\gamma \equiv (1 - u^2/c^2)^{-1}$ is the Lorentz factor, c is the speed of light, $\boldsymbol{v}$

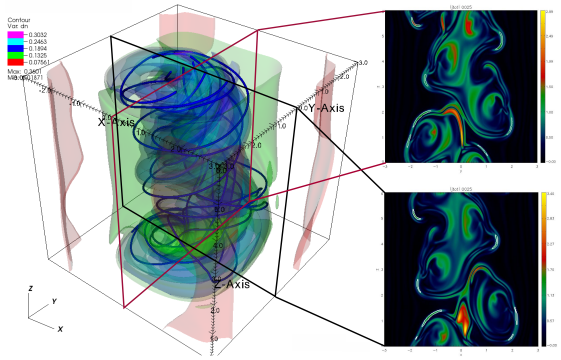

Figure 1. Left shows a three-dimensional density isosurfaces, the solid blue lines correspond to the magnetic field lines, and the color scales give the values of the density. Right panels show the central xz and yz cut of the jet at $t = 50$ in code units, the figures shows the current-density distribution in code units.

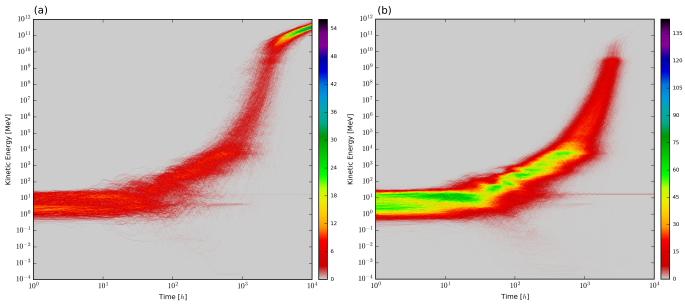

Figure 2. Histogram of energy of test particles injected in the snapshot $t = 50$ of Figure 1 (a) periodic injection of 1,000 test particles and (b) 10,000 test particles injection with periodic re-injection only in the z direction of the jet.

is the plasma velocity, $\boldsymbol{u}$, m and q are the particle velocity, mass and electric charge, respectively. In the current study we do not include particle losses, therefore test particles can gain or lose energy only through the interactions with the moving magnetized plasma an its fluctuations. The trajectory of the particles was integrated for two different cases: periodic bondaries in all directions, and periodic in the z direction only with outflow bondaries in the x & y directions.

3. Preliminary Results

Figure 1 (right panels) shows the current density distribution in two-dimensional cuts at the center of the simulated jet. We can see clearly the formation of current sheets near the axis at the bottom, where the test particles are probably mostly accelerated in our tests. We used an algorithm (developed by L. Kadowaki in our group) to identify the current sheets where there are magnetic reconnection regions (which is based in Zhdankin et al. 2013). We encounter that in $t = 50$ there are more regions of reconnection than in other times. For this reason we have taken this snapshot to inject test particles. In the left part of the Figure 2, we show the particle kinetic energy evolution of 1,000 particles for a periodic injection in the three-directions. This periodic re-injection continued until $t = 10^4$ hours. The re-injection of the particles tries to mimic the large extension of these sources, since in our simulations we only consider a small portion of real jet domains. We note that after $t \sim 2.5 \times 10^3$ hours, the exponential growth saturates. At this stage the particles' Larmour radius have become larger than the size of the accelerating zones and the particles can no longer be accelerated by reconnection. They only suffer linear drift acceleration from this time on (see Kowal et al. 2012; del Valle et al. 2016). In the right of the Figure 2 we injected 10,000 test particles with a periodic re-injection in z direction only and with an outflow scape condition in the x & y directions. These preliminary results of test particles in magnetic reconnection sites show that the particles start to be accelerated exponentially after $\sim$ 100 hours of injection. From 1,000 particles on, they are accelerated from 10^4 MeV to 10^{11} MeV in a few hundreds hours only, indicating that once the particles enter the acceleration zones the process is very fast, as predicted by de Gouveia Dal Pino & Lazarian 2005, Kowal et al. 2011, 2012; de Gouveia Dal Pino et al. 2016. In these tests, we considered a magnetic field of the order of 0.01 G. For velocities of the order of the light speed and a time interval of several hundreds hours, the dimension scale of the acceleration region is of the order of $ct \sim 10^{14}$ cm or 10^{-4} pc, which is compatible with the dimensions of the acceleration zones producing the observed gamma-ray flares in luminous AGN jets, like the blazars (Giannios et al. 2009, Aharonian et al. 2007).

References

Aharonian, F. et al. 2007, ApJ, 664, L71
Bell, A. R. 2013, arXiv, arXiv:1311.5779
de Gouveia Dal Pino, E. M., & Lazarian, A. 2005, A&A, 441, 845
de Gouveia Dal Pino, E. M., & Kowal, G. 2015, Magnetic Fields in Diffuse Media, Astr. Sp. Sc. Library, 407, 373
Giannios, D. 2010, MNRAS, 408, L46
Giannios, D., Uzdensky, D. A., & Begelman, M. C. 2009, MNRAS, 395, L29
Kadowaki, L.H.S., de Gouveia Dal Pino, E. M., & Singh, C. B. 2015, ApJ, 802, 113
Khiali, B., de Gouveia Dal Pino, E. M., & del Valle, M.V. 2015a, MNRAS, 449, 34
Khiali, B., de Gouveia Dal Pino, E. M., & Sol, H. 2015b, arXiv, arXiv:1504.07592
Kowal, G., de Gouveia Dal Pino, E. M., & Lazarian, A. 2011, ApJ, 735, 102
Kowal, G., de Gouveia Dal Pino, E. M., Lazarian, A. 2012, PRL 108, 241102
Mizuno, Y., Lyubarsky, Y., Nishikawa, K. I., & Hardee, P. E. 2012, ApJ, 757, 16
Mizuno, Y., Nishikawa, K. I., Koide, S., Hardee, P., & Fishman, G. J. 2006, arXiv:astro-ph/0609004
Singh, C.B., de Gouveia Dal Pino, E. M., & Kadowaki, L.H.S. 2015, ApJ, 799, L20
Singh, C.B., Mizuno, Y. & de Gouveia Dal Pino, E. M. 2016, ApJ, 824, 48
Sironi, L., & Spitkovsky, A. 2014, ApJ, 783, L21
Uzdensky D. A. 2011, Space Sci. Rev., 160, 45
del Valle, M. V., de Gouveia Dal Pino, E. M. & Kowal, G. 2016, MNRAS 463, 4331
Zhdankin, V., Uzdensky, D. A., Perez, J. C., & Boldyrev, S. 2013, ApJ, 771, 124

Boletim da Sociedade Astronômica Brasileira, **30**, no. 1, 249-250

A radiative transfer algorithm to calculate the spectral evolution in relativistic jets

Mohammad A. Nawaz[1,3], Alexander Y. Wagner[2], E. M. de Gouveia Dal Pino[3], D. A. Falceta-Gonçalves[1]

[1] Escola de Artes, Ciencias e Humanidades, University of Sao Paulo, Brasil e-mail: mohammad.nawaz@iag.usp.br
[2] Center for Coumputer Science, Tsukuba University, Japan
[3] Instituto de Astronomia, Geofisica e Ciencias Atmosfericas, University of Sao Paulo, Brasil

Abstract. A major challenge in the study of relativistic jets is the determination of the jet plasma's physical state, such as density, pressure, velocity or magnetic field from the observed radio synchrotron emission by the non-thermal particles. When predicting emission maps and spectra from relativistic jets, it is important to consider special relativistic Doppler boosting and time delays between different emission region, non thermal radiative losses by the emitting particles, modulation by the intermediate space between the source and the observer by Faraday rotation and opacity, particle acceleration at shocks, magnetic reconnection. Magneto-hydrodynamic simulations need to be complemented by additional schemes that track the evolution of the non-thermal particle distribution and perform the ray tracing taking into account all the above-listed effects. In this first stage, we evolve a power-law particle distribution in post-process considering the adiabatic changes and frequency dependent synchrotron radiative losses of the non thermal electrons. We apply our synthetic radio emission calculations to simulations of relativistic jets with the hydrodynamical code PLUTO. The simulations include models of the radio galaxy Hydra A focussing on the role of spectral evolution in the brightness of inner knots, and the flaring zones.

Resumo. Um grande desafio no estudo de jatos relativísticos é a determinação do estado físico do plasma do jato, tais como densidade, pressão, velocidade ou campo magnético a partir da emissão radiossincrotrônica observada pelas partículas não térmicas. Na previsão de mapas e espectros de emissão de jatos relativísticos, é importante considerar o aumento estimulante Doppler relativista e atrasos de tempo entre diferentes regiões de emissão, perdas radiativas não térmicas pelas partículas emissoras, modulação pelo espaço intermediário entre a fonte e o observador pela rotação e opacidade de Faraday, aceleração das partículas nos choques, reconexão magnética. As simulações magneto-hidrodinâmicas precisam ser complementadas por esquemas adicionais que acompanhem a evolução da distribuição de partículas não térmicas e realizem o rastreamento de raios levando em consideração todos os efeitos acima mencionados. Nesta primeira etapa, desenvolvemos uma distribuição de partículas de poder em pós-processo considerando as mudancas adiabáticas e as perdas radiativas dependentes da frequência de sincronismo dos eletrons não-térmicos. Aplicamos nossos cálculos sintéticos de radioemissão a simulações de jatos relativísticos com o código hidrodinâmico PLUTO. As simulações incluem modelos da radiogaláxia Hydra A focando o papel da evolução espectral no brilho dos nós internos e as zonas de fulguração.

Keywords. Galaxies: jets – Radiative transfer – Methods: numerical

1. Introduction

Relativistic jets are collimated magnetised flows emanating from the vicinity of central supermassive blackholes of active galactic nuclei. They can extend from few tens of Schwarzschild radii to very large ten to hundreds kilo parsec scale structures. Modern powerful supercomputers allow us to perform detailed numerical hydrodynamic modelling of jets from parsec to kpc scale. However, incorporation of non-thermal particle evolution and radiative transfer in the hydrodynamic calculation is still computationally challenging because it introduces additional dimensions (particle energy, frequency and direction of radiation) to the problem. Furthermore, because the timescale associated with the transport microphysics is often smaller than the dynamic timescale of the jet, subgrid recipes, for example for shock acceleration, need to be invoked. Therefore, alternative post-process calculations of the evolution of non-thermal particle distributions and associated non-thermal emission have been used to study relativistic jets (Komissarov & Falle 1996; Mimica et al. 2009; Nawaz et al. 2014, 2016).

In this study, our goal is to set up a numerical scheme to calculate spectral evolution of non-thermal particles in relativistic jets and apply this to new simulations using the hydrodynamic code PLUTO. In particular, we shall revisit the internal and global structure of the Hydra A radio galaxy, an archetypal precessing FRI radio source in a cool core cluster. We use a Lagrangian scheme for calculating the transport of non-thermal particles, based on that of Mimica et al. (2009). In this method, the distribution of the non-thermal particles is tracked in both spatial and energy space. The initial positions of the NTPs, at the jet base, advect following the background velocity field while the energy space and the particle distribution evolve according to

$$\frac{dp}{dt} = a(t)p + b(t)p^2 \tag{1}$$

where, p is the momentum of NTP. Factors $a(t)$ and $b(t)$ account for the adiabatic and synchrotron losses, respectively. The NTP distribution is discretized in the energy domain and approximated by a The synchrotron emissivities and absorption coefficients are calculated directly from the NTP distribution and the thermodynamic quantities of the background relativistic fluid. Finally, we will compute emission solving the radiative transfer equation along the line of sight.

2. Jet intracluster medium interaction

We develop an axisymmetric model for a magnetised relativistic jet interacting with the intracluster medium (ICM). The jet parameters are set by a constant jet power $P_{\rm jet}$, that is related to

Table 1. Summary of simulation parameters.

Parameter	Value
Jet Power, $P_{\rm jet}$	10^{45} erg/s
Jet inlet radius, $r_{\rm jet}$	0.1 kpc
Jet density parameter , $\chi_{\rm jet}$	12.67
Jet over pressure ratio, $p_{\rm jet}/p_{\rm a}$	5
Lorentz factor, Γ	1.7
Plasma $\beta = 2p_{\rm jet}/B^2$	10

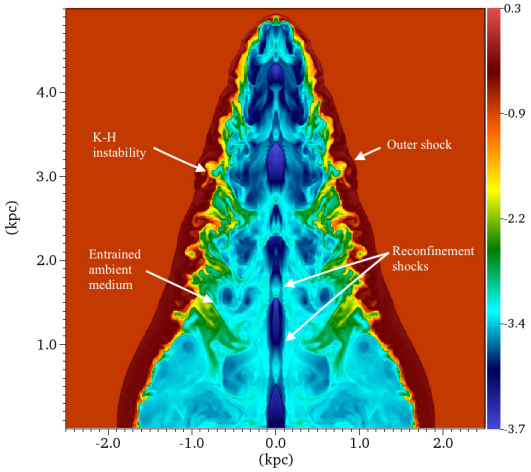

Figure 1. Logarithmic density snapshot of the jet-ICM interaction model. Biconical reconfinement shocks form as the jet expands and interacts with the environment. At the contact discontinuity Kelvin-Helmholtz instability develops.

other jet parameters, such as, jet cross-section $A_{\rm jet} = \pi r_{\rm jet}^2$, where $r_{\rm jet}$ is the jet inlet radius, jet pressure $p_{\rm jet}$, jet density parameter $\chi_{\rm jet} = \rho_{\rm jet}c^2/(p_{\rm jet} + \varepsilon_{\rm jet})$, where $\rho_{\rm jet}$ and $\varepsilon_{\rm jet}$ are the rest mass density and internal energy density of the jet, jet velocity $v_{\rm jet}$, jet Lorentz factor Γ and the magnetic field B^i.

$$P_{\rm jet} = A\left[\frac{\gamma}{\gamma-1}p_{\rm jet}\Gamma^2 v_{\rm jet}\left(1+\frac{\Gamma-1}{\Gamma}\chi_{\rm jet}\right)+\Gamma^2B^2v^i - B^iv_iB^i\right] \quad (2)$$

Here, γ is the adiabatic index. We set a hydrostatic environment based on the X-ray data of the Hydra A cluster. The jet is initialised with best fit values obtained from a previous study of the source (Nawaz et al. 2014).

The simulation parameters are summarised in Table 1. Different features developed in the earlier stage of jet evolution are shown in the logarithmic density slice in Figure. 1.

3. Synchrotron emission map

We are in the initial stage in developing the spectral evolution code. However, we produce a synthetic radio map from the estimated Stokes synchrotron emissivity for each cell assuming that the nonthermal particle pressure is proportional to thermal pressure (Wagner & Bicknell 2011). Here we consider the effects of relativistic aberration and Doppler boost. This method does not consider particle transport, nevertheless, it successfully captures features like bright inner jet knots and terminal hot spot. Figure. 2 shows synthetic radio map of the modelled jet at a line of sight angle 90°.

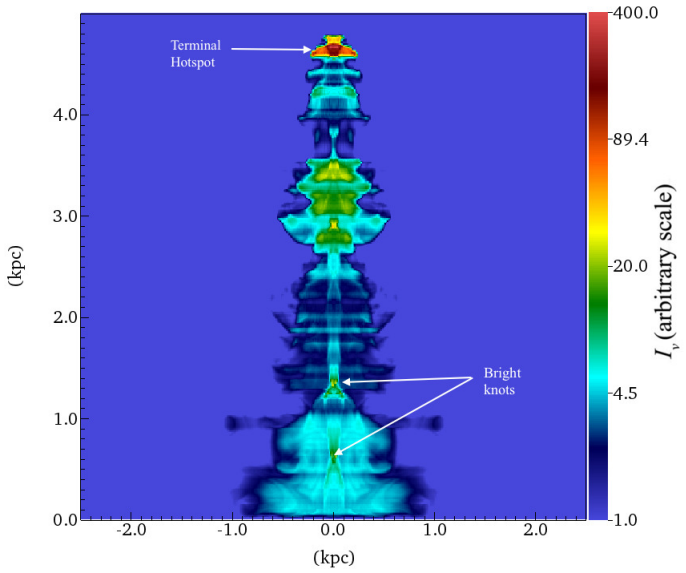

Figure 2. Synthetic radio map of the axisymmetric model. Inner bright knots develop due to reconfinement shocks and a terminal hotspot develops where the jet hits the cavity wall.

4. Summary

In the first stage of our study we develop an axisymmetric jet-ICM model. The key features we obtain with our model are: i) bright knots, ii) outer shock, iii) terminal hotspot and iv) entrainment layer of shocked jet and ambient plasma.

Once developed, the spectral evolution code will be incorporated with the hydrodynamical output to calculate emission from relativistic jets. Focussing on a prominent radio galaxy Hydra A, we will utilise the algorithm to study the role of evolutionary history of nonthermal particles on the observed jet features. This code will be an efficient tool to study two poorly understood features of Hydra A jets: i) The increasing brightness of inner jet knots along the jet axis, and ii) The bright zones where the initially collimated jets flare to form wide plumes.

Acknowledgements. MAN acknowledges support from a FAPESP grant (2015/25126-2).

References

Komissarov, S. S., & Falle, S. A. E. G. 1996, Energy Transport in Radio Galaxies and Quasars, 100, 173
Mimica, P., Aloy, M.-A., Agudo, I., et al. 2009, ApJ, 696, 1142
Nawaz, M. A., Bicknell, G. V., Wagner, A. Y., Sutherland, R. S., & McNamara, B. R. 2016, MNRAS, 458, 802
Nawaz, M. A., Wagner, A. Y., Bicknell, G. V., Sutherland, R. S., & McNamara, B. R. 2014, MNRAS, 444, 1600
Wagner, A. Y., & Bicknell, G. V. 2011, ApJ, 728, 29

Índice (continua)

Índice (continua)

Boletim da Sociedade Astronômica Brasileira

Índice

Vol. 30

Artigos de Proceedings

Capa: Conchas mareais e correntes estelares da Galáxia NGC 474 (crédito: CFHT, Coelum, MegaCam, J.-C. Cuillandre & G. A. Anselmi)

Publicado pela Sociedade Astronômica Brasileira

http://www.sab-astro.org.br

ISSN: 0101-3440